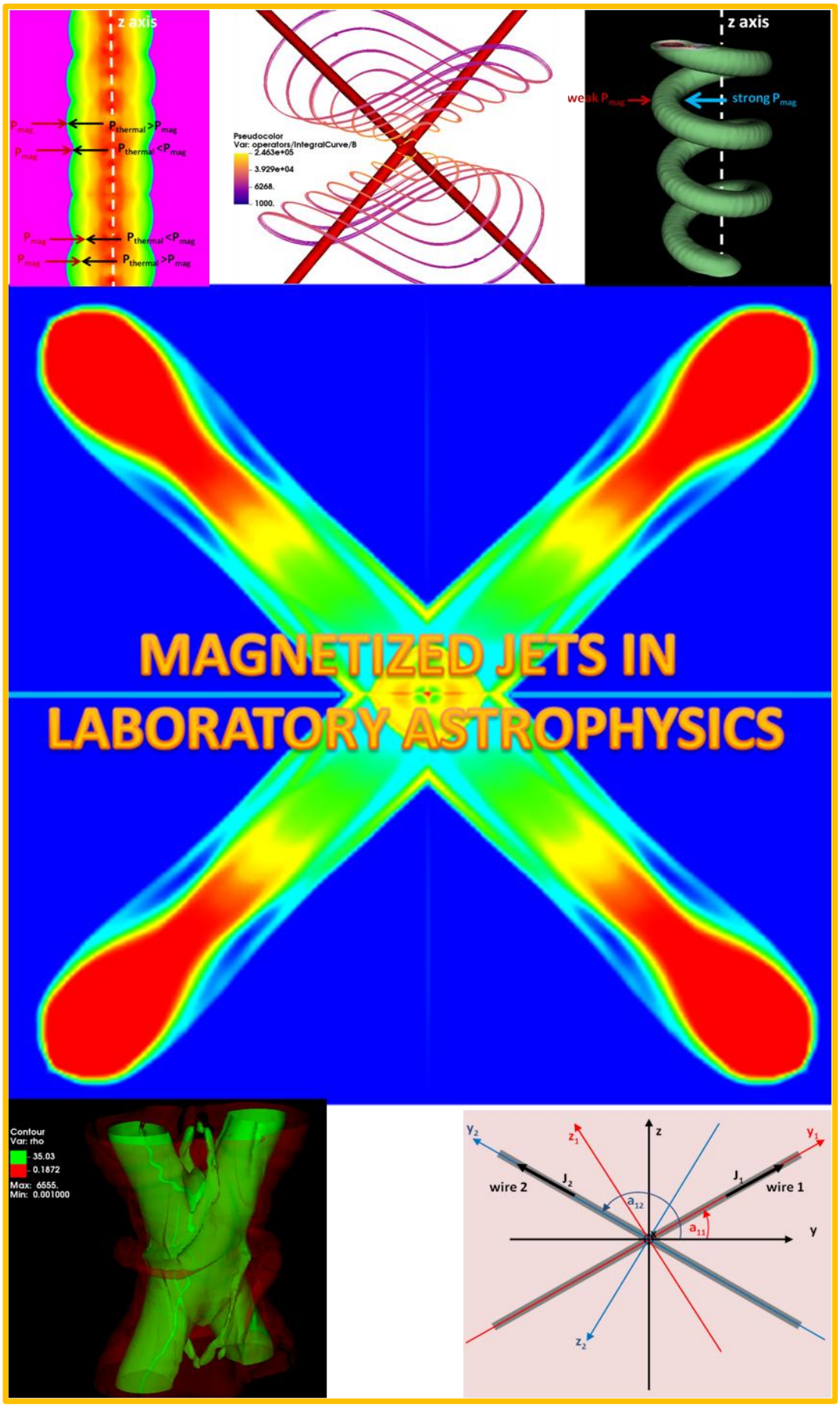
z axis
P_mag
P_thermal >P_mag
P_mag
P_thermal <P_mag
P_mag
P_thermal <P_mag
P_mag
P_thermal >P_mag
Pseudocolor
Var: operators/IntegralCurve/B
2.463e+05
3.929e+04
6268.
1000.
z axis
weak P_mag
strong P_mag
MAGNETIZED JETS IN
LABORATORY ASTROPHYSICS
Contour
Var: rho
35.03
0.1872
Max: 6555.
Min: 0.001000
y2
z1
z
y1
wire 2
J2
J1
wire 1
a12
a11
y
z2

NATIONAL AND KAPODISTRIAN UNIVERSITY OF ATHENS (NKUA)

/Magnetized jets in Laboratory Astrophysics/
/Μαγνητισμένοι πίδακες στην Εργαστηριακή Αστροφυσική/

A dissertation submitted in partial fulfillment of the requirements for the degree of Doctor of Philosophy in Physics

By

George D. Koundourakis

NKUA id: 2013516

April 2022

NATIONAL AND KAPODISTRIAN UNIVERSITY OF ATHENS (NKUA)

/Magnetized jets in Laboratory Astrophysics/ /Μαγνητισμένοι πίδακες στην Εργαστηριακή Αστροφυσική/

By

George D. Koundourakis

Advisory Committee	Thesis Examination Committee
Dr. Nektarios Vlahakis (Supervisor)	**Dr. Ioannis A. Daglis**
Professor Section of Astrophysics, Astronomy and Mechanics of the Department of Physics, NKUA	Professor Section of Astrophysics, Astronomy and Mechanics of the Department of Physics, NKUA
Dr. Michael Tatarakis (Co-supervisor)	**Dr. Apostolos Mastichiadis**
Professor Department of Electronic Engineering of the Faculty of Engineering, HMU /Institute of Plasma Physics and Lasers	Professor Section of Astrophysics, Astronomy and Mechanics of the Department of Physics, NKUA
Dr. Nektarios A. Papadogiannis (Co-supervisor)	**Dr. Maria Petropoulou**
Professor Vice-Rector of the Hellenic Mediterranean University (HMU) /Institute of Plasma Physics and Lasers	Assistant Professor Section of Astrophysics, Astronomy and Mechanics of the Department of Physics, NKUA
	Dr. Vasilis Dimitriou
	Associate Professor Institute of Plasma Physics and Lasers of the HMU

In memory of my Dad

Dedicated to my children Giorgos, Vasilis and Panayiotis

Motivation phrases

"Carpe Diem"

"Ad astra per aspera"

"There is no royal path to conquer knowledge"

"It is never too late. Try hard for your life dreams and surely, one or two, will become true"

"You have to remember that, sometimes, the journey counts, not the destination!"

Abstract

The main goal of this work is the numerical investigation of the plasma dynamic evolution of Z-pinch and X-pinch devises. A more thorough investigation of the jet formation mechanisms and dynamic evolution of a two-wire tungsten X-pinch formation along with experimental validation is presented. Additionally a possible correlation to astrophysical jets of YSO and HH objects is discussed. Specifically this study contributes to the estimation of the scalability factors and all the relevant numbers and parameters for a low current X-pinch tungsten plasma configuration.

In order to achieve robust, flexible and realistic computational simulation models, a variety of different numerical and physical schemes is needed. An extra study for this dissertation, is the synthesizing process of extracting physical formulas for all the dissipative terms for all density and temperature regimes. The synthesis of different physical formulas for piece-wise functions or correction factors to already known formulas or combination formulas, provide flexibility for any MHD numerical scheme and also, for any Z or X-pinch configuration at any density, thermal pressure and plasma temperature regime. The graphic presentation of these formulas, as a comparison evaluation tool with experimental/semi-empirical or other studies data, is provided and estimated by the author.

The mathematical transformation of any Local plasma configuration to the Global coordinate system is a supplementary and necessary study, as it provides the appropriate spatial profiles for all the physical variables and assisting for the best spatial resolution that can be computationally executable. Moreover, the mathematical transformations through rotation and displacement matrices are presented correlating the mass density, thermal pressure and magnetic field Local components to the Global ones. The latter is important due to the novelty of the initial condition spatial implementation of the magnetic field. Examples of Z and X-pinch configurations are discussed according to these transformations. Information over the physical, mathematical and numerical implementation procedure of the new modifications to the code and the significance they have along the simulation run, is presented and discussed. The choice of the appropriate Riemann solver, the radiation transport module, the appropriate boundary conditions for the computational box, the magnetic field initial topology and the correct updating along the simulation run are, among others, subjects of this thesis analysis!

Two specific simulation applications of these transformations are preliminary tested and evaluated, through the experimental and other simulation studies bibliographic data. The first is a "cold" start X-pinch configuration using two unmerged metallic tungsten wires, starting just before the ablation phase and the merging in a denser cross-point area. The focus of this simulation is at the cross-point area. The study ends when the merging is succeeded and the formation of the axial jets is initiated. Similarities with astrophysical jet mechanisms, are discussed. The second is a four

tungsten, thin wire, low current Z-pinch array configuration study till the stagnation phase. Both studies present novel and very promising results for future work.

The computational results study presents the dynamic behavior of 1/4 spatial model of a single tungsten Z-pinch wire evaluating the contribution of the radiation transport module to the appropriate plasma evolution. A 1/16 spatial model, of an X-pinch tungsten plasma configuration for a wide wire angle, is subsequently studied. The spatiotemporal plasma jet formation and evolution is presented and discussed. The simulated areal mass density is compared with the experimentally measured dense opaque region to enlighten the dense plasma evolution. In addition, the measured experimental areal electron density is compared to the simulation results. The main jet formation mechanisms are analyzed and discussed in relation to the influence of the **J×B** force and the mass momentum density.

The physical and numerical modeling differences of GORGON and PLUTO and their influence on the simulation results are demonstrated and analyzed, for a sharp two-wire tungsten load X-pinch geometry. Six different computational MHD schemes are presented at a specific spatial moment only for PLUTO. The model comparison provides valuable information on the improvement of flexible and efficient X-pinch models according to the experimental data and offer crucial insights on the mechanisms of plasma evolution and jet formation.

The scalability and jet astrophysical relevancy estimation, for the wide wire angle X-pinch pulsed power configuration, is attempted. All relevant dimensionless numbers are calculated for the X-pinch plasma and compared to the ones of other laboratory astrophysics experiments and to the ones of YSOs, HHs and other astrophysical objects.

Keywords: MHD, plasma, Astrophysical jets, YSO, Laboratory Astrophysics, PLUTO code, GORGON code

Σύντομη Περίληψη

Η ερευνητική συνεισφορά της παρούσης διατριβής αφορά τρείς επιμέρους εργασίες. Πρώτον, τη μαθηματική και γεωμετρική μοντελοποίηση των αρχικών συνθηκών που αφορούν την πυκνότητα ύλης, τη θερμική πίεση και του αντίστοιχου μαγνητικού πεδίου στο μαγνητοϋδροδυναμικό κώδικα για τη βέλτιστη χωροχρονική εξέλιξη και συμπεριφορά του πλάσματος. Δεύτερον, τη συνθετική εργασία φυσικής μοντελοποίησης όλων των φυσικών παραμέτρων που επηρεάζουν τη δυναμική εξέλιξη του πλάσματος και του μαγνητικού πεδίου, όπως, η ηλεκτρική και θερμική αγωγιμότητα, το ιξώδες, ο λογάριθμος Coulomb, οι καταστατικές εξισώσεις, ο βαθμός ιονισμού, η μεταφορά και η απώλεια της ακτινοβολίας του πλάσματος. Η δεύτερη αυτή εργασία, προσφέρει λύση στη φυσική μοντελοποίηση που αφορά όλες τις περιοχές πυκνοτήτων και θερμοκρασιών του πλάσματος. Ο τρίτος και κύριος στόχος εστιάζει στην αριθμητική διερεύνηση και μοντελοποίηση της δυναμικής εξέλιξης του πλάσματος και του παραγόμενου μαγνητικού πεδίου παραγόμενο από οπτοηλεκτρονικές διατάξεις Z-pinch και X-pinch, μονών, διπλών και πολλών μεταλλικών καλωδίων υπό συνθήκες μεγάλης πυκνότητας κι θερμοκρασίας, για την εξαγωγή συμπερασμάτων του τρόπου δημιουργίας και της δυναμικής εξέλιξης συγκεκριμένων ασταθειών, της κεντρικής περιοχής του X-pinch αλλά κυρίως για τον τρόπο σχηματισμού των πιδάκων πλάσματος που προκύπτουν από διατάξεις X-pinch. Για το λόγο αυτό, ένας αρχικά αστροφυσικός κώδικας, ο PLUTO, έχει διαμορφωθεί και μοντελοποιηθεί με επιτυχία, για την μελέτη των προαναφερθέντων διατάξεων πλάσματος. Ένας δεύτερος κώδικας, ο GORGON, χρησιμοποιείται ως εργαλείο σύγκρισης και αξιολόγησης σε μοντέλα διατάξεων X-pinch. Τα συμπεράσματα που εξάγονται δίνουν πολύτιμες πληροφορίες για τον τρόπο σχηματισμού των πιδάκων πλάσματος και των μαγνητοϋδροδυναμικών ασταθειών. Καταληκτικά παρουσιάζεται η πιθανή συσχέτιση των εργαστηριακών πιδάκων πλάσματος με τους αντίστοιχους πίδακες που προκύπτουν από νεαρά αστροφυσικά αντικείμενα (YSO's) και αντικειμένων Herbig Haro (HH). Συγκεκριμένα αυτή η εργασία συνεισφέρει στην εκτίμηση των παραγόντων κλίμακας και όλων των σχετικών αδιάστατων αριθμών και παραμέτρων που αφορούν τη συσχέτιση των αστροφυσικών και εργαστηριακών πιδάκων πλάσματος που παράγονται από μία διάταξη X-pinch, δύο καλωδίων Βολφραμίου, χαμηλού παλμικού ρεύματος.

Acknowledgments

This is the end of a long, seven year old, journey (or as I prefer to see it, the end of a beautifull research beginning!)! The work described in this thesis begun at 2014 and finished at 2021 as a member of the Institute for Plasma Physics and Lasers (IPPL) research community of Mediterranean Hellenic University (MHU) in collaboration with the National and Kapodistrian University of Athens (NKUOA). It would not have been possible to finish it without the help of my friends and colleagues who were always there for me through every difficulty.

First of all, I would like to thank Professor Nektarios Vlahakis for accepting me as a PhD candidate in the University of Athens. Although our communication was mainly from distance, our few meetings and talks were very constructive. Especially at early years where my ignorance in computational physics was a certain problem, he gave me all the support that I needed to go further. I still remember our all day talks and discussions in his homeland Agios Nikolaos, on his vacation summer days, teaching me how to use PLUTO in MHD problems. Or on the Christmas days in Athens checking the rotation of Axis and the physical implementations for the computational problem of an X-pinch configuration. Thank you very much.

Secondly, the man that offered me the opportunity to follow my dream, encouraging me all the time, was the Professor Nektarios A. Papadogiannis. His HiPER presentation and our talks through years were the catalyst to take the researcher path. Thank you very much.

Then a big thanks goes to Professor Michael Tatarakis that his scientific work and research is the most relevant to my PHD thesis. It is obvious that his support and scientific expertise are priceless for my progress. Michael and Nektarios thank you very much. I consider you both, my friends.

I would like to thank Associate Professor Vasilios Dimitriou for his continuous guidance in the computational methods and his valuable advises at our common conferences presentations. His support was also important at the educational part of two Summer schools where I presented the PLUTO code and the computational modules of our work. His instructions where valuable for the construction of my writings at my papers. Thank you Vasilis.

I could not forget Professor Andrea Ciardi of Sorbonne University in Paris. He provided the GORGON code to our research group while he provided us all the valuable information we needed for a proper use. His visits at the IPPL were very educating, exchanging valuable informations for our MHD simulations. Thank you Professor.

I would like to thank all the other members of the examination committee, honoring me by participating to it, and for their valuable comments and suggestions: Professor Ioannis A. Daglis, Professor Apostolos Mastichiadis and Assistant Professor Maria Petropoulou. Thank you all.

We share the same office and spend most of my Institute time together. Evaggelos Kaselouris is a patient and very reluctant colleague that helped me a lot through the years giving me very useful programming advises or using computational tools like MATLAB. He was very helpful also for the scientific language that I should use in my writings. Thank you Vangelis.

Last but not least is Alekos Skoulakis. Without his help I would have a serious problem on the programming part. He also executed the X-pinch experiments that I presented in my work. We had a lot of arguments about selecting the right tools or the appropriate physics modules to execute our simulation runs but I think at the end we had the best of results. Thank you Alekos.

I would like to thank all the people at the IPPL and the Department of Astrophysics of the University of Athens because wherever I needed something they were there for me. Thank you all.

I thank my friends Antonis Bouzakis, Dimitrios Monahos and Vasilios Doulgerakis for their interest along this journey. Especially Antonis was there for me through every difficulty and helped me to overcome a lot of my personal problems having with him the nicest of talks. His company provided me all the software and hardware stuff that I needed. Also a huge thanks to Xrysanta. Her support and encouragement at the late writing and presentation time was catalytic! Thank you all.

This work is dedicated to my family and especially to my kids. I wish them health, prosperity and good luck in their lives. I hope they succeed their life dreams and have a happy life. We mustn't forget that nothing is impossible and it's never too late to pursue your dreams.

A huge thanks for the team of ‘ARIS’ National HPC Infrastructure of the Greek Research and Technology Network (GRNET). Our projects LAMIS, Plups-I & -II and LaMIPlaS-I, -II and -III provide the most of the simulation results of this work. We wouldn’t have done that much as a computational team without the resources and the support of the 'ARIS' team. Thank you all guys.

This work was supported by the project “ELI-LASERLAB Europe Synergy, HiPER & IPERION-CH.gr” (MIS 5002735) which is implemented under the Action “Reinforcement of the Research and Innovation Infrastructure”, funded by the Operational Programme "Competitiveness, Entrepreneurship and Innovation" (NSRF 2014-2020) and co-financed by Greece and the European Union (European Regional Development Fund).

Contents

List of figures

List of tables

Εκτενής Περίληψη

Α. Χρονική παρουσίαση, συσχέτιση και εξέλιξη των καινοτομιών της παρούσης διδακτορικής διατριβής με τη σύγχρονη έρευνα σε αριθμητικά και υπολογιστικά μοντέλα διατάξεων Z και X-pinch.

Οι παλμικές διατάξεις παραγωγής πλάσματος όπως οι Z-pinch και X-pinch, προσφέρουν ένα μοναδικό περιβάλλον για την ανάπτυξη και κατανόηση των ιδιοτήτων του πλάσματος εξαιτίας της πολύ απλής δομής τους. Είναι ένα πεδίο με μεγάλο και συνεχές ενδιαφέρον λόγω των σημαντικά αναδυόμενων εφαρμογών. Τέτοιες είναι στη φυσική υψηλών ενεργειών, στην ελεγχόμενη πυρηνική σύντηξη, στην εργαστηριακή αστροφυσική, στην σημειακά εκπεμπόμενη ραδιογραφία αλλά και στην συναρπαστική βασική εμπλεκόμενη φυσική. Οι φορητές γεννήτριες παλμικής ηλεκτρικής ισχύος (Z-pinch , X-pinch) μεταφέροντας μερικές δεκάδες kA στο φορτίο (σύρμα) σε μερικά ns, έχουν μία μεγάλη ιστορία εφαρμογών όπως επίσης και βασικών ερευνητικών δυνατοτήτων π.χ. σημειακής εκπομπής ραδιογραφία μαλακών και σκληρών αχτίνων X (π.χ. διατάξεις X-pinch), μελέτη της δυναμικής πυκνού πλάσματος υψηλής ενέργειας και πιδάκων αστροφυσικού πλάσματος (π.χ. διατάξεις κωνικών περιοχών πολλαπλών καλωδίων Z-pinch (Z-pinch arrays)). Επιπλέον μπορούν να παίξουν σημαντικό ρόλο στη μελέτη της δυναμικής του πλάσματος αποσκοπώντας στην κλιμάκωση των συνθηκών του πλάσματος που δημιουργούνται από μεγαλύτερα ρεύματα.

Τα τελευταία 20 χρόνια υπάρχει έντονο ενδιαφέρον στην ανάπτυξη των αριθμητικών προσομοιώσεων τέτοιων διατάξεων λόγω της πολύ ενεργής αναπτυσσόμενης έρευνας στον τομέα της ελεγχόμενης πυρηνικής σύντηξης αλλά και στην εφαρμογή τέτοιων διατάξεων στην εργαστηριακή αστροφυσική και στη μελέτη φαινομένων που είναι δύσκολο να παρατηρηθούν και να μελετηθούν αναλυτικά με τα σημερινά τηλεσκόπια. Οι προσομοιώσεις προσφέρουν ένα πολύ άμεσο και εύκολο προς μελέτη περιβάλλον αλλά ταυτόχρονα βρίσκονται αντιμέτωπες με μία συνεχή πρόκληση, για την σωστή εισαγωγή όλων των απαιτουμένων παραμέτρων και φυσικών όρων, ώστε να μπορούν να έχουν παραπλήσια και φυσικά αναμενόμενα αποτελέσματα σύμφωνα με το πείραμα και την παρατήρηση. Το "πρόβλημα των συνοριακών συνθηκών" στα όρια του υπολογιστικού χώρου αλλά και στις διεπιφάνειες των υλικών της προσομοίωσης, αποτελεί μία δεύτερη πρόκληση κυρίως για τη σωστή συμπεριφορά του μαγνητικού πεδίου, την μη ανάπτυξη αφύσικων θερμοκρασιών στο πλάσμα αλλά και την αποφυγή δημιουργίας αριθμητικών "κρουστικών" μετώπων πίεσης και θερμοκρασίας και αφύσικων φαινομένων διάχυσης, παραμορφώσεων και ανακλάσεων. Μία τρίτη πρόκληση για μία απαιτητική προσομοίωση με πολλούς φυσικούς όρους και πολύ καλή χωρική διακριτοποίηση είναι η απαιτούμενη υπολογιστική ισχύς. Για το λόγο αυτό τα τελικά μοντέλα, όλων των επιστημονικών μελετών που αφορούν τέτοιες διατάξεις αλλά και απαιτητικών αστροφυσικών προσομοιώσεων, χρειάζονται τη συνδρομή υπέρ-υπολογιστικών

συστημάτων χρησιμοποιώντας ταυτόχρονα, κατά την εκτέλεση της προσομοίωσης, αρκετές εκατοντάδες ή χιλιάδες υπολογιστικούς πυρήνες. Λόγω της συμμετρίας των διατάξεων Z και X-pinch με κατάλληλες μετατροπές στις συνοριακές συνθήκες, τα μοντέλα μπορούν να προσομοιάσουν το 1/4, 1/8 ή 1/16 του πλήρους σχηματισμού, μειώνοντας με αυτόν τον τρόπο τον αριθμό των απαιτούμενων πυρήνων αλλά και αυξάνοντας ταυτόχρονα την ικανότητα καλύτερης χωρικής διακριτοποίησης.

Τον 21ο αιώνα πολλοί αριθμητικοί κώδικες δημιουργήθηκαν, αναπτύχθηκαν και εξελίχθηκαν ώστε να μπορούν να μελετήσουν εργαστηριακά και αστροφυσικά πλάσματα. Αρκετές φορές, κατά τη διάρκεια αυτής της εξέλιξης, τροποποιήθηκαν ώστε να μπορούν να περιγράψουν διαφορετικά φυσικά προβλήματα από τον αρχικό σχεδιασμό τους [1-25]. Καθαροί Οϊλεριανοί (Eulerian) όπως ο GORGON [1,9-15] ή καθαροί Λαγκραντζιανοί (Lagrangian) όπως ο MULTI-2D [20,21] ή μεικτοί Οϊλεριανοί-Λαγκραντζιανοί (Arbitrary Lagrangian Eulerian (ALE)) όπως οι ALEGRA [2-6] και MACH2 [18,22] μπορούν να περιγράψουν εργαστηριακά και αστροφυσικά πλάσματα. Ακόμα και καθαροί αστροφυσικοί κώδικες όπως οι ATHENA και ZEUS [16,18] ή αρχικά αστροφυσικοί όπως ο FLASH [17], έχουν αξιολογηθεί και δοκιμαστεί σε προβλήματα Z-pinch μονού καλωδίου αλλά και σε μοντέλα διατάξεων Z-pinch πολλών καλωδίων, μελετώντας την ένρηξη και συμπίεση του πλάσματος στην κεντρική περιοχή της διάταξης για την μελέτη φαινομένων που εμφανίζονται στην πυρηνική σύντηξη.

Ειδικά ο GORGON τα τελευταία χρόνια έχει χρησιμοποιηθεί και χρησιμοποιείται για τη μελέτη μαγνητο-υδροδυναμικών πλασμάτων που αφορούν εφαρμογές όπως μαγνητισμένα jet που παράγονται από διατάξεις laser, Z-pinch και X-pinch διατάξεων μονών και πολλών καλωδίων, τα οποία προσομοιάζουν πειραματικά εργαστηριακά jet αλλά και εργαστηριακά jet ειδικά σχεδιασμένα για τη μελέτη υπό κλίμακα αντίστοιχων αστροφυσικών που παράγονται κυρίως από Νεαρά Αστρικά Αντικείμενα (Young Stellar Objects (YSO)) που σχηματίζουν "κόμβους" φωτοβολούντος αερίου, γνωστοί ως αντικείμενα Χέρμπιγκ-Άρο (Herbig-Haro (HH)). Για αυτό το λόγο επιλέχθηκε σε αυτήν την διατριβή αυτός ο κώδικας, σαν ένας δεύτερος κώδικας αξιολόγησης, μαζί με τον κύριο, αρχικά αστροφυσικής περιγραφής, Οϊλεριανό κώδικα PLUTO [26-27].

Η παρούσα διδακτορική διατριβή έχει σαν κύριο αντικείμενο τη μελέτη της δυναμικής εξέλιξης πλάσματος παραγόμενο από εργαστηριακές οπτοηλεκτρονικές διατάξεις παλμικής ισχύος χαμηλού και μεσαίου ηλεκτρικού ρεύματος (~50kA) με χρόνο ανόδου της τάξης των 50ns (διατάξεις X-pinch και Z-pinch). Τα μαγνητο-υδροδυναμικά μοντέλα που χρησιμοποιήθηκαν μελέτησαν τη δυναμική συμπεριφορά των πιδάκων πλάσματος (jet) που παράγονται από διατάξεις X-pinch, τη δυναμική εξέλιξη της κεντρικής περιοχής (cross-point) καθώς και των μαγνητο-υδροδυναμικών ασταθειών που δημιουργούνται (π.χ. μαγνητικές Rayleigh-Taylor (MRT)). Διεξήχθη μελέτη υπό κλίμακα για τις φυσικές παραμέτρους των jet και τη συσχέτιση τους με τις αντίστοιχες που αφορούν Αστροφυσικά jet που προέρχονται από Νεαρά Αστρικά Αντικείμενα (YSOs). Ένας δεύτερος στόχος είναι η πλήρη μαθηματική και φυσική περιγραφή ενός μαγνητο-υδροδυναμικού μοντέλου καθώς και μία όσο γίνεται πλήρη

αριθμητική προσέγγιση για τον μαγνητο-υδροδυναμικό κώδικα PLUTO. Με αυτόν τον τρόπο ο συγκεκριμένος αστροφυσικός κώδικας έγινε ικανός στο να μπορεί να προσομοιώσει τα παραπάνω εργαστηριακά πλάσματα μέσω των αλλαγών των φυσικών του παραμέτρων και φυσικών μεγεθών που υπεισέρχονται στο σύστημα των μαγνητο-υδροδυναμικών διαφορικών του εξισώσεων αλλά και μέσω της προσαρμογής των ήδη υπαρχόντων τεχνικών του κώδικα στα συγκεκριμένα εργαστηριακά δεδομένα και αρχικές συνθήκες. Επίσης η πλήρη φυσική και μαθηματική μελέτη για όλο το εύρος θερμοκρασιών, πιέσεων και πυκνοτήτων έδωσε τη δυνατότητα για την εξαγωγή συναρτήσεων σύνθεσης και αντίστοιχων αριθμητικών δεδομένων, τα οποία παρουσιάζονται με αντίστοιχες γραφικές παραστάσεις έτσι ώστε να μπορεί οποιοσδήποτε αντίστοιχος κώδικας να περιγράψει αντίστοιχα πλάσματα σε οποιαδήποτε περιοχή που δεν μπορεί να προσεγγιστεί με μία απλή μαθηματική σχέση. Τα φυσικά μεγέθη που αναλύονται σε αυτήν την μελέτη αφορούν:

i. την ηλεκτρική αγωγιμότητα του πλάσματος

ii. την θερμική αγωγιμότητα του πλάσματος

iii. το ιξώδες

iv. τη μεταφορά και εκπομπή ακτινοβολίας για οπτικά διαφανές και μη διαφανές πλάσμα

v. την αριθμητική συσχέτιση του βαθμού ιονισμού του πλάσματος με την θερμοκρασία και την ηλεκτρονιακή πυκνότητα

vi. καταστατικές γραφικές παραστάσεις που συσχετίζουν αριθμητικά την πίεση με την πυκνότητα και την θερμοκρασία καθώς και καταστατικές γραφικές παραστάσεις συσχέτισης της εσωτερικής ενέργειας με την πυκνότητα και τη θερμοκρασία.

Όλες αυτές οι αναλύσεις αφορούν πλάσμα που προέρχεται από το μέταλλο Βολφράμιο αλλά μπορούν εύκολα να επεκταθούν σε οποιοδήποτε μεταλλικό πλάσμα με κατάλληλη τροποποίηση των αρχικών αριθμητικών τιμών και φυσικών μεγεθών και παραμέτρων.

Η διδακτορική διατριβή ξεκίνησε και συνεχίστηκε με μία αγαστή συνεργασία μεταξύ του τομέα Αστροφυσικής, Αστρονομίας και Μηχανικής του Εθνικού Καποδιστριακού Πανεπιστημίου Αθηνών (ΕΚΠΑ) και του Ινστιτούτου Φυσικής Πλάσματος και Λέιζερ (IPPL) του Ελληνικού Μεσογειακού Πανεπιστημίου (ΕΛΜΕΠΑ) στην περιοχή τρία Μοναστήρια Ρεθύμνου. Ξεκίνησε τον Απρίλιο του 2014 με το γενικό τίτλο " Μαγνητισμένα jets στην Αστροφυσική και στο Εργαστήριο". Στις 10 Μαΐου του 2021 ζητήθηκε και εγκρίθηκε από το τμήμα και τον τομέα του η αλλαγή του τίτλου σε "Μαγνητισμένοι πίδακες στην εργαστηριακή Αστροφυσική". Η κύρια δουλειά της ερευνητικής δραστηριότητας προσανατολίστηκε προς τη θεωρητική διερεύνηση και μελέτη μέσω αριθμητικών προσομοιώσεων της δυναμικής συμπεριφοράς του πλάσματος που παράγεται από διατάξεις Z και X-pinch. Για το λόγο αυτό χρησιμοποιήθηκε ο ελεύθερης πρόσβασης αστροφυσικός κώδικας PLUTO. Λόγω των σύνθετων γεωμετρικών δομών που έπρεπε να έχει η αρχική δομή του πλάσματος και το αντίστοιχο μαγνητικό πεδίο, μοντελοποιήθηκε, μέσω χωρικών μετατοπίσεων και

στροφών, η αρχική δομή του πλάσματος και των φυσικών του παραμέτρων όπως η πυκνότητα, η θερμική πίεση και το μαγνητικό πεδίο για οποιαδήποτε χωρική/γεωμετρική κατανομή τους. Ελέγχοντας την αποτελεσματικότητα αυτής της αρχικής μοντελοποίησης, ένα τρισδιάστατο μοντέλο μίας διάταξης X-pinch, δύο καλωδίων βολφραμίου, μελέτησε την χωροχρονική εξέλιξη των δημιουργούμενων πιδάκων πλάσματος καθώς και των αντίστοιχων μαγνητο-υδροδυναμικών (MHD) ασταθειών που σχηματίζονται. Τα αποτελέσματα της αριθμητικής προσομοίωσης συγκρίθηκαν με αντίστοιχα πειραματικά αποτελέσματα σκιαγραφικών (shadowgraphy) εικόνων και εικόνων ιντερφερομετρίας (interferometry). Οι εικόνες προήλθαν από πειράματα που διεξήχθηκαν στο IPPL. Η συμφωνία πειράματος-προσομοίωσης αυτής της πρώτης προσέγγισης ήταν αρκετά ικανοποιητική επιδεικνύοντας τον γρήγορο σχηματισμό MHD ασταθειών και τη συσχέτιση τους με την τοπολογία και ισχύ του μαγνητικού πεδίου. Τα αποτελέσματα της μελέτης αυτής παρουσιάστηκαν και δημοσιεύτηκαν σε ένα επιστημονικό συνέδριο που διεξήχθη το Νοέμβριο του 2015 στην Αθήνα [28].

Λόγω των μεγάλων αριθμητικών απαιτήσεων και σχετικά υψηλού βαθμού διακριτοποίησης τα τελικά μοντέλα προσομοίωσης δεν ήταν δυνατόν να επιλυθούν και να φτάσουν στο τελικό στάδιο από ένα απλό προσωπικό υπολογιστή. Με αυτόν τον "υποχρεωτικό" περιορισμό ξεκίνησε τον Νοέμβριο του 2016 αρχικά για τις υπολογιστικές απαιτήσεις των προσομοιώσεων της παρούσης διατριβής μία συνεργασία με το Εθνικό Δίκτυο Υποδομών Τεχνολογίας και συγκεκριμένα της υποδομής ARIS [29]. Η συνεργασία αυτή συνεχίζεται μέχρι σήμερα παρέχοντας κατά μέσο όρο 1.5-2.0 εκατομμύρια υπολογιστικές ώρες ανά έτος για όλες τις απαιτητικές προσομοιώσεις του IPPL. Τα τελικά μοντέλα των προσομοιώσεων με τη βέλτιστη διακριτοποίηση απαιτούν περίπου 48 ώρες για να ολοκληρωθούν σε ένα σύστημα 1000 πυρήνων των 64GB υπολογιστικής μνήμης κατά μέσο όρο.

Το επόμενο βήμα στη βελτιστοποίηση του κώδικα για την ικανότητα περιγραφής των εργαστηριακών πλασμάτων ξεκίνησε το 2016 και αφορούσε την εισαγωγή νέων αλγορίθμων στον κώδικα. Συγκεκριμένα εισήχθηκαν:

α. Μία τροποποιημένη καταστατική εξίσωση μεταξύ πυκνότητας, πίεσης, θερμοκρασίας και εσωτερικής ενέργειας χρησιμοποιώντας αριθμητικά δεδομένα από την βάση δεδομένων SESAME και την τροποποιημένη καταστατική εξίσωση MGGB του Εθνικού εργαστηρίου του Los Alamos ειδικά για το Βολφράμιο [30].

β. Απώλειες ακτινοβολίας για οπτικά αραιά πλάσματα χρησιμοποιώντας τη βάση δεδομένων από τον FLYCHK κώδικα [31].

γ. Προσδιορισμός της πυκνότητας του πλάσματος κατά τη διάρκεια της εκτέλεσης, συσχετίζοντας την με το βαθμό ιονισμού και τη θερμοκρασία. Για αυτόν τον σκοπό χρησιμοποιούνται αριθμητικές τιμές για το υλικό του Βολφραμίου πάλι από τον FLYCHK κώδικα [31].

δ. Τροποποιημένο μοντέλο μεταφοράς ακτινοβολίας που χρησιμοποιούσε σε υδροδυναμικές αστροφυσικές περιπτώσεις ο κώδικας ώστε να συμπεριλάβει και

εργαστηριακά μαγνητο-υδροδυναμικά πλάσματα από μεταλλικά υλικά (π.χ. Βολφράμιο) [32].

ε. Εισαγωγή της ηλεκτρικής αγωγιμότητας χρησιμοποιώντας μία τροποποιημένη εκδοχή της ευρέως γνωστής μαθηματικής σχέσης του Spitzer.

Οι τροποποιήσεις αυτές δοκιμάστηκαν με επιτυχία σε μία απλή διάταξη Z-pinch μονού καλωδίου Βολφραμίου, δίνοντας κοντινά αποτελέσματα για τη θερμοκρασία και την εξάπλωση του πλάσματος σε σχέση με αντίστοιχο πείραμα της διεθνούς βιβλιογραφίας. Επίσης διαπιστώθηκε η σημαντική συνεισφορά του μοντέλου μεταφοράς της ακτινοβολίας για τη σωστή ανάπτυξη και μορφολογία του πλάσματος διαμορφώνοντας ταυτόχρονα τα επίπεδα της θερμοκρασίας στα αντίστοιχα επίπεδα του πειράματος και της βιβλιογραφίας.

Τα αποτελέσματα αυτά παρουσιάστηκαν τον Ιούνιο του 2018 σε συνέδριο που διεξήχθη στη πόλη των Χανίων με αντίστοιχη δημοσίευση [33]. Το Νοέμβριο του ίδιου έτους παρουσιάστηκαν επίσης σε διεθνές συνέδριο που πραγματοποιήθηκε στην πόλη του Ρεθύμνου με ανάρτηση αντίστοιχου Πόστερ και περίληψης [34].

Μοντέλα για την τελική προσομοίωση και τη σύγκριση με τα εργαστηριακά δεδομένα, ολοκληρώθηκαν και αξιολογήθηκαν. Τα μοντέλα αφορούσαν διάταξη X-pinch με κύριο στόχο τη δυναμική μελέτη του πλάσματος, των φυσικών παραμέτρων που το χαρακτηρίζουν και τη μελέτη του jet που παράγεται. Η μορφολογία του καθώς και η ταχύτητά του εμφανίζει ομοιότητες με τα αντίστοιχα μεγέθη αστροφυσικών jet που προέρχονται από YSOs. Επιλέχθηκε ένα τελικό μοντέλο που προσεγγίζει καλύτερα τη δυναμική και φυσική συμπεριφορά του πλάσματος, με γνώμονα τα πειραματικά και άλλων εργασιών, αποτελέσματα. Τα αντίστοιχα πειραματικά αποτελέσματα προήλθαν από αντίστοιχη διάταξη του IPPL. Εργασία που παρουσίασε αναλυτικά όλη αυτή τη μελέτη υποβλήθηκε στο επιστημονικό περιοδικό Plasma Physics and Control Fusion (PPCF) το καλοκαίρι του 2020, αξιολογήθηκε, έγινε δεκτή και δημοσιεύτηκε ηλεκτρονικά τον Οκτώβριο του ίδιου χρόνου [35].

Παράλληλα ωστόσο έγινε εκτενής θεωρητική μελέτη και διερεύνηση όλων των φυσικών παραμέτρων και των φυσικών όρων που είναι υπεύθυνοι για τις απώλειες και τη δημιουργία ασταθειών και φαινομένων διάλυσης της μορφολογίας του πλάσματος (π.χ. ιξώδους, ηλεκτρικής αγωγιμότητας, θερμικής αγωγιμότητας). Αποτέλεσμα αυτής της πολύμηνης συνθετικής εργασίας ήταν η εξαγωγή γραφημάτων, αριθμητικών δεδομένων και συνδυαστικών μαθηματικών σχέσεων για τους κυρίαρχους αυτούς φυσικούς όρους όπου θα μπορούσαν να χρησιμοποιηθούν και να εισαχθούν σε οποιοδήποτε μαγνητο-υδροδυναμικό κώδικα για όλο το εύρος των πυκνοτήτων, θερμοκρασιών και θερμικών πιέσεων που συναντάμε σε εργαστηριακό και αστροφυσικό πλάσμα. Με αυτόν τον τρόπο διορθώθηκαν οι τιμές φυσικών όρων όπως π.χ. της ηλεκτρικής αγωγιμότητας στην περιοχή της θερμής και πυκνής ύλης (Warm Dense Matter (WDM)) όπου η μαθηματική σχέση του Spitzer έδινε μεγάλες αποκλίσεις. Αυτή η μελέτη παρουσιάζεται εκτενώς στα δύο μέρη του τρίτου

κεφαλαίου της διδακτορικής διατριβής. Μία από αυτές τις νέες προσεγγίσεις για την ηλεκτρική αγωγιμότητα προστέθηκε στο μαγνητο-υδροδυναμικό μοντέλο του PLUTO.

Επίσης καινούργιοι όροι και τεχνικές προστέθηκαν και ενεργοποιήθηκαν στον κώδικα με αποτέλεσμα τη βελτίωση της υπολογιστικής συμπεριφοράς και της ικανότητας για δημιουργία μικρότερων χωρικών μοντέλων, ώστε να υπάρχει καλύτερη διακριτοποίηση και εστίαση σε συγκεκριμένες περιοχές του πλάσματος. Επιγραμματικά ενεργοποιήθηκε ο όρος της θερμικής αγωγιμότητας και προστέθηκε ένας τρίτος όρος σε αυτήν, στο αρχικό σύστημα του κώδικα, όπου λαμβάνει υπόψη του τη θερμική διάχυση σε κατεύθυνση κάθετη στο επίπεδο που ορίζουν η κλίση της θερμοκρασίας και το μαγνητικό πεδίο. Επίσης τεχνικές όπως η απενεργοποίηση του μαγνητο-υδροδυναμικού επιλύτη (Riemann Solver) στην περιοχή του κενού, έδωσαν την δυνατότητα για καλύτερη χωροχρονική εξέλιξη του μαγνητικού πεδίου και την καλύτερη δυναμική εξέλιξη του πλάσματος χωρίς αυτό να επηρεάζεται από αφύσικες ανακλάσεις και παραμορφώσεις από τα υπολογιστικά χωρικά όρια.

Οπότε μία δεύτερη μελέτη ολοκληρώθηκε ώστε να εξεταστούν και να αξιολογηθούν οι καινούργιες προσθήκες και αλλαγές. Αφορά την αξιολόγηση του μαγνητο-υδροδυναμικού κώδικα PLUTO με τις καινούργιες προσθήκες, για την ίδια πειραματική διάταξη X-pinch, δύο καλωδίων Βολφραμίου αλλά με πιο στενή γωνία μεταξύ τους. Για τη μελέτη αυτή χρησιμοποιήθηκε και ένας δεύτερος διεθνώς αναγνωρισμένος κώδικας, ο GORGON. Ο κώδικας αυτός έχει χρησιμοποιηθεί και χρησιμοποιείται σε εργαστηριακά πλάσματα και πλάσματα προσομοίωσης εργαστηριακής αστροφυσικής με πολύ μεγάλη επιτυχία. Αυτή η προσθήκη στο υπολογιστικό τμήμα του IPPL πραγματοποιήθηκε με τη βοήθεια του καθηγητή Andrea Ciardi του Πανεπιστημίου της Σορβόννης. Η συνεργασία αυτή ξεκίνησε το καλοκαίρι του 2019 και συνεχίζεται μέχρι σήμερα.

Έξι μοντέλα, με διαφορετικές φυσικές παραμέτρους για τον PLUTO και ένα για τον GORGON, ολοκληρώθηκαν και χρησιμοποιήθηκαν για τη μελέτη αυτή. Στην εργασία αυτή αξιολογούνται όλες οι φυσικές παράμετροι της δυναμικής διαμόρφωσης του jet και της κεντρικής περιοχής (cross-point area). Η αξιολόγηση των δύο προσεγγίσεων δίνει πολύ ικανοποιητικά και παρεμφερή αποτελέσματα. Τα έξι διαφορετικά μοντέλα του PLUTO δίνουν διαφωτιστικές προσεγγίσεις για το πώς επηρεάζουν η θερμική αγωγιμότητα και η μετάδοση ακτινοβολίας τη δυναμική του πλάσματος, τη δημιουργία μαγνητο-υδροδυναμικών ασταθειών και της εξέλιξης τους. Επίσης αν και διαφορετικές οι προσεγγίσεις της αρχικής εισαγωγής του μαγνητικού πεδίου στους δύο κώδικες αλλά και ο τρόπος του χρονικού επαναπροσδιορισμού του, υπάρχει αξιοσημείωτη συμφωνία στην μορφολογία και τοπολογία του μέχρι και μεταγενέστερους χρόνους. Αυτό αποτελεί μία ισχυρή ένδειξη της σωστής προσέγγισης του χρονικού επαναπροσδιορισμού του μαγνητικού πεδίου στον PLUTO ικανοποιώντας συνεχώς, χωροχρονικά, το νόμο του Ampere και το θεώρημα του Stokes σε όλο το υπολογιστικό κουτί. Η εργασία έχει αξιολογηθεί έγινε δεκτή και δημοσιεύτηκε ηλεκτρονικά στα τέλη Δεκεμβρίου του 2021 [36].

Β. Περιληπτική παρουσίαση του θέματος κάθε κεφαλαίου

Η Διδακτορική διατριβή αποτελείται από τρία κύρια μέρη. Στο πρώτο μέρος που αφορά τα κεφάλαια 1 και 2 γίνεται μία εκτενής παρουσίαση γιατί ξεκίνησε και τι αφορά αυτή η διατριβή, εξηγώντας ταυτόχρονα τι έχει γίνει μέχρι σήμερα παγκόσμια στον τομέα των αντίστοιχων αριθμητικών προσομοιώσεων ειδικά τις τελευταίες 2 δεκαετίες. Εξηγούνται οι τεχνικές και τα φυσικά μοντέλα που μελετούν οι κώδικες αυτοί, με γνώμονα πάντα τα εργαστηριακά πλάσματα Z και X-pinch διατάξεων.

Β1. Α μέρος-Κεφάλαια 1 και 2

Συγκεκριμένα στο εισαγωγικό κεφάλαιο 1 παρουσιάζεται και εξηγείται το κίνητρο που οδήγησε στην συγκεκριμένη διατριβή και την ερευνητική της κατεύθυνση οδηγώντας με αυτόν τον τρόπο στη συνεργασία του ΕΚΠΑ και του IPPL. Παρουσιάζονται οι εργαστηριακοί και αστροφυσικοί κώδικες που χρησιμοποιούνται διεθνώς τα τελευταία χρόνια. Εξηγούνται περιληπτικά ο τεχνικές που χρησιμοποιούν για να προσομοιώσουν επιτυχώς τα εργαστηριακά και αστροφυσικά πλάσματα και για να επιλύσουν τα προβλήματα που παρουσιάζονται κατά την διάρκεια εκτέλεσης της προσομοίωσης. Στη συνέχεια παρουσιάζεται περιληπτικά ο αστροφυσικός, μη τροποποιημένος, κώδικας PLUTO που αποτελεί το κύριο αριθμητικό εργαλείο της παρούσης διατριβής. Εξηγούνται οι λόγοι που οδήγησαν στην επιλογή του συγκεκριμένου κώδικα και τα αριθμητικά/υπολογιστικά πλεονεκτήματα που είχε ήδη ενσωματωμένα στο κύριο μαγνητο-υδροδυναμικό μέρος του, ώστε να αποτελεί ένα αρκετά ευέλικτο εργαλείο, δίνοντας αρκετές εναλλακτικές ως προς την επιλογή του επιλύτη, των συνοριακών συνθηκών, την επιλογή καταστατικών εξισώσεων κ.α. Στο προτελευταίο μέρος του κεφαλαίου γίνεται μία παρουσίαση όλων των τεχνικών και των φυσικών παραμέτρων που έπρεπε να εισαχθούν ώστε να μπορεί ο αρχικός κώδικας να τροποποιηθεί και να μπορεί να προσομοιώσει εργαστηριακές διατάξεις πλάσματος. Στο τελευταίο μέρος του κεφαλαίου παρουσιάζεται ο στόχος της διατριβής και επιγραμματικά η θεματολογία του κάθε κεφαλαίου.

Στο κεφάλαιο 2 γίνεται αναλυτική παρουσίαση της διεθνούς επιστημονικής έρευνας των τελευταίων χρόνων σε διατάξεις Z-pinch μονού και πολλών καλωδίων, σε διατάξεις δύο καλωδίων X-pinch και σε διατάξεις παραγωγής εργαστηριακών jet που προσομοιάζουν αντίστοιχα αστροφυσικά από YSOs και Herbig-Haro (HHs) αντικείμενα. Εξηγούνται και αναλύονται όλα τα εμπλεκόμενα φυσικά φαινόμενα στο πείραμα καθώς και οι δυσκολίες και οι τεχνικές που χρησιμοποιούν οι προσομοιώσεις ώστε να τα περιγράψουν με επιτυχία. Συγκεκριμένα παρουσιάζεται η σχέση του Bennet όπου εξηγείται και αποδεικνύεται αναλυτικά (εξισώσεις 2.1-2.8, 2.11-2.15) η στατική ισορροπία που μπορεί να υπάρξει μεταξύ της θερμικής πίεσης-εκτόνωσης συγκρινόμενη με τη μαγνητική πίεση-συμπίεσης διαμορφώνοντας με αυτόν τον τρόπο ένα παραβολικό προφίλ για την πυκνότητα μάζας και την θερμική πίεση σε ένα μονό καλώδιο Z-pinch (σχηματικές και γραφικές απεικονίσεις 2.1-2.3). Η σχέση αυτή

καταλήγει σε μία συσχέτιση μεταξύ του συνολικού ρεύματος, της θερμοκρασίας και του αριθμού σωματιδίων ανά μονάδα μηκους. Η τελική εξίσωση 2.15 έχει εισαχθεί στον κώδικα και η απόκλιση από την ισορροπία διαμορφώνει τις αρχικές συνθήκες πίεσης και θερμοκρασίας του πλάσματος δίνοντας ένα ακόμα εργαλείο για την καταλληλότερη προσέγγιση των αρχικών συνθηκών (συνήθως οι διατάξεις Z και X-pinch δεν ικανοποιούν αρχικά την εξίσωση Bennet) [37]. Σε πολύ μικρές αντιστάσεις στο εσωτερικό του πλάσματος, το φαινόμενο του επιδερμικού ρεύματος (skin effect current) παίζει σημαντικό ρόλο στην τοπολογία του ηλεκτρικού ρεύματος και του παραγόμενου μαγνητικού πεδίου (εξισώσεις 2.9-2.11). Είναι επίσης μία νέα προσθήκη στον κώδικα η οποία παράγει ρεαλιστικότερα φυσικά μοντέλα και δίνει ευελιξία στην καλύτερη απεικόνιση των αρχικών συνθηκών του πλάσματος.

Στη συνέχεια αναλύεται η σημασία της εισαγωγής των απωλειών ενέργειας σε ένα μαγνητο-υδροδυναμικό κώδικα μέσω ακτινοβολίας και μεταφοράς ακτινοβολίας από οπτικά λεπτό και οπτικά πυκνό πλάσμα. Εξηγείται η σημασία που μπορεί να έχει αυτή η φυσική διαδικασία σε πλάσματα Z-pinch τόσο στη θερμοκρασιακή συμπεριφορά όσο και στη δημιουργία ασταθειών, τοπικών φαινομένων συμπίεσης, στην αύξηση του ιονισμού και της διέγερσης του πλάσματος καθώς και στο φάσμα εκπομπής του. Συνήθως οι περισσότεροι κώδικες λαμβάνουν υπόψη τους τις απώλειες λόγω εκπομπής ακτινοβολίας από οπτικά λεπτό πλάσμα κυρίως (π.χ. ακτινοβολία πέδησης) αλλά δεν έχουν πολλοί το πλήρες πακέτο όλων των φαινομένων ακτινοβολίας. Στον ανανεωμένο PLUTO λαμβάνονται υπόψη και τα φαινόμενα μεταφοράς αλλά και εκπομπής ακτινοβολίας, με αναλυτική παρουσίαση όλου του φυσικού και αριθμητικού μοντέλου στο επόμενο κεφάλαιο. Ένα ενδιαφέρον φυσικό φαινόμενο, που μπορεί να εμφανιστεί στην κεντρική περιοχή του X-pinch ή σε διατάξεις Z-pinch σχετιζόμενες με την μελέτη της σύντηξης, είναι η κατάρρευση λόγω ακτινοβολίας (radiative collapse). Το πλάσμα τότε καταρρέει σε πυκνότητες στερεού ή και περισσότερο. Το ρεύμα που επιτυγχάνεται αυτή η κατάρρευση ονομάζεται Πις-Μπραζίνσκι (Pease-Braginskii (PB) current) (εξίσωση 2.16). Η διαδικασία αυτή είναι πολύ σημαντική για τον σχηματισμό m=0 ασταθειών και μικρό Z-pinch σχηματισμών στην κεντρική περιοχή του X-pinch.

Οι διατάξεις Z και X-pinch είναι πολύ ασταθείς και σε μικρό χρονικό διάστημα εμφανίζουν m=0 (αστάθεια "λουκάνικου") και m=1 (αστάθεια συστροφής ή περιέλιξης) μαγνητο-υδροδυναμικές αστάθειες. Ο ρυθμός ανάπτυξης των ασταθειών καθορίζει σε μεγάλο ποσοστό την εξέλιξη της προσομοίωσης αλλά και του πειράματος. Οι αστάθειες m=0 δημιουργούν περιοχές με λαιμούς και εξογκώματα κατά μήκος της κυλινδρικής διάταξης του καλωδίου τα οποία ενισχύονται η εξασθενούν από την τοπολογία του μαγνητικού πεδίου. Στις αστάθειες συστροφής το τοπικό μαγνητικό πεδίο της μίας πλευράς του καλωδίου διαφοροποιείται σε σχέση με της άλλης με αποτέλεσμα το κυλινδρικό πλάσμα να αποκτά μία μορφή που θυμίζει έλικα. Ο συνδυασμός αυτών των δύο ασταθειών δημιουργεί τελικά καταστάσεις διάλυσης και διάχυσης του πλάσματος (απεικόνιση σχημάτων 2.5 και 2.6). Η μελέτη

της δημιουργίας και ενίσχυσης/εξασθένισης των ασταθειών είναι ακόμα ένα ενεργό ερευνητικό κομμάτι. Το ερευνητικό κέντρο IPPL προσανατολισμένο προς αυτήν την κατεύθυνση, ερευνώντας τον μηχανισμό και την αρχική προέλευση των ασταθειών σε μονό καλώδιο χαλκού Z-pinch καταλήγει σε πρόσφατη έρευνα [38-40] ότι ένα μεγάλο μέρος της αρχικής διαταραχής που μεταβιβάζεται από τη στερεή ,στην υγρή και τελικά στην αέρια φάση και φάση πλάσματος, οφείλεται στις παραμορφώσεις του καλωδίου ήδη από τη στερεή του φάση. Η αντίστοιχη αστάθεια ονομάζεται ηλεκτρο-θερμο-μηχανική αστάθεια (electro-thermo-mechanical (ETM) instability). Αυτή μπορεί να δημιουργήσει την αρχική προϋπόθεση για τη δημιουργία ασταθειών συστροφής σε μονά ή και πολλά καλώδια διατάξεων Z-pinch. Για το κομμάτι της δυναμικής συμπεριφοράς του καλωδίου στη φάση του πλάσματος χρησιμοποιήθηκε ο PLUTO. Τα αποτελέσματα αυτής της έρευνας αποτελούν ιδανικό εφαλτήριο για τη μελλοντική διερεύνηση της δυναμικής συμπεριφοράς, από πολύ πρώιμες χρονικές στιγμές και για τις διατάξεις που αφορούν τη παρούσα διατριβή.

Κατόπιν γίνεται εκτενής ανάλυση για τις διατάξεις X-pinch δύο καλωδίων και τον τρόπο σχηματισμού του αραιού στεφανιαίου πλάσματος (coronal plasma) από την αποδόμηση των εξωτερικών επιφανειών των καλωδίων, τον σχηματισμό των αξονικών πιδάκων πλάσματος (axial jets) από την ακτινική εξάπλωση του πλάσματος από τα καλώδια αλλά και από την κεντρική περιοχή, σε μεταγενέστερες χρονικές στιγμές και την διαμόρφωση διαδοχικών μικρό-σχηματισμών Z-pinch (cascading) και διακλαδώσεων (bifurcation) στην περιοχή του "λαιμού" της κεντρικής περιοχής (σχήμα 2.7) [41-43]. Παρουσιάζεται το "μοντέλο ρουκέτας" (rocket model) που περιγράφει αρκετά ικανοποιητικά τον τρόπο που γίνεται η αναπλήρωση του στεφανιαίου πλάσματος από τις εσωτερικές περιοχές των καλωδίων κατά την αποδόμησή τους, σε διατάξεις X-pinch αλλά και Z-pinch περιοχών πολλών καλωδίων (εξίσωση 2.19).

Δίνεται ιδιαίτερη έμφαση στον τρόπο σχηματισμού των πιδάκων πλάσματος όπου δύο κύριοι μηχανισμοί διαμορφώνουν τη δυναμική συμπεριφορά τους. Αρχικά κυρίαρχη είναι η ακτινική εξάπλωση του στεφανιαίου πλάσματος από τα εξωτερικά στρώματα των καλωδίων όπου αυτό συμπιέζει και συμπιέζεται υδροδυναμικά στην κατακόρυφη διεύθυνση δημιουργώντας τους αρχικούς σχηματισμούς των πιδάκων. Σε μεταγενέστερες χρονικές στιγμές οι δυνάμεις Λαπλάς (Laplacian forces) αναλαμβάνουν ενεργό ρόλο εκτοξεύοντας πλάσμα από την εσωτερική κεντρική περιοχή κατά μήκος του κατακόρυφου άξονα ενισχύοντας σημαντικά την πυκνότητα πλάσματος στις εσωτερικές περιοχές του πίδακα, δημιουργώντας ταυτόχρονα και περιοχές υψηλότερης θερμοκρασίας λόγω της μαγνητικής συμπίεσης. Σε αυτή την φάση του σχηματισμού η κεντρική περιοχή της διάταξης εμφανίζει ταυτόχρονα και καυτά σημεία (hot spots) τα οποία εκπέμπουν εντονότερα ακτινοβολία στην περιοχή των ακτίνων X. Στη παρούσα διατριβή δίνεται ιδιαίτερη έμφαση και μελετάται διεξοδικά στο κεφάλαιο 5 ο τρόπος σχηματισμού των πιδάκων μέσω προσομοίωσης και σύγκρισης με το πείραμα καθώς και οι αντίστοιχοι σχηματισμοί που εμφανίζονται στην περιοχή του "λαιμού".

Στο τελευταίο μέρος του κεφαλαίου παρουσιάζεται η σύγχρονη ερευνητική δραστηριότητα (και σχετικές προσομοιώσεις) που είναι σχετική με την μελέτη αστροφυσικών αντικειμένων, όπως τα YSO και οι αντίστοιχοι πίδακες πλάσματος που μπορούν να εμφανίσουν δομή HH (εικόνες σχήματος 2.8).

Παρουσιάζονται σε μορφή πίνακα (πίνακας 2.1) όλες οι αδιάστατες σταθερές που είναι σημαντικές για τη μελέτη των αστροφυσικών και εργαστηριακών πλασμάτων, δείχνοντας ότι οι υδροδυναμικά σχετιζόμενες έχουν σχετικές τιμές αλλά οι μαγνητο-υδροδυναμικές έχουν και αρκετές αποκλίσεις. Παρουσιάζονται οι δύο εξισώσεις που πρέπει να ληφθούν υπόψη για την αντιστοίχιση των εργαστηριακών πιδάκων πλάσματος με τους αστροφυσικούς. Οι δύο σημαντικές παράμετροι είναι ο αριθμός Μαχ (Mach number) και το πλάσμα βήτα (plasma β) δίνοντας αντιστοιχίσεις μερικών μηνών χρόνου σε αντίστοιχα ns εργαστηρίου και μερικά mG αστροφυσικού μαγνητικού πεδίου σε εκατοντάδες χιλιάδες Gauss εργαστηριακού μαγνητικού πεδίου. Μία αναλυτική παρουσίαση των αδιάστατων παραμέτρων, γραφική τους απεικόνιση και μελέτη μαζί με την εργαστηριακή αντιστοίχιση πιδάκων πλάσματος διάταξης X-pinch σε αντίστοιχους αστροφυσικούς γίνεται στο τελευταίο μέρος του κεφαλαίου 5 της παρούσης διατριβής.

Β2. Β μέρος-Κεφάλαια 3 και 4

Στο δεύτερο μέρος της διατριβής, που αντιστοιχούν τα κεφάλαια 3 και 4, συναντάμε κυρίως την παρουσίαση και ανάπτυξη των φυσικών, μαθηματικών και υπολογιστικών μοντέλων και σχεδίων που χρησιμοποιούνται αλλά και μπορεί να χρησιμοποιηθούν στο μέλλον από τον PLUTO και άλλους μαγνητο-υδροδυναμικούς κώδικες (π.χ. τον GORGON).

Στο κεφάλαιο 3/Μέρος Ι αναπτύσσεται το κομμάτι του μαγνητο-υδροδυναμικού κώδικα που έχει σχέση με την επιλογή των καταστατικών εξισώσεων και την εισαγωγή των όρων των διαφορικών εξισώσεων που είναι υπεύθυνοι για τις απώλειες και τη μεταφορά ακτινοβολίας, κυρίως στον PLUTO. Με αυτόν τον τρόπο μέσα από τα αντίστοιχα γραφήματα και τις αντίστοιχες εξισώσεις δίνεται ο τρόπος συσχετισμού της θερμικής πίεσης-πυκνότητας-εσωτερικής ενέργειας και θερμοκρασίας κατά τη διάρκεια της εξέλιξης της υπολογιστικής προσομοίωσης. Στο δεύτερο μέρος του ίδιου κεφαλαίου περιγράφονται και αναλύονται όλοι οι όροι απωλειών και μεταφοράς που μπορούν να χρησιμοποιηθούν και χρησιμοποιούνται από τον κώδικα για την καλύτερη μαγνητο-υδροδυναμική προσέγγιση του πλάσματος. Σκοπός της μελέτης αυτής είναι να υπάρξει μία συνθετική προσέγγιση για τους φυσικούς μαγνητο-υδροδυναμικούς όρους, μέσα από συνδυαστικές σχέσεις και διορθωτικούς παράγοντες, παρέχοντας μία ολοκληρωμένη φυσική προσέγγιση οποιουδήποτε εργαστηριακού ή αστροφυσικού πλάσματος σε όλες τις συνθήκες πυκνότητας-θερμοκρασίας-θερμικής πίεσης και μαγνητικού πεδίου.

Συγκεκριμένα στο πρώτο μέρος παρουσιάζεται το πλήρες σετ των μαγνητο-υδροδυναμικών εξισώσεων, στη διατηρητική τους μορφή, συμπεριλαμβάνοντας τους

κυρίαρχους όρους απωλειών όπως η ηλεκτρική αντίσταση, η θερμική αγωγιμότητα και το ιξώδες (εξισώσεις 3.1-3.13). Το σετ ολοκληρώνεται με τις καταστατικές εξισώσεις της εσωτερικής ενέργειας και της θερμικής πίεσης σε συνάρτηση με τη θερμοκρασία και την πυκνότητα μάζας (εξίσωση 3.14). Οι καταστατικές του ιδανικού αερίου είναι οι πιο απλές που μπορούν να χρησιμοποιηθούν (εξισώσεις 3.15 και 3.16) αλλά αποτελούν ικανοποιητική προσέγγιση μόνο για πολύ αραιό πλάσμα (< ~0.1gr/cm^3), υψηλής πίεσης (> ~10^{8}dyn/cm^2) και θερμοκρασίας (> μερικά eV) ανάλογα φυσικά και με το μέταλλο από το οποίο προέρχεται το πλάσμα. Αυτές οι καταστατικές χρησιμοποιήθηκαν στο μοντέλο X-pinch της πρώτης δημοσίευσης του 2015 [28]. Το επόμενο βήμα ήταν να συμπεριληφθεί ένα πληρέστερο μοντέλο καταστατικών εξισώσεων που να μπορεί να περιγράφει πληρέστερα και ακριβέστερα τη συμπεριφορά της εσωτερικής ενέργειας και της θερμικής πίεσης σε όλες τις τιμές θερμοκρασίας και πυκνότητας μάζας. Παρουσιάζεται αναλυτικά η προσέγγιση MGGB (Mie–Grüneisen–Guggenheim–Barnes approximation) όπου τα δεδομένα από τη βιβλιοθήκη SESAME των εργαστηρίων του LOS-ALAMOS εξελίσσονται μέσω αυτής της προσέγγισης. Το σετ των εξισώσεων 3.17-3.22 των αντίστοιχων ενεργειών και θερμοδυναμικών μεγεθών όπου μπορούν να χρησιμοποιηθούν συναρτήσεις για την εξαγωγή δεδομένων, έχει σαν βάση την ελεύθερη ενέργεια του Helmholtz [30]. Δίνεται μία γραφική απεικόνιση της αρχικής SESAME καταστατικής εξίσωσης της πίεσης μέσω ισόθερμων σε συνάρτηση με την πυκνότητα μάζας για το μέταλλο αλουμίνιο (σχήμα 3.1). Στις γραφικές παραστάσεις αναλύονται και παρουσιάζονται και οι 5 διαφορετικές περιοχές των καταστάσεων της ύλης. Παρόμοιες γραφικές παραστάσεις ισχύουν και για το μέταλλο Βολφράμιο οι οποίες παρουσιάζονται μέσω 24 διαφορετικών ισόθερμων, αλλά με την βελτιωμένη MGGB προσέγγιση, σε συνάρτηση με την πυκνότητα μάζας για την εσωτερική ενέργεια αλλά και για την θερμική πίεση (θερμοκρασίες από 298K έως ~10^{8}K). Αντίστοιχες γραφικές παρουσιάζονται και για τον ξηρό αέρα αφού τα δύο αυτά υλικά είναι τα δύο που χρειάζονται στις προσομοιώσεις και υπάρχουν μέσα στον πειραματικό θάλαμο (σχήμα 3.2). Η MGGB προσέγγιση είναι ιδανική για αλληλεπιδρώντα υλικά που βρίσκονται σε καταστάσεις τοπικής θερμοδυναμικής ισορροπίας (Local Thermodynamic Equilibrium (LTE)) αποφεύγοντας τις προβληματικές ασυνέχειες που παρουσιάζονταν στα αρχικά δεδομένα της SESAME βιβλιοθήκης (σύγκριση εικόνων σχήματος 3.1 και 3.2). Αυτές οι καταστατικές χρησιμοποιούνται από τον PLUTO, για το μέταλλο Βολφράμιο, για όλες τις επόμενες προσομοιώσεις μετά το 2015.

Κατόπιν παρουσιάζεται το μοντέλο της εκπομπής και μεταφοράς ακτινοβολίας για οπτικά αραιά και πυκνά πλάσματα. Τα εμπλεκόμενα φυσικά μεγέθη στη παρουσίαση αυτή είναι ο βαθμός ιονισμού (Z_{eff}) και η σταθερά Λ που αντιπροσωπεύει την πυκνότητα της ακτινοβολούμενης ενέργειας ανά μονάδα χρόνου. Για τα δύο αυτά μεγέθη παρουσιάζονται γραφικά, για το Βολφράμιο και το Άζωτο το κυριότερο συστατικό του αέρα, η εξάρτηση τους από τη θερμοκρασία και την ηλεκτρονιακή πυκνότητα. Τα αριθμητικά δεδομένα προέρχονται από τη βιβλιοθήκη FLYCHK [31].

Στον πίνακα 3.1 γίνεται σύγκριση των δεδομένων αυτών με δύο άλλες μελέτες που χρησιμοποιούν και πειραματικά δεδομένα για θερμοκρασίες από 50 eV έως 100000eV. Η συμφωνία είναι αξιοσημείωτη, αποδεικνύοντας την ορθή επιλογή της βιβλιοθήκης αυτής. Ο PLUTO επομένως χρησιμοποιεί τα αριθμητικά δεδομένα για το Z_{eff} και το Λ του Βολφραμίου και του Αέρα, χρησιμοποιώντας την διαφορική εξίσωση που συνδέει το ρυθμό απωλειών της εσωτερικής ενέργειας με την ηλεκτρονιακή πυκνότητα και το Z_{eff} (εξισώσεις 3.23 και 3.24). Στη συνέχεια παρουσιάζεται μία δεύτερη προσέγγιση για το ρυθμό απωλειών της εσωτερικής ενέργειας μέσω της διαφορικής εξίσωσης που τη συνδέει με τη θερμοκρασία, τον ιονισμό και την ενέργεια επανασύνδεσης (εξισώσεις 3.25-3.26). Παρουσιάζονται δύο διαφορετικές αναλύσεις για τον υπολογισμό των απωλειών χρησιμοποιώντας αρχικά τα δεδομένα του Z_{eff} από το FLYCHK και στη συνέχεια τα δεδομένα του Z_{eff} από το μοντέλο του Thomas-Fermi (εξίσωση 3.27 και πίνακας 3.2). Σε κάθε ανάλυση δείχνεται χωριστά η συνεισφορά της ακτινοβολίας πέδησης (Bremsstrahlung) και της αθροιστικής συνεισφοράς αυτής με την ενέργεια επανασύνδεσης (γραφικές παραστάσεις των σχημάτων 3.5 και 3.6). Αποδεικνύεται με αυτόν τον τρόπο ότι και οι δύο προσεγγίσεις έχουν απόκλιση για τις απώλειες δύο και τρείς τάξεις μεγέθους (ή και περισσότερο) σε σχέση με τα δεδομένα του FLYCHK. Πρέπει επομένως να χρησιμοποιηθεί ένας διορθωτικός πολλαπλασιαστικός παράγοντας για να ληφθούν έμμεσα οι απώλειες λόγω μεταβάσεων από μία στάθμη σε μία άλλη (κάτι που λαμβάνει υπόψη του ο κώδικας FLYCHK). Ο GORGON χρησιμοποιεί το σύστημα αυτών των εξισώσεων με την προσέγγιση Thomas-Fermi, οπότε χρησιμοποιούμε ένα ανάλογο διορθωτικό παράγοντα για όλες τις προσομοιώσεις του κώδικα στη διάταξη καλωδίων Βολφραμίου X-pinch που μελετάμε στη συνέχεια.

Η ανακατανομή της ακτινοβολίας μέσα και έξω από το πλάσμα μέσω απορρόφησης και εκπομπής φωτονίων είναι ο λόγος ύπαρξης του μοντέλου της ακτινοβολίας λόγω μεταφοράς (radiation transport module). Οι αντίστοιχες εξισώσεις 3.28-3.33 που χρησιμοποιούνται στο PLUTO παρουσιάζονται και αναλύονται χρησιμοποιώντας δύο βασικά φυσικά μεγέθη, την επιτάχυνση λόγω ακτινοβολίας (a_{rad}) και την πυκνότητα ενέργειας ακτινοβολίας (E_{rad}). Επίσης χρησιμοποιούνται οι μέσες τιμές των σταθερών αδιαφάνειας του Planck και του Rosseland (Rosseland and Planck mean opacities). Το σύστημα των εξισώσεων 3.34-3.36 χρησιμοποιείται για την εξαγωγή τους. Οι αριθμητικές τιμές για τις δύο αδιαφάνειες για τον ξηρό αέρα δίνονται γραφικά στο σχήμα 3.7 [44] ενώ οι προσεγγιστικές τελικές σχέσεις των δύο σταθερών, για το Βολφράμιο σε συνάρτηση με την πυκνότητα μάζας και τη θερμοκρασία, δίνονται από τις σχέσεις της 3.37 [45]. Το μοντέλο αυτό χρησιμοποιείται από τον PLUTO. Αποδεικνύεται πολύ χρήσιμο στην καλύτερη ανακατανομή της ενέργειας στον κώδικα και του ελέγχου της μη φυσικής αύξησης της θερμοκρασίας και θερμικής πίεσης καθώς και του περιορισμού της μη φυσικής ακτινικής εξάπλωσης του πλάσματος.

Στο δεύτερο μέρος του κεφαλαίου 3 γίνεται αναλυτική παρουσίαση των φυσικών μεγεθών απωλειών και διάχυσης. Συγκεκριμένα αναλύονται τρία φυσικά μεγέθη, η

ηλεκτρική αγωγιμότητα/αντίσταση, η θερμική αγωγιμότητα και το ιξώδες. Ο σκοπός της μελέτης αυτής, όπως προαναφέραμε, είναι να παρουσιάσει παραμετρικές εξισώσεις σύνθεσης για αυτά τα μεγέθη, ώστε να μπορούν να εφαρμοστούν σε οποιαδήποτε διάταξη εργαστηριακού/αστροφυσικού πλάσματος, σε οποιαδήποτε περιοχή θερμικής πίεσης, θερμοκρασίας, πυκνότητας μάζας και μαγνητικού πεδίου. Κάποιες προσεγγίσεις έχουν εισαχθεί ή θα εισαχθούν στον PLUTO ενώ γίνεται συζήτηση και για τις προσεγγίσεις των αντίστοιχων μεγεθών του GORGON. Συγκεκριμένα αναλύονται και απεικονίζονται:

α. Τέσσερις διαφορετικές φυσικές και μαθηματικές προσεγγίσεις για την ηλεκτρική αγωγιμότητα/αντίσταση, δίνοντας όμως παραπλήσια γραφικά αποτελέσματα για μεγάλο εύρος περιοχών θερμοκρασίας και πυκνότητας πλάσματος.

β. Τρείς διαφορετικές προσεγγίσεις για τη θερμική αγωγιμότητα, παρουσιάζοντας γραφικά παρεμφερή αποτελέσματα σε δύο από αυτές.

γ. Μοντέλο εισαγωγής της μήτρας του ιξώδους παρουσιάζοντας δύο διαφορετικές προσεγγίσεις, χρησιμοποιώντας αναλυτικές εξισώσεις και εξισώσεις πολλαπλού τύπου. Παρουσιάζονται γραφικά, σε 3D γραφήματα, ισόθερμες που συσχετίζουν το συντελεστή ιξώδους με το μαγνητικό πεδίο και τη πυκνότητα του πλάσματος για όλο το πιθανό εύρος τιμών.

Ειδικότερα για την ηλεκτρική αγωγιμότητα/αντίσταση η πρωταρχική προσέγγιση που χρησιμοποιήθηκε στα πρώτα μοντέλα ήταν η εξίσωση του Spitzer. Όμως η συγκεκριμένη σχέση δίνει μεγάλες αποκλίσεις από τις πειραματικές τιμές στην περιοχή των υψηλών πυκνοτήτων και χαμηλών θερμοκρασιών όπως προαναφέρθηκε.

Στη πρώτη προσέγγιση της εξαγωγής μίας συνάρτησης πολλαπλού τύπου για την ηλεκτρική αγωγιμότητα τροποποιείται η σχέση Spitzer χρησιμοποιώντας διορθωμένες τιμές για το μέσο βαθμό ιονισμού στις χαμηλές θερμοκρασίες. Ταυτόχρονα χρησιμοποιείται μία συνάρτηση για να προσεγγίσει χωριστά την περιοχή των υψηλών πυκνοτήτων ($\rho<10gr/cm^3$) χαμηλής θερμοκρασίας και μία δεύτερη για πολύ υψηλές πυκνότητες ($10gr/cm^3<\rho<100gr/cm^3$) οποιασδήποτε θερμοκρασίας. Δύο διαφορετικές συναρτήσεις χρησιμοποιούνται για τη στερεή και υγρή φάση. Η εξαγωγή αυτής της πολλαπλής συνάρτησης έγινε χρησιμοποιώντας εργαστηριακά και ημι-εμπειρικά δεδομένα από προηγούμενες εργασίες (εξισώσεις 3.38-3.51). Η σύγκριση της τελικής συνάρτησης πολλαπλού τύπου (εξίσωση 3.57) με τα πειραματικά και ημι-εμπειρικά δεδομένα μέσω γραφημάτων (γραφικές σχήματος 3.18) δίνει πολύ καλή συμφωνία ενώ η τροποποιημένη προσέγγιση του Spitzer είναι ικανοποιητική για υψηλές θερμοκρασίες και αραιά πλάσματα. Αυτή η προσέγγιση είναι χρήσιμη για όποιον μαγνητο-υδροδυναμικό κώδικα χρησιμοποιεί μεγάλο εύρος πυκνοτήτων και θερμοκρασιών χωρίς την ανάγκη χρησιμοποίησης αριθμητικών δεδομένων αλλά μόνο συναρτήσεων. Ακόμα και ο μέσος βαθμός ιονισμού που υπολογίζεται αριθμητικά από τα δεδομένα του FLYCHK, μπορεί να προσεγγιστεί με την αναλυτική συνάρτηση του μοντέλου Thomas-Fermi όπως προαναφέρθηκε.

Στη δεύτερη προσέγγιση της ηλεκτρικής αγωγιμότητας χρησιμοποιείται μία απλή σχέση όπου η διορθωμένη σχέση του Spitzer πολλαπλασιάζεται με ένα διορθωτικό παράγοντα λαμβάνοντας υπόψη την πυκνότητα του πλάσματος στο εργαστηριακό "κενό" (εξίσωση 3.58). Με αυτό τον τρόπο υπάρχει μία ομαλή μετάβαση μεταξύ του κυρίως μεταλλικού πλάσματος του Βολφραμίου και του πολύ αραιού πλάσματος του ατμοσφαιρικού αέρα που θεωρείται το περιβάλλον πολύ αραιό πλάσμα υποβάθρου (low density background plasma or vacuum plasma). Αυτή η προσέγγιση χρησιμοποιήθηκε με επιτυχία στον κώδικα για τη μελέτη της δυναμικής συμπεριφοράς της διάταξης X-pinch και της σύγκρισής της με το πείραμα (εξισώσεις 3.58-3.60) [35].

Στην τρίτη κατά σειρά προσέγγιση χρησιμοποιείται μία γραμμική σχέση δύο όρων για την ηλεκτρική αντίσταση του μεταλλικού πλάσματος. Ο πρώτος όρος περιγράφει την αλληλεπίδραση ιόντων-ηλεκτρονίων και ο δεύτερος την αλληλεπίδραση ουδέτερων ατόμων και ηλεκτρονίων (εξισώσεις 3.61, 3.63 και 3.65-3.67). Η συσχέτιση των πληθυσμών ιόντων-ουδετέρων ατόμων χρησιμοποιεί τη εξίσωση Saha (εξίσωση 3.62). Μία μεγάλη επίσης διαφοροποίηση στις σχέσεις των αντιστάσεων/αγωγιμοτήτων είναι η χρησιμοποίηση του ενεργού κβαντικού λογάριθμου Coulomb (effective quantum Coulomb logarithm), όπως υπολογίζεται από την προσέγγιση Born και το δυναμικό Debye (εξισώσεις 3.64). Με αυτόν τον τρόπο επιτυγχάνεται η εξασφάλιση της θετικής τιμής του λογαρίθμου για όλες τις τιμές θερμοκρασίας και αριθμητικής ηλεκτρονιακής πυκνότητας κάτι που δεν συμβαίνει στις κλασικές σχέσεις του κλασσικού λογαρίθμου όπου χρησιμοποιείται ένα ελάχιστο κατώφλι (~1). Ταυτόχρονα χρησιμοποιώντας την προσέγγιση αυτή του λογαρίθμου, διορθώνεται η υπερεκτίμηση της αγωγιμότητας στις μεγάλες πυκνότητες και χαμηλές θερμοκρασίες (WDM) (γραφικές παραστάσεις του σχήματος 3.19) ενώ παίρνουμε πάλι παρεμφερή αποτελέσματα σε σχέση με την πρώτη προσέγγιση της συνάρτησης πολλαπλού τύπου. Μία όμοια προσέγγιση, ως τελευταία προσθήκη στον PLUTO, χρησιμοποιείται στην τελευταία εργασία προς δημοσίευση [36] με μόνη διαφορά ότι ο αριθμός των ουδετέρων ατόμων σχετίζεται με τον αριθμό των ιόντων μέσω μίας συνάρτησης υπερβολικής εφαπτομένης και όχι με την εξίσωση του Saha (εξίσωση 5.4.8).

Στην τελευταία (τέταρτη) προσέγγιση της ηλεκτρικής αγωγιμότητας χρησιμοποιείται μία αναλυτική εξίσωση που βασίζεται στο μοντέλο του Braginskii [46], εισάγοντας και την επιρροή του μαγνητικού πεδίου σε αυτήν. Η συγκεκριμένη προσέγγιση χρησιμοποιεί πάλι ένα μείγμα ηλεκτρονίων, ιόντων και ουδέτερων ατόμων. Η μίξη εφαρμόζεται όχι πια στις αγωγιμότητες αλλά στις συχνότητες συγκρούσεων, λαμβάνοντας υπόψη την συνεισφορά του ανώμαλου όρου σύγκρουσης με την χαμηλή υβριδική συχνότητα (low hybrid frequency) (εξισώσεις 3.68) [47-49]. Δίνονται δύο διαφορετικά γραφήματα. Το πρώτο χωρίς τη συνεισφορά του ανώμαλου όρου και το δεύτερο με την παρουσία του (σχήματα 3.20 και 3.21-3.22 αντίστοιχα). Χρησιμοποιείται και στις δύο περιπτώσεις η προσέγγιση του κβαντικού λογάριθμου

όπως αναφέρθηκε προηγουμένως. Η απουσία του ανώμαλου όρου δίνει παρεμφερή αποτελέσματα με τις προσεγγίσεις ένα και τρία (κυρίως με την τελευταία). Η παρουσία του ανώμαλου όρου (3D γράφημα 3.21 και 2D 3.22) διαμορφώνει πολύ χαμηλές τιμές της αγωγιμότητας (υψηλές ηλεκτρικής αντίστασης) στις χαμηλές πυκνότητες. Η συμπεριφορά αυτή ενισχύεται με την αύξηση της τιμής του μαγνητικού πεδίου. Με αυτόν τον τρόπο ο κώδικας δημιουργεί υψηλές τιμές της αντίστασης στις περιοχές χαμηλής πυκνότητας, που είναι συνήθως οι περιοχές του κενού, ώστε η μεγάλη αγωγιμότητα, άρα και το ρεύμα να διέρχεται από το κυρίως μεταλλικό πλάσμα. Μία όμοια προσέγγιση με αυτή της τέταρτης χρησιμοποιεί ο GORGON με εξαίρεση τον λογάριθμο Coulomb όπου χρησιμοποιεί την κλασσική και όχι κβαντική προσέγγιση.

Συμπερασματικά η χρησιμοποίηση του κβαντικού λογάριθμου και η γραμμική προσέγγιση των δύο τελευταίων αναλύσεων δίνουν μία ικανοποιητική συμπεριφορά της ηλεκτρικής αγωγιμότητας για όλες τις τιμές των πυκνοτήτων και θερμοκρασιών αποφεύγοντας τη χρήση πολλαπλού τύπου της πρώτης προσέγγισης η οποία δίνει κατά τα άλλα παρεμφερή αποτελέσματα με αυτές τις δύο.

Η θερμική αγωγιμότητα έχει τρείς διαφορετικούς συντελεστές τους $k_{||,}$ $k_{\perp}$ και $k_{x.}$ Οι δύο πρώτοι είναι ο παράλληλος και ο κάθετος αντίστοιχα στο μαγνητικό πεδίο ενώ ο τρίτος είναι κάθετος στο επίπεδο που ορίζουν η βαθμίδα θερμοκρασίας και το μαγνητικό πεδίο. Ορίζονται και οι τρείς ανεξάρτητα για τα ηλεκτρόνια και τα πρωτόνια του πλάσματος δηλαδή μπορούμε να χρησιμοποιήσουμε έξι συνολικά συντελεστές.

Η πιο απλή πρώτη προσέγγιση που μπορεί να χρησιμοποιηθεί εύκολα, περιλαμβάνει μία συνάρτηση διπλού τύπου. Η προσέγγιση Seydel–Fucke για θερμοκρασίες $3695K<T_e<6000K$ και η προσέγγιση μέσω του νόμου Wiedemann-Franz για την παράλληλη ηλεκτρονιακή τιμή για όλες τις υπόλοιπες θερμοκρασίες (εξισώσεις 3.70-3.71). Η γραφική απεικόνιση χρησιμοποιεί την τροποποιημένη εξίσωση του Spitzer και συγκρίνεται με πειραματικά και ημι-εμπειρικά δεδομένα για τις θερμοκρασίες 10000K, 20000K και 40000K με πολύ καλή συμφωνία (γραφήματα σχήματος 3.23). Η έλλειψη πειραματικών δεδομένων για πλάσματα με υψηλότερες θερμοκρασίες επισημαίνεται ενώ ταυτόχρονα υπογραμμίζεται η αξιοπιστία της συγκεκριμένης προσέγγισης μέσω της σύγκρισης με τους ευρέως διαδεδομένους τύπους του Braginskii που δίνουν παρεμφερή αποτελέσματα στη συνέχεια [46].

Η δεύτερη απλή επίσης προσέγγιση, που χρησιμοποιείται συχνά στην αστροφυσική, περιλαμβάνει την παράλληλη συνεισφορά των ηλεκτρονίων του θερμικού συντελεστή και την κάθετη συνιστώσα του που αφορά την συνεισφορά των ιόντων μέσω τροποποιημένων σχέσεων της εξίσωσης Spitzer (εξισώσεις 3.72-3.73). Αυτές είναι και οι κυρίαρχες συνεισφορές όπως εξηγείται στην τρίτη προσέγγιση που περιλαμβάνει και τους έξι όρους.

Στην τρίτη προσέγγιση αναλύονται και οι έξι όροι μέσω της προσέγγισης του μοντέλου του Braginskii [46] (εξισώσεις 3.74-3.82 και στο κεφάλαιο 5 οι εξισώσεις 5.4.13-5.4.14). Ο αρχικός κώδικας PLUTO είχε ενσωματωμένο στο σύστημα των

εξισώσεών του τη παράλληλη και την κάθετη συνεισφορά ηλεκτρονίων και ιόντων αντίστοιχα. Η τρίτη συνιστώσα k_x προστέθηκε στον κώδικα δίνοντας τη δυνατότητα για πληρέστερη περιγραφή του μοντέλου της θερμικής αγωγιμότητας. Ο PLUTO χρησιμοποιεί μαγνητο-υδροδυναμική προσέγγιση ενός ρευστού μη διαχωρίζοντας ανεξάρτητα τη συνεισφορά ιόντων και ηλεκτρονίων. Για το λόγο αυτό χρησιμοποιείται μία γραμμική άθροιση των συνεισφορών από τα ηλεκτρόνια και τα ιόντα για τους όρους της παράλληλης και κάθετης συνιστώσας και μία αφαίρεση των αντίστοιχων συνεισφορών στην συνιστώσα k_x, σύμφωνα με τη μορφή των μαγνητο-υδροδυναμικών εξισώσεων. Ο GORGON χρησιμοποιεί και αυτός την ίδια προσέγγιση κατά Braginskii λαμβάνοντας υπόψη του ξεχωριστά την συνεισφορά από τα ιόντα και τα ηλεκτρόνια. Δεν έχει ενσωματωμένο στο σύστημα των εξισώσεών του τη συνεισφορά της τρίτης συνιστώσας k_x.

Για την παράλληλη συνιστώσα των ηλεκτρονίων γίνεται γραφική μελέτη όπως και με την πρώτη προσέγγιση δίνοντας πάλι ικανοποιητική συμφωνία με το πείραμα (γραφικές παραστάσεις του σχήματος 3.24). Δίνονται 2 διαφορετικές γραφικές, μία με την κλασσική προσέγγιση του λογαρίθμου Coulomb και μία με την κβαντική. Στη δεύτερη περίπτωση βλέπουμε πάλι όμοια συμπεριφορά στις υψηλές πυκνότητες, χαμηλής θερμοκρασίας με αυτήν της ηλεκτρικής αγωγιμότητας όταν λαμβάνεται υπόψη η συνεισφορά του κβαντικού λογάριθμου. Στη περιοχή αυτή των πυκνοτήτων οι ισόθερμες αρχίζουν να συγκλίνουν προς κοινές τιμές ηλεκτρικής ή θερμικής αγωγιμότητας. Ανάλογη συμπεριφορά βλέπουμε και στο ιξώδες του πλάσματος όπως θα δούμε στη συνέχεια.

Το ιξώδες είναι το τελευταίο φυσικό μέγεθος που αναλύεται στο κεφάλαιο 3. Γίνονται δύο διαφορετικές προσεγγίσεις για την εισαγωγή της μήτρας του ιξώδους στις μαγνητο-υδροδυναμικές εξισώσεις, μία βασιζόμενη στην εργασία του Braginskii και άλλη μία βασιζόμενη στην μαγνητο-υδροδυναμική προσέγγιση του Νευτώνειου ρευστού/αερίου. Προτείνονται επίσης και κοινές εξισώσεις των συντελεστών του ιξώδους και για τις δύο προσεγγίσεις (διάγραμμα ροής σχήματος 3.29).

Σε εργαστηριακά και αστροφυσικά πλάσματα μπορούν να χρησιμοποιηθούν και οι 5 μήτρες της εργασίας του Braginskii [46], εισάγοντας 5 ανεξάρτητους συντελεστές για το ιξώδες ν_0, ν_1, ν_2, ν_3 και ν_4 (εξισώσεις 3.83 και 3.85-3.87). Οι συντελεστές αυτοί απλοποιούνται αν θωρήσουμε αμελητέα τη συνεισφορά του μαγνητικού πεδίου (εξισώσεις 3.84). Η πλήρης μήτρα του ιξώδους επομένως περιλαμβάνει τους πέντε όρους Π_0, Π_1, Π_2, Π_3 και Π_4. Ο πρώτος όρος δημιουργεί διαφοροποιήσεις της ταχύτητας κατά μήκος του μαγνητικού πεδίου. Ο δεύτερος και τρίτος όρος αντίστοιχα διαφοροποιεί την ταχύτητα κάθετα στο μαγνητικό πεδίο. Οι δύο τελευταίοι αφορούν τάσεις διάτμησης, κάθετες συνεχώς στην ταχύτητα του πλάσματος, οι οποίες παίζουν πολύ σημαντικό ρόλο σε φαινόμενα μαγνητικής επανασύνδεσης (magnetic reconnection) ή σε πλάσματα συσκευών Tokamak. Δίνονται τρισδιάστατες γραφικές παραστάσεις των ισόθερμων, των συνιστωσών ν_2 και ν_4, σε συνάρτηση με την πυκνότητα και το μαγνητικό πεδίο καθώς και δισδιάστατες γραφικές για σχεδόν

αμαγνήτιστο πλάσμα και πολύ ισχυρά μαγνητισμένο (γραφικές παραστάσεις των 3.26 και 3.27). Προκύπτουν πολύ χρήσιμα συμπεράσματα για την εξάρτηση των συντελεστών από το μαγνητικό πεδίο, τη θερμοκρασία, την πυκνότητα και τη μεταξύ των συντελεστών συσχέτιση.

Στη δεύτερη προσέγγιση, η οποία βρίσκεται ενσωματωμένη στον PLUTO, η μήτρα του ιξώδους περιλαμβάνει δύο όρους, τον ογκομετρικό (bulk) όρο παραμόρφωσης $\mathbf{\Pi_b}$ και τον διατμητικό (shear) όρο $\mathbf{\Pi_s}$ (επιφανειακής παραμόρφωσης) (εξίσωση 3.10). Ο πρώτος όρος δημιουργεί ογκομετρικές παραμορφώσεις συμπίεσης και αποσυμπίεσης, αν θεωρήσουμε το πλάσμα συμπιεστό. Ο δεύτερος είναι ο διατμητικός όρος, που είναι και ο πιο συνηθισμένος.

Δίνονται τρείς διαφορετικές προσεγγίσεις για τους όρους ν_s, με αμελητέα συνεισφορά του μαγνητικού πεδίου ($\mathbf{B\rightarrow 0}$), με τον ένα να χρησιμοποιεί την προσέγγιση του Braginskii και τους άλλους δύο να στηρίζονται στο μοντέλο του Spitzer και της μοριακής δυναμικής προσέγγισης (Spitzer like equilibrium molecular dynamics (MD) approximation) (εξισώσεις 3.100). Ο πρώτος από τους δύο είναι εφαρμόσιμος για σταθερές σύζευξης Γ<10 ενώ ο δεύτερος είναι πολύ γενικότερος και εφαρμόσιμος για σταθερές 0.01<Γ<200. Δίνονται αντίστοιχες γραφικές ισόθερμων σε συνάρτηση με την πυκνότητα για το διατμητικό συντελεστή ν_s και για τις τρείς προσεγγίσεις (γραφικές παραστάσεις σχήματος 3.25). Στην παράσταση της τρίτης προσέγγισης φαίνεται πάλι στην περιοχή των υψηλών πυκνοτήτων η σύγκλιση των ισόθερμων ακριβώς όπως συμβαίνει και στην περίπτωση της ηλεκτρικής και θερμικής αγωγιμότητας (σχήματα 3.18-3.24). Επίσης προτείνονται σχέσεις αν έχουμε ογκομετρικές παραμορφώσεις του πλάσματος ($\nu_b\neq 0$) (εξισώσεις 3.101).

Στη συνέχεια προτείνονται εξισώσεις για το ν_s και ν_b για μικρές και μεγάλες τιμές του μαγνητικού πεδίου. Με αυτόν τον τρόπο σε αυτή την απλούστερη προσέγγιση των δύο όρων των μητρών του ιξώδους, δεν αγνοούμε τη συνεισφορά του μαγνητικού πεδίου, η οποία είναι εμφανής στη περιοχή των χαμηλών πυκνοτήτων (γραφικές παραστάσεις των σχημάτων 3.26 και 3.27) (εξισώσεις 3.84, 3.100 και 3.102).

Τελικά δίνεται ένα παράδειγμα εφαρμογής των πέντε μητρών του ιξώδους παρουσία μαγνητικού πεδίου, για ένα μονό καλώδιο Z-pinch κατά μήκος του άξονα Z (εξισώσεις 3.106-3.109).

Ο PLUTO θα τροποποιηθεί στο άμεσο μέλλον ώστε να μπορεί να συμπεριλάβει και τις πέντε μήτρες του ιξώδους αλλά και τη μοριακή δυναμική προσέγγιση (MD), βοηθώντας τη δυνατότητα εκκίνησης της προσομοίωσης από πολύ αρχικές χρονικές στιγμές πειράματος (συνθήκες "κρύου ξεκινήματος" (cold start conditions)).

Στο κεφάλαιο 4 περιγράφεται αναλυτικά ο μαγνητο-υδροδυναμικός κώδικας PLUTO. Αναλύεται και παρουσιάζεται όλη η αριθμητική, φυσική/μαθηματική προσέγγιση καθώς και όλες οι αλλαγές που έπρεπε να γίνουν στο ήδη υπάρχον σύστημα του κώδικα ώστε να είναι ικανός να περιγράφει με επιτυχία εργαστηριακά πλάσματα μεταλλικών διατάξεων μονών ή πολλών καλωδίων. Επίσης αναλύεται και εξηγείται ο τρόπος που συσχετίζονται μαθηματικά, μέσω πινάκων μετατοπίσεων και

στροφών, ο τρόπος γραφής της πυκνότητας, της πίεσης και του μαγνητικού πεδίου για οποιαδήποτε γεωμετρική κατανομή τους (εξισώσεις 4.1-4.20). Με αυτόν τον τρόπο έχουμε πάντα τη σωστή αρχική κατανομή αυτών των μεγεθών στον κώδικα αρκεί να υπάρχει και η κατάλληλη αρχική διακριτοποίηση στο αντίστοιχο μοντέλο.

Δίνονται συγκεκριμένα παραδείγματα εφαρμογής των συγκεκριμένων μετασχηματισμών και μαθηματικών σχέσεων, για ένα μονό καλώδιο Z-pinch, μία διάταξη καλωδίων X-pinch, μία διάταξη πολλών καλωδίων Z-pinch (Z-pinch array) και μία κωνική διάταξη πολλών καλωδίων Z-pinch (conical wire array) (εξισώσεις 4.21-4.35). Με αυτόν τον τρόπο ο χρήστης μπορεί να εισάγει στον κώδικα την ακριβή γεωμετρική δομή του πλάσματος και του μαγνητικού πεδίου στις αρχικές συνθήκες της προσομοίωσης.

Δύο συγκεκριμένα παραδείγματα προσομοίωσης παρουσιάζονται ως εφαρμογή των παραπάνω. Το πρώτο αφορά μία διάταξη X-pinch, δύο καλωδίων Βολφραμίου, με αρχικές συνθήκες "κρύου" ξεκινήματος (χαμηλής αρχικής θερμοκρασίας πλάσματος και εφαπτόμενης διάταξης των καλωδίων στη κεντρική περιοχή). Η αρχική χρονική εξέλιξη της προσομοίωσης έδειξε μεταφορά στροφορμής από το κύριο κεντρικό κομμάτι της διάταξης προς τα παραγόμενα jet, θυμίζοντας αντίστοιχες συμπεριφορές σε αστροφυσικά πλάσματα! Μία δεύτερη διάταξη εφαρμογής του μαθηματικού μοντέλου εισαγωγής αφορά ένα σχηματισμό Z-array τεσσάρων καλωδίων Βολφραμίου δίνοντας επίσης παρεμφερή προκαταρκτικά αποτελέσματα με άλλα πειράματα και προσομοιώσεις διεθνών αντίστοιχων επιστημονικών εργασιών.

Στη τελευταίο μέρος του κεφαλαίου παρουσιάζονται και αναλύονται επιγραμματικά όλα τα εργαλεία του PLUTO που είναι χρήσιμα για τις προσομοιώσεις των πειραματικών διατάξεων της διατριβής. Συγκεκριμένα αναλύονται:

α. Η επιλογή της διακριτοποίησης του πλέγματος και η επιλογή του συστήματος συντεταγμένων.

β. Η πολύ σημαντική επιλογή του επιλύτη Riemann για την ακριβέστερη επίλυση και την απόσβεση των μη γραμμικών κυμάτων κατά τη διάρκεια της υπολογιστικής προσομοίωσης.

γ . Το σχέδιο ανακατασκευής (reconstruction scheme) το οποίο κατευθύνει τη χωρική σειρά υπολογισμών κατά την εκτέλεση της προσομοίωσης.

δ. Το σχέδιο χρονικού βηματισμού (time stepping scheme) που καθορίζει το πόσο μικρό ή μεγάλο χρονικά θα είναι κάθε υπολογιστικό βήμα. Παρουσιάζονται οι επιμέρους αλγόριθμοι χρονικού βηματισμού, ο αριθμός Courant (Courant-Friedrichs-Lewy (CFL) number) και ο τρόπος επιλογής της αριθμητικής ολοκλήρωσης των παραβολικών όρων διάχυσης.

ε. Το σχέδιο αριθμητικής ικανοποίησης του νόμου του Gauss στο μαγνητισμό **($\nabla \cdot \mathbf{B} = 0$).**

στ. Η τεχνική της Ntracer-passive scalar multi-material διαδικασίας η οποία βοηθάει στον έλεγχο μη φυσικών μεταβολών (π.χ. απότομη αύξηση της θερμοκρασίας και μη

φυσική διάχυση του μαγνητικού πεδίου και ηλεκτρικού ρεύματος) όταν η προσομοίωση περιλαμβάνει παραπάνω από ένα υλικά.

ζ. Οι συνοριακές συνθήκες (boundary conditions) που είναι από τα πιο σημαντικά κομμάτια των προσομοιώσεων και ίσως από τα δυσκολότερα για την ομαλή και φυσική εξέλιξή τους.

Για όλα τα παραπάνω παρουσιάζεται και προτείνεται η καλύτερη/καλύτερες επιλογές που θα μπορούσε να έχει ο χρήστης για οποιαδήποτε προσομοίωση αφορά διατάξεις Z-pinch μονού ή πολλών καλωδίων και για διατάξεις X-pinch. Δίνεται επίσης ιδιαίτερη έμφαση στην επιλογή των συνοριακών συνθηκών στα όρια του υπολογιστικού κουτιού και στα εσωτερικά όρια. Η επιλογή των εσωτερικών ορίων δίνει τη δυνατότητα απενεργοποίησης της επίλυσης (με εξαίρεση το μαγνητικό πεδίο) στην περιοχή του πολύ αραιού πλάσματος του κενού, αν κρίνεται απαραίτητο από τις συνθήκες του φυσικού προβλήματος, δίνοντας ένα μεγάλο υπολογιστικό πλεονέκτημα για επιλογή καλύτερης διακριτοποίησης και περιορισμού του υπολογιστικού κουτιού.

Β3. Γ μέρος-Κεφάλαιο 5

Τα αποτελέσματα των προσομοιώσεων του PLUTO και η αξιολόγησή τους με βάση το πείραμα και ένα δεύτερο κώδικα τον GORGON, είναι το αντικείμενο του τελευταίου κεφαλαίου 5 το οποίο χρησιμοποιεί και τα δημοσιευμένα αποτελέσματα για την πραγματοποίηση της διατριβής. Αναλυτικότερα:

i. Στην ενότητα 5.1 παρουσιάζεται αναλυτικά η πειραματική διάταξη των δύο καλωδίων Βολφραμίου που χρησιμοποιείται για την αξιολόγηση των υπολογιστικών προσομοιώσεων στις επόμενες ενότητες. Επίσης εξηγούνται οι τεχνικές που χρησιμοποιήθηκαν για τον υπολογισμό της επιφανειακής πυκνότητας του πλάσματος και τον τρόπο αξιολόγησης των σκιαγραφικών εικόνων και εικόνων ιντερφερομετρίας.

ii. Στην ενότητα 5.2 ένα 1/4 χωρικό μοντέλο Z-pinch, μονού καλωδίου Βολφραμίου, μελετάται. Η μοντελοποίηση της διεπιφάνειας μεταξύ πλάσματος και κενού (αραιό πλάσμα αέρα) βασίζεται σε 4 διαφορετικές προσεγγίσεις και δύο διαφορετικούς επιλύτες. Γίνεται η τελική αξιολόγηση και η κατάληξη σε ένα συγκεκριμένο συνδυασμό επιλύτη και προσέγγισης (εικόνες των σχημάτων 5.2.2-5.2.5). Επίσης διερευνάται η συνεισφορά της ακτινοβολίας μέσω μεταφοράς όπου αποδεικνύεται πολύ σημαντική για την καλύτερη αναμενόμενη χωροχρονική εξέλιξη του πλάσματος (εικόνες του σχήματος 5.2.6) [33,34].

iii. Στην 5.3 ενότητα ένα 1/16 χωρικό μοντέλο X-pinch διπλού καλωδίου Βολφραμίου για γωνία 100^{o} παρουσιάζεται σε σύγκριση με το πείραμα. Ο χώρο-χρονικός σχηματισμός του jet και η εξέλιξή του παρουσιάζεται και αναλύεται. Η επιφανειακή πυκνότητα της μάζας του μοντέλου συγκρίνεται με την αντίστοιχη του πειράματος εμφανίζοντας αξιοσημείωτη συμφωνία (εικόνες των σχημάτων 5.3.2-5.3.4). Ο μηχανισμός παραγωγής του jet αναλύεται παρουσιάζονται οι αντίστοιχες υπερηχητικές ταχύτητες (Mach~6) και επεξηγείται η επιρροή των εμφανιζόμενων

δυνάμεων Laplace και του μηχανισμού μεταφοράς μάζας μέσω της αντίστοιχης πυκνότητας ορμής (εικόνες των σχημάτων 5.3.5, 5.3.6) [35].

iv. Στην 5.4 υποενότητα χρησιμοποιούνται ο GORGON και ο PLUTO για να προσομοιώσουν διάταξη X-pinch καλωδίων Βολφραμίου με μικρότερη γωνία (50^o). Το φυσικό και αριθμητικό μοντέλο αναλύεται και συγκρίνεται για τους δύο κώδικες (εικόνες του σχήματος 5.4.2). Έξι διαφορετικές παραλλαγές του μοντέλου παρουσιάζονται σε μία συγκεκριμένη χρονική στιγμή για τον PLUTO (εικόνες του σχήματος 5.4.3 και πίνακας 5.4.1). Οι διαφοροποιήσεις αφορούν την μοντελοποίηση της θερμικής και ηλεκτρικής αγωγιμότητας, δίνοντας χρήσιμες πληροφορίες για τον τρόπο που επηρεάζουν την χώρο-χρονική εξέλιξη του μοντέλου [36].

v. Στην τελευταία ενότητα γίνεται μία αναλυτική παρουσίαση των φυσικών παραμέτρων και των αδιάστατων φυσικών μεταβλητών που αφορούν την υπό κλίμακα μελέτη (εξισώσεις 5.5.1-5.5.3) των παραγόμενων πιδάκων πλάσματος και τη συσχέτισή τους με αντίστοιχους αστροφυσικούς από Νεαρά Αστρικά Αντικείμενα. Αρκετοί αδιάστατοι αριθμοί αποδεικνύεται ότι είναι κοντά και στις δύο προσεγγίσεις (εξισώσεις 5.5.3). Συγκεκριμένα παρουσιάζονται και αναλύονται με εικόνες και γραφικά:

α. Ο αριθμός Mach (M), ο γρήγορος και αργός μαγνητο-ηχητικός (M_f/Ms), ο αριθμός Alfvén (M_A) και οι αντίστοιχες ταχύτητες (εικόνες των σχημάτων 5.5.1, 5.5.2).

β. Ο αριθμός Reynolds (R_e) και ο μαγνητικός (R_m) αντίστοιχος (εικόνες των σχημάτων 5.5.3, 5.5.4).

γ. Ο αριθμός Peclet (P_e) (εικόνες των σχημάτων 5.5.5, 5.5.6).

δ. Η παράμετρος χ (cooling parameter) και το πλάσμα β (εικόνες των σχημάτων 5.5.8, 5.5.9).

ε. Η παράμετρος τοπικότητας (localization parameter δ) (εικόνες του σχήματος 5.5.10).

Τα αποτελέσματα της ανάλυσης των παραπάνω εικόνων και γραφημάτων παρουσιάζονται στο πίνακα 5.5.1. Η ανάλυση αυτή δίνει κοντινά αποτελέσματα με άλλες εργαστηριακές αστροφυσικές μελέτες [50-52]. Η αντιστοίχηση κλίμακας δίνει μερικές δεκάδες ns εργαστηρίου να αντιστοιχούν σε μερικά χρόνια των αστροφυσικών jet, μερικά mGauss διαστημικών μαγνητικών πεδίων σε δεκάδες χιλιάδες του εργαστηρίου και μερικά mm εργαστηριακού πλάσματος σε ~10AU αστροφυσικού.

Γ. Μελλοντικές προοπτικές

Οι προοπτικές ανάπτυξης, περαιτέρω εφαρμογής και βελτίωσης για το άμεσο μέλλον είναι:

- Εισαγωγή στον PLUTO, με όμοιο τρόπο της αντίστοιχης του Βολφραμίου και άλλων μεταλλικών υλικών όπως το Αλουμίνιο, ο Χαλκός και ο Μόλυβδος. Με αυτόν τον τρόπο θα γίνει ο κώδικας πιο ευέλικτος και θα μπορεί να περιγράψει και άλλα εργαστηριακά πλάσματα όπως επίσης και να προσομοιώσει με καλύτερο τρόπο εργαστηριακά αστροφυσικά μοντέλα.

- Εισαγωγή του πλήρη τένσορα του ιξώδους ώστε να μοντελοποιηθούν καλύτερα οι διατμητικές τάσεις για να μπορεί το πλάσμα να ξεκινάει από πολύ αρχικές χρονικές στιγμές, σχεδόν στη φάση της αρχικής μεταλλικής διάταξης με ταυτόχρονη συνύπαρξη υγρού, αερίου και πλάσματος.
- Οι δύο κώδικες (GORGON και PLUTO) μπορούν να χρησιμοποιηθούν ταυτόχρονα αλλά και ανεξάρτητα μεταξύ τους ώστε να περιγράψουν όλα τα αντίστοιχα πειράματα διατάξεων Z και X-pinch του IPPL.
- Και οι δύο κώδικες μπορούν να χρησιμοποιηθούν σε διατάξεις X-pinch πολλών καλωδίων ώστε να μπορέσουν να μελετήσουν εργαστηριακά jet που θα προσομοιώνουν αντίστοιχα αστροφυσικά έχοντας αρκετές ομοιότητες με διατάξεις κωνικών Z-pinch arrays.

ΑΝΑΦΟΡΕΣ

[1] F. N. Beg et al., "Jet Formation and Current Transfer in *X*-Pinches**",** IEEE TRANSACTIONS ON PLASMA SCIENCE, VOL. 34, NO. 5, OCTOBER 2006. (GORGON).

[2] William Neal and Christopher Garasi, "High Fidelity Studies of Exploding Foil Initiator Bridges, Part 3: ALEGRA MHD simulations", AIP Conf. Proc. 1793, 080008-1–080008-5. (ALEGRA Eulerian mesh)

[3] E. Love, M. K. Wong, "Lagrangian Continuum Dynamics in ALEGRA", SAND2007-8104 Unlimited Release Printed December 2007. (ALEGRA Lagrangian mesh)

[4] Allen C. Robinson , Christopher J. Garasi "Three-dimensional z-pinch wire array modeling with ALEGRA-HEDP", *Computer Physics Communications,* 164 (2004), pp. 408–413. (ALEGRA)

[5] Robinson AC et al. 2008, "ALEGRA: An Arbitrary Lagrangian-Eulerian Multimaterial, Multiphysics Code", in 46th AIAA Aerospace Sciences Meeting and Exhibit, Reno, Nevada. (ALEGRA FULL ANALYSIS)

[6]A. C. Robinson, J.H.J. Niederhaus, V.G.Weirs and E. Love, "Arbitrary Lagrangian–Eulerian 3D ideal MHD algorithms", INTERNATIONAL JOURNAL FOR NUMERICAL METHODS IN FLUIDS, Int. J. Numer. Meth. Fluids 2011; **65**:1438–1450. (LAGRANGIAN-EULERIAN ALEGRA)

[7] Derek Mariscal et al., "Investigation of Current Transport in 2×2 Wire Array Plasmas, IEEE TRANSACTIONS ON PLASMA SCIENCE, VOL. 43, NO. 8, AUGUST 2015. (GORGON)

[8] Matteo Bocchi et al., "Numerical simulations of Z-pinch experiments to create supersonic differentially-rotating plasma flows", High Energy Density Physics 9 (2013) 108-111. (GORGON)

[9] G. F. Swadling et al., "Oblique shock structures formed during the ablation phase of aluminium wire array z-pinches", PHYSICS OF PLASMAS 20, 022705 (2013). (GORGON)

[10] C.A. Jennings et al., "3D Resistive, Radiative MHD Modeling of Z-pinches", American Institute of Physics 808, 57 (2006); doi: 10.1063/1.2159319. (GORGON)

[11] G W Collins IV et al , "Effect of the global to local magnetic field ratio on the ablation modulations on X-pinches driven by 80 kA peak current", New Journal of Physics 14 (2012) 043021. (GORGON)

[12] F. Suzuki-Vidal et al., "Interaction of radiatively cooled plasma jets with neutral gases for laboratory astrophysics studies", High Energy Density Physics 9 (2013) 141-147. (GORGON)

[13] F Suzuki-Vidal et al., "Laboratory astrophysics experiments studying hydrodynamic and magnetically-driven plasma jets", Journal of Physics: Conference Series **370** (2012) 012002. (GORGON)

[14] J P Chittenden *et al* 2004 *Plasma Phys. Control. Fusion* **46** B457. (GORGON)

[15] B. Jones et al, "Doppler measurement of implosion velocity in fast *Z*-pinch x-ray sources", PHYSICAL REVIEW E **84**, 056408 (2011). (GORGON)

[16] Jun Huang et al., "Numerical investigation on the implosion dynamics of wire-array Z-pinches in (r,θ) geometry", PHYSICS OF PLASMAS 19, 062701 (2012). (ZEUS CODE)

[17] P. Tzeferacos et al., "FLASH magnetohydrodynamic simulations of shock-generated magnetic field experiments", High Energy Density Physics 8 (2012) 322-328. (FLASH- Noh Z pinch)
[18]A. L. Velikovich et al., "Exact self-similar solutions for the magnetized Noh Z pinch problem", PHYSICS OF PLASMAS 19, 012707 (2012). (ATHENA-MACH2)
[19] R. Ramis J. Meyer-ter-Vehn, J. Ramirez, "MULTI2D – a computer code for two-dimensional radiation hydrodynamics", Computer Physics Communications 180 (2009) 977–994. (MULTI 2D HYDRODYNAMIC ORIGINAL FORM)
[20] Fuyuan Wu, Rafael Ramis, Zhenghong Li , "A conservative MHD scheme on unstructured Lagrangian grids for Z-pinch hydrodynamic simulations" , Journal of Computational Physics, Volume 357, 15 March 2018, pp. 206-229 (2018). (MULTI 2D HYDRODYNAMIC, IMPLEMENTATION OF MHD FORM)
[21] Fuyuan Wu et al., "Numerical studies on the radiation uniformity of Z-pinch dynamic hohlraum",. Matter and Radiation at Extremes 3 (2018) 248-255 (MULTI2D WITH MHD SHEME)
[22] Frank J. Wessel et al., "Fusion in a Staged *Z*-Pinch", IEEE TRANSACTIONS ON PLASMA SCIENCE, VOL. 43, NO. 8, AUGUST 2015. (MACH2 2-1/2 D)
[23] Alexey S. Boldarev et al., "OBJECT-ORIENTED CODE MARPLE3D: SIMULATIONS OF RADIATIVE HYDRODYNAMIC/MHD EFFECTS AT HIGH-PERFORMANCE COMPUTER SYSTEMS", European Congress on Computational Methods in Applied Sciences and Engineering (ECCOMAS 2012) 7007-7027. (MARPLE 3D)
[24] Ding Ning et al., "Simulation Studies of the Wire-Array Z-Pinch Implosions", 2013 IEEE 25th Symposium on Fusion Engineering (SOFE),13846232. (MARED)
[25] N. Ding et al., "Theoretical and Numerical Research of Wire Array Z-pinch and Dynamic Hohlraum in the IAPCM", Matter and Radiation at Extremes ,Volume 1, Issue 3, May 2016, 135-152. (MARED)]
[26] "PLUTO: A Numerical Code for Computational Astrophysics" Mignone et al., The Astrophysical Journal Supplement Series, Volume 170, Issue 1, pp. 228-242
[27] http://plutocode.ph.unito.it/
[28] **G. Koundourakis et al,** "Experimental and numerical investigation of the plasma dynamics and jet formation in low current table-top X-pinch plasma devices", Proceedings of the SCinTE 2015, VOL.3, 19-22.
[29] hpc.grnet.gr
[30] Kashiwa, B. A. The MGGB Equation-of-State for Multifield Applications: A Numerical Recipe for Analytic Expression of Sesame EOS Data, LA-1442 Issued: September 2010. http://www.doe.gov/bridge.
[31] Tungsten Charge State Distribution by FLYCHK NLTE Kinetics Calculation at NIST by International Atomic Energy Agency- Atomic Molecular Data Services provided by the Nuclear Data Section.
[32] Kolb, S.M., Stute, M. Kley, W. and A. Mignone (2013), "Radiation hydrodynamics integrated in the PLUTO code", *Astronomy and Astrophysics*, Vol. 559, pp. A80.
[33] **A. Skoulakis-G. Koundourakis et al**, 2018 9th GRACM International Congress on Computational Mechanics pp 294.
[34] **G. Koundourakis et al**, 2018, Computational study of plasma dynamic evolution produced by low current table-top pinch plasma devic.es *ECLIM Abstract book* pp 118.
[35] **G. Koundourakis et al**, "A numerical study on laboratory plasma dynamics validated by low current X-pinch experiments", Plasma Phys. Control. Fusion **62** (2020) 125012 (14pp)/ https://iopscience.iop.org/article/10.1088/1361-6587/abbebf
[36] **A. Skoulakis-G. Koundourakis et al**, " High performance simulations of a single X-pinch", Plasma Phys. Control. Fusion **64** (2022) 025003 (11pp).
[37] J. P. (HANS) GOEDBLOED AND STEFAAN POEDTS, "PRINCIPLES OF MAGNETO-HYDRODYNAMICS with Applications to Laboratory and Astrophysical Plasmas" , Cambridge University Press 2004, pg .74-77.
[38] E Kaselouris et al, "Preliminary investigation on the use of low current pulsed power Z-pinch plasma devices for the study of early stage plasma instabilities", Plasma Phys. Control. Fusion 60 (2018) 014031 (8pp).

[39] E. Kaselouris et al, "The influence of the solid to plasma phase transition on the generation of plasma instabilities", NATURE COMMUNICATIONS | DOI: 10.1038/s41467-017-02000-6.
[40] E Kaselouris, "Study of matter behavior dynamics governed by the interaction with laser pulses and external strong currents", PhD thesis TECHNICAL UNIVERSITY OF CRETE SCHOOL OF PRODUCTION ENGINEERING & MANAGEMENT.
[41] J. P. Chittenden et al, "Structural Evolution and Formation of High-Pressure Plasmas in *X* Pinches", PRL **98,** 025003 (2007).
[42] S. A. Pikuz et al, "X-Pinch. Part I", Plasma Physics Reports, 2015, Vol. 41, No. 4, pp. 291–342.
[43] S. A. Pikuz et al, "X-Pinch. Part II, "Plasma Physics Reports, 2015, Vol. 41, No. 6, pp. 445–491.
[44] TOPS Opacities/Opacities of mixtures (calculated by TOPS using ATOMIC or LEDCOP elemental opacities) https://aphysics2.lanl.gov.
[45] G. D. TSAKIRIS and K. EIDMANN, "AN APPROXIMATE METHOD FOR CALCULATING PLANCK AND ROSSELAND MEAN OPACITIES IN HOT, DENSE PLASMAS", J. Quant. Spectrosc. Radiat. Transfer Vol. 38, No. 5, pp. 353-368, 1987.
[46] S.I Braginskii , "Transport processes in a plasma", Reviews of Plasma Physics, Volume 1, 206-311 (1965).
[47] J. P. Chittenden, "The effect of lower hybrid instabilities on plasma confinement in fiber Z pinches", Physics of Plasmas **2**, 1242 (1995); doi: 10.1063/1.871401.
[48] J. P. Chittenden, "Structural Evolution and Formation of High-Pressure Plasmas in *X* Pinches", PRL **98,** 025003 (2007).
[49] J. P. Chittenden et al, "Plasma formation in metallic wire *Z* pinches", PHYSICAL REVIEW E VOLUME 61, NUMBER 4 APRIL 2000.
[50] Andrea Ciardi, "Laboratory Studies of Astrophysical Jets", Lect. Notes Phys. **793**, 31–50 (2010).
[51] G. Revet et al, "Laboratory disruption of scaled astrophysical outflows by a misaligned magnetic field", NATURE COMMUNICATIONS | (2021) 12:762 | https://doi.org/10.1038/s41467-021-20917-x.
[52] S. V. Lebedev et al, "LABORATORY ASTROPHYSICS AND COLLIMATED STELLAR OUTFLOWS: THE PRODUCTION OF RADIATIVELY COOLED HYPERSONIC PLASMA JETS", THE ASTROPHYSICAL JOURNAL, 564:113-119, 2002 January 1.

CHAPTER 1

INTRODUCTION

1.1 Motivation for this dissertation

If we look high above in the clear night sky we can see approximately, from the north hemisphere, 3000 "plasma balls" glowing with their flickering light. We call them stars with plasma as their main material. Plasma is often called “the fourth state of matter,” along with solid, liquid and gas. It is superheated matter – so hot that the electrons are ripped away from the atoms forming an ionized gas but could also have a potential collective behavior of any ordinary fluid. It comprises over 96% of the visible matter in the universe. In the night sky, plasma glows in the form of stars, nebulas, and even the auroras which sometimes ripple above the north and south poles. Those lightning formations are plasma and so are the neon signs of our cities and our life-giving sun, the closest star to this planet. Those wonders always made me curious and finally ignited a "plasma spark" in my mind for further investigation.

Since so much of the universe is made of plasma, its behavior and properties are of intense interest to scientists from various disciplines. For example, researchers have used the properties of plasma as a charged gas to confine it with magnetic fields and to heat it to temperatures hotter than the core of the sun aiming to Inertial Confinement Fusion (ICF) application. Over the last decades, plasma devices have been used to study physics phenomena such as: fusion, laboratory astrophysics, x-ray spectroscopy, radiation-plasma interaction, MHD instabilities study. The study of plasma dynamics concerns a lot of interacting physics variables such as plasma density, temperature, ionization state, thermal pressure, magnetic pressure, internal energy and radiation energy.

The initial motivation for this thesis was enhanced by the aforementioned potentiality and the vast plasma applications. In the 21st century, experiments on pulsed power plasma facilities as well as with high-power lasers have been executed for studying astrophysical phenomena in the laboratory, providing promising results. The study focuses especially on the jet formation of Young Stellar Objects (YSOs), the interaction with the interstellar medium and their knotted Herbig-Haro (HH) structure formation (figure 2.10 Chapter 2) [1-18]. The exact spatiotemporal formation mechanisms of these jets and their interaction with the magnetic field and the interstellar winds are under ongoing research via both experiments and simulations [6-14].

The inspiration for this thesis is associated with the existence of pulsed power plasma devises at the Institute for Plasma Physics and Lasers (IPPL) of the Hellenic Mediterranean University at Tria Monastiria in Rethymno [19] along with the collaboration IPPL with the Astrophysics department of the National and Kapodistrian University of Athens [20]. Furthermore, watching dedicated talks and having conversations with leading professors of IPPL about the “Fundamental Science Program ” of the ESFRI research infrastructure HiPER, inspired me with extra motivation to engage in plasma physics research [19,21]. The laser- produced fusion is an artificial way to achieve in a micro-scale the same physical procedure which takes place at the stars cores. These are still fascinating subjects and current research areas.

The main research fields of IPPL are: i. High Power Laser Matter Interactions, ii. Plasma Science & Technology, iii. Numerical Modeling & Simulations. A part of the experiments that are carried out concerns the use of table-top Z and X-pinch pulsed powered plasma devises (figure 1.1) for plasma physics studies. The phase transition from solid to plasma is priority research at IPPL. Valuable assets to this study for each phase transition are the numerical codes [19,22-25].

For a Z-pinch single wire configuration, numerical simulations based on the Finite Element Method (FEM), combined with Finite Volume Method (FVM) fluid simulations were developed to provide valuable insights for important parameters such as temperature, density and expansion rate of the exploded wire material from solid to plasma phase. The initiation of Magneto-Hydro-Dynamic (MHD) instabilities in the plasma phase and the influence of the thermo-elasto-plastic regime on their creation were investigated using the original 4.2 version of PLUTO MHD code [22-25]. The successful description and evaluation attained through the experiment, of the matter phase transition and the instabilities origin and growth rate, are a strong indication of the need of the transition phase multi-physics simulation research. Furthermore the MHD numerical schemes and simulations could give valuable information for the final stages of the matter behavior, ending the matter evolution study. The same study of the Z-pinch wire could be expanded to the X-pinch and other plasma configurations (i.e. for ICF studies or laser produced plasmas) which are still a very active scientific research field.

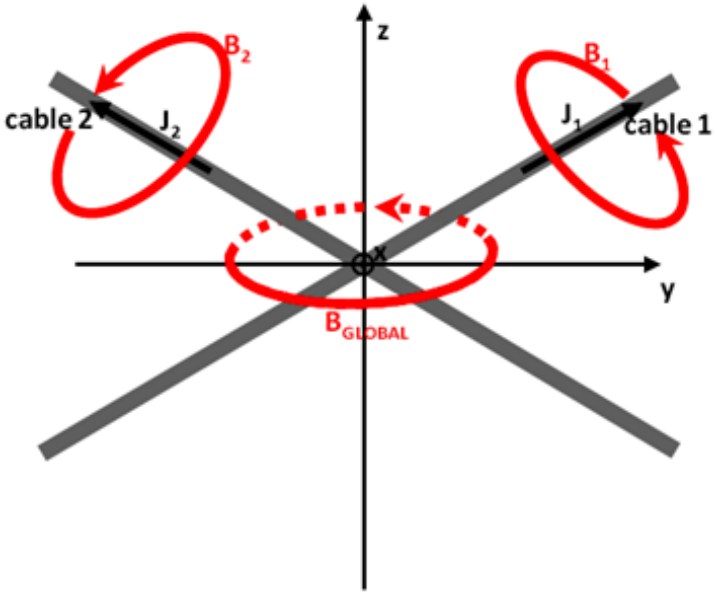

Figure 1.1: *Presentation of the yz level slice of the Global coordinate system and the schematic depiction of the plasma cylinders slices and the magnetic field of a two wire X-pinch configuration.*

In an X-pinch discharge, a large current is pulsed through the two wires, which are arranged in the form of an 'X' between the electrodes. Initially, work on X pinches was concentrated upon their development as versatile laboratory radiographic tool. The micrometer scale source size, the keV photon range and the short 10–100 ps burst duration make the X pinch an ideal source for point-projection radiography of rapidly evolving objects, like laboratory plasmas [26-29], biological samples with a much finer resolution than any ordinary radiography [29-31,32]. Furthermore, the small size and predictable location of the radiation source(s) within the X-pinch make it attractive for applications

such as x-ray backlighting [32] and microlithography [33,34]. This intense burst of x ray comes from plasma with material densities close to solid (or even beyond), electron densities up to ~10^{22}-10^{23}e/cm^3 and electron temperatures in the hundreds of eV to keV range. On the contrary, the surrounding corona plasma has many order of magnitude lower densities while the cold wire core can have till later simulation/experimental times, temperatures only of a few eV or even less [35]. The X-pinch geometry is essentially three-dimensional and as a result, in order to accurately describe the plasma evolution, 3D MHD modeling should be used resulting to computational demanding models.

Interest in the plasma jets formation was increased when their applicability to those observed in astrophysics was realized [26,36,37]. Correlation and scaling to large scale astrophysical plasma jets have been investigated in the past [36,37] but mainly for other large scale infrastructures like Z-pinch machines [15-17,38-40]. The scaling factors and all the relevant physics numbers and parameters can be estimated for a low current X-pinch configuration, investigating any correlation to the YSOs and HHs objects jets.

The plasma numerical/simulation study of the very small (millimeter scale) laboratory sizes of an X-pinch configuration and the astrophysical scaling to hundreds of astronomical units (AU) for an YSO jet, where someone needs a MHD computational scheme, functional for every density, temperature, magnetic field and pressure, was the primary goal of this dissertation.

1.2 Simulation models of MHD laboratory/astrophysical numerical codes

The study of plasma generation and evolution is a complex multiphysics problem. Such problems demand the development of advanced computational models and simulation schemes to provide insights to the experiments. In the 21st century a lot of codes were developed and evolved describing, during this evolution process, different physical problems than their original design [26,41-64]. Purely Eulerian grid codes like GORGON [15-17,26,46-54] or purely Lagrangian like MULTI-2D [58-60] or Arbitrary Lagrangian Eulerian (ALE) codes like ALEGRA [41-45] and MACH2 [57,61] are capable of describing astrophysical and laboratory plasmas. Some of them, like MULTI-2D , begun as hydrodynamic codes and lately adopted MHD schemes with radiation transport and other dissipative effects aimed to describe Inertial Confinement Fusion (ICF) models [58-59]. Even purely astrophysical codes like ATHENA or ZEUS and originally astrophysically developed like FLASH were evaluated and tested on the Noh Z-Pinch problem or on investigating the implosion dynamics of wire-array Z-pinches [55-57].

Specifically the GORGON 3D resistive Eulerian MHD code has been used for MHD plasma applications such as laser-produced magnetized jets [1,16,18,65], Z and X-pinch wire configurations [26,27,36,50], Z-pinch wire arrays [6,8,9,30,31,54], conical arrays, radial wire arrays and foils that create magnetically driven outflows, which are studied in laboratory astrophysics experiments mainly for YSO's and HH jets [1,15-18,51-53]. The flexibility and the wide range applicability are the main reasons why we use this code as a supplementary evaluation tool along with the main code of this dissertation, PLUTO [66,67]. Our choice for PLUTO is analytically presented and explained at the section 1.3.

Different schemes are used in these codes for the magneto-hydrodynamics and radiation transport modules. The diffusion equation of the magnetic field **B** is solved implicitly with an iterative method in

MACH2 [57,61], and ZEUS-2D [55], while an implicit solver for the equation of magnetic vector potential **A** is employed in GORGON to ensure a divergence-free magnetic field **B** [17]. A radiation cooling model or a flux-limited diffusion model is available in MACH2 [57,61]. Radiation effects are included through an optically thin radiation loss model in GORGON, which does not consider the radiation energy transfer inside the plasma [17]. A full radiation transport algorithm which is applicable in both thin and thick media is utilized in ZEUS-2D [55]. MULTI-2D [58-60] has the ability to treat radiation transport in both optically thick and thin regimes, with angular resolution, on a unstructured mesh in axisymmetric coordinates. ALEGRA [41-44] has two different approximations for the thermal radiation transport. The most accurate is a multigroup Implicit Monte Carlo (IMC) package while a faster, but less accurate approximation, is a flux limited diffusion package [44].

The thermal conduction module and the appropriate Equation Of State (EOS) are two important implementations for plasma evolution. Especially for situations with no radiation transport, the thermal conduction module is the one replenishing the energy exchange and transfer, smoothing the localized energy sources which can be developed due to Joule heating, lowering unnatural increment of the plasma temperature**.** Multi-material support with tabulated EOS and opacities is included in FLASH, while the thermal conductivity diffusion equation is referred to the Spitzer electron thermal conductivity using the electron specific heat [56]. ALEGRA supports an implicit thermal conduction modeling in the operators' split methodology. The moving mesh elements are using interface reconstruction method algorithms for transporting material interfaces, while fluid pressure P, mass density ρ and total energy E_{total} are correlated through appropriate thermodynamic equations which can use bulk modulus weighted schemes. The MHD scheme is accomplished through a model which combines hydrodynamics and Maxwell's equations in moving media with displacement currents neglected [44]. GORGON has both the ion and electron thermal fluxes, using Braginskii-like transport coefficients while there are two energy exchange rates between ions and electrons (Δ_{ei}=-Δ_{ie}) that couple the ion and electron energy equations. The thermal pressure and internal energy are correlated through an ideal EOS with the addition of an extra term at the electron equation, representing the ionization potential energy depending on the average ionization charge Z_{eff} of the plasma. The latter is calculated with the use of an average-ion Thomas-Fermi model [17]. In MACH2 and 3 the equation of state and caloric equation of state prescribe the fluids pressure and specific internal energy based on number densities and temperatures. Similarly the transport equations define the transport coefficients, such as electrical diffusivity and thermal conductivity. MACH can use a provided set of analytical models, including the ideal gas model and Gruneisen model [68], or can be extended to include additional tabular data models of plasma EOS and transport variables such as radiation opacities, obtained from semiempirical tables [61]. These equations can usually be provided via the SESAME data tables generated by the T-4 group of the Theoretical Division at Los Alamos National Laboratory [69-71]. The purpose of (Magnetically Accelerated Radiative Plasma Explorer, 3D version) MARPLE 3D is to provide numerical tools capable of performing large-scale 3D simulations in the field of high temperature hydrodynamics and High Energy Density Plasmas (HEDP). The demands of such physical problems need a full package of electron-ion energy relaxation, energy dissipation, and spectral multigroup radiative transfer and conduction. There are a lot of similarities and applications like the ones in ALEGRA due to the need of the whole four phases of matter and the wide range of

plasma density and temperature description. The equation of state is implemented as a C++ class hierarchy, which allows the use of various types of state equations (analytic, tabular etc.). These equations correlate the ion and electron temperature, thermal ion and electron pressure as functions of mass density and internal ions and electron energy. The thermal conduction solver models the ion and electron thermal conductivity and the energy relaxation between ions and electrons. The expressions for the thermal conductivity coefficients k_e and k_i and the electron-ion relaxation k_{ei} are taken from the polymorphic object describing the properties of matter (EOS, etc) [62]. Astrophysical codes like ATHENA or ZEUS-2D and 3-D usually use ideal EOS, while in many cases the thermal conduction module is absent [55,57]. Nevertheless, expanding ZEUS in ZEUS-EW [55] using the appropriate EOS Thomas–Fermi–Kirzhnits model and a modified Lee–More–Desjarlais model, a successive investigation of the dynamics of a wire array aluminum explosion is achieved where radiation and heat conduction are ignored. Heat conduction model with a flux limiter is implemented in the MULTI-2D too. In the current implementation, energy transfer via radiation and heat conduction are solved together with a single application. Sometimes heat flux under extreme gradients is modeled, imposing a maximum allowable value fulfilling this requirement by using a nonlinear conductivity instead of k [58]. The temperatures of the electrons and the ions are regarded as equal. Tabulated equations of state are generated by the QEOS model or the ideal gas model [62].

The electron transport coefficient (density and temperature dependent electrical conductivity) has been proved to be an implementation with a key role to the simulation. The WDM regime at low temperatures is a considerable factor in the proper electrical resistivity implementation. The Spitzer resistivity model is sound in the ideal gas regime for high temperature and low-density plasma, whereas it is not applicable within the phase transition zone, particularly, in the WDM regime with high density close to the solid state. Additionally in most numerical schemes a high artificial resistivity is considered at the vacuum area minimizing the level of Ohmic heating and thermal energy transport. The resistivity in GORGON has an anomalous component and is Braginskii-like, including two components, the classical ion-electron contribution and the electron-neutral contribution [17,72]. The ion-electron resistivity is taking into consideration the anomalous collision term with the low hybrid frequency [72]. Thus, a high resistive vacuum is regarded where only the vacuum form of Maxwell's equations are solved [17], while the inclusion of anomalous resistivity, due to the lower hybrid micro-instability, is numerically convenient, providing a physically justifiable scaling from finite plasma resistivity to virtually infinite vacuum resistivity, preventing a large discontinuity in the resistivity coefficient at the boundary [73]. Non-conducting regions are treated as being highly resistive in ALEGRA too; modeling environments which include magneto-solid dynamic motion transitioning into melted and vaporized material interacting with magnetic fields. Thus the flow can range from an Ideal to a high diffusive regime. The Lee-More Desjarlais (LMD) models provide the crucial material modeling of the high temperature state transitions and in particular how the conductivity varies with density and temperature, giving practical improvements to the Lee-More conductivity near the metal-insulator transition [74,75]. The electrical conductivity can be obtained from semi-empirical (LANL SESAME) tables or from the LMD electron transport model also in MACH2 code [57,61]. Modified LMD models are used in ZEUS-EW [55], as we already mentioned, simulating the dynamics of aluminum wire explosions. A perpendicular and parallel Spitzer magnetic resistivity with respect to the field line,

according to the prescription of Braginskii, is the most common option in FLASH code [56,76-78]. Braginskii/Spitzer like or of zero or constant value transport formulas are commonly used in Astrophysical codes like ATHENA [57], CRONOS, ZEUS [55], FLASH [56,77], PLUTO [66,67] due to the low density and high temperature plasmas.

The purpose of any MHD code development should be to provide numerical tools capable of performing large-scale 3D simulations in the field of high temperature magneto-hydrodynamics, HEDP and WDM which are the more demanding physical regimes for accurate simulations. The experimental data for these extreme plasma conditions are also lacking the abundance of the dilute and low temperature plasma regime data. Such tools should be properly designed and adjusted to modern supercomputer systems. Due to complexity of physical processes which should be taken into account and the wide range of spatiotemporal non-uniformity scales observed experimentally, the more demanding pinch problems like X-pinch and wire array configurations are so intricate and computationally expensive that may be comprehensively studied by use of distributed high-performance computing only, especially in the 3D case. The development of parallel codes and computational processing for these simulations are a real challenge for the specialists. In our case the high computational demanding simulations are being performed on the state-of-the-art HPC facility of GRNET S.A., ARIS (National Infrastructures for Research and Technology S.A.) [79]. Both PLUTO and GORGON have a built-in system module of MPI routines/compilers for the parallel run execution.

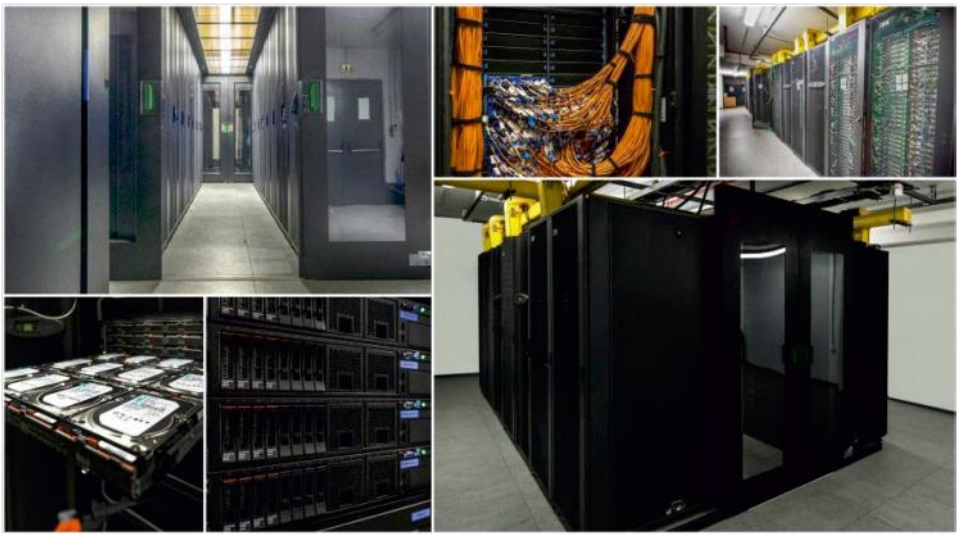

Figure 1.2: *HPC facility of Hellenic supercomputer ARIS, consisting of 532 computational nodes.*

There is a variety of computational schemes and the applicability of each code in most cases is not for all the plasma configurations, densities and temperatures regimes. Proper boundary conditions and solvers for flux computation (i.e. Riemann), appropriate plasma-vacuum interface correlation, control of the numerical dissipation, elimination of the numerical pathologies, physically consistent magnetic field spatiotemporal evolution, are matters to be considered, having no simple answers in complex plasma configurations.

1.3 PLUTO advantages and benefits analysis

Open source Eulerian MHD codes are usually astrophysical due to the vast variety of space plasmas and their interaction with self-produced or external magnetic fields. An Eulerian, easily programmed in C language with HD and MHD module is PLUTO [66,67].

PLUTO can describe any plasma formation at the ideal or dissipative term regime having a system of (nearly) conservation laws, of the form:

$$\frac{\partial \mathbf{U}}{\partial \mathrm{t}} + \nabla \cdot \mathbf{T}(\mathbf{U}) = \mathbf{S}(\mathbf{U}) \tag{1.1}$$

where $\mathbf{U}$ represents a set of conservative quantities, $\mathrm{T}(\mathbf{U})$ is the flux tensor and $\mathrm{S}(\mathbf{U})$ are the source terms [66,67]. The main advantages of this code, suitable for this work, are:

1. It includes four different choices of the EOS system where the Pressure-Volume-Temperature-Energy (PVTE) EOS is the most suitable, correlating the internal energy ,thermal pressure, mass density and plasma temperature, considering different plasma materials. Tabulated versions of EOS can replace expensive and not so accurate function evaluations.

2. Includes Explicit or Super Time Stepping (STS, accelerating the Explicit computations) resistivity modules.

3. The thermal conduction module is implemented, including $k_{||}$ and $k_{\perp}$ thermal conduction coefficients along and across the magnetic field of the classical thermal conduction flux.

4. Includes a viscosity stress term, entering the MHD equation by a viscous stress tensor, using the shear (ν_1) and bulk (ν_2) parameters of viscosity respectively.

5. Includes time dependent optically thin radiative losses with five different cooling module selection. The tabulated module is the most suitable for laboratory metal plasmas where the internal energy equation is solved using a tabulated heating/cooling function $\Lambda(\mathrm{T})$.

6. Radiation transport effects are included in the two-temperature approximation with an additional equation for the radiation energy. This was firstly distributed with the 4.1 version of the code and can be implemented to newer versions [80].

7. Includes six different embodied boundary conditions that can be applied at the ghost zones of the computational domain. Along with the potentiality of user defined boundary conditions and the internal boundary condition switch where the user has a full control over the solution array, boundaries are a strong suit for PLUTO.

8. Includes seven different Riemann solvers, five different reconstruction schemes for spatial order integration and five different time-stepping algorithms set a variety of choices for a robust and more accurate simulation run.

The **1-6** modules are analytically presented at Chapters 3 and 4 while the **7** and **8** are described at Chapter 4.

The original code has been successfully used as we already mentioned, as a supplementary tool, via a FEM/MHD coupled model that simulates the final plasma phase evolution in a copper Z-pinch single wire configuration using an ideal EOS and Spitzer's resistivity [22-25]. Preliminary results for an X-pinch low current configuration have also been presented considering an ideal EOS and constant resistivity in

[81]. In this specific study the “plasma neck” braking, the formation of the axial plasma jets as well as the development of MHD instabilities were the main physical phenomena that were demonstrated, in comparison with the experiments, verifying the potential even of the specific unmodified MHD code. Since the original PLUTO code operates in the C.G.S metric system, all the formula presentations and mathematical analysis of Chapters 3,4 and 5 are in the same system.

1.4 Modifications and module implementations in PLUTO for laboratory metal plasmas

Pluto has been used to the past without major modifications from the original code. Our new approach in the code is essential to make an independent plasma phase study from a low temperature start plasma (first nanoseconds of current rise) to later times up to the point the MHD approach is still valid. Thus, the originally astrophysical code is majorly modified being able to simulate laboratory plasmas, throwing light in the understanding of complicated phenomena in astrophysical plasmas. The physical model in the code is able to simulate a single tungsten wire Z-pinch, a two wire X-pinch and can also be extended in Z-pinch wire arrays or any geometric plasma formulation of tungsten or other metal materials. For this purpose, new algorithms for the PLUTO, which extend the field of applicability of the code modules, are being developed for these laboratory plasmas. Three regions for the connection of the pure vacuum with the material plasma are implemented to make the spatiotemporal derivatives smoother. This distinction creates an extra material plasma vacuum environment interacting (or not) with the wire plasma. The new modules seeded in the code aim to produce a robust computational domain, describing as good as possible and according to the literature data/experimental data, the plasma spatiotemporal evolution, reducing its size relative to the real experimental chamber, focusing in a specific domain area of interest and last but not least, saving valuable computational time and space. These major modifications are listed below:

1. Use of the PVTE EOS, which is modified to include metal material plasma and plasma air, using tabulated data by the MGGB/SESAME Database [69-71]. Given the thermal pressure and the mass density via the curvilinear mapping p=p(ρ,T), the temperature is evaluated and afterwards the internal energy density ρe is computed using the ρe=ρe(ρ,T) table and vice versa. Five different mixing methods of metal plasma and plasma vacuum provide flexibility to the MHD computational scheme (analysis in Chapter 3/PART I and 5.2 section of Chapter 5).

2. Two main choices for the electrical resistivity are included,

i. the simple modified Spitzer-like formula equation as presented in equations 3.52-3.55 and 3.58 in Chapter 3.

ii. a linear mix formula considering the electron-ion and ion-neutral contribution [82],

$$n_{total} = n_{ei} + n_{en} \tag{1.2}$$

where n_{en} is the electron-neutral resistivity and n_{ei} is the electron-ion resistivity. The analytic presentation is discussed at the 3.4.1.3 subsection in the third Chapter and at the 5.4.1 in the Results Chapter.

3. the optically thin radiative losses module are taken into account using tabulated data with the help of the FLYCHK code [83,84] (Chapter 3/Part I).

4. the k_x is the component coefficient of the thermal conduction flux, transverse to the plane of **B** and ∇T, which is added to the source files of the code to approximate better the metal plasma temperature and the energy exchange spatiotemporal profile. The classical Braginskii components are used for the three thermal conduction coefficients. Due to the fluid nature of PLUTO, a linear sum of the electron and ion component for the parallel and normal coefficients and the subtraction of the two for the transverse one according to the MHD equations form, is used [78,85,86] (equations 3.74-3.82 in 3.4.2.3 subsection of the third Chapter).

5. a modified radiation transport module is implemented, able to include metal plasma materials, described analytically at the Chapter 3/ Part I relative section [80].

6. plasma density is determined along simulation run using the effective ionization charge state Z_{eff}, with the help of tabulated values that FLYCHK code provides [83,84] (Chapter 3/Part I).

7. the inclusion of a passive scalar function is used for the intermediate transition zone among the metal plasma and plasma vacuum region for the multimaterial approximation, helping to have a smoother behavior at the tungsten plasma-vacuum air interface, avoiding deformations and extra dissipation (section 5.3 in Chapter 5).

8. the magnitude of the magnetic field is updated in the whole computational domain, at the necessary time steps using the experimentally measured current. The magnetic field satisfies the Ampere's law and the Stokes theorem along the execution run for the whole volumetric computational territory. Therefore the energy inflow is imposed avoiding the limitations of using a time dependent magnetic field at the boundary planes (more detailed discussion at Chapters 4 and 5).

9. a Bennet deviation factor defines the initial radial temperature distribution as a function of the thermal pressure, the magnetic field magnitude and maximum radius, allowing LTE initial plasma conditions (or not) and a cold/hot plasma core relative to the plasma wire outer thinner/corona-like regions (Chapters 2 and 4).

10. skin depth implementation module also defines the initial current density distribution affecting the initial radial profile of the magnetic field distribution (Chapter 2.1.1 subsection).

11. the flexible boundary condition system in PLUTO provides three main computational schemes for the Z and X-pinch simulations,

i. the standard PLUTO set of symmetric-periodic and outflow boundary condition, appropriate to simulate mainly axisymmetric models of Z-pinch wires (Chapter 5.2 models).

ii. the user defined X-pinch configuration setting the appropriate boundaries at the wire end-boundary interface (Chapter 5.3 and 5.4 model)

iii. the Riemann solver of PLUTO is deactivated in the vacuum region through the internal boundary switch, without any loss of the generality of the numerical approximation, setting fixed values for the thermal pressure, mass density and plasma temperature there. This allows for smaller spatial computational models without the diffusive behavior of other boundary implementation schemes (Chapter 5.4 models).

Switches for the upper and lower values of vacuum mass density, thermal pressure and a lower value switch for the vacuum temperature preserve the simulation of negative and unphysical values.

The mass density and thermal pressure initial profiles implementations follow a radial Gaussian or parabolic (outcome of the Bennet equilibrium relation for thermal pressure) or a combination of these two distributions, providing a smoother radial transition from the denser metal plasma region to the thin plasma vacuum area.

The flexible PLUTO architecture sets an ideal environment for these and any future implementations.

1.5 Objectives of this dissertation

The main goal of this thesis is to numerically investigate the plasma dynamic evolution of Z and X-pinch devises. A more thorough investigation of the jet formation mechanisms and dynamic evolution of a two-wire tungsten X-pinch formation along with experimental validation is presented. Additionally a possible correlation to astrophysical jets of Young Stellar and HH objects is discussed.

In order to achieve robust, flexible and realistic computational simulation models, a variety of different numerical and physical schemes is needed. An extra study of this work is the synthesizing process of extracting physical formulas for all the dissipative terms for all density and temperature regimes. The mathematical transformation of any Local plasma configuration to the Global coordinate system is a supplementary and necessary study, as it provides the appropriate spatial profiles for all the physical variables and assisting for the best spatial resolution that can be computationally executable.

In Chapter 2 there is a state of the art presentation of the Z and X-pinch configurations and numerical work. Laboratory experiments and astrophysical related jets are also included, mainly for Young Stellar and HHs objects presentation along with the relative simulation studies.

In Chapter 3/PART I, the MHD module which is relative mostly to the conservative form of the PLUTO code, is presented. The thin/thick radiation module implementation is analyzed and the EOS tabular data set is explained, defining the mass density-thermal pressure-internal energy-plasma temperature correlation**.**

In Chapter 3/PART II, all the dissipative terms that are implemented or can be implemented in the future in any MHD code, are introduced. The synthesis of different physical formulas for piece-wise functions or correction factors to already known formulas or combination formulas, provide flexibility for any MHD numerical scheme and also, for any Z or X-pinch configuration at any density, thermal pressure and plasma temperature regime. The graphic presentation of these formulas provides a comparison evaluation tool with experimental/semi-empirical or other studies, data**.**

In Chapter 4 the one fluid MHD code PLUTO is described, the numerical and mathematical/physical schemes implemented or improved at the already embodied numerical-tool system. The new modifications which are essential to the code to describe laboratory metal plasmas, such as tungsten, of X-pinch or Z-pinch configurations surrounded by a second thin plasma material, such as plasma air, considered as the low density plasma background, are presented. Moreover, the mathematical transformations through rotation and displacement matrices are presented correlating the mass density, thermal pressure and magnetic field Local components to the Global ones. Examples of Z and X-pinch configurations are discussed according to these transformations. Two specific simulation applications of these transformations are preliminary tested and evaluated. The first is a "cold" start X-

pinch configuration using two unmerged metallic tungsten wires, starting just before the ablation phase and the merging in a denser cross-point area. The focus of this simulation is at the cross-point area. The study ends when the merging is succeeded and the formation of the axial jets is initiated. The second is a four tungsten, thin wire, low current Z-pinch array configuration study till the stagnation phase. Both studies present novel and very promising results for future work.

The computational results are presented in Chapter 5. The section order has as follows:

i. In section 5.1 the experimental devise of the X-pinch configuration is presented , used to evaluate the simulation results. The experimental techniques and the software processing package are briefly presented.

ii. In section 5.2, a 1/4 spatial model of a single tungsten Z-pinch wire is studied. The modeling of the interface region is based on four approximations and two different PLUTO solvers are used for the simulation. The simulations are repeated with the temperature of vacuum constrained, resulting to sixteen simulation cases evaluation. The contribution of the radiation transport module to the appropriate plasma evolution is presented through a specific model [87].

iii. In section 5.3 a study of a 1/16 spatial model, of an X-pinch tungsten plasma configuration for a wide wire angle, is presented. The spatiotemporal plasma jet formation and evolution is presented and discussed. The simulated areal mass density is compared with the experimentally measured dense opaque region to enlighten the dense plasma evolution. In addition, the measured experimental areal electron density is compared to the simulation results. The main jet formation mechanisms are analyzed and discussed in relation to the influence of the J×B force and the mass momentum density [88].

iv. In section 5.4 GORGON and PLUTO are used to simulate a sharp two-wire tungsten load X-pinch geometry. The physical and numerical modeling differences of GORGON and PLUTO as well as their influence on the simulation results are demonstrated and analyzed. Six different computational MHD schemes are presented at a specific spatial moment only for PLUTO. The model comparison provides valuable information on the improvement of flexible and efficient X-pinch models according to the experimental data and offer crucial insights on the mechanisms of plasma evolution and jet formation [89].

v. In section 5.5, the scalability and jet astrophysical relevancy estimation for the 5.3 section's X-pinch pulsed power configuration is attempted. All relevant dimensionless numbers are calculated for the X-pinch plasma and compared to the ones of other laboratory astrophysics experiments and to the ones of YSOs, HHs and other astrophysical objects.

References

[1] G. Revet et al, "Laboratory disruption of scaled astrophysical outflows by a misaligned magnetic field", NATURE COMMUNICATIONS | (2021) 12:762 | https://doi.org/10.1038/s41467-021-20917-x (GORGON).

[2] M. Koenig et al, "Radiative Shocks And Plasma Jets As Laboratory Astrophysics Experiments", CP926, Atomic Processes in Plasmas—15th International Conference on Atomic Processes in Plasmas, 2007 American Institute of Physics 978-0-7354-0436-6/07.

[3] C D Gregory et al, "Astrophysical jet experiments", Plasma Phys. Control. Fusion 50 (2008) 124039 (7pp) doi:10.1088/0741-3335/50/12/124039

[4] C D Gregory et al, "ASTROPHYSICAL JET EXPERIMENTS WITH COLLIDING LASER-PRODUCED PLASMAS", The Astrophysical Journal, 676:420–426, 2008 March 20.
[5] Dawei Yuan et al, "Laboratory Investigation of Astrophysical Collimated Jets with Intense Lasers", The Astrophysical Journal, 860:146 (7pp), 2018 June 20.
[6] John I. Castor , "Astrophysical Radiation Dynamics: The Prospects for Scaling", Astrophys Space Sci (2007) 307:207–211.
[7] R. Bonito et al Astronomy & Astrophysics 484, 389 (2008).
[8] P. Hartigan et al, "FLUID DYNAMICS OF STELLAR JETS IN REAL TIME: THIRD EPOCH *HUBBLE SPACE TELESCOPE* IMAGES OF HH 1, HH 34, AND HH 47", The Astrophysical Journal, 736:29 (20pp), 2011 July 20.
[9] F. H. Shu, J. R. Najita, H. Shang, and Z.-Y. Li, in Protostars and Planets IV, edited by V. Mannings, A. P. Boss, and S. S. Russell (Tucson, AZ: Univ. Arizona Press, 2000) pp. 789–814.
[10] A. Konigl and R. E. Pudritz, in Protostars and Planets IV, edited by V. Mannings, A. P. Boss, and S. S. Russell (Tucson, AZ: Univ. Arizona Press, 2000) p. 759.
[11] A. Frank, T. P. Ray, S. Cabrit, P. Hartigan, H. G. Arce, F. Bacciotti, J. Bally, M. Benisty, J. Eisloffel, M. Gudel, S. Lebedev, B. Nisini, and A. Raga, in Protostars and Planets VI (University of Arizona Press, 2014) pp. 451– 474,
[12] P. Hartigan et al, The Astrophysical Journal 559, L157 (2001).
[13] T. Matsakos et al, "Two-component jet simulations I. Topological stability of analytical MHD outflow solutions", A&A 477, 521–533 (2008)/DOI: 10.1051/0004-6361:20077907.
[14] O. Teşileanu et al, "Young stellar object jet models: From theory to synthetic observations", A&A 562, A117 (2014)/DOI: 10.1051/0004-6361/201322627.
[15] A. Ciardi, Laboratory Studies of Astrophysical Jets. Lect. Notes Phys. **793**, 31–50 (2010). (GORGON)
[16] S. V. Lebedev et al, "Exploring astrophysics-relevant magnetohydrodynamics with pulsed-power laboratory facilities", REVIEWS OF MODERN PHYSICS, VOLUME 91, APRIL–JUNE 2019. (GORGON)
[17] A. Ciardi et al, "The evolution of magnetic tower jets in the laboratory", PHYSICS OF PLASMAS **14**, 056501 (2007). (GORGON)
[18] A. Ciardi et al, Astrophysics of Magnetically Collimated Jets Generated from Laser-Produced Plasmas, PRL 110, 025002 (2013). (GORGON)
[19] Hellenic Mediterranean University Institute of Plasma Physics & Lasers, *www.ippl.hmu.gr.*
[20] http:Uoa Department of Physics-Astronomy-Astrophysics-Mechanics/en.phys.uoa.gr.
[21] http://www.hiper-laser.org/index.html.
[22] E. Kaselouris et al, "Plasma instabilities: the influence on plasma instabilities during the solid-plasma phase transition",*27th Symposium on Plasma Physics and Technology (Prague/*Czech*/ 20-23 June 2016).*
[23] Kaselouris et al. (2017), "The influence of the solid to plasma phase transition on the generation of plasma instabilities", Nature Communications, Vol 8, pp. 1713.
[24] E Kaselouris et al, "Preliminary investigation on the use of low current pulsed power Z-pinch plasma devices for the study of early stage plasma instabilities", Plasma Phys. Control. Fusion 60 (2018) 014031 (8pp).
[25] E Kaselouris, "Study of matter behavior dynamics governed by the interaction with laser pulses and external strong currents", PhD thesis TECHNICAL UNIVERSITY OF CRETE SCHOOL OF PRODUCTION ENGINEERING & MANAGEMENT.
[26] F. N. Beg et al., "Jet Formation and Current Transfer in *X*-Pinches**",** IEEE TRANSACTIONS ON PLASMA SCIENCE, VOL. 34, NO. 5, OCTOBER 2006. (GORGON).
[27] J. P. Chittenden **"**Structural Evolution and Formation of High-Pressure Plasmas in *X* Pinches", PRL **98,** 025003 (2007). (GORGON)
[28] Douglass J.D., "An Experimental Study of Tungsten Wire-Array Z-Pinch Plasmas Using Time-Gated Point-Projection X-Ray Imaging ". PhD thesis, Cornell University,(2007).
[29] Shelkovenko, T. A., S. A. Pikuz, and D. A. Hammer. "A review of projection radiography of plasma and biological objects in X-Pinch radiation." Plasma Physics Reports 42.3 (2016): 226-268.
[30] Song, Byung Moo, et al. "X pinch x-ray radiation above 8 keV for application to high-resolution radiography of biological specimens." IEEE Transactions on Nuclear Science 51.5 (2004): 2514-2519.
[31] Beg, F. N., et al. "Compact X-pinch based point x-ray source for phase contrast imaging of inertial confinement fusion capsules." Applied physics letters 89.10 (2006): 101502.

[32] Aranchuk et al, "Experimental study of X-pinch in a sub-microsecond regime." IEEE transactions on plasma science 33.2 (2005): 990-996.
[33] Hammer, D. A., et al. "X-pinch soft x-ray source for microlithography." Applied physics letters 57.20 (1990): 2083-2085.
[34] Shelkovenko, T. A., et al. "Accelerated electrons and hard X-ray emission from X-pinches." Plasma physics reports 34.9 (2008): 754-770.
[35] G. S. Sarkisov et al, "Transformation of a tungsten wire to the plasma state by nanosecond electrical explosion in vacuum", PHYSICAL REVIEW E **77**, 056406 (2008). (MACH2 2D)
[36] D.M. Haas et al, "Supersonic jet formation and propagation in x-pinches", Astrophys Space Sci DOI 10.1007/s10509-011-0599-8. (GORGON)
[37] G. S. Jaar and R. K. Appartaim, "Axial plasma jet characterization on a microsecond x-pinch", JOURNAL OF APPLIED PHYSICS 123, 213301 (2018).
[38] S. V. Lebedev et al, "LABORATORY ASTROPHYSICS AND COLLIMATED STELLAR OUTFLOWS: THE PRODUCTION OF RADIATIVELY COOLED HYPERSONIC PLASMA JETS", THE ASTROPHYSICAL JOURNAL, 564:113-119, 2002 January 1.
[39] S V Lebedev et al, "Production of radiatively cooled hypersonic plasma jets and links to astrophysical jets", Plasma Phys. Control. Fusion **47** (2005) B465–B479.
[40] P. M. Bellan et al, "Astrophysical jets: Observations, numerical simulations, and laboratory experiments", PHYSICS OF PLASMAS **16**, 041005 (2009).
[41] William Neal and Christopher Garasi, "High Fidelity Studies of Exploding Foil Initiator Bridges, Part 3: ALEGRA MHD simulations", AIP Conf. Proc. 1793, 080008-1–080008-5. (ALEGRA Eulerian mesh)
[42] E. Love, M. K. Wong, "Lagrangian Continuum Dynamics in ALEGRA", SAND2007-8104 Unlimited Release Printed December 2007. (ALEGRA Lagrangian mesh)
[43] Allen C. Robinson , Christopher J. Garasi "Three-dimensional z-pinch wire array modeling with ALEGRA-HEDP", *Computer Physics Communications,* 164 (2004), pp. 408–413. (ALEGRA)
[44] Robinson AC et al. 2008, "ALEGRA: An Arbitrary Lagrangian-Eulerian Multimaterial, Multiphysics Code", in 46th AIAA Aerospace Sciences Meeting and Exhibit, Reno, Nevada. (ALEGRA FULL ANALYSIS)
[45]A. C. Robinson, J.H.J. Niederhaus, V.G.Weirs and E. Love, "Arbitrary Lagrangian–Eulerian 3D ideal MHD algorithms", INTERNATIONAL JOURNAL FOR NUMERICAL METHODS IN FLUIDS, Int. J. Numer. Meth. Fluids 2011; **65**:1438–1450. (LAGRANGIAN-EULERIAN ALEGRA)
[46] Derek Mariscal et al., "Investigation of Current Transport in 2×2 Wire Array Plasmas, IEEE TRANSACTIONS ON PLASMA SCIENCE, VOL. 43, NO. 8, AUGUST 2015. (GORGON)
[47] Matteo Bocchi et al., "Numerical simulations of Z-pinch experiments to create supersonic differentially-rotating plasma flows", High Energy Density Physics 9 (2013) 108-111. (GORGON)
[48] G. F. Swadling et al., "Oblique shock structures formed during the ablation phase of aluminium wire array z-pinches", PHYSICS OF PLASMAS 20, 022705 (2013). (GORGON)
[49] C.A. Jennings et al., "3D Resistive, Radiative MHD Modeling of Z-pinches", American Institute of Physics 808, 57 (2006); doi: 10.1063/1.2159319. (GORGON)
[50] G W Collins IV et al , "Effect of the global to local magnetic field ratio on the ablation modulations on X-pinches driven by 80 kA peak current", New Journal of Physics 14 (2012) 043021. (GORGON)
[51] F. Suzuki-Vidal et al., "Interaction of radiatively cooled plasma jets with neutral gases for laboratory astrophysics studies", High Energy Density Physics 9 (2013) 141-147. (GORGON)
[52] F Suzuki-Vidal et al., "Laboratory astrophysics experiments studying hydrodynamic and magnetically-driven plasma jets", Journal of Physics: Conference Series **370** (2012) 012002. (GORGON)
[53] J P Chittenden *et al* 2004 *Plasma Phys. Control. Fusion* **46** B457. (GORGON)
[54] B. Jones et al, "Doppler measurement of implosion velocity in fast *Z*-pinch x-ray sources", PHYSICAL REVIEW E **84**, 056408 (2011). (GORGON)
[55] Jun Huang et al., "Numerical investigation on the implosion dynamics of wire-array Z-pinches in (r,θ) geometry", PHYSICS OF PLASMAS 19, 062701 (2012). (ZEUS CODE)
[56] P. Tzeferacos et al., "FLASH magnetohydrodynamic simulations of shock-generated magnetic field experiments", High Energy Density Physics 8 (2012) 322-328. (FLASH- Noh Z pinch)

[57]A. L. Velikovich et al., "Exact self-similar solutions for the magnetized Noh Z pinch problem", PHYSICS OF PLASMAS 19, 012707 (2012). (ATHENA-MACH2)
[58] R. Ramis J. Meyer-ter-Vehn, J. Ramirez, "MULTI2D – a computer code for two-dimensional radiation hydrodynamics", Computer Physics Communications 180 (2009) 977–994. (MULTI 2D HYDRODYNAMIC ORIGINAL FORM)
[59] Fuyuan Wu, Rafael Ramis, Zhenghong Li , "A conservative MHD scheme on unstructured Lagrangian grids for Z-pinch hydrodynamic simulations" , Journal of Computational Physics, Volume 357, 15 March 2018, pp. 206-229 (2018). (MULTI 2D HYDRODYNAMIC, IMPLEMENTATION OF MHD FORM)
[60] Fuyuan Wu et al., "Numerical studies on the radiation uniformity of Z-pinch dynamic hohlraum",. Matter and Radiation at Extremes 3 (2018) 248-255 (MULTI2D WITH MHD SHEME)
[61] Frank J. Wessel et al., "Fusion in a Staged *Z*-Pinch", IEEE TRANSACTIONS ON PLASMA SCIENCE, VOL. 43, NO. 8, AUGUST 2015. (MACH2 2-1/2 D)
[62] Alexey S. Boldarev et al., "OBJECT-ORIENTED CODE MARPLE3D: SIMULATIONS OF RADIATIVE HYDRODYNAMIC/MHD EFFECTS AT HIGH-PERFORMANCE COMPUTER SYSTEMS", European Congress on Computational Methods in Applied Sciences and Engineering (ECCOMAS 2012) 7007-7027. (MARPLE 3D)
[63] Ding Ning et al., "Simulation Studies of the Wire-Array Z-Pinch Implosions", 2013 IEEE 25th Symposium on Fusion Engineering (SOFE),13846232. (MARED)
[64] N. Ding et al., "Theoretical and Numerical Research of Wire Array Z-pinch and Dynamic Hohlraum in the IAPCM", Matter and Radiation at Extremes ,Volume 1, Issue 3, May 2016, 135-152. (MARED)
[65] D. P. Higginson et al, "Enhancement of Quasi-stationary Shocks and Heating via Temporal Staging in a Magnetized Laser-Plasma Jet", PRL 119, 255002 (2017). (GORGON)
[66] "PLUTO: A Numerical Code for Computational Astrophysics" Mignone et al., The Astrophysical Journal Supplement Series, Volume 170, Issue 1, pp. 228-242
[67] http://plutocode.ph.unito.it/
[68] Brian J. Parma, "Three-Dimensional Modeling and Analysis of Magneto-plasma-dynamic", Thesis Presented in Partial Fulfillment of the Requirements for the Degree Master of Arts ARIZONA STATE UNIVERSITY, August 2011.
[69] T-4 Handbook of Material Properties Data Bases, Vol Ic: Equations of State, LA-101 SO-MS, UC-34, Issued November 1984.
[70] SESAME THE LOS ALAMOS NATIONAL LABORATORY EQUATION OF STATE DATABASE, LA-UR_92_3407.
[71] Kashiwa B.A., "The MGGB Equation-of-State for Multifield Applications: A Numerical Recipe for Analytic Expression of Sesame EOS Data", LA-1442 ,September 2010. http://www.doe.gov/bridge
[72] J. P. Chittenden, "The effect of lower hybrid instabilities on plasma confinement in fiber Z pinches", Physics of Plasmas **2**, 1242 (1995).
[73] J. P. Chittenden et al ,"Two-dimensional magneto-hydrodynamic modeling of carbon fiber Z -pinch experiments", Phys. Plasmas **4** (12), December 1997.
[74] Desjarlais, M. P., "Practical improvements to the Lee-More conductivity near the metal-insulator transition," Contributions to Plasma Physics, Vol. 41, No. 2-3, March 2001, pp. 267–270.
[75] Desjarlais, M. P., Kress, J. D., and Collins, L. A., "Electrical conductivity for warm, dense aluminum plasmas and liquids," Physical Review E, Vol. 66, No. 2, Aug. 2002, pp. 025401(R).
[76] Atzeni, S. and Meyer-Ter-Vehn, J. 2004, The Physics of Inertial Fusion: Beam Plasma Interaction, Hydrodynamics, Hot Dense Matter (Oxford Science Publications).
[77] FLASH User's Guide, Version 4.5, December 2017.
[78] S.I Braginskii , "Transport processes in a plasma", Reviews of Plasma Physics, Volume 1, 206-311 (1965).
[79] HPC| National HPC Infrastructure - http://doc.aris.grnet.gr/system/hardware/
[80] Stefan M. Kolb, Matthias Stute, Wilhelm Kley, Andrea Mignone, "Radiation hydrodynamics integrated in the code PLUTO", A&A 559, A80 (2013).
[81] G. Koundourakis et al., "Experimental and numerical investigation of the plasma dynamics and jet formation in low current table-top X-pinch plasma devices", Proceedings of the SCinTE 2015, VOL.3, 19-22.
[82] Zhijian Fu et al, "Electrical conductivity of warm dense tungsten", High Energy Density Physics , Volume 9, Issue 4, 2013, Pages 781-786.

[83] Tungsten Charge State Distribution by FLYCHK NLTE Kinetics Calculation at NIST by International Atomic Energy Agency- Atomic Molecular Data Services provided by the Nuclear Data Section.
[84] H.-K. Chung et al., "FLYCHK: Generalized population kinetics and spectral model for rapid spectroscopic analysis for all elements", High Energy Density Physics 1 (2005) 3-12.
[85] Frank Modica et al, "The Braginskii model of the Rayleigh-Taylor instability. I. Effects of self-generated magnetic fields and thermal conduction in two dimensions", High Energy Density Physics 9 (2013) 767-780.
[86] Richardson A S 2019 NRL Plasma Formulary.
[87] A. Skoulakis et al 2018 9th GRACM International Congress on Computational Mechanics pp 294.
[88] G. Koundourakis et al, "A numerical study on laboratory plasma dynamics validated by low current X-pinch experiments", Plasma Phys. Control. Fusion **62** (2020) 125012 (14pp)/ https://iopscience.iop.org/article/10.1088/1361-6587/abbebf.
[89] A. Skoulakis-G. Koundourakis et al, " High performance simulations of a single X-pinch", Plasma Phys. Control. Fusion **64** (2022) 025003 (11pp)

CHAPTER 2

LITERATURE REVIEW

PINCH PLASMA DEVISES AND LABORATORY ASTROPHYSICS

2.1 Literature review of Z-pinch plasma experiments and simulations

Over the last decades, interest in pulsed power plasma devices remains high, since they are simple to implement and can be used to produce extremely high plasma-energy-densities in the laboratory.

The simplest pulsed power plasma device is the Z-pinch loaded with a thin in diameter solid wire or with a gas in a gas puff configuration. [1-11]. A Z-pinch plasma device is a plasma confinement system which uses currents to generate the compression magnetic field. The current heats, ablates and converts the solid, in the case where a solid wire is used as target, into plasma. The plasma consists of a colder core and a hot expanding corona plasma. Interplay between magnetic pressure P_{mag}, and thermal pressure $P_{thermal}$, modulates the plasma evolution and the creation of MHD instabilities. Bremsstrahlung effects, Ohmic heating and radiation transport phenomena also affect the plasma temperature and expansion [12].

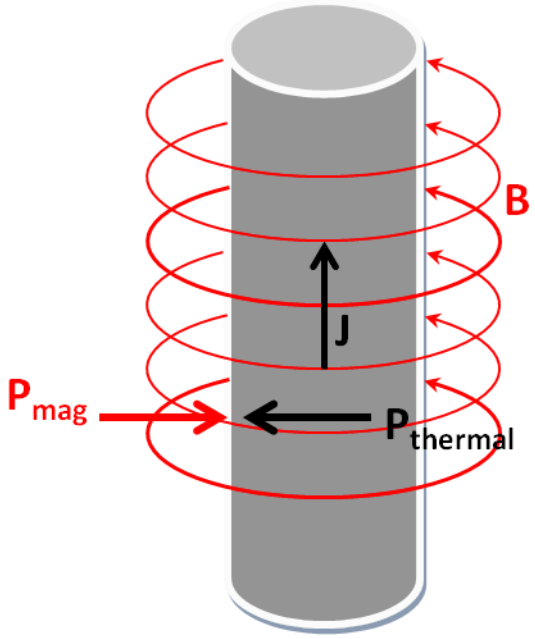

Figure 2.1: *A wire Z-pinch design presenting the upwards current density **J**, the azimuthal magnetic field **B** and the inwards and outwards local magnetic and thermal pressure respectively.*

The Z-pinch configuration is a vacuum discharge plasma device, which uses a current to heat and convert matter into the plasma state. During the heating process strong magnetic fields are generated which subsequently compress the plasma. Such plasma confinement devices consist of an energy storage unit (i.e. a MARX bank) (figure 2.2), a pulse forming line and a metallic wire attached between two electrodes, the anode and cathode. Initially, the wire is heated up until it becomes a plasma,

which then continues to drive the current along the axial direction. The advantages of the Z-pinch are that large volumes of plasma are produced with very high energy density.

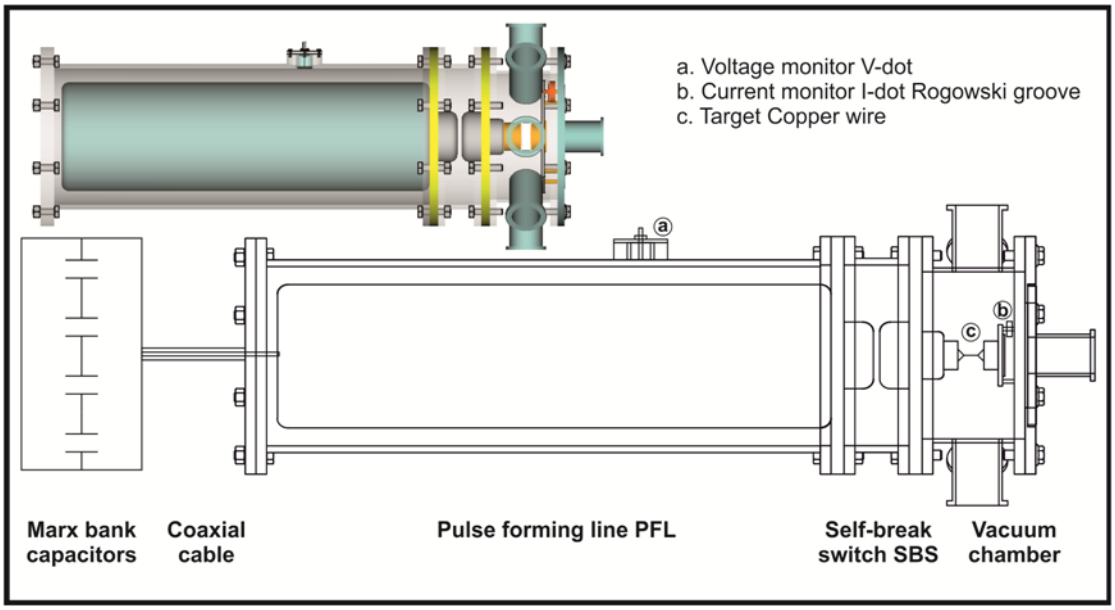

Figure 2.2: *A 3D CAD model and the detailed cross section of a wire Z-Pinch device [4].*

Z-pinches are frequently used in the study of fundamental problems such as among others laboratory astrophysics, material's equation of state research, generation of X-ray sources and magnetic confinement fusion research. There are two main types of Z-pinch devices: the equilibrium Z-pinch [4-10] and the dynamic or "fast" Z-pinch [2]. The former is a simple form of magnetically confined plasma, susceptible to MHD instabilities while it is not an effective magnetic fusion energy (MFE) scheme. The latter is a highly efficient plasma radiation source (PRS). Examples of such devises are the solid single wire Z-pinches [1-10], the Z-pinch liners [18,19], the wire array Z-pinches [9,14-17], the fiber Z-pinches [7,8], the Z foil liners [13] and the gas-puff Z-pinches [20-22,24]. More precisely, cylindrical foil liners are often used in scale Z-pinch experiments to study physics relevant to Inertial Confinement Fusion (ICF), while 3D extended Magneto-Hydro-Dynamic (MHD) simulations are used to study these experiments [13]. 2D [8,9] and 3D MHD codes like PERSEUS [13], GORGON [17], MACH2 [19,24], ALEGRA [16,23], MARED [15] and many others are developed and implemented to simulate Z-pinch experiments. The original version of PLUTO has also been used to study the MHD instabilities in a single wire Z-pinch configuration [4-6] and for the study of the Magneto-Rayleigh–Taylor (MRT) instability in thin liner implosions [18].

2.1.1 Pinch equilibria and Bennett relation

As an example of a simple equilibrium Z-pinch, a cylindrical plasma column currying a strong electric current along the z axis, is considered. The current creates a magnetic field, resulting in a **J×B** force directed radially inwards, resulting in the so called pinch effect (figure 2.1). For a perfectly conducting plasma with a current density **J**, it is possible to examine the steady-state equilibrium conditions

through a MHD treatment [12,25]. Considering steady-state, where the plasma velocity is neglected and also neglecting viscosity, the MHD equations are simplified to the magneto-hydrostatic case:

$$\boldsymbol{\nabla} \mathrm{P} = \frac{\mathbf{J} \times \mathbf{B}}{\mathrm{c}} \tag{2.1}$$

$$\nabla \times \mathbf{B} = \frac{4\pi \mathbf{J}}{\mathrm{c}} \tag{2.2}$$

$$\nabla \cdot \mathbf{B} = 0 \tag{2.3}$$

where P is the thermal pressure [25]. The azimuthal symmetry and the radial gradient direction, considering also the current flow along z axis, transform this system to the next system of equations:

$$\frac{\mathrm{dP}}{\mathrm{dr}} = -\frac{\mathrm{J_Z B_\theta}}{\mathrm{c}} \tag{2.4}$$

$$\text{where } \mathrm{J_Z} = \frac{\mathrm{c}}{4\pi \mathrm{r}} \frac{\partial (\mathrm{r B_\theta})}{\partial \mathrm{r}} \tag{2.5}$$

and z, θ and r are the cylindrical coordinates. Combining 2.4 and 2.5 we find:

$$\frac{\mathrm{dP}}{\mathrm{dr}} = -\frac{\mathrm{B_\theta}}{4\pi \mathrm{r}} \frac{\partial (\mathrm{r B_\theta})}{\partial \mathrm{r}} \tag{2.6}$$

For simplicity, we can choose a constant current density profile $\mathrm{J_Z}$=const. This determines the thermal pressure and magnetic field profile inside the plasma cylinder of radius $\mathrm{r_0}$, as:

$$\mathrm{B_\theta} = \frac{2\pi \mathrm{r}}{\mathrm{c}} \mathrm{J_Z}, 0 \le \mathrm{r} \le \mathrm{r_0} \tag{2.7}$$

and

$$\mathrm{P} = \mathrm{P_0} \left(1 - \frac{\mathrm{r}^2}{{\mathrm{r_0}}^2} \right), 0 \le \mathrm{r} \le \mathrm{r_0} \tag{2.8}$$

where

$$\mathrm{P_0} = \frac{\pi}{\mathrm{c}^2} {\mathrm{r_0}}^2 {\mathrm{J_Z}}^2$$

Outside the plasma cylinder the thermal pressure and current density have zero values, while the magnetic field obeys the inverse radius law resulting from the Ampere's law.

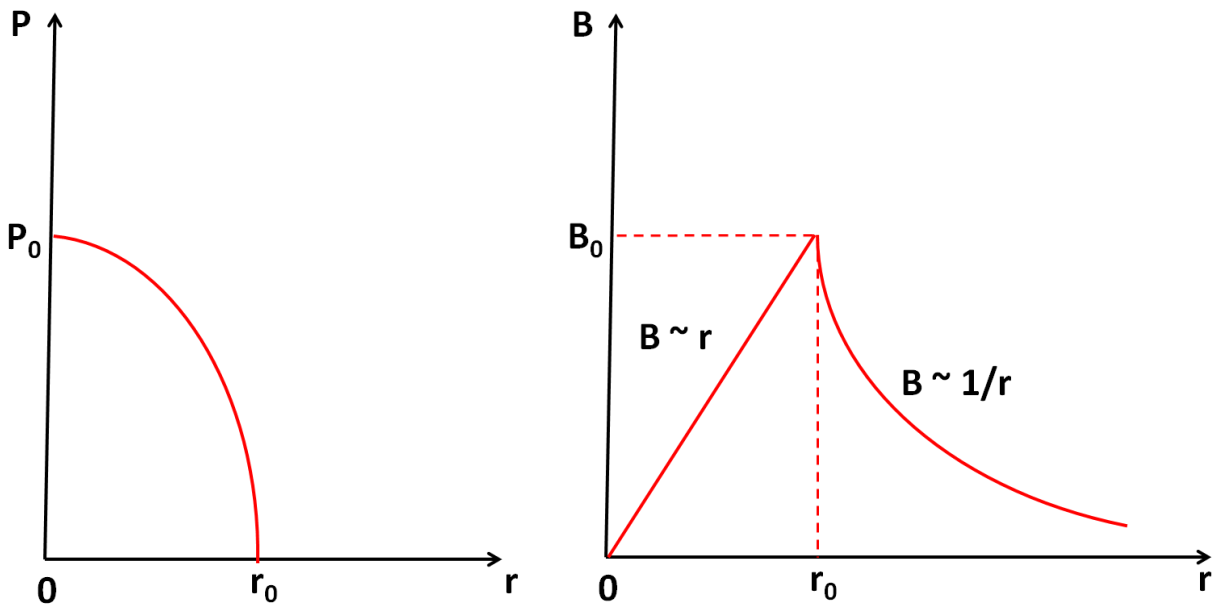

Figure 2.3: *Parabolic radial thermal pressure profile (at the left) and the radial distribution of the magnetic field magnitude (at the right) produced from a constant current density of a plasma cylinder with a radius r_0.*

Thus, the pressure balance determines the internal structure. If we consider a constant temperature profile (isothermal), the mass density ρ is proportional to thermal pressure and has also a radial parabolic profile. This is used as a parabolic initial condition for the MHD simulation when considering an equilibrium state with a high internal resistivity value.

If we consider a small resistivity inside the plasma (high conductivity metal), the **skin effect** can play a significant role in the spatiotemporal radial plasma density, temperature and magnetic field distributions. We assume the surface magnetic pressure is balanced by the internal thermal pressure, while a uniform density and temperature can be considered. With regard to the skin effect [26], a piece-wise function which relates the current density, is introduced:

$$J_z(r) = J_o \cdot \begin{cases} e^{-\frac{R_{max}-(r+\Delta r)}{\delta}} & \text{if} \quad 0 \le r \le R_{max} - \Delta r \\ e^{-((r-(R_{max}-\Delta r))/w)^2} & \text{if} \quad R_{max} - \Delta r < r \end{cases} \tag{2.9}$$

where R_{max} is the radius of the maximum magnetic field while $\Delta r = \sqrt{2}\, w$ and w is chosen for the J_2 function to reach $J_2(R_{max}) = J_o/e^2$. The equation of current density, for R_{max}-Δr<r, is applied in order to achieve a smooth transition to zero values. The skin depth δ is defined as:

$$\delta = \frac{c}{\sqrt{2\pi\mu_r\omega\sigma}} \tag{2.10}$$

where σ is the conductivity, ω the angular frequency, c the speed of light and μ_r the relative permeability (μ_r is 1 for most cases).

This current density profile modulates the magnetic field inside the plasma cylinder. The magnitude of the magnetic field $B(r)$ is defined through Ampere's law from the current density profile $J=f(r)$ and the radius r, decreasing as $1/r$ outside the plasma cylinder. Thus, the magnetic field magnitude is:

$$B(r) = \frac{4\pi}{c}\frac{\int_0^r J_z(r) r dr}{r} \tag{2.11}$$

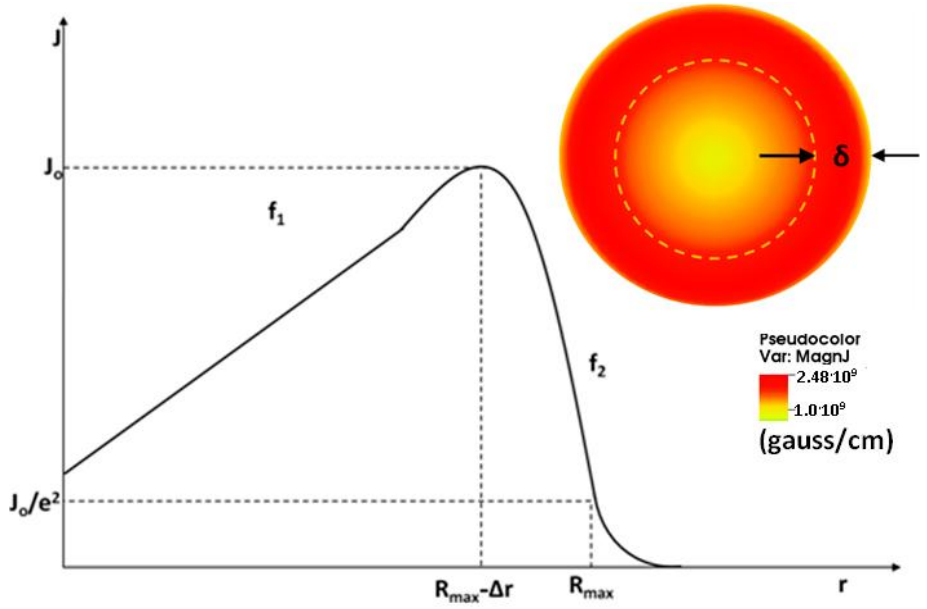

Figure 2.4: *Presentation of a typical distribution of current density along plasma radius for a smooth skin effect as described by the functions of equation 2.9. The inset picture presents the skin depth radial profile, where the red are the high current density values and the orange/yellow the lower (PLUTO simulation).*

The thermal pressure radial profile can be derived from the equation 2.6, resulting to a Gaussian one. If we consider a constant plasma temperature we have the same profile for mass density too. **The resistivity, the current density radial profile and the assumption of LTE conditions (or not) can alter the temperature profile, the thermal pressure and the mass density radial distribution.**

If equations 2.6 and 2.11 are applied for a plasma cylinder of radius r_0, the enclosed current $I_z(r)$ is obtained:

$$\frac{dI_z(r)}{dr} = 2\pi r J_z(r) \tag{2.12}$$

where

$$I_0 = \int_0^{r_0} 2\pi r J_z(r)\, dr = I_z(r_0) \tag{2.13}$$

Combining the equations 2.6, 2.11 and 2.12, 2.13, and after integration, we get:

$${I_0}^2 = 4\pi c^2 \int_0^{r_0} r P(r)\, dr \tag{2.14}$$

If we use the ideal gas relation: $P=N_i k_B T_i + N_e k_B T_e = (Z_{eff}+1) N_i k_B T$ where N_i and N_e are the number density of ions and electrons respectively, Z_{eff} is the mean ionization state, k_B is the Boltzmann constant, and we assume that $T_i \simeq T_e = T$, the equation 2.14 becomes:

$$I_0{}^2 = 2c^2(Z_{eff}+1)N_{il}k_B T, \text{where } N_{il} = \int_0^{r_0} 2\pi r N_i(r)\, dr \tag{2.15}$$

It should be noted here that N_{il} defines the number of particles per unit length of the plasma column. Equation 2.15 is called the **Bennet relation**. It calculates the total current which must be discharged through the plasma column in order for the confinement to take place at a specific temperature for a given N_{il}.

2.1.2 Radiation losses and transport in Z-pinch plasmas

Radiation transport is the redistribution of energy within a nonlinearly coupled medium by the emission, movement, and absorption of photons. Radiation absorption, re-emission and photo-ionization are considered in radiation transport studies.

Below, the principal effects of radiation transport in Z-pinches are presented:

i. The emitted power can be significantly reduced, compared with the optically thin case, by the absorption of radiation within the pinch. Optically thin means that the size and/or density of the pinch are small enough so that emitted photons escape without being absorbed: **most Z-pinches are not optically thin.**

ii. Localized radiative heating or cooling can occur within the pinch.

iii. Reabsorption and/or scattering of photons can often increase bound-state excitation and sometimes ionization.

iv. Even in the rare instance of uniformity in a pinch plasma, boundary effects on the radiation field can introduce gradients in excitation and/or ionization.

v. The emitted spectrum can be significantly affected, sometimes enhancing its diagnostic value.

High current Z-pinches incorporate increasingly larger masses of plasma and are nearly always optically thick to some or most of the photons that they produce. Modelling of the radiation transport is an important element not only in attaining an overall picture of the physics of Z-pinches, but also in optimizing their properties for applications [27]. For instance, radiation uniformity is important for Z-pinch dynamic hohlraum-driven fusion. MHD codes like MULTI-2D are employed to investigate the related physical processes. Today, the radiation transport algorithms can usually handle accurately optically thick and optically thin regions simultaneously [28,29]. We present two typical cases. The 2D Radiation Magneto-Hydro-Dynamics (RMHD) code MARED along with the 1D RMHD code CRMHA which implement more detailed radiation model are used for the radiation study of a wire array Z-pinch and Dynamic Hohlraum [15]. 3D ALEGRA-HEDP is used to simulate the thermal radiation transport in wire array configurations using two different approximations to the Boltzmann Equation [16,30]. Nowadays, the coupling of the radiation field with the HD/MHD schemes are being studied [31,32].

One interesting phenomenon, which is possible in a Z-Pinch is the so called "radiative collapse." When the temperature and density of the plasma are high enough, losses from radiation will exceed Ohmic heating. The pinch will collapse to densities much higher than the solid ones (overdense regime). Related to this phenomenon are the X-pinch crosspoint area dynamics that will be presented at the next section and pinch plasma devises related to ICF studies [33, 34].

The current at which this collapse occurs is referred to as the Pease-Braginskii (PB) current I_{PB}. For a steady state plasma, in which the Bennett relation is satisfied, the power deposited by Ohmic heating will be in balance with the power radiated through bremsstrahlung at I_{PB}. For a uniform single species Z-pinch the PB current is [12,36]:

$$I_{PB} = 2I_A \left(\frac{8\ln\Lambda}{aF_B}\right)^{0.5} \frac{(Z_{eff}+1)}{Z_{eff}} \tag{2.16}$$

where a=1/137 (Sommerfeld's constant), $F_B=(2\pi/27)^{0.5}$, Z_{eff} the mean ionization state and I_A the Alfvén-Lawson current [36]. The square root ratio considers the cross-sections for the collisions that are responsible for heating ($\sim 8\ln\Lambda$) and the energy loss from bremsstrahlung ($\sim aF_B$).

Initially during the pinching process, the current is lower than I_{PB}, the radial growth rate is positive and the column expands. In this case Ohmic heating dominates, depositing energy in the plasma and raising the thermal pressure. As the current increases and surpasses I_{PB}, the radial growth rate becomes negative indicating a contraction of the plasma. At this point, bremsstrahlung effects dominate and the plasma cools down, reducing the outward pressure. At the same time, the still rising current increases the inward $\mathbf{J}\times\mathbf{B}$ force, aiding in the contraction of the plasma. This compression will abide by the Bennett relation, adjusting the column radius (and therefore density) in order to maintain the temperature. The constriction will continue until the opacity of the plasma becomes important. The power emitted by bremsstrahlung radiation is proportional to the square of electron density N_e^2. As the plasma radius becomes smaller, the cooling rate increases, hastening the contraction. This runaway process is therefore referred to as a radiative collapse and will occur when current exceeds I_{PB} [12]. The radiative collapse process is also important for the neck formation of m=0 instabilities in high density Z-pinches and micro Z-pinches formation at the crosspoint area of plasma X-pinches [33]. The former is presented below, while the latter is a topic at the next section 2.2 related to the X-pinch configuration.

2.1.3 Z-pinch plasma stability

Z pinch are highly MHD unstable. To characterize the instability, the plasma is treated as an electrically conducting fluid with zero viscosity using an ideal MHD single fluid model. A small radial perturbation δr is applied to the surface of an initially cylindrical plasma column, changing its distance to the central z axis. In cylindrical coordinates δr is expressed:

$$\delta r = \xi_0(r) e^{i(kz-\omega t+m\theta)} \tag{2.17}$$

where ξ_0 is the amplitude of the plasma displacement, k is the wavenumber and m is the azimuthal mode number of the instability which determines its θ period [6,12].

The **m = 0** and **m = 1** instabilities are commonly referred to as the **sausage** and **kink** instabilities, respectively. The m=0 mode consists of a series of necks (constricted regions) and bulges (expanded regions) along the pinch column, while the m=1 mode is the one where the plasma column is in the form of a 3D helix or a "snake" 2D shape (experimental images of figure 2.5 and simulation results of figure 2.6). Higher m modes do not perturb the column on axis and appear as a twisted multistranded cable. Figure 2.5 illustrates typical images of the main instability modes taken from Z-pinch experiments, while figure 2.6 presents 2D and 3D simulation images of m=0 and m=1 helix like instabilities, pointing local spatial maxima and minima of magnetic and thermal pressure.

The sausage instability exhibits a quasi-periodic structure, in which the 'necks' have a smaller radius than their neighbouring (bulging) regions. In the expanded regions a dispersion of the B-field lines results in low magnetic field strengths, which coerce an expansion of the plasma. However, at the small radii the magnetic field is large creating a high PB which serves to compress the plasma further. As the deformation continues, the magnetic pressures of the bulges and necks decrease and increase respectively and the increasing disparity of PB accelerates the deformation. The relative high pressure created at the necks drives an axial flow away from the compressions and into neighbouring regions. As a result, there is no rise in the internal pressure to counteract the increasing magnetic pressure. That way, the difference in magnetic pressure causes the increase in growth rate of the surface perturbations and the unstable behaviour of the plasma [6,12].

The m=0 instability grows as $e^{\gamma t}$ and the growth rate γ [37] is:

$$\gamma = \frac{V_A}{R} \text{ with } V_A = \frac{B}{(4\pi\rho)^{0.5}} \ (c.g.s) \tag{2.18}$$

where R is the column radius, V_A is the Alfvén velocity, ρ the plasma density and B the magnetic field magnitude.

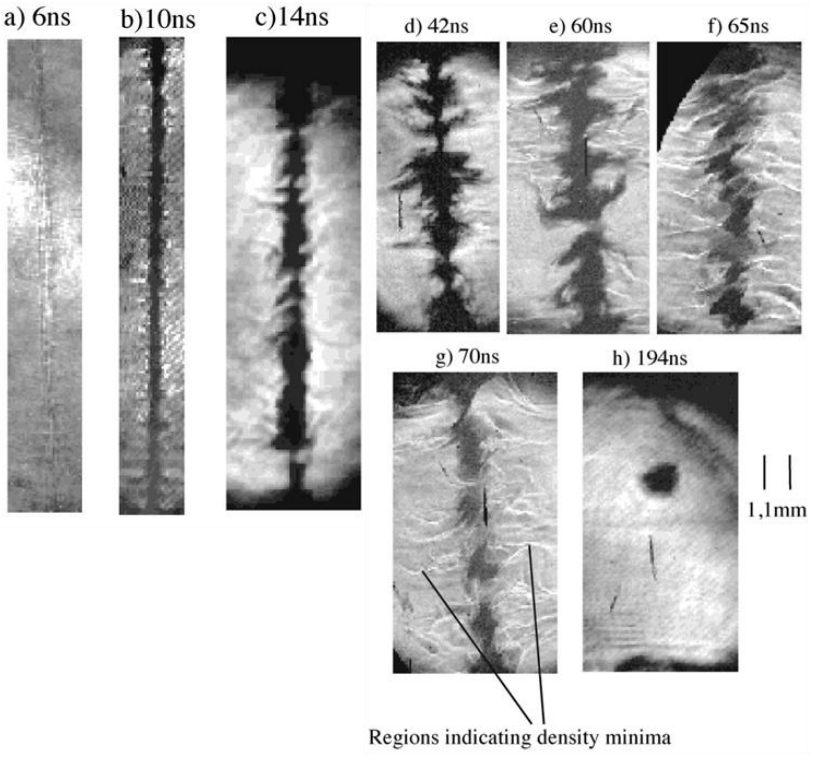

Figure 2.5: *A time sequence of experimental laser shadowgrams (a to h images) showing the plasma dynamics and the MHD instabilities' development in Z-pinch plasmas (i.e. m=0, m=1) [7].*

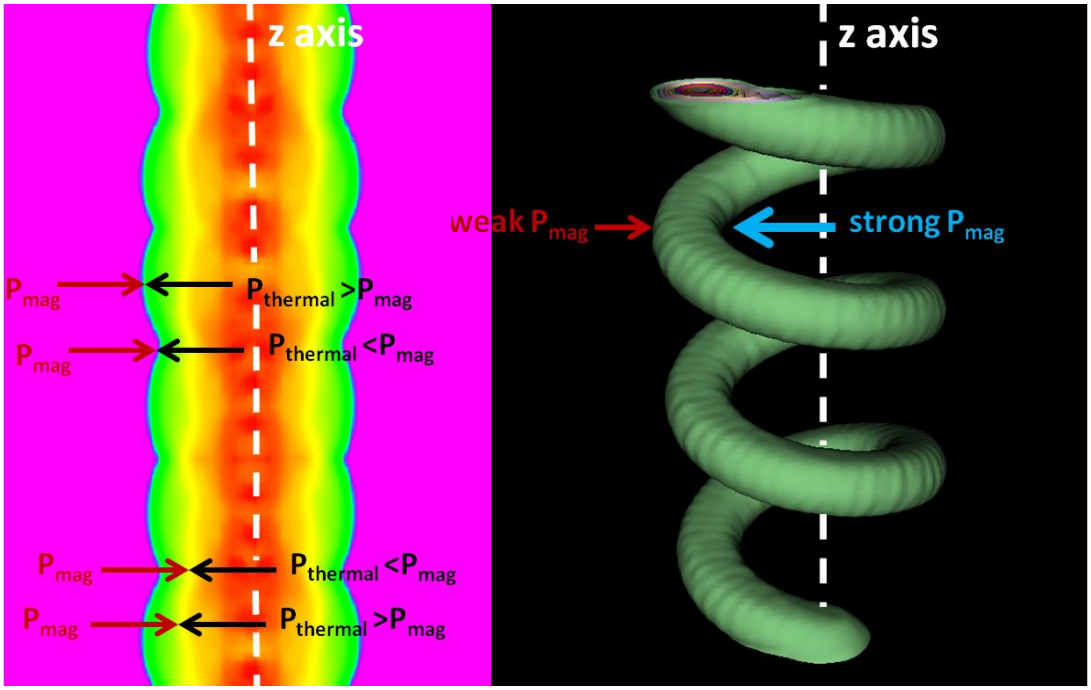

Figure 2.6: *2D density simulation images of the m=0 instability (left), at the inner plasma core and outer corona plasma, and m=1 (helical formation) 3D density isocontour simulation image (right side). The simulations were performed with code PLUTO for the purposes of this thesis.*

At the m = 1 or kink instability, the plasma column is deviated from the original axis, resulting in 2D bends or 3D 'kinks'. Build-up of the magnetic field inside the bends region creates high magnetic pressure, while the field dispersion on the outside results in regions of low PB and low magnetic pressure. In response, the plasma moves from the high to low pressure regions, increasing the amplitude of the perturbations. As the displacement becomes more pronounced, the bends become sharper and the pressure difference grows, increasing the rate of deformation [12,38].

The study of the seeding mechanisms for the generation of plasma instabilities is of crucial importance for investigating mitigation strategies of their growth rates. Experimental and numerical studies, at IPPL facilities provide this interpretation in single Z-pinch metal wires. These studies suggest that the physical processes that occur during the thermo-elasto-plastic regime of the interaction at the solid-liquid phase act as seeding for the initiation of plasma instabilities. Experiment and simulation present a remarkable agreement [5].

The inclusion of the material's physical properties modifies the electro-thermal instability (ETI) into an instability, which is called electro-thermo-mechanical (ETM) instability, having growth rates at least one order of magnitude larger than those found in the literature. Moreover, the ETM instability may act as seeding mechanism for the helical instability structures observed in pre-magnetized liner experiments and could lead to the dynamic evolution of the aforementioned instabilities of this section [4-6].

This section analysis is valid also for the initial conditions' implementations in X-pinch plasma simulations.

2.2 State of the art of X-pinch plasma configurations

The X-pinch is a plasma device in which plasmas are produced by using two or more thin crossed wires, in the form of an X [33,39-51]. Ohmic heating causes the wires to explode into a hot, dense plasma. However, since a plasma is very efficient at carrying a current, the current continues to flow and the induced magnetic field around the wires acts to confine the plasma. In a two wire X-pinch the current is divided between the two legs, with the full current only being concentrated at the central crossing point where the magnetic pressure that confines the plasma has a maximum value. Typically, a small instability will lead to plasma implosion under the magnetic pressure at the central crossing point, resulting in an intense burst of X-rays which lasts for only a few nanoseconds. The combination of radiative cooling and axial mass loss, leads the pinch to collapse rapidly and form the so called micro-Z-pinch creations as well as the density islands [33].

As we already mentioned in the introduction, the major application of the X-pinch is as a bright-point (small size) source of X-ray radiation for point–projection radiography [33,42-46,51].

Regarding the physical processes that occur in a X-pinch wire configuration, each leg of the X-pinch experiences a local, self-induced magnetic field (B_{Local}), while the configuration as a whole is surrounded by a global magnetic field (B_{Global}) (depiction of these at Chapters 1 and 4 in figures 1.1 and 4.9 respectively). In areas with a dynamically significant B_{Global}, the coronal plasma is accelerated from the wires by the $\mathbf{JxB_{Global}}$ force (where **J** is the current density) towards the vertical axis of the X. The wire cores ablate, feeding the coronal plasma, contributing to the formation of plasma jets which

propagate bi-directionally towards the electrodes [39-44,48] (further analysis at the 5.3 relative section). The crosspoint area is compressed by a significant $\mathbf{JxB}_{\mathbf{Global}}$ force and starts the micro-Z pinch formation resulting to a bifurcation or neck cascading [45,46,48,52-55]. Almost immediately after the generation of the X-ray pulse, the neck breaks and a gap forms in which the plasma density is several orders of magnitude lower than that in the neck. This process leads to the formation of a mini-diode and the generation of electron and ion beams [41,43,47,48]. The main physical events, along the spatiotemporal plasma evolution, for a two wire X-pinch, are presented at figure 2.7.

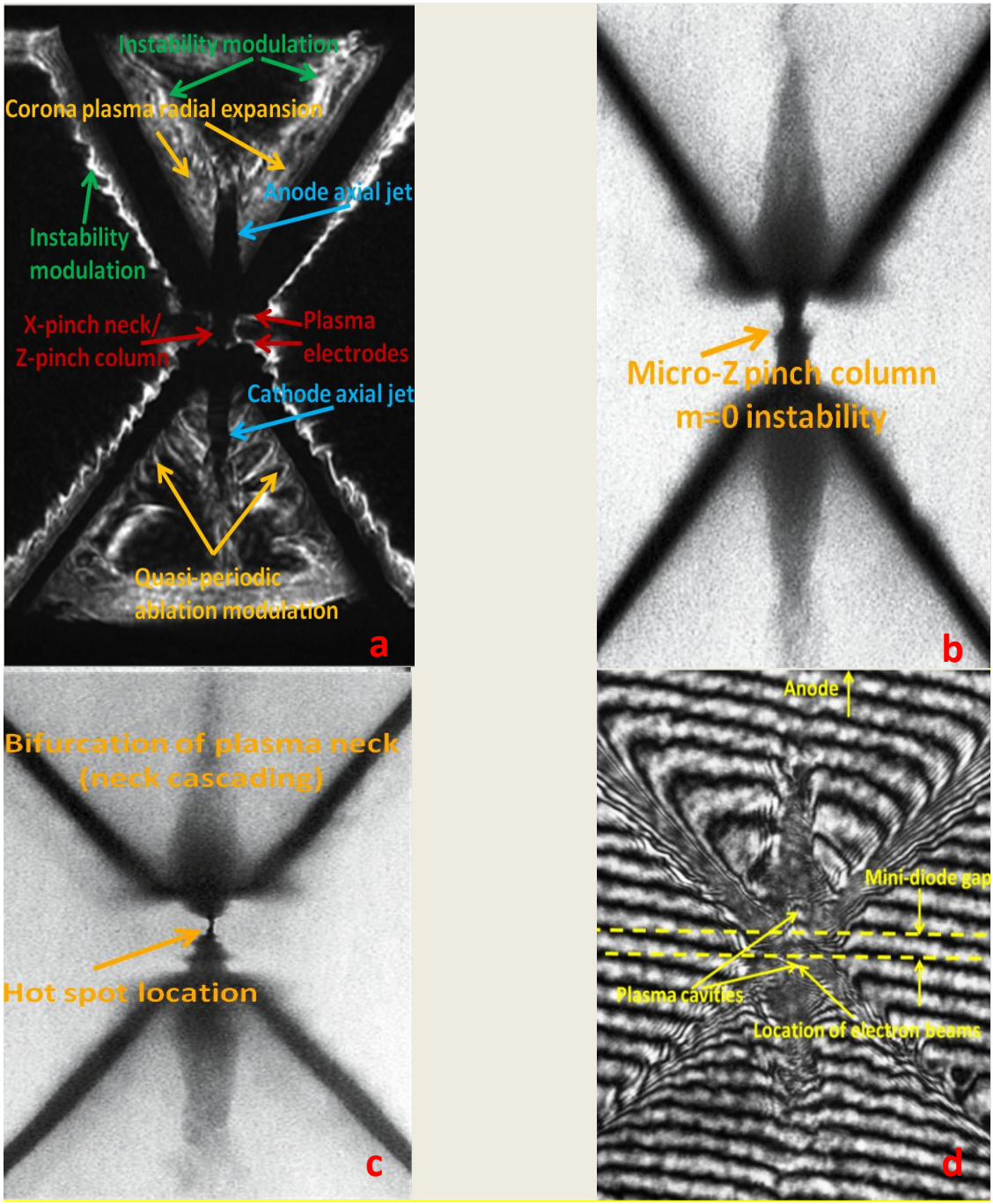

Figure 2.7: *Two wire Molybdenum X-pinch Schlieren image* (a) *[41], two wire Molybdenum X-pinch X-ray radiographs images* (b,c) *[48] and two wire Tungsten X-pinch interferometry image* (d) *[IPPL experiment], presenting the main physical X-pinch formations till the mini-diode gap presence.*

Analytical presentations of each physical process and the state of the art experimental and simulation work worldwide about X-pinch configurations, are the main subject of the next sub-sections.

2.2.1 Initial stage and wire ablation

The initial stage of the X-pinch is determined by two main processes. The first is associated with the formation and interaction of dense wire cores, while the second determines the paths of the discharge current through the diode and is associated with the formation of the coronal plasma. During the first ns, the wire material is heated to high temperature. As a result the resistivity increases [48] and the current decreases [48,49].

Evidence of non-uniform wire ablation has been seen in wire experiments, including X-pinches [56,57]. Electrical current passing through the wires, whether fast rising or slow rising, causes Ohmic heating. A substantial current causes sufficient Ohmic heating to ablate the wire material, creating coronal plasma around the relatively cold wire core. The wire ablation characteristics in X-pinches vary from the cross-point towards the electrodes, as the ratio of Global to Local magnetic field changes [43]. Additionally, the rate of wire core ablation is determined by the Global magnetic field strength and is thus a strong function of the axial position [33]. The main stages during the ablation phase are [48]: (i) heating of the wires by the current flowing through them; (ii) partial evaporation of the wire surfaces and formation of wire cores and conducting plasma channels; (iii) complete evaporation of the wires in the wire crossing and formation of a plasma load in it.

Experimental study in combination with simulation study, using GORGON code, by G. W. Collins et al [58], about the behaviour of ablation modulations in X-pinches, was carried out as a function of distance from the cross-point, and consequently as a function of the Global to Local magnetic field ratio. This study demonstrates a dependence between the magnetic field ratio and ablation properties, suggesting a transition to a classical m=0 instability far from the cross-point [41] (picture **a** in 2.7 figure). The increase in the average wavelength of the ablation flares moving away from the cross-point indicates that the relative magnetic field strengths play a dynamic role in the ablation structure. This plasma behavior was confirmed for three metals, W, Ni and Cu. These ablation modulations are also present at the 5.4 Result section using also GORGON code for a tungsten two wire, sharp angle of 50^{o}, configuration.

The rate at which mass is ablated from the wire cores, for a Z-pinch array, to replenish the corona is in general well approximated by a **rocket model**, assuming a fixed velocity of the ablated material [59]:

$$V_{abl}\frac{dm}{dt} = -\frac{I^2}{c^2 \cdot R_0}\ (c.g.s) \tag{2.19}$$

where V_{abl} is the fixed "ablation" velocity, dm/dt is the mass ablation rate per unit length, I is the drive current, R_0 is the array radius and c the speed of light. This has been observed by both laser imaging

and radiography at different current levels for many different experiments including X-pinches [60]. Specifically Simon C. Bott et al in [61] investigated the ablation of wires in two-wire tungsten *X*-pinches driven by an 80kA current. The applicability of the momentum balance assumed in the rocket model was also valid in the X-pinch configuration, using a fixed ablation velocity of 150km/s despite the changing $\mathbf{J}\times\mathbf{B}_{\mathrm{Global}}$ force in these experiments, an average Z_{eff}~10, ablation plasma temperature ~15eV and R_0~1mm.

The neck formation is submitted, generally, to a specific ablation process. In the beginning of this stage, the wires are melted and heated up to the point where they cease to exhibit metallic conduction. This results in an electrical explosion of the wires followed by expansion of their material. At the end of this stage, a micro-Z pinch neck is formed in the wire crossing region due to implosion of the wire material [54]. The intense ablation rate due to the $\mathbf{B}_{\mathrm{Global}}$ near the cross-point area forms in most cases the electrode gap after the X-ray pulse, while the wire cores and surrounding corona plasma are still present far from the central area (picture **d** in figure 2.7) [40,41,45].

2.2.2 Coronal plasma dynamics

The formation of the corona plasma is a very early process beginning almost right away from the current start. Electric breakdown of the evaporated wire material or the gas desorbed as a result of the wire heating takes place and the plasma corona appears. The current through the load increases abruptly; however, the current flowing through the wires is shunted by the corona plasma, so energy release in the wires almost terminates at this early stage [48].

The corona plasma contributes mainly to the wire radial expansion at the first stages of X-pinch evolution. The streaming plasma converges to form jets on both sides of the cross point. As the distance from the cross point increases, the coronal plasma's effect of merging becomes less pronounced. At this time, no compression of the plasma at the cross point is observed, the main contribution to the jets being the streaming plasma from the wires [42]. Simulations by GORGON code confirm the aforementioned corona spatiotemporal evolution while a similar 3D spatiotemporal dynamic evolution is presented and discussed in section 5.3 for a two wire wide angle of 100^{o} X-pinch configuration.

Some studies on the behaviour of the coronal plasma formed in a 450 kA X-pinch have been carried out. Mitchell et al [44,47] showed with optical and XUV framing images that the low density coronal plasma contributes to jet formation. The jets were formed due to sweeping of the coronal plasma to the mid plane of the X-pinch. In Beg et al [42] X-ray images were recorded with a framing camera transmitting x-rays above 1 keV. In these experiments, a significant change in the dynamics of the coronal plasma was observed when the angle of the x-pinch was narrowed from 120^{o} to 81^{o}. The change in behaviour of the pinch has been attributed to the stronger global magnetic field near the cross-point, which extends to the electrodes. The central plasma was also observed to be m=1 unstable as soon as it made contact with the electrodes. Kink modulations are also observed in plasma jets in four different materials by G. S. Jaar and R. K. Appartaim [40] in a microsecond X-pinch through light-field schlieren imaging and optical framing photograph. These results demonstrate that the coronal plasma plays a significant role in the X-pinch dynamics, especially in jet and plasma instability formation and dynamic evolution.

Experiments using two wire X-pinches from both bare and gold coated molybdenum have been presented by D. M. Haas et al [41]. The formation of a sheath initially occurred close to the wire cross point, both as a result of the proximity of the wires to each other, and the increased magnetic field at smaller radii. This sheath then extended towards the electrodes at ~70km/s, with the anode side of the cross-point displaying a slightly higher velocity than the cathode side. The high emission regions of the XUV images corresponded to the coronal plasma, which was forming the sheath, and to the jet when this was formed. The wire cores, still at their initial position, showed little emission during this process. This suggested that the drive current flew mainly through the coronal plasma and in the jet as it was formed. The path of the current moved away from the wire cores and eventually flew through the formed Z-pinch when the jets reached both electrodes (~40 ns). Similar observations were made in [62] by showing similar processes for thinner wires (13μm here versus 125μm in the referenced work). The current was supported by very low density plasma; $N_e<5.5\cdot10^{18}cm^{-3}$ since the current path was not observed on comparable Schlieren imaging. The inward moving current carrying plasma appeared to show a variation in emission along its length as well as a low amplitude modulation at later times. These could be due to the MHD (m = 0 and m=1) instabilities which were a result of the current flowing in the low density plasma, or as an effect of the deceleration of the plasma flow by the magnetic field [63].

2D simulations were executed to test the empirical law $G\cdot I^p$ of the mass production rate of cold plasma, where G is a numerical factor which reflects the material properties and should be found empirically, I is the current through the wire and p is an adjustable parameter, which was close to 2 (a similar law of the rocket model presented earlier). Simulation results for various G factors indicated the sensitivity of the plasma evolution to this parameter. A clear difference in the coronal plasma formation and dynamics was observed for low versus high G factors [41].

2.2.3 Axial jet formation

Another common feature of X-pinches is the development of plasma columns on the X-pinch axis, which appear to start at the crossing point and increase in length toward both the anode and the cathode. The density of the plasma in these columns is considerably lesser than that of the solid core but similar to that of the limb corona. These columns of plasma have been observed in schlieren, shadowgraphy, interferometry and soft x-ray pinhole images of X-pinches [39-44,46-49,61,64].

A thorough study by Mitchell et al [44,47] presented a quite revealing spatiotemporal analysis of the jet columns formation for a two Aluminum wires of 10μm at 100kA. It is believed that the plasma in the column comes from several different sources. One source is a low density, supersonic component expanding from the limbs which was not detected by the interferometer. The authors suggested that another component of the plasma may come from the corona plasma in the parts of the limbs close to the crossing point. This plasma was observed to expand and reach the axis where it could stream at the sound speed into the low field region. The final source of the column plasma was the axial expulsion of material from the crossing point due to the pinching process. The initial stages of jet formation were from the coalescing on the axis of a low density expansion from the corona plasma of the X-pinch limbs, similar to the formation of the precursor in wire array Z pinches, while at the next stages the jet was fed from corona plasma from the limbs near the cross-point and material from the

main cross-point area due to the plasma pinching. This spatiotemporal jet formation is also supported by the analysis of the simulation results in 5.3 section of this dissertation.

The confinement of the plasma column is also a two process mechanism [44,47,33,64]. The first collimation process is due the bombardment of the incoming material from the X-pinch legs. Current flow in the plasma column may also contribute to the observed confinement. The presence of an azimuthal B field has been shown to be a good confinement mechanism for plasma jets and simulations of wire array Z pinches have shown that a combination of supersonic bombardment and an azimuthal B field confines the precursor plasma. However, the increased symmetry in the case of the wire array Z pinch would make the confinement due to bombardment more effective than in the X pinch. This two-process mechanism is also simulation supported by this dissertation. Furthermore, it is supported by the analysis of J. P. Chittenden et al [33] and F. N. Beg et al [42] for 2 wire Molybdenum X-pinch experiments along with 2D and 3D simulations by GORGON code having a high Mach number and low divergence which are similar to jets formed in conical wire array Z-pinches.

The jets produced on a microsecond X-pinch have been studied by G. S. Jaar and R. K. Appartaim [40] through light-field schlieren imaging and optical framing photographs across 4 different materials: Al, Ti, Mo, and W. The axial velocity of the jets was measured and exhibited no dependence on atomic number Z of the wire material. There may be a dependence on another factor namely, the current rise rate and/or the value of the peak current. The average axial jet velocity across all four materials was measured to be ~29.6km/s. Similar velocities of ~25km/s were measured by Beg et al [42] for Molybdenum and Aluminum wires for X-pinch discharges driven by a 160 kA/80ns pulse. Supersonic jet propagation with a velocity of 33±0.6 km/s in low-current X-pinches comprising of four 7.5 μm diameter tungsten wires driven by an 80 kA/50 ns current pulse were presented by D. M. Haas et al. This is a close estimation of this dissertation's ~39 km/s for two tungsten plasma wires driven by a 45 kA/50 ns current pulse presented in 5.3 section.

The average jet diameter and the average radial jet expansion rate display inverse relationships with Z, which may be attributed to radiative cooling and inertia. The mean divergence angle of the jet varies with wire material and is correlated inversely with the thermal conductivity of the cold wire [40]. Asymmetry between the anode and cathode jet behavior is thought to be caused by electron beam activity and is observed in many different experimental studies and materials [40-42,44,47-49].

A strong radiative cooling rate results to low temperature profile and strong collimation of the main jet body. The inclusion of thermal conductivity terms and optically thin losses and/or radiation transport modules support this behavior in a MHD simulation (further analysis in 5.4 section) [33,39,42,64]. Temperatures of 20eV-30eV were observed in [42], 35ns from the current start, at the converging streams region while they were decreasing along jet's length due to the radiation losses. The temperature of the jet above the convergence region was ~6eV, which agreed with the experiment estimate in [39], 140ns from the current start. The simulated jet Mach number was >20. The jet is cooler than the surrounding matter, which was >10 eV. This supported the radiative cooling expected in these jets [39,65]. Temperatures of ~15eV [64], near the cross-point area, along the symmetry axis of plasma jet, reducing to ~2eV at the jets tip, are estimated 49ns from the current start, presented at 5.4 and 5.5 sections of this study.

Kink modulations have been observed in X-pinch jets after making contact with the electrodes, indicating current flow through them [42]. Also kink modes were experimentally observed at jet formations as a result of current flowing through the dilute corona plasma and the deceleration of the plasma flow by the magnetic field as we already mentioned earlier [40,41,63]. The kink modulations along with the multilayer structure is also present in astrophysical jets [40]. A possible scalability to astrophysical jets due to the relative Mach number and the hydrodynamic nature of the jets was mentioned in [39]. The scalability and a thorough relevant astrophysical parameter estimation for a two tungsten wire X-pinch configuration is discussed at 5.5 section.

2.2.4 Cross-point dynamics

Cross-point dynamics is one of the more interesting physical studies in X-pinch configurations, related to the production of Hot-Spot(s) (HS), X-ray pulses and electron-ion beams from the formed mini-diode gap [33,45,46,48,49,53-55].

A general two process evolution of plasma neck formation and implosion was discussed in [54] by V. I. Oreshkin et al for two or four molybdenum wires of different diameter. The first stage is neck formation. This stage begins with an electrical explosion of the wires forming the X-pinch and at the end of the stage, a micro-pinch (neck) is formed in the region where the wires are crossed (pictures **a** and **b** in figure 2.7). The second stage is neck implosion. The implosion is accompanied by outflow of matter from the neck region, resulting in the formation of a “hot spot” (picture **c** in figure 2.7). Analytical estimates obtained in this study indicate that these stages are approximately equal in duration. The hot spot was formed at the final stage of neck formation, and its axial and radial dimensions were both much less than the length of the neck [33,48,49,53-55]. The thermo-dynamical parameters of the hot spot of an X-pinch were determined from its radiative characteristics. The hot spot was formed under conditions close to Bennett equilibrium [equation 2.15] and a soft x-ray pulse was generated once almost the whole of the material has flown out from the hot spot. In the experiment, the pinch mass per unit length at the final stage of implosion made some tenths of one percent of its initial value. Having analyzed the neck implosion dynamics, they verified a scaling, which makes it possible to explain the observed dependences of the time of occurrence of an x-ray pulse on the X-pinch current and mass. They also proposed an experimental-based formula and a theoretical formula for the micro Z-pinch neck length estimation suggesting that the time of occurrence of an x-ray pulse in an X-pinch is determined by the neck length.

2 wire Molybdenum X-pinch experiments by J. P. Chittenden et al in [33] also presented simulation pictures by GORGON code for the structure of the neck formation and evolution just before, during and just after peak compression (~30ns from the current start) and comparisons of synthetic radiographs (areal density maps) with experimental data. As time progresses, a longer length of the wire core ablates and compresses to the axis and this combined with the axial $j_r B_\theta$ force serves to elongate the cylindrical micro-Z pinch that forms at the cross point. The combination of radiative cooling and axial mass loss means pinch rapidly collapses to small size (as described in 2.1.2 subsection). The mass per unit length of the micro-*Z* pinch is smallest where the axial $j_r B_\theta$ force is largest, i.e., at the ends of the Z-pinch and, consequently, in a simulation without any perturbation, result to two tightly compressing regions at the ends of the micro-*Z* pinch, with an isolated island of

plasma at the center. This spatiotemporal behavior of plasma neck is observed in GORGON and PLUTO simulations of an X-pinch configuration, at 60ns from the current start, resulting to one or two denser spot formations (possible HS's area) along with the density island at the center, as presented in 5.4 section of this study [66].

The simulations provide quite enlightening information and details for the neck evolution and the bifurcation or cascading process (picture c in figure 2.7) [33,49,53]. In [33], parts of the micro-*Z* pinch have collapsed below the resolution of the 10 μm of the simulation's resolution at ~30ns, presenting an upper limit for the cascading process necks diameters. The evolution of the rest of the X-pinch is still consistent with experiment. Late in time, the axial Lorentzian force drives a strong shock into the plasma electrode structures. Since the magnetic field is largest on axis, the center of the electrode reaches higher velocity than the edges producing a characteristic quasi-spherical shock wave as observed in experiment. Once the length of the neck region becomes long compared to its radius, both the thermal pressure forces and the Lorentzian along the central jet axis are large at the ends of the neck region and negligible at the center. Mass depletion at the center therefore ceases and this region stops collapsing. The ends of the neck region start to form two identical, smaller, collapsing necks. This ‘‘bifurcation’’ or ‘‘cascading’’ process of the neck regions continues until 8 or 16 necks are formed, depending on the resolution [33]. In experiments, such a symmetric perturbation will not occur, so while this process may explain why multiple x-ray bursts are often observed, the bifurcation process is unlikely to repeat itself to the extent seen in simulation. 2D simulations with similar observations were conducted by S. A. Pikuz et al [49] and by G. V. Ivanenkov et al [53] for two Molybdenum X-pinch wires of 2x20μm focusing on the cascading process of neck evolution and HSs formations.

The physical processes occurring in the X-pinch plasma neck and the HSs formation and emittion were extendedly studied by S. A. Pikuz et al [48,49]. Their X-pinch configuration consisted of two or four metallic wires of Tungsten, Molybdenum and Aluminum of different diameters. The results of measurements obtained in experiments with different X-pinches showed that, if one succeeded to fix the time close to the instant of maximum compression, then the position of the emitting region (HS) always almost exactly corresponds to the position of the neck with the minimal diameter. It is obvious that, due to cascading, the HS position almost never corresponds not only to the center of the wire crossing, but also to the centers of low-order necks. Data on higher order necks (higher than fourth) are very scarce, because, for them to be observed, it is necessary that parallel X-pinch emission pulses be separated in time by no more than 100 ps. At the instant of X-ray generation, the well-localized fast energy release occurs in the HS and the processes in the neck region acquire the character of a point explosion. Both axial and radial ejections of the neck material are observed in the images, and its expansion rapidly becomes quasi-spherical (also observed in [33]), causing the generation of shock waves in the X-pinch plasma. The shock wave and the relevant axial plasma motion can affect the pinching process in the neighbouring regions of the neck and even completely destroy it. Therefore, HSs may arise either very close in time (if they are located in the close vicinity of explosion) or sufficiently far in space (i.e., in regions to which the shock wave propagates over a time longer than the time during which the maximum compression is reached in them). This explains the characteristic double macrostructure of the X-pinch HS observed already in the initial stage of experiments. Such a

double structure corresponds to second-order necks separated by a distance at which their mutual influence is still insufficient to violate the implosion process [48,49].

The activation of the adaptive mesh refinement (AMR) tool for a fine resolution at the cross-point area at the 4.3 PLUTO version (or to a next version), including the MHD-PIC related option, could be a robust simulation scheme for the cascading neck study and the formation of HSs resulting to the evolution of the electrode gap and the ejection of electron and ion beams.

2.3 Astrophysical entities and laboratory Astrophysics experiments and corresponding simulations

In the last decades, experiments on pulsed power facilities and high-power lasers have been conducted aiming at studying astrophysical phenomena in the laboratory. More precisely the study of magnetically driven jets in conical wire arrays (a modification of the wire array Z-pinch) [67-72], radial wire arrays and foils (also a modification of wire array Z-pinch and Z-pinch foils) [67,71-74] were developed over the past two decades. Jets obtained by means of suitable de Laval nozzles propagating along the longitudinal axis of a modular cylindrical vacuum vessel [75] or by expanding plasma outflow, generated by ablating plasma from a solid by a high-power laser, were used for scaling experiments for astrophysical jets originating around Young Stellar Objects (YSOs) [70,76-80]. The similar structure and Mach numbers among YSOs jets and X-pinch axial jets, were discussed in [39] and [40].

Emerging areas of research have been aimed at producing complex dynamical phenomena, such as compressible hydrodynamic mixing, hypersonic jets, shock physics, radiation hydrodynamics and photo-ionized plasmas. These can help to understand the physics of phenomena associated with a wide range of astrophysical objects, including proto-stellar and Active Galactic Nucleus (AGNs) jets, HH objects, supernovae explosions and the subsequent generation of remnants and photo-evaporated molecular clouds. The presentation of these Astrophysical objects is at the 2.3.1 subsection mainly for the ones that have jet similarities with the appropriate laboratory experiments.

The scaling for physical systems can be described by a small set of partial differential equations. The central point is the non-dimensionality of the equations, which leads to a minimum set of non-dimensional parameters of which must all match in order for one system to be the scaled version of the other. A brief explanation of the parameters for several astronomical environments is presented at the next subsections. Also, several laboratory environments that may be proposed as scaling candidates are presented [67,68,72,81].

2.3.1 Presentation of astrophysical objects relevant to laboratory astrophysics studies

Young Stellar Objects (YSOs) are stars in the first phase of their lives, before they enter the main sequence of the Hertzsprung-Russell diagram and are fed by hydrogen fusion. YSOs are formed by contraction (and fragmentation) of molecular clouds (schematic presentation in **a** at figure 2.8). They are always surrounded by an accretion disk of matter illuminated by the central star (**b** figure 2.8).

Jets and outflows produced during star-formation are observed on many scales: from the “micro-jets” which extend over a few hundred Astronomical Units to the “super-jets”, which propagate over distances of a few parsecs [67]. Protostellar (and galactic jets) are thought to be powered by the

combination of rotation and magnetic fields, which extract the rotational energy from the accreting system and create magnetic stresses which accelerate and collimate the flow. Jets associated with low-luminosity ($L_{bol} < 10^3 L_\odot$) YSOs have velocities in the range ~150−400 $km \cdot s^{-1}$, large Mach numbers (>20), and inferred mass outflow rates ~10^{-9}–10^{-7} $M_\odot \cdot yr^{-1}$. They are collimated on scales of a few tenths of AU, and exhibit opening angles as small as ~3^o to 5^o on scales of 10^3 – 10^4 AU. High-resolution observations of optically visible jets from classical T Tauri stars reveal an onion-like morphology, with the regions closer to the axis having higher velocities and excitations and appearing to be more collimated.

YSO jets are supersonically ejected into the ambient medium and often show a well collimated chain of knots detected in several bands, e.g. optical and X-ray bands (pictures **b**,**c** and **d** in figure 2.8) [82,83]. Proper motions of Herbig–Haro (HH) objects (the brightest shocks within jets) were first observed decades ago. These observations showed the shocked nature of the bipolar flows, while the vastly superior spatial resolution provided by the Hubble Space Telescope (HST) made it possible to clearly resolve cooling zones and individual shocks in each region [83].

YSO jets are detected during the early stages of evolution (class 0 and class I) and in Classical T Tauri Stars, when accretion of material onto the central object is still at work, while they are not observed in more evolved stages when the accretion process is no longer active. YSOs outflow genesis originates from magneto-centrifugally accelerated disk or stellar winds. Most models envision a centrifugally driven wind of accreted matter (figure 2.8). What is debated is whether the wind is launched from the stellar surface or its vicinity by the stellar magnetic field or whether it originates further out in the disk and involves the interstellar magnetic field [84-86]. The collimation process is more controversial [76,87].

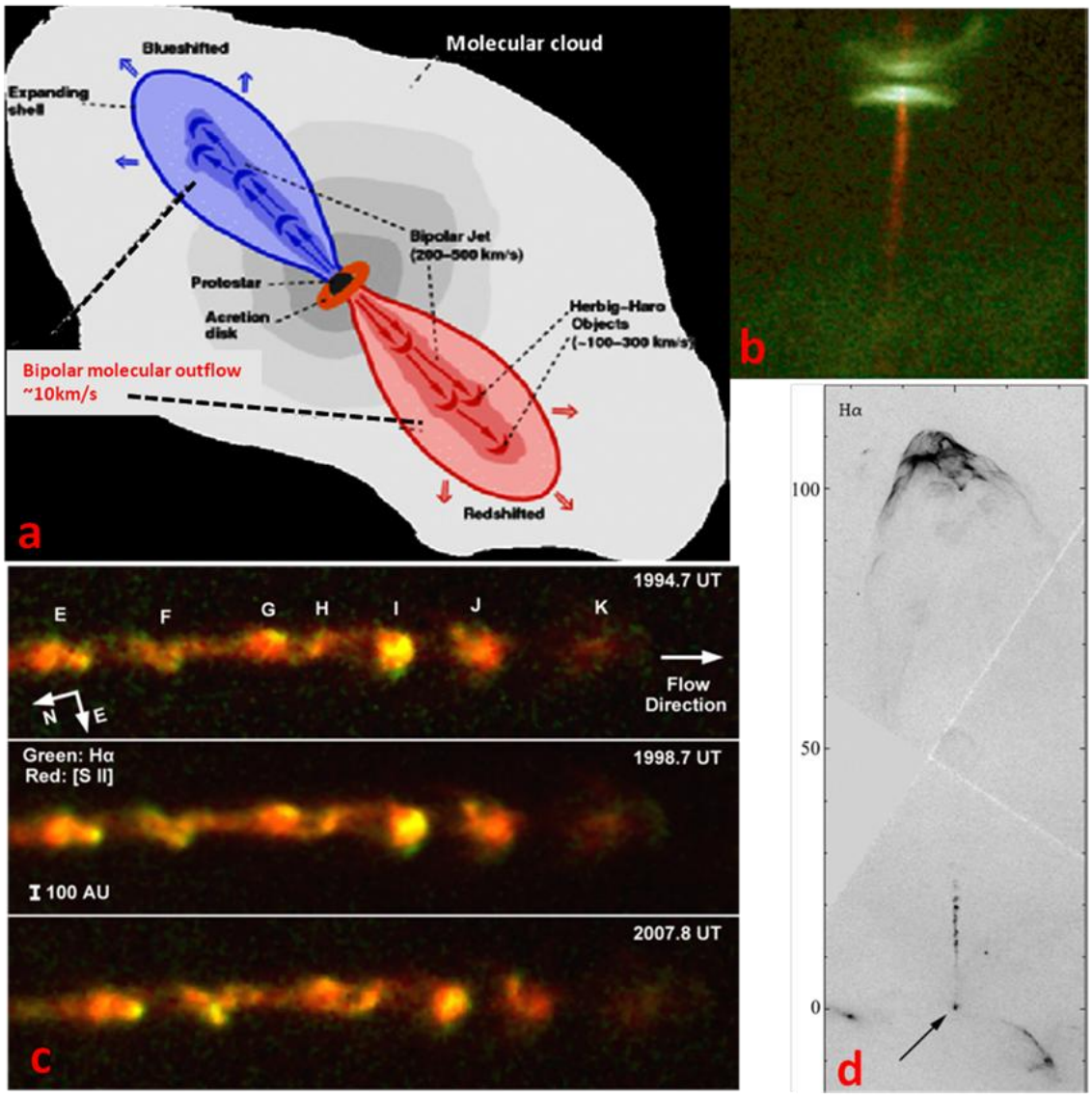

Figure 2.8: [a] *Disk-jet scenario valid in the formation of stars of all masses.* [b] *Hubble Space Telescope image of HH-30 jet (NASA press release of June 6, 1995). An accretion disk observed edge on is seen at the top of the image as a dark band between its outer parts illuminated by the central star. The young stellar object is obscured by the densest part of the disk [71].* [c] *Colour composite of the brightest portion of the HH 34 jet. Hα is in green, [S ii] in red, and yellow denotes emission in both filters. The flow moves from left to right. The bottom of knot F has become nearly pinched off in the last image. Knots I, J, and K all faded significantly between 1998 and 2007 (third-epoch Hubble Space Telescope images)[83].* [d] *A jet from a young star. The star situated inside the lowest knot (indicated by the arrow) is obscured by a compact reflection nebula. A knotty structure of the jet is obvious. Visible at the top of the figure is a bow shock produced by the interaction of the jet with the ambient medium [71].*

Numerical and simulation investigation of a two-component outflow were reported by T. Matsakos et al and O. Teşileanu et al in [88[and [89] respectively where a central stellar component around the jet axis was surrounded by an extended disk wind. They stated that the precise contribution of each component may depend on the intrinsic physical properties of the YSO-disk system as well as its

evolutionary stage. The analysis of the two-component jet simulations was carried out by the simulation models of PLUTO code [90,91]. The values for the along the axis density, temperature, and velocity provided by the simulations were within the typical range of protostellar outflows. They outlined a well-collimated and knot-structured jet, which was surrounded by a less dense and slower wind. The jet was found to have a small opening angle and a radius that was also comparable to observations [89]. A sophisticated cooling function (MINEq cooling module in [91]) incorporated optically thin energy losses in the dynamics, allowing a self-consistent treatment of the jet evolution.

Axisymmetric resistive magnetohydrodynamic (MHD) simulations for a generalized solution of the Blandford & Payne type were performed in [92], and compared with the corresponding analytical and numerical ideal-MHD solutions. They introduced $R_\beta=(\beta/2)R_m$ with β the plasma beta and R_m the magnetic Reynolds number, measuring the importance of the resistive effects in the energy equation. The presented simulations revealed that for a range of magnetic diffusivities corresponding to $R_\beta \geq 1$ the flow remained close to the ideal-MHD self-similar solution. The NIRVANA code was used in these simulations, while the ideal MHD simulations had also been confirmed (88), by using the PLUTO code.

Conclusions of the aforementioned numerical work summarized that the jet radius, as well as the opening angle, were also found to be close to typical YSO jets. The dense and hot inner part of the jet emitted strongly, with the synthetic emission maps showing a well-collimated outflow that closely resembled real observations.

Other simulation works using advanced Astrophysical codes produced similar results enhancing the two and three component YSO and AGN jets formation, focusing on the magnetic field contribution and the radiation energy exchange for the jet's collimation and temperature profile. For example, the effect of large scale magnetic field on the formation of two-component jets in magnetohydrodynamic disk winds simulations was presented by Jan Staff et al [93] using the ZeusMP astrophysical code. Excellent agreement between features seen in the simulations and of Herbig-Haro objects from multi-epoch Hubble Space Telescope observations was reported by E. C. Hansen et al using AstroBEAR, a highly parallelized adaptive mesh refinement (AMR) multi-physics code. They concluded that YSO jets may be dominated by heterogeneous structures such as knots or clamps and that interactions between these structures and the shocks they produce can account for many details of YSO jet evolution [94]. FLASH AMR multi-physics code, taking into account thermal conduction and radiative losses, was also used to analyze the Chandra X-ray telescope observations of HH 154 by investigating the evolution of its X-ray source [95]. They concluded that the X-ray emission from HH 154 is consistent with a diamond shock originating from a nozzle through which the jet was launched into the ambient medium. PLUTO code was also used to study HH 154 jet and the jet associated with DG Tau, a Class II disk-bearing source or classical T Tauri star (CTTS) [96]. They performed a set of 2.5D magnetohydrodynamic numerical simulations that modelled two component supersonic jets ramming into a magnetized medium. Axisymmetric MHD jet launching was simulated by AMR PLUTO models, including photoionization and optically thin losses in a recent work also by Z. Ahmane et al. They were performed to study the effect of X-ray photoionization, coming from the vicinity of the central star, on the ionization fraction inside the jet that can be advected at large distances [97].

Three dimensional MHD simulations of magnetically driven, radiatively cooled laboratory jets were and are produced (i.e. in [70-74]) with an outflow structure comprising an expanding magnetic cavity

which is collimated by the pressure of an extended plasma background medium, and a magnetically confined jet which develops within the magnetic cavity. “Knotty” jets emerge from the system with similar morphology observed in many astrophysical jets like the ones we already described. Such structures are conical wire arrays or radial wire arrays or other laboratory configurations as the ones we presented earlier. The scaling and similarities of these jets with the astrophysical ones is discussed at the next two sub-sections [82-106].

2.3.2 Prospects for scaling

The dynamic range of the scaling parameters for the astronomical environments is, much larger than the range among the available laboratory experiments. A large part of the range covered by the astronomical environments is inaccessible in the laboratory. This means that the odds of successfully simulating a given astronomical environment in the laboratory are little. However, the odds of a given laboratory environment having an analogue in astronomy are much better [81]. In this thesis we will focus on this analogy.

Other studies also presented the estimation of similar dimensionless values. A. Ciardi presented a general estimation for YSOs and laboratory experiments [67], while G Revet et al presented these numbers for the DG Tau A object and its associated HH 158 jet in its launching region and the relevant experiment of this study [76]. Six dimensionless parameters were presented for stellar jets and the related values for conical wire arrays of W, Fe and Al, by S. V. Lebedev et al in [68]. Dawei Yuan et al listed also dimensionless parameters of laboratory jets compared with that of typical HH objects in a recent study [80]. Table 2.1 presents the typical values of the most important dimensionless parameters of the aforementioned studies.

Dimensionless Parameters	YSOs [ref 67]	Lab [ref 67]	DG TAU A/HH 158 [ref 76]	Lab [ref 76]	Stellar jets [ref 68]	Lab [ref 68]	HHs [ref 80]	Lab Au jet [ref 80]
Mach number	>>5	5-40	13	3	>10	≥20	≥5	~15-20
R_e	$>10^8$	$>10^4$	20	$5\cdot10^4$	-	$>10^4$	$\sim10^8$	$\sim10^8$-10^9
R_m	$>10^{15}$	10-10^3	$4\cdot10^{17}$	$3\cdot10^3$	-	-	-	-
Plasma β	10^{-2}-10^2	10^{-2}-10^2	-	-	-	-	-	-
P_e	$>10^7$	50-10^4	$2\cdot10^4$	2	-	>10	$\sim10^7$	$\sim10^3$-10^4
χ	<1	10^{-2}-10	-	-	≤1	≤1	<1	~0.2-0.3
Localization parameter δ	$<10^{-6}$	$<10^{-4}$	-	-	-	$\leq10^{-4}$	-	-

Table 2.1: *Presentation of seven dimensionless parameters for laboratory and astrophysical jets prepared for the purposes of this thesis. The localization parameter $\delta=\lambda_{mfp,\perp}/r_j$ is the ratio of the mean free path $\lambda_{mfp,\perp}$ of plasma particles perpendicular to the jet flow to jet radius r_j.*

A thorough estimation, presentation and scaling estimation of these seven and other dimensionless parameters for X-pinch plasma tungsten laboratory jets, is presented at the section 5.5 of the Results Chapter.

2.3.3 Laboratory-Astrophysics jets experiments and simulations

Collimated outflows (jets) are observed in different types of astrophysical objects, spanning a very broad range of spatial scales. Some examples include bipolar outflows from galaxies, with typical lengths of thousands of light-years, to jets from young stellar objects, with characteristic lengths of hundreds of astronomical units. Astrophysical jets are typically studied with high resolution observations and computer simulations. Nevertheless, there are still many open questions regarding their dynamics (i.e. the jet-launching mechanism close to the ejection source), and the mechanisms which generate and sustain the high degree of collimation in the outflows far from the launching point.

Study of astrophysical phenomena by the means of carefully designed scaled experiments, has seen major advances in the past years due to the development of High-Energy Density Physics (HEDP) facilities. One of the applications of this new research area is the study of astrophysical jets from young stars. Astrophysical jets can be appropriately scaled to laboratory conditions if their dimensionless parameters are sufficiently similar to those in the laboratory system i.e. Mach, Reynolds, magnetic Reynolds, Peclet numbers [67,74,76,98] (scaling properties analyzed in the previous subsection).

A recent work by Paul M. Bellan [99] presented experiments and models of MHD jets and their relevance to astrophysics and solar physics. MHD-driven jets presented different mechanisms dominating in different parts of the jet. A detailed analysis is the following (**a** in 2.9 figure):

i. The jet main column is squeezed by the pinching resulting from the toroidal magnetic field and is accelerated on axis by the gradient of the axial pressure gradient resulting from the axial gradient of this squeezing.
ii. Off axis magnetic forces resulting from the axial gradient of the toroidal field provide axial acceleration. The jet tip has a retarding force because of the strong curvature of the poloidal magnetic field at the apex.
iii. This results in an axial non-uniformity of the jet velocity such that the tip velocity moves more slowly than the fluid behind the tip. The stagnation in the jet frame resulting from this axial non-uniformity, compresses embedded toroidal magnetic flux, thereby amplifying the frozen-in toroidal magnetic field and so enhancing the pinching to produce collimation of the jet.

Because the ideal MHD equations have no intrinsic scale, these conclusions can be relevant to solar and astrophysical plasmas as well as laboratory plasmas [99,100]. Experimental measurements supported these arguments. S. You et al [100] proposed a universal magnetohydrodynamic pumping process explaining why such collimated, plasma-filled magnetic-flux tubes are ubiquitous presenting experimental evidence from carefully diagnosed laboratory simulations of astrophysical jets. They emphasized that strong flows and collimation could be driven by even modest amounts of current, before reaching the kink instability (high current) threshold (**b** in figure 2.9).

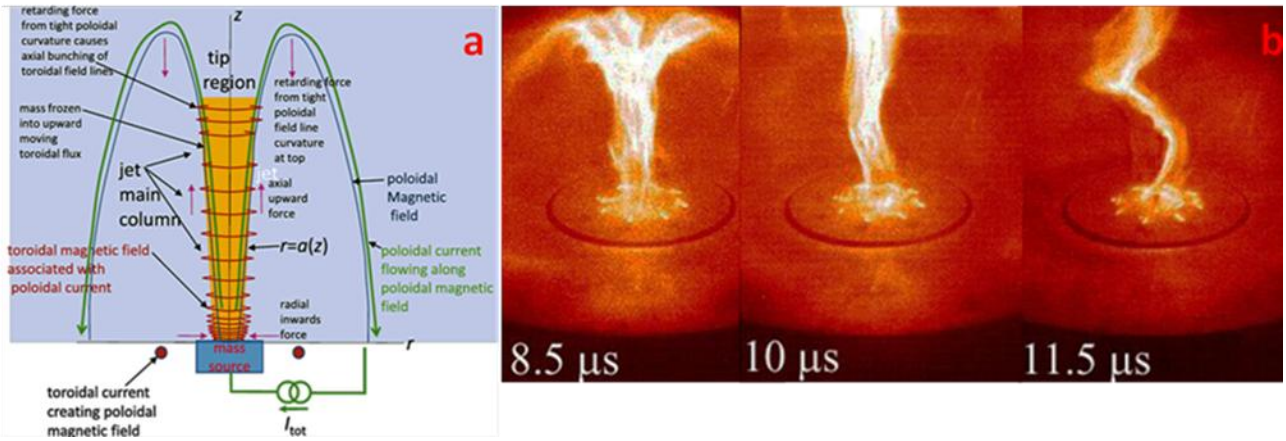

Figure 2.9: *Typical laboratory/simulation produced jets scaling YSOs Astrophysical jets.* [a] *Jet at the later stage. The stretching of the poloidal field causes the poloidal field to be nearly straight except at the apex, where it makes a sharp turn-around. This sharp curvature at the top provides a downwards/retarding force that slows down the jet near its upper tip. The velocity gradient provides an axial compression in the jet frame of the jet plasma and its embedded toroidal flux. This compression increases the toroidal flux density, i.e., amplifies the toroidal field. The radially inward curvature and gradient forces of the amplified toroidal field collimate the jet [99].* [b] *Dynamical evolution of laboratory simulation of astrophysical jet. Magnetic pressure due to toroidal magnetic field inflates poloidal field resulting in magnetic tower configuration. Collimation results from pileup of frozen-in toroidal flux near the top. At later stages, the jet undergoes kink instability [100].*

Jets produced on the MAGPIE Z-pinch facility [68,72,74] are analysed and presented in [67]. The experiments demonstrated that magnetic acceleration and collimation, occurring within a framework of strongly episodic outflow activity, can be effective in producing well-collimated and heterogeneous jets similar with the ones of Astrophysical cases [67,71,72].

Experiments [68,72] with conical wire arrays using different materials (Al, Fe, and W) presented that a highly supersonic (V_{jet}~200km/s and $M_s \geq 20$), well-collimated jet was generated when the radiative cooling rate of the plasma is significant. Higher atomic numbers of the wires' material increased the plasma cooling rate, lowering its temperature and leading to the formation of more collimated jets (with higher Mach numbers). Collimation, stability, and jet-cloud interactions were scale similar of astrophysically stellar jets of YSOs and Planetary Nebulae (PNs).

Jet creation and propagation were presented [80] using a C-shaped target golden/plastic (Au/CH) foil with diameter of 800 μm and thickness of 50 μm (**a** in figure 2.10). FLASH code simulations were executed, along with the experiments, concluding that both the radiation effect and the surrounding medium contributed to the jet collimation (**b** in figure 2.10). These radiative jets can be well-scaled to the astrophysical jets (their relevant numbers are presented in table 2.1/ref [80]). They concluded that these well collimated jets could be also applied to the study of other relevant astrophysical events, such as jet deflection behavior, X-ray emission from the protostellar jet, accretion formation and accretion shocks formations.

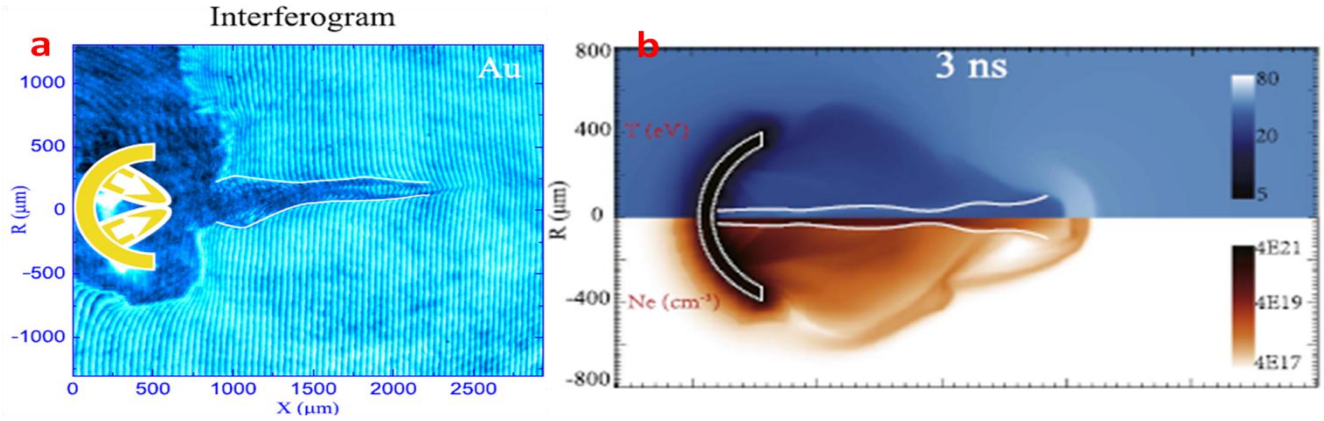

Figure 2.10: [a] *Experimental shadowgraph of the Au-jet generated by Au C-shaped foil at 3 ns.* [b] *FLASH code simulated jet evolution presenting the spatial-temporal evolution of the temperature (upper) and electron density (below) of the Au-jet at 3 ns [80].*

The dynamics of curved HH astrophysical jets were investigated presenting simulations of both laboratory and astrophysical curved jets and results from laboratory experiments [67,72,76,98,101]. Herbig-Haro jets often show some degree of curvature along their path, in many cases produced by the ram pressure of a side wind. In [98], they presented simulations of both laboratory and astrophysical curved jets and results from laboratory experiments. The 3D MHD numerical simulations were performed with GORGON code. The properties and similarities of the laboratory and astrophysical flows were discussed showing the formation of internal shocks and working surfaces. The results illustrated how the breakup of the bow shock and clumps in the flow were produced without invoking jet variability. They also discussed how jet rotation reduced the growth of the Rayleigh-Taylor instability in curved jets. Moreover, parabolic jet trajectory was discussed in astrophysical models of jet deflection which gave a relation between the radius of curvature and physical jet and wind variable. This jet trajectory and dynamic evolution was also captured by the 3D simulations.

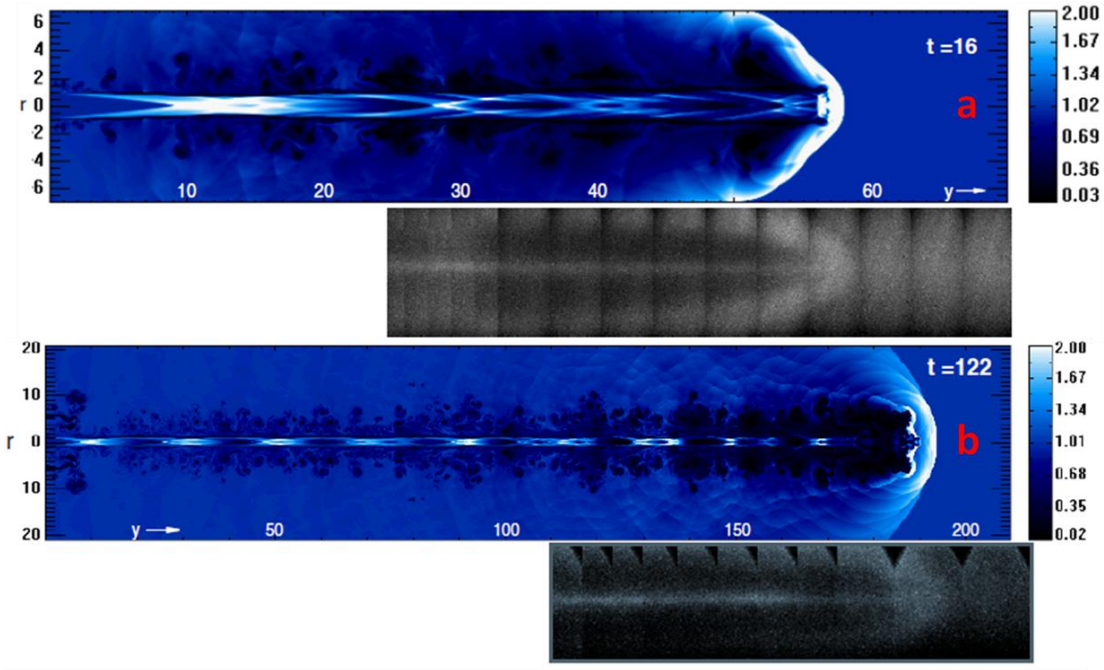

Figure 2.11: [a] *Helium jet in Xenon, M_s = 15.3, η = 1.4. Space unit r_0 = 35.7 mm, time unit τ = 230 μs.* **[b]** *Helium jet in Xenon, M_s = 10.9, η = 1.2. Space unit r_0 = 12 mm, time unit τ = 69 μs. The colored are the PLUTO simulation photos and the black and white the corresponding experimental [75,105].*

M. Belan et al studied the propagation of hypersonic hydrodynamic jets (M_s>5) in a laboratory vessel designed and built specifically for this purpose. They made comparisons with numerical simulations by PLUTO code of axially symmetric flows with the same initial and boundary conditions aiming the Astrophysical study of the YSOs jets (**a** and **b** in figure 2.11). The agreement between experiments and numerical simulations was satisfactory in most of the comparisons. The resulting scaled flow velocities and elapsed times were close to the ones shown by observations. The morphologies of the density distributions agreed with the observed ones too. The laboratory and the simulated hypersonic jets were all pressure-matched. They maintained their collimation for long distances in terms of the initial jet radii (figure 2.15), without including magnetic confinement effects, yielding a qualitatively good agreement with the observed YSO jet morphologies.

Observations of collimated supersonic jet propagation in low-current X-pinches is common. D. M. Haas et al [39] demonstrated that highly supersonic, freely propagating plasma jets can be produced by a low current 80 kA, 50 ns current pulse from a compact pulser, using a four 7.5 μm diameter tungsten wires configuration. These jets gave an average Mach number of M_s~6 and cooling parameter χ~<1, demonstrating a potential scalability to astrophysics. G. S. Jaar and R. K. Appartaim [40] produced hypersonic jets on a microsecond X-pinch configuration ($T_{1/4}$~1μs, dI/dt ~ 0.35 kA/ns) studying 4 different materials: Al, Ti, Mo, and W. Optical images indicated a two-layer structure in Al jets, which may be caused by standing shocks, resembling phenomena observed in astrophysical jet formation and collimation. They observed bright edges with a darker core at these images, which could be indicative of radiative shock fronts. Astrophysical jets, such as He 3–1475, are thought to be collimated by a conical shock mechanism, which could be similar to what is observed in the X-pinch jets [103,106]. Other behaviors of the jets such as bending and kinks, may also be similar to what is noticed in astrophysical entities. Due to the X-pinch study in this thesis, an astrophysical scaling estimating all the relevant dimensionless parameters and physical variables, is attempted. Lacking a more thorough literature study, this attempt is quite enlightening for the jet laboratory scaled creation and propagation.

References

[1] M. G. Haines, A review of the dense Z-pinch, *Plasma Phys. Control. Fusion* **53**, 093001 (2011).

[2] D. D. Ryutov, M. S. Derzon, M. K. Matzen, The physics of fast Z pinches, *Reviews of Modern Physics,* **72(1)**, 167-223 (2000).

[3] M. G. Haines, S. V. Lebedev, J. P. Chittenden, F. N. Beg, S. N. Bland and A. E. Dangor, The past, present, and future of Z pinches, *Phys. Plasmas* **7**, 1672-1680 (2000).

[4] E Kaselouris et al, "Preliminary investigation on the use of low current pulsed power Z-pinch plasma devices for the study of early stage plasma instabilities", Plasma Phys. Control. Fusion 60 (2018) 014031 (8pp).

[5] E. Kaselouris et al, "The influence of the solid to plasma phase transition on the generation of plasma instabilities", NATURE COMMUNICATIONS | DOI: 10.1038/s41467-017-02000-6.

[6] E Kaselouris, "Study of matter behavior dynamics governed by the interaction with laser pulses and external strong currents", PhD thesis TECHNICAL UNIVERSITY OF CRETE SCHOOL OF PRODUCTION ENGINEERING & MANAGEMENT.

[7] M. Tatarakis et al, "Optical probing of fiber Z-pinch plasmas", PHYSICS OF PLASMAS VOLUME 5, NUMBER 3 MARCH 1998.
[8] J. P. Chittenden et al, "Two-dimensional magneto-hydrodynamic modelling of carbon fiber Z -pinch experiments", Phys. Plasmas **4** (12), December 1997.
[9] J. P. Chittenden et al, "Plasma formation in metallic wire *Z* pinches", PHYSICAL REVIEW E VOLUME 61, NUMBER 4 APRIL 2000.
[10] Ruiz-Camacho, J. et al. (1999), "Z-pinch discharges in aluminum and tungsten wires", *Physics of Plasmas*, Vol. 6, pp. 2579-2587.
[11] F. N. Beg et al, "Plasma dynamics during the evolution of two wire Z-pinch", Plasma Phys. Control. Fusion **46** (2004) 1–10.
[12] Haas D M 2011, "Investigation of the dynamics and emission characteristics of x-pinch plasmas", PhD thesis University of California San Diego.
[13] J. M. Woolstrum et al, "Extended magnetohydrodynamics simulations of thin-foil Z-pinch implosions with comparison to experiments", Phys. Plasmas 27, 092705 (2020); doi: 10.1063/5.0012170.
[14] J. D. Hare et al, "An experimental platform for pulsed-power driven magnetic reconnection", PHYSICS OF PLASMAS 25, 055703 (2018).
[15] Ning Ding et al, "Theoretical and Numerical Research of Wire Array Z-pinch and Dynamic Hohlraum in the IAPCM", Volume 1, Issue 3, May 2016, pp 135-152.
[16] C. J. Garasi et al, "Multi-dimensional high energy density physics modeling and simulation of wire array Z-pinch physics", PHYSICS OF PLASMAS VOLUME 11, NUMBER 5 MAY 2004.
[17] Felipe Veloso et al, "Ablation dynamics in wire array Z-pinches under modifications on global magnetic field topology", PHYSICS OF PLASMAS 22, 072509(2015)| https://doi.org/10.1063/1.4926581.
[18] Xiao-Guang Wang et al ,"Numerical study on magneto-Rayleigh–Taylor instabilities for thin liner implosions on the primary test stand facility", Chin. Phys. B Vol. 28, No. 3 (2019) 035201.
[19] F. J. Wessel et al, "Fusion in a Staged Z-pinch", Norman Rostoker Memorial Symposium, Irvine, CA August 25, 2015, DOI: 10.1063/1.4944028.
[20] D. Mikitchuk et al, "Effects of a Pre-embedded Axial Magnetic Field on the Current Distribution in a Z-Pinch Implosion", PHYSICAL REVIEW LETTERS 122, 045001 (2019).
[21] J. L. Giuliani and R. J. Commisso, "A review of the gas-puff z-pinch as an x-ray and neutron source", IEEE Transactions on Plasma Science, 43(8):2385–2453, August 2015.
[22] P. W. L. de Grouchy et al, "Observations of the magneto-Rayleigh-Taylor instability and shock dynamics in gas-puff Z-pinch experiments", PHYSICS OF PLASMAS 25, 072701 (2018).
[23] PAVEL B. BOCHEV et al, "TOWARDS ROBUST 3D Z-PINCH SIMULATIONS: DISCRETIZATION AND FAST SOLVERS FOR MAGNETIC DIFFUSION IN HETEROGENEOUS CONDUCTORS", Electronic Transactions on Numerical Analysis, Volume 15, pp. 186-210, 2003.
[24] U. Shumlak et al, "Equilibrium, flow shear and stability measurements in the Z-pinch", Nucl. Fusion **49** (2009) 075039 (9pp) | doi:10.1088/0029-5515/49/7/075039.
[25] J. P. (HANS) GOEDBLOED AND STEFAAN POEDTS, "PRINCIPLES OF MAGNETO-HYDRODYNAMICS with Applications to Laboratory and Astrophysical Plasmas" , Cambridge University Press 2004, pg .74-77.
[26] Jackson J D 1975 Classical Electrodynamics (New York, John Wiley and Sons) pp 298, 481.
[27] John P. Apruzese and John L. Giuliani, "Radiation Transport in Z-Pinches", IEEE TRANSACTIONS ON PLASMA SCIENCE, 10.1109/TPS.2015.2420992.
[28] Fuyuan Wu et al ,"Numerical studies on the radiation uniformity of Z-pinch dynamic hohlraum", Matter and Radiation at Extremes 3 (2018) 248-255.
[29] Fuyuan Wu et al, "Numerical Simulation of the Interaction between Z-Pinch Plasma and Foam Converter Using Code MULTI (#18353)", FUSION SCIENCE AND TECHNOLOGY, American Nuclear Society,
DOI: https://doi.org/10.1080/15361055.2017.1347458.
[30] Robinson AC et al. 2008, "ALEGRA: An Arbitrary Lagrangian-Eulerian Multimaterial, Multiphysics Code", in 46th AIAA Aerospace Sciences Meeting and Exhibit, Reno, Nevada.

[31] Nicolas-Pierre Louis Niasse, "Development of a Pseudo Non-LTE model for Z-pinch simulations", ", PhD thesis, The Blackett Laboratory, Imperial College London, September 2011.
[32] Stefan M. Kolb, Matthias Stute, Wilhelm Kley, Andrea Mignone, "Radiation hydrodynamics integrated in the code PLUTO", A&A 559, A80 (2013).
[33] J. P. Chittenden et al, "Structural Evolution and Formation of High-Pressure Plasmas in *X* Pinches", PRL **98,** 025003 (2007).
[34] Zhenghong Li et al, "Experimental investigation of Z-pinch radiation source for indirect drive inertial confinement fusion", Matter Radiat. Extremes 4, 046201 (2019); doi: 10.1063/1.5099088.
[35] G. C. Burdiak et al, "Cylindrical liner Z-pinch experiments for fusion research and high-energy-density physics", J. Plasma Physics, page 1-20, Cambridge University Press 2015 | doi:10.1017/S0022377815000318.
[36] Nino R. Pereira, "A simple derivation of the Pease–Braginskii current", Physics of Fluids B: Plasma Physics 2, 677 (1990); doi: 10.1063/1.859303.
[37] M. Coppins, Ideal magnetohydrodynamic linear instabilities in the Z-pinch, Plasma Physics and Controlled Fusion **30**(3), 201 (1988).
[38] R. J. Taylor, "Hydro-magnetic Instabilities of an Ideally Conducting Fluid", *Proceedings of the Physical Society* **B70** 1049 (1957).
[39] D.M. Haas et al., "Supersonic jet formation and propagation in x-pinches", Astrophys Space Sci (2011) 336:33–40.
[40] G. S. Jaar and R. K. Appartaim, "Axial plasma jet characterization on a microsecond x-pinch", JOURNAL OF APPLIED PHYSICS 123, 213301 (2018).
[41] D Haas et al., "Dynamics of low density coronal plasma in low current x-pinches", Plasma Phys. Control. Fusion **49** (2007) 1151–1162.
[42] F. N. Beg et al., "Jet Formation and Current Transfer in *X*-Pinches", IEEE TRANSACTIONS ON PLASMA SCIENCE, VOL. 34, NO. 5, OCTOBER 2006.
[43] G. W. Collins IV et al., "Study of X-pinch dynamics using a low current (25 kA) and slower current (400 ns) pulse", PHYSICS OF PLASMAS 20, 042704 (2013).
[44] I. H. Mitchell et al., "Investigation of the plasma jet formation in X-pinch plasmas using laser interferometry", Phys. Plasmas, Vol. 7, No. 12, December 2000.
[45] T. A. Shelkovenko et al., "Evolution of the structure of the dense plasma near the cross point in exploding wire X pinches", Phys. Plasmas, Vol. 6, No. 7, July 1999.
[46] G.V. Ivanenkov et al., "Experimental Study of X-pinch Dynamics", Plasma Physics Reports, Vol.22, No5, 1996
[47] R. Aliaga-Rossel, et al., "Plasma Jet Formation in X-pinch Plasmas", AIP Conference Proceedings **563**, 270 (2001).
[48] S. A. Pikuz et al, "X-Pinch. Part I", Plasma Physics Reports, 2015, Vol. 41, No. 4, pp. 291–342.
[49] S. A. Pikuz et al, "X-Pinch. Part II, "Plasma Physics Reports, 2015, Vol. 41, No. 6, pp. 445–491.
[50] A Robledo-Martinez *et al* 2017 *J. Phys.: Conf. Ser.* **792** 012042.
[51] T. A. Shelkovenko *et al,* "A Review of Projection Radiography of Plasma and Biological Objects in X-Pinch Radiation", *Plasma Physics Reports, 2016, Vol. 42, No. 3, pp. 226–268.*
[52] V.V. Vikhrev et al, "MHD Simulation of X-pinch plasma dynamics", *35th EPS Conference on Plasma Phys. Hersonissos, 9 - 13 June 2008 ECA Vol.**32D**, P-2.154 (2008).*
[53] G.V. Ivanenkov et al, "The dynamics of Non-Equilibrium plasmas of the neck of X-pinch, 31st EPS Conference on Plasma Phys. London, 28 June - 2 July 2004 ECA Vol.**28G**, P-5.040 (2004).
[54] V. I. Oreshkin et al, "X-pinch dynamics: Neck formation and implosion", PHYSICS OF PLASMAS 21, 102711 (2014).
[55] V. I. Oreshkin et al, "Simulation of the radiation from the hot spot of an X-pinch", PHYSICS OF PLASMAS 24, 012703 (2017).
[56] Hutchinson I H, 2002, "*Principles of Plasma Diagnostics*", (Cambridge: Cambridge University Press). https://doi.org/10.1017/CBO9780511613630.
[57] S. M. Zakharov et al, "Plasma of an Exploding Multiwire Load in the Diode of a High current Accelerator," *Sov. J. Plasma Phys*., **13**, 115 (1987).
[58] G W Collins IV et al, "Effect of the global to local magnetic field ratio on the ablation modulations on X-pinches driven by 80 kA peak current", 2012 New J. Phys. 14 043021.

[59] S. V. Lebedev et al, "Effect of discrete wires on the implosion dynamics of wire array *Z* pinches, "*Phys. Plasmas*, vol. 8, no. 8, pp. 3734–3747, Aug. 2001.
[60] S. M. Zakharov et al, "Plasma of an exploding multiwire load in the diode of a high-current accelerator," *Sov. J. Plasma Phys.*, vol. 13, p. 115, 1987.
[61] Simon C. Bott et al, "Quantitative Measurements of Wire Ablation in Tungsten *X*-pinches at 80 kA", IEEE TRANSACTIONS ON PLASMA SCIENCE, VOL. 36, NO. 5, OCTOBER 2008.
[62] Mitchell I. H. et al 2005 Plasma Sources Sci. Technol. **14** 501.
[63] Ciardi A et al 2003 *Bull. Am. Phys. Soc.* **48** 242.
[64] G. Koundourakis et al, "A numerical study on laboratory plasma dynamics validated by low current X-pinch experiments", Plasma Phys. Control. Fusion **62** (2020) 125012 (14pp)/ https://iopscience.iop.org/article/10.1088/1361-6587/abbebf.
[65] Ampleford D.J. et al, AIP Conf. Proc. **1088**, 83 (2009)
[66] A. Skoulakis-G. Koundourakis et al, " High performance simulations of a single X-pinch", Plasma Phys. Control. Fusion **64** (2022) 025003 (11pp)
[67] Andrea Ciardi, "Laboratory Studies of Astrophysical Jets", Lect. Notes Phys. **793**, 31–50 (2010)/[Radial and Conical wire array].
[68] S. V. Lebedev et al, "LABORATORY ASTROPHYSICS AND COLLIMATED STELLAR OUTFLOWS: THE PRODUCTION OF RADIATIVELY COOLED HYPERSONIC PLASMA JETS", THE ASTROPHYSICAL JOURNAL, 564:113-119, 2002 January 1/[Conical wire array].
[69] G.W.Collins et al ,"Role of collisionality and radiative cooling in supersonic plasma jet collisions of different materials", PHYSICAL REVIEW E **101**, 023205 (2020)/[Conical wire array].
[70] P. M. Bellan et al, "Astrophysical jets: Observations, numerical simulations, and laboratory experiments", PHYSICS OF PLASMAS **16**, 041005 (2009)/[Conical arrays and Laser jets].
[71] S. V. Lebedev et al, "Exploring astrophysics-relevant magnetohydrodynamics with pulsed-power laboratory facilities", REVIEWS OF MODERN PHYSICS, VOLUME 91, APRIL–JUNE 2019/[Radial foils and Conical wire array].
[72] S V Lebedev et al, "Production of radiatively cooled hypersonic plasma jets and links to astrophysical jets", Plasma Phys. Control. Fusion **47** (2005) B465–B479/ [Radial and Conical wire array].
[73] Andrea Ciardi et al, "3D MHD Simulations of Laboratory Plasma Jets", Astrophys Space Sci (2007) 307:17–22/DOI 10.1007/s10509-006-9215-8/[Radial wire array].
[74] F Suzuki-Vidal et al, "Laboratory Astrophysics Experiments with Magnetically Driven Plasma Jets", Journal of Physics: Conference Series **511** (2014) 012050/[Radial foil].
[75] M. Belan et al, "The hydrodynamics of astrophysical jets: scaled experiments and numerical simulations", A&A 554, A99 (2013) .
[76] G. Revet et al, "Laboratory disruption of scaled astrophysical outflows by a misaligned magnetic field", NATURE COMMUNICATIONS | (2021) 12:762 | https://doi.org/10.1038/s41467-021-20917-x.
[77] M. Koenig et al, "Radiative Shocks And Plasma Jets As Laboratory Astrophysics Experiments", CP926, *Atomic Processes in Plasmas—15th International Conference on Atomic Processes in Plasmas,* 2007 American Institute of Physics 978-0-7354-0436-6/07.
[78] C D Gregory et al, "Astrophysical jet experiments", Plasma Phys. Control. Fusion 50 (2008) 124039 (7pp) doi:10.1088/0741-3335/50/12/124039
[79] C D Gregory et al, "ASTROPHYSICAL JET EXPERIMENTS WITH COLLIDING LASER-PRODUCED PLASMAS", The Astrophysical Journal, 676:420–426, 2008 March 20.
[80] Dawei Yuan et al, "Laboratory Investigation of Astrophysical Collimated Jets with Intense Lasers", The Astrophysical Journal, 860:146 (7pp), 2018 June 20.
[81] John I. Castor , "Astrophysical Radiation Dynamics: The Prospects for Scaling", Astrophys Space Sci (2007) 307:207–211.
[82] R. Bonito et al Astronomy & Astrophysics 484, 389 (2008).
[83] P. Hartigan et al, "FLUID DYNAMICS OF STELLAR JETS IN REAL TIME: THIRD EPOCH *HUBBLE SPACE TELESCOPE* IMAGES OF HH 1, HH 34, AND HH 47", The Astrophysical Journal, 736:29 (20pp), 2011 July 20.

[84] F. H. Shu, J. R. Najita, H. Shang, and Z.-Y. Li, in Protostars and Planets IV, edited by V. Mannings, A. P. Boss, and S. S. Russell (Tucson, AZ: Univ. Arizona Press, 2000) pp. 789–814.
[85] A. Konigl and R. E. Pudritz, in Protostars and Planets IV, edited by V. Mannings, A. P. Boss, and S. S. Russell (Tucson, AZ: Univ. Arizona Press, 2000) p. 759.
[86] A. Frank, T. P. Ray, S. Cabrit, P. Hartigan, H. G. Arce, F. Bacciotti, J. Bally, M. Benisty, J. Eisloffel, M. Gudel, S. Lebedev, B. Nisini, and A. Raga, in Protostars and Planets VI (University of Arizona Press, 2014) pp. 451– 474,
[87] P. Hartigan et al, The Astrophysical Journal 559, L157 (2001).
[88] T. Matsakos et al, "Two-component jet simulations I. Topological stability of analytical MHD outflow solutions", A&A 477, 521–533 (2008)/DOI: 10.1051/0004-6361:20077907.
[89] O. Teşileanu et al, "Young stellar object jet models: From theory to synthetic observations", A&A 562, A117 (2014)/DOI: 10.1051/0004-6361/201322627.
[90] A. Mignone et al, "PLUTO: A Numerical Code for Computational Astrophysics" The Astrophysical Journal Supplement Series, Volume 170, Issue 1, pp. 228-242
[91] http://plutocode.ph.unito.it/.
[92] Čemeljić et al, "Resistive jet simulations extending radially self-similar magnetohydrodynamic models," in *Monthly Notices of the Royal Astronomical Society*, vol. 389, no. 3, pp. 1022-1032, Sept. 2008.
[93] Jan Staff et al, "Two-component jets from 3-dimensional magnetohydrodynamic jet simulations of disk winds at sub-parsec scales", EPJ Web of Conferences **61** 02006 (2013)/[ZeusMP code].
[94] E. C. Hansen et al, "The Shock Dynamics of Heterogeneous YSO Jets:3D Simulations Meet Multi-epoch Observations", The Astrophysical Journal, 837:143 (16pp), 2017 March 10/[AstroBEAR code].
[95] R. Bonito et al, "X-RAY EMISSION FROM PROTOSTELLAR JET HH 154: THE FIRST EVIDENCE OF A DIAMOND SHOCK?", The Astrophysical Journal, 737:54 (7pp), 2011 August 20/[Flash code].
[96] S. Ustamujic et al, "Structure of X-ray emitting jets close to the launching site: from embedded to disk-bearing sources", A&A 615, A124 (2018).
[97] Z. Ahmane et al, "Simulations of protostar-driven photoionization in Herbig-Haro jets", Astrophys Space Sci (2020) 365:94.
[98] A. Ciardi et al, "CURVED HERBIG-HARO JETS: SIMULATIONS AND EXPERIMENTS", The Astrophysical Journal, 678:968-973, 2008 May 10.
[99] Paul M. Bellan, "Experiments and models of MHD jets and their relevance to astrophysics and solar physics", PHYSICS OF PLASMAS **25**, 055601 (2018)/ https://doi.org/10.1063/1.5009571.
[100] S. You et al, "Dynamic and Stagnating Plasma Flow Leading to Magnetic-Flux-Tube Collimation", PRL **95**, 045002 (2005).
[101] A. C. Raga et al, "Curved Herbig-Haro jets immersed in a stellar wind", A&A **493**, 115–118 (2009)/DOI: 10.1051/0004-6361:200810900.
[102] Miljenko Čemeljić, "Resistive magnetohydrodynamic jets from protostellar accretion disks", May 2004, PhD Thesis, University of Potsdam, Germany.
[103] Borkowski et al., "COLLIMATION OF ASTROPHYSICAL JETS: THE PROTO–PLANETARY NEBULA He 3-1475", THE ASTROPHYSICAL JOURNAL, 482 :L97–L100, 1997 June 10.
[104] Atzeni, S. et al, "Fluid and kinetic simulation of inertial confinement fusion plasmas", Computer Phys. Commun. **169**, 153–159 (2005).
[105] M. Belan et al, "AN INVESTIGATION OF THE HYDRODYNAMICS OF HYPERSONIC JETS IN ASTROPHYSICAL CONDITIONS", EAS Publications Series, **58** (2012) 137–141.
[106] G. Mellema and A. Frank, Mon. Not. R. Astron. Soc. 292, 795 (1997).

CHAPTER 3

THEORETICAL PHYSICS MODULES STRUCTURAL SYNTHESIS AND EVALUATION

This chapter is focused on the work of the author in presenting, analyzing and synthesizing the conservative form of the MHD equations including most of the dissipative terms. It specifically analyzes the tungsten plasma and the surrounding plasma air, providing state of the art formulas and tabular data for all the physical variables involved. In most cases, more than one formula is presented, allowing to compare and evaluate the results for the best suited simulation implementation. The physics modules that will be discussed, are :

i. EOS for plasma tungsten and thin plasma air.

ii. Radiation transport module.

iii. Module of optically thin losses (a tabular and a mixing function-tabular related data).

iv. Electrical resistivity/conductivity formula (four different approximations).

v. Thermal heat conductivity module (three different approximations).

vi. Viscosity tensor module for unmagnetized/low magnetized to high magnetized plasmas, one Newtonian fluid based approximation and another magnetically defined, analytical and piece-wise functions for specific cases.

We will separate this Chapter in two parts. The first (PART I) describes the radiation relevant module, while the second (PART II) describes all the relative dissipative terms/effects of the MHD scheme.

PART I: MHD EQUATIONS AND RADIATION MODULE

3.1 Conservation laws and set of MHD equations

The dynamics of laboratory and astrophysics magnetically confined plasmas can be studied as an one-fluid model description, the so called Magneto-Hydro-Dynamic (MHD). The MHD equations can be written in a primitive or in a conservative form. Each presentation has its advantages but here we will thoroughly discuss the conservative one. The conservation form is expressed as:

$$\frac{\partial \mathbf{U}}{\partial \mathrm{t}} + \nabla \cdot \mathbf{T}(\mathbf{U}) = \mathbf{S}(\mathbf{U}) \tag{3.1}$$

where $\mathbf{U}$ represents a set of conservative quantities, $\mathbf{T}(\mathbf{U})$ is the flux tensor and $\mathbf{S}(\mathbf{U})$ defines the source terms. An equivalent set of primitive variables $\mathbf{V}$ is more conveniently used for assigning initial and boundary conditions in the computational domain when it is needed.
The sets of conservative and primitive variables $\mathbf{U}$ and $\mathbf{V}$ are given by,

$$\mathbf{U} = (\rho, \mathbf{m}, \mathrm{E_t}, \mathbf{B})^{\mathrm{T}}, \qquad \mathbf{V} = (\rho, \mathbf{u}, \mathrm{P}, \mathbf{B})^{\mathrm{T}} \tag{3.2}$$

where, ρ is the material's density, **m** is the momentum density with $\mathbf{m}=\rho\mathbf{u}$, $\mathrm{E_t}$ is the total energy density, **B** is the magnetic field, P is the thermal pressure and **u** the bulk velocity. The total energy density is:

$$\mathrm{E_t} = \rho\cdot\mathrm{e} + \frac{\mathbf{m}^2}{2\rho} + \frac{\mathbf{B}^2}{2} \tag{3.3}$$

where e is the specific internal energy (erg/gr) and ρ·e is the density of internal energy. Resistivity, thermal conductivity, viscosity and other dissipative effects can be implemented as source terms **S(U).**

The main MHD module including resistivity is of the form:

$$\frac{\partial\rho}{\partial \mathrm{t}} + \boldsymbol{\nabla}\cdot(\rho\mathbf{u}) = 0 \tag{3.4}$$

$$\frac{\partial\mathbf{m}}{\partial \mathrm{t}} + \boldsymbol{\nabla}\cdot\left[\mathbf{m}\mathbf{u} + \left(\mathrm{P} + \frac{1}{2}\mathrm{B}^2\right)\mathbf{I} - \mathbf{B}\mathbf{B}\right] = 0 \tag{3.5}$$

$$\frac{\partial \mathrm{E_t}}{\partial \mathrm{t}} + \boldsymbol{\nabla}\cdot\left[\left(\mathrm{E_t} + \mathrm{P} + \frac{1}{2}\mathrm{B}^2\right)\mathbf{u} + (\mathbf{u}\cdot\mathbf{B})\mathbf{B}\right] = -\boldsymbol{\nabla}\cdot[(\mathrm{n_D}\cdot\mathbf{J})\times\mathbf{B}] \tag{3.6}$$

$$\frac{\partial\mathbf{B}}{\partial \mathrm{t}} + \boldsymbol{\nabla}\cdot(\mathbf{u}\mathbf{B}\text{-}\mathbf{B}\mathbf{u}) = -\boldsymbol{\nabla}\times(\mathrm{n_D}\cdot\mathbf{J}) \text{ with } \mathbf{J} \equiv \boldsymbol{\nabla}\times\mathbf{B} \tag{3.7}$$

where $\mathrm{n_D}=(4\pi)^{-1}\mathrm{c}^2\cdot\mathrm{n}$ is the magnetic diffusivity term in cm^2/s, c the speed of light and n the resistivity term in seconds. A factor of $1/\sqrt{4\pi}$ has been engaged in the magnetic field **B** [1,2].

Other sources that can be implemented are viscosity and thermal conductivity. The viscous stresses enter the MHD equations with two parabolic diffusion terms in the momentum and energy equations. So 3.5 and 3.6 become:

$$\frac{\partial\mathbf{m}}{\partial \mathrm{t}} + \boldsymbol{\nabla}\cdot\left[\mathbf{m}\mathbf{u} + \left(\mathrm{P} + \frac{1}{2}\mathrm{B}^2\right)\mathbf{I} - \mathbf{B}\mathbf{B}\right] = \boldsymbol{\nabla}\cdot\Pi \tag{3.8}$$

$$\frac{\partial \mathrm{E_t}}{\partial \mathrm{t}} + \boldsymbol{\nabla}\cdot\left[\left(\mathrm{E_t} + \mathrm{P} + \frac{1}{2}\mathrm{B}^2\right)\mathbf{u} + (\mathbf{u}\cdot\mathbf{B})\mathbf{B}\right] = -\boldsymbol{\nabla}\cdot[(\mathrm{n_D}\cdot\mathbf{J})\times\mathbf{B}] + \boldsymbol{\nabla}\cdot(\mathbf{u}\cdot\Pi) \tag{3.9}$$

where Π represents the second order viscous tensor with components:

$$(\Pi)_{\mathrm{ij}} = 2\nu_{\mathrm{s}}\mathrm{D_{ij}} + \left(\nu_{\mathrm{b}} - \frac{2}{3}\nu_{\mathrm{s}}\right)\boldsymbol{\nabla}\cdot\mathbf{u}\delta_{\mathrm{ij}} = (\Pi)_{\mathrm{bij}} + (\Pi)_{\mathrm{sij}} \text{ where i, j} = 1,2,3$$

and

$$\mathrm{D_{ij}} = \frac{1}{\mathrm{h_i h_j}}\left(\frac{1}{2}\left(\frac{\partial \mathrm{u_i}}{\partial \mathrm{x_j}} + \frac{\partial \mathrm{u_j}}{\partial \mathrm{x_i}}\right)\right)(\text{deformation tensor}) \tag{3.10}$$

This is the Newtonian approximation and holds for an isotropic viscous stress, giving a symmetric tensor $(\Pi)_{\mathrm{ij}}$. The ν_{s} and ν_{b} are the shear and bulk parameter of viscosity respectively and are suitable for the HD case and for low magnetized plasmas. The $\mathrm{h_i}$ and $\mathrm{h_j}$ are the geometry elements of the respective dimension (i.e. $\mathrm{h_i}=\mathrm{h_j}=1$ for the Cartesian geometry). A more thorough study, of the MHD high and low magnetic field case, is presented at the 3.4.3 subsection.

Thermal conduction can be added at the energy equation by introducing an additional divergence flux term:

$$\frac{\partial \mathrm{E_t}}{\partial \mathrm{t}} + \boldsymbol{\nabla} \cdot \left[\left(\mathrm{E_t} + \mathrm{P} + \frac{1}{2}\mathrm{B}^2 \right) \mathbf{u} + (\mathbf{u} \cdot \mathbf{B})\mathbf{B} \right] = \boldsymbol{\nabla} \cdot \mathbf{F_c} \tag{3.11}$$

(of course if we include resistivity and viscosity the right side terms of 3.9 will be added too). The flux expression $\mathbf{F_c}$ is given by:

$$\mathbf{F_c} = \mathbf{F}_{\mathrm{class}} \left(\frac{\mathrm{F_{sat}}}{\mathrm{F_{sat}} + |\mathbf{F}_{\mathrm{class}}|} \right) \tag{3.12}$$

where

$$\mathbf{F}_{\mathrm{class}} = \mathrm{k}_{||} \frac{\mathbf{B}(\mathbf{B} \cdot \boldsymbol{\nabla}\mathrm{T})}{\mathrm{B}^2} + \mathrm{k}_{\perp} \left(\boldsymbol{\nabla}\mathrm{T} - \frac{\mathbf{B}(\mathbf{B} \cdot \boldsymbol{\nabla}\mathrm{T})}{\mathrm{B}^2} \right) + \mathrm{k}_{\times} \left(\frac{\mathbf{B}}{\mathrm{B}} \times \boldsymbol{\nabla}\mathrm{T} \right) \tag{3.13}$$

$$\text{and } \mathrm{F_{sat}} = 5\varphi\rho\mathrm{c_s}^3$$

The $\mathbf{F}_{\mathrm{class}}$ and $\mathrm{F_{sat}}$ are the classical and saturated thermal conduction regimes where $\mathrm{c_s}$ is the isothermal sound speed, and ϕ is a free parameter, a number of the order of unity (0<φ<1) [2,3,4]. The classical expression is given by 3.13 where the $\mathrm{k}_{||}$ and $\mathrm{k}_{\perp}$ are the thermal conduction coefficients along and across the magnetic field. The $\mathrm{k_x}$ is the component coefficient of the thermal conduction flux transverse to the plain of $\mathbf{B}$ and $\boldsymbol{\nabla}\mathrm{T}$. The last term is sometimes ignored and it will not be discussed at the thermal conduction, section but only at the Results Chapter, at section 5.4. The saturated expression is selected by making the flux independent of $\boldsymbol{\nabla}\mathrm{T}$ for very large temperature gradients.

The final equation which relates internal energy, thermal pressure, mass density and temperature is the Equation Of State (EOS) that usually correlates ρe and/or P with ρ and temperature T. That is:

$$\rho \cdot \mathrm{e} = \rho \cdot \mathrm{e}(\rho, \mathrm{T}) \text{ and } \mathrm{P} = \mathrm{P}(\rho, \mathrm{T}) \tag{3.14}$$

The above system is a closed system of equations which are of the form that PLUTO uses [2]. The description of the code will be part of the next chapter. The radiation transport and optically thin losses module along with resistivity, viscosity, thermal conductivity and the appropriate EOS for plasma tungsten and plasma air will be discussed right away at the next sections.

3.2 Equation of state model (EOS)

The equation of state (EOS) defines matter's thermodynamic characteristics in a functional form correlating physical values such as thermal pressure P, mass density ρ, internal energy E and temperature T. These correlations can be expressed in graphs, tables or analytic functions [5].

The most common EOS is the thermal ideal gas equation, where the thermal equation between pressure and temperature is:

$$\mathrm{P} = \mathrm{nK_B T} \text{ (thermal pressure (dyn/cm}^2\text{))} \tag{3.15}$$

where P is the thermal pressure, n is the total particle number density , $\mathrm{K_B}$ is the Boltzmann constant and T is the temperature. The internal energy density can be expressed as a function of thermal pressure:

$$E = \rho \cdot e = \frac{P}{\Gamma - 1} \text{ (internal energy density (erg/cm}^3\text{))} \tag{3.16}$$

where Γ the ratio of specific heats is considered constant for a calorically ideal gas. In plasma state for low densities and high temperatures it could be a sufficient model but for other cases (e.g. condensed matter) the deviations are large and this is an inappropriate description.

A more sophisticated approach is the SESAME EOS that covers all the range of densities, pressure, internal energy and temperature for a wide range of materials [6]. The Aluminum EOS is shown in figure 3.1 as an example and is used for the presentation of all different regions of the SESAME EOS .

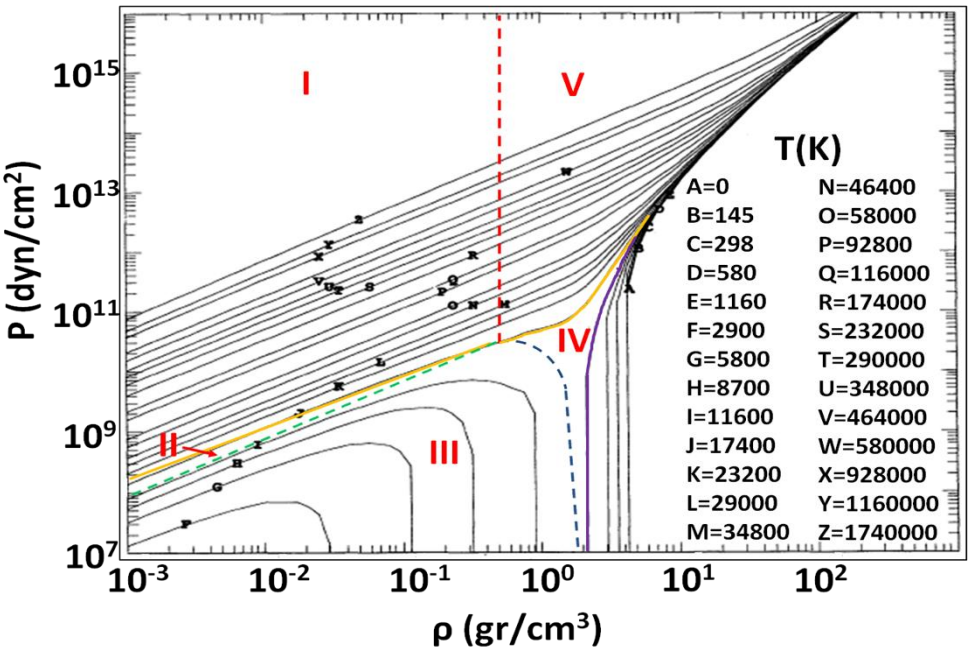

Figure 3.1: *Aluminum LOS ALAMOS original P-ρ graph EOS isotherms [7].The three colour dashed line identifies the saturation curve, which has a branch–cut extending from the critical temperature to infinity (red part). Yellow line is the critical isotherm; purple is the cold curve. Region I is supercritical and to the expanded side of the saturation curve; Region II is subcritical and to the expanded side of the saturation curve; Region III is the coexistence region; Region IV is the subcritical condensed–phase region; and Region V is supercritical condensed phase.*

The analysis from now on is for tungsten, the main plasma material of this work. There is a similar pressure depiction as a function of density and temperature for tungsten. Its EOS is calculated with the Thomas-Fermi-Dirac theory for the electrons. A Lennard-Jones tail is used for densities less than ρ_0 (19.2 gr/cm^3). The nuclear vibrations contributions are also based on the Dugdale-MacDonald form of Grüneisen-Debye theory, but with a transition to ideal gas at high temperatures [6].

The main part of the modified EOS of this work follow the MGGB version [8]. This approach is an evolution of the SESAME data, appropriate for problems in dynamics that involve several distinct materials, separated in space, interacting with material interfaces, which Local Thermodynamic Equilibrium (LTE) is a good approximation (LTE will be explained at the radiation part section 3.3). This is the most suitable choice for this study considering the two materials' coexistence in the chamber

(i.e. metal plasma cable and the surrounding plasma air) including solid, dense matter, gas and plasma phase, having one ion/atom temperature that is convenient for the one fluid model assumed. Sesame data for the EOS functions are derived from a Helmholtz free energy expressed as the sum of thermal (fluctuational) and collisional (condensed–phase) contributions, thus the free energy is of the Mie–Gruneisen form. The phase–coexistence region is defined using a parameterised saturation curve by extending the form introduced by Guggenheim, which scales the curve relative to conditions at the critical point. The zero–temperature condensed–phase contribution is used, which extends the Thomas–Fermi–Dirac equation to zero pressure. Thus, the functional form of the EOS could be called MGGB (for Mie–Grüneisen–Guggenheim–Barnes). Substance's specific parameters are obtained by fitting the low–density energy to data from the SESAME library. Thus MGGB can be thought of as a numerical recipe for rendering the tabular SESAME EOS data in an analytic form which includes a proper coexistence region, and which permits the accurate calculation of derivatives associated with compressibility, expansivity, Joule coefficient and specific heat, all of which are required for multifield applications, avoiding the discontinuities of the original SESAME data (figure 3.2).

In accordance with the adiabatic approximation, where and when functions can be derived, the Helmholtz free energy of matter depending on mass density ρ and temperature T is treated as a sum of ionic F_i and electronic F_e components:
$F(\rho, T) = F_c(\rho) + F_i(\rho, T) + F_e(\rho, T)$ where the $F_c(\rho)$ is the cold free energy contribution. Units for F are erg/gr. The basic thermodynamic quantities are:

$$e = F + TS = F - T\left(\frac{\partial F}{\partial T}\right)_V \text{ (specific internal energy(erg/gr))} \tag{3.17}$$

$$h = e + \frac{P}{\rho} \text{ (specific enthalpy (erg/gr))} \tag{3.18}$$

$$P = \rho^2\left(\frac{\partial F}{\partial \rho}\right)_T \text{ (pressure (dyn/cm}^2\text{))} \tag{3.19}$$

$$C_V = \left(\frac{\partial e}{\partial T}\right)_V \text{ (specific heat at constant volume (erg} \cdot \text{gr}^{-1} \cdot \text{K}^{-1}\text{))} \tag{3.20}$$

$$C_P = \left(\frac{\partial h}{\partial T}\right)_P \text{ (specific heat at constant pressure (erg} \cdot \text{gr}^{-1} \cdot \text{K}^{-1}\text{))} \tag{3.21}$$

$$\Gamma = \frac{C_P}{C_V} \text{ (ratio of specific heats)} \tag{3.22}$$

The range of interest in this study is for temperatures in the range from 0.1 eV to a few thousands eV and densities in the range from a few gr/cm^3 to 10^{-9}gr/cm^3 (for the tungsten plasma of our interest in this study and the dry air in the chamber). There is an extraction of tabular data from the graphs used for the runs in PLUTO. The aforementioned graphs are the graphs of figure 3.2. There is a linear extrapolation fit for densities smaller than 10^{-4} gr/cm^3.

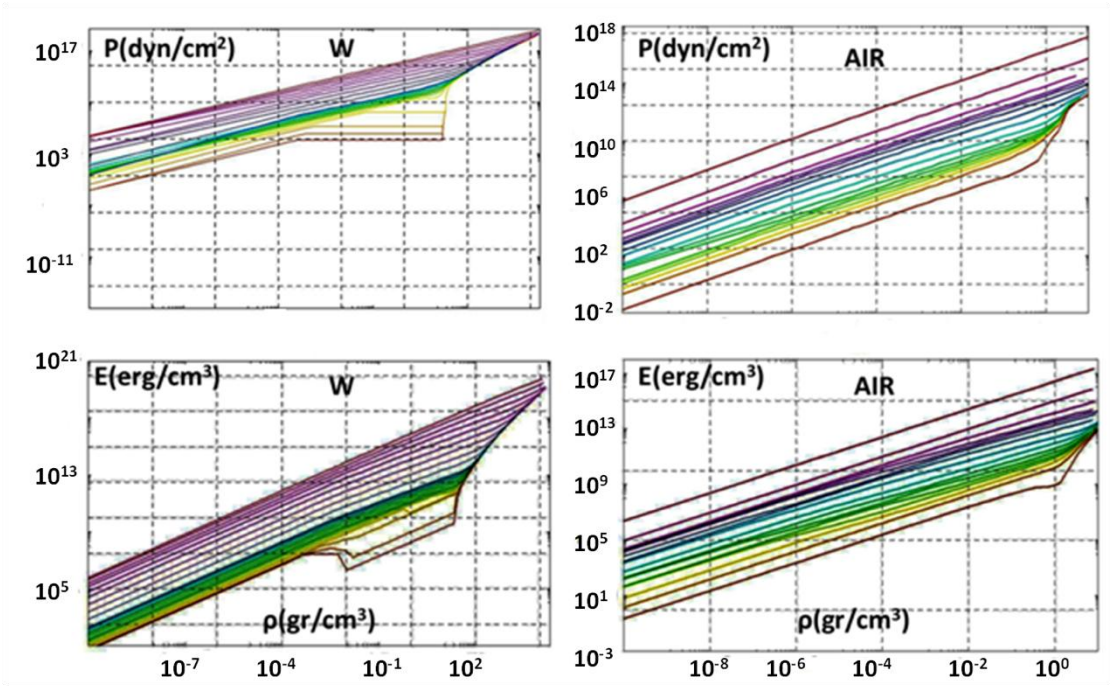

Figure 3.2 Thermal pressure and Internal density energy as a function of density for different temperatures calculated for use in the modified PLUTO code. *Top row: Thermal pressure P isotherms as a function of ρ for tungsten and air through the modified SESAME(MGGB) data. Bottom row: Internal energy density E (or ρe) isotherms as a function of ρ for Tungsten and air through the modified SESAME (MGGB) data. These are logarithmic curves. The temperatures have a range from 298K to* $1.06 \cdot 10^8$*K for tungsten and 184K to* $2.91 \cdot 10^8$*K for dry air equally spaced in logarithmic scale (*$\log T_{i+1} - \log T_i = 0.23$*, T in eV) depicting 24 isotherms.*

The smoother transition from low to high densities is obvious for the low temperature isotherms compared to the original data (figure 3.1). Also there are no discontinuities avoiding jump conditions and infinities at derivatives.

3.3 Radiation module

Radiative emission and transport play a crucial role in the dynamics' evolution and correct physics behaviour of many high-energy-density laboratory plasma experiments. The optically thin radiative losses and radiation transport phenomena should be considered just to have better plasma description for the thinner corona and denser core interaction evolving in the very thin low density background (e.g. plasma air) [9].

The most common computational study is of the Local Thermodynamic Equilibrium (LTE). When this is true at a given point in the plasma, the plasma conditions can be described by a single temperature ($T=T_{electron}=T_{radiation}=T_{ion}$). The rate at which atomic process occurs is exactly balanced by the rate of its inverse process (this condition simplifies the physics model in relation to Non-LTE (NLTE) and introduce a much faster simulation run time). The energy distribution of the free electrons in the plasma is described by a Maxwellian distribution and the radiation field is described by a Planck function at the same temperature.

On the contrary, Non Local Thermodynamic Equilibrium cases (NLTE) are changing so rapidly that electron and/or photon energy distributions do not reach thermal equilibrium (i.e. Maxwellian or Planckian is not valid, lasers emittion, $T_{electron} \neq T_{radiation}$, etc). This is the case for many laboratory plasmas, especially fusion related plasma simulations [10]. Also, for these cases, optically thin radiation energy can escape and is not available to provide LTE balance among the fundamental atomic processes. If an NLTE study is necessary, a model that contains all the relevant fundamental atomic physics data should be considered (energy levels, radiative rates, collisional rates, etc). NLTE calculations can take as much as 3-4 orders of magnitude more computational time than LTE calculations and are more delicate at computational discrepancies and divergence behaviour, thus making it time demanding, in order to take in consideration all the physical phenomena of interest [11]. There is no strict separation which case is better for every problem. The advantages and disadvantages should be considered, evaluating and validating the computational results with literature and experiment [9-12].

The implemented radiation module, compatible with the PLUTO code will be analysed in the next two subsections, in which the LTE case is considered.

3.3.1 Optically thin losses

Radiative losses is an important energy loss mechanism of plasmas, containing medium to high Z elements and it is critical to quantify the total energy balance of plasma and consequently temperature predictions [9]. Screened Hydrogenic Level (SH) models provide a quick and reasonable estimate for radiative loss rates when a model of detailed atomic structure is difficult to build. This is an approach adopted from the FLYCHK code [13] and the relevant formulas of PLASMA FORMULARY [14]. The optically thin radiative losses give an extra differential equation in the system, correlating the internal energy density rate with the electron and ion density. It can be equivalently built in equation 3.9 as an extra dissipative sunk term. This rate is essentially a proportional function of electron and ion density product (equations 3.23 and 3.26). The crucial part is the "correct" knowledge of the multiplication variable Λ as a function of plasma density and temperature. The presentation below gives an estimation of this factor through two different approaches. The first one is tabulated using the FLYCHK [13] code and the second is mainly functional using the Bremsstrahlung and recombination electron contribution and separately for Z_{eff} the FLYCHK data and the estimation of an average Thomas-Fermi model [14].

3.3.1.1 Tabulated Optically thin losses using FLYCHK code

Time-dependent optically thin radiative losses are taken into account by:

$$\frac{\partial \rho e}{\partial t} = -\Lambda(\rho, T) N_e N_i \tag{3.23}$$

where $\Lambda(T,\rho)$ is the radiative cooling coefficient, calculated by tabulated data from the FLYCHK code, with N_i the ion density, m_i the ion mass. For the relation of the electron and ion plasma density it holds that:

$$N_i = \rho m_i^{-1} \text{ and } N_e = Z_{eff}(\rho, T) N_i = Z_{eff} \rho m_i^{-1} \tag{3.24}$$

where Z_{eff} is the effective ionization charge state calculated through tabulated data from the FLYCHK code and in this case is a function of electron density and temperature [13]. The code takes into account the free-free (Bremsstrahlung), free-bound (recombination) and bound-bound radiation contribution [15]. The tabulated data for Λ and Z_{eff} are presented in figure 3.3. The code plots isodensities of energy rate per ion (second row) and Z_{eff} (first row) as a function of electron temperature. The range for densities is, $10^{12} e \cdot cm^{-3} < N_e < 10^{24} e \cdot cm^{-3}$ and for temperatures, $0.5eV < T_e < 10^5 eV$. The Λ coefficient then can be estimated by the ratio of energy per ion rate and electron density N_e, both originating from the code data. Thus, the result is energy rate per ion, per electron, times unit volume, as can be expected for the Λ coefficient in 3.23.

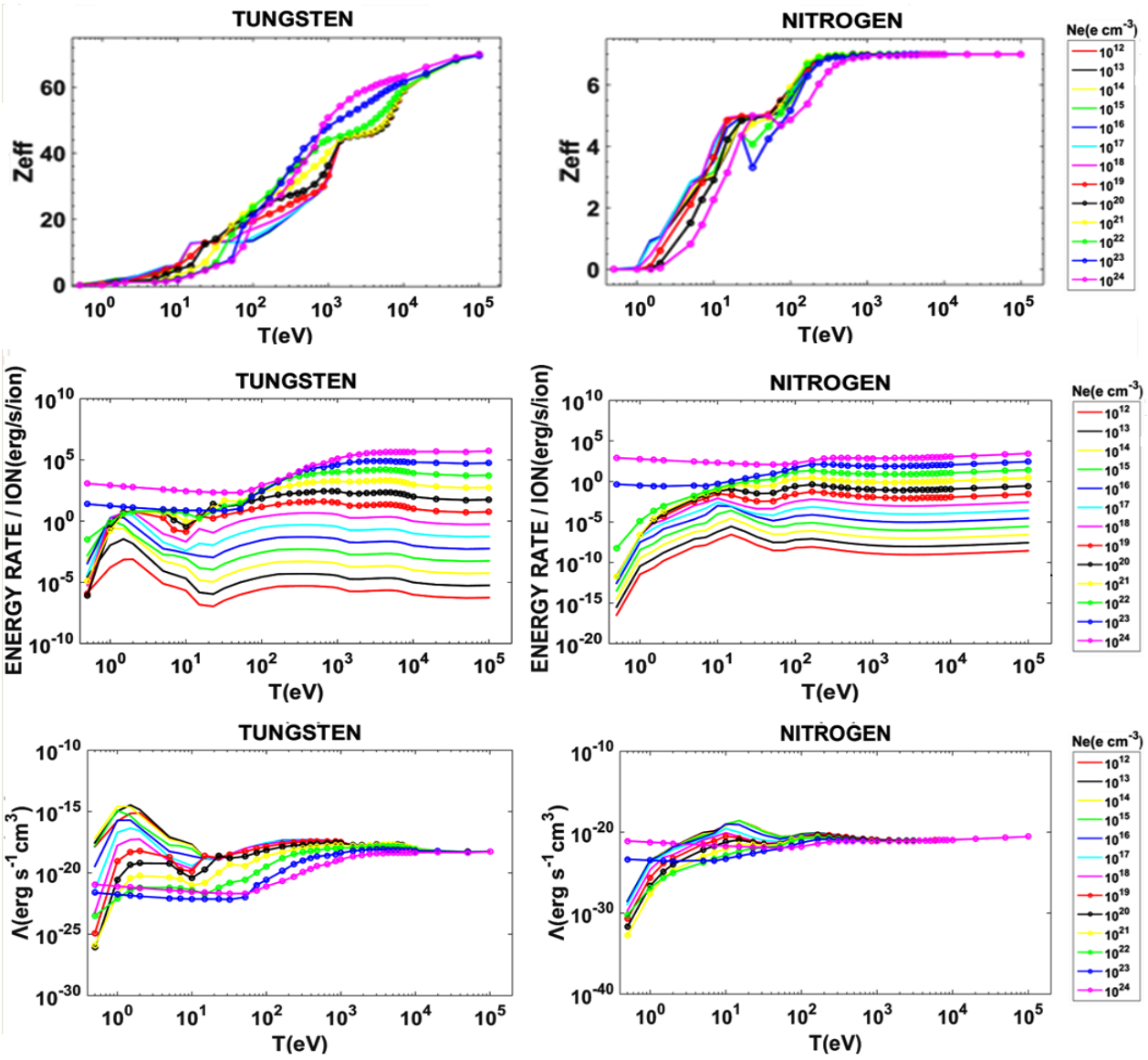

Figure 3.3: *Radiative cooling coefficient Λ and Z_{eff} as a function of temperature for different electron densities for the tungsten and for the main component of the air, nitrogen calculated using FLYCHK code. The electron densities have a range from $10^{12} e/cm^3$ to $10^{24} e/cm^3$ and the temperatures from*

0.5eV to 10^5eV. The second row depicts the energy rate per ion from the original FLYCHK data. The third row depicts the Λ coefficient of 3.23. The first row uses semi logarithmic axes, while the rest are logarithmic. The legend column replies to all graphs [13-15].

This approach has the advantage of a more realistic fitting than using analytic functions, taking into account a big range of temperature and electron densities. But at the same time it holds only for one metal material and has to be extracted from FLYCHK data separately for another plasma material. This is for computational implementation, a demanding task (doable nevertheless!).

Using the expression of 3.23 and the data from figure 3.3 we derive figure 3.4 for the radiation emission energy density rate.

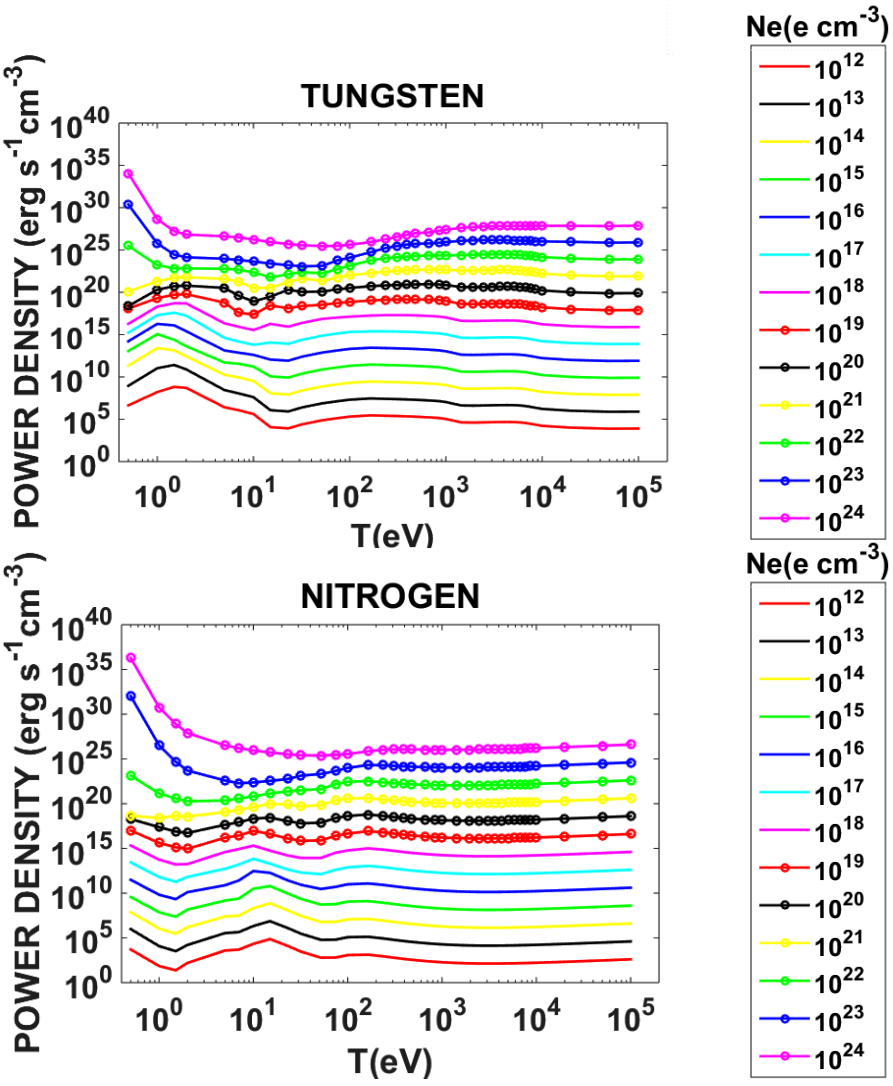

Figure 3.4: *Radiation energy density rate for optically thin cooling plasma tungsten and nitrogen. The temperature and electron density range are the same as those depicted at figure 3.3.*

The estimation of the optically thin radiative losses of plasma tungsten in figure 3.4 is evaluated for the region of low density plasmas and high temperatures through literature [16,17] . More specifically the radiation rates and charge states of atoms in the high-temperatures range 2eV< T_e <10^5eV and low-density plasmas with N_e<10^{16}e·cm^{-3}, is estimated by D. E. Post et al [17], using the equation 3.23

for elements with Z>26. Also T. Pütterich et al [16], in a recent work, calculates and compares with the experiment, the cooling factor of tungsten for N_e~10^{14} $e \cdot cm^{-3}$ and for temperatures in the range 30eV<T_e<40000eV. The comparison is presented in table 3.1.

T(eV)	Λ(FLYCHK)(c.g.s) [10^{12}<Ne (e/cm^3)< 10^{16}]	Λ(T. Pütterich et al.) (c.g.s) [Ne (e/cm^3)~ 10^{14}]	Λ(Post et al.) (c.g.s) [Ne (e/cm^3)<10^{16}]
50	$9.88 \cdot 10^{-19}$	$2.55 \cdot 10^{-18}$	_
100	$2.75 \cdot 10^{-18}$	$1.67 \cdot 10^{-18}$	~$3.0 \cdot 10^{-18}$
200	$4.87 \cdot 10^{-18}$(for 235eV)	$1.65 \cdot 10^{-18}$	~$1.6 \cdot 10^{-18}$
1000	$3.48 \cdot 10^{-18}$	$4.21 \cdot 10^{-18}$	~$6.0 \cdot 10^{-18}$
3000	$2.04 \cdot 10^{-18}$	$2.28 \cdot 10^{-18}$	~$1.9 \cdot 10^{-18}$
10000	$9.77 \cdot 10^{-19}$	$1.33 \cdot 10^{-18}$	~$1.0 \cdot 10^{-18}$
20000	$6.44 \cdot 10^{-19}$	$7.30 \cdot 10^{-19}$	~$5.4 \cdot 10^{-19}$
40000		$4.95 \cdot 10^{-19}$	~$4.6 \cdot 10^{-19}$
70000	$5.21 \cdot 10^{-19}$(for 50000eV)	_	~$4.3 \cdot 10^{-19}$
100000	$5.58 \cdot 10^{-19}$	_	~$4.8 \cdot 10^{-19}$

Table 3.1: *Comparison of FLYCHK tabular data to the ones of Pütterich et al and Post et al for densities up to 10^{16} $e \cdot cm^{-3}$ and temperatures from 50eV to 10^5eV. The values of FLYCHK code are average estimations for electron densities 10^{12} $e \cdot cm^{-3}$ up to 10^{16} $e \cdot cm^{-3}$ [16,17].*

There is a quite good agreement of the three approaches especially for temperatures higher than 100eV. The deviations at this region are up to 50% (except for the 235 eV temperature in FLYCHK, developing a value overestimation of Λ relative to the other two while for the 100eV Pütterich et al presents a pretty smaller estimation relative to FLYCHK and Post et al. This is an indication that FLYCHK is in good agreement with other codes and experimental data at intermediate temperatures and very thin plasma regions. It is also mentioned at the web page of the FLYCHK code that for very low N_e, FLYCHK may underestimate the radiative loss rates for near-neutral plasmas due to lack of Δn=0 transitions (n is the principal quantum number) but for highly ionized plasmas and intermediate electron densities introduces better results [13,15]. For our case, a satisfactory agreement, at low densities, medium ionized tungsten plasma and intermediate to high temperatures, is confirmed.

3.3.1.2 Analytical function of Optically thin losses

Taking into account the free-free (Bremsstrahlung from hydrogen-like plasma) and free-bound (recombination) contribution to the optically thin radiation energy density rate, we obtain the following formula[14]:

$$\frac{\partial \rho e}{\partial t} = -1.69 \cdot 10^{-25}\, N_e T_e^{0.5} \sum Z^2\, N_i(Z) \left(1 + \frac{E_\infty{}^{Z-1}}{T_e}\right) (cgs) \qquad (3.25)$$

The temperature and E_∞ are in eV and all other variables in cgs units. Z is the charge state (Z = 0 refers to a neutral atom), the sum is over all ionization states Z and $E_\infty{}^{Z-1}$ is the ionization energy of the recombined state.

If we want to simplify this formula avoiding the fractional abundances of the ionization stages, we can use Z_{eff} again, limiting the sum just to one term:

$$\frac{\partial \rho e}{\partial t} = -1.69 \cdot 10^{-25}\, N_e T_e^{\,0.5} Z_{eff}^{\,2} N_i \left(1 + \frac{E_\infty^{\,Z-1}}{T_e}\right) (cgs) \qquad (3.26)$$

The first term is the Bremsstrahlung contribution and the second the recombination density energy rate. Bremsstrahlung radiation will only dominate at very high temperatures and once the ion is fully ionized. There are graphic depictions of equation 3.26 in figures 3.5 and 3.6 with and without the Bremsstrahlung term investigating the latter allegation. The mean ionization state will be implemented with two different data formats. The first is the tabulated FLYCHK data estimation of the figure 3.3. The second is an estimation from an average ion Thomas-Fermi model [18]. The ionization energies E_∞ for plasma tungsten are the ones of P. Beiersdorfer et al [19]. Another more thorough estimation is from Alexander E. Kramida et al presenting similar values [20].

Finally a comparison will take place with the first graph of figure 3.4 for the tungsten plasma.

A. The mean ionization state from the FLYCHK data

For this case, we use equation 3.26, where Z_{eff} originates from the FLYCHK data of 3.3 figure.

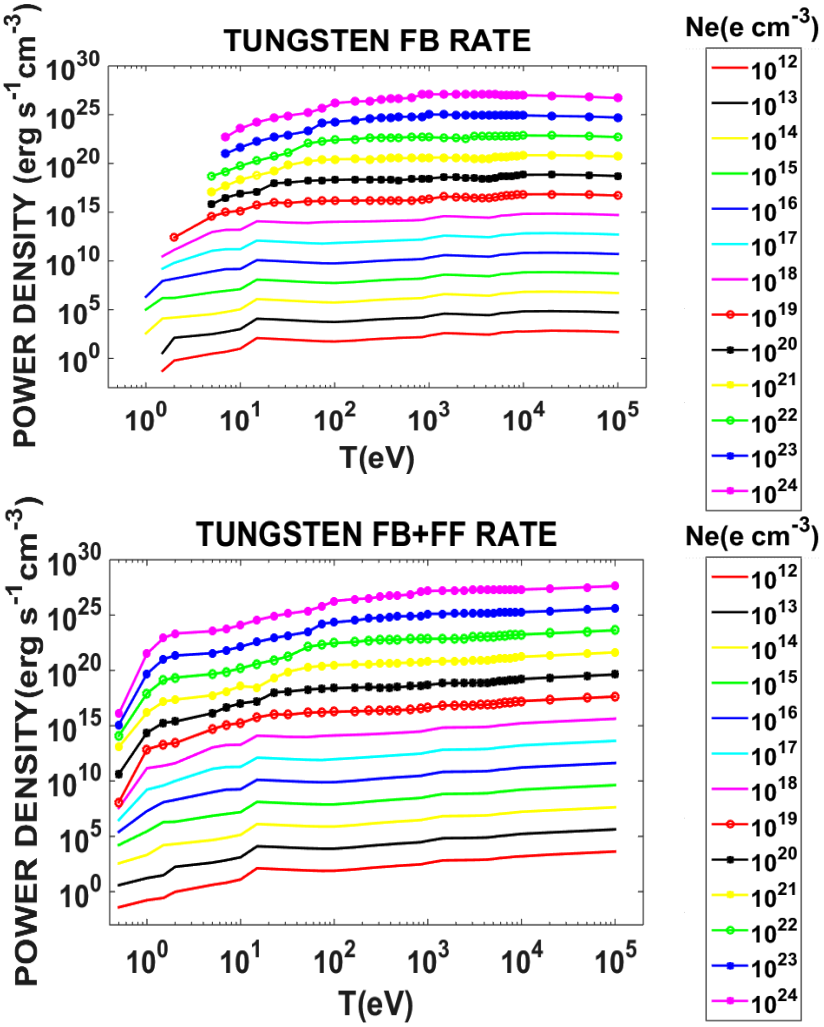

Figure 3.5: *Radiation energy density rate for optically thin cooling plasma tungsten calculated for the purpose of this thesis using the FLYCHK code. The temperature and electron density range are the same of the 3.3 figure and Z_{eff} is implemented from the FLYCHK tabular data. The top graph depicts the free-bound contribution, while the bottom the sum of the free-bound and the free-free (Bremsstrahlung) radiation power density loss.*

As mentioned earlier, the free-free contribution produces a small rise of energy rate especially at the high temperature region. Furthermore, it has non zero values at ionization states lower than unity in contradiction to the free-bound term, due to the zero value ionization energies $E_{\infty}{}^{Z-1}$. Nevertheless, the significant observation is the three or four orders (or more) of magnitude underestimation of the energy rate for the low density and low temperature region in comparison with the one in figure 3.4. For high temperatures and densities the disagreement is lower. This comparison confirms the observation by T. Pütterich et al [16], which calculates the line emission contribution by two orders of magnitude higher than the other two for the electron density of ~10^{15} e/cm^3. This is crucial if someone wants to use formula 3.26 for the thin radiation losses. Last but not least, a correction factor should be considered for the simulation runs, in order to match the lack of the bound-bound contribution.

B. The mean ionization state from the Thomas-Fermi model

The Thomas-Fermi estimation for the ionization level is obtained by an expression [18] which is a function of mass density and plasma temperature, fitted to the numerical solution of:

$$Z_{\text{eff}} = Z \cdot \frac{y}{1 + y + \sqrt{1 + 2y}} \tag{3.27}$$

The y function and all the related constants and other functions are shown in Table3.2

$R=\rho\cdot(Z\cdot A)^{-1}(gr\cdot cm^{-3})$ ($Z=74$ & $A=183.84$ for W)	$a= 14.3139$
$T_o= T\cdot Z^{-4/3}$ (eV)	$b= 0.6624$
$T_f= T_o(1+T_o)^{-1}$	$c_1= -0.366667$
$A= a_1T_o{}^{a2}+ a_3T_o{}^{a4}$	$c_2= 0.983333$
$B= -\exp(b_o+b_1T_f+b_2T_f{}^2)$	$b_o= -1.7630$
$C=c_1T_f + c_2$	$b_1= 1.43175$
$Q_1=A\cdot R^B$	$b_2= 0.315463$
$Q=(R^C + Q_1{}^C)^{1/C}$	$a_1= 0.003323$
$y=a\cdot Q^b$	$a_2= 0.971832$
	$a_3= 9.26148\cdot10^{-5}$
	$a_4=3.10165$

Table 3.2: *The equation and constant set for the estimation of the mean ionization state from 3.27 ,of any one material plasma with atomic number Z and atomic weight A, as a function of mass density and temperature.*

The mean ionization state calculated from equation 3.27 has the advantage that uses only analytic functions correlating solely with plasma temperature and mass density, using some global constants

and factors. It is a general approach for the ionization of every plasma with known atomic number Z and atomic weight A. As a result, there is no need for the separate knowledge of the $Z_{eff} = Z_{eff}(\rho, T)$ through tabular data for each different plasma material and the implementation in any code could be global and easier. The depiction of Z_{eff} along with the two energy rate losses as a function of temperature is presented in figure 3.6.

To compare the two different approaches, the same values of mass density and temperature range should be considered in the FLYCHK code. Consequently the mass density values originate from formula 3.24 using the same data for the Thomas-Fermi model, correlating these values also with the tabular plasma temperature values that FLYCHK gives (figure 3.3). Hence, the electron density is $10^{12} e \cdot cm^{-3} < Ne < 10^{24} e \cdot cm^{-3}$ and the temperature $0.5eV < T < 10^5 eV$.

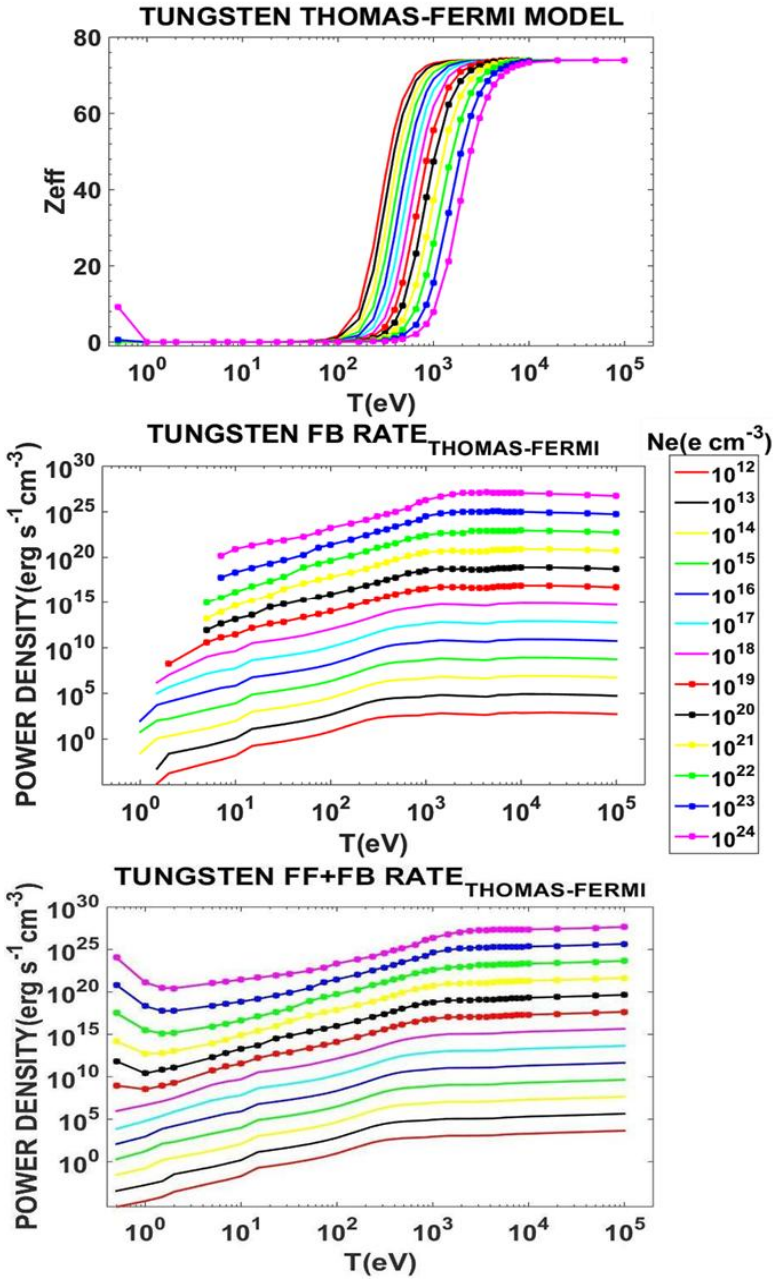

Figure 3.6: *Radiation energy density rate for optically thin cooling plasma tungsten. The temperature and mass density range are the same of* figure 3.3 *and Z_{eff} is calculated from an average Thomas-Fermi model. The top graph depicts the Z_{eff} , the second the energy density rate from the free-bound contribution, while the bottom the sum of the free-bound (recombination) and the free-free (Bremsstrahlung) radiation power density loss.*

Some observations for the values of Z_{eff} from these two different estimations:

i. The FLYCHK data (figure 3.3) present a density dependent value at low temperatures with high densities, having Z_{eff} values different than the lower ones. This is absent in the Thomas-Fermi model that gives almost identical values between 1 eV and 100eV for all densities. An exception is observed at the high densities of 10^{22}-10^{24} $e \cdot cm^{-3}$ that have mean ionization states, between 0.5eV and 1eV, higher than those of bigger temperatures (especially the 10^{24} $e \cdot cm^{-3}$ that has a 9 value ionization at 0.5 eV).
ii. The Thomas-Fermi model has an abrupt rise of the mean ionization for temperatures 100eV< T<10000 eV, while the FLYCHK model presents a smoother rise from 10 eV to 100000eV.
iii. The higher ionization state is 70 for the FLYCHK approach, while the Thomas-Fermi model is fully ionized, for all plasma densities, for temperatures higher than ~10000eV.

Now we can understand the importance of the bound-bound transitions for the radiation energy rates. Some last observations are:

i. The correction factor is necessary, especially for low and medium temperatures, for ff and fb expressions if anyone wants to have thin radiation losses of the correct order of magnitude.
ii. The free-free radiation is important at high temperatures but also gives non-zero values to the ff-fb contribution at low temperatures (~0.5eV to ~5eV) for all isodensities curves (figures 3.5 and 3.6).
iii. There is no significant difference between the power densities shown in figures 3.6 and 3.5 when the fb rate is taken into account. But when the ff contribution is added, the Thomas-Fermi model estimates higher rates and of the same form of the FLYCHK data in figure 3.4 which lucks in the figure 3.5.
iv. The differences with FLYCHK data at low temperatures and high densities are much smaller for the ff-fb Thomas-Fermi model than the ff-fb FLYCHK one.
v. Both models with the ff-fb rates underestimate the radiation losses by some (or many) orders of magnitude at lower temperatures.
vi. All energy isodensities at high temperatures (>10^3 eV) are of the same order of magnitude for all estimations.

3.3.2 Radiation transport module

Radiation transport redistributes energy within a medium through the emission and reabsorption of photons. These are quantum phenomena which need to be modelled [9]. One can simplify this modelling by averaging at all frequencies taking the mean opacities at the equations. The matching of the MHD equations and the radiation transport module can be accomplished then by adding extra source terms at the 3.5 and 3.6 equations. These are transformed to equations 3.28 and 3.29 adding

an extra equation including the radiation flux and the heating cooling term in parenthesis at the right hand side of 3.30.

$$\frac{\partial \mathbf{m}}{\partial t} + \boldsymbol{\nabla} \cdot \left[\mathbf{mu} + \left(P + \frac{1}{2} B^2 \right) \mathbf{I} - \mathbf{BB} \right] = \rho \mathbf{a_{rad}} \tag{3.28}$$

$$\frac{\partial E_t}{\partial t} + \boldsymbol{\nabla} \cdot \left[\left(E_t + P + \frac{1}{2} B^2 \right) \mathbf{u} + (\mathbf{u} \cdot \mathbf{B}) \mathbf{B} \right] = - \boldsymbol{\nabla} \cdot [(n_D \cdot \mathbf{J}) \times \mathbf{B}] + \rho \mathbf{u} \cdot \mathbf{a_{rad}} - k_P \rho c (a_R T^4 - E_{rad}) \tag{3.29}$$

$$\frac{\partial E_{rad}}{\partial t} + \boldsymbol{\nabla} \cdot \mathbf{F} = k_P \rho c (a_R T^4 - E_{rad}) \tag{3.30}$$

The E_{rad} is the radiation density energy and $\mathbf{F}$ denotes the radiation flux [21]. All equations are solved in the co-moving frame in the frequency independent (grey) approximation. In general, it is necessary to solve the equations for each frequency which appears in the physical problem. However, this makes the problem more complicated and computational demanding. So the grey approximation in which all radiative quantities, including the opacities, are integrated over all frequencies, simplifies it. All the scattering phenomena are not accounted for directly, but are included at the constants a_R, k_p and k_R, which are the radiation constant , Planck mean opacity and Rosseland mean opacity respectively (a more thorough explanation after equation 3.33). Specifically the radiation constant is:

$$a_R = \frac{8\pi^5 {k_B}^4}{15 c^3 h^3} = 7.56 \cdot 10^{-15} \mathrm{erg} \cdot c m^{-3} K^{-4} \tag{3.31}$$

The plasma fluid is influenced by the radiation in two different ways. First, the radiation may be absorbed or emitted by the fluid leading to variation of its energy density. This variation is given by the parenthesis expression at equations 3.29 and 3.30. The second effect is that of radiation pressure acceleration, $\mathbf{a_{rad}}$, introduced in the momentum and energy equations. This acceleration is given by the radiation flux through the following expression:

$$\mathbf{a_{rad}} = \frac{k_p}{c} \mathbf{F} \tag{3.32}$$

where $\mathbf{F}$ denotes the radiative flux, k_p the Planck mean opacity and c the speed of light.

The radiation flux is given by a diffusion approximation:

$$\mathbf{F} = -\lambda \frac{c}{k_R \cdot \rho} \boldsymbol{\nabla} E_{rad} \tag{3.33}$$

where E_{rad} is the radiation energy density and k_R the Rosseland mean opacity. The flux-limiter λ describes approximately the transition from very optically thick to optically thin regimes [21].

The two opacities are given in cm^2/gr. They are calculated via the frequency dependent k_ν. The opacity k_ν describes the coupling between matter and radiation via electron-photon interactions. It is composed of various contributions summarized as $k_\nu = k_{BB} + k_{BF} + k_{FF} + k_{SCAT}$, meaning the sum of bound-bound(BB), bound-free(BF), free–free(FF) and scattering(SCAT) contributions. It is a macroscopic quantity built up from fundamental cross-sections. The mean (gray) opacity represents, in a single number, the tendency of a material (at a specific ρ and T) to absorb/scatter radiation of all frequencies. This is a big advantage in practice, avoiding monochromatic opacities that are not commonly used in radiation transport calculations because they are too computational expensive [22].

The Rosseland and Planck mean opacities are density and temperature dependent. The Rosseland mean opacity yields the correct value for the integrated energy flux for an **optically thick** plasma while the Planck mean opacity for the **optically thin**. Planck opacity uses the normalized Planck black body radiation energy density distribution,

$$B_\nu(T) = \frac{2h\nu^3 \, {k_B}^4}{15c^2(e^{h\nu/k_B T} - 1)} \tag{3.34}$$

as a weighting function and averages k_ν directly, where k_ν is the frequency-dependent opacity and σ is the Stephan-Boltzmann constant

$$k_P = \frac{\int_0^\infty k_\nu \, B_\nu(T) d\nu}{\int_0^\infty B_\nu \, (T) d\nu)} = \frac{\pi}{\sigma T^4} \int_0^\infty k_\nu \, B_\nu(T) d\nu \tag{3.35}$$

Rosseland opacity, uses a temperature derivative of the Planck distribution as the weighting function, and averages ${k_\nu}^{-1}$:

$$\frac{1}{k_R} = \frac{\int_0^\infty {k_\nu}^{-1} \frac{\partial \, B_\nu}{\partial t} d\nu}{\int_0^\infty \frac{\partial \, B_\nu}{\partial t} d\nu} \tag{3.36}$$

For dry air the two opacities are calculated from TOPS Opacities webpage [23]. The tabular data are implemented in the code and the following 2-D graphs are produced (figure 3.7).

For temperatures in the range of 30 eV < T < 1.0 keV and densities in the range of 0.1 gr/cm^3< ρ <10.0 g/cm^3, the two opacities for the tungsten are calculated using an exponential fit as presented in Equation 3.37, with T in keV and ρ in gr·cm^{-3} [24]:

$$k_P = 646.4 \frac{\rho^{0.199}}{T^{1.225}} (cm^2 gr^{-1}), \qquad k_R = 244.12 \frac{\rho^{0.005}}{T^{1.119}} (cm^2 gr^{-1}) \tag{3.37}$$

For temperatures lower than 30 eV both opacities follow a~T^{-1} behaviour providing a good approximation, if we use 3.37. For lower densities (ρ<0.1 gr/cm^3) and temperatures T<100eV, the opacities follow a similar behaviour according to the above expressions. All the physical quantities are in CGS units.

This analysis presents a global radiation energy exchange for thinner and thicker plasma regions for a wide range of densities and temperatures. For the dissipative source variables and for a wide range of mass density and temperature values there will be a presentation in section PART II section.

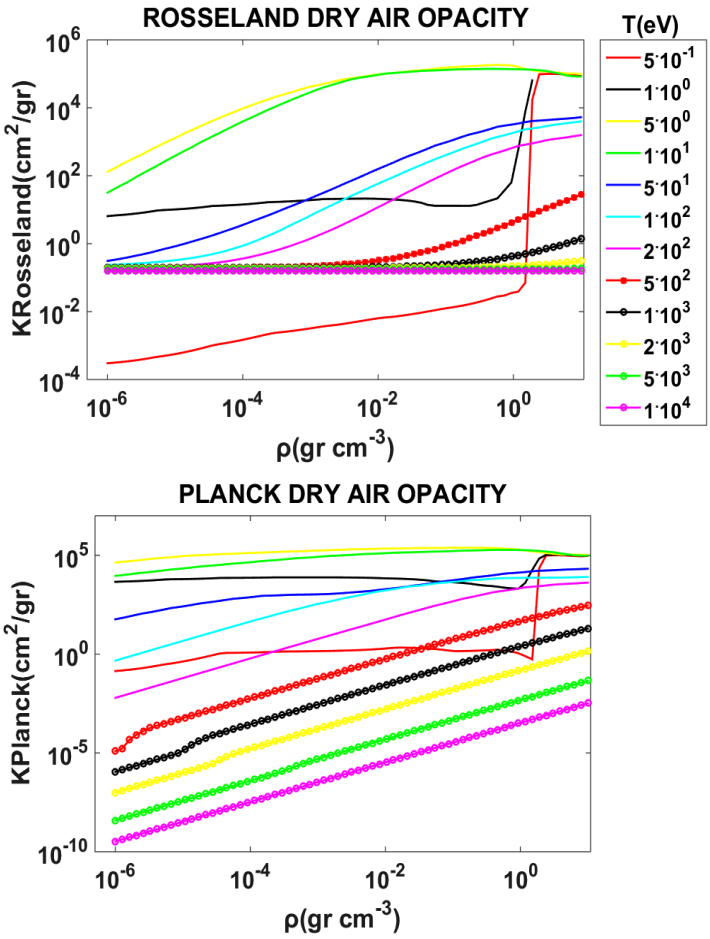

Figure 3.7: *The two opacities of dry air as a function of mass density and temperature calculated from the* from TOPS Opacities webpage*. The mixture is composed of 78% Nitrogen and 22% Oxygen. The temperatures are from 0.5eV to 10^4eV and the densities from 10^{-6}gr/cm^3 to 10gr/cm^3 having 12 isotherms depicted [23].*

References

[1] J. P. (HANS) GOEDBLOED AND STEFAAN POEDTS, "PRINCIPLES OF MAGNETO-HYDRODYNAMICS with Applications to Laboratory and Astrophysical Plasmas" , Cambridge University Press 2004, pg .178-183

[2] http://plutocode.ph.unito.it/PLUTO User's Guide v.4.2.

[3] L. Spitzer Jr., "Physics of Fully Ionized Gases" Interscience Publishers ING, New York, 1962.

[4] Lennox L. Cowie and Christopher F. McKee, "THE EVAPORATION OF SPHERICAL CLOUDS IN A HOT GAS. I. CLASSICAL AND SATURATED MASS LOSS RATES", The Astrophysical Journal, 211:135-146, 1977 January 1.

[5] V.E. Fortov, I.V. Lomonosov, "Equations of State of Matter at High Energy Densities", The Open Plasma Physics Journal, **3**, 122-130, (2010).

[6] T-4 Handbook of Material Properties Data Bases, Vol Ic: Equations of State, LA-101 SO-MS, UC-34, Issued November 1984.

[7] SESAME THE LOS ALAMOS NATIONAL LABORATORY EQUATION OF STATE DATABASE, LA-UR_92_3407.

[8] Kashiwa B. A., "The MGGB Equation-of-State for Multifield Applications: A Numerical Recipe for Analytic Expression of Sesame EOS Data", LA-1442 ,September 2010. http://www.doe.gov/bridge

[9] Yuri Ralchenko, "Modern Methods in Collisional-Radiative Modelling of Plasmas", Springer International Publishing Switzerland 2016.

[10] J. J. MacFarlane, P. Wang, G. A. Moses, "Non-LTE radiation transport in moderate-density plasmas", Laser and Particle Beams (1990), vol. 8, no. 4, pp. 729-740.
[11] J. P. Apruzese et al, "The physics of radiation transport in dense plasmas", PHYSICS OF PLASMAS VOLUME 9, NUMBER 5 MAY 2002.
[12] I. Yu. Vichev, V. G. Novikov, and A. D. Solomyannaya , "Modelling of the Emission Spectra of Tungsten Plasma" , Mathematical Models and Computer Simulations, 2009, Vol. 1, No. 4, pp. 470–481.
[13] Tungsten Charge State Distribution by FLYCHK NLTE Kinetics Calculation at NIST by International Atomic Energy Agency- Atomic Molecular Data Services provided by the Nuclear Data Section.
[14,] A. S. Richardson, NRL PLASMA FORMULARY, 2019.
[15] H.-K. Chung et al., "FLYCHK: Generalized population kinetics and spectral model for rapid spectroscopic analysis for all elements", High Energy Density Physics 1 (2005) 3-12.
[16] T. Pütterich et a., "Calculation and experimental test of the cooling factor of tungsten", Nucl. Fusion **50** (2010) 025012 (9pp).
[17] D. E. POST et al, "STEADY-STATE RADIATIVE COOLING RATES FOR LOW-DENSITY, HIGH-TEMPERATURE PLASMAS", ATOMIC DATA AND NUCLEAR DATA TABLES 20, 397-439 (1977).
[18] J. Larsen Ionization, "In Foundations of High-Energy-Density Physics: Physical Processes of Matter at Extreme Conditions" 2017 (pp. 122-184), Cambridge University Press, doi:10.1017/9781316403891.005.
[19] P. Beiersdorfer et al, "Atomic physics and ionization balance of high-Z Ions: Critical ingredients for characterizing and understanding high-temperature plasmas", High Energy Density Physics 8 (2012) 271-283
[20] Alexander E. Kramida , Joseph Reader, "Ionization energies of tungsten ions: W2+ through W71+", Atomic Data and Nuclear Data Tables 92 (2006) 457–479.
[21] Stefan M. Kolb, Matthias Stute, Wilhelm Kley, Andrea Mignone, "Radiation hydrodynamics integrated in the code PLUTO", A&A 559, A80 (2013).
[22] J. Colgan et al., "A NEW GENERATION OF LOS ALAMOS OPACITY TABLES", The Astrophysical Journal, 817:116 (10pp), 2016 February 1.
[23] TOPS Opacities/Opacities of mixtures (calculated by TOPS using ATOMIC or LEDCOP elemental opacities) https://aphysics2.lanl.gov.
[24] G. D. TSAKIRIS and K. EIDMANN, "AN APPROXIMATE METHOD FOR CALCULATING PLANCK AND ROSSELAND MEAN OPACITIES IN HOT, DENSE PLASMAS", J. Quant. Spectrosc. Radiat. Transfer Vol. 38, No. 5, pp. 353-368, 1987.

CHAPTER 3

PART II: DISSIPATIVE EFFECTS

3.4 Analysis of MHD (one fluid temperature model)

In the second part of this chapter, we introduce an appropriate plasma resistivity-/conductivity, thermal conductivity and viscosity MHD implementation, aiming for a global description of tungsten's plasma dissipative terms, for every density and temperature, including solid-liquid material at low temperatures and/or higher densities of condensed matter (dense/overdense region). The aim is to take in consideration the early plasma stages of solid/nearly solid densities ("cold" start conditions) and low temperatures of plasma, to the situations of condensed matter and high temperature plasma phases. Having in mind the separation regimes of the SESAME/MGGB data (figure 3.1), we present the following analysis, novel synthetic formula construction, graphic depiction and evaluation through experimental/semiempirical data.

3.4.1 Electrical Resistivity/Conductivity

Electrical resistivity/conductivity is one of the most crucial physical variables for the MHD equations and the most important diffusive term. Estimation of the resistivity/conductivity function (n/σ) will be presented using four different approaches.

The first one is a more thorough piecewise function equation valid for all densities of tungsten plasma from the solid and early liquid phase to the very thin plasma region and temperatures from very low, solid-liquid phase and early plasma formation, to very high values. Even for higher than solid densities, a fixed value or a linear/parabolic fitting is proposed.

The second method is a simpler direct approach of one function using low plasma background density (plasma air) as a parametric value fitting.

The third one is based on a linear mixture conductivity formula. It incorporates one electron-ion term and one neutral-ion term using the non-ideal Saha equation. It also introduces a better estimation of the Coulomb logarithm giving a smoother profile at the warm dense and overdense matter region for temperatures up to 10^5K.

The fourth method is a Braginskii like, magnetically dependent conductivity, including the non-ideal Saha equation, considering also the anomalous collision frequency term.

3.4.1.1 Piecewise function of electrical resistivity/conductivity of solid/liquid and tungsten plasma

The plasma conductivity is a strong function of the density and, at a high density, is almost-independent of temperature. As the density falls, the effect of temperature is more apparent. At lower temperatures, the conductivity falls to a minimum at a few percent of solid density, then rises with further decrease in density, eventually approaching the Spitzer conductivity which is valid for dilute plasmas [25]. Efforts of combining experimental data and theoretical work according to Spitzer based,

Lee-More, linear mixture atom-ion and electron density models, valid for specific density matter regimes have already been presented in the literature [25-33].

This study will introduce a general estimation of the conductivity/resistivity of a tungsten plasma resulting to a global fit for a wide range of densities and temperatures. Specifically, the value range for temperature is $0.01\text{eV}<\text{T}<165\text{eV}$, for the mass density $10^{-11}\text{gr/cm}^3<\rho<10^2\text{gr/cm}^3$ and for the electron density $10^{12}\text{e/cm}^3<\text{N}_e<10^{24}\text{e/cm}^3$. There will be a polynomial fitting and graphic presentation for several different solid/liquid/plasma temperatures at specific ranges of mass density. According to this we have:

i. A thorough examination by P. Tolias et al, of the W electrical resistivity, presents a very good polynomial fitting for low solid/liquid tungsten temperatures. The White–Minges fit for solid Tungsten in the temperature range $100<\text{T(K)}<3695$ and the Seydel–Fucke fit for liquid phase. The first one is:

$$\text{n} = -1.075\cdot 10^{-18} + 2.141\cdot 10^{-20}\text{T} + 8.688\cdot 10^{-24}\text{T}^2 - 2.055\cdot 10^{-27}\text{T}^3 + 2.310 \cdot 10^{-31}\text{T}^4 \ (\text{c.g.s units})$$

while the Seydel–Fucke fit in the temperature range $3695\text{K}\leq\text{T(K)}\leq 6000\text{K}$ for all liquid densities ($13.75\ \text{gr/cm}^3<\rho_{liq}<16.36\ \text{gr/cm}^3$) is

$$\text{n} = 15\cdot 10^{-17} - 2.0\cdot 10^{-21}(\text{T}-\text{T}_\text{m}) + 5.0\cdot 10^{-23}(\text{T}-\text{T}_\text{m})^2 \ (\text{c.g.s units}) \tag{3.38}$$

where T_m is the melting temperature (3695K) and n electrical resistivity in seconds.

Another option is the Wilthan–Cagran–Pottlacher fit where:

$$\text{n} = 25.7\cdot 10^{-17} - 5.1\cdot 10^{-20}\text{T} + 6.3\cdot 10^{-24}\text{T}^2 \ (\text{c.g.s units}) \tag{3.39}$$

and gives similar results as Seydel–Fucke [26]. A constant estimation for the liquid phase is given by R.S.Hixson and M.A.Winkler [27]:

$$\text{n} = 1.62\cdot 10^{-16}\text{s} \tag{3.40}$$

and is in good average agreement with the results from the previous polynomials.

ii. A polynomial fit is used for the electrical conductivity fitting, extrapolating data from A.W. DeSilva and J.D.Katsouros [25], for densities $10^{-3}\text{gr/cm}^3<\rho<10\text{gr/cm}^3$ and for temperatures $6000\text{K}<\text{T}<10000\text{K}$. For T=6000K the polynomial fit is:

$$\log\sigma = 0.4795\cdot\text{x}^2 + 1.9217\cdot\text{x} + 14.343\ , \qquad \text{x} = \log\rho \ (\text{c.g.s units}) \tag{3.41}$$

For T=8000K the polynomial fit is:

$$\log\sigma = 0.3904\cdot\text{x}^2 + 1.497\cdot\text{x} + 14.461 \ (\text{c.g.s units}) \tag{3.42}$$

The polynomial fit for T=10000K is:

$$\log\sigma = 0.3339\cdot\text{x}^2 + 1.2584\cdot\text{x} + 14.593 \ (\text{c.g.s units}) \tag{3.43}$$

However, another option for T=10000K is the prediction made by Kuhlbrodt et al. with COMPTRA04 [28].The polynomial fit is:

$$\log\sigma = 0.5127 \cdot x^2 + 1.3346 \cdot x + 13.965 \text{ (c.g.s units)} \quad (3.44)$$

There will be no graph presentation here due to the later modified fitting at these temperatures and a thorough graphic presentation (figures 3.15-3.17).

A combination of the theoretical data from A. W. DeSilva and J. D. Katsouros [25], with the ones from COMPTRA04 [28], experimental data from D. Sheftman and Y.E.Krasik [29] and A. D. Rakhel et.al [30], gives the data curve below for T=10000K.

The density range is 10^{-3}gr/cm^3<ρ<19.3gr/cm^3. The polynomial fit is:

$$\log\sigma = 0.3799 \cdot x^2 + 1.1235 \cdot x + 13.96 \text{ (c.g.s units)} \quad (3.45)$$

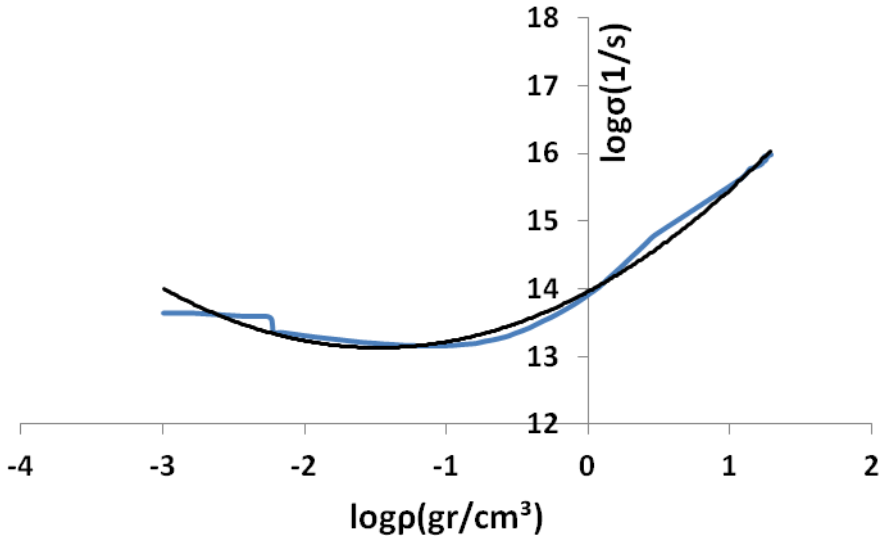

Figure 3.8: *The combination blue curve and the fitting polynomial one at 10000K for the conductivity and for densities 10^{-3}gr/cm^3<ρ<19.3gr/cm^3.*

For T=30000K experimental data from D.Sheftman and Y.E.Krasik [29], for densities 0.81 gr/cm^3<ρ<19.3 gr/cm^3, form the bottom data curve. A data merging with the ones of 10000K for lower densities is considered:

$$\log\sigma = 0.144 \cdot x^2 + 0.9192 \cdot x + 14.582 \text{ (c.g.s units)} \quad (3.46)$$

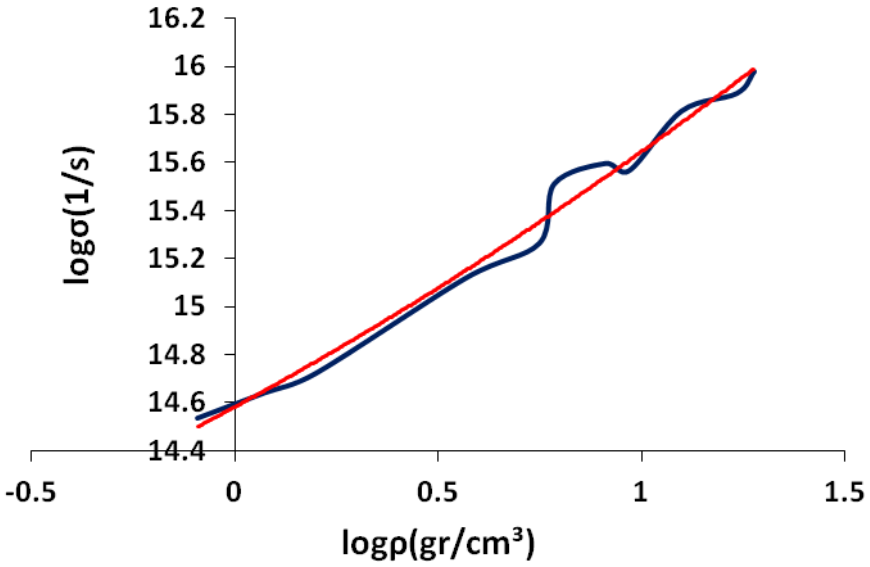

Figure 3.9: *The polynomial fitting of conductivity is the red curve and the deep blue the experiment. The temperature is 30000K for densities 10^{-3}gr/cm^3<ρ<19.3gr/cm^3.*

A combination fitting for T=30000K from D. Sheftman and Y. E. Krasik [29], A. W. DeSilva and Rakhel [33], A. D. Rakhel et.al [30] for densities 0.02gr/cm^3<ρ<19.3gr/cm^3 gives the curve below. The polynomial is:

$$\log\sigma = 0.347 \cdot x^2 + 0.8577 \cdot x + 14.413 \text{ (c.g.s units)} \tag{3.47}$$

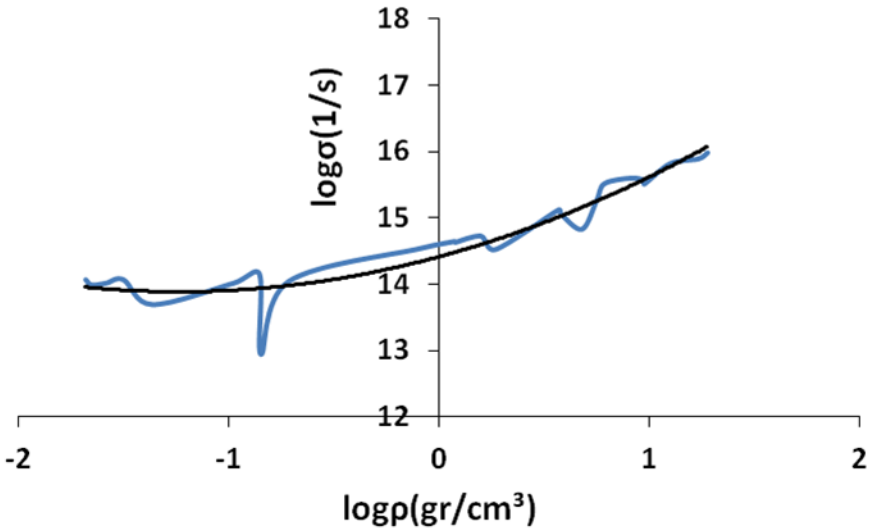

Figure 3.10: *The combination blue curve and the fitting polynomial one at 30000K for the conductivity and for densities 0.02 gr/cm^3<ρ<19.3 gr/cm^3.*

For T=50000K experimental data from D.Sheftman and Y.E.Krasik [29] and densities 0.51gr/cm^3<ρ<19.3gr/cm^3, form the following data curve. A data merging with the ones of 10000K for near metal densities is considered. The polynomial fitting is the linear green curve:

$$\log\sigma = 0.7513 \cdot x + 14.958 \text{ (c.g.s units)} \tag{3.48}$$

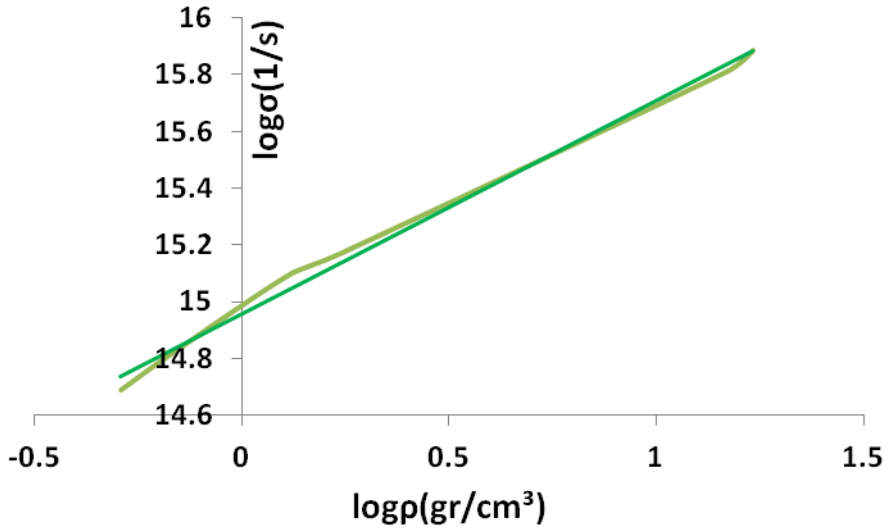

Figure 3.11: *The polynomial fitting linear green curve and the experimental one at 50000K for the conductivity and for densities 0.51 gr/cm^3<ρ<19.3 gr/cm^3.*

For T=50000K merging data from D.Sheftman and Y.E.Krasik [29] and A.D. Rakhel et.al [30] and densities 0.51gr/cm^3<ρ<19.3gr/cm^3, give the bottom data curve. The polynomial is:

$$\log\sigma = 0.2101 \cdot x^2 + 0.5028 \cdot x + 14.904 \ (\text{c.g.s units}) \tag{3.49}$$

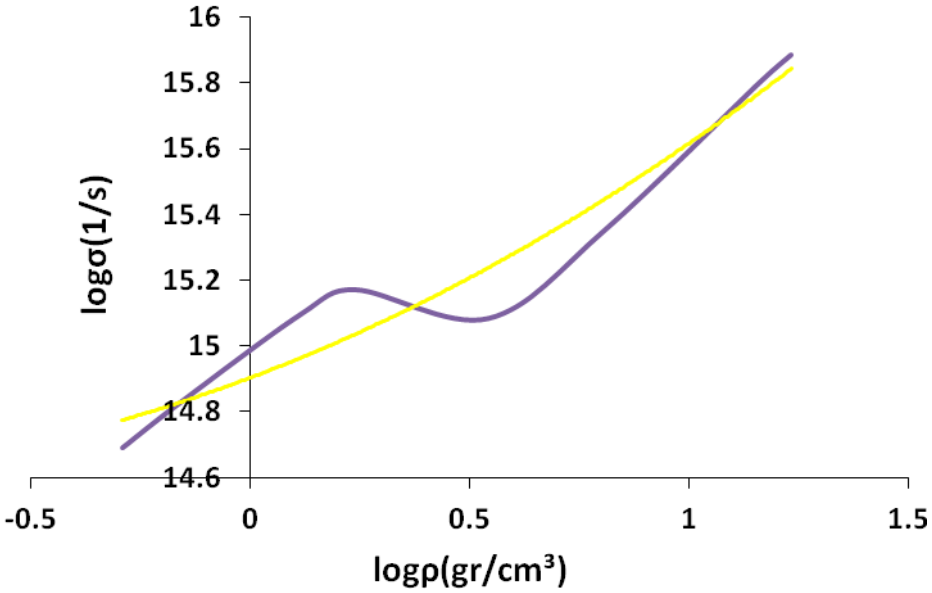

Figure 3.12: *The combination purple curve and the fitting yellow polynomial one at 50000K for the conductivity and for densities 0.51 gr/cm^3<ρ<19.3 gr/cm^3.*

For T=70000K experimental data from D.Sheftman and Y.E.Krasik [29] and densities 0.51gr/cm^3<ρ<19.3gr/cm^3, give the bottom data curve. The polynomial fitting is:

$$\log\sigma = 0.6275 \cdot x + 15.119 \ (\text{c.g.s units}) \tag{3.50}$$

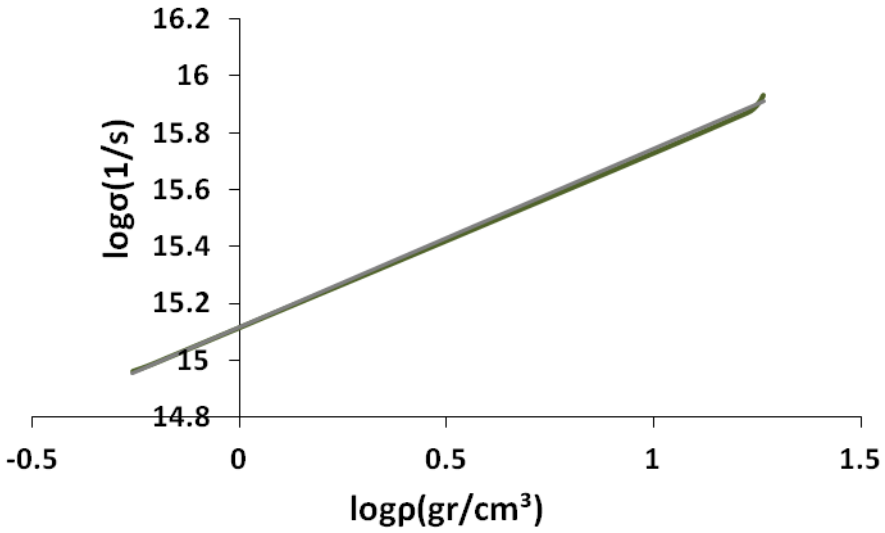

Figure 3.13: *The experimental near linear green curve and the linear fitting polynomial one at 70000K for the conductivity and for densities 0.51 gr/cm^3<ρ<19.3 gr/cm^3.*

For T=90000K, experimental data from D.Sheftman and Y.E.Krasik [29] and densities 0.51gr/cm^3<ρ<19.3gr/cm^3, form the bottom data curve. A data merging with the ones of 10000K for near metal densities is considered. The polynomial fitting is:

$$\log\sigma = 0.5278 \cdot x + 15.232 \ (\text{c.g.s units}) \tag{3.51}$$

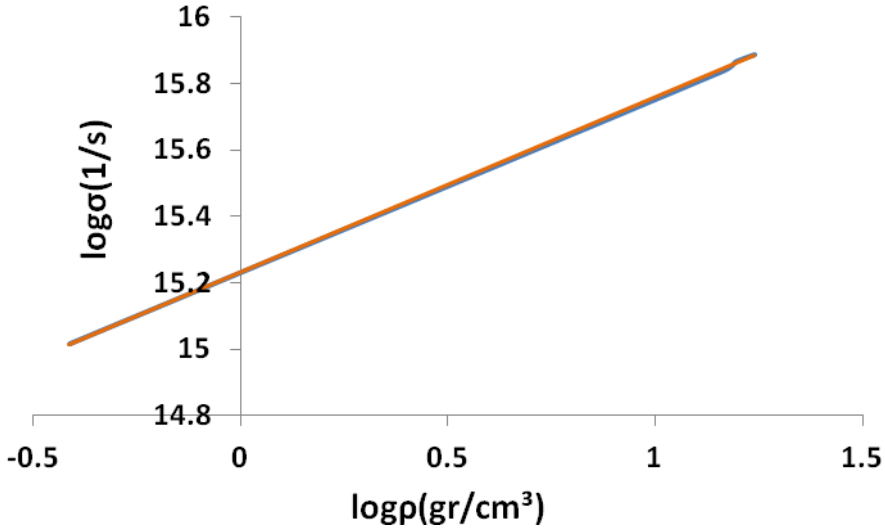

Figure 3.14: *The experimental near linear blue curve and the linear brown fitting polynomial one at 90000K for the conductivity and for densities 0.51gr/cm^3<ρ<19.3gr/cm^3.*

Some observations for the above resistivities (conductivities):

i. the resistivity of liquid tungsten weakly depends on temperature and has a very slow decrease right after the melting point followed by an increase again at a much slower rate than the solid state increase [25].
ii. a plasma-like dependence of the electrical resistivity of expanded tungsten on temperature takes place at a density which is 8–16 times lower than the standard solid density [30].

iii. For plasma densities near and above metal tungsten the dependence on the temperature is very weak [25,27,30].

iv. If the plasma density is smaller than 10^{-2}gr/cm^3, the conductivity rises with the decreasing of density and approaches Spitzer's formula for all temperatures above 6000K.

v. The fitting for specific high temperatures (e.g. 30000K) is repeated at different density areas and is merged to the data of lower temperatures at lower densities (e.g. 10^{-3}gr/cm^3<ρ<0.5 gr/cm^3) trying to accomplish a fitting for all densities at each temperature where Spitzer's formula is inaccurate.

iii. The Spitzer's resistivity/conductivity is given by:

$$\sigma_{\text{Spitzer}} = \frac{1}{\eta_{\perp}} = 6.96 \cdot 10^7 \frac{{T_e}^{1.5}}{Z_{\text{eff}} \ln\Lambda} \ (1/\text{s}) \tag{3.52}$$

where the electron temperature T_e is in K and Z_{eff} is given from the graph in figure 3.3 [14]. This equation is valid for low densities (ρ<10^{-3}gr/cm^3) for all plasma temperatures above 6000K. The original Coulomb's logarithm for electron-electron collision is:

$$\ln\Lambda = 23.5 - \ln\left({T_e}^{-1.25} {N_e}^{0.5}\right) \tag{3.53}$$

for all temperatures (in eV) and densities (in cm^{-3}) [14]. For high electron densities this gives negative values, so a cut-off value can be used (e.g. $\ln\Lambda$=0.5). The Z_{eff} ionization state is considered nearly constant and independent of the temperature for temperatures up to 10000K. It is nearly zero for these temperatures, for all electronic densities except for those that are near the solid ones (figure 3.3). FLYCHK calculations are known to give better results for highly ionized plasmas and intermediate electron densities. For very low N_e, FLYCHK overestimates the meta-stable state population, which may affect Z_{eff}. Especially for most elements with atomic numbers > 18, the near-neutral ion results are incorrect. For very high N_e, FLYCHK may give inadequate results due to simple continuum lowering model and lack of degenerate states contribution**.** Some modifications were made to correct these miscalculations, as will be discussed later on.

It is assumed that:

$$Z_{\text{eff}} \cdot N_i = N_e \text{ and } \rho = N_i \cdot m_i (\, m_i >> m_e) \text{ giving } \ \rho = \frac{N_e \cdot m_i}{Z_{\text{eff}}} \tag{3.54}$$

where m_i=183.84amu=305·10^{-24}g. The mass density can be calculated from the previous relation. Data from figure 3.3 can be extrapolated, where Z_{eff} is calculated as a function of temperature. Like this, an estimation of electrical conductivity σ, as a function of ρ for a specific temperature, could be extracted from equations 3.52 and 3.53. The graphic presentation of σ from the Spitzer formula for all the above temperatures and for densities ~10^{-10}gr/cm^3<ρ<~10^2gr/cm^3 is presented at figures 3.15 and 3.16. There is a comparison with the experimental and semiempirical data for the relative density region of this section's just presented study. The electron density range is 10^{12}gr/cm^3<N_e<10^{24}gr/cm^3.

For T=6000K, 8000K and 10000K, we take the graph 3.15, comparing the polynomial fit (for densities 10^{-3} gr/cm^3<ρ<19.25 gr/cm^3) to the Spitzer's formula plots (for the aforementioned densities). For these graphs (figure 3.15, 3.16) the used Coulomb logarithm for electron-ions collisions is:

$$\ln\Lambda = 25 - \ln\left(T_e^{-1.5} N_e^{0.5}\right) \text{ valid for } T_e < 10eV \tag{3.55}$$

The Z_{eff} data are the unmodified ones coming from the FLYCHK code for figure 3.15.

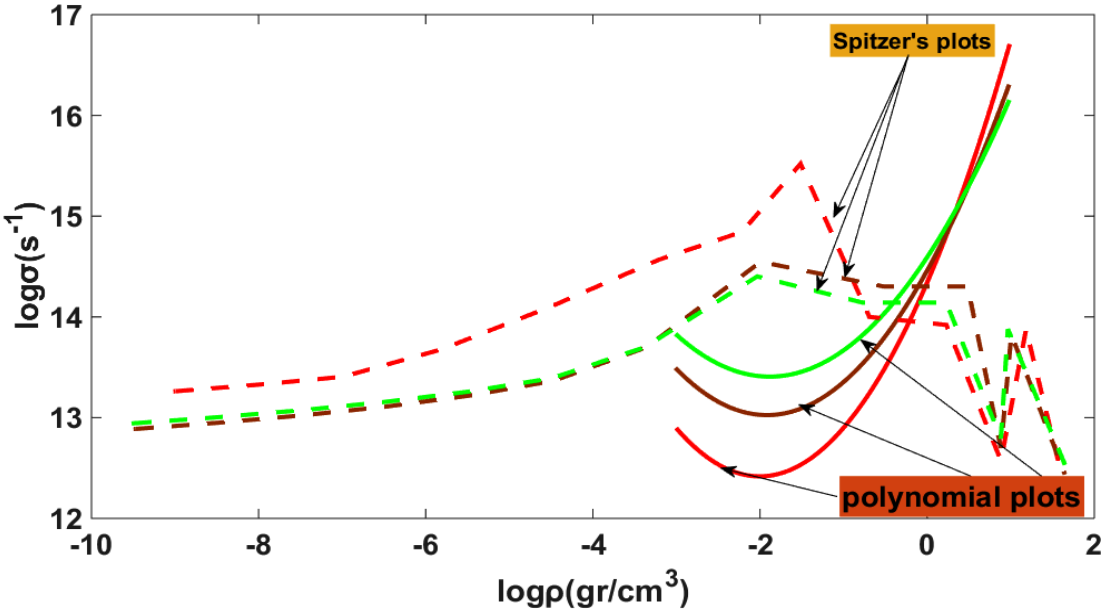

Figure 3.15: *The dashed lines are the Spitzer's plots and the solid ones the polynomials. The red line is for 6000K, the brown for 8000K and the green for 10000K.*

As can be seen the dashed lines predict different conductivities than these of the references for the warm dense matter region (WDM). Especially at 6000K, there is the maximum discontinuity at 10^{-3} gr/cm^3 while it is reduced at 8000 K and disappears at 10000K. Spitzer overestimates the conductivity for 6000K-10000K according to the polynomial fit curves. The 6000K conductivity presents higher values than those of 8000K and 10000K.

So modification is made for Z_{eff} correcting the discrepancies of the FLYCHK code. More specifically, we want to avoid more than two orders of magnitude at the estimation of Z_{eff} for each electron density. This, for different electron densities, could give the same mass density value (3.54 equation), but different calculations for the resistivity and the transport coefficients (thermal conductivity, viscosity). Additionally, for temperatures lower than a few eV the FLYCHK overestimates the high electron density region (specifically for Ne=10^{23}e/cm^3 and Ne=10^{24}e/cm^3 as presented in figure 3.3). A modification to lower values is necessary. The Coulomb logarithm $\ln\Lambda$ is calculated through 3.55. Cut off value is $\ln\Lambda$=0.5 (even though it is out of theory's limit it is a good low limit for the curves fitting). Thus, the value range in equation 3.55 is from 0.5 to ~12 for all temperature and density ranges. The modified Spitzer's formula presents better plots for the dense matter region (10^{-3} gr/cm^3<ρ<19.25 gr/cm^3), compared to the ones of figure 3.15, temperatures smaller than 10000K and very close results

to the experimental and semiempirical data for temperatures higher than 10000K (figure 3.16). But of course the discrepancy for 6000K, 8000K and 10000K still exists!

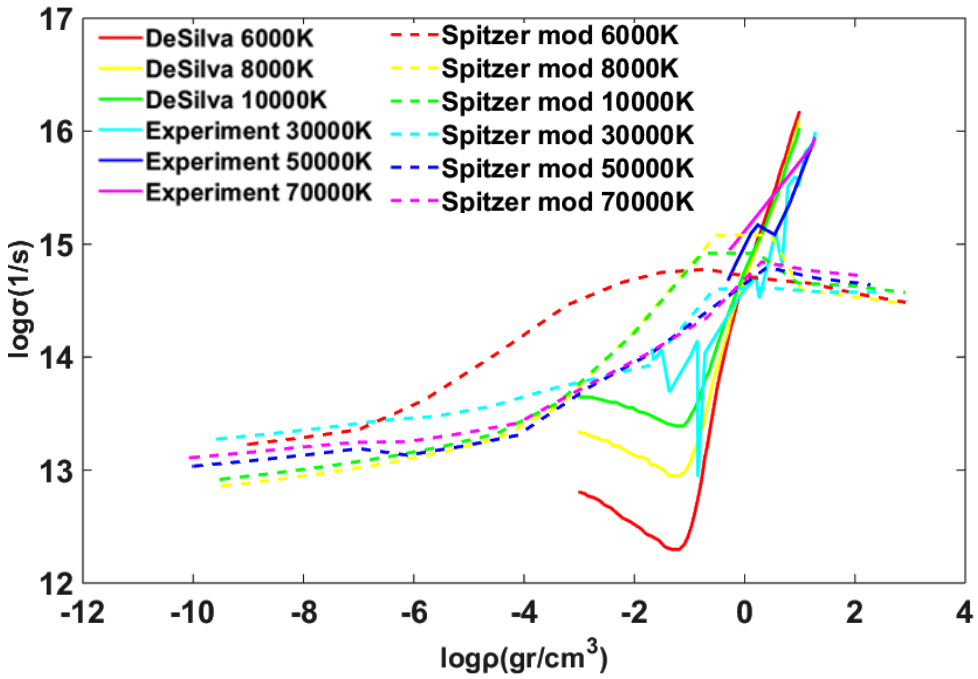

Figure 3.16: *The dashed lines are the modified Spitzer's plots and the solid ones the experimental and semiempirical data. The previous polynomials fittings are depicted only at DeSilva's work (mostly) for 6000K, 8000K and 10000K. The rest are lines of the raw experimental data. The red line is for 6000K, the yellow for 8000K, the green for 10000K, the cyan for 30000K, the blue for 50000K and the magenta one for 70000K.*

A new modification adjustment to the Spitzer's electrical conductivity has to be made so it can conclude the warm dense matter region (WDM), as presented in figure 3.16, for temperatures smaller than 10000K. A Gaussian fit is implemented having its peak at 0.1gr/cm^3. The comparison of figures 3.15 and 3.16 reveals a large difference between experimental and theoretical studies. Thus, the proposed formula for the new modification is:

$$\log\sigma_{\mathrm{mod}} = \log\sigma_{\mathrm{Spitzer}} \cdot \left(1 - \frac{T_0}{T} e^{-(\log\rho+1)^2/b}\right) \tag{3.56}$$

where T_0=1000K in our case, b=1 and 6000K<T<10000K. Depending on the problem, the coefficients T_0 and b can be modified properly. With this transformation we have a correction of one or two orders of magnitude for electrical conductivity close to the 0.1gr/cm^3 density. Using the above function the corrected isotherm plots are depicted in figure 3.17.

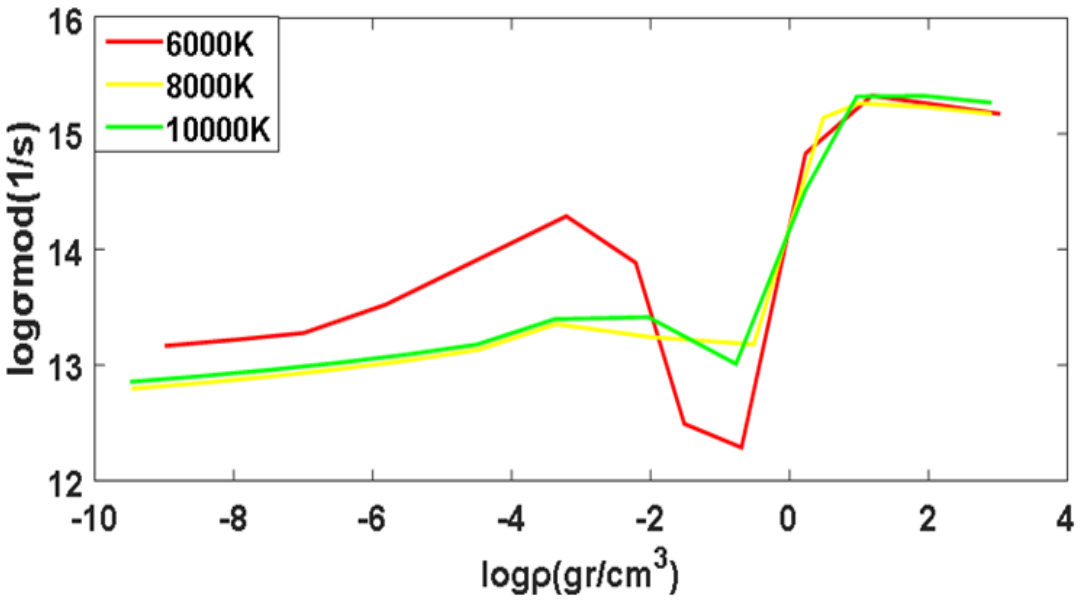

Figure 3.17: *Plots of the three temperatures with the exponential fit correction to the originally modified Spitzer formula.*

Comparison of these graphs with the ones in figure 3.16, reveals that, for the whole range of densities, the modified Spitzer and the experimental/ semiempirical plots are merged presenting satisfying agreement to the literature of dense matter and low temperatures. Exception is the dense/overdense matter region (solid/beyond solid) that probably underestimates the experiment.

It must also be mentioned that the thermal conductivity coefficient disagrees with these plots in the dense region below 10000K, as will be presented later. The original modified Spitzer plots of 3.16 will be used there.

A similar approach could be adopted for every metal plasma combining experimental and semiempirical data along with function fitting. The produced formula would be similar to the one of 3.56 equation adjusting the parameters T_0 and b.

Thus concluding in a general conductivity/resistivity formula for every density and temperature, we have:

$$\log\sigma = \begin{cases} \log\left(\dfrac{1}{-1.075\cdot10^{-18}+2.141\cdot10^{-20}\mathrm{T}+8.688\cdot10^{-24}\mathrm{T}^2-2.055\cdot10^{-27}\mathrm{T}^3+2.310\cdot10^{-31}\mathrm{T}^4}\ \mathrm{s}^{-1}\right), & 100\mathrm{K}<T<3695K \\ \log\left(\dfrac{1}{25.7\cdot10^{-17}-5.1\cdot10^{-20}\mathrm{T}+6.3\cdot10^{-24}\mathrm{T}^2}\ \mathrm{s}^{-1}\right), & 3695\mathrm{K}<T<6000K \\ \log\sigma_{\mathrm{Spitzer}}\cdot\left(1-\dfrac{\mathrm{T}_0}{\mathrm{T}}\mathrm{e}^{-\frac{(\log\rho+1)^2}{\mathrm{b}}}\right), & 6000\mathrm{K}<T<10000K \\ \log(\sigma_{\mathrm{Spitzer}}), & 10000\mathrm{K}<T \\ a\log\rho+\mathrm{b}\ \text{where a}\sim1.0\ \text{and b}\sim15, & \rho>\sim10\ \mathrm{gr}\cdot\mathrm{cm}^{-3}\ \text{for all T} \end{cases} \quad (3.57)$$

The density's validity for the first one is for the solid regime, the second for densities 13.75 gr/cm^3 < ρ_{liq} < 16.36 gr/cm^3 while the third one is for the whole range 10^{-9}gr/cm^3<ρ<~10gr/cm^3 and the fourth for ~10 gr/cm^3<ρ< ~100gr/cm^3.

For densities a little lower and higher than the solid ones, we see the experimental curves rising away from the Spitzer's and having temperature independence. Thus, a mean fixed value can be used due to this independency (i.e. 10^{15} to 10^{16} s^{-1}) or one linear or parabolic fitting for all temperatures ($\log\sigma=a\cdot\log\rho+b$ or $\log\sigma=a\cdot\log^2\rho+b\cdot\log\rho+c$ with $a<0$, where a, b and c are adjustable variables, matching the experimental curves). We have to be careful and uncertain to our estimations though, due to the lack of data for densities much higher than the solid ones (the validity of this fitting is approximately up to 10^2 gr/cm^3).

If there are overlapping regions from the above analysis (density varying mostly), in which more than one approach is valid we select the most global fitting and the closer value estimation to the neighbour regions (i.e. the third relation in system 3.57 is overlapping the liquid phase as we will present right away at figure 3.18).

These estimations are presented at the final figure 3.18 where all temperature and density depended conductivities are shown. There, all the modifications and formulas of the 3.57 equation system are included. The experimental and semiempirical/theoretical data of other works are more than satisfying matched to the present work suggestions. Of course there is a maximum of two orders difference for a narrow density region $\sim10^{-3}gr/cm^3<\rho<\sim10^{-2}gr/cm^3$ of the 6000K curve to the one of Da Silva's and other work combination study [25,33]. The curve could be better matched if someone changed the exponential constants. But it also reminds us that Spitzer's formula is inadequate at the very low liquid/plasma phase transition and overestimates the conductivity as we also present in figures 3.16 and 3.17.

More specifically, the density independence of solid and liquid conductivity is presented at the top graph as single cross and star points for the solid (19.25 gr/cm^3) and liquid density of ~15 gr/cm^3 respectively. As the temperature rises, the solid phase conductivity is rising too. The liquid phase conductivity presents very similar values at 4000K, 5000K and 6000K. These star points are overlapped from the 6000K, 8000K and 10000K of Da Silva's data that have similar values at this density region.

The mid graph is for temperatures up to 90000K having also the specific modified curve of Spitzer formula that is absent to the previous figures. The relevant experimental work is the one of D. Sheftman's and Y.E.Krasik's presented in figure 3.14. As we can see, the higher temperature values give a slight higher conductivity than the lower ones at the diluted plasma region while they are rising and are of the same values with the ones of the top graph at the dense matter region. The 30000K curve presents higher values at low densities due to the uncertainty at the mean ionization states and Coulomb's logarithm. This discrepancy and the one for 6000K has to be considered at the implementation phase in the code. Moreover, the dash-dotted line presenting the exponential fit proves that this modification is less consistent at this temperature with the experimental data than the one without, as it is clearly depicted in the 3.18 figure. Nevertheless, the experimental and semiempirical data of other works are very close and have, for almost any temperature, a mean value curve very close to the one predicted from these Spitzer curves at the dense matter region.

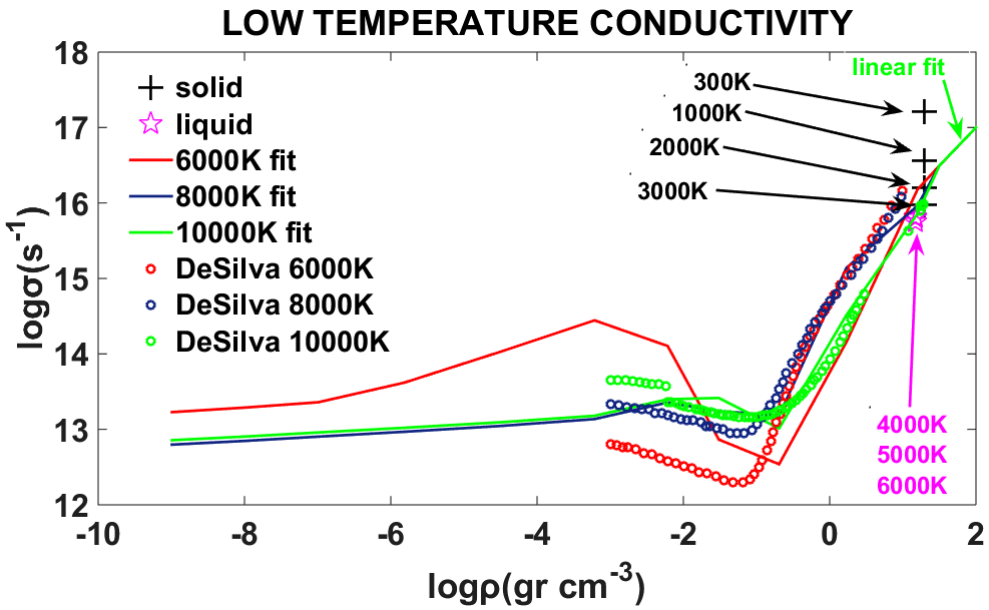
LOW TEMPERATURE CONDUCTIVITY
solid
liquid
6000K fit
8000K fit
10000K fit
DeSilva 6000K
DeSilva 8000K
DeSilva 10000K
linear fit
300K
1000K
2000K
3000K
4000K
5000K
6000K
logσ(s-1)
logρ(gr cm-3)

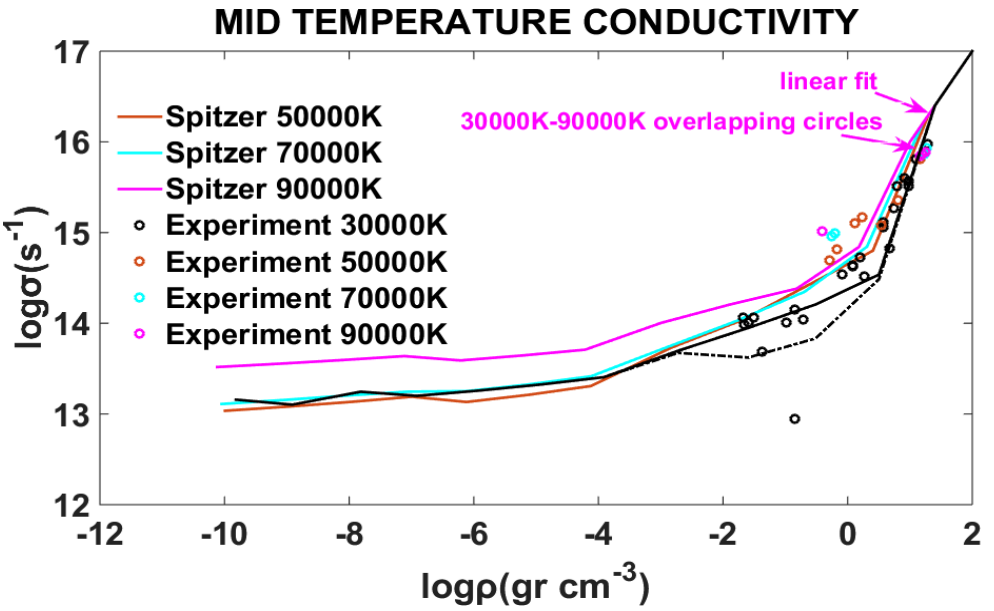
MID TEMPERATURE CONDUCTIVITY
Spitzer 50000K
Spitzer 70000K
Spitzer 90000K
Experiment 30000K
Experiment 50000K
Experiment 70000K
Experiment 90000K
linear fit
30000K-90000K overlapping circles
logσ(s-1)
logρ(gr cm-3)

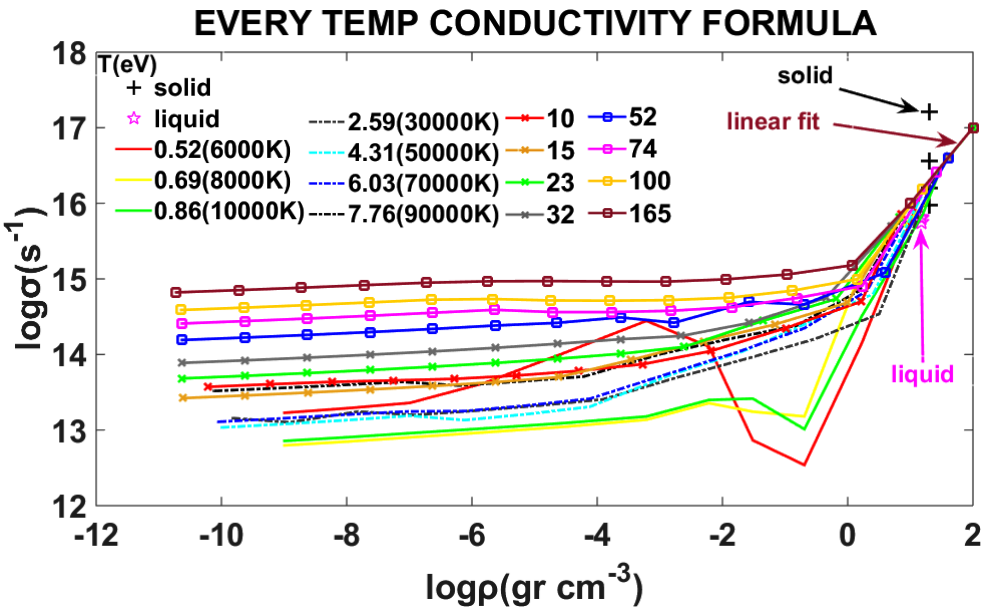
EVERY TEMP CONDUCTIVITY FORMULA
T(eV)
solid
liquid
0.52(6000K)
0.69(8000K)
0.86(10000K)
2.59(30000K)
4.31(50000K)
6.03(70000K)
7.76(90000K)
10
15
23
32
52
74
100
165
solid
linear fit
liquid
logσ(s-1)
logρ(gr cm-3)

Figure 3.18 i. Top graph: *Plots of the low temperatures up to 10000K. The cross points are of the solid tungsten density, the pink stars of liquid phase at 15 gr/cm^3 and the three temperatures of figure 3.17 with the exponential fit correction and the linear fit for the overdense region proposed at 3.57 equation system. The circle points are (mostly) Da Silva's extended semiempirical and experimental data of the polynomial fitting.*
ii. Mid graph: *Plots of temperature range, 30000K up to 90000K. Four temperatures depiction of the modified Spitzer formula with linear fitting for the overdense region proposed at 3.57 equation system. The black solid line is the Spitzer modified formula while the dash-dotted is with the exponential fit. The circle points are experimental and theoretical semiempirical literature data of the previous analysis without function fitting.*
iii. Bottom graph: *Plots of every temperature from 0.025eV (300K) to 165eV (1914660K) that is mentioned in this theoretical study without the experimental and literature data points. The Spitzer plots or temperatures >10eV are unmodified, using the original FLYCHK data for Z_{eff} while the $\ln\Lambda=26-\ln(T^{-1}N_e^{0.5})$ valid for T>10eV. All curves are linear fitted at the overdense region (>~10 gr/cm^3).The solid and liquid temperature symbols are the same of the top graph. The electron densities have a range from 10^{12}e/cm^3 to 10^{24}e/cm^3 for all graphs and mass density from ~10^{-11}gr/cm^3 to 10^2gr/cm^3.*

The bottom graph is the one that depicts all the temperature ranges from the very early solid phase to the main plasma phase with ionization levels of the order of 20-30. The depiction includes not only the proposed theoretical curves of the first two graphs but also unmodified Spitzer curves up to the 165eV temperature. The exception is the linear fit at the overdense region presenting a temperature independence profile. The similarities of these curves morphology with the ones of the SESAME/MGGB curves in figure 3.2 is noticeable**.** The value range is also in good agreement with other theoretical works that are suitable for the warm dense matter regime considering various interactions of electrons with electrons, atoms, and ions by a linear mixture rule [32]. A modified version of the linear mixture technique will be presented at subsection 3.4.1.3.
A disadvantage of this approach is that it can be computational difficult in implementation. The solution time-step can be dramatically reduced due to discrepancies between different transition zones. The crossings of some graphs at different temperatures has to be considered for the implementation of this function (i.e. at 3.17 or 3.18 figures). The safest way is to extract tabular data from the graphs, properly modifying them to avoid crossings, while an interpolation procedure can evaluate the conductivities/resistivities of all densities and temperatures of interest. Last but not least, a linear extrapolation fitting could be used for densities higher than the solid ones introducing closer results to the experimental data of figure 3.16. It's the same procedure of the linear fitting in equation 3.57, but tabulated, and similar to the one proposed for the EOS in section 3.2.

3.4.1.2 A simple function of electrical resistivity/conductivity of plasma tungsten

A simpler approach considering the smooth transition from the metal plasma to the low density background (vacuum regions) follows the form presented in equation:

$$n = \eta_{\perp}(1 + \frac{k\rho_{vac}}{\rho}) \tag{3.58}$$

where $\eta_{\perp}$ is the transverse Spitzer resistivity presented in 3.52, ρ_{vac} is the initial low density background (which is considered to be 10^{-6}gr/cm^3 for the problems studied here), ρ is the plasma density and k is the resistivity coefficient of the low density background [34]. This model is representative of resistive MHD codes which smooth the transition to a large background resistivity.

According to the parametrical numerical study, the computed optimal value to address this smooth transition was determined to be the number 24 for the selected vacuum value and the material of plasma tungsten. This value also prevents the solution time-step to be dramatically reduced (tested in 5.3 section for a PLUTO simulation). When thermal electron-ion collisions are concerned, it holds for the Coulomb's logarithm:

$$\ln\Lambda = 25 - \ln\left({T_e}^{-1.5}{N_e}^{0.5}\right) \text{ valid for } T_e < 10eV \tag{3.59}$$

and

$$\ln\Lambda = 26 - \ln\left({T_e}^{-1}{N_e}^{0.5}\right) \text{ valid for } T_e > 10eV \tag{3.60}$$

This is a modified version of the classical electron–ion collisions formula that provides slightly higher values, enabling a smoother transition to the large resistivity of the low density background [14]. It cannot avoid though the discrepancies of the 6000K to 10000K, presented earlier, but still remains a quick computational and easy to implement solution.

3.4.1.3 Linear mixture, Saha based, conductivity formula

Another tested formula as we mentioned earlier at subsection 3.4.1.1, especially suitable at the expanded fluid domain to the warm dense matter regime (WDM), is the linear mixture rule considering various interactions of electrons with electrons, atoms, and ions [32]. The same team, of [32], has evaluated and tested this formula for the warm dense tungsten plasma and also for dense nickel and iron plasmas [35]. Mofreh R. Zaghloul uses the same technique to evaluate and calculate the electrical conductivity of the non-ideal copper plasma [36]. Their work correlates and uses the neutral electron cross-section evaluation of M.P. Desjarlais that gives practical improvements to the Lee-More conductivity near the metal-insulator transition [37].

Here we will present a modified/combination formula, combining the previous reference methods, giving a global fitting formula for all densities ~10^{-11}gr/cm^3<ρ<~10^2gr/cm^3 and temperatures from liquid-plasma phase up to 10^5K (or even more!). The Z_{eff} data are again FLYCHK originating. The linear mixture rule is simple. It considers a linear sum contribution of the electron-ion and electron-atom resistivity or the inverse sum of the respective conductivities [32,35,36]:

$$\eta_{total} = \eta_{ei} + \eta_{en} \quad \text{or} \quad {\sigma_{total}}^{-1} = {\sigma_{ei}}^{-1} + {\sigma_{en}}^{-1} \tag{3.61}$$

The neutral-ion percentage is given by the non-ideal Saha equation for a single species plasma in thermodynamic equilibrium:

$$\frac{N_i}{N_n} = \frac{1}{x} \simeq 2.42 \cdot 10^{15} T^{1.5} N_i^{-1} e^{-\frac{E_{ion}}{K_B T}\left[1-\left(\frac{c_1 e^2}{E_{ion} \cdot a}\right)^{c_2)}\right]}$$

$$\text{where } a = \left(\frac{3}{4\pi N_i}\right)^{\frac{1}{3}} \text{ and } f = \frac{1}{2}\left[(x^2 + 4x)^{0.5} - x\right] \tag{3.62}$$

The non-ideal Saha equation of 3.62 equation is used to the electron-ion conductivity via the f factor (as will be presented at 3.64) and a is the Wigner-Seitz radius, using the N_i ion density. The second term in exponential parentheses gives a semi-empirical pressure ionization correction [37]. The constants c_1 and c_2 are selected to give the best curve fitting to the experimental and semiempirical data of subsection 3.4.1.1. The constants for all temperatures are 1.5 and 1.5 respectively, and are the same as of reference [37]. In general, they could differ and have close values to the ones proposed, having always in mind the evaluation through experiment. The argument of the exponential changes sign at $c_1 e^2 E_{ion}^{-1} a^{-1} = 1$. This is consistent with Likalter's percolation criterion $c_1 e^2 E_{ion}^{-1} r^{-1} \approx 1/3$ for the metal-insulator transition for the selected values of constant c_1 [37]. The E_{ion} is the first ionization energy for plasma tungsten equal to 7.68eV [20]. All units are in c.g.s system.

The electron-ion conductivity is then given by the next formula:

$$\sigma_{ei} = \frac{6.96 \cdot 10^7 T^{1.5}}{Z_{eff} \ln\Lambda} \gamma_e \tag{3.63}$$

where

$$\gamma_e = \frac{3\pi}{32}\left(1 + \frac{153 \cdot Z_{eff}^2 + 509 \cdot Z_{eff}}{64 \cdot Z_{eff}^2 + 345 \cdot Z_{eff} + 288}\right)$$

The above formula is a Spitzer like 3.52 equation with the addition of γ_e factor that takes into account the electron-electron scattering and can be neglected at a first approximation, since it is of the order of unity. The Z_{eff} is the mean ionization state that is extracted from the FLYCHK data. The Coulomb logarithm that is used here is the one proposed by Ebeling et al, representing the effective quantum Coulomb logarithm, as calculated from the Born approximation and Debye potential [38]. This is a more physical way for the Coulomb logarithm approach taking into consideration the quantum phenomena than the "artificial" corrections and cut-offs of the classical Coulomb logarithm approach which is not valid for values lower than unity [14]. The validity of the quantum formula is at all densities of our interest for the low temperature regime, while the classical formula presents similar values for high temperatures. It also introduces appropriate values at the dense matter region, that are much lower than unity, presenting a smooth, almost linear rising profile, which is the one we "artificially" implemented at the 3.4.1.1 subsection approximation. This fitting will be presented in the next figure. The proposal of the Mofreh R. Zaghloul et al [39,40] gives an improved formula but is not of much different value regime than the simpler one that we use here. Also the latter uses the $\bar{b}_o$, which is an average thermal impact parameter that has to be evaluated carefully [41,42]. Both

approximations are valid for this task and give no negative values at the dense matter region at the low temperature regime. The analytical function and the related variables are as follows:

$$\ln\Lambda = \frac{1}{2}\left[\ln\left(1+\frac{(2\cdot\lambda_D)^2}{{l_o}^2}\right)-\frac{(2\cdot\lambda_D)^2}{(2\cdot\lambda_D)^2+{l_o}^2}\right] \simeq \frac{1}{4}\ln\left(1+\frac{(2\cdot\lambda_D)^4}{{l_o}^4}\right)$$

$$\text{where } l_o = \frac{\hbar}{(2M_r K_B T)^{0.5}} \text{ (average thermal wave length)}$$

$$\lambda_D = \left(\frac{K_B T}{4\pi N_i {q_i}^2}\right)^{0.5} = \left(\frac{K_B T}{4\pi N_e e^2 Z_{eff}}\right)^{0.5} \text{ (Debye ion length)} \quad (3.64)$$

$$\text{and } M_r = \frac{m_i m_e}{m_i + m_e} \text{ (reduced ion} - \text{electron mass)}$$

Here we use the fourth power approximate formula of equation 3.64.

The electron-atom conductivity formula is the following:

$$\sigma_{en} = \left(\frac{\pi}{8K_B m_e}\right)^{0.5} \frac{e^2 Z_{eff}}{f\cdot T^{0.5} Q_{en}} \quad (3.65)$$

The f is the Saha based blending neutral-ion factor that was previously discussed at equation 3.62. The Q_{en} is the electron-neutral momentum transfer cross section calculated in the Born approximation. It is approximately [32,35,37,38]:

$$Q_{en} = \frac{\pi^3\left(\frac{a_D}{2r_o a_B}\right)^2}{{A_k}^2 + 3B_k k r_o + 7.5C_k(kr_o)^2 - 3.4D_k(kr_o)^3 + 10.6668E_k(kr_o)^4} \quad (3.66)$$

All the constants and physical variables that are presented at this formula are depicted at the following equations:

$$k_D = \frac{1}{\lambda_D} \text{ (inverse screaning length)}$$

$$k = \frac{1}{\hbar}\left(\frac{8K_B m_e}{\pi}T\right)^{0.5} \text{ (electron wave number)}$$

$$a_B = 5.291\cdot 10^{-9}\text{cm (Bohr radius)}$$

$$a_D = (68 \mp 15){a_B}^3 \text{ (dipole polarizability)} \quad (3.67)$$

$$r_o = \left(\frac{a_D a_B}{2{Z_{eff}}^{1/3}}T\right)^{0.25} \text{ (cut off radius)}$$

$$A_k = 1 + 2k_D r_o + \frac{7}{\pi^2}(k_D r_o)^2 + \frac{\pi}{7}(k_D r_o)^3$$

$$B_k = e^{-18k_D r_o}$$

$$C_k = \frac{1 + 22k_D r_o - 11.3(k_D r_o)^2 + 33(k_D r_o)^4}{1 + 6k_D r_o + 4.7(k_D r_o)^2 + 2(k_D r_o)^4}$$

$$D_k = \frac{1 + 28k_D r_o + 13.8(k_D r_o)^2 + 3.2(k_D r_o)^3}{1 + 8k_D r_o + 10(k_D r_o)^2 + (k_D r_o)^3}$$

$$E_k = 1 + 0.1k_D r_o + 0.3665(k_D r_o)^2$$

The a_D dipole polarizability is the one that is proposed from the 2018 Table of static dipole polarizabilities of the neutral elements in the periodic table [43]. There is a value uncertainty range, so we chose the $68a_B{}^3$ value for plasma tungsten that is the intermediate one.

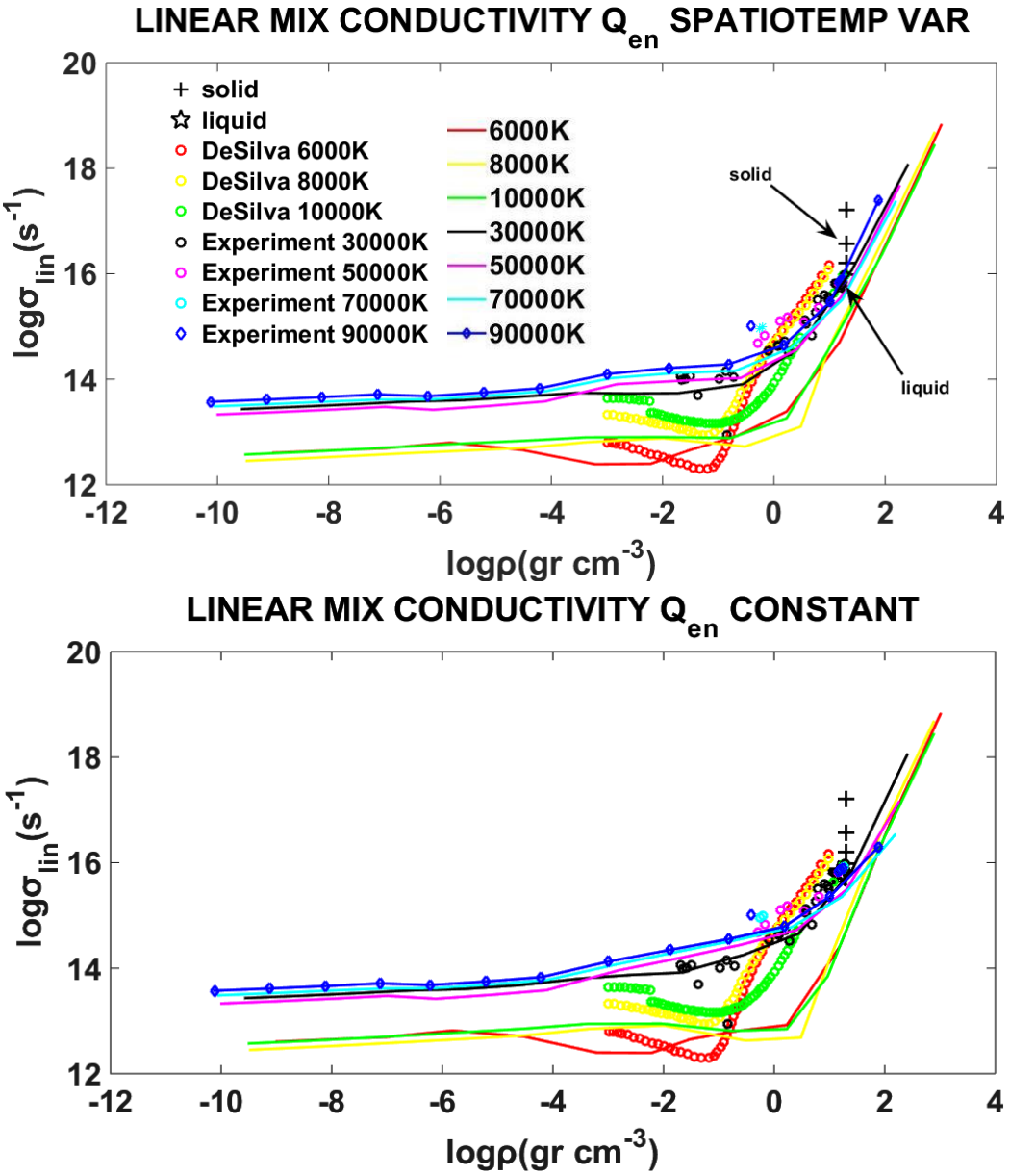

Figure 3.19 i. Top graph: *Plots of temperature range, 6000K up to 90000K. The cross and star black points are the solid and liquid of figure 3.18. The circle points are (mostly) Da Silva's extended*

semiempirical and experimental data of the polynomial fitting. The experimental data of the other works up to 90000K are the same as in figure 3.18. The Q_{en} electron-neutral momentum transfer is the spatiotemporal formula of equation 3.66. The density and electron density have the same value range as the ones in figure 3.18.

ii. Bottom graph: *The same plots are depicted here but with Q_{en} having a mean constant value of 10^{-13} cm^2 for the 6000K, 8000K and 10000K and $10^{-15}cm^2$ for the rest curves.*

Here we present two different conductivity group graphs. The first has a varying Q_{en} cross-section and the second a mean constant value equal to one. Even though at reference [32] the constant value is not considered a valid approximation with this modified approach, we see that both group graphs have similar behavior and a very good agreement according to the experimental data. $10^{-13}cm^2$ up to $10^{-15}cm^2$ are good mean values for this task for plasma tungsten. In addition to that, the fixed cross section value has been tested succesfully by Mofreh R. Zaghloul et al for copper plasma at the WDM regime [36].

The benefit of using the quantum Coulomb logarithm of the previous discussion is the anticipated almost linear rising at the WDM region that we achieved with the piece wise function of 3.4.1.1. We also see a smoother transition to the independent temperature behavior at the dense and overdense regime especially at the first graph! The values at the dilute plasma area are of the same order to the ones of the previous estimations. The discrepancies we see at the 6000K,8000K and 10000K with the experimental data are smaller at the first graph, while for higher temperatures the fittings are experimentally closer at the second graph. We must not forget though that the experimental points of these temperatures are mostly of DeSilva's work and are theoretically fitted from the work of Ebeling et al [25]. These points are, at major percent, the ones we used here and in 3.4.1.1. The experimental points of 6000K, 8000K and 10000K have a much larger area dispersion and a lot of them coincide with the theoretical data points of these curves. Our curves have almost the same fitting behavior with the ones proposed of Ebeling et al at the WDM region [25]! The work by D. Sheftman, Y.E.Krasik [29] and A.D. Rakhel et al [30], has similar modifications and also similarities with this presentation at specific temperatures at the WDM region!

3.4.1.4 Anomalous Braginskii-like, Saha-based, magnetically determined conductivity

A final presentation of a very good choice for implementation at ~~an~~ a MHD code is a Braginskii like magnetic dependent conductivity formula that takes a mixture of electrons, ions and neutrals plasma. The analytic expression for the electron collision frequency had been provided in Braginskii's original work. Braginskii's result for resistivity is identical to Spitzer's for high magnetized plasmas (χ_i>>1). The same expressions can be used in the absence of magnetic field **B**, assuming that the parallel transport coefficients are the same with and without **B.** This is due to the strong effect of the magnetic field to the transverse transport coefficients when χ_i>>1, leaving the longitudinal ones unaffected [44].

Having this in mind, a more thorough examination of the effect of the magnetic field at the transverse resistivity coefficient is in order. We also take a mixture of ion, electron and neutral plasma to evaluate the collision frequency and the inverse relevant time. It is a similar technique with the previous one of the conductivity linear mix. The mixture instead in conductivities is applied to the

collision frequencies taking into consideration the anomalous collision term with the low hybrid frequency, as will be presented immediately after [45]. Moreover, the mixture of plasma particles makes the nonlinear Saha equation the appropriate choice to evaluate the ratio of neutrals and ions as the one of equation 3.62 including the correction fittings of the ionization potentials. The Coulomb logarithm is the one of the previous estimation by the Born approximation of equation 3.64. Thus, the electron collision time has two terms, one of the classical electron-ion collision and one electron-neutral using neutrals density N_n originating from the Saha equation. The electron-neutral cross-section Q_{en} we used is a fixed value suitable for the plasma tungsten**.** The E_{ion} is the first ionization energy for plasma tungsten and is 6.7 eV, the same as in [19], instead of using 7.68eV of [20].

The resistivity has an anomalous component and is a Braginskii-like [45-48] where,

$$\nu = \nu_{ei} + \nu_{an} \text{ (collision frequency with anomalous term)}$$

$$\text{where } \nu_{an} = \frac{1}{2}\left(\frac{\pi}{2}\right)^{0.5} \omega_{LH} \frac{u_D{}^2}{c_s{}^2} \text{ (anomalous collision frequency)}$$

$$\text{and } \omega_{LH} = \frac{\omega_{pi}}{\left(1 + \frac{\omega_{pe}{}^2}{\omega_{ce}{}^2}\right)^{0.5}} \text{ (low hybrid frequency)}$$

$$\text{and } \omega_{pi} = Z_{eff} e \left(\frac{4\pi N_i}{m_i}\right)^{0.5},\ \omega_{pe} = e \left(\frac{4\pi N_e}{m_e}\right)^{0.5} \text{ (plasma frequency)} \qquad (3.68)$$

$$\text{and } u_D = \frac{J(\text{current density})}{N_e e} \text{(diamagnetic drift velocity)}$$

$$\text{and } c_s = \left(\frac{1.5\,(N_e + N_i + N_n) K_B T_e(K)}{(N_i + N_n) m_i}\right)^{0.5} \text{ (sound speed)}$$

Now the total collision time is defined as:

$$(\tau_e)_{total} = \frac{1}{\frac{1}{\tau_e} + 3 \cdot Q_{en} \cdot N_n \cdot \left(\frac{3 K_B T_e(K)}{m_e}\right)^{0.5}} \text{ (total collision time)}$$

$$\text{where } Q_{en} = 5 \cdot 10^{-15} \text{cm}^2 \text{ (cross-section)}$$

$$\text{and } \tau_{ei} = \frac{1}{\nu_{ei}} = \frac{3 \cdot m_e{}^{0.5} (K_B T_e(K))^{1.5}}{4(2\pi)^{0.5} N_e \ln\Lambda \cdot Z_{eff} \cdot e^4}$$

$$\text{and } \tau_e = \frac{1}{\nu} = \frac{1}{\nu_{ei} + \nu_{an}}$$

$$\text{and } \chi_e = \omega_{ce} \cdot (\tau_e)_{total} \text{ and } \omega_{ce} = \frac{eB}{c \cdot m_e} \text{ (eletron cyclotron frequency)}$$

$$\text{The resistivity is: } n = \frac{1}{\sigma} = \frac{m_e}{N_e e^2 \cdot (\tau_e)_{total}} \left(1 - \frac{3.1\chi_e + 1.89}{{\chi_e}^2 + 6.2\chi_e + 2.8}\right)(s)$$

,$\mathbf{J}$ is the plasma current density, $\mathbf{u_D}$ the diamagnetic drift velocity and along with the low hybrid frequency ω_{LH} formulate the anomalous collision frequency. Due to the presence of the magnetic field the plasma frequencies of electrons and ions and the electron cyclotron frequency modulate the anomalous/low hybrid frequency and the resistivity term respectively. The Braginskii-like resistivity/conductivity uses the total electron collision time and the dimensionless factor χ_e that is the standard parameter to all the Braginskii magnetized conductivity, thermal conductivity and viscosity coefficient formulas. For the last two, a similar analysis will follow at the relevant subsections.

If the magnetic field is negligible and Z_{eff}<1, we can ignore the anomalous collision frequency term. The absence and presence of this term is something that we will discuss right away. We will compare the results with the ones of the unmagnetized, Saha based linear mixture conductivity of the previous subsection.

In a pinch plasma configuration the anomalous resistivity causes the formation of a low-density, highly resistive, coronal plasma, while the lower hybrid microinstabilities caused by the anomalous term make radiative collapse more difficult to be achieved with radial pressure balance affected too [45].

If the radial pressure balance is preserved while the current rises, high density can be maintained while the plasma is Ohmically heated. This could be very important for fusion temperatures to be achieved. Thus the implementation of this form of resistivity could provide insights for the plasma behavior concerning, the radial pressure, microinstabilities formation and the heating mechanism of the plasma [46,47]. The inclusion of an anomalous component to the electron-ion collision frequency in the evaluation of electrical resistivity and electron thermal conductivity, serves to limit the electron drift velocity to less than the ion sound speed, providing a physically justifiable scaling from finite plasma resistivity to virtually infinite vacuum resistivity and preventing a large discontinuity in transport coefficients at the vacuum/plasma boundary [47]. It has been successfully tested and implemented in the MHD code GORGON [48]. The difference and the crucial part here is the usage of the specific expression of the Coulomb logarithm and the Saha equation that gives a very good matching with the experimental and semiempirical data at the WDM region for the low temperature regime. The first estimation is depicted at the graph 3.20 with three different graphs of one no magnetized and two magnetized cases. The one that is mainly valid for the plasma tungsten case of our concern is the middle one of 10^5 Gauss due to the magnetic field range of our X-pinch plasmas experiments of ~10^4-~10^5 Gauss magnetic fields at the peak of plasma current. Most of the experimental data are overlapped and are depicted at the WDM region from ~10^{-2}gr/cm^3 to 10gr/cm^3 having the same value range as in figures 3.18 and 3.19 (~10^{13} s^{-1} to 10^{16} s^{-1}). The same narrow range of values holds for most isothermal theoretical curves at the same density area.

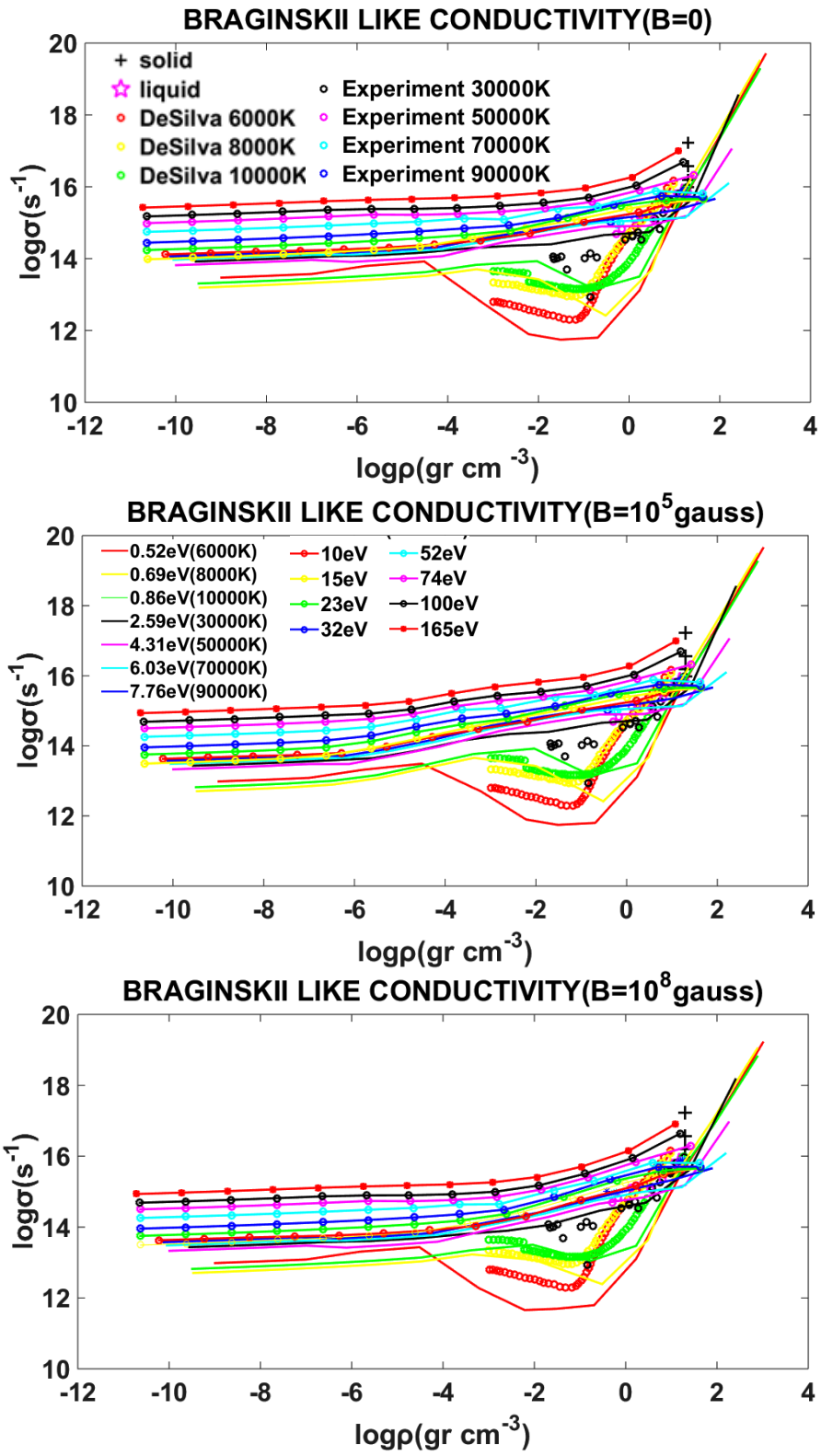

Figure 3.20 i. Top graph: *Plots of temperature range, 0.52eV up to 165eV for the unmagnetized case (**B=0**). The cross and star black and magenta points are the solid and liquid of figure 3.18/3.19. The circle points are (mostly) Da Silva's extended semiempirical and experimental data of the polynomial fitting. The experimental data of the other works up to 90000K are the same of figure 3.18/3.19. The density and electron density have the same value range as the ones in figure 3.18.*

ii. Middle and bottom graph: *The same plots are shown for the B=10^5 gauss and B=10^8 gauss respectively. The legend columns are common for all graphs.*

Usefull observations for the above graphs are:

1. All three cases have a similar behavior in comparison to the linear resistivity mixture case of the previous subsection.
2. The agreement with the experimental and semiempirical data till the 90000K is very good. Nevertheless, the no magnetized and mid magnetized case present closer estimations to the WDM region at temperatures of 6000K, 8000K and 10000K compared to the one of the experiment. The high magnetized case presents lower values for these temperatures and has slightly higher differences with the experiment.
3. The high magnetized case presents better estimations for the 30000K curve than the other two while all three are practically the same for the 50000K, 70000K and 90000K at their predictions.
4. The no and mid magnetized case are very similar to the Saha-based and Spitzer modified case of the previous subsections for the dense and dilute plasma region, while the high magnetized curves introduce slight higher predictions at the dilute plasma regime.
5. The conductivity value range is very narrow for most of the plasma density area and is ~$10^{13}s^{-1}$-~$10^{15}s^{-1}$.
6. Someone could use the spatiotemporal electron-neutral cross-section as the one presented at 3.4.1.2 for a better fitting.

Considering the full expression for the conductivity of the 3.68 equation with the anomalous term implemented. For the current density we use Ampere's law:

$$\frac{c}{4\pi}\nabla \times \mathbf{B} \sim \frac{c}{4\pi}\frac{\mathbf{B}}{l_0} = \mathbf{J} \tag{3.69}$$

The l_0 is the characteristic discretization spatial length of our simulations, approximately 10μm but it could be one order of magnitude smaller or higher (depending on the size of the computational box, the main plasma size configuration and the detailed analysis we want). Thus, the important term of the diamagnetic drift velocity is calculated along with the other terms of equation 3.68. The magnetic field magnitude range is from 10^0 to 10^8 Gauss shown at the 3D graph in figure 3.21. The conductivity isotherms varies from 0.52eV to 165eV. We also present the 2D graphs for B=1Gauss, 10^5Gauss and 10^8 Gauss in figure 3.22 just to estimate the differences with the conductivity without the anomalous collision frequency term of figure 3.20.

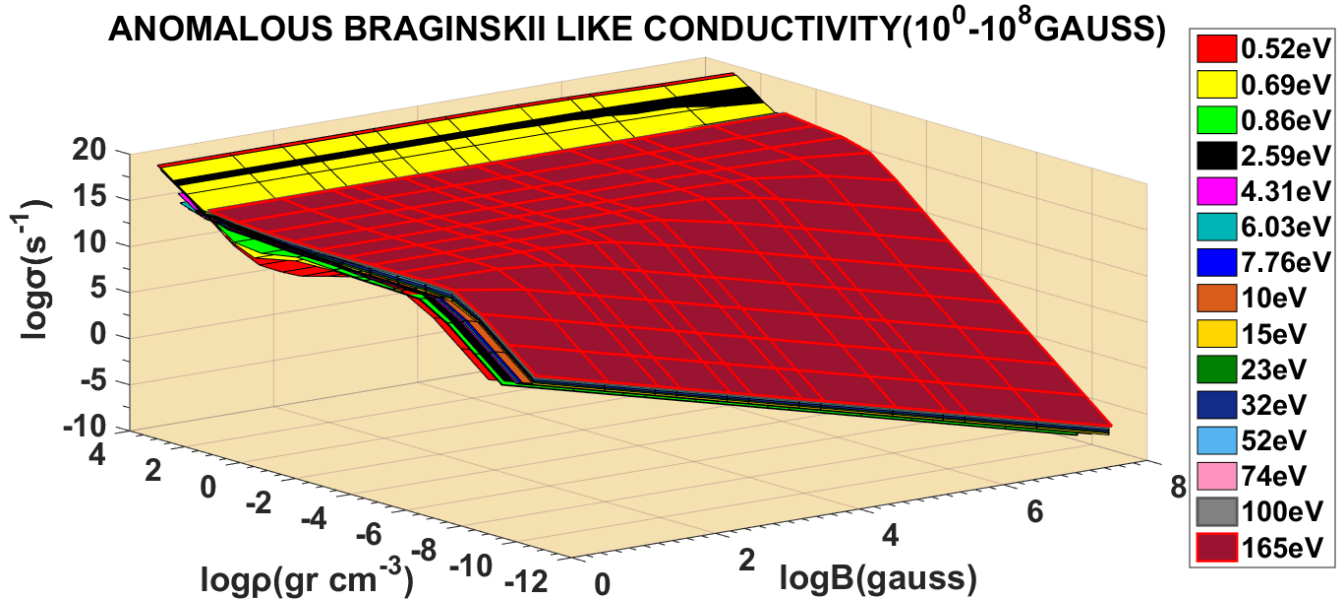

Figure 3.21: *The 3D isotherm surfaces as a function of magnetic induction and mass density. The magnetic field range is 10^0-10^8 Gauss and the mass density is ~10^{-11}gr/cm^3-~10^3gr/cm^3. The isotherms are from 0.52eV to 165eV.*

The 3D graph presents very low conductivities at the dilute plasma region at every magnetic field magnitude. For the very low case of ~1 Gauss, the mass density dependence is very near to the one of the unmagnetized case and goes like this up to ~10^{-6}gr/cm^3. Then the conductivity has a linear-like reducing till the value of ~$10^{6.5}$s^{-1}. The conductivity of the metallic tungsten is ~10^{17}s^{-1} at the 300K thus the conductivity is of this order or one order of magnitude lower at the dense matter region, but it can go till ten orders of magnitude lower at the dilute plasma region. This behaviour of lowering the conductivity at the dilute region is enhanced for higher magnetic fields. The ~10^4-~10^5 gauss magnetic fields have this lowering value behavior much sooner at the ~10^{-3}gr/cm^3, while at the very strong magnetic field region we see an almost continuous lowering of the conductivity reaching ~10^{-4}s^{-1} and ~10^{-10}s^{-1} at the dilute plasma region respectively (twenty seven orders of magnitude lower than the solid tungsten's)! It is, practically, a zero value conductivity or an almost infinite computational resistivity.

We select three different magnitudes of the magnetic field B=1 gauss (low), B=10^5 gauss (mid) and B=10^8 gauss (high) and we present the 2D graphs of figure 3.22 to estimate clearer the value range of conductivity for every density and temperature. We observe the aforementioned behaviour for the conductivity, presenting low values at the dilute plasma region, while the high magnetic fields present lower conductivity values at the same densities than the low magnetic field ones. The agreement with the experimental data is very good at the low magnetized case. The mid magnetized case is reducing the conductivity value very soon at the 6000K,8000K and 10000K isotherms having a discrepancy there. This is not the case for higher temperatures, where the experimental data are better fitted to the theoretical curves. The high magnetized case introduces very low conductivities for the low temperatures compared to the experiment at WDM region, but is still valid for higher temperatures, where the experiment is within the theoretical value range.

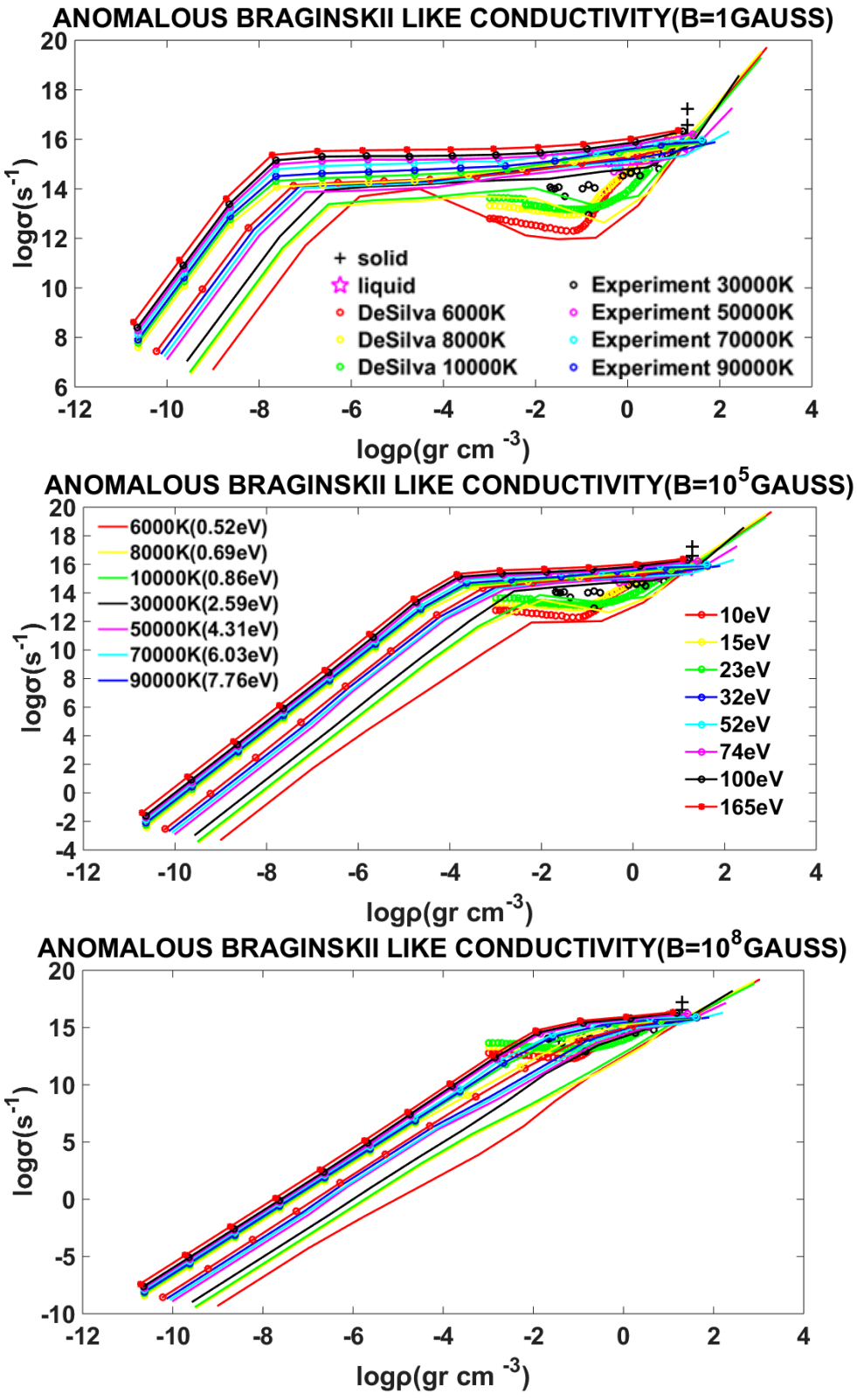

Figure 3.22: *The 3D isotherm surfaces as a function of mass density. The magnetic field is 10^0 gauss at the top graph, 10^5 gauss at the middle and 10^8 gauss at the bottom. The mass density is ~10^{-11}gr/cm^3-~10^3gr/cm^3 and the isotherms of 0.52eV-165eV hold for all three graphs. The experimental and semiempirical data are the same as in figures 3.18, 3.19 and 3.20.*

As we mentioned before, the inclusion of an anomalous component to the electron-ion collision frequency provides a physically justifiable scaling from finite plasma resistivity to virtually infinite vacuum resistivity, thus preventing a large discontinuity in transport coefficients at the vacuum/plasma boundary. This is a valid approximation also to the dilute plasma region when we have one component plasma in our computational box, having very high resistivities there, thus better control of the diffusion of the physical variables retaining an isothermal and high resistivity vacuum (i.e. the current density and the magnetic field of the vacuum) [46-47].

Conclusively, the anomalous term can be neglected or implemented at the conductivity formula depending on the needs of the simulation run and the effects to the corona thinner density areas expansion and the instability formation [46-48]!

3.4.2 Thermal Conductivity for liquid-plasma tungsten

The thermal conductivity is implemented at the MHD energy equation as a dissipative term. It is a divergence flux term as shown in equation 3.11. In the MHD case, thermal conductivity is highly anisotropic being suppressed in the direction transverse to the magnetic field. The thermal conductivity has three components in the MHD approach. The $k_{||}$ and $k_{\perp}$ are the thermal conduction coefficients along and across the magnetic field respectively. The classical hydrodynamic case has only the parallel contribution with the known expression $\mathbf{F}_{\text{class}} = k_{||}\boldsymbol{\nabla}T$, denoting it [2]. Also often the $k_{||}$ >> $k_{\perp}$ when the particles essentially free-stream with very long collisional mean free paths parallel to the magnetic field, but not perpendicular to it [49]. The k_x is the component coefficient of the thermal conduction flux transverse to the plain of $\mathbf{B}$ and $\boldsymbol{\nabla}T$. This term is oftenly ignored and will be evaluated separately at the Results Chapter 5. All three components of thermal conductivity are implemented in equation 3.13 of PART I.

The thermal transport phenomena are significant for the plasma energy exchange, especially when the radiation transport is ignored. Numerous studies have shown that heat transfer can affect the growth rates of instabilities (i.e. the Rayleigh Taylor instability) and the self generated magnetic fields. This is due to reduction of temperature and density gradients due to conduction [50,51].

3.4.2.1 Thermal conduction parallel coefficient for liquid-plasma tungsten through a piece-wise function

In condensed matter, heat transfer is mediated by the collisional transport of valence electrons and lattice waves. In metals, the electron contribution dominates over the phonon contribution. Due to the fact that the valence electrons are responsible for both charge and heat transfer in metals, a proportionality between the thermal conductivity and the electrical conductivity can be expected. This is expressed by the so-called Wiedemann–Franz law that is an appropriate fit for WDM matter and fusion applications.

A first approach is a piece-wise presentation for the $k_{||}$ that is evaluated from:

i. The Seydel–Fucke fit [26] in the temperature range for liquid tungsten 3695K<T_e<6000K,

$$k_{||} = 66.62 \cdot 10^5 + 2.086 \cdot 10^3 (T_e - T_m) - 0.376 (T_e - T_m)^2 \ (\text{c.g.s}) \tag{3.70}$$

where $T_m(K)$ is the melting temperature (3695 K).
ii. The Wiedemann-Franz law for T_e >6000K that has the following expression:

$$k_{||} = \frac{2.45 \cdot 10^{-12} T_e(K)}{9} \sigma \quad (c.g.s.) \tag{3.71}$$

where T_e in K and σ is the electrical conductivity (in 1/s), and is given from the modified version of 3.52 that is plotted in figure 3.16 [28]. A graphic presentation of the above formula and a comparison with experimental /semiempirical results is:

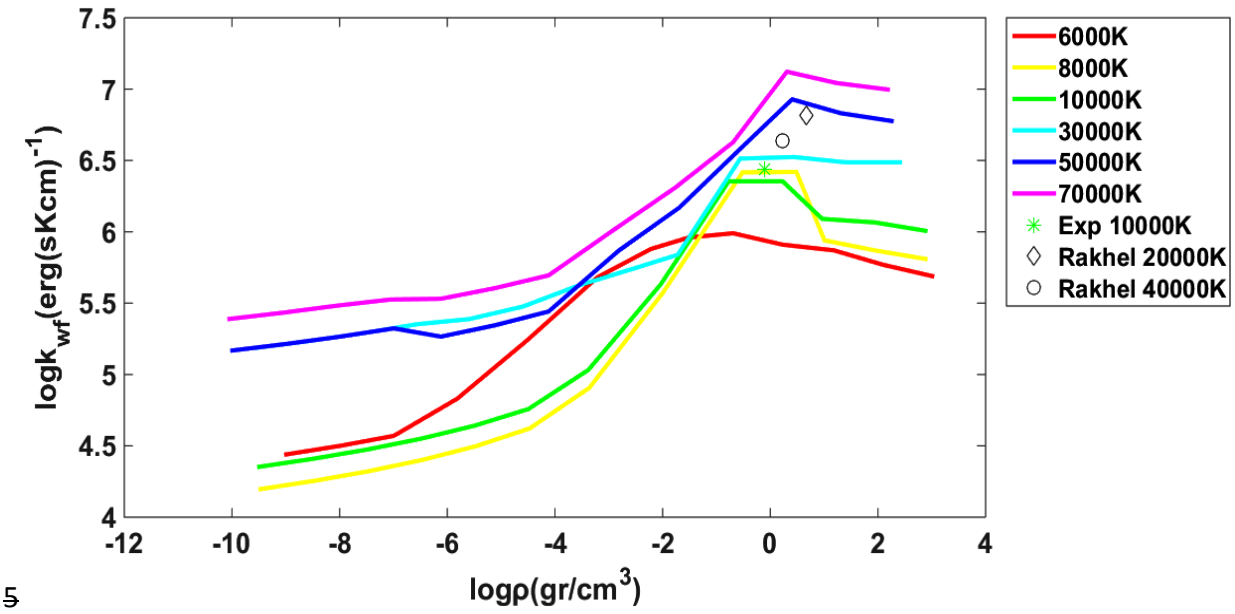

Figure 3.23: *Parallel component of thermal conductivity $k_{//}$ estimated by Wiedermann-Franz law substituting σ from the modified Spitzer (dashed lines of 3.16 plots). The star point, depicts the result obtained in the experimental study by Satoshi Sugimoto et al [52]. The circle and diamond point plots are semi-empirical estimates obtained using the Wiedermann-Franz law with Rakhel's results [28].*

The prediction of the parallel component of thermal conductivity from the Wiedermann-Franz law with the modified Spitzer (of 3.16 figure), presents similar results to the experimental data of the WDM region at 10000K (green line and star point). For higher temperatures in the same density range, the predictions are similar. As a result, with this modification, the Wiedermann-Franz law is a good approximation for thermal conductivity in a big temperature range for the dense matter region (comparison of the experimental/semiempirical points and the law curves at figure 3.23).

Another observation is that if we use Wiedermann-Franz law with the modified Spitzer formula for electrical conductivity, for temperatures smaller than 10000K and densities smaller than 0.1gr/cm^3, one or two order of magnitude lower values than the ones of the dense matter are evaluated for the thermal conductivity. This behaviour is smoother for 30000K and more abrupt at 50000K and 70000K. It has to be tested and evaluated from the experiment. An observation also by Satoshi Sugimoto et all gives an experimental independent temperature behaviour at $0.04\rho_{solid}$~0.8gr/cm^3 for temperatures 8000K to 13000K [52]. This is the case here for the yellow, green and blue curves for the density range

of 1gr/cm^3 to 0.01gr/cm^3. For smaller densities the law has to be compared with another tested formula (i.e. Braginskii's) and experimental data at every temperature above liquid phase.

3.4.2.2 Thermal conduction coefficients for plasma tungsten through modified Spitzer's formulas

A simple formula for the parallel thermal conduction coefficient, is a modified Spitzer that is commonly used in astrophysical simulations:

$$k_{||} = 5.6 \cdot 10^{-7} T_e(K)^{2.5} \quad (c.g.s.) \tag{3.72}$$

The $k_{\perp}$ coefficient is evaluated from:

$$k_{\perp} = \frac{3.3 \cdot 10^{-16} {N_e}^2}{T_e(K)^{0.5} B^2 {Z_{eff}}^2} \ (c.g.s.) \tag{3.73}$$

where B is the magnitude of the magnetic field and N_e the electron density. This is also a modified Spitzer formula [53,54]. Both coefficients are in units of erg·(s·K·cm)$^{-1}$.

Till now we have not separated the thermal contribution of the electrons from the ions. This job is presented with the next approach by Braginskii's formulas.

3.4.2.3 Thermal conduction coefficients for liquid-plasma tungsten through Braginskii's formulas

A third and more complete evaluation for the thermal conductivity components comes from the formulas of Braginskii's model [14,44,50,51]. As presented before, the electron component is dominant at low temperatures and dense matter. If someone has to choose for one thermal conductivity coefficient for the whole temperature range, this has to be the electron one for the parallel component and the ion one for the transverse (it will be explained through this analysis). The formulas 3.70-3.73 were chosen having in mind the former observation.

The parallel component is evaluated from:

$$k_{||}{}^{e} = \frac{\gamma_0 \cdot N_e {K_B}^2 T_e \tau_e}{m_e} = 4.61 \cdot 10^{-5} \frac{T_e(K)^{2.5}}{\ln\Lambda \cdot Z_{eff}} (c.g.s.), \qquad \text{if } \gamma_0 = 8 \tag{3.74}$$

and the transverse:

$$k_{\perp}{}^{e} = \frac{N_e {K_B}^2 T_e \tau_e}{m_e} \cdot \left(\frac{{\gamma_1}' {\chi_e}^2 + {\gamma_0}'}{\Delta_e}\right) \tag{3.75}$$

$$\text{where } \tau_e = \frac{3 \cdot {m_e}^{0.5} (K_B T_e)^{1.5}}{4(2\pi)^{0.5} N_i \ln\Lambda \cdot {Z_{eff}}^2 e^4}, \qquad \chi_e = \omega_{ce}\tau_e \text{ and } \omega_{ce} = \frac{eB}{m_e c} \tag{3.76}$$

For the ions the thermal coefficients are:

$$k_{||}{}^{i} = \frac{3.9 \cdot N_i K_B{}^2 T_i \tau_i}{m_i} \tag{3.77}$$

and the transverse:

$$k_{\perp}{}^{i} = \frac{N_i K_B{}^2 T_i \tau_i}{m_i} \cdot \left(\frac{2\chi_i{}^2 + 2.645}{\Delta_i}\right) \tag{3.78}$$

$$\text{where } \tau_i = \frac{3 \cdot m_i{}^{0.5} (K_B T_i)^{1.5}}{4\pi^{0.5} N_i \ln\Lambda \cdot Z_{eff}{}^4 e^4}, \qquad \chi_i = \omega_{ci}\tau_i \text{ and } \omega_{ci} = \frac{Z_{eff} eB}{m_i c}$$
$$\text{with } \Delta_i = \chi_i{}^4 + 2.7\chi_i{}^2 + 0.677 \text{ and } \Delta_e = \chi_e{}^4 + \delta_1 \chi_e{}^2 + \delta_0 \tag{3.79}$$

In the limit of large fields ($\chi_i >> 1$ & $\chi_e >> 1$) the equations 3.75 and 3.78 have a simpler form (the second and third term at Δ_e and Δ_i are ignored) :

$$k_{\perp}{}^{e} = \frac{\gamma_1' N_e K_B{}^2 T_e \tau_e}{m_e \chi_e{}^2} = \frac{\gamma_1' N_e K_B{}^2 T_e}{m_e \omega_{ce}{}^2 \tau_e}$$

and (3.80)

$$k_{\perp}{}^{i} = \frac{2.0 \cdot N_i K_B{}^2 T_i \tau_i}{m_i \chi_i{}^2} = \frac{2.0 \cdot 10^{-16} N_e{}^2 \ln\Lambda}{T_i(K)^{0.5} B^2} \text{ (c.g.s.)}$$

All units are in c.g.s and T_e , T_i in K. The values of γ_0, δ_1, δ_0, γ_1' and γ_0' are defined in [44. For the simulation runs in Chapter 5 we use mean values of these constants. If we set $Z_{eff}=1$, $\gamma_0=3.2$, $\gamma_1'=4.7$ we get the same formulas of reference [14] (multiplied by the Boltzmann constant).

Therefore a convenient choice for a simulation run of a heavy plasma ion material with high Z_{eff} is to use the system of 3.74-3.79 displacing the 3.75 and 3.78 with 3.80 for a simpler computational implementation (but someone could use the whole package without replacing).
Comparing the parallel coefficients of electron and ion we set $T_e=T_i$, $N_e=Z_{eff} \cdot N_i$ and we have:

$$\frac{k_{||}{}^{e}}{k_{||}{}^{i}} = \frac{\gamma_0 \cdot Z_{eff}{}^3}{3.9} \left(\frac{m_i}{m_e}\right)^{0.5} \tag{3.81}$$

We know that γ_0 values are from ≈3 to ≈13 and for $Z_{eff}=1$ to ∞ [31]. Z_{eff} is of the order of 10 for a few eV temperatures (figure 3.3) and m_i=183.84 amu≈$3.35 \cdot 10^5 m_e$, for plasma tungsten. This is an obvious dominance of the electron contribution to the parallel thermal coefficient (thousands to millions times higher as long as Z_{eff} is bigger than unity).

A similar comparison, finding the ratio for the transverse coefficients of 3.80, we get:

$$\frac{k_{\perp}{}^{i}}{k_{\perp}{}^{e}} = \frac{2^{0.5}}{\gamma_1' \cdot Z_{eff}} \left(\frac{m_i}{m_e}\right)^{0.5} \tag{3.82}$$

Although the result is not as high as that of 3.81 (as long as Z_{eff} is bigger than unity also), the transverse ion coefficient is much higher than the electron (substituting $\gamma_1' \approx 4$ and Z_{eff} of the order of 10).

The Braginskii's model and the Wiedemann-Franz law with the modified Spitzer are used to all density regions from 6000K to 70000K (the same value range of figure 3.16). The Braginskii's parallel electron component is shown in figure 3.24 considering the constant γ_0 as a function of T_e and Z_{eff} [44]. Their value correlation is depicted at Table 3.3.

T(K)	Z_{eff}	γ_0
6000	<1	3
8000	~ 1	3
10000	~ 1	3
30000	$[1.1 , 1.6]$	3.5
50000	$[1.2 , 4.0]$	6.0
70000	$[1.8 , 4.0]$	6.0

Table 3.3: *Values of γ_0 that are used for every temperature that is depicted at figure 3.24. Z_{eff} is estimated through the FLYCHK tabular data while γ_0 estimation correlates with Z_{eff}. Thus, a mean qualitative approximation of the original values of Braginskii's work is considered [44].*

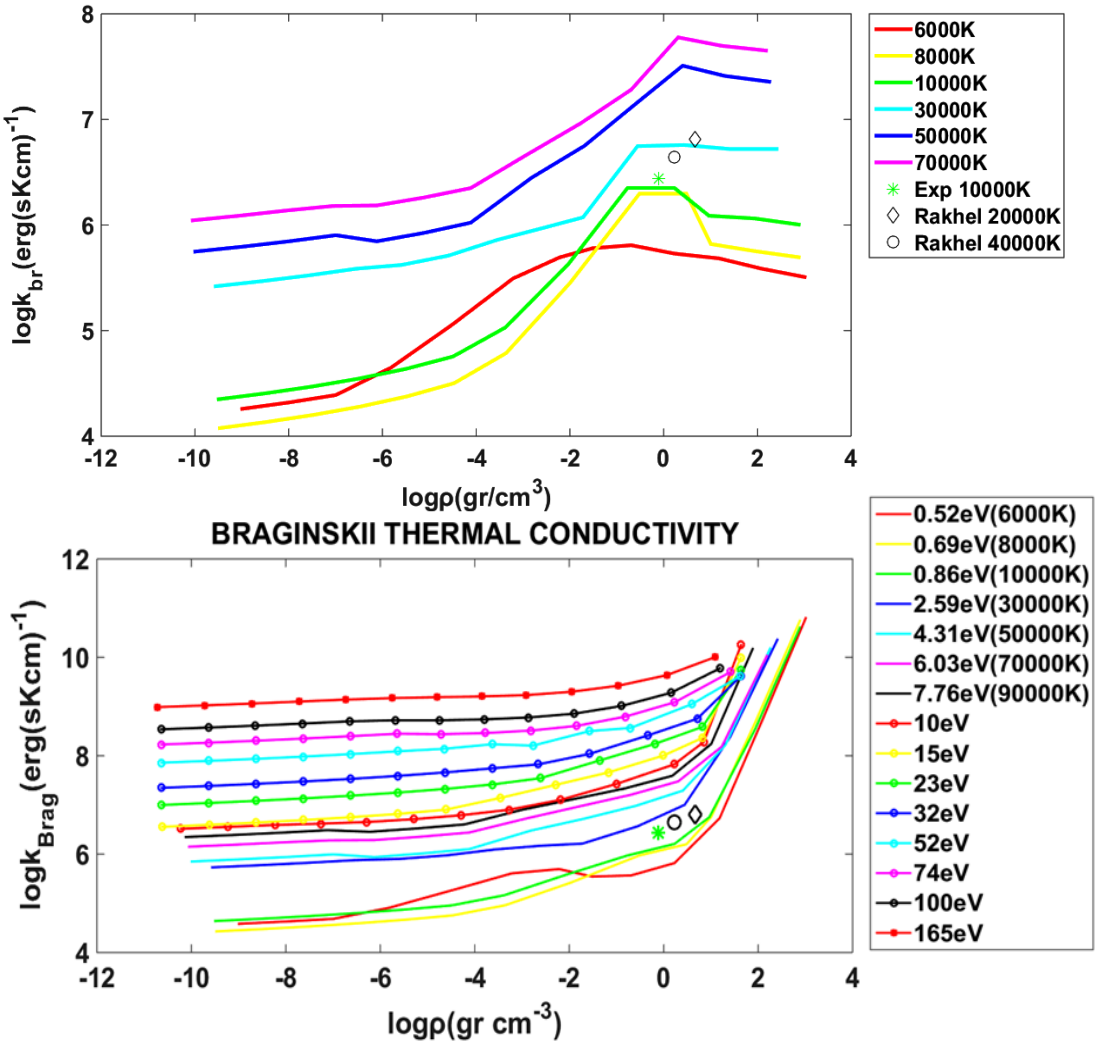

Figure 3.24 Top graph: *Parallel component of thermal conductivity $k_{//}$ estimated by* Braginskii's model. *The result obtained in the experimental study by Satoshi Sugimoto et al is depicted as a star point[52]. The circle and diamond point plots are semi-empirical estimates obtained using the Wiedermann-Franz law with Rakhel's results [28]. The temperature range is 0.52eV-6.03eV.*
Bottom graph: *The same component is depicted using the same model, experimental and semiempirical data but for $ln\Lambda$ we use the effective quantum Coulomb logarithm as calculated from the Born approximation and Debye potential of 3.64. The temperature range is 0.52eV-165eV.*

Comparison of figures 3.23 and 3.24 shows similarities but considerable differences also.

i. The WDM region has similar results for the two approximations but closer to the experiment and semiempirical data is the Wiedemann-Franz's law results.
ii. The experimental 10000K star point is very near to the same temperature curve for both cases, but Braginskii's model does not introduce the independent temperature behaviour at 0.8gr/cm^3 that is observed at the experiment [52].
iii. Wiedermann-Franz's law curve of 30000K underestimates the semiempirical data of Rakhel but Braginskii presents a better fitting.
iv. Braginskii's 50000K is one order of magnitude higher than the semiempirical data by Rakhel, in contradiction to the proximity of the Wiedemann-Franz's law results at the WDM.
v. On the other hand Braginskii's is a global fit for all plasma temperatures having formulas for all four components of the thermal coefficients that could be implemented in the code.
vi. The two other cross components k_x are not considered in this Chapter but are included at the conservative equations MHD system as presented in equation 3.13 and are described and used at the fourth section of the results Chapter [14,44,50]).
vii. The 6000K-30000K curves have values of the same order at both approximations, while the 50000K and 70000K differ from one order of magnitude at all plasma densities.
viii. Temperatures higher than 70000K should be better implemented with the Braginskii formula due to the repeatedly simulation testing i.e. with the GORGON MHD code [48,51].
ix. The quantum Coulomb logarithm is used to the second of figure 3.24 for a better linear fitting at the dense matter region as the one we used at the Saha linear mixture technique at sub-section 3.4.1.3. It is a better fitting than the classic case of the Coulomb logarithm that we used previously and also introduces the anticipated temperature independence behavior at the WDM.
x. Temperatures of 10eV and more have the same Spitzer-like behavior of figure 3.18 and are depicted here at the second graph of 3.24.

A piece-wise function could be used in the simulations combining these approximations. Furthermore, more experimental/semiempirical and theoretical data could help to have better conclusions for the best fitting.

Some useful observations for the three approximations are:

i. Caution with the Boltzmann constant that is absent at the original Braginskii's formulas [44,50] while it is considered in [14]. But the coefficients in the latter are in cm^{-1}s^{-1}, while the K_B is implemented in the spatial derivatives of temperature at the MHD equations. Here the

presented formulas have the same c.g.s dimensions as the ones of figures 3.23/3.24 and K_B is implemented at them having this way the correct units in equation 3.13.

ii. The most important thermal component at the hydrodynamic and WDM regime is the parallel thermal coefficient.

iii. For high magnetic fields the transverse coefficients are smaller than the parallel.

iv. The electron contribution is dominant at the parallel and the ion contribution at the transverse component coefficient especially in high atomic number and low ionized plasmas (small temperatures).

v. The simple form of equations 3.72 and 3.73 lack the presence of the Coulomb logarithm. Nevertheless, they are of the same order compared to the Braginskii's formulas for large fields, for almost every Z_{eff} and $\ln\Lambda$ of our interest range.

3.4.3 Viscosity Tensor components from low to high magnetized one-fluid plasmas- Application to any pinch plasma configuration

The relation between the viscous stress $\boldsymbol{\Pi_{ij}}$ and the deformation tensor $\mathbf{D_{ij}}$ of equation 3.10 is achieved through the ν_s shear viscosity coefficient [55,56]. The presence of the magnetic field in the MHD case leads to significant differences for the momentum transfer along and across the magnetic field. This case complicates the aforementioned relation, "demanding" the presence of five independent viscosity coefficients of proportionality. This holds for ions and electrons. The ion viscosity is always much larger than the electrons, in an one-fluid approximation, so the viscosity of plasma is determined essentially by ions.

The five viscosity coefficients are defined in Braginskii's original work [44]:

$$\begin{aligned} \nu_0 &= 0.96 N_i K_B T_i \tau_i \\ \nu_2 &= N_i K_B T_i \tau_i \left(\frac{1.2\chi_i^2 + 2.23}{\Delta} \right) \\ \nu_4 &= N_i K_B T_i \tau_i \left(\frac{\chi_i^3 + 2.38\chi_i}{\Delta} \right) \end{aligned} \tag{3.83}$$

$$\nu_1 = \nu_2(2\chi_i) \text{ and } \nu_3 = \nu_4(2\chi_i) \text{ and } \Delta = \chi_i^4 + 4.03\chi_i^2 + 2.33$$

where the χ_i and τ_i are the same as the ones of the thermal conductivity's subsection in equation 3.79. All units are expressed in the c.g.s system and T in Kelvin. The same form of ν holds for the electron coefficients, but with different polynomials at the parenthesis [44]. If we choose the high magnetized situation ($\chi_i >> 1$) the viscosity ion coefficients become:

$$\begin{aligned} \nu_0 &= 0.96 N_i K_B T_i \tau_i \\ \nu_2 &= \frac{1.2 N_i K_B T_i \tau_i}{\chi_i^2} \end{aligned} \tag{3.84}$$

$$\nu_4 = \frac{N_i K_B T_i \tau_i}{\chi_i}$$

$$\nu_2 \simeq 3.3\nu_1 \text{ and } \nu_4 = 2\nu_3$$

Now we will define all the relevant tensor implementation and we will clear the notification index form along with the analytical matrix one.

For a Cartesian system [55-56] the deformation tensor D_{ij} holds:

$$\mathbf{D_{ij}} = \begin{bmatrix} \frac{\partial \mathbf{u_x}}{\partial x} & \frac{1}{2}\left(\frac{\partial \mathbf{u_y}}{\partial x} + \frac{\partial \mathbf{u_x}}{\partial y}\right) & \frac{1}{2}\left(\frac{\partial \mathbf{u_z}}{\partial x} + \frac{\partial \mathbf{u_x}}{\partial z}\right) \\ \frac{1}{2}\left(\frac{\partial \mathbf{u_x}}{\partial y} + \frac{\partial \mathbf{u_y}}{\partial x}\right) & \frac{\partial \mathbf{u_y}}{\partial y} & \frac{1}{2}\left(\frac{\partial \mathbf{u_z}}{\partial y} + \frac{\partial \mathbf{u_y}}{\partial z}\right) \\ \frac{1}{2}\left(\frac{\partial \mathbf{u_x}}{\partial z} + \frac{\partial \mathbf{u_z}}{\partial x}\right) & \frac{1}{2}\left(\frac{\partial \mathbf{u_y}}{\partial z} + \frac{\partial \mathbf{u_z}}{\partial y}\right) & \frac{\partial \mathbf{u_z}}{\partial z} \end{bmatrix} \text{ and } i, j = x, y, z \quad (3.85)$$

The $\mathbf{u=(u_x, u_y, u_z)}$, are the three components of plasma velocity at the Cartesian system.

In order to describe the viscosity tensor in a magnetized plasma, it is helpful to redefine the presentation of the viscosity tensor and insert the spatial-rate-of-strain tensor [44,57-60] which is :

$$\mathbf{W_{ij}} = \mathbf{2D_{ij}} - \frac{2}{3}(\boldsymbol{\nabla} \cdot \mathbf{u})\delta_{ij} =$$

$$= \begin{bmatrix} \frac{4}{3}\frac{\partial \mathbf{u_x}}{\partial x} - \frac{2}{3}\left(\frac{\partial \mathbf{u_y}}{\partial y} + \frac{\partial \mathbf{u_z}}{\partial z}\right) & \left(\frac{\partial \mathbf{u_y}}{\partial x} + \frac{\partial \mathbf{u_x}}{\partial y}\right) & \left(\frac{\partial \mathbf{u_z}}{\partial x} + \frac{\partial \mathbf{u_x}}{\partial z}\right) \\ \left(\frac{\partial \mathbf{u_x}}{\partial y} + \frac{\partial \mathbf{u_y}}{\partial x}\right) & \frac{4}{3}\frac{\partial \mathbf{u_y}}{\partial y} - \frac{2}{3}\left(\frac{\partial \mathbf{u_x}}{\partial x} + \frac{\partial \mathbf{u_z}}{\partial z}\right) & \left(\frac{\partial \mathbf{u_z}}{\partial y} + \frac{\partial \mathbf{u_y}}{\partial z}\right) \\ \left(\frac{\partial \mathbf{u_x}}{\partial z} + \frac{\partial \mathbf{u_z}}{\partial x}\right) & \left(\frac{\partial \mathbf{u_y}}{\partial z} + \frac{\partial \mathbf{u_z}}{\partial y}\right) & \frac{4}{3}\frac{\partial \mathbf{u_z}}{\partial z} - \frac{2}{3}\left(\frac{\partial \mathbf{u_x}}{\partial x} + \frac{\partial \mathbf{u_y}}{\partial y}\right) \end{bmatrix} \quad (3.86)$$

This definition introduces a more compact form of the viscous stress tensor which is magnetically field dependent:

$$\mathbf{\Pi_{kl}} = \sum_{a=0}^{4} \mathbf{\Pi_{akl}} = \sum_{a=0}^{4} (\pm)\nu_a \mathbf{W_{akl}} = \nu_0 \mathbf{W_{0kl}} + \nu_1 \mathbf{W_{1kl}} + \nu_2 \mathbf{W_{2kl}} - \nu_3 \mathbf{W_{3kl}} - \nu_4 \mathbf{W_{4kl}} \quad (3.87)$$

$$\text{and } k, l = x, y, z$$

The magnetic field dependence is at the $\mathbf{W_{akl}}$ five components tensors which will be presented below. We have also to take into consideration that the signs of the viscosity coefficients are the opposite than those of the literature [44, 55-63]. This is due to the right hand side presentation of the viscous stress tensor $\mathbf{\Pi}$, retaining positive signs at equations 3.8 and 3.9 source terms and keeping the same form of equation 3.1.

Now we will clarify all the tensors, symbols and matrices that we present,

$$\mathbf{i})\ \delta_{ij} = \begin{cases} 1 \text{ if } i = j \\ 0 \text{ if } i \neq j \end{cases} \qquad \textbf{Kronecker's Delta}$$

$$\mathbf{ii})\ \varepsilon_{ijk} = \begin{cases} 1 \text{ if } \{ijk\} = xyz, zxy, yzx \\ -1 \text{ if } \{ijk\} = yxz, zyx, xzy \\ 0 \qquad\qquad \text{otherwise} \end{cases} \qquad \textbf{Levi-Civita Epsilon Symbol}$$

$$\mathbf{iii})\ \mathbf{I} = \begin{bmatrix} 1 & 0 & 0 \\ 0 & 1 & 0 \\ 0 & 0 & 1 \end{bmatrix} \qquad \textbf{Unity Matrix} \tag{3.88}$$

$$\mathbf{iv})\ \mathbf{b} = \frac{\mathbf{B}}{|\mathbf{B}|} = \left(\mathbf{b_x}, \mathbf{b_y}, \mathbf{b_z} \right) \qquad \textbf{magnetic unity vector}$$

$$\mathbf{v})\ \mathbf{I_{\perp}} = \mathbf{I} - \mathbf{bb}\ (\textbf{vector dyadic product}) = \begin{bmatrix} \mathbf{1 - b_x}^2 & \mathbf{-b_x b_y} & \mathbf{-b_x b_z} \\ \mathbf{-b_y b_x} & \mathbf{1 - b_y}^2 & \mathbf{-b_y b_z} \\ \mathbf{-b_z b_x} & \mathbf{-b_z b_x} & \mathbf{1 - b_z}^2 \end{bmatrix}, \textbf{ projector on the perpendicular plane of the magnetic field}$$

$$\mathbf{vi})\ \mathbf{bb}:\nabla\mathbf{u} = \sum_{\mathbf{i=x,y,z}}^{\mathbf{j=x,y,z}} \mathbf{b_i}\, \mathbf{b_j} \frac{\partial \mathbf{u_i}}{\partial j} = \mathbf{b_x}^2 \frac{\partial \mathbf{u_x}}{\partial x} + \mathbf{b_y}^2 \frac{\partial \mathbf{u_y}}{\partial y} + \mathbf{b_z}^2 \frac{\partial \mathbf{u_z}}{\partial z} +$$

$$+\mathbf{b_x b_y}\left(\frac{\partial \mathbf{u_x}}{\partial y} + \frac{\partial \mathbf{u_y}}{\partial x}\right) + \mathbf{b_y b_z}\left(\frac{\partial \mathbf{u_y}}{\partial z} + \frac{\partial \mathbf{u_z}}{\partial y}\right) + \mathbf{b_x b_z}\left(\frac{\partial \mathbf{u_x}}{\partial z} + \frac{\partial \mathbf{u_z}}{\partial x}\right)$$

The first viscosity stress presentation is the symbol index using Kronecker's Delta and Levi-Civita Epsilon at the rate strain tensors. This is the choice in the original Braginskii's work [44,57]:

$$\mathbf{W_{0kl}} = \frac{3}{2}(\mathbf{b_k b_l} - \frac{1}{3}\delta_{kl})(\mathbf{b_i b_j} - \frac{1}{3}\delta_{ij})\mathbf{W_{ij}} \tag{3.89}$$

$$\mathbf{W_{1kl}} = ((\delta_{ki} - \mathbf{b_k b_i})(\delta_{lj} - \mathbf{b_l b_j}) - \frac{1}{2}(\delta_{kl} - \mathbf{b_k b_l})\mathbf{b_i b_j})\mathbf{W_{ij}} \tag{3.90}$$

$$\mathbf{W_{2kl}} = ((\delta_{ki} - \mathbf{b_k b_i})\mathbf{b_l b_j} - (\delta_{lj} - \mathbf{b_l b_j})\mathbf{b_k b_i})\mathbf{W_{ij}} \tag{3.91}$$

$$\mathbf{W_{3kl}} = \frac{1}{2}((\delta_{ki} - \mathbf{b_k b_i})\varepsilon_{lmj} + (\delta_{lj} - \mathbf{b_l b_j})\varepsilon_{kmi})\mathbf{b_m W_{ij}} \tag{3.92}$$

$$\mathbf{W_{4kl}} = (\mathbf{b_k b_i}\varepsilon_{lmj} + \mathbf{b_l b_j}\varepsilon_{kmi})\mathbf{b_m W_{ij}} \text{ where m=x, y, z} \tag{3.93}$$

$$\text{and } \mathbf{W_{kl}} = \mathbf{W_{0kl}} + \mathbf{W_{1kl}} + \mathbf{W_{2kl}} \tag{3.94}$$

The Einstein summation convention is employed here.

Another, maybe more compact way to depict the rate of strain tensor, is using the matrix presentation, dyadic and double inner products [61-63]:

$$\mathbf{W_0} = 3\left(\mathbf{bb} - \frac{1}{3}\mathbf{I}\right)\left(\mathbf{bb} - \frac{1}{3}\mathbf{I}\right) : \boldsymbol{\nabla}\mathbf{u} \tag{3.95}$$

$$\mathbf{W_1} = -[\mathbf{I}_\perp \cdot \mathbf{W} \cdot \mathbf{I}_\perp + \frac{1}{2}\mathbf{I}_\perp(\mathbf{b} \cdot \mathbf{W} \cdot \mathbf{b})] \tag{3.96}$$

$$\mathbf{W_2} = -[\mathbf{I}_\perp \cdot \mathbf{W} \cdot \mathbf{bb} + \mathbf{bb} \cdot \mathbf{W} \cdot \mathbf{I}_\perp] \tag{3.97}$$

$$\mathbf{W_3} = \frac{1}{3}[\mathbf{b} \times \mathbf{W} \cdot \mathbf{I}_\perp - \mathbf{I}_\perp \cdot \mathbf{W} \times \mathbf{b}] \tag{3.98}$$

$$\mathbf{W_4} = [\mathbf{b} \times \mathbf{W} \cdot \mathbf{bb} - \mathbf{bb} \cdot \mathbf{W} \times \mathbf{b}] \tag{3.99}$$

The double dot product at 3.95 should be interpreted according to the example of equation 3.88. The total viscosity tensor is again the expression of 3.87 (without the **k, l** indices).

These are two equivalent presentations of the tensor/matrix formulation of the viscous stresses. They are both useful for the implementation to the general magnetized MHD plasma case at any computational attempt. They also introduce the same asymptotic behaviours. Let's see independently each of the five tensor components and understand the effect they have at the plasma behaviour.

The first is $\boldsymbol{\Pi_0}=\nu_0\mathbf{W_0}$, the so called parallel viscosity tensor [61,65]. This is the one that controls the variation of plasma velocity component along the magnetic field lines. As long as the $\mathbf{W_{ii}}$ components survive we have a compression viscous tensor. In this case $\nu_0 \equiv \nu_b$ and is also called the compressive/bulk velocity coefficient of the viscosity tensor. Especially at the HD case it is always true according to the 3.10 equation and the term $\nu_0(\boldsymbol{\nabla}\mathbf{u})\mathbf{I}$ [55,56,59]. But if the shear indices survive ($\mathbf{D_{ij}}$ with $i \neq j$) we have also shear viscosity behaviour. This is true only when the MHD Braginskii case is concerned. The parallel viscosity is unchanged from the unmagnetized case of the two fluid kinetic theory ($\mathbf{B}$=0) [44]. It is also obvious $\mathbf{W_{ij}}$ should be zero for plasmas with **u**=constant, as for uniform isotropic compressions, meaning compressions of no elementary volumetric deformation [44]. For many astrophysical and laboratory plasmas the ν_0 coefficient could be several orders of magnitude higher than the other coefficients [59,60].

The $\boldsymbol{\Pi_1}=\nu_1\mathbf{W_1}$ and $\boldsymbol{\Pi_2}=\nu_2\mathbf{W_2}$ represent the perpendicular viscosity tensors [61]. They control the variation of plasma velocity component across the magnetic field lines. The ν_1 coefficient can be derived from the same formula of ν_2 replacing χ_i with $2\chi_i$ in 3.74, as mentioned before. Practically, they represent the shear stress impulse coefficients per unit surface to the plasma layers ($dyn \cdot s/cm^2$), perpendicular to the magnetic field line. Although it could be several orders of magnitude smaller than the parallel one it has a significant effect to the heating mechanisms of astrophysical plasmas (i.e. Solar corona) and its magnitude is comparable to the resistivity heating [59]. The presence of shear viscosity mechanism and its dissipation are relevant for astrophysical plasma jets. It is also the dominant deformation mechanism when the parallel components are negligible and give shear dissipation mechanisms, experimentally tested, in weakly magnetized ions plasmas at the radial direction of axial laboratory plasma jets [64].

The last two are the $\mathbf{\Pi_3}=-\nu_3\mathbf{W_3}$ and $\mathbf{\Pi_4}=-\nu_4\mathbf{W_4}$ the so called gyroviscosity tensors [61,66]. The ν_3 and ν_4 are the gyroviscous coefficients where the ν_3 can be similarly derived from ν_4 replacing χ_i with $2\chi_i$. They are not actual viscosities, since the associated viscous stresses are always perpendicular to the velocity, implying that there is no dissipation (i.e. viscous heating) associated with this effect. But gyroviscous forces are significant in collisional toroidal plasmas (i.e. Tokamaks) [65] or in weakly collisional but highly magnetized electron-ion plasmas where magnetic reconnection phenomena are present [66].

The appearance of all $\mathbf{\Pi_a}$ tensor components in the momentum and energy equations lead to the evolution of extra shear or bulk or gyro plasma deformations and extra heating mechanisms beyond the classical Ohming, pressure and radiation. This is a difficult task to implement in a computational code, but it would be enlightening to estimate the differences in plasma formations/deformations and plasma evolution in configurations with plasma jets, like single X-pinch or wire arrays and conical arrays. The equations 3.8 and 3.9 should have the full expression of 3.87.

Despite the complexity of this task some specific regimes are easy to study and implement.

A. If we get the Newtonian fluid/gas MHD approach, it is exactly the one of 3.8, 3.9 and 3.10 equations (remember, the one PLUTO uses), using for the bulk and shear coefficients the formulas of Braginskii or Spitzer or other appropriate literature fits [67-71].

I. The unmagnetized/low magnetized limit ($\chi_i = 0$ or $\chi_i << 1$) which should lead to the original form of equation 3.10 cannot be derived from the magnetized one ($\mathbf{B\rightarrow 0}$), at least with the Braginskii's formula presentation, creating simultaneously null magnetic points that create infinities at the simulation runs [67]. The original work, starting from kinetic theory and building to a two-fluid description of the plasma, treats separately this case leaving only the parallel coefficient present and the $\mathbf{\Pi_0}=\nu_0\mathbf{W_0}$ viscosity tensor (given by 3.86 expression) [44,61]. This is not the case if we consider the plasma as one fluid and derive the stress tensor from the HD Newtonian fluid approximation that preserves both the bulk and shear components (equation 3.10) [2,55,56].

a. If we set $\mathbf{B\rightarrow 0}$ and consider that there is no elementary volumetric deformation at the plasma volume, we can set ν_b, bulk component, zero and leave only the shear component contribution. This is a common implementation at the one-fluid studies of MHD and HD cases, where plasma is considered as a classical unmagnetized or low magnetized liquid [55,64,68]. The MHD heavy plasma metals often use this assumption, but in most cases for the low temperature range [64,69]. The choices for the formula of ν_s, could be:

$$\mathbf{i}.\ \nu_{sa} = 0.16 \cdot 10^{-2}\, e^{\frac{3.97\cdot T_m}{T_i}} \left(\frac{dyn \cdot s}{cm^2}\right) (\mathbf{Arrhenius - Ishikawa\ fit})$$

$$\mathbf{ii}.\ \nu_{sb} = 0.96 N_i K_B T_i \tau_i \ (\mathbf{Braginskii\ formula})$$

$$\mathbf{iii}.\ \nu_{ss1} = \frac{5}{4}\left(\frac{m}{\pi}\right)^{0.5} \frac{(K_B T_i)^{2.5}}{(Z_{eff}\cdot e)^4} \frac{0.466}{\ln(1 + 1.493 \cdot e^{\ln\Lambda})} \ (\mathbf{Spitzer/MD\ like\ formula}) \qquad (3.100)$$

$$\textbf{iv.}\ \nu_{ss2} = \frac{0.795 \cdot a^2 m_i N_i \omega_p}{\Gamma^{2.5} \ln\left(1+\frac{0.862}{\Gamma^{1.5}}\right)} \frac{1 + 4.256 \cdot 10^{-2}\Gamma + 2.057 \cdot 10^{-3}\Gamma^2 + 7.036 \cdot 10^{-5}\Gamma^3}{1 + 4.299 \cdot 10^{-2}\Gamma - 2.707 \cdot 10^{-4} \cdot \Gamma^2 + 3.254 \cdot 10^{-6}\Gamma^3 - 1.150 \cdot 10^{-8}\Gamma^4}$$

$$= \frac{0.59625 \cdot (3m)^{0.5} \frac{(K_B T_i)^{2.5}}{(Z_{eff} \cdot e)^4}}{\pi \cdot \ln\left(1+\frac{0.862}{\Gamma^{1.5}}\right)} \frac{1 + 4.256 \cdot 10^{-2}\Gamma + 2.057 \cdot 10^{-3}\Gamma^2 + 7.036 \cdot 10^{-5}\Gamma^3}{1 + 4.299 \cdot 10^{-2}\Gamma - 2.707 \cdot 10^{-4} \cdot \Gamma^2 + 3.254 \cdot 10^{-6}\Gamma^3 - 1.150 \cdot 10^{-8}\Gamma^4}$$

(**Spitzer/MD like formula**)

$$\text{where } \Gamma = \frac{(Z_{eff} \cdot e)^2}{a \cdot K_B T_i} \text{ (c.g.s) (}\textbf{Coulomb coupling parameter}\text{)}$$

$$\text{and } a = \left(\frac{3}{4\pi N_i}\right)^{\frac{1}{3}} \text{ (}\textbf{Wiegner} - \textbf{Sietz radius}\text{) and } \omega_p = Z_{eff} \cdot e \cdot \left(\frac{4\pi N_i}{m_i}\right)^{0.5} \text{(}\textbf{plasma frequency}\text{)}$$

The **first** formula is an Arrhenius fit of the form $\nu = \nu_0 \cdot e^{E/RT}$ that provides an accurate description for the entire liquid phase, where R is the ideal gas constant and E the activation energy. This is valid only at the liquid metal phase while ionization and bulk deformation are absent. Validity range is from 3695K to 10000K approximately while T_m is 3695K for tungsten [26,69].

The second formula is the classic Braginskii formula of no magnetic dependence that is referred to the parallel or perpendicular coefficient (they are the same for the low magnetized limit).

The third one is a straightforward modification of the traditional Landau-Spitzer formula for the shear viscosity coefficient of the one-component plasma which is calculated with very high accuracy using equilibrium molecular dynamics (MD) simulations [70]. It is valid for all the one component ionized plasmas with coupling strength parameter $\Gamma < 10$.

The fourth one is an advanced formula of the third one which is a practical fit that reproduces the viscosity coefficient across coupling regimes, from the weakly coupled regime to the solid-liquid transition one, using equilibrium molecular dynamics simulations and the Green-Kubo relation. It is valid for all the one component ionized plasmas with coupling strength parameter Γ. This formula is very accurate across the entire fluid regime for every coupling parameter Γ, while it has been successfully validated with other MD works for $0.01 < \Gamma < 200$. This fit will be the reference ideal fitting for the estimation of the other presented formulas here. The third and fourth ones are Spitzer like formulas, where the latter, is a global fitting for every coupling and temperature regime [67]. Additionally, these last two theoretical fits are accurate for identical ions of charge $Z \cdot e$, and the one component plasma (OCP), modelling strongly coupled Coulomb systems and, in particular, ions in strongly coupled plasmas. If $\Gamma << 1$ we are at the nearly collisionless, gaseous regime, while the transition to bigger values till $\Gamma >> 1$ is expressed through an increasingly correlated, liquid-like regime to the Wigner crystallization to a lattice near Γ. The gas-like to liquid-like crossover manifests itself in several ways in the microscopic properties of the OCP. This approximation is flexible and appropriate for one fluid codes (i.e. plutocode). Nevertheless instead of a constant mean ionization state these formulas could use the mean ionization data of FLYCHK code. This implemantation could be tested

through the simulations giving them a more dynamic plasma interaction through different plasma densities and temperatures, correlating spatially different mean ionization states at the same instant.

For the better estimation of the value range of the previous formulas there is a graphic presentation depiction at figure 3.25. The Z_{eff} tabular data are extracted from FLYCHK code for tungsten plasma and the τ_i formula is the one of 3.79. These formulas are shown as isotherm functions of mass density. The density, electron density and temperature range are the ones of the resistivity section of figure 3.18. The $\ln\Lambda$ is estimated from the Coulomb logarithm formula of the resistivity section. A cut off value is used.

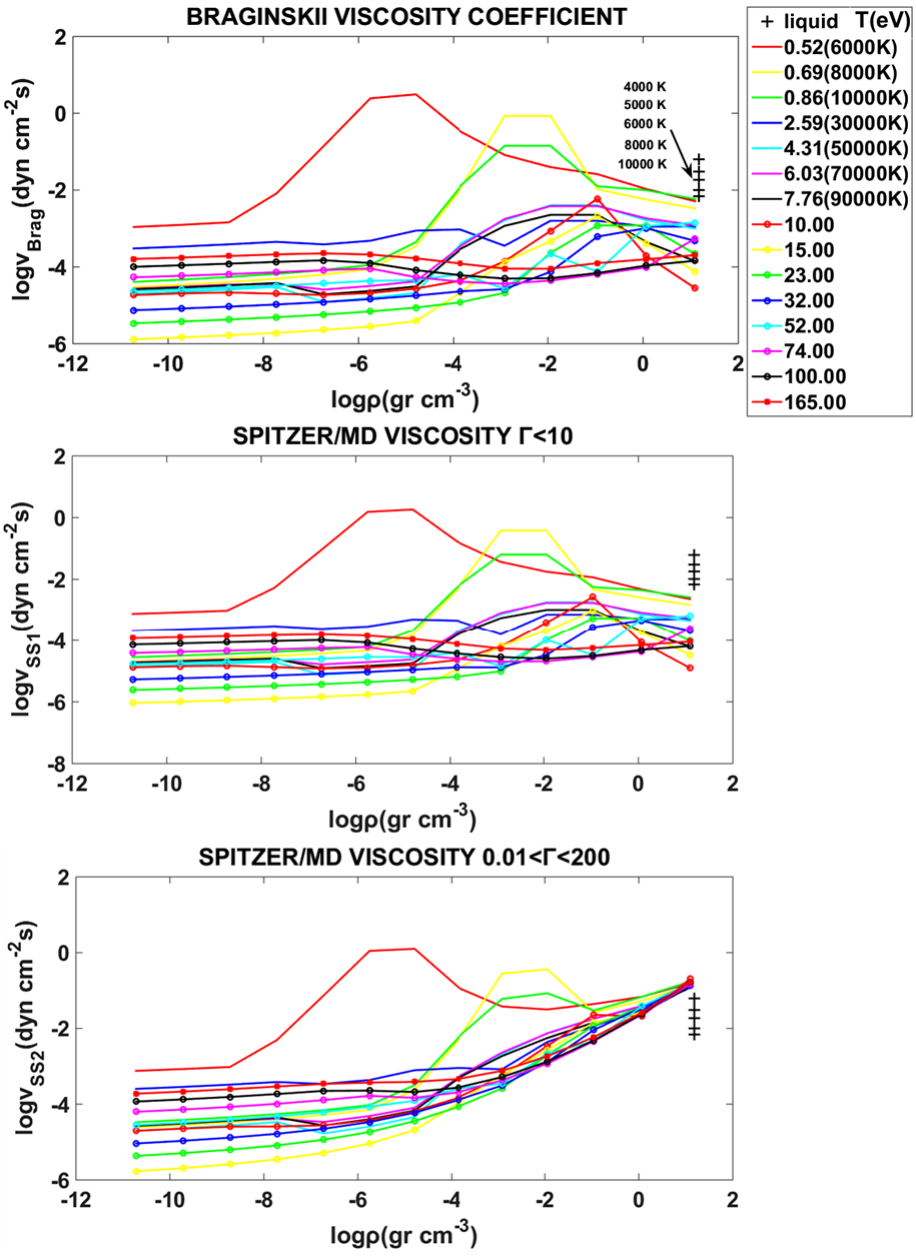

Figure 3.25: *Braginskii and Spitzer like, MD based shear viscosity coefficients. The temperature values are the same as the ones of figure 3.18 at the resistivity section. The mean ionization state Z_{eff} is extracted from the modified tabular data of the FLYCHK code. The Coulomb logarithm used is lnΛ=23-*

ln($Z_{eff}T^{-1.5}Ne^{0.5}$), taking into account the Z_{eff} of the ions (cut off value is 2). The liquid viscosity is depicted at 15 gr/cm^3.

Some useful observations are:

i. The unmagnetized Braginskii case (top graph) introduces the same density and temperature behaviour as the unmagnetized weak coupled Spitzer/MD like (second graph) at all temperatures range. They are of the order ~10^{-6}gr·cm^{-1}s^{-1} to ~10^{0}gr·cm^{-1}s^{-1} for all temperatures. The low temperatures of 6000K, 8000K and 10000K, have a maxima of ~10^{0}gr·cm^{-1}s^{-1} at (approximately) the dense matter region while they are of the same order to the other temperature range (~10^{-2}gr·cm^{-1}s^{-1} to ~10^{-6}gr·cm^{-1}s^{-1}) at the dense and low density plasma region.

ii. The liquid cross marks, that are experimentally matched [69], are very close to the Braginskii/Spitzer weak coupled case having slightly higher values till one order of magnitude smaller than the ones to the global fit case of the third graph. We consider the third graph as a reference case and we must not forget that at the experimental cases we could have one to two times different values discrepancies at our estimations [64]. This could also mean that the plasma dense region behaviour differs than the one of the liquid-plasma phase [64,69].

iii. The third graph is the one that is multi-theoretical evaluated and is the one that is fitted for all plasma regime from the weak coupled plasma to the solidification threshold [70]. We observe, once again, at the dense matter region the linear density behaviour and the temperature independence (similar behaviour at the EOS and resistivity/conductivity section). The values for densities higher than 10^{-4}gr·cm^{-3} are rising and go beyond the 10^{-2}gr·cm^{-1}s^{-1}

b. The dependence of the growth rate of Kelvin Helmholtz instability (KHI) [71] or magnetoviscous [68] and other viscous stress related [59], has a straightforward dependence from the viscous bulk and shear component coefficient.

If we set $\mathbf{B\rightarrow 0}$ and consider that there is volumetric deformation, meaning having a compressible plasma, we have to take in consideration both ν_b and ν_s. So possible combinations presented already from this work, are:

$$\begin{gathered}
\mathbf{i}.\ \nu_b = 0 \\
\text{and } \nu_s = \nu_{sa} \text{ for } 3695\text{K} < T < 10000K \\
\mathbf{ii}.\ \nu_b = \nu_s = 0.96 N_i K_B T_i \tau_i \text{ for } \text{T} > 10000K \\
\mathbf{iii}.\ \nu_b = 0.96 N_i K_B T_i \tau_i \text{ for } \text{T} > 10000K \\
\text{and } \nu_s = \nu_{ss1} \\
\mathbf{iv}.\ \nu_b = 0.96 N_i K_B T_i \tau_i \text{ for } \text{T} > 10000K \\
\text{and } \nu_s = \nu_{ss2}
\end{gathered} \tag{3.101}$$

where the symbols of the shear coefficients are the same as the ones in equation 3.100.

II. If we take in consideration the magnetized plasma we have, the intermediate case ($\chi_i \neq 0$) and the high magnetized one ($\chi_i >> 1$).

a. So the intermediate case can take in consideration the Braginskii formulas of 3.83 equations along with the ones of 3.100 and 3.101. If we have only shear coefficient we can take:

$$\begin{gathered}\textbf{i.}\ \nu_b = 0 \\ \text{and } \nu_s = \nu_{sa} \text{ for } 3695\text{K} < T < 10000K \\ \textbf{ii.}\ \nu_b = 0 \\ \text{and } \nu_s = \nu_1 \text{ or } \nu_s = \nu_2 \text{ for T} > 10000K\end{gathered} \tag{3.102}$$

where the symbols of the shear coefficients are the same as the ones in equation 3.83. We have to be careful though that shear component here means that in every Cartesian direction partial spatial derivatives of plasma velocity could survive. This is not necessarily the same as the perpendicular viscosity coefficient of the magnetic field. It is something to be tested at the simulation runs and find the better fitting. We will discuss this according to some specific plasma configurations.

b. For the case of magnetized plasma, but with freedom for compression deformation along each component of plasma derivative, we have also the bulk coefficient that could be any choice of Spitzer-like or Braginskii-like formula of equation 3.100, since they all have the same temperature, ionization Z_{eff} and Coulomb logarithm dependence. For the shear coefficient, we can take again the same formula of equation 3.102.

c. For the high magnetized case we can take the Braginskii coefficients of 3.84 instead of 3.83. All the other combinations could be the ones of **II.a** or **II.b** case.

We will now discuss and present the perpendicular and gyroviscous coefficients, concerning this part of analysis as also the oncoming full component magnetized case after a few pages. The behaviour of the ν_2 and ν_4 magnetized coefficients are depicted as a function of magnetic field and mass density in figures 3.26 and 3.27 as isotherm surfaces 3D figures diagrams respectively.

Some observations are useful at this point to validate the previous and the subsequent estimations for the perpendicular and gyroviscous coefficients:

i. The low magnetized perpendicular case introduces the same density and temperature behaviour as the unmagnetized of the parallel coefficient of figure 3.25.
ii. The high magnetized area has similar magnitude values, as the ones of the low magnetized, at the dense plasma region, while it has 10 orders of magnitude reduce at the dilute plasma region for all temperature range. These observations are profoundly demonstrated at the 2D graphs.
iii. The low magnetized plasma presents a ν_2 coefficient of the same order of magnitude as the parallel ν_0 (depicted at figure 3.25), but as the magnetic field rises, the perpendicular one reduces several orders of magnitude. This justifies the choice of taking only the parallel coefficient at some cases [60,66,67].
iv. The viscosity coefficient mass density dependence is similar up to a magnetic field equal to 100 Gauss. Then, the coefficient decreases rapidly for higher magnetic values, at the low density region, reaching the high magnetized profile of the 2D graph.

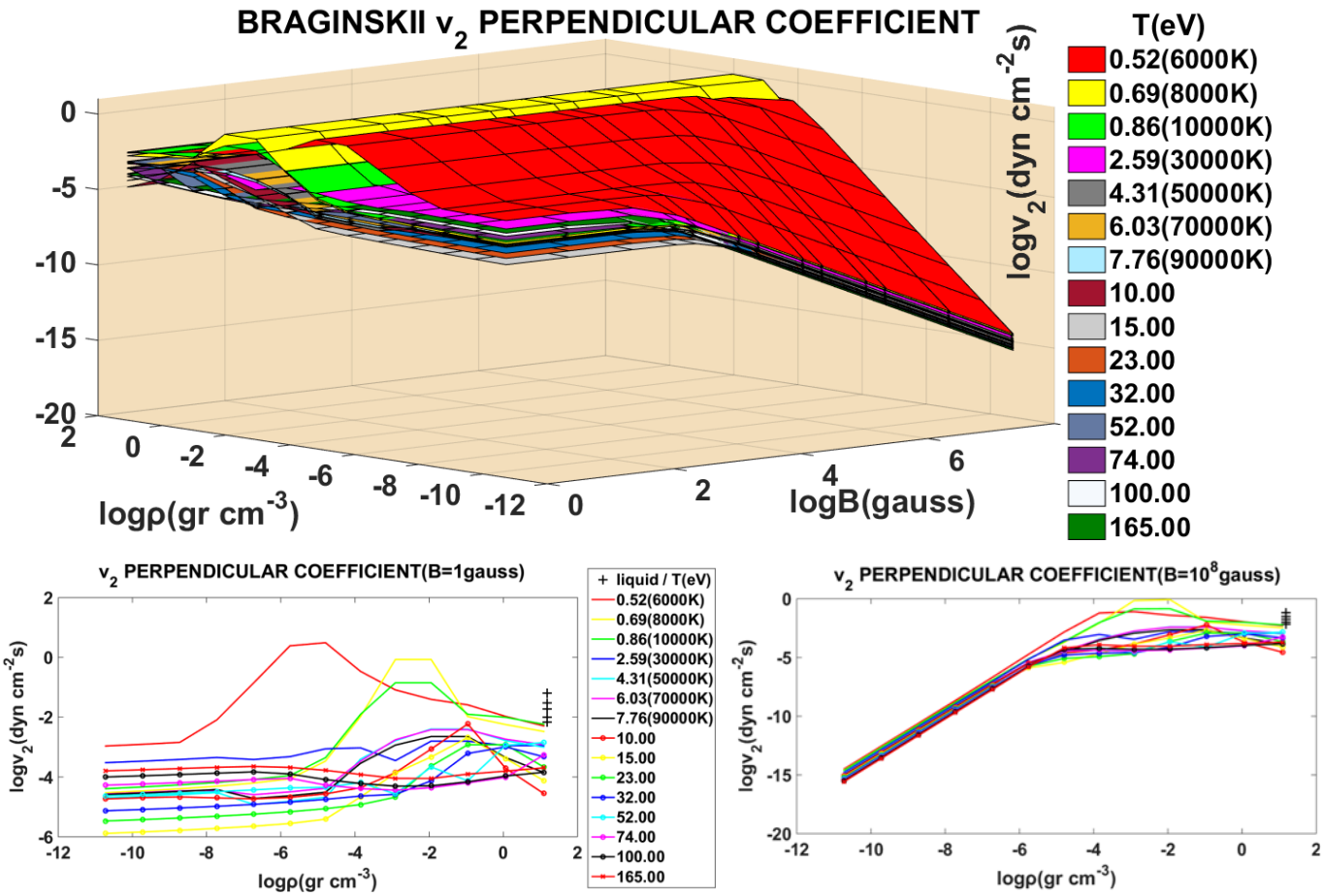

3.26 Figure: *3D isotherm surfaces of ν_2 Braginskii viscosity coefficient as a function of mass density ρ and magnetic field strength B. The magnetic field magnitude range is 10^0gauss<B<10^8gauss. The mass density is from solid to very thin plasma (19,2gr/cm^3<ρ<~10^{-11}gr/cm^3), electron density 10^{12}e/cm^3<N_e<10^{24}e/cm^3 and the temperature values are the same as the ones of the figures 3.18 and 3.25. The 2D graphs are the lowest (B=1 gauss) and the highest (B=10^8 gauss) magnetized slices of the 3D graph. The mean ionization state Z_{eff} is extracted from the modified tabular data of the FLYCHK code. The Coulomb logarithm used is lnΛ=23-ln(Z_{eff}·$T^{-1.5}$·$Ne^{0.5}$), taking into account the Z_{eff} of the ions (cut off value is 2). The liquid viscosity is depicted at 15 gr/cm^3 at the 2D graphs and the temperatures are the same of figure 3.25.*

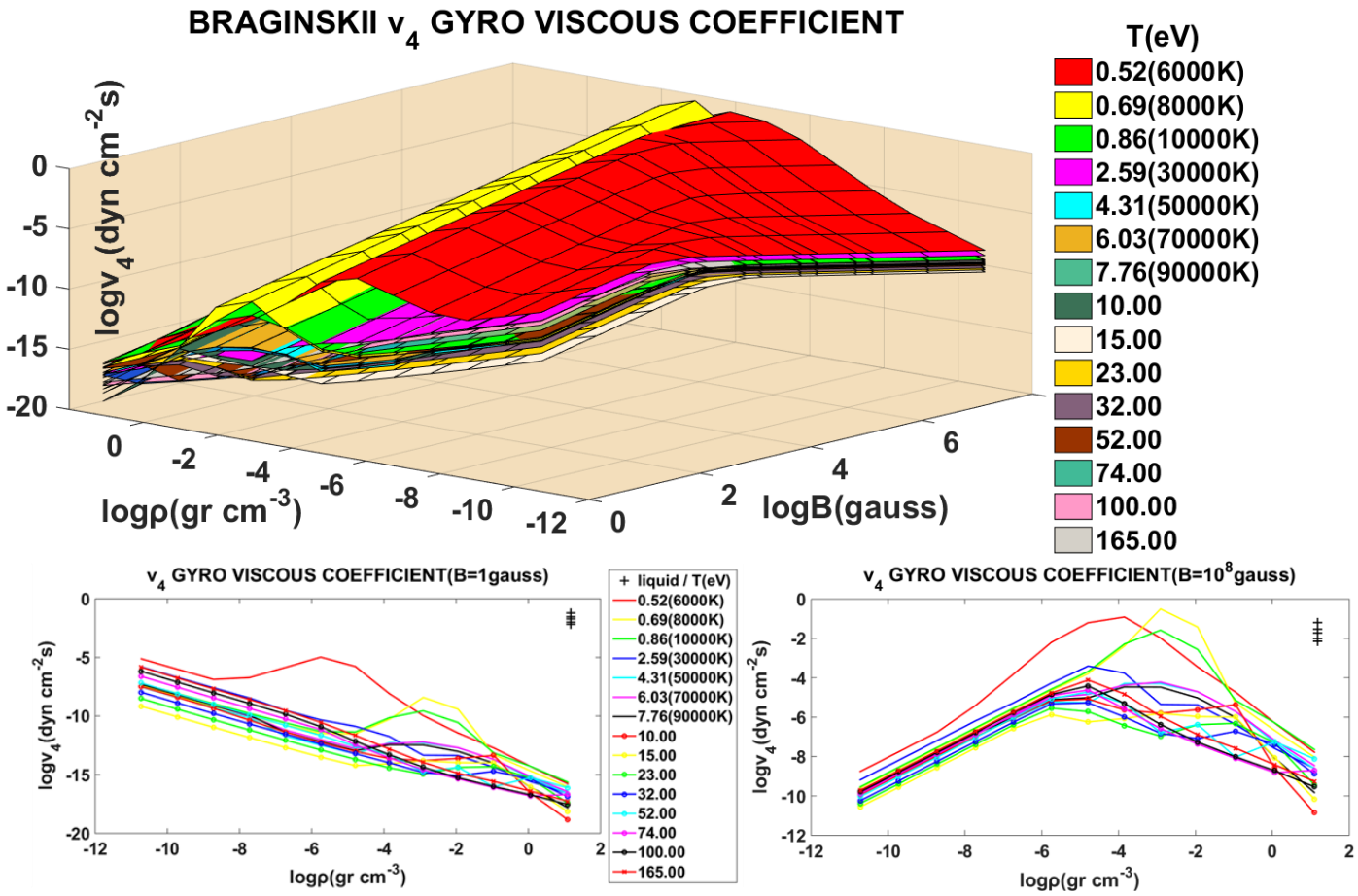

3.27 Figure: *3D isotherm surfaces of v_4 Braginskii viscosity coefficient as a function of mass density ρ and magnetic field strength B. The magnetic field magnitude range is 10^0Gauss<B<10^8Gauss. The mass density area range goes from the solid to the very thin plasma (19,2gr/cm^3<ρ<~10^{-11}gr/cm^3), the electron density 10^{12}e/cm^3<N_e<10^{24}e/cm^3 while the temperature values are the same as the ones of figures 3.18, 3.25 and 3.26. The 2D graphs are the lowest (B=1 gauss) and the highest (B=10^8 gauss) magnetized slices of the 3D graph. The mean ionization state Z_{eff} is extracted from the modified tabular data of the FLYCHK code. The Coulomb logarithm used is lnΛ=23-ln($Z_{eff}T^{-1.5}Ne^{0.5}$) taking into account the Z_{eff} of the ions (cut off value is 2). The liquid viscosity is depicted at 15 gr/cm^3 at the 2D graphs and the relevant temperatures are the same of figure 3.25.*

i. The low magnetized case gyroviscous component has the lowest values compared to the perpendicular and parallel coefficients at all temperatures, varying from 10^{-5}gr·cm^{-1}s^{-1} till ~10^{-18}gr·cm^{-1}s^{-1}. The dense plasma region presents the smallest values up to 15 orders of magnitude lower than the other two at the same densities. The low density plasma region has up to ~four orders of magnitude lower values than the other two coefficients.

ii. The low magnetized case presents an almost linear decrease for all temperatures from the dilute plasma region to the dense and solid one.

iii. The linear decrease continues up to ~100 Gauss for the magnetic field variable, while for higher values it is transformed at the dilute plasma regime, concluding to the parabolic like shape of the right 2D graph. It is the same transition value as the one of the perpendicular graph.

iv. The high magnetized case presents a parabolic-like behaviour having its maxima at the intermediate plasma values (~10^{-4}gr/cm^{-3}), while at both edges the values are similar, of the order of ~10^{-10}gr·cm^{-1}s^{-1}. The intermediate plasma densities, at the high magnetized case have approximately the same values for all three viscosity coefficients as presented in figures 3.25, 3.26 and 3.27. This is something that should not be neglected in the implementation of the viscosity tensor.

Now we can make some general remarks, concerning all Braginskii viscosity coefficients. Even though the perpendicular coefficient could be several orders of magnitude smaller than the parallel at the magnetized case, it could play a significant role at the shear viscosity heating mechanisms in the corona plasma (i.e. the Solar corona) [59]. Braginskii full viscosity tensor i.e. anisotropic transport of momentum with respect to the direction of the magnetic field, could be of prime importance for studies of the weakly collisional plasma in laboratory and astrophysical plasmas (i.e. in corona plasma for both cases) [59,67]. Magnetic reconnection phenomena in weakly collisional highly magnetized plasmas are affected from the presence of the parallel and gyroviscous components of the viscosity tensor [66]. The shear dynamic plasma viscosity mitigates the R-T instability in Z-pinch configurations [75]. The full Braginskii viscosity tensor mitigates the m=0 and m=1 modes, and can stabilize the short-wavelength perturbations in Z-pinches [76]. As the shear viscosity increases, the growth rate of the MRT instability is reduced rapidly in a Z-pinch configuration [77]. The gyroviscous components are important for the explanation of experimental confinement results in collisional strong rotated Tokamak plasmas [65].

As a conclusion of this analysis we can propose a viscous plan implementation in a fluid based MHD code like PLUTO. First we will deal with the bulk and shear coefficients of the two component fluid viscosity tensor.

If a single metal wire of a Z-pinch configuration has to be studied from the early plasma face to the late magnetized plasma, we could take any of the aforementioned combinations without the bulk ν_b viscosity coefficient. We can consider the Z axis as the one of the plasma cable and we have an azimuthal magnetic field at the XY plane. So we have bulk plasma velocities mainly at this plane leaving the shear components to affect the creation of instabilities. But as recently presented by E. Kaselouris et al, at early metal transition to liquid and plasma phase, plasma presents a "memory" ETM instability dependence. It begins from the solid phase, affects the fluid and plasma instability, morphology, creation and evolution, while the contribution of the fixed wire ends at the electrodes, producing a Z axis stress and compression at the early plasma phase [72-74]. As a consequence, what needs to be tested is the effect of the bulk viscosity component to the plasma density and instability evolution and the differences we can observe without its contribution.

If we have a Z-pinch wire array, X-pinch or a Z-pinch conical wire array configuration the most obvious choice is to take both bulk and shear components into consideration. This is due to the presence of jets and more complicated plasma formations. The shear and bulk components would affect the plasma jet, across and along the plasma velocities and magnetic field components. Also there are denser, compressed and stagnation phase areas, like the X-pinch neck and central wire arrays jet collision that would need the presence of the bulk component to contribute to denser island formations, deformations, modulation on instability growth (i.e. MRT,KH,ETM instability e.t.c.) and extra heating mechanisms [71-77].

Someone could also try to combine the MD plasma coupling formulas of equation 3.101 with the magnetized ones of Braginskii, replacing the $N_i K_B T_i \tau_i$ part with the one of **iii** or **iv** of equation 3.100, taking in consideration the Coulomb ion-ion coupling, while simultaneously ignoring the effect of the magnetic field to the viscosity coefficient. For instance, if we combine the iv of equation 3.100 considering the appropriate MD fitting with the ν_1 or ν_2 Braginskii perpendicular coefficients we could achieve at the 3.26 graphs the linear behaviour we observe at the dense matter region in the third graph of 3.25. It is an interesting alternative and has to be simulation tested (an analogous mixture is proposed to the anomalous Braginskii, Saha-based, magnetically determined conductivity of 3.4.1.3 sub-section)!

B. If we use the two-fluid kinetic theory approximation for the formula of the viscosity tensor, we should implement the whole Braginskii expression of equation 3.87 replacing the rates-of-strain-tensors from 3.89-3.94 or 3.95-3.99. This is not a problem for one or two fluid MHD codes as long as we replace $\mathbf{\Pi}$ in 3.8 and 3.9 with the one of equation 3.87. It has been partially implemented in some specific cases to other works and is called the Braginskii extended MHD model [57,62,67]. We should also have in mind the previous observations and the graph depiction of figures 3.25-3.27.

I. Setting $\mathbf{B \to 0}$ at the low magnetized limit at the viscosity coefficients, we get:

$$\nu_0 = \nu_1 = \nu_2 = 0.96 N_i K_B T_i \tau_i \text{ and } \nu_3 = \nu_4 = 0 \tag{3.103}$$

This is a $\nu \sim T_i^{2.5}$ dependence and it is a common formula to the simulations for the bulk and/or shear viscosity coefficient for both Braginskii and Spitzer formulas [44,61,64,66,68].

II. The high one is the simplest magnetized case. Then the unmagnetized component $\nu_{0>>} \nu_1, \nu_2, \nu_3, \nu_4$ (for a direct estimation we should consider the figures 3.25-3.27). The simplest form of the viscosity tensor originates from the equations 3.87 and 3.89, ignoring the magnetized components and assuming the magnetic field is along Z axis, we have[60]:

$$\mathbf{\Pi_{ij}} = \nu_0 \mathbf{W_{ij}} = \nu_0 \begin{bmatrix} \frac{\mathbf{W_{xx}} + \mathbf{W_{yy}}}{2} & 0 & 0 \\ 0 & \frac{\mathbf{W_{xx}} + \mathbf{W_{yy}}}{2} & 0 \\ 0 & 0 & \mathbf{W_{zz}} \end{bmatrix} \tag{3.104}$$

where the components $\mathbf{W_{ij}}$ originate from equation 3.86. (We must not forget that $\mathbf{W_{ij}}$ is a traceless matrix giving $\mathbf{W_{xx} + W_{yy} + W_{zz} = 0}$ thus $\mathbf{W_{zz} = -W_{xx} - W_{yy}}$ simplifying further the presentation of 3.104 and 3.105 matrix form).

III. The intermediate magnetized case ($\chi_i \neq 0$) preserving all five components for a Z axis directed magnetic field, leads to [44,59]:

$$\begin{aligned} \mathbf{\Pi_{xx}} &= \nu_0 \frac{\mathbf{W_{xx}} + \mathbf{W_{yy}}}{2} + \nu_1 \frac{\mathbf{W_{xx}} - \mathbf{W_{yy}}}{2} + \nu_3 \mathbf{W_{xy}} \\ \mathbf{\Pi_{yy}} &= \nu_0 \frac{\mathbf{W_{xx}} + \mathbf{W_{yy}}}{2} - \nu_1 \frac{\mathbf{W_{xx}} - \mathbf{W_{yy}}}{2} - \nu_3 \mathbf{W_{xy}} \\ \mathbf{\Pi_{xy}} &= \mathbf{\Pi_{yx}} = \nu_1 \mathbf{W_{xy}} - \nu_3 \frac{\mathbf{W_{xx}} + \mathbf{W_{yy}}}{2} \end{aligned} \tag{3.105}$$

$$\mathbf{\Pi_{xz} = \Pi_{zx} = \nu_2 W_{xz} + \nu_4 W_{yz}}$$
$$\mathbf{\Pi_{yz} = \Pi_{zy} = \nu_2 W_{yz} - \nu_4 W_{xz}}$$
$$\mathbf{\Pi_{zz} = \nu_0 W_{zz}}$$

IV. If we consider the case of a single Z-pinch wire for the magnetized case ($\chi_i \neq 0$) and the cable is along Z axis, the magnetic field components are on the XZ plane according to figure 3.28,

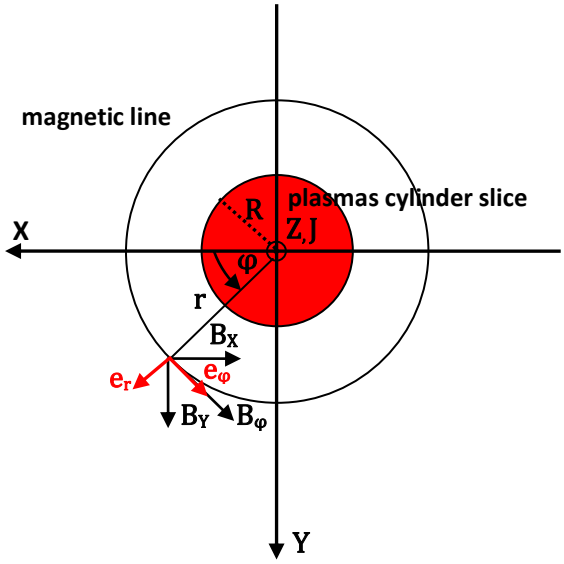

Figure 3.28: *Slice of a Z-pinch plasma cylinder, radius R, at the XY plane.*

where the **Z** positive direction and the current density **J** are pointing outwards to the observer's eye.

The radial distance and the magnetic field components are related to the Cartesian coordinates through the expressions:

$$r = \sqrt{y^2 + x^2} \tag{3.106}$$

and for the azimouthal magnetic field :

$$\mathbf{B_\varphi} = |\mathbf{B}|(r)\hat{\mathbf{e}}_{\boldsymbol{\varphi}} = |\mathbf{B}|(r)\begin{bmatrix} -\cos\varphi\,\hat{\imath} \\ \sin\varphi\,\hat{\jmath} \\ 0 \end{bmatrix} = |\mathbf{B}|(r)\begin{bmatrix} -\frac{x}{r}\hat{\imath} \\ \frac{y}{r}\hat{\jmath} \\ 0 \end{bmatrix} \tag{3.107}$$

where the r and ϕ are the polar coordinates, $\mathbf{e_\varphi}$, $\mathbf{e_r}$ are the unit polar vectors, **i, j, k** are the unit Cartesian vectors and x,y are the Cartesian coordinates of the origin of the magnetic field vector. The aforementioned unity vector **b** of the previous analysis becomes,

$$\mathbf{b_\varphi} = \frac{|\mathbf{B}|(r)}{|\mathbf{B}|(r)}\hat{\mathbf{e}}_{\boldsymbol{\varphi}} = \begin{bmatrix} -\cos\varphi\,\hat{\imath} \\ \sin\varphi\,\hat{\jmath} \\ 0 \end{bmatrix} = \begin{bmatrix} -\frac{x}{r}\hat{\imath} \\ \frac{y}{r}\hat{\jmath} \\ 0 \end{bmatrix} \tag{3.108}$$

and supposing the situation of the dominant ν_0 coefficient of the **II** magnetized case we have:

$$\mathbf{\Pi_{ij}} \equiv \mathbf{\Pi_{0ij}} = \nu_0 \mathbf{W_{0ij}} \text{ where}$$

$$\mathbf{\Pi_{0xx}} = \frac{3\nu_0(\mathbf{b_x}^2 - \frac{1}{3})(\mathbf{b_x}^2\mathbf{W_{xx}} + \mathbf{b_y}^2\mathbf{W_{yy}} + \mathbf{2b_x b_y W_{xy}})}{2}$$

$$\mathbf{\Pi_{0yy}} = \frac{3\nu_0(\mathbf{b_y}^2 - \frac{1}{3})(\mathbf{b_x}^2\mathbf{W_{xx}} + \mathbf{b_y}^2\mathbf{W_{yy}} + \mathbf{2b_x b_y W_{xy}})}{2} \tag{3.109}$$

$$\mathbf{\Pi_{0xy}} = \mathbf{\Pi_{0yx}} = \frac{3\nu_0\mathbf{b_x b_y}(\mathbf{b_x}^2\mathbf{W_{xx}} + \mathbf{b_y}^2\mathbf{W_{yy}} + \mathbf{2b_x b_y W_{xy}})}{2}$$

$$\mathbf{\Pi_{0zy}} = \mathbf{\Pi_{0yz}} = \mathbf{\Pi_{0xz}} = \mathbf{\Pi_{0zx}} = \mathbf{0}$$

$$\text{where } \mathbf{b} = (\mathbf{b_x}, \mathbf{b_y}, 0) = \left(-\frac{\mathbf{x}}{\mathbf{r}}, \frac{\mathbf{y}}{\mathbf{r}}, 0\right) \text{ and } \mathbf{W_{zz}} = -(\mathbf{W_{xx}} + \mathbf{W_{yy}})$$

These are some cases of the non/low magnetized and magnetized viscosity case. Again the coefficients could properly change at the high magnetized limit. The IV magnetized case is an example of one experimental occasion at the high magnetized limit mostly ignoring again the perpendicular and gyroviscous coefficients. The X-pinch and wire array cases could implement the whole package of the five viscosity components, as mentioned previously, due to the three component presence of the magnetic field, especially at later simulation times, where the jets are a significant part of the plasma formation. Coronal plasma evolution and mitigation of the magnetoviscous instabilities are considerably affected by the full component viscosity as we previously discussed [75-77]. The plasma viscosity also presents a stabilization effect and the effectiveness of such a mechanism is enhanced with the perturbation wavenumber and the value of the viscosity parameter increasing, as mentioned in [77]. Similar and more bold approaches have been recently tested by J. D. Pecover and J. P. Chittenden [78], implementing a material strength model in GORGON to improve simulation of the solid phase of liner implosions which, when applied to simulations exhibiting the Electro-Thermal Instability (ETI) and “Electro-Choric” Instability (ECI), gave a significant increase in wavelength and amplitude, having a better simulation agreement with the experiment than previous randomly initialized results.

Concentrating the proposed viscous analysis, the flow chart below presents the possible combinations of the Newtonian fluid/gas approximation and the magnetized Braginskii one.

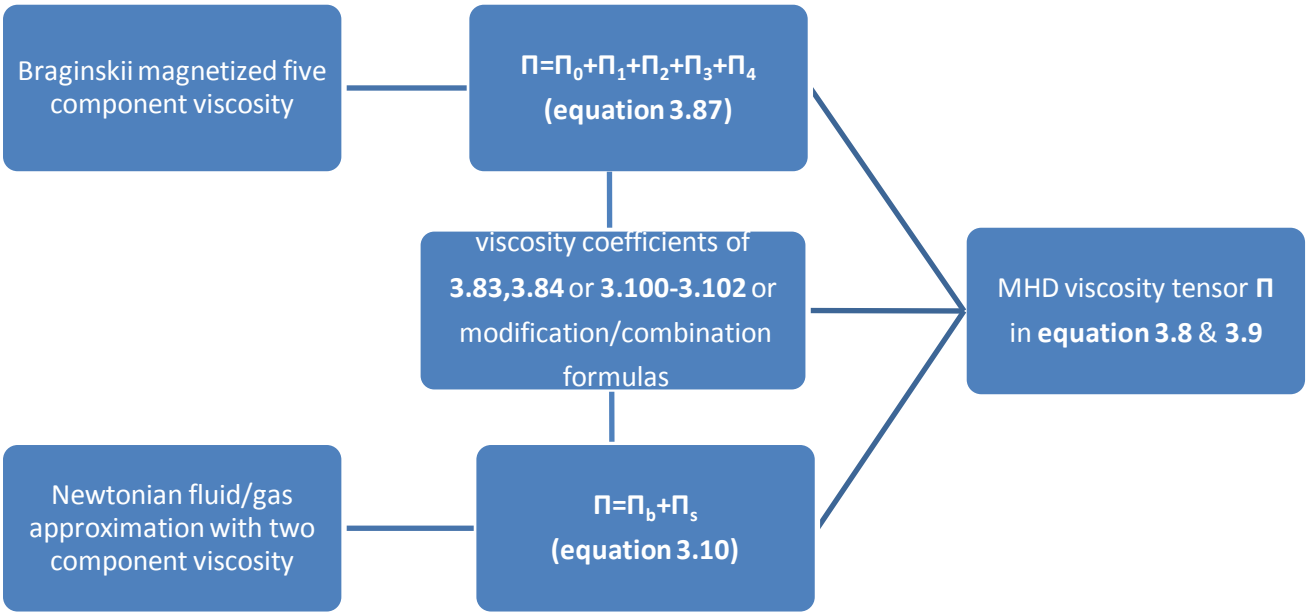

Figure 3.29: *Flow chart of the viscosity tensor scheme through the two different approach approximation of this analysis.*

3.5 Summary/Conclusions

All these propositions and fittings are for an MHD, one-fluid plasma scheme. General observations for the radiation transport, optically thin losses, conductivity/resistivity, thermal conductivity, viscosity scheme and propositions for the best fittings are as follows:

1. The aforementioned fits in this chapter are for every phase of the matter evolution (solid, liquid/gas, plasma) useful for codes that are using transition matter phases. The electrical conductivity, thermal conductivity and viscosity have piece-wise fittings from the solid phase density and temperature of 100K till temperatures of hundreds (or more) of eV and densities from the dense/overdense matter ~10^{2}gr/cm^{3} to the very dilute region of ~10^{-11}gr/cm^{3}.

2. The classical theory of the Coulomb logarithm is not valid at the dense matter region for low temperatures presenting non-physical values. This is fixed using the Born approximation! If we consider the classical formula a lower cut-off value is needed, but the discrepancies there are obvious at the dense matter (especially at lower temperatures), introducing underestimations of some orders of magnitude at the dense/overdense regime.

3. The maxima at the thermal conductivity and viscosity coefficients graphs for 6000K, 8000K and 10000K and all the low temperature regime, should be tested further for its accuracy. Even though we have good agreement with three other results for the thermal conductivity from experiment and semiempirical data, it does not prove that another fitting could not be more appropriate. The introduction of the Coulomb logarithm by the Born approximation introduces a similar-like behaviour of these two with the conductivity graphs (presenting local minima instead of maxima at the dense matter/low temperature region i.e. in figure 3.24). We must not also forget that the estimations from the FLYCHK code for Z_{eff} have larger uncertainties at the low temperature/dense matter range and were modified.

4. On the contrary we see (surprisingly?!) a similar behaviour of every physical variable isotherm as a function of mass density. More specifically:

i. The conductivity $\sigma=f(\rho,T)$, thermal conductivity coefficient $k_{||}= f(\rho,T)$, and viscosity unmagnetized coefficient $\nu_0= f(\rho,T)$, have an almost steady density and almost linear temperature rise dependence at the dilute plasma region. The MGGB/SESAME based EOS $P=f(\rho,T)$ has a linear rise behaviour as a function of density also at the same low density region.

ii. The dense matter region ($>10^{-1}$gr/cm^3) for temperatures of 6000K, 8000K and 10000K has local minima at ~10^{-1}gr/cm^3-~10^{0}gr/cm^3 (i.e. in conductivity, thermal conductivity, EOS presentation) or maxima (unmagnetized viscosity coefficient) displaced at the lower density matter region (10^{-2}gr/cm^3-10^{-5}gr/cm^3).

iii. The dense/overdense matter region presents a linear rise-like behaviour as a function of mass density, almost temperature independent for all cases (EOS, conductivity, thermal conductivity, unmagnetized parallel/MD viscosity). This is achieved effortlessly for the conductivity and thermal conductivity through the usage of the Coulomb logarithm by the Born approximation, otherwise we need a piece wise function with an exponential and linear/parabolic fit, as we saw at the conductivity subsection!

iv. The local minima of the resistivity/conductivity is implemented with an exponential fit through a piece wise function, but it can be fitted (probably better) with a linear mixture of the resistivities or collision frequencies including, to the model, populations of neutral atoms that are defined from the non-ideal Saha equation.

The agreement with the experiment and literature is remarkable for the conductivity/resistivity variable at any approximation fitting!

5. The implementation of the magnetic field presents a similar behaviour with the unmagnetized one at the very low value regime of the magnetic induction, but at the mid and high value region we see a correction of the conductivity (anomalous Braginskii-like) and viscosity's components parallel and perpendicular to the magnetic field that could reach 15 orders of magnitude lower values! The same holds for the transverse coefficients of the thermal conductivity but there is no depiction at the relative subsection. The growth rate and dynamic evolution of the plasma instabilities are key sensitive to the magnetic field modulation of these physical variables, especially at the dilute plasma region where the differences with the unmagnetized one are many orders of magnitude as we just mentioned.

Conclusively, these formulas provide us a major variety of combinations and extra cases that are not discussed here, but could be simulation implemented, tested and experimentally validated.

Moreover, we must not forget that we could try piece wise functions at different plasma areas due to different physical modules that could be dominant there. For instance, at the plasma vacuum interface and at the low density background plasma we could use equation 3.58 formula for resistivity that is representative of MHD codes that smooth the transition to a large background resistivity. For the thick metal plasma region we could use the 3.57 piece wise or the Saha-based linear mix formula of 3.61 and so on!

Another situation of different implementation areas could be the use of fluid/gas viscosity coefficients at the corona plasma of a Z-pinch or at the corona and the plasma jet of an X-pinch

configuration and magnetically defined at the thicker core and pinch area. The transition switch could be the magnitude of the magnetic field **|B|**.

All these equations , functions and tabular data are compatible and can be implemented in the one-fluid MHD code PLUTO or to any other MHD code that uses similar equation scheme.

References

[1] J. P. (HANS) GOEDBLOED AND STEFAAN POEDTS, "PRINCIPLES OF MAGNETO-HYDRODYNAMICS with Applications to Laboratory and Astrophysical Plasmas", Cambridge University Press 2004, pg .178-183

[2] http://plutocode.ph.unito.it/PLUTO User's Guide v.4.2.

[3] L. Spitzer Jr., "Physics of Fully Ionized Gases" Interscience Publishers ING, New York, 1962.

[4] Lennox L. Cowie and Christopher F. McKee, "THE EVAPORATION OF SPHERICAL CLOUDS IN A HOT GAS. I. CLASSICAL AND SATURATED MASS LOSS RATES", The Astrophysical Journal, 211:135-146, 1977 January 1.

[5] V.E. Fortov, I.V. Lomonosov, "Equations of State of Matter at High Energy Densities", The Open Plasma Physics Journal, **3**, 122-130, (2010).

[6] T-4 Handbook of Material Properties Data Bases, Vol Ic: Equations of State, LA-101 SO-MS, UC-34, Issued November 1984.

[7] SESAME THE LOS ALAMOS NATIONAL LABORATORY EQUATION OF STATE DATABASE, LA-UR_92_3407.

[8] Kashiwa B. A., "The MGGB Equation-of-State for Multifield Applications: A Numerical Recipe for Analytic Expression of Sesame EOS Data", LA-1442 ,September 2010. http://www.doe.gov/bridge

[9] Yuri Ralchenko, "Modern Methods in Collisional-Radiative Modeling of Plasmas", Springer International Publishing Switzerland 2016.

[10] J. J. MacFarlane, P. Wang, G. A. Moses, "Non-LTE radiation transport in moderate-density plasmas", Laser and Particle Beams (1990), vol. 8, no. 4, pp. 729-740.

[11] J. P. Apruzese et al, "The physics of radiation transport in dense plasmas", PHYSICS OF PLASMAS VOLUME 9, NUMBER 5 MAY 2002.

[12] I. Yu. Vichev, V. G. Novikov, and A. D. Solomyannaya , "Modeling of the Emission Spectra of Tungsten Plasma" , Mathematical Models and Computer Simulations, 2009, Vol. 1, No. 4, pp. 470–481.

[13] Tungsten Charge State Distribution by FLYCHK NLTE Kinetics Calculation at NIST by International Atomic Energy Agency- Atomic Molecular Data Services provided by the Nuclear Data Section.

[14,] A. S. Richardson, NRL PLASMA FORMULARY, 2019.

[15] H.-K. Chung et al., "FLYCHK: Generalized population kinetics and spectral model for rapid spectroscopic analysis for all elements", High Energy Density Physics 1 (2005) 3-12.

[16] T. Pütterich et a., "Calculation and experimental test of the cooling factor of tungsten", Nucl. Fusion **50** (2010) 025012 (9pp).

[17] D. E. POST et al, "STEADY-STATE RADIATIVE COOLING RATES FOR LOW-DENSITY, HIGH-TEMPERATURE PLASMAS", ATOMIC DATA AND NUCLEAR DATA TABLES 20, 397-439 (1977).

[18] J. Larsen Ionization, "In Foundations of High-Energy-Density Physics: Physical Processes of Matter at Extreme Conditions" 2017 (pp. 122-184), Cambridge University Press, doi:10.1017/9781316403891.005.

[19] P. Beiersdorfer et al, "Atomic physics and ionization balance of high-Z Ions: Critical ingredients for characterizing and understanding high-temperature plasmas", High Energy Density Physics 8 (2012) 271-283

[20] Alexander E. Kramida , Joseph Reader, "Ionization energies of tungsten ions: W2+ through W71+", Atomic Data and Nuclear Data Tables 92 (2006) 457–479.

[21] Stefan M. Kolb, Matthias Stute, Wilhelm Kley, Andrea Mignone, "Radiation hydrodynamics integrated in the code PLUTO", A&A 559, A80 (2013).

[22] J. Colgan et al., "A NEW GENERATION OF LOS ALAMOS OPACITY TABLES", The Astrophysical Journal, 817:116 (10pp), 2016 February 1.

[23] TOPS Opacities/Opacities of mixtures (calculated by TOPS using ATOMIC or LEDCOP elemental opacities) https://aphysics2.lanl.gov.

[24] G. D. TSAKIRIS and K. EIDMANN, "AN APPROXIMATE METHOD FOR CALCULATING PLANCK AND ROSSELAND MEAN OPACITIES IN HOT, DENSE PLASMAS", J. Quant. Spectrosc. Radiat. Transfer Vol. 38, No. 5, pp. 353-368, 1987.
[25] A. W. DeSilva and J. D. Katsouros, "Measurement of the Electrical Conductivity of Metals in the Vicinity of the Critical Point", International Journal of Thermophysics, Vol. 20, No. 4, 1999, pp. 1267-1277.
[26] P. Tolias, "Analytical expressions for thermophysical properties of solid and liquid tungsten relevant for fusion applications", Nuclear Materials and Energy 13 (2017) pp. 42–57.
[27] R.S. Hixson and M.A. Winkler," Thermophysical Properties of Solid and Liquid Tungsten" , International Journal of Thermophysics, Vol. 11, No. 4, 1990, pp. 709-718.
[28] Toru Sasaki et al, "A Semiempirical Evaluation of the Thermal Conductivity in Ablated Dense Tungsten Plasma" , IEEE TRANSACTIONS ON PLASMA SCIENCE, vol. 40, NO. 12, DECEMBER 2012, pp. 3455-3457.
[29] D. Sheftman and Ya. E. Krasik, "Investigation of electrical conductivity and equations of state of non-ideal plasma through underwater electrical wire explosion", PHYSICS OF PLASMAS **17**, 112702 (2010).
[30] A. D. Rakhel, V.N. Korobenko, A. I. Savvatimski and V. E. Fortov, "Electrical Conductivity of Tungsten in a Continuous Transition from Condensed to Gaseous State", International Journal of Thermophysics, Vol. 25, No. 4, July 2004, pp. 1203-1214.
[31] A.W. DeSilva and A. D. Rakhel, "Electrical Resistivity and Thermodynamic Properties of Dense Tungsten Plasma", International Journal of Thermophysics, Vol. 26, No. 4, July 2005, pp. 1137-1149.
[32] Zhijian Fu et al, "Electrical conductivity of warm dense tungsten", High Energy Density Physics , Volume 9, Issue 4, December 2013, Pages 781-786.
[33] A.W. DeSilva and A. D. Rakhel, "Progress in Measurements of the Electrical Conductivity of Metal Plasmas", Contrib. Plasma Phys. **45**, No. 3-4, 236–242 (2005).
[34] Jun Huang et al, "Numerical investigation on the implosion dynamics of wire-array Z-pinches in (r,θ) geometry", PHYSICS OF PLASMAS 19, 062701 (2012).
[35] Z J Fu et al, ''Electrical conductivity and nonmetal–metal transition of dense iron and nickel plasmas'', Phys. Scr. **85** (2012) 045502 (8pp)
[36] Mofreh R. Zaghloul, "A simple theoretical approach to calculate the electrical conductivity of nonideal copper plasma", PHYSICS OF PLASMAS **15**, 042705 2008
[37] M. P. Desjarlais, "Practical Improvements to the Lee-More Conductivity Near the Metal-Insulator Transition", Contrib. Plasma Phys. **41** (2001) 2-3, pp. 267–270.
[38] W. Ebeling et al "Thermophysical Properties of Hot Dense Plasmas", Teubner-Verlag, Stuttgart, 1991, Chap. 6, Sec. 5.
[39] Mofreh R. Zaghloul et al, "Energy-averaged electron–ion momentum transport cross section in the Born Approximation and Debye–Huckel potential: Comparison with the cut-off theory", Physics Letters A 266 (2000)34–40
[40] Mofreh R. Zaghloul et al, "On the average electron–ion momentum transport cross-section in ideal and non-ideal plasmas", Physics Letters A 262 (1999) 86–89
[41] P. Mulser et al, "Revision of the Coulomb logarithm in the ideal plasma", PHYSICS OF PLASMAS 21, 042103 (2014).
[42] M. Mitchener, C.H. Kruger, Partially Ionized Gases, Wiley, New York, 1973
[43] Peter Schwerdtfeger & Jeffrey K. Nagle (2018): 2018 Table of static dipole polarizabilities of the neutral elements in the periodic table, Molecular Physics, DOI: 10.1080/00268976.2018.1535143
[44] S.I Braginskii , "Transport processes in a plasma", Reviews of Plasma Physics, Volume 1, 206-311 (1965).
[45] J. P. Chittenden, "The effect of lower hybrid instabilities on plasma confinement in fiber Z pinches", Physics of Plasmas **2**, 1242 (1995); doi: 10.1063/1.871401.
[46] J. P. Chittenden, "Structural Evolution and Formation of High-Pressure Plasmas in *X* Pinches", PRL **98,** 025003 (2007).
[47] J. P. Chittenden et al, "Plasma formation in metallic wire *Z* pinches", PHYSICAL REVIEW E VOLUME 61, NUMBER 4 APRIL 2000.
[48] A. Ciardi et al, "The evolution of magnetic tower jets in the laboratory", PHYSICS OF PLASMAS **14**, 056501 2007.
[49] Stephen Jardin, " Computational Methods in Plasma Physics", CRC press, Taylor and Francis Group 2010, LLC.
[50] Satoshi Sugimoto et al, " Observation of the thermal conductivity of warm dense tungsten plasma generated by a pulsed-power discharge using laser-induced fluorescence", PHYSICS OF PLASMAS **24**, 072703 (2017).

[51] Frank Modica et al, "The Braginskii model of the Rayleigh-Taylor instability. I. Effects of self-generated magnetic fields and thermal conduction in two dimensions", High Energy Density Physics 9 (2013) 767-780.
[52] Xiao-Guang Wang et al, "Numerical study on magneto-Rayleigh–Taylor instabilities for thin liner implosions on the primary test stand facility", ,Chin. Phys. B Vol. 28, No. 3 (2019) 035201.
[53] S. Orlando et al, "THE IMPORTANCE OF MAGNETIC-FIELD-ORIENTED THERMAL CONDUCTION IN THE INTERACTION OF SNR SHOCKS WITH INTERSTELLAR CLOUDS", The Astrophysical Journal, 678:274-286, 2008 May 1.
[54] Leonardo Di G. Sigalotti et al, "Propagation of thermal and hydro-magnetic waves in an ionizing-recombining hydrogen plasma", PHYSICS OF PLASMAS VOLUME 11, NUMBER 4 APRIL 2004.
[55] Eleuterio F. Toro, "Riemann solvers and numerical methods for fluid dynamics", 2 ed., Springer-Verlag Berlin Heidelberg, 1997.
[56] L. D. Landau, E. M. Lifshitz, "Fluid mechanics", 2 ed., Pergamon Press, Oxford, 1987.
[57] R. Erdélyi, Marcel Goossens, "Viscous computations of resonant absorption of MHD waves in flux tubes by fem", Astrophysics and Space Science March 1994.
[58] Steven A. Balbus, "VISCOUS SHEAR INSTABILITY IN WEAKLY MAGNETIZED, DILUTE PLASMAS", The Astrophysical Journal, 616:857–864, 2004 December 1.
[59] L. Ofman, J.M. Davila, "Coronal heating by the resonant absorption of Alfvén waves: The effect of viscous stress tensor", The Astrophysical Journal, 421:360-371, 1994 January 20.
[60] Alemayehu Mengesha, S. B. Tessema, " Effect of viscosity on propagation of MHD waves in astrophysical plasma", J. Plasma Physics (2013), vol. 79, part 5, pp. 535–544.
[61] Richard Fitzpatrick, "lecture notes a graduate level lecture course", The Institute for Fusion Studies, The University of Texas at Austin Spring 1998.
[62] S. S. Cerri et al, "Extended fluid models: Pressure tensor effects and equilibria", PHYSICS OF PLASMAS 20, 112112 (2013).
[63] Thomas Berlok et al, "Braginskii viscosity on an unstructured, moving mesh accelerated with super-time-stepping", *Monthly Notices of the Royal Astronomical Society*, Volume 491, Issue 2, January 2020, Pages 2919–2938, https://doi.org/10.1093/mnras/stz3115.
[64] L.A. Dorf et al, "Measurements of velocity shear and ion viscosity profile in a magnetohydrodynamic plasma jet", PHYSICS OF PLASMAS **17**, 102101 (2010).
[65] W. M. Stacey Jr. and D. J. Sigmar, "Viscous effects in a collisional tokamak plasma with strong rotation", Phys. Fluids Vol. 28, No. 9, September 1985.
[66] Richard Fitzpatrick**,** "Magnetic reconnection in weakly collisional highly magnetized electron-ion plasmas", PHYSICS OF PLASMAS **17**, 042101 (2010).
[67] D. MacTaggart et al, "Braginskii magnetohydrodynamics for arbitrary magnetic topologies: coronal applications, J. Fluid Mech. (2017), vol. 826, pp. 615-635.
[68] Tanim Islam, Steven Balbus, "DYNAMICS OF THE MAGNETOVISCOUS INSTABILITY", The Astrophysical Journal, 633:328–333, 2005 November 1.
[69] T. Ishikawa et al, " Viscosity of molten Mo, Ta, Os, Re, and W measured by electrostatic levitation", J. Chem. Thermodynamics 65 (2013) 1–6.
[70] Jérôme Daligault et al , "Determination of the shear viscosity of the one-component plasma", PHYSICAL REVIEW E **90**, 033105 (2014).
[71] E. Roediger et al, "Viscous Kelvin–Helmholtz instabilities in highly ionized plasmas", MNRAS **436,** 1721–1740 (2013).
[72] E. Kaselouris et al, "The influence of the solid to plasma phase transition on the generation of plasma instabilities", NATURE COMMUNICATIONS | DOI: 10.1038/s41467-017-02000-6.
[73] E Kaselouris et al, "Preliminary investigation on the use of low current pulsed power Z-pinch plasma devices for the study of early stage plasma instabilities", Plasma Phys. Control. Fusion 60 (2018) 014031 (8pp).
[74] E. Kaselouris et al, "Growth rate studies of the electro-thermo-mechanical instability and its role as seeding mechanism for the generation of plasma instabilities" (to be published in PRL).
[75] QIU Xiao-Ming et al, " Stabilization of Viscosity on Rayleigh-Taylor Instability in Z Pinches", CHIN.PHYS.LETT., Vol. 21, No. 4 (2004) 689.

[76] P. M. Cox, "Resistive and viscous effects on z-pinch stability", Plasma Physics and Controlled Fusion, Vol. 32, No. 7, pp. 553 - 563, 1990.
[77] Zhang Yang, Ding Ning, "Stability analysis of viscous Z-pinch plasma with a sheared axial flow", Chinese Physics B, Vol 17 No 8, August 2008.
[78] J. D. Pecover and J. P. Chittenden, "Instability growth for magnetized liner inertial fusion seeded by electro-thermal, electro-choric, and material strength effects", PHYSICS OF PLASMAS 22, 102701 (2015).

CHAPTER 4

INTRODUCING PHYSICAL AND MATHEMATICAL MODULES IN PLUTO

In this chapter, the one-fluid MHD code PLUTO is described as well as the numerical and mathematical schemes implemented and/or improved, by the author, and the new modifications performed. Such modifications are essential to describe laboratory metallic plasmas such as tungsten, copper or aluminum used in X-pinch or Z-pinch configurations surrounded by a second thin plasma material like plasma air that is perceived as the low density plasma background.

Most of the physical modifications are discussed at Chapter 3, but here we will introduce extra information over the physical, mathematical and numerical implementation procedure of these modifications to the code and the significance they have along the simulation run.

GORGON is the second code, already widely tested, for laboratory plasmas which was used in this research as supplementary tool to evaluate our implementations.

The choice of the appropriate Riemann solver and boundary conditions for the computational box are also analyzed and discussed here! The magnetic field initial topology and the correct updating along the simulation run are among of the most important parameters for the dynamic plasma evolution, pinching procedures and the interplay between thermal and magnetic pressure! The magnetic field topology is seeded here at the very first moment of the simulation, satisfying the Ampere's law and the Stokes theorem along the execution run for the whole volumetric computational territory, correlating the magnetic induction with the current density, updating the induction magnitude as a function of time accordingly with the temporal sinusoidal form of the experimental current (more detailed discussion at the Results Chapter).

The temperature deviations and the diffusion of all the physical variables are affected from the radiation modules of optically thin losses, but mostly from the radiation transport module (also see physics analysis at Chapter 3 PART I and the Results Chapter at the 5.2 and 5.4 section). These are some of the modules and code switches we used and are presented in this Chapter.

Furthermore, there will be a thorough discussion for the initial conditions of the primitive physics variables and the best implementation scheme for specific plasma configurations**.** Not only do we describe the nowadays work, but we also display examples for future work and configurations such as Z-pinch wire arrays and conical arrays. In addition, we introduce mathematical details for the coordinate transformation concerning the spatial plasma and magnetic field implementation from the Local to the Global Cartesian coordinate system.

There are more than one set of suitable initial conditions at most cases, so we will present alternative choices wherever it is convenient. More specifically, there is a presentation of four different pinch configurations initial condition analysis focusing on the coordinate transformation (from the Local to the Global system) of the primitive physics variables and the magnetic field topology. Testing the validity of this transformation, creating "cold" start initial conditions, preliminary results are presented for a two cable X-pinch configuration, providing insights for the physical mechanisms at the initial stages of the plasma jets creation. The spatiotemporal evolution of the Local and the Global magnetic field and the mass density, of a low current, four cable Z-array configuration, is also presented and discussed.

The version of PLUTO used for this work is v.4.2, so all the implementations and modifications are for this specific version (of course it can be expanded to v.4.3 and other future versions). The details for the code, the modules and the download procedure can be found in reference [1].

It should me mentioned here, that all the implementations, modulations and mathematical transformations that are discussed here can be introduced to any MHD one-fluid (or two-fluid) code.

4.1 Mathematical/Physical model of Local plasma centered Z-pinch and X-pinch configuration

In this section we will describe the coordinate relation of a Local centered plasma formation to the Global Cartesian coordinate system x,y,z. There will be a thorough presentation for the geometry fitting of the physical variables, analyzing especially the magnetic field topology being the most difficult task (along with the boundary conditions) for an MHD simulation. The "secret" is the migration from a Local coordinate system of a specific plasma formation to the Global and vise versa. It is crucial because the simulation run is very sensitive for its evolution to the initial condition set and the appropriate spatial geometry of the physics variables at the same moment. These geometry implementations can be seeded at any MHD computational code. So apart from PLUTO we, at the next section present an X-pinch example simulation of another MHD code, GORGON.

Suppose we have one random Local plasma formation, inside a Global spatial domain that has its spatial center at the origin of the local $X_iY_iZ_i$ Cartesian system. A convenient plasma geometry that applies in our case is the cylindrical Local centered formation of a Z-pinch plasma. The understanding of the Local behavior at this formation is the key to describe the initial conditions for the other complex formations like X-pinch, Z-pinch wire arrays and conical wire arrays. This analysis also has no limits for the plasma geometry as long as we can express all the physical variables to Local Cartesian coordinate functions. Then a superposition of the physics variables, of all the Local plasma configurations, is adopted to describe the whole plasma variable formation to the Global system.

From now on, along this analysis, the Local spatially displaced coordinate system will be denoted as (X_i,Y_i,Z_i), the Global coordinate as (x,y,z) and the Local rotated as (x_i,y_i,z_i). If displacement and rotation take place, we will use the convenient notation of the last one, (x_i,y_i,z_i).

4.1.1 Mathematical description of the displacement and rotation of the Local Axis coordinate system relative to the Global one

Suppose the origin of a single wire is displaced to the (x_{0i},y_{0i},z_{0i}) point of the Global system where $i=1,\ldots,n$ and n denotes the number of the Local plasma formations (figure 4.1). The Galilean relations between the Local and Global coordinates are:

$$\begin{aligned} X_i &= x - x_{0i} \\ Y_i &= y - y_{0i} \\ Z_i &= z - z_{0i} \end{aligned} \qquad (4.1)$$

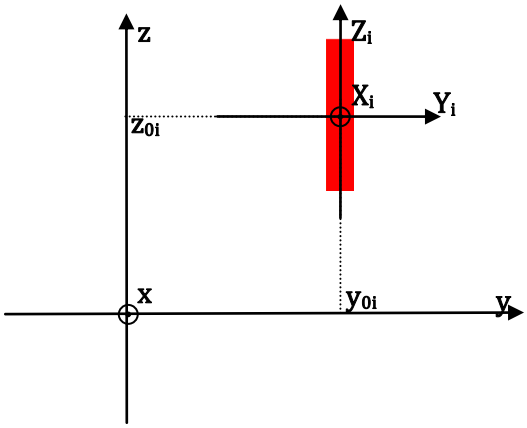

Figure 4.1: *Presentation of the Local coordinate (X_i,Y_i,Z_i) and its displacement to the Global (x,y.z).*

Then we can rotate the Local system with the rotation axis as the Local X_i, counter clockwise with a positive rotation angle a_{1i} (consider right handed Cartesian systems). The new coordinates are related to the old ones through the rotation matrix **Rx**:

$$\begin{bmatrix} x_i \\ y_i \\ z_i \end{bmatrix} = \begin{bmatrix} 1 & 0 & 0 \\ 0 & cosa_{1i} & sina_{1i} \\ 0 & -sina_{1i} & cosa_{1i} \end{bmatrix} \begin{bmatrix} X_i \\ Y_i \\ Z_i \end{bmatrix} = Rx \begin{bmatrix} x - x_{oi} \\ y - y_{oi} \\ z - z_{oi} \end{bmatrix} \tag{4.2}$$

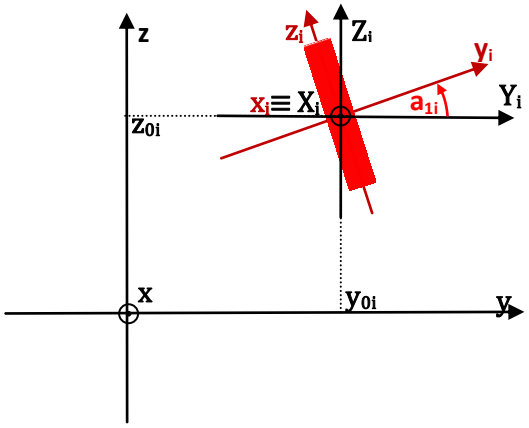

Figure 4.2: *Presentation of the Local coordinate (x_i,y_i,z_i) and its rotation angle a_{1i} compared with the Local (X_i,Y_i,Z_i) and its displacement to the Global (x,y,z).*

If the rotation is similar but to the Y_i axis with a positive rotation angle $a_{2i,}$ the coordinates are related:

$$\begin{bmatrix} x_i \\ y_i \\ z_i \end{bmatrix} = \begin{bmatrix} cosa_{2i} & 0 & -sina_{2i} \\ 0 & 1 & 0 \\ sina_{2i} & 0 & cosa_{2i} \end{bmatrix} \begin{bmatrix} X_i \\ Y_i \\ Z_i \end{bmatrix} = Ry \begin{bmatrix} x - x_{oi} \\ y - y_{oi} \\ z - z_{oi} \end{bmatrix} \tag{4.3}$$

and finally for the Z_i rotation axis with a positive rotation angle $a_{3i,}$ we have:

$$\begin{bmatrix} x_i \\ y_i \\ z_i \end{bmatrix} = \begin{bmatrix} cosa_{3i} & sina_{3i} & 0 \\ -sina_{3i} & cosa_{3i} & 0 \\ 0 & 0 & 1 \end{bmatrix} \begin{bmatrix} X_i \\ Y_i \\ Z_i \end{bmatrix} = Rz \begin{bmatrix} x - x_{oi} \\ y - y_{oi} \\ z - z_{oi} \end{bmatrix} \tag{4.4}$$

These rotations are separate from each other. If we want to rotate more than once, we have to multiply the Local Galilean system with the Rotation matrices, i.e. :

$$\mathbf{RxRyRz}\begin{bmatrix}\mathbf{X_i}\\ \mathbf{Y_i}\\ \mathbf{Z_i}\end{bmatrix} = \mathbf{RxRy}\begin{bmatrix}\mathbf{X'_i}\\ \mathbf{Y'_i}\\ \mathbf{Z'_i}\end{bmatrix} = \mathbf{Rx}\begin{bmatrix}\mathbf{X''_i}\\ \mathbf{Y''_i}\\ \mathbf{Z''_i}\end{bmatrix} = \begin{bmatrix}\mathbf{x_i}\\ \mathbf{y_i}\\ \mathbf{z_i}\end{bmatrix} \tag{4.5}$$

This is a rotation first around the Z_i axis, second a rotation around the new $\mathbf{Y_i}'$ axis and third a rotation around the second rotation $\mathbf{X_i}''$ axis. So with these displacements of the axes origin and the rotation matrices we can have any symmetric plasma configuration of one or more parts anywhere in space and with any orientation inside the computational domain.

When cylindrical plasma geometry is considered, we introduce some extra definitions for the Local system. The presentation is also for the magnetic field components that are vital to have a correct geometry displacement and rotation for the initial conditions of the problem. In this case, for simplicity reasons, we consider no displacement of the Local Axis origin due to the Global one. If there is such a displacement after the rotation transformation, we can use the 4.1 Galilean equation correlation and replace the Local X_i,Y_i,Z_i at the 4.3, 4.4 and 4.5 with the ones of 4.1. A specific example of both rotation and displacement is the Conical array case that will be presented in a few pages**.** Our assumption is for an infinite plasma cylinder that has an azimuthal magnetic field topology! This holds for the central plasma of an X-pinch or a Z-pinch configuration and is not correct for the plasma near the electrodes. This analysis is valid for most cases due to the smaller computational domain than the experimental one.

a. If the plasma cylinder is along the $\mathbf{x_i}$ Local axis with current density **J** at the same direction of the positive $\mathbf{x_i}$ axis, we have:

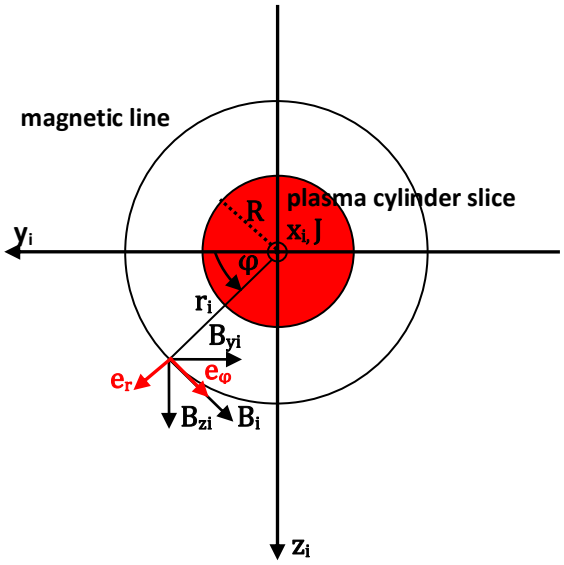

Figure 4.3: *Presentation of the y_iz_i slice of the Local coordinate system, the illustration of the plasma cylinder slice and the azimuthal magnetic field line.*

$$r_i = \sqrt{z_i^2 + y_i^2} \tag{4.6}$$

and for the azimouthal magnetic field :

$$\mathbf{B_i} = B_i(r_i)\mathbf{e_\varphi} = B_i(r_i)\begin{bmatrix}\mathbf{0}\\ \mathbf{-sin\varphi}\\ \mathbf{cos\varphi}\end{bmatrix} = B_i(r_i)\begin{bmatrix}\mathbf{0}\\ -\frac{\mathbf{z_i}}{\mathbf{r_i}}\\ \frac{\mathbf{y_i}}{\mathbf{r_i}}\end{bmatrix} \tag{4.7}$$

i. If the rotation is around the X_i Axis we have:

$$\mathbf{B_i} = B_i(r_i)\begin{bmatrix}\mathbf{0}\\ \mathbf{-sin\varphi}\ \hat{\mathbf{j}}_\mathbf{1}\\ \mathbf{cos\varphi}\ \hat{\mathbf{k}}_\mathbf{1}\end{bmatrix} = \left(\frac{B_i(r_i)}{r_i}\right)[\,\mathbf{0}\quad -\mathbf{z_i}\quad \mathbf{y_i}]\mathbf{Rx}\begin{bmatrix}\hat{\mathbf{i}}\\ \hat{\mathbf{j}}\\ \hat{\mathbf{k}}\end{bmatrix} = \left(\frac{B_i(r_i)}{r_i}\right)\begin{bmatrix}\mathbf{0}\\ (-\mathbf{z_i cosa_{1i}} - \mathbf{y_i sina_{1i}})\hat{\mathbf{j}}\\ (-\mathbf{z_i sina_{1i}} + \mathbf{y_i cosa_{1i}})\hat{\mathbf{k}}\end{bmatrix} \tag{4.8}$$

where $\hat{\mathbf{i}}_\mathbf{1}$, $\hat{\mathbf{j}}_\mathbf{1}$, $\hat{\mathbf{k}}_\mathbf{1}$ are the rotated unit vectors of the Local system and $\hat{\mathbf{i}}$, $\hat{\mathbf{j}}$, $\hat{\mathbf{k}}$ are the ones of the Global.

ii. If the rotation is around the Y_i Axis :

$$\mathbf{B_i} = B_i(r_i)\begin{bmatrix}\mathbf{0}\\ \mathbf{-sin\varphi}\ \hat{\mathbf{j}}_\mathbf{1}\\ \mathbf{cos\varphi}\hat{\mathbf{k}}_\mathbf{1}\end{bmatrix} = \left(\frac{B_i(r_i)}{r_i}\right)[\,\mathbf{0}\quad -\mathbf{z_i}\quad \mathbf{y_i}]\mathbf{Ry}\begin{bmatrix}\hat{\mathbf{i}}\\ \hat{\mathbf{j}}\\ \hat{\mathbf{k}}\end{bmatrix} = \left(\frac{B_i(r_i)}{r_i}\right)\begin{bmatrix}\mathbf{y_i sina_{2i}}\hat{\mathbf{i}}\\ -\mathbf{z_i}\hat{\mathbf{j}}\\ \mathbf{y_i cosa_{2i}}\hat{\mathbf{k}}\end{bmatrix} \tag{4.9}$$

iii. If the rotation is around the Z_i Axis :

$$\mathbf{B_i} = B_i(r_i)\begin{bmatrix}\mathbf{0}\\ \mathbf{-sin\varphi}\ \hat{\mathbf{j}}_\mathbf{1}\\ \mathbf{cos\varphi}\hat{\mathbf{k}}_\mathbf{1}\end{bmatrix} = \left(\frac{B_i(r_i)}{r_i}\right)[\,\mathbf{0}\quad -\mathbf{z_i}\quad \mathbf{y_i}]\mathbf{Rz}\begin{bmatrix}\hat{\mathbf{i}}\\ \hat{\mathbf{j}}\\ \hat{\mathbf{k}}\end{bmatrix} = \left(\frac{B_i(r_i)}{r_i}\right)\begin{bmatrix}\mathbf{z_i sina_{3i}}\hat{\mathbf{i}}\\ -\mathbf{z_i cosa_{3i}}\hat{\mathbf{j}}\\ \mathbf{y_i}\hat{\mathbf{k}}\end{bmatrix} \tag{4.10}$$

b. If the plasma cylinder is along the $\mathbf{y_i}$ Local axis with current density **J** at the ~~same~~ direction of the positive $\mathbf{y_i}$ axis, we have:

$$r_i = \sqrt{z_i^2 + x_i^2} \tag{4.11}$$

and for the azimouthal magnetic field :

$$\mathbf{B_i} = B_i(r_i)\mathbf{e_\varphi} = B_i(r_i)\begin{bmatrix}\mathbf{cos\varphi}\\ \mathbf{0}\\ \mathbf{-sin\varphi}\end{bmatrix} = B_i(r_i)\begin{bmatrix}\frac{\mathbf{z_i}}{\mathbf{r_i}}\\ \mathbf{0}\\ -\frac{\mathbf{x_i}}{\mathbf{r_i}}\end{bmatrix} \tag{4.12}$$

i. If the rotation is around the X_i Axis we have:

$$\mathbf{B_i} = \mathrm{B_i(r_i)}\begin{bmatrix} \frac{\mathbf{z_i}}{\mathbf{r_i}}\widehat{\mathbf{i}_1} \\ \mathbf{0} \\ \frac{-\mathbf{x_i}}{\mathbf{r_i}}\widehat{\mathbf{k}_1} \end{bmatrix} = \left(\frac{\mathrm{B_i(r_i)}}{\mathrm{r_i}}\right)[\,\mathbf{z_i}\ \ \mathbf{0}\ \ -\mathbf{x_i}]\mathbf{Rx}\begin{bmatrix} \hat{\boldsymbol{\imath}} \\ \hat{\boldsymbol{\jmath}} \\ \widehat{\boldsymbol{k}} \end{bmatrix} = \left(\frac{\mathrm{B_i(r_i)}}{\mathrm{r_i}}\right)\begin{bmatrix} \mathbf{z_i}\hat{\mathbf{i}} \\ \mathbf{x_i sina_{1i}}\hat{\mathbf{j}} \\ -\mathbf{x_i cosa_{1i}}\hat{\mathbf{k}} \end{bmatrix} \tag{4.13}$$

ii. If the rotation is around the Y_i Axis:

$$\mathbf{B_i} = \mathrm{B_i(r_i)}\begin{bmatrix} \frac{\mathbf{z_i}}{\mathbf{r_i}}\widehat{\mathbf{i}_1} \\ \mathbf{0} \\ \frac{-\mathbf{x_i}}{\mathbf{r_i}}\widehat{\mathbf{k}_1} \end{bmatrix} = \left(\frac{\mathrm{B_i(r_i)}}{\mathrm{r_i}}\right)[\,\mathbf{z_i}\ \ \mathbf{0}\ \ -\mathbf{x_i}]\mathbf{Ry}\begin{bmatrix} \hat{\boldsymbol{\imath}} \\ \hat{\boldsymbol{\jmath}} \\ \widehat{\boldsymbol{k}} \end{bmatrix} = \left(\frac{\mathrm{B_i(r_i)}}{\mathrm{r_i}}\right)\begin{bmatrix} (\mathbf{z_i cosa_{2i}} - \mathbf{x_i sina_{2i}})\hat{\mathbf{i}} \\ \mathbf{0} \\ (-\mathbf{z_i sina_{2i}} - \mathbf{x_i cosa_{2i}})\hat{\mathbf{k}} \end{bmatrix} \tag{4.14}$$

iii. If the rotation is around the Z_i Axis:

$$\mathbf{B_i} = \mathrm{B_i(r_i)}\begin{bmatrix} \frac{\mathbf{z_i}}{\mathbf{r_i}}\widehat{\mathbf{i}_1} \\ \mathbf{0} \\ \frac{-\mathbf{x_i}}{\mathbf{r_i}}\widehat{\mathbf{k}_1} \end{bmatrix} = \left(\frac{\mathrm{B_i(r_i)}}{\mathrm{r_i}}\right)[\,\mathbf{z_i}\ \ \mathbf{0}\ \ -\mathbf{x_i}]\mathbf{Rz}\begin{bmatrix} \hat{\mathbf{i}} \\ \hat{\mathbf{j}} \\ \hat{\mathbf{k}} \end{bmatrix} = \left(\frac{\mathrm{B_i(r_i)}}{\mathrm{r_i}}\right)\begin{bmatrix} \mathbf{z_i cosa_{3i}}\hat{\mathbf{i}} \\ \mathbf{z_i sina_{3i}}\hat{\mathbf{j}} \\ -\mathbf{x_i}\hat{\mathbf{k}} \end{bmatrix} \tag{4.15}$$

c. Finally, if the plasma cylinder is along the $\mathbf{z_i}$ Local axis with current density $\mathbf{J}$ at the direction of the positive $\mathbf{z_i}$ axis, we have:

$$\mathrm{r_i} = \sqrt{\mathrm{y_i^2} + \mathrm{x_i^2}} \tag{4.16}$$

and for the azimouthal magnetic field :

$$\mathbf{B_i} = \mathrm{B_i(r_i)}\mathbf{e_\varphi} = \mathrm{B_i(r_i)}\begin{bmatrix} -\mathbf{sin\varphi} \\ \mathbf{cos\varphi} \\ \mathbf{0} \end{bmatrix} = \mathrm{B_i(r_i)}\begin{bmatrix} -\frac{\mathbf{y_i}}{\mathbf{r_i}} \\ \frac{\mathbf{x_i}}{\mathbf{r_i}} \\ \mathbf{0} \end{bmatrix} \tag{4.17}$$

i. If the rotation is around the X_i Axis we have:

$$\mathbf{B_i} = \mathrm{B_i(r_i)}\begin{bmatrix} -\frac{\mathbf{y_i}}{\mathbf{r_i}}\widehat{\mathbf{i}_1} \\ \frac{\mathbf{x_i}}{\mathbf{r_i}}\widehat{\mathbf{j}_1} \\ \mathbf{0} \end{bmatrix} = \left(\frac{\mathrm{B_i(r_i)}}{\mathrm{r_i}}\right)[-\mathbf{y_i}\ \ \mathbf{x_i}\ \ \ \mathbf{0}]\mathbf{Rx}\begin{bmatrix} \hat{\mathbf{i}} \\ \hat{\mathbf{j}} \\ \hat{\mathbf{k}} \end{bmatrix} = \left(\frac{\mathrm{B_i(r_i)}}{\mathrm{r_i}}\right)\begin{bmatrix} -\mathbf{y_i}\hat{\mathbf{i}} \\ \mathbf{x_i cosa_{1i}}\hat{\mathbf{j}} \\ \mathbf{x_i sina_{1i}}\hat{\mathbf{k}} \end{bmatrix} \tag{4.18}$$

ii. If the rotation is around the Y_i Axis:

$$\mathbf{B_i} = \mathrm{B_i(r_i)}\begin{bmatrix} -\frac{\mathbf{y_i}}{\mathbf{r_i}}\widehat{\mathbf{i}_1} \\ \frac{\mathbf{x_i}}{\mathbf{r_i}}\widehat{\mathbf{j}_1} \\ \mathbf{0} \end{bmatrix} = \left(\frac{\mathrm{B_i(r_i)}}{\mathrm{r_i}}\right)[-\mathbf{y_i}\ \ \mathbf{x_i}\ \ \ \mathbf{0}]\mathbf{Ry}\begin{bmatrix} \hat{\mathbf{i}} \\ \hat{\mathbf{j}} \\ \hat{\mathbf{k}} \end{bmatrix} = \left(\frac{\mathrm{B_i(r_i)}}{\mathrm{r_i}}\right)\begin{bmatrix} -\mathbf{y_i cosa_{2i}}\hat{\mathbf{i}} \\ \mathbf{x_i}\hat{\mathbf{j}} \\ \mathbf{y_i sina_{2i}}\hat{\mathbf{k}} \end{bmatrix} \tag{4.19}$$

iii. If the rotation is around the Z_i Axis:

$$\mathbf{B_i} = \mathrm{B_i}(\mathrm{r_i})\begin{bmatrix} -\frac{\mathbf{y_i}}{\mathbf{r_i}}\hat{\mathbf{i}} \\ \frac{\mathbf{x_i}}{\mathbf{r_i}}\hat{\mathbf{j}} \\ \mathbf{0} \end{bmatrix} = \left(\frac{\mathrm{B_i}(\mathrm{r_i})}{\mathrm{r_i}}\right)[-\mathbf{y_i} \quad \mathbf{x_i} \quad \mathbf{0}]\mathbf{Rz}\begin{bmatrix} \hat{\mathbf{i}} \\ \hat{\mathbf{j}} \\ \hat{\mathbf{k}} \end{bmatrix} = \left(\frac{\mathrm{B_i}(\mathrm{r_i})}{\mathrm{r_i}}\right)\begin{bmatrix} (-\mathbf{y_i cosa_{3i}} - \mathbf{x_i sina_{3i}})\hat{\mathbf{i}} \\ (\mathbf{x_i cosa_{3i}} - \mathbf{y_i sina_{3i}})\hat{\mathbf{j}} \\ \mathbf{0} \end{bmatrix} \quad (4.20)$$

It should be mentioned here that all the Cartesian coordinates of the Local system (x_i,y_i,z_i) that we present at the final equality of each of the above equations, are correlated to the ones of the Global (x,y,z) through the rotations and displacements of the 4.1 to 4.5 equation system!

4.1.2 Specific Examples

All examples discussed here are based on a cylindrical plasma configuration geometry of single-wire (Z-pinch) or more displaced cylinders (wire array Z-pinch) or rotated cylinders (two- wire X-pinch) or a combination of rotation and displacement (conical arrays Z-pinch).

A. Z-pinch of a single wire

The single wire Z-pinch configuration is the simplest one. The Local and Global system can be identical for this case. We can have any of the Local/Global Axis as the plasma cylinder's Axis e.g. z Axis. If we consider no rotation we have:

$$\begin{gathered} \mathrm{i}=1 \text{ due to single wire} \\ (\mathbf{x_{01}}, \mathbf{y_{01}}, \mathbf{z_{01}})=(0,0,0) \\ (\mathbf{a_{11}}, \mathbf{a_{21}}, \mathbf{a_{31}})=(0,0,0) \\ \mathbf{x_1}=\mathbf{X_1}=\mathbf{x} \\ \mathbf{y_1}=\mathbf{Y_1}=\mathbf{y} \\ \mathbf{z_1}=\mathbf{Z_1}=\mathbf{z} \\ \text{with } \mathrm{r_1} = \sqrt{\mathrm{y_1^2} + \mathrm{x_1^2}} \end{gathered} \quad (4.21)$$

For the scalar variables such as thermal pressure P and mass density ρ we perform a Local Gaussian or Parabolic fit distribution (satisfying the Bennet equilibrium relation) or a Linear combination of these two. Depiction of mass density profiles and the related lineout graphs at the initial simulation time will be given at the related sub-section of section 4.2 from the output data of the code.

These approaches permit us to consider only one function for the whole computational domain that is rapidly decreasing outside the plasma cylinder. For the azimouthal magnetic field we have:

$$\mathbf{B_1} = B_1(r_1)\mathbf{e_\varphi} = B_1(r_1)\begin{bmatrix}-\sin\varphi\\ \cos\varphi\\ 0\end{bmatrix} = B_1(r_1)\begin{bmatrix}-\frac{y_1}{r_1}\hat{\mathbf{i}}\\ \frac{x_1}{r_1}\hat{\mathbf{j}}\\ 0\end{bmatrix} \tag{4.22}$$

The definition of r_1 can also affect the current density profile if we want to take into account the skin effect [2] (discussed in 2.1.1 sub-section).

Thus, the magnetic field magnitude in equation 4.22 for a single plasma cylinder in c.g.s is:

$$B_1(r_1) = \frac{4\pi}{c}\frac{\int_0^{r_1} J_z(r)rdr}{r_1} \tag{4.23}$$

These profiles will be presented at visualization section 4.2.

Of course any displacement for the axes origin and any rotation according to the previous analysis can be used.

B. Wire Array Z-pinch configuration

The Wire Array configuration consists of n parallel cables that have one of the Global axis as the symmetry axis, i.e. z axis and have the same angle displacement θ from each other. If we consider no rotation we have:

$$\mathbf{i=1,\ldots,n} \tag{4.24}$$

where n is the number of plasma cylinders. The origin of each Local cable is displaced to the Global point:

$$\mathbf{(x_{0i},y_{0i},z_{0i})=(R_{0i}\cos(\theta_0+(i-1)\cdot\theta),\ R_{0i}\sin(\theta_0+(i-1)\cdot\theta),\ 0)} \tag{4.25}$$

where θ_0 is the positive angle of R_{01} relative to the x Global axis and

$$\begin{gathered}\mathbf{(a_{1i},a_{2i},a_{3i})=(0,0,0)}\\ \mathbf{x_i=X_i=x-x_{0i}}\\ \mathbf{y_i=Y_i=y-y_{0i}}\\ \mathbf{z_i=Z_i=z}\\ R_{01}=R_{02=\ldots=}R_{0n}\\ r_i=\sqrt{y_i^2+x_i^2}\ (z_i \text{ is the Local symmetry plasma axis})\end{gathered} \tag{4.26}$$

while the azimouthal magnetic field derives from:

$$\mathbf{B_i} = B_i(r_i)\mathbf{e_\varphi} = B_i(r_i)\begin{bmatrix}-\sin\varphi_i\\ \cos\varphi_i\\ 0\end{bmatrix} = B_i(r_i)\begin{bmatrix}-\frac{y_i}{r_i}\hat{\mathbf{i}}\\ \frac{x_i}{r_i}\hat{\mathbf{j}}\\ 0\end{bmatrix} = \begin{bmatrix}B_{xi}\hat{\mathbf{i}}\\ B_{yi}\hat{\mathbf{j}}\\ B_{zi}\hat{\mathbf{k}}\end{bmatrix} \tag{4.27}$$

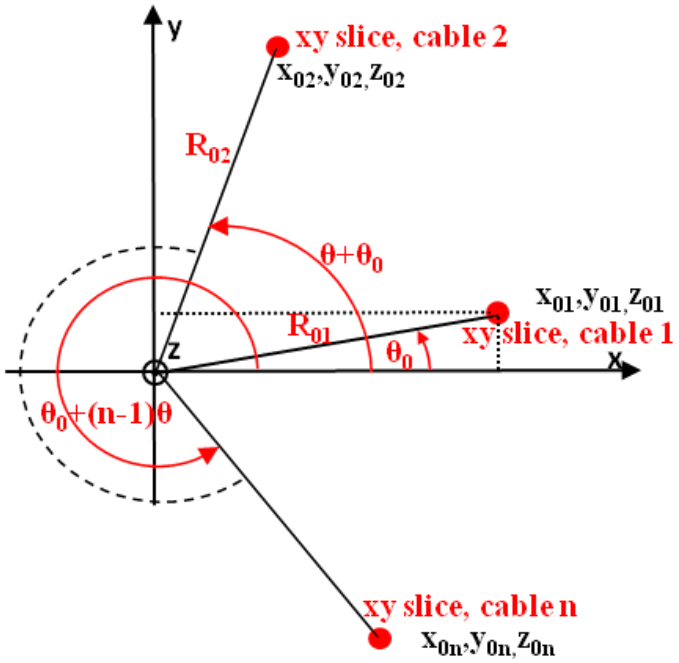

Figure 4.4: *Presentation of the xy slice of the Global coordinate system, the depiction of the plasma cylinders slices, the displacement radius R_{0i} and the rotation angle ϑ_n.*

As for the Global values of the physic variables, we can consider for both scalar and vectors that we can add the components of each plasma cable to take the total value. So:

$$\mathbf{B_{GLOBAL}} = \begin{bmatrix} \sum_{i=1}^{n} \mathbf{B_{xi}\hat{i}} \\ \sum_{i=1}^{n} \mathbf{B_{yi}\hat{j}} \\ \sum_{i=1}^{n} \mathbf{B_{zi}\hat{k}} \end{bmatrix}$$

$$\mathbf{P_{GLOBAL}} = \sum_{i=1}^{n} \mathbf{P_i} \qquad (4.28)$$

$$\boldsymbol{\rho}_{\mathbf{GLOBAL}} = \sum_{i=1}^{n} \boldsymbol{\rho}_{\mathbf{i}}$$

where the thermal pressure and mass density profiles resemble the ones described previously for one wire for each Local system

C. X-pinch of two wires

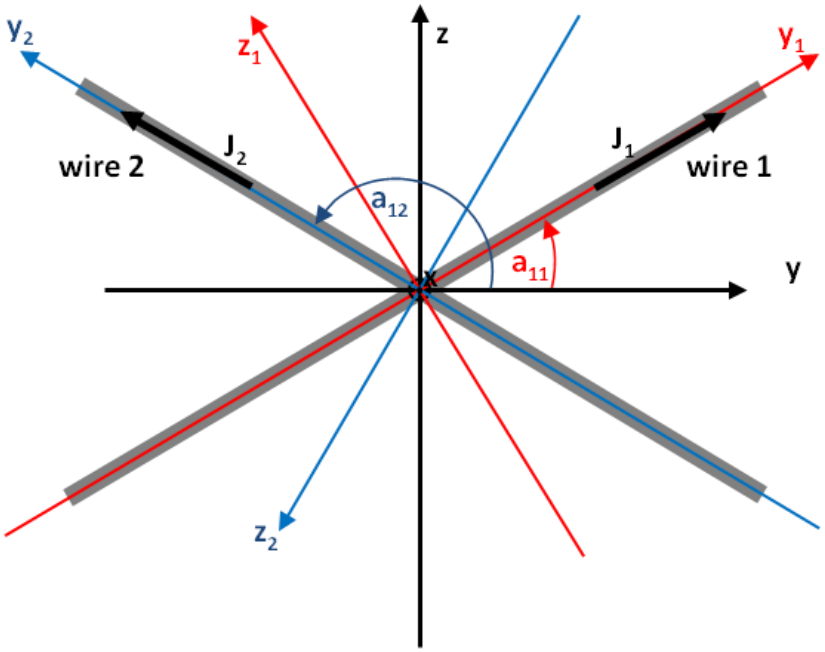

Figure 4.5: *Schematic representation of the yz slice of the Global coordinate system and the illustration of the plasma cylinder slices of the X-pinch configuration. The Local (x,y_1,z_1) and (x,y_2,z_2) coordinate systems and the rotation angles a_{11} and a_{12} of each X wire are depicted with red and blue colours respectively.*

The cartesian coordinate system is shown in the above figure, where the x axis is vertical to the yz plane. The X-pinch configuration is centered at the original xyz cartesian system. The rotated coordinate systems have a common x axis and the rotation angle is a_{11} for the y_1 and z_1 and a_{12} for the y_2 and z_2 axis respectively to the original xyz cartesian system. They are named y_1 and z_1 axis and they form a new coordinate system with the common x axis. Along the y_1 axis is the one of the two axisymmetric plasma wires of the X-pinch configuration with the current density J_1 pointing at the possitive direction of the axis. We have similar spatial distribution for the second plasma wire along of y_2 axis of the other rotated system. We consider that the initial formation of the X-pinch consists of two independent cylindrical wires. At the crosspoint we consider the coexistence of the two wires while the values of all physics variables are considered as the linear sum of the components of each plasma wire as we present below:

$$\mathbf{i=1,2} \text{ due to two independent plasma cylinders}$$

$$\begin{gathered}(\mathbf{x_{01}, y_{01}, z_{01}})=(0,0,0)\\(\mathbf{a_{11},a_{21},a_{31}})=(\mathbf{a_{11}},0,0)\\(\mathbf{a_{12},a_{22},a_{32}})=(\mathbf{a_{12}},0,0)\\\text{where } \mathbf{a_{12}=\pi- a_{11}}\end{gathered} \tag{4.29}$$

We define:

$$r_1 = \sqrt{x_1^2 + z_1^2}$$

$$r_2 = \sqrt{x_2^2 + z_2^2} \tag{4.30}$$

$$\mathbf{B_1} = B_1(r_1)\begin{bmatrix} \frac{\mathbf{z_1}}{\mathbf{r_1}}\hat{\mathbf{i}}_1 \\ \mathbf{0} \\ \frac{-\mathbf{x_1}}{\mathbf{r_1}}\hat{\mathbf{k}}_1 \end{bmatrix} = \left(\frac{B_1(r_1)}{r_1}\right)[\,\mathbf{z_1} \quad \mathbf{0} \quad -\mathbf{x_1}]\mathbf{Rx}\begin{bmatrix}\hat{\mathbf{i}}\\ \hat{\mathbf{j}}\\ \hat{\mathbf{k}}\end{bmatrix} = \left(\frac{B_1(r_1)}{r_1}\right)\begin{bmatrix}\mathbf{z_1}\hat{\mathbf{i}}\\ \mathbf{x_1 sina_{11}}\hat{\mathbf{j}}\\ -\mathbf{x_1 cosa_{11}}\hat{\mathbf{k}}\end{bmatrix} = \begin{bmatrix}\mathbf{B_{x1}}\hat{\mathbf{i}}\\ \mathbf{B_{y1}}\hat{\mathbf{j}}\\ \mathbf{B_{z1}}\hat{\mathbf{k}}\end{bmatrix}$$

$$\mathbf{B_2} = B_2(r_2)\begin{bmatrix} \frac{\mathbf{z_2}}{\mathbf{r_2}}\hat{\mathbf{i}}_2 \\ \mathbf{0} \\ \frac{-\mathbf{x_2}}{\mathbf{r_2}}\hat{\mathbf{k}}_2 \end{bmatrix} = \left(\frac{B_2(r_2)}{r_2}\right)[\,\mathbf{z_2} \quad \mathbf{0} \quad -\mathbf{x_2}]\mathbf{Rx}\begin{bmatrix}\hat{\mathbf{i}}\\ \hat{\mathbf{j}}\\ \hat{\mathbf{k}}\end{bmatrix} = \left(\frac{B_2(r_2)}{r_2}\right)\begin{bmatrix}\mathbf{z_2}\hat{\mathbf{i}}\\ \mathbf{x_2 sina_{12}}\hat{\mathbf{j}}\\ -\mathbf{x_2 cosa_{12}}\hat{\mathbf{k}}\end{bmatrix} = \begin{bmatrix}\mathbf{B_{x2}}\hat{\mathbf{i}}\\ \mathbf{B_{y2}}\hat{\mathbf{j}}\\ \mathbf{B_{z2}}\hat{\mathbf{k}}\end{bmatrix}$$

A xz_1 and xz_2 slice of the wires 1 and 2 are shown in figure 4.6. We consider that the maximum of the Local magnetic field is at R_1 and R_2 respectively, while the magnetic field spatial distribution follows the Ampere's law. The magnetic field profile has an azimuthal form.

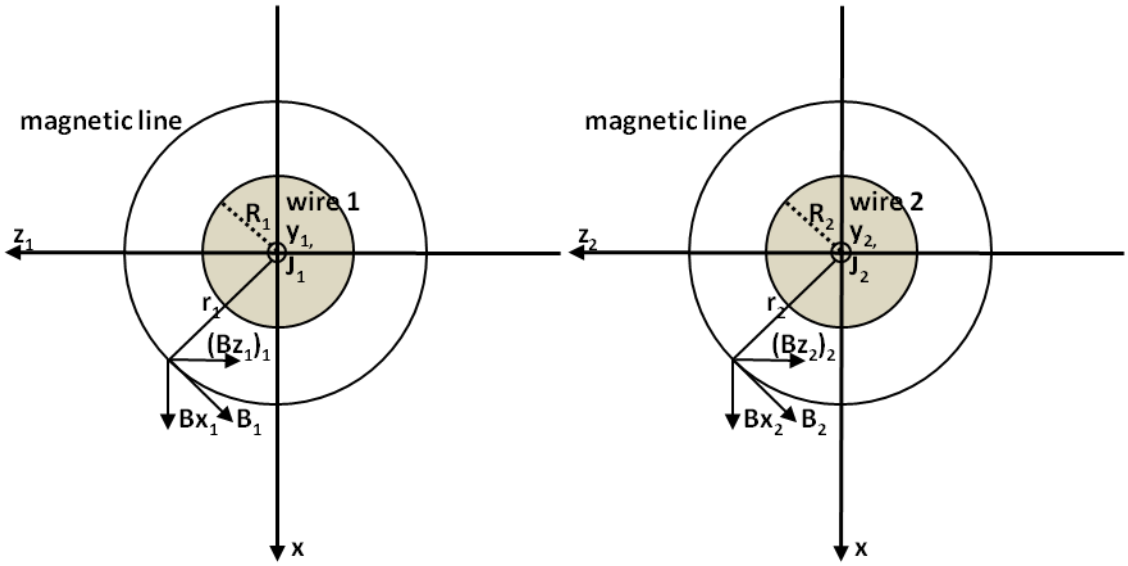

Figure 4.6: *Presentation of the xz_1 and xz_2 slice of the Local coordinate system of the plasma cylinders of the X-pinch configuration. The azimuthal magnetic field and the magnetic field lines are shown outside the plasma cylinder.*

When the Global values of the variables are concerned, we can take into consideration -for the scalar and vector variables- the components of each plasma wire, adding them to take the total Global value. As a result:

$$\mathbf{B_{GLOBAL}} = \begin{bmatrix} \sum_{i=1}^{2} \mathbf{B_{xi}\hat{i}} \\ \sum_{i=1}^{2} \mathbf{B_{yi}\hat{j}} \\ \sum_{i=1}^{2} \mathbf{B_{zi}\hat{k}} \end{bmatrix}$$

$$\mathbf{P_{GLOBAL}} = \sum_{i=1}^{2} \mathbf{P_i} \qquad (4.31)$$

$$\boldsymbol{\rho}_{\mathbf{GLOBAL}} = \sum_{i=1}^{2} \boldsymbol{\rho}_{\mathbf{i}}$$

where the thermal pressure and mass density profiles resemble the ones described previously for one wire for each Local system.

D. Conical wire Arrays

The Conical Wire Array configuration consists of n parallel wires that have one of the Global axis as the symmetry axis, i.e. z Axis for the centres of masses of plasma cylinders and have the same displacement angle θ from each other at the xy Global plane. We consider:

$$\mathbf{i=1,\ldots,n} \qquad (4.32)$$

where n is the number of plasma cylinders. The origin of each Local cable is displaced to the Global point:

$$\mathbf{(x_{0i},y_{0i},z_{0i})=(R_{0i}\cos(\theta_0+(i-1)\cdot\theta),\ R_{0i}\sin(\theta_0+(i-1)\cdot\theta),\ 0)} \qquad (4.33)$$

where θ_0 is the positive angle of R_{01} relative to the x Global axis and

$$\begin{gathered} \mathbf{(a_{1i},a_{2i},a_{3i})=(a,0,0)} \\ \mathbf{x_i=X_i=x-x_{0i}} \\ \mathbf{Y_i=y-y_{0i}} \\ \mathbf{Z_i=z} \\ R_{01}= R_{02=\ldots=} R_{0n} \end{gathered} \qquad (4.34)$$

with $r_i = \sqrt{z_i^2 + x_i^2}$ (y_i is the Local symmetry plasma axis)

$$\text{where} \begin{bmatrix} \mathbf{x_i} \\ \mathbf{y_i} \\ \mathbf{z_i} \end{bmatrix} = \begin{bmatrix} \mathbf{1} & \mathbf{0} & \mathbf{0} \\ \mathbf{0} & \mathbf{cosa} & \mathbf{sina} \\ \mathbf{0} & \mathbf{-sina} & \mathbf{cosa} \end{bmatrix} \begin{bmatrix} \mathbf{X_i} \\ \mathbf{Y_i} \\ \mathbf{Z_i} \end{bmatrix} = \mathbf{Rx} \begin{bmatrix} \mathbf{x - x_{oi}} \\ \mathbf{y - y_{oi}} \\ \mathbf{z} \end{bmatrix}$$

The positive angle a is the rotation angle of y_i and z_i axis of each Local system. Before rotation we have displaced the cylinder centres as in the Z array configuration of the B case. Then we can rotate again as in equation 4.2 the Local system with rotation axis the Local X_i, counter-clockwise with the positive rotation angle a. The new coordinates are related to the previous through the rotation matrix **Rx**, while the azimuthal magnetic field derives from:

$$\mathbf{B_i} = B_i(r_i)\begin{bmatrix} \frac{\mathbf{z_i}}{\mathbf{r_i}} \\ \mathbf{0} \\ \frac{-\mathbf{x_i}}{\mathbf{r_i}} \end{bmatrix} = \left(\frac{B_i(r_i)}{r_i}\right)[\,\mathbf{z_i} \quad \mathbf{0} \quad -\mathbf{x_i}]\mathbf{Rx}\begin{bmatrix} \hat{\mathbf{i}} \\ \hat{\mathbf{j}} \\ \hat{\mathbf{R}} \end{bmatrix} = \left(\frac{B_i(r_i)}{r_i}\right)\begin{bmatrix} \mathbf{z_i}\hat{\mathbf{i}} \\ (\mathbf{x}-\mathbf{x_{oi}})\mathbf{sina}\hat{\mathbf{j}} \\ -(\mathbf{x}-\mathbf{x_{oi}})\mathbf{cosa}\hat{\mathbf{k}} \end{bmatrix} \tag{4.35}$$

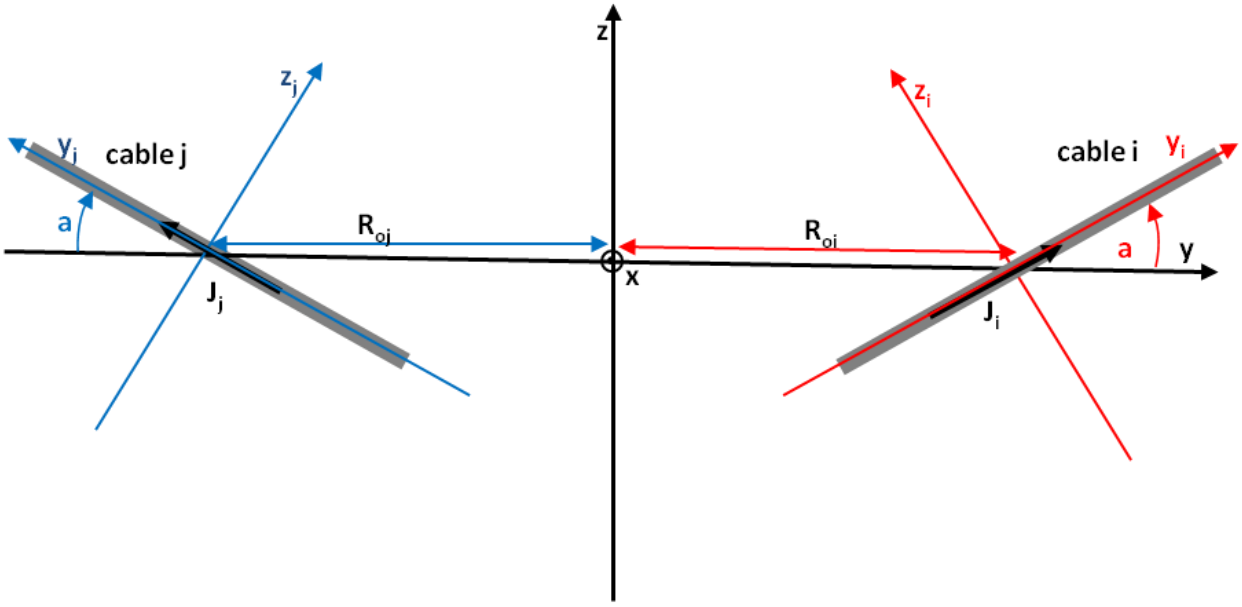

Figure 4.7: *Presentation of the yz slice of the Global coordinate system, the illustration of two random plasma cylinder slices i and j with y_i and y_j Local axis of symmetry respectively, the displacement radius R_{0i} and R_{0j} of their origin and the rotation angle around the x_i and x_j axis of the Local axis system. For reasons of simplicity, we consider that the two cylinders have their origins before rotation on the y axis, while the x_i axis is pointing vertically outside the yz plane and the x_j inside it, corresponding to a ϑ_j-ϑ_i=180^0 angular axis origin displacement.*

The Global thermal pressure, mass density and the magnetic field components are defined from a similar system as the one of equations 4.28. The depiction of $B=B(r)$ taking into consideration the skin effect will be presented at the next subsection for a single plasma wire.

These are the plasma cylinder-based configurations implemented in the PLUTO code or in any MHD computational code defining from time zero the correct plasma spatial mass density and magnetic field distribution, using Local functions transformed and projected to the Global coordinate system.

4.2 Mathematical/Physical model application in PLUTO and GORGON code- Initial conditions analysis for four different cases-Preliminary results for an X-pinch and a Z-array configuration

Now we will present the visualization outcome of some example cases simulated with the PLUTO and GORGON Eulerian MHD codes. The GORGON code description is not a subject of this work since it is used in this research only for calibration and comparison purposes**.** Nevertheless, specific equations and modules that this code uses will be presented within this and the next Chapter in order to be connected to the present research. The mathematical model used for the initial conditions is the one described in the previous section for all the physical variables and the magnetic field (only for PLUTO) initial distribution based on the correlation of the Local and Global coordinate system.

The visualization tool we use is the VisIt 3.0.2 version [3]. It is a very convenient visualization program, appropriate for large computational data, illustrating 3D and 2D pictures of any physics variable output and any physics expression presented from now on.

4.2.1 Z-pinch single wire initial conditions visualization

The first 3D and 2D pictures are the ones of a single plasma Z-pinch cable and the illustration is for the mass density ρ, the magnetic field **B** and the current density **J** in the skin effect mode. All pictures are at the zero moment of the simulation, emphasizing to the appropriate initial conditions of the problem (see equations 4.21 to 4.23). The axis of symmetry is the z axis, while the Local and Global systems are identical here, as mentioned earlier.

The figure below illustrates a tungsten plasma cylinder with initial radius of 20μm, while the length along z axis is 0.4 mm. This is an eight times higher radius than the experiment's cold metal tungsten wire of 2.5μm radius. The distance from anode to cathode is 15mm long, while the current has a rise time (10%-90%) of 65ns and a peak value of 160kA. This is the initial simulation time, corresponding to a 3ns to 5ns experimental time, counting from the experimental current start. The correct choice for the simulation initial time (t_{sim}=0) due to the experiment is a very delicate procedure performed through a testing error-correct procedure from the best dynamic plasma evolution at later simulation times. A more thorough description and evaluation of the simulation through a specific literature, single wire Z-pinch experiment, is presented at the Result Chapter, section 5.2.

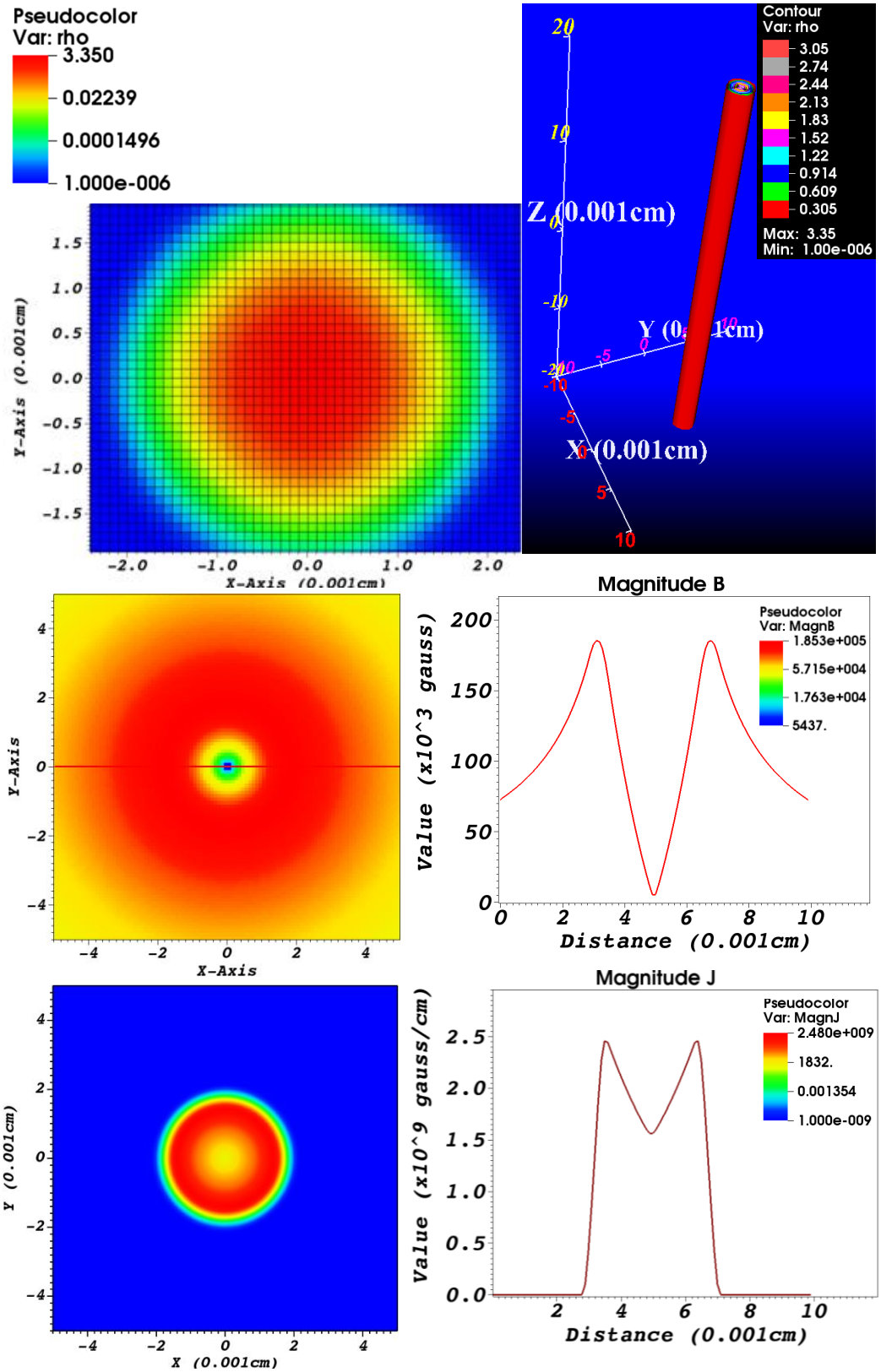

Figure 4.8 Top row: *3D model of the mass density (in gr/cm^3) in cylindrical geometry of a single wire Z-pinch plasma cable for t=0. The left picture is the xy slice at Z=0 illustrating the mass density inside the computational grid. The resolution grid cell has 1μm length at each dimension while the unit program length is 10μm (0.001cm). The right 3D contour plot picture presents the bounding box axis system at*

the edges of the box for better visualization. The Global axis centre is displaced 100μmx100μmx200μm (xyz) on each direction respectively, while the Local/Global axes origin (0,0,0) is at the centre of plasma cylinder.
Second row: *The left picture is the xy slice of the magnitude of magnetic induction (in gauss) at the Z=0 plane. A lineout is taken from -50μm to 50μm along X axis at Y=0. The right picture shows the lineout curve of the magnetic induction of the left picture.*
Bottom row: *The left picture is the xy slice of the magnitude of current density (in gauss/cm) at the Z=0 plane. A lineout is taken from -50μm to 50μm, along X axis at Y=0. The right picture shows the lineout curve of current density from the lineout of the left picture.*

The computational grid that is used here has static cubic cells of 1μm spatial resolution, while the VisIt unit length is 10μm. This is a good spatial resolution providing smooth curve illustration of the plasma cylindrical boundary, despite the use of a Cartesian coordinate system. It is presented at the up left image of figure 4.8. The mass density distribution follows a Gaussian profile reducing the maximum value at 3.35 gr/cm^3 compared to the solid tungsten density of 19.25 gr/cm^3. Nevertheless, it is the higher maximum value than any other profile we could use, i.e. parabolic, due to the narrow width of the Gaussian function. The Gaussian function presents a smoother transition from the main plasma tungsten area to the thin plasma area and is usually preferred due to the enhancing of the computational robustness.

The magnetic field inside the plasma cylinder near the R_{max} radius obeys an almost linear rise law, while its maximum value is $1.85 \cdot 10^5$ Gauss and the minimum at the centre is 5437 Gauss. The current density profile is the one of a more smooth skin effect than the one presented in figure 4.4 having a skin depth $\delta=1.4R_{max}$. The current density along the plasma radius has a maximum value of $2.48 \cdot 10^9$ Gauss /cm at $R_{max}-\Delta r_1$ (see figure 2.4 in Chapter 2) and a lower value of $1.6 \cdot 10^9$ Gauss /cm at the centre. This current density profile is an intermediate from the uniform one of a cold thin metallic cylindrical wire and the surface current density profile of an intense skin effect [2]. These magnetic and current density profiles also introduce non-zero values at the centre of the cylinder, thus avoiding the infinities at the derivatives of the variables during the simulation run. This way we have more robust scenarios with higher and steadier simulation time-steps. Furthermore, the smooth transition of the current density from low values to the zero value at the plasma vacuum for $r>R_{max}$ contribute to this steady execution behaviour. We should mention here, that the finer spatial resolution results to lower values for the magnetic field and the current density (than of worse spatial resolution) at the centre of the plasma cylinder approaching better the correct values of the skin effect theory. The grid resolution is very crucial for the evolution of the simulation run, for the time-step value and for the numerical instabilities growth. These parameters have to be considered for the fittest spatial resolution. The resources, the nodes and the parallel processing scheme are also important for the optimum choice of the spatial resolution and the computational box. These matters will be discussed later at this section and section 4.3.

The definition of the current density here is the same as the one in equation 3.7 neglecting the factor $4\pi/c$. The resolution unit length of $l_0=1\mu m$ will produce the appropriate dimensions of Gauss/cm through the formula:

$$\boldsymbol{\nabla}_{\mathbf{unit}} \times \mathbf{B} \sim \frac{\boldsymbol{\nabla}_{\mathbf{unitless}} \times \mathbf{B}}{l_0} \equiv \mathbf{J} \tag{4.36}$$

Thus the correct expression is depicted at the VisIt program (third row pictures of figure 4.8). The smaller l_0 produces, a better approximation of the density current values, as we mentioned earlier.

4.2.2 X-pinch of two wires initial conditions visualization

The second configuration we will visualize is an X-pinch two plasma tungsten wire of initial cold radius, at each wire 2.5μm, initial angle of the two wires 100^0, 15mm long at z axis from the anode to cathode electrodes, experimental rise time (10%-90%) of ~50ns and maximum current density of 46kA. It is an experimental configuration description from our lab facilities of the Institute of Plasma Physics and Lasers in Rethymnon (IPPL–www.ippl.hmu.gr). This simulation-experimental comparison and analysis is presented at the Result Chapter 5 in the third section.

The initial simulation time (t_{sim}=0) corresponds again at 3ns-5ns from the experimental current start. The initial tungsten plasma cylinder radius is again eight times bigger (20μm). The Local axis of each cable is the y_1 and y_2 respectively while the rotation angles are $a_{11}=40^o$ and $a_{12}=180^o$-$40^o=140^o$. The equations that we use for the correct geometrical spatial contribution of the mass density, thermal pressure and magnetic field induction are the ones of 4.29-4.31 system. The plasma cylinders are considered crossed and separate Z-pinches that at every spatial point all the physics variables are the sum of each plasma cylinder variable (equation 4.31). This way the crosspoint area is formed from t_{sim}=0 and the domination of the Local magnetic field away from this area around the plasma cables and the Global magnetic field formation near this area, is clear from the same moment too. The depiction of all these observations is at the following figure.

As we can see at the 3D pictures of the first row, we have two plasma wires that form an angle of 100^0. The two wires have gone through the ablation face and they have merged into a common area at the cross-point (right picture). The zero simulation time at this depiction corresponds to a 3ns experimental time relative to the current start. The correct magnitude of the radial contribution of the magnetic field is evaluated through the current density. This is a function that considers the skin effect as we already presented, while the magnitude of the current density is also evaluated from the initial value of the sinusoidal form of the experimental current (presented at section 5.1). The updating of the magnetic field is a subject of discussion at the Results Chapter 5 section relative to the X-pinch simulation results.

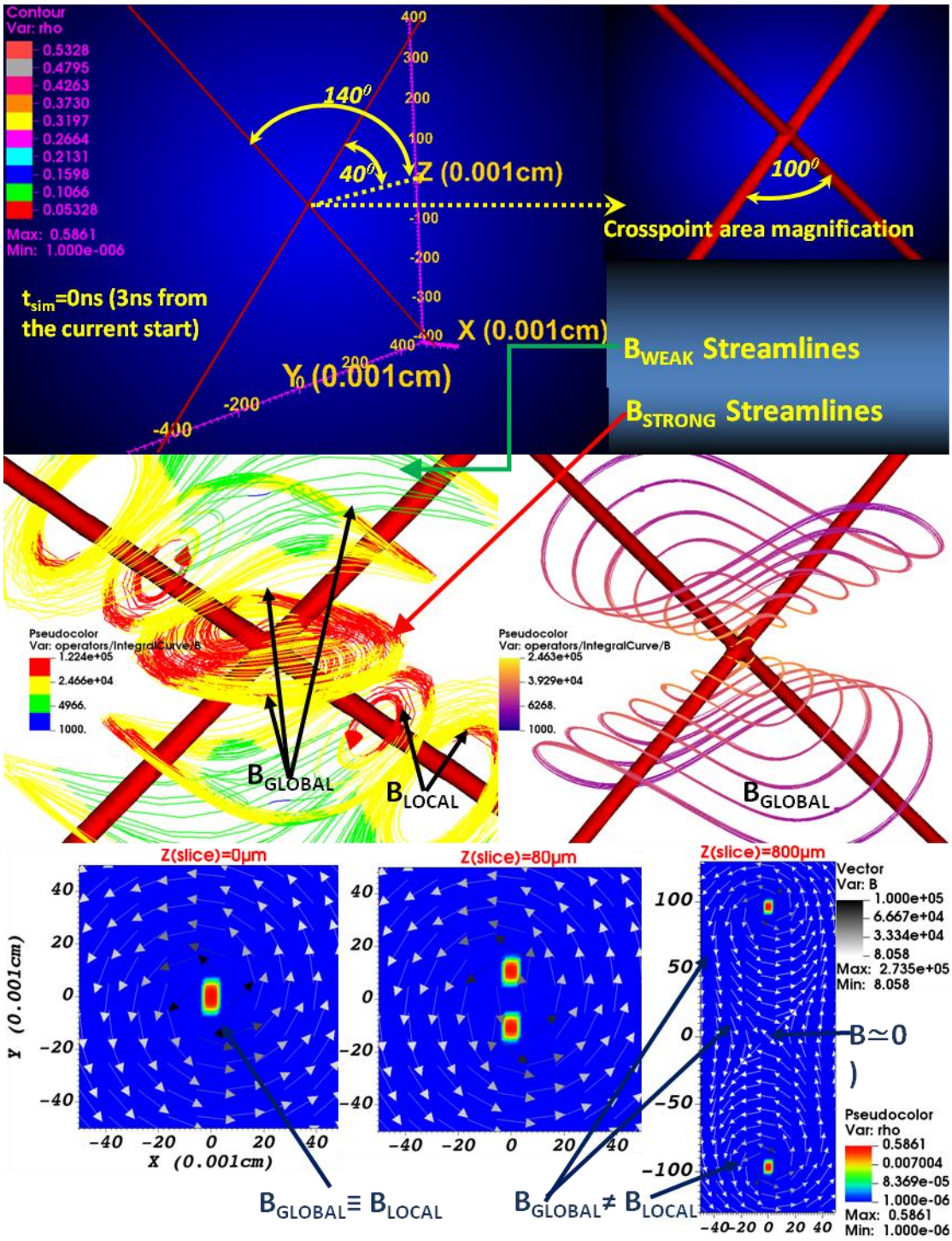

Figure 4.9 Top row: *The left picture is a 3D X-pinch two wire configuration at t_{sim}=0 (3ns from the current start). The radius of each cable is 20μm (8 times the cold metal radius), while the computational box is 1mmx10mmx8mm (x-y-z). The center of the Global axis system is displaced 100μmx100μmx200μm (x-y-z) at each direction respectively while the Local/Global axes origin (0,0,0) is at the crosspoint of the two plasma cylinders. The right picture is a magnification of the crosspoint area depicting the merged ablated plasma cylinders with an initial angle of 100^0. The a_{11} and a_{12} rotation angles are 40^0 and 140^0 respectively.*

Middle row: *The left picture is a presentation of the magnetic field streamlines depicting the spatial areas of the B_{Local} and B_{Global} dominance. The right picture is of the same configuration depicting only the Global magnetic field.*
Bottom row: *From left to the right we see Z=0, Z=0.08mm and Z=0.8mm depiction of parallel Z planes. The B_{Global} dominancy at the crosspoint area (Z=0) is gradually transformed (Z=0.08mm) to Local magnetic spatial areas near and around the plasma wires, while the B_{Global} is dominant at the intermediate and far away zones (Z=0.8mm). All units are in c.g.s. system.*

The second row depicts the 3D pictures of the mass density with the magnetic streamlines of the Local and Global magnetic field. The Local magnetic field is depicted clearly away from the crosspoint and near each plasma wire, while the rest of the spatial area has a Global magnetic profile (left picture). The right picture depicts only this Global behavior. The contoured color selection presents, four different levels of the magnetic field strength. As we see, the areas near the crosspoint and plasma cables outside the X formation are the ones with the strongest magnetic field. This is something that plays a key role for the pinching procedure at later simulation times! The magnitude of the magnetic field topology is also very important for the formation of the plasma jets, the corona plasma and the plasma "migration" from the plasma wires and crosspoint area to the plasma jets. A relevant discussion and analysis is presented at the Results Chapter for the X-pinch configuration.

The third row depicts the sequence from the Global magnetic field dominance at the crosspoint area at lower Z levels (Z=0 and Z=80μm) to the Local like behavior near each plasma cable and the Global at the intermediate area at higher ones (Z=800μm). This dominance of B_{Global} near the cross-point area and its rapid decrease moving towards the electrode area have been studied and simulated at other works emphasizing of the importance of this initial magnetic distribution [4]. The Local magnetic field vectors have the higher depiction value of 10^5 gauss at the $r=R_{max}$ circle, while this is rapidly decreasing as we go further away from each wire. This holds for the first and third picture at the last row, but is valid only at the outside $r=R_{max}$ area for each cylinder at the second intermediate level picture (Z=80μm). The topology of the magnetic field at Z=0.8mm plane has also similarities to the one that has a Z-pinch array with the central area having the lowest value (practically B=0), while there is an enclosing B_{Local} at each plasma cable and an enclosing B_{Global} for the whole array area [5-7].

The initial magnetic field distribution and the advection/diffusion of the magnetic field along the run are essential for the appropriate plasma dynamic evolution. This analysis continues at the next subsections concerning both Z-pinch tungsten wire array and X-pinch two tungsten wire formations.

4.2.3 X-pinch of two initially tangent plasma wires-Preliminary results at early simulation/experimental times-"Cold" start like conditions

An additional choice for the initial simulation time that is strictly defined as far as the magnetic field and plasma distribution are concerned is the so called "cold start". We can assume that the plasma wires are at the ablation phase, tangentially begin to merge, starting the plasma phase evolution and the creation of the crosspoint territory. We can assume that the initial temperatures are of the liquid tungsten phase or even lower (~0.026eV corresponding to room temperature to ~0.5eV of the liquid/melting phase).

It is a novel presentation for a purely MHD code including the crosspoint formation procedure that its dynamic formation and evolution can have a significant role to the plasma jets, rotational instability creation and pinching phenomenon. A preliminary analysis follows in a few lines, while a more focused presentation is at the fourth section of the Result Chapter 5.

The origin of each Local system is displaced from the Global one (let's say along x axis), where the displacement could be $0 \leq d \leq R_c$, where d is the displacement distance and R_c the initial metallic cylinder radius. The smaller the displacement at x axis, the bigger is the merging of plasma cables and a later current start time we have for the $t_{sim}=0$. The displacement here is chosen to be $0.9R_c$ (almost at the beginning of merging), while the initial tungsten radius is 3μm (20% higher than the metal radius of 2.5μm). The temperature we assume is 0.5eV (melting temperature of solid tungsten). This way the $t_{sim}=0$ time we choose can be theoretically very close to experimental current start time (here we choose 0.5ns less than the one of 3ns to 5ns we mentioned earlier).

The MHD code we use here are both PLUTO and GORGON. The initial plasma tangential cable formation is depicted at figure 4.10 and there are photos from the PLUTO code. Figure 4.11 depicts simulation run photos from the early jet creation that originate from the GORGON relevant run.

The distance d is not a constant one, but it begins with a $d_{max}=0.9R_c$ value at the $z=0$ plane and ends at the $z=z_{max}$ plane with a zero value. The $z_{max}=7.5mm$ for our case corresponds to the electrode distance from the crosspoint at the experimental chamber. The analytic relation for the $d=d(z)$ is:

$$d = d_{max}(1 - |\frac{z}{z_{max}}|) \tag{4.37}$$

This is a simple way to take into consideration the bending of the plasma cables at the cross-point, while the end of the cables at $z=z_{max}$ (the electrode surface) are on the x Global axis (d=0) (see the first picture of picture 4.10 points A and B). The Local radial coordinates r_1 and r_2 of equation 4.32 become:

$$r_1 = \sqrt{(x_1 + d)^2 + z_1^2}$$

$$r_2 = \sqrt{(x_2 - d)^2 + z_2^2} \tag{4.38}$$

We selected the Local plasma center of cable 1 to be displaced at (d,0,0) Global point and the other cable 2 to the (-d,0,0) Global point.

The curvature of the cables is very small compared to the length of plasma cables. The correct distribution of the magnetic field for each plasma cable is given by the Biot-Savart law. Due to $d<<z_{max}$, a very good approximation is that the magnetic field magnitude for each cable is of the same radial form as the one we presented earlier using the integral form of the Ampere's law and the skin effect replacing r_1 and r_2 radial distances from equation 4.38. This change and replacing the x_1 Local coordinate to x_1+d and x_2 to x_2+d is adequate of providing the correct implementation formulas for

the magnetic field and plasma distribution that are depicted at figure 4.10, even though the Local axes y_1 and y_2 have been (slightly) bended.

The initial cylinder radius of these pictures is $r_c=1.2R_c=3\mu m$, expanded 20% from the metallic tungsten cable of 2.5μm, thus we have to choose for a nearly constant plasma density profile decaying sharply at the boundaries of plasma cylinder. A sharp parabolic profile is suitable for this task. The crosspoint area is at the very beginning of its creation and the plasma density there, is the sum of the parabolic profile from each wire.

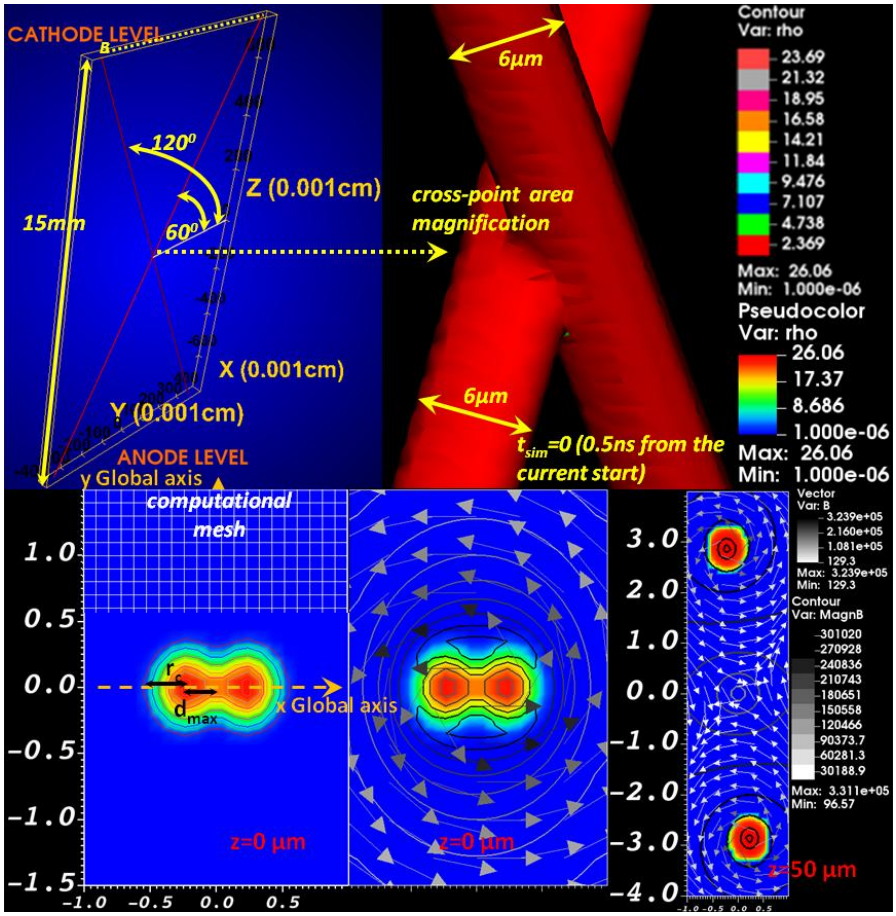

Figure 4.10 Top row: *The left picture is a full experimental scale 3D X-pinch two cable configuration of PLUTO code at t_{sim}=0 (0.5ns from the current start). The radius of each cable is 3μm (1.2 times the cold metal radius), while the computational box is 20μmx8000μmx15000μm (x-y-z). The right picture is a magnification of the crosspoint area depicting the initial merging phase of the ablated plasma cylinders with an initial angle of 60^0. The a_{11} and a_{12} rotation angles are 60^0 and 120^0 respectively. The displacement distance at the x Global axis of each Local center is 90% of the cold metal wire (2.25 μm).* Bottom row: i. *The left picture depicts the mass density of the xy plane at z=0 Global axis system. The computational mesh has 1μm spatial unit cell, while the displacement d_{max}=2.25μm and plasma cable radius r_c=3μm are presented. The density isocontours depict a clearer view of the cable center and displacement.* **ii.** *The intermediate picture depicts the vectors of the magnetic field and the isocontours magnetic field lines at z=0 Global plane.***iii.** *The right picture depicts the same physical values at the z=50μm plane. The twisting of the magnetic field lines is obvious due to the cables x displacement.*

All units are in c.g.s. system.

The initial displacement d_{max} is depicted at the bottom row in the left 2D picture along with the wire radius. This displacement vanishes at the very top of the X-pinch configuration, where we can see the A and B touching points of the plasma wires at the cathode level. The 3D left picture of the top row presents the full scale X-pinch configuration from bottom (anode level) to the top (cathode level). The AB line segment lies on the xz Global plane giving a very close to the X-pinch experiment spatial initial formation with displacement d=0 as we just mentioned. Of course a more realistic initial spatial mass formation according to the experimental procedure should include the 180^0 or 360^0 twisting of the touching cables at the cross-point. This complicates more the magnetic field topology and the mass density distribution rotational functions, consequently this specific presentation is an adequate first approximation for the "cold start" scheme.

The experimental chamber height from anode to cathode is 15mm, while the anode/cathode plate has a diameter ~40mm. This experimental presentation is part of the subject of the first section at the Result chapter 5.

The computational box has a y axis width of 8mm and a x axis depth of 0.02mm. The rotation angles a_{11} and a_{12} are 60^0 and 120^0 respectively, thus having a wire angle of 60^0. The magnification of the cross-point area at the right picture of the top row clearly presents the separate plasma cables at the beginning of merging for the cross-point area creation.

The bottom row has a 2D left picture of the mass density pseudocolor and isocontours depicting clearly the common area of the two cables at the center of the global axis system and the separate radial area of each cable. This spatial geometry plasma distribution produces from the very beginning the Local magnetic field area inside and around each plasma cable, while the Global magnetic field encloses the whole formation. This is true, even for the z=0 plane area, as we can see at the intermediate picture of the vector arrows and isocontours lines of the magnetic field. It goes on till the upper and lower z planes and the anode and cathode levels. Due to the x displacement of plasma wires, we can see a twisting of the magnetic field lines to a rotational clockwise pattern from the z=0 plane to the higher planes. This is clear if we compare the intermediate and right picture of the bottom row.

The twisting of the magnetic field lines along with the displacement of plasma wires introduce an interesting perspective for the initial stage of cross-point creation, jet formation and the rotation of the plasma streams originating from the crosspoint and cable branches area. The cross-point creation from experimental studies for many X-pinch formations with different materials describe a similar early stage creation that its general scenario is: cold wires → formation of wire cores→ formation of corona→ merging of the cores→ creation of the neck [8,9]. It could take several nanoseconds, depending on the diameter of plasma wires and the magnitude of current density, to have a full merging of the wire cores at the cross-point. We see that the direct merging of the wires at t_{sim}=0 could be a lesser method for the best description of plasma dynamic evolution for the appropriate X-pinch, cross-point, geometry.

The azimuthal asymmetry due to the geometry of the initial contact of the wires and the crucial role at the discharge asymmetry in an X-pinch configuration is something that is also pointed by G. V.

Ivanenkov et al. It is responsible for the creation and pinching mechanism of hot spots (HSs) far from the mini-diode (MD) area and like-snake formations from the intersection of the wires [10]! It has also been demonstrated by Shelkovenko et al [9] and mentioned again by Mitchell et al [11,12] that the development of the plasma in the crossing point undergoes three distinct phases. The first one is established as, "the individual wires which form the limbs of the X-pinch explode, resulting in a dense core (probably containing solid wire material) surrounded by a low density, higher temperature coronal plasma". This initial wire phase describes two initially separate plasma wires touching at the cross-point! These observations are pointing to the importancy of the initial separate plasma wire touching phase implementation if we want to study the dynamic evolution of a small, high resolution, area around the crosspoint!

The novel approach from the very beginning of plasma phase evolution will also provide insights for the two lobes jet displaced initial creation and evolution (see figure 4.11), the rotational plasma stream behavior along with the creation of possible rotational instability formation i.e. kink (m=1) and gyroviscous with possible magnetic reconnection related phenomena (assuming the inclusion of gyroviscous terms in the MHD equations), enhancing all these phenomena due to the cable initial bending at the cross-point [13]. Kinks at the jet columns are experimentally observed, but without a clear interpretation yet [14]. It could be an interesting simulation observation if we see such structures formed due to the wire crossing displacement!

For the first time we will present a preliminary numerical study of this evolution for the two cable X-pinch plasma tungsten configuration in small angles using GORGON Eulerian MHD code. This study will be a priority to the near future work.

The GORGON code is the one we will use here for the presentation of the initial stages evolution of the former X-pinch configuration. It uses Fortran 90 as a programming language, while the PLUTO code uses basically C language. The MHD scheme is similar to PLUTO with the bigger differences to be the two temperature electron/ion model, the energy exchange rates between ions and electrons and the initial boundary implementation of the magnetic field [15]. It includes optically thin radiative losses and thermal conduction, but it lacks a radiation transport scheme. Additional information for the GORGON MHD code is presented at the Result Chapter 5 and Introduction Chapter, while a lot of physical terms that it uses are similar to the ones at the Chapter 3 relative sections (i.e. Braginskii thermal conduction and anomalous resistivity) [16,17].

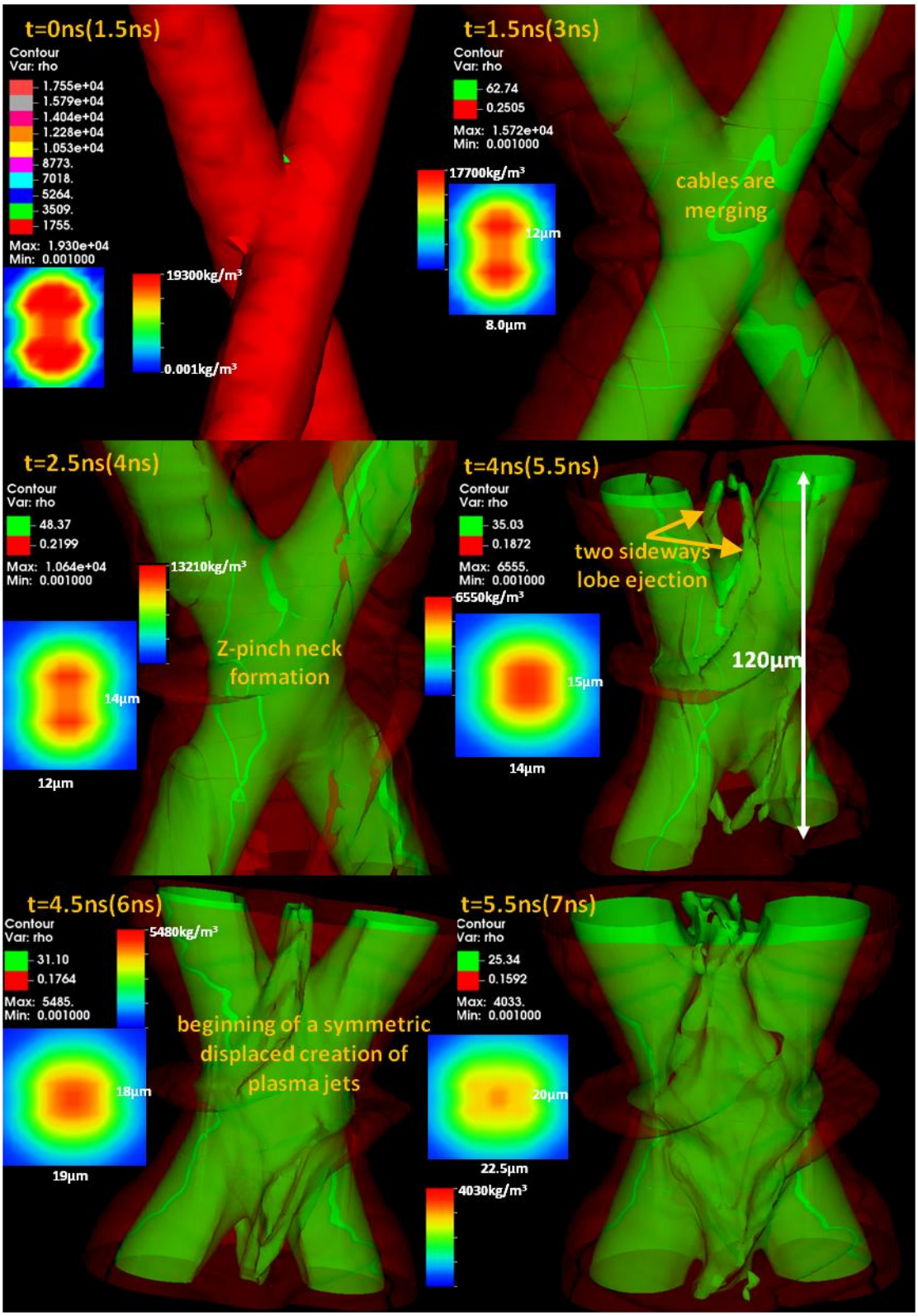

Figure 4.11: *A time sequence photo depiction from t_{sim}=0ns till 5.5ns (the parenthesis time is measured from the current start). This is a GORGON code model having at t_{sim}=0ns the initial cold metallic radius of 2.5µm and initial tungsten metal density of 19300 kg/m^3. All units are in SI. The spatial resolution is 1.25 µm. The two-contour depiction focuses on the thinner plasma evolution. The insert 2D pseudocolor*

photos are of the xy Global plane at z=0 and they are not at the same scale of the 3D pictures. The legend pseudocolor column has at all photos the same lower value of 0.001kg/m^3.

The initial conditions here are slightly different than the ones in PLUTO code. The initial radius at t_{sim}=0 is $r_c=R_c=2.5\mu m$ and $d_{max}=0.9R_c$, while for the plasma density profile we use practically the solid density of 19300kg/m^3 for the whole plasma cable having a sharp decrease to the vacuum value at the cable boundaries with the vacuum area. The initial experimental start is considered to be 1.5ns from the current start having a slight higher current value than the previous one. The initial temperature is considered spatially constant of 0.026eV inside and outside the plasma cable (room temperature). Although GORGON has not appropriate EOS for solid tungsten, at the very first steps of the simulation run the temperature rises to some eV's due to the dissipative terms of Ohmic heating and thermal conductivity and this discrepancy is fixed considering the plasma evolution after this moment to be sufficiently approximated. Additionally, initial conditions with lower resolution, very low temperatures and cold start-like conditions have been used at the past for other pinch configurations i.e. carbon fiber Z-pinch with a good representation of the experimental results and m=0 instability creation and growth rate [18,19], Z-pinch wire arrays implosions [20] and magnetic tower jets [15].

The time sequence has as follows:

i. t=0ns (1.5ns) → beginning of merging of plasma cables for the creation of the crosspoint area. The 2D insert pseudocolor photo depicts the separate sliced two cable area. The contour plot depicts from solid to ten times lower density.

ii. t=1.5ns (3ns) → plasma cables are almost merged. The contour depiction uses only two contours, one of the thicker corona plasma that is of the order of tenths of kg/m^3 (green one) and the other of the thinner one that is approximately two orders of magnitude lower (red colour). The insert photo shows mass transfer from the cables to the central area. The thin corona plasma begins to form and expand (2D cyan colour and 3D red contour).

iii. t=2.5ns (4ns) → plasma cables are still merging (2D) and the crosspoint area is Z-pinch shaped (3D) (micro Z-pinch creation). The dilute corona red isocontour has a rotational structure, breaking the symmetric form expansion of a single symmetric plasma column.

iv. t=4.0ns (5.5ns) → plasma lobes are ejected sideways having a rotation trajectory that will merge within the central plasma bulb to create the two plasma jets. The 2D picture presents the merged plasma cables. These angular momentum plasma transfer could be scale associated even with Young Stellar Objects (YSOs) similar formation mechanisms from the accretion disk to the plasma jets [14,15].

v. t=4.5ns (6ns) → two plasma jets are formed and are asymmetrically expanding to the anode and cathode direction. The magnetic compression forms a wider x than y cross-section for the first time since the beginning of the simulation.

vi. t=5.5ns (7ns) → the corona plasma is ejected all around the cross-point neck area feeding with material the neck and jet expansion. The 2D photo presents the continuing of plasma expansion, the widening of the cross-section at the x axis and the compression at the y.

The initial geometry of plasma cables enables the **JxB** forces to "break" the symmetry of plasma expansion sideways and along z axis that we observe at all simulation studies. This is something new

that could provide a more realistic dynamic evolution closer to the experimental (not so symmetric) results.

This analysis can focus on the physics phenomena around and at the cross-point area from the very beginning of the plasma creation. Experimental results for the initialization of the plasma neck formation and implosion enhance this time sequenced analysis [21].

The resolution analysis we need is at least equal to the initial metal cable radius. This resolution for our case, due to the very small radius of 2.5μm, is very demanding for the computation run and only a "super-computer" parallel processing can give us the computational power to complete the task. We use for our simulation runs the computer system ARIS of the Greek Research & Technology Network (GRNET) in the National HPC facility [22]. Even then the full scale model is out of the system's capability and we have to take smaller computational boxes or/and 1/4 or 1/8 symmetric models with the appropriate boundary conditions that will be discussed at the next section.

This high resolution first nanoseconds plasma study can be also used for the best estimation of the physics values at the very first nanoseconds that will be used as initial conditions to a bigger computational box with lower resolution. This way we can have the "appropriate" initial condition values of the mass density expansion, temperature profile and thermal pressure and we can study the model till the final evolution time of our interest**.** For example, the initial plasma radius and temperature profile we use at the third section of Result Chapter 5 is estimated to be 8 times the 2.5μm of cold wire and 1.5eV maximum value respectively at t_{sim}=0 (5ns from the current start). This estimation is in quite a good agreement with the above pictures that depict a ~20μm maximum radius at ~5ns to ~7ns from the current start!

4.2.4 Z-pinch array of four plasma wires-Preliminary results till the stagnation phase

The last simulation model that is presented is the simplest wire Z-array configuration of four tungsten plasma cables of initial 7.5μm wire radius, experimental rising time (10%-90%) of 65ns and maximum current of 50kA [23]. Accordingly to the symbolic notation of 4.24-4.28 equations, for the displacement of the plasma wires, we have:

$$\mathbf{i=1,2,3,4} \tag{4.39}$$

The origin of each Local cable is displaced to the Global point:

$$\mathbf{(x_{0i},y_{0i},z_{0i})=(R_{0i}\cos(\theta_0+(i-1)\cdot\theta),\ R_{0i}\sin(\theta_0+(i-1)\cdot\theta),\ 0)} \tag{4.40}$$

where $\theta_0=0^0$, $\theta=90^0$ and

$$\begin{gathered}\mathbf{x_i=X_i=x-x_{0i}}\\ \mathbf{y_i=Y_i=y-y_{0i}}\\ \mathbf{z_i=Z_i=z}\\ R_{01}=R_{02}=R_{03}=R_{04}=1.5\text{mm}\end{gathered} \tag{4.41}$$

We consider a computational box of 2mmx2mmx0.2mm of 10 μm spatial resolution. The depiction of the physical variables are at figure 4.12. The simulation considers an initial time of 5ns from the current start. The plasma radius of each wire is four times the initial radius of the cold plasma cable.

The density and temperature profile is Gaussian. The distribution of the current density takes yet again the skin effect into consideration. Radiation optically thin losses and radiation transport are used.

The aim of this simulation is to present a qualitative description of the initial stages of the plasma ejection from the plasma wires, the dynamics of ablation streams and precursor plasma under the temporal variations of the global magnetic field topology. Then we will present similarities and variations from the literature experimental and simulation results, even though this is a smaller and a few wire model with a lower maximum current value (equal to the one of the previous X-pinch configuration) [5-7,20,24].

The boundary condition problem is significant here and we will present two different spatial distributions of the plasma wires emphasizing to the significance of the appropriate spatiotemporal magnetic field evolution regarding the boundaries and the low density background (plasma vacuum) implication.

The initial variable depiction is for mass density, magnetic field vector topology and magnitude, and the magnitude of the current density. The latter is defined as in equation 4.36 in gauss/cm. The vacuum consists of plasma air of 10^{-6} gr/cm^3 with a constant temperature there at 0.05eV along the simulation run.

The 3D pictures depict the mass density distribution (left picture) along with the vectors of the magnetic field (right picture) presenting a clear view of the Local magnetic field domination around each plasma wire and the Global field near the center and the boundary area of the computational box. The depiction range of 10^4 Gauss<B<10^5 Gauss emphasizes on the best presentation of the magnetic field vectors around each plasma wire (Local field) presenting the expected highest value (red arrows at the right picture) just outside the common array area tangentially to the cable.

The 2D pictures of the magnetic field at the middle row introduce a lower value of 1 gauss focusing on the zero value area of the Global magnetic field at the box center (blue and green area at the right picture), while the higher value of 10^5gauss depicts similar behavior for the Local magnetic field around each plasma wire as the previous 3D one (black and grey arrows at the left picture).

The mass density and the temperature 2D presentation present the same spatial Gaussian profile with 1gr/cm^3 and 1.363eV higher values respectively. The linear profile of the current density has a similar spatial morphology as the mass density and temperature (not a Gaussian profile though), while the lineout profile for each plasma wire is the same as the one presented for a single Z-pinch configuration in figure 4.8 due to the skin effect implementation. Due to the ten times lower resolution at this simulation we do not see the clear skin effect profile of the current density of figure 4.9, while the higher value of $2.509 \cdot 10^8$ Gauss/cm is ten times reduced relatively to the one of figure 4.9. We see here the effect of the resolution to the physical variables calculation, especially to the ones that are a spatiotemporal derivative outcome.

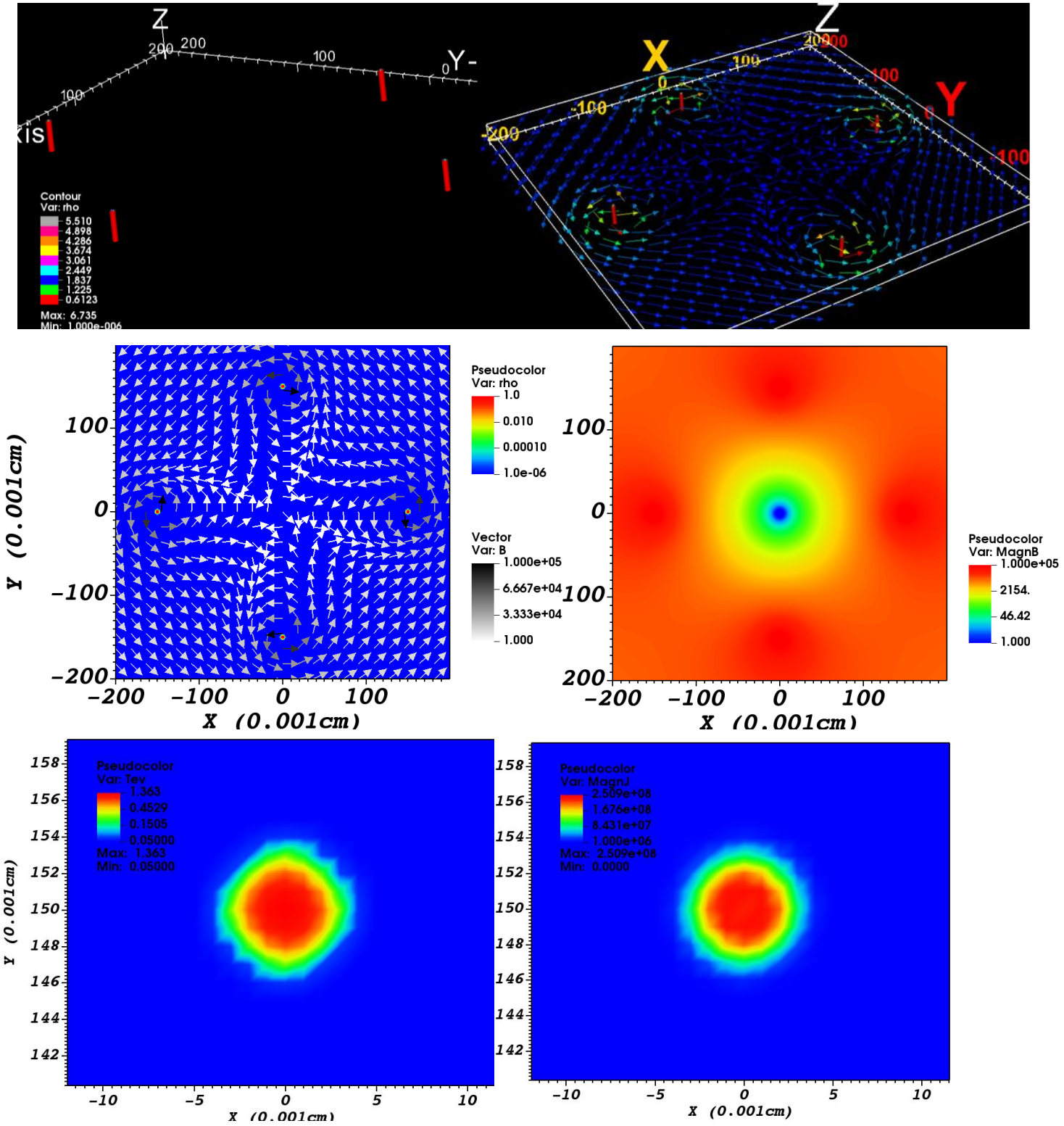

Figure 4.12 Top row: *3D pictures of mass density at the left and mass density with magnetic field vectors at the right. The vector depiction has 10^4 Gauss lower value and 10^5 Gauss maximum.*
Middle row: *2D pictures of the mass density's xy plane with the magnetic field vectors at the left and the magnitude of the magnetic field at the right. The lowest value is 1 Gauss.*
Bottom row: *2D pictures of the initial temperature distribution of the top cable (left picture in logarithmic scale) and the magnitude of the current density (right picture in linear scale).*

The next figure presents the mass density and magnetic field for two different spatial distributions at the same instant (20ns from the current start and 15ns from the simulation start). The right one (rotated by 45^0 relevant to the left one) seems unaffected preserving the azimuthal Local/Global magnetic field behavior around the plasma wires, while at the left we see a clear affection from the boundaries, reversing the magnetic field vectors at the corners of the computational box and around the plasma cables.

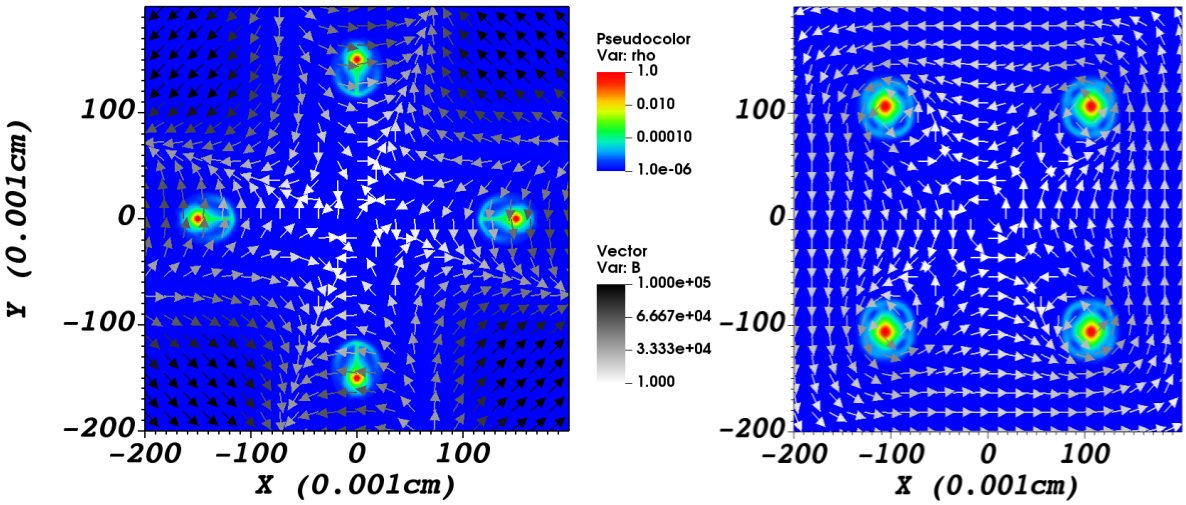

Figure 4.13: *The left picture has the four plasma wires placed by pairs symmetrically on the x and y axes depicting the mass density and the magnetic field vectors at 20ns from the current start. The right picture has the centers of the wires rotated counter clock by 45^0 depicting the same time.*

More specifically, we see that the magnetic field at the corners of the left box is enhanced and reversed compared to the one at the right box. The ablation/plasma streams are elongated and already have a beam shape, while the ones of the right are just formed. The higher values of the magnetic field at the left picture are around the plasma cables (grey scale) and much lower than the higher values of the other formation (black and grey scale at the corners and near the plasma cables).
Solutions for a better simulation with lesser affection from the boundaries are:
i. A bigger computational box placing the plasma cylinders as far as possible from the sideways boundaries and corners. This is very difficult due to the limitations of the computational power and the real experiment's chamber size that could be several mm long at each dimension of the xy plane.
ii. A lower resolution with bigger computational cells. This also creates deformations and miscalculations at the physics variables along the simulation run. A minimum cell length should be at least equal to the diameter of the initial plasma wire.
iii. Reducing the computational box to the 1/2 or 1/4 of the real spatial Z array area taking the appropriate boundary conditions (equatorial-symmetric, reflective and periodic. They will be described at the next section of this Chapter). This is something that we use also for the single wire Z-pinch and two-wire X-pinch formation at the next Chapter allowing us to take a bigger computational box at each semi-axis with better resolution. A similar approximation is used in reference 5. Of course if we have more than six plasma cables, equally angular displaced, the two pictures of figure 4.13 will be either identical or similar.

iv. A radical solution is to switch off the Riemann solver (more details for the solver choice at the next section) at the vacuum region allowing only the magnetic field evolution there and fixing at a constant value all the other "vacuum" variables. This is something that is tested and evaluated for an X-pinch configuration at the next Chapter along with the similar technique that GORGON uses. As we present there, the deformations of the magnetic field vanish and the size of the computational box can be reduced focusing on the area of interest. This is valid if we have a "very good" experimental vacuum that does not affect the main plasma evolution. For instance, shock waves and bow shocks could be the result of a main plasma component interaction with a surrounding plasma air of higher than "vacuum" condition density. At this work we want, mainly, to avoid these interactions. This technique offers us the opportunity to consider only the surrounding magnetic field as the modulation mechanism at the plasma-vacuum interface and study instabilities and deformations there (i.e. MRT instabilities!).

The next figure presents 2D pictures of the mass density evolution till ~250ns from the current start corresponding to a nearly full period of the experimental current. The depiction of the mass density is escorted by the bulk velocity vectors for a better understanding of the plasma evolution, especially at the center of the precursor plasma column, where at later simulation times we have plasma contractions, plasma bouncing and collimation due to the thermal pressure and/or magnetically driven expansions/contractions, resulting in mass density temporal variations [24]. An interesting case for further future investigation is the clarification of the main spatiotemporal dominant mechanisms that are creating the pinching and expansion of the precursor column area i.e. the interplay between the JxB forces and $\nabla P_{\text{thermal}}$ along with the plasma momentum spatiotemporal evolution. A similar investigation is presented for an X-pinch configuration relatively to the jet creation at the third section of the next Chapter.

The time evolution depiction at the above graph represents the sequence we described before beginning from the initial plasma stream formation (picture A) till the beginning of the expansion of the denser precursor column area (pictures F,G,H). Specifically:

The first picture presents the initial stage of the plasma stream formation from each plasma cable. Picture B depicts the initial precursor plasma column creation and the elongated plasma streams that are guiding the main plasma stream ejection that are radially expanded we have(better visualization of the precursor column at the next figure due to the lower value density depiction). The origin of the elongated plasma stream formations is mainly from the radial corona plasma trajectories that are swept around the wire cores producing radial streams due to the **JxB** forces [20]. A similar corona origin mechanism exists in the two-wire X-pinch devise that is thoroughly presented at section 5.3 of the next Chapter. The third picture presents the narrow plasma precursor column that is clearly observed. The time sequence from this moment goes beyond the current peak time. The next two pictures (D and E) have radially expanded plasma streams around each column, while in the central area a compressed plasma column is beginning to form. The Z-array center at the latter is full of corona plasma and the central column is ready to expand having even higher density than the previous one of D.

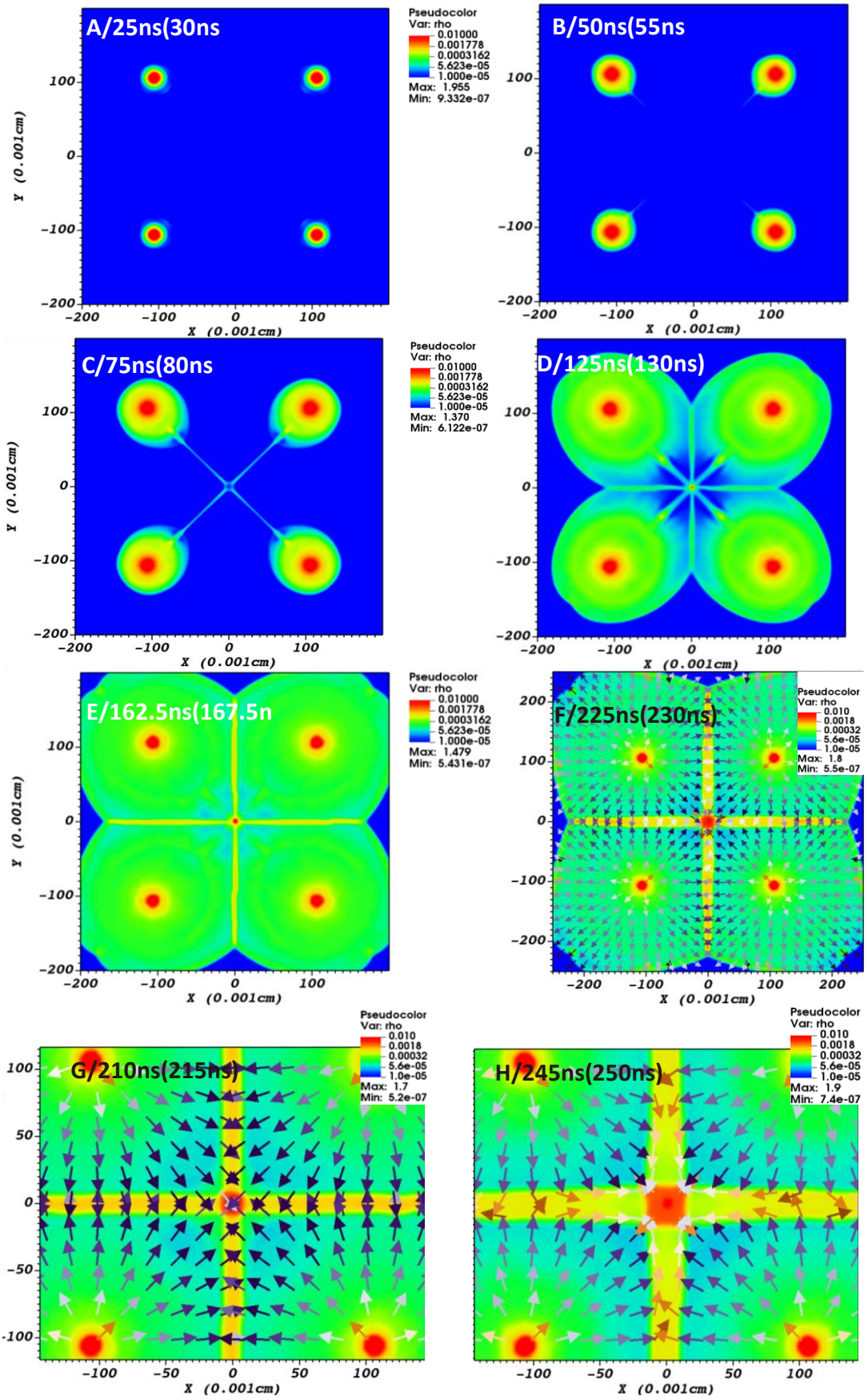

Figure 4.14: *The time sequence of the four tungsten wire array at xy plane. The temporal instants are from 30ns to 250ns from the current start (parenthesis values), depicting the initial ejection of the*

plasma streams till the expansion of the central plasma column. The mass density legend goes from $5 \cdot 10^{-5}$gr/cm^3 to 0.1gr/cm^3, while have the bulk velocity from 100m/s to 10km/s.

The "cross shape" formation of the denser matter we observe along x and y axes is created due to the development of the neighbourhood plasma streams that are compressed hydro-dynamically. As time passes, these get thicker and denser. These formations are also observed to other simulations [5,7,20,24] at the initial stages of the precursor plasma column.

The last three pictures F,G and H also present the vectors of the plasma bulk velocities. This is due to the implosion phase sequence clarifying this way the relation of the plasma movement to the contraction and expansion of the precursor column. We see an interesting depiction at G and H. The expansion of the plasma column is a fact at G, but the bulk velocities are still pointing at the column center. This means that plasma material is deposited from the four main streams to the column producing a volumetric rising. This is a fact till ~225ns. Then the expansion consists of two procedures, the continuing deposition from the streams and the expansion of the main plasma column (depiction at F and H). This is a similar time sequence to the one of the jet creation of the X-pinch configuration in Chapter 5, where we observe deposition from the limbs and at later times deposition from the crosspoint due to the magnetic forces. It could be interesting to present the spatiotemporal affection from the thermal and the magnetic interplay, but this goes beyond this preliminary study, as we mentioned earlier.

The mass density maximum has a higher value of ~2gr/cm^3 at the first picture, decreases to lower value ~1.3gr/cm^3 and finally reaches a higher value of 1.9gr/cm^3 at the last picture. Small upside-down variations of the maximum value at F, G and H develop due to the former mechanism of the previous paragraph.

The temporal sequence is similar to the one presented in literature [5,20,24]. But the spatial evolution presents some differences with the other simulations. Two are the main ones.

The first is the very close approximation of the four plasma cables that is at least four times smaller than a typical Z-array [4,6,20,24]. This choice has been made to avoid the demanding computational power and for enhancing the physical phenomena we want to study (i.e. the Local and Global magnetic field morphology evolution) due to the small distance of the plasma cylinders. Another reason is the small value of the peak current limiting this way the distance we can place the tungsten cables if we want to have reasonable ablation and mass transfer at the central area. Higher peak currents and larger spatial Z-arrays will be simulation tested in the near future (a higher peak current of 160kA, 1/4 model is presented, at the initial precursor phase, at the boundary section of this Chapter).

The second difference is the narrow width of the initial streams, creating the initial stages of the precursor column before the main streams reach the central area at ~130ns.

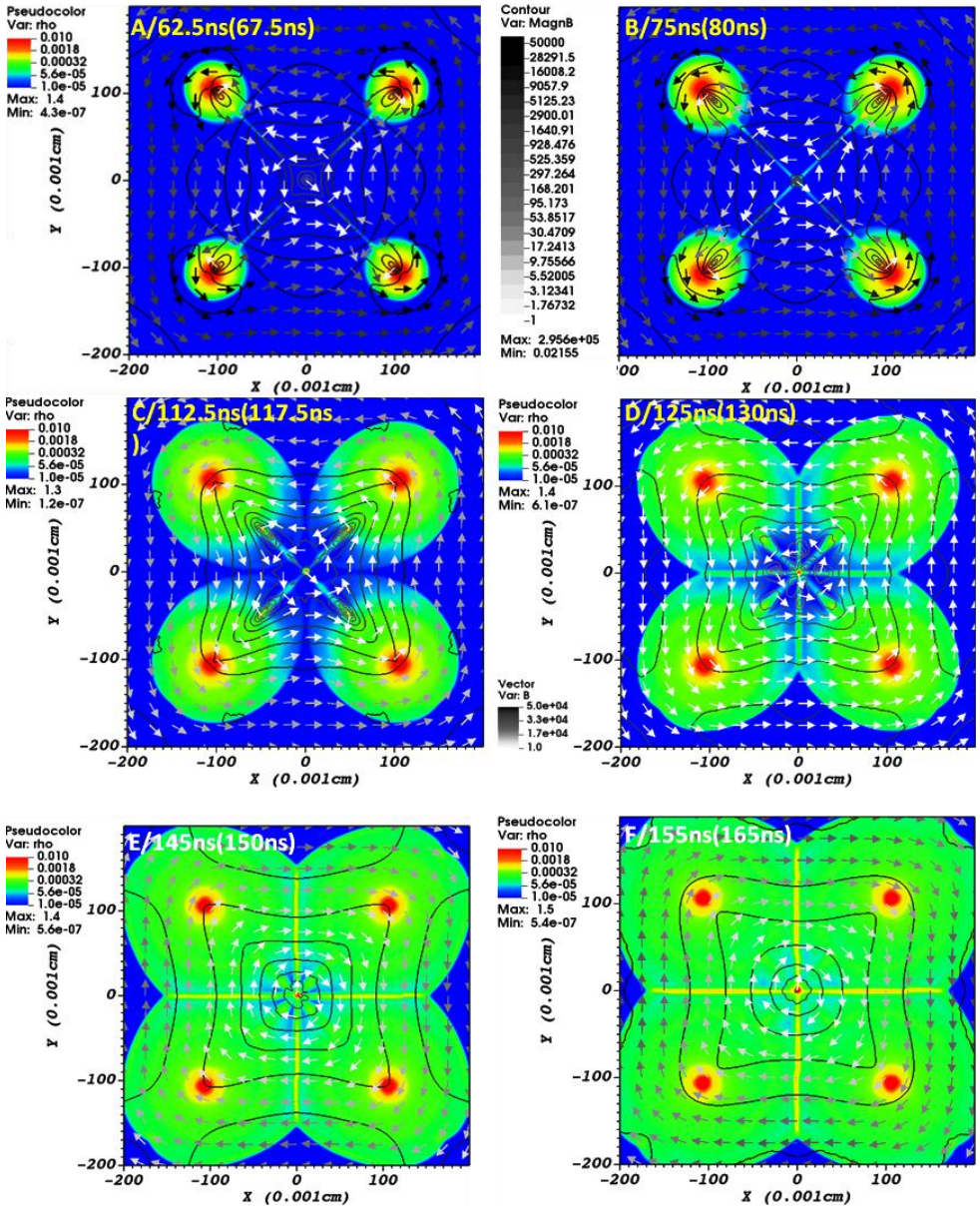

Figure 4.15: *The evolution of the Local/Global magnetic field isocontours from 67.5ns to ~200ns depicting the evolution of the Local magnetic field around plasma cables, the Global at the central area and the area around the array formation and the beginning of the Local formation around the precursor column at later simulation times.*

The last figure 4.15 depicts the evolution of the magnetic field isocontours and vectors. The initial time of 67.5ns (picture A) from the current start is at the peak current where the magnetic field around the precursor plasma column and the Local magnetic field near each plasma column are distinct. The magnetic field vectors and contours have the same range of 10^0gauss to $5 \cdot 10^4$gauss. The second picture B presents a similar magnetic field topology.

This is something we do not see at the next two pictures C and D. The Global magnetic field at these pictures is the one we see surrounding the four wire array while each isocontour has a Global topology. The **B** vectors introduce a Global counter clockwise depiction for all the Z-array area. These pictures present similarities to the ones of other laboratory Z-array simulations concerning the central

and the surrounding magnetic field topology along the precursor plasma and the dense central area formation [5,7].

The last two pictures E and F depiction reveal a reversed rotation of the magnetic field vectors due to the inversed current density, since the time sequence is after the semi-period of the experimental current (the temporal updating of the magnetic field along the simulation run has been already mentioned). The magnetic field at the center of the precursor column presents a Z-pinch like topology (picture F).

4.3 Pluto physical and numerical tools description

A lot of the physical modules that are implemented and discussed here have already been analyzed at the previous Chapter 3 (PART I and PART II) and whenever it is required we will give the appropriate references for the reader to this Chapter. The numerical tools we use are mainly the ones already implemented in the code and can be activated through the appropriate switches, but here we focus on the best implementation scheme and numerical modifications concerning the Z-pinch single wires and the X-pinch two single wires configurations. A mixture of similar strategies can be used at the Z-arrays and conical Z-arrays configurations.

4.3.1 Introduction to PLUTO MHD set of equations-Modified EOS correlating primitive to conservative tabular data and vise versa

Plutocode is an one-fluid HD/MHD code that can operate at the non Relativistic/Relativistic regime depending on the magnetic field strength and magnitude of plasma velocities. The code can describe any plasma formation at the Ideal or Dissipative term regime having a system of (nearly) conservation laws, of the form:

$$\frac{\partial \mathbf{U}}{\partial \mathrm{t}} + \nabla \cdot \mathbf{T}(\mathbf{U}) = \mathbf{S}(\mathbf{U}) \tag{4.42}$$

where $\mathbf{U}$ represents a set of conservative quantities, $\mathrm{T}(\mathbf{U})$ is the flux tensor and $\mathrm{S}(\mathbf{U})$ are the source terms [1,25]. The full set of equations with the dissipative terms that are valid for our case has been presented at the 3.1 section of Chapter 3 (PART I) from 3.1 to 3.13 equation system. These equations are used or will be used for future work concerning metal plasmas configurations (Z-pinch single wire and X-pinch two-wire for the time being at the Result Chapter 5). The plasma material that we study in this work is tungsten with a surrounding plasma air. The MHD equation system includes radiation and resistivity modules that are presented analytically at the relative sections of Chapter 3 PART I and PART II respectively. The plasma velocities and plasma wave velocities are at least ~1000 times smaller than the speed of light, so we are at the non Relativistic regime. There is an analytical presentation of all plasma and wave velocities in the Result Chapter 5 at the third, fourth and fifth sections.

PLUTO uses both conservative and primitive physical quantities. The conservative form is convenient for the execution, while the primitive description is more convenient for assigning the initial and boundary conditions of the physical problem. The updating of the fluxes **F** though, uses the primitive variable tensor as we present at the next subsection.

The sets of conservative to primitive variables U and V and vise versa are depicted in the following flow chart:

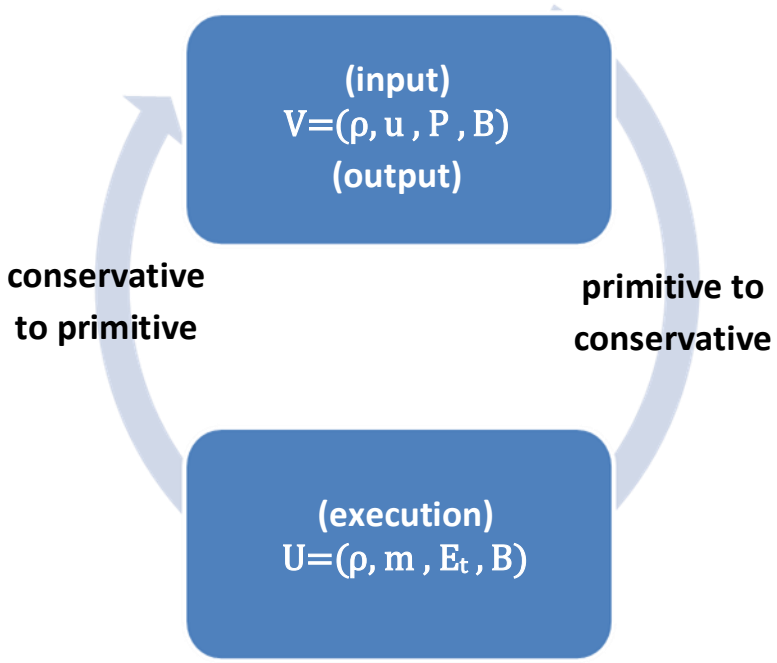

Figure 4.16: *The input data in the code is at the primitive form, the execution uses the conservative and the output again is at the primitive form.*

The input data of thermal pressure P, mass density ρ, bulk velocity $\mathbf{u}$ and magnetic field $\mathbf{B}$ are in the primitive form while the execution goes on with the total energy density $\mathrm{E_t}$, the mass density ρ, the momentum density $\mathbf{m}$ and the magnetic field $\mathbf{B}$ (there is an exception concerning the fluxes **F** that are discussed at the next subsection). The output data are again at the primitive form [1,25,26].

This is a convenient sequence for this work to implement the initial condition mass density, thermal pressure and magnetic field distribution for any plasma model configuration, evaluate along the simulation run the total energy density $\mathrm{E_t}$ or the internal energy density ρe and then return as output all the primitive variables along with the energy data.

As we mentioned at the previous Chapter, we use modified tabular data for the thermal pressure and internal energy as a function of mass density ρ and electron temperature T from the MGGB/SESAME data base [27-29]. These data are depicted at graph 3.2. We also correlate the effective ionization plasma state $\mathrm{Z_{eff}}$ as function of mass density/electron density and electron temperature through the FLYCHK tabular data as presented at figure 3.3 [30,31].

Given the thermal pressure and the mass density via the curvilinear mapping $\mathrm{P=P(\rho,T)}$ the temperature is evaluated at the execution and afterwards the internal energy density is computed using the $\mathrm{\rho e=\rho e(\rho,T)}$ table and vice versa. As PLUTO works with the conservative variables and produces as output the primitive, the temperature is the common value that relates the thermal pressure P and mass density ρ with internal energy density ρe, ionization state $\mathrm{Z_{eff}}$ and electron density $\mathrm{N_e}$. This is also the safest way to estimate the real spatiotemporal temperature profile from the graph tabular data of 3.2 and 3.3 figures filling in the gap of the temperature calculation profile of the

original code that also ignores the dynamic evolution of $Z_{eff}= Z_{eff}(\rho,T)$ for metal plasmas materials! This cyclic correlation is depicted at flow chart/smart-art diagram 4.17:

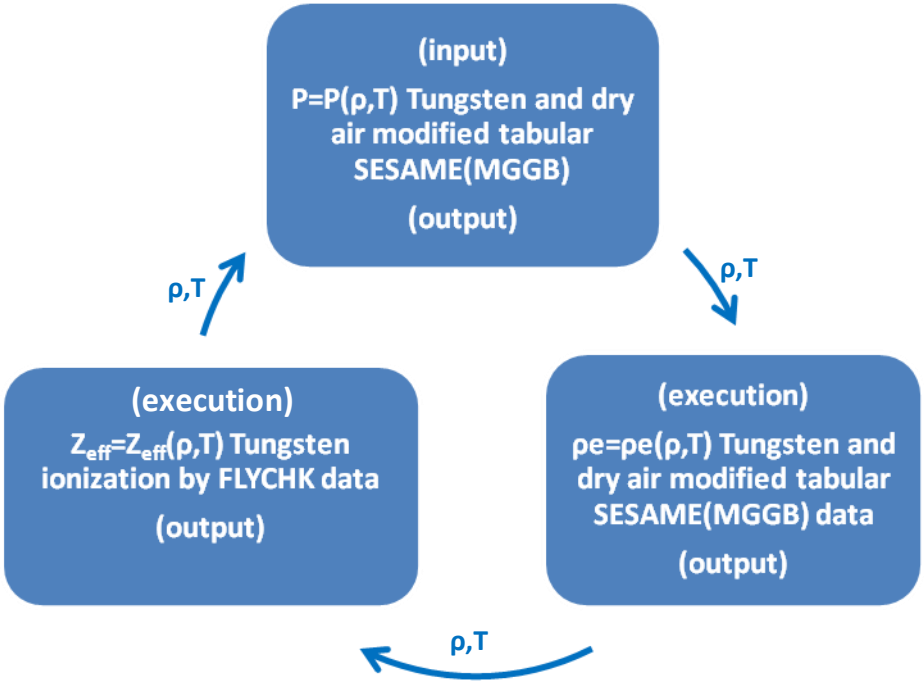

Figure 4.17: *The input/output data of thermal pressure P cyclic correlation with internal energy ρe and effective ionization charge state Z_{eff}.*

All the physics variables can be evaluated along the simulation run through the appropriate expressions of the aforementioned variables and can be extracted as output data from the code (i.e. the Spitzer resistivity formula of the 3.52 equation that is $\sigma=f(Z_{eff}, \rho, T)$).

4.3.2 The spatial grid and coordinate system

Our plasma materials consist of simple cylindrical geometry configurations (i.e. Z-pinch single cable or wire arrays) to more complex ones (i.e. X-pinch two wire or conical Z-pinch arrays). The most appropriate coordinate system that is valid at any case is the Cartesian one. The correct initial condition expressions implementation for the mass density, current density and the magnetic field to these systems are analytically discussed along the sections 4.1 and 4.2.

PLUTO is a finite volume/ finite difference code. Thus, the computational grid consists of 3D static spatial cells that at the base grid case correspond to level 0, while higher levels are used at the AMR version of the code [32]. The discretization is defined at each axis from the number of points that are specified. If a uniform computational grid is formed, the grid spacing is defined at each direction from the ratio of the length of each computational box dimension to the number of points that are taken at this direction. This ratio outcome should be the same for each of the three directions for a **uniform** grid.

The next figure presents an example of the computational mess, the cubic unit cells and the discretization at each axis depicting the initial mass density (in gr/cm^3) distribution of a Z-pinch plasma.

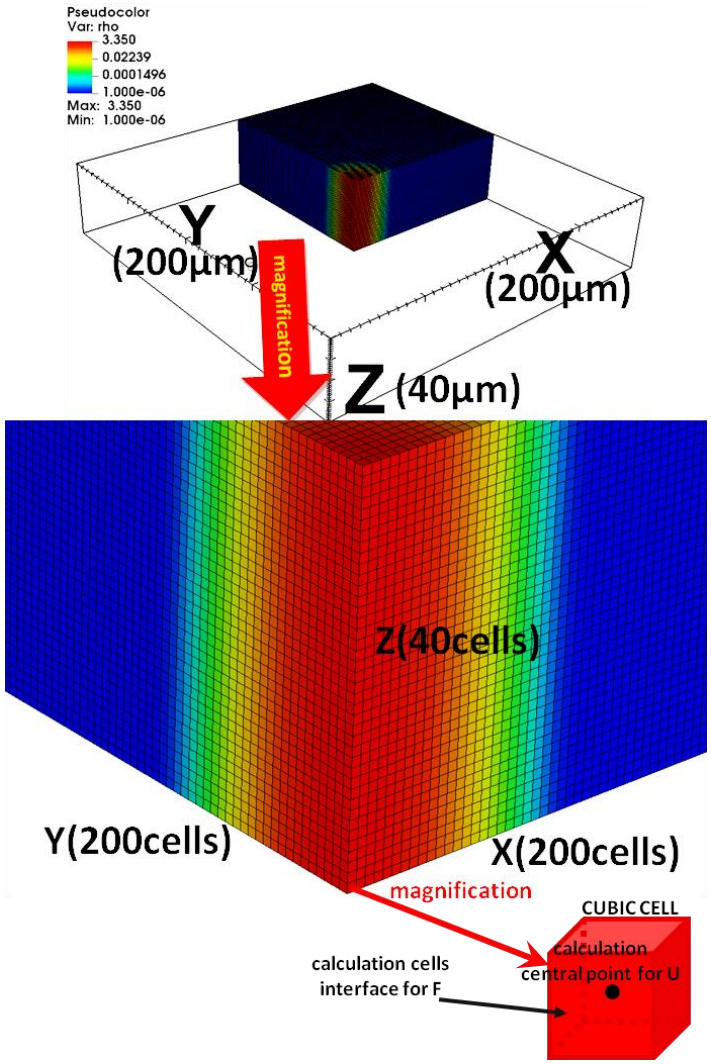

Figure 4.18: *The top picture depicts the Z-pinch formation of the 4.9 figure with the Cartesian computational mesh depiction of the 1/4 spatial distribution of the computational box. A magnification picture is the one at the bottom left, depicting the computational cubic cells, while the magnification of one cubic cell of 1μm edge is the one at the right bottom picture. The grid consists of 200x200x40 cubic cells at X-Y-Z axis respectively.*

However, the cell aspect ratio can be different than one leading to a rectangular unit cells domain. This is a strategy we use for the Z-pinch and X-pinch configuration at the next Chapter where we want a finer resolution at the YX and YZ plane respectively due to the study of the plasma radial expansion (Z-pinch) and jet evolution (X-pinch). The other options are the streched grid, logarithmic grid [1] and the adaptive mesh refinement (AMR) functionality through the Chombo library [32]. This work uses only the uniform cubic and rectangular cell spatial domain.

In PLUTO, volume averages are first reconstructed using piecewise monotonic interpolants inside each computational cell. Although the components of conservative variables **U** are the primary variables being updated, fluxes **F** are more conveniently computed using the primitive vector **V** [1,26,32]. A Riemann problem is then solved at each interface with discontinuous left and right states, and the solution is finally evolved in time for **U**. This is a supplementary description of the conservative

variables updating along time for the simulation run as we discussed before (see figures 4.16 and 4.17).

When the computational grid is generated, each processor owns a domain portion defined by the global integer variables IBEG ≤ i ≤ IEND, JBEG ≤ j ≤ JEND and KBEG ≤ k ≤ KEND. Ghost cells are added outside the local computational domain to complete the stencil at the boundaries. This is depicted at the next figure 4.19. The global variables NX1, NX2 and NX3 define the total number of points (boundaries excluded) such as IEND - IBEG + 1 = NX1, JEND - JBEG + 1 = NX2, KEND - KBEG + 1 = NX3. The total number of zones (for a given processor, boundaries included) is given by the global variables NX1 TOT, NX2 TOT and NX3 TOT (see figure 4.19) [1,26]. For our Cartesian case X1,X2,X3 represent the X,Y,Z spatial directions respectively.

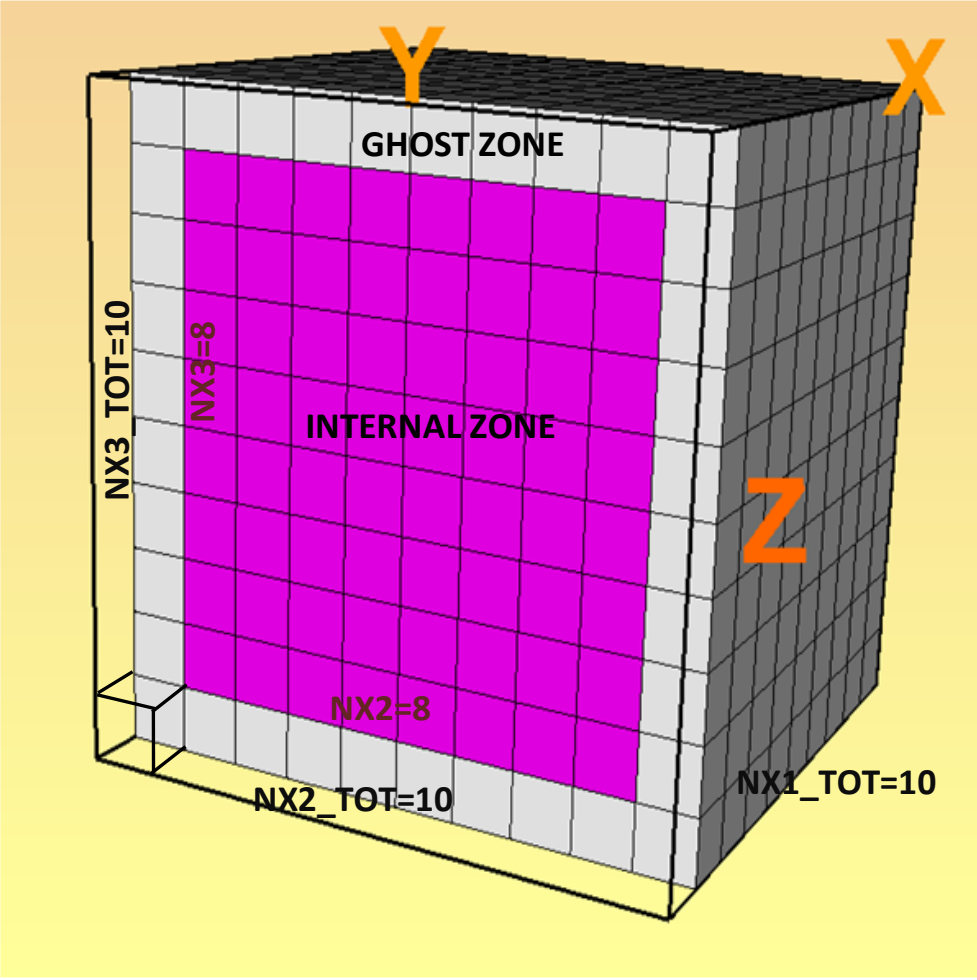

Figure 4.19: 3D *computational grid with NX1 = NX2 = NX3=8 and 1 ghost zone cells giving NX1_TOT = NX2_TOT = NX3_TOT=10. Internal zones (magenta boxed) are spanned by IBEG ≤i ≤IEND, JBEG ≤ j ≤ JEND and KBEG ≤ k≤ KEND. Grey colored boxes represent boundary ghost zones. The front line ghost cells are not depicted except the transparent first at the left corner.*

4.3.3 The Riemann solver for flux computation

The exact solution to the Riemann problem involves the decay of a set of nonlinear waves and can be a rather challenging task to achieve. The standard PLUTO code version has seven different Riemann solvers which are: two shock, roe, ausm+, hlld, hllc, hll, tvdlf, from the most accurate to the most diffusive ones.

We have run a numerous amount of Z and X-pinch models. We conclude that more accurate Riemann solvers may introduce insufficient numerical dissipation for certain flow morphologies. Sporadically, this could lead to a number of numerical pathologies such as the increase of diffusive behavior especially at the magnetic field, odd-even couplings or lack of positivity-preserving properties such as mass density, thermal pressure and internal energy density [26]. This is due to the complexity of our configurations, especially the X-pinch ones.

The ones we thoroughly tested for a single Z-pinch configuration and present at the second section of the next Chapter are the hllc (more accurate) and the tvdlf (more diffusive) solvers. The roe is more sensitive to our simulations, sometimes not preserving the positivity of the physical variables till the end of the execution runs. The same holds for the hlld but not for the hll. The other two are used only for HD problems [1].

After a long testing period and the evaluation presented at the next Chapter, the most appropriate choice for our problems seems to be the tvdlf solver (a Total Variation Diminishing (TVD) Riemann solver for the computation flux, that is based on a Lax-Friedrichs scheme (TVDLF)) [26]. Of course this is not the only choice depending on the nature of the simulation run and the computational scheme. If the Riemann solver is deactivated at the vacuum area (as we discussed earlier and analyze at the 4.3.8 sub-section) the hll and hllc are also robust choices.

The radiation transport PLUTO version uses two different solvers for the matrix equation. The first one is the built in SOR solver that uses the Successive Over Relaxation (SOR) method and a faster and more flexible solver that uses the PETSc library [33]. In our simulations, the built in SOR solver is used.

4.3.4 The reconstruction scheme

The reconstruction scheme sets the spatial order of integration. Interpolation routines are designed to reconstruct a piece-wise polynomial approximations P(x) to the primitive variables **V** inside each cell for the output values of the physics variables [26]. Reconstruction methods have to satisfy monotonicity constraints in order to avoid false oscillations in proximity of discontinuities and sharp gradients. The built in options are [1]:

FLAT: first order reconstruction. The stencil is 1 point.

LINEAR: piecewise TVD linear reconstruction is applied to primitive variables. It is 2nd order accurate in space. Stencil is 3 point wide.

WENO3: provides 3rd order weighted essentially non-oscillatory reconstruction inside a cell using is 3-point stencil.

LimO3: provides 3rd order limiter function based on a 3-point stencil.

PARABOLIC: piecewise parabolic method (PPM) as implemented by A. Mignone [A. Mignone 2014]. The stencil requires 5 zones.

In our simulations for the Z-pinch single-wire configurations due to the simpler azimuthal form of the magnetic field topology and the nearly cylindrical symmetry of the physical variables both LINEAR and WENO3 are effective till later simulation times. For the X-pinch configurations we use WENO3 that employs a local three-point stencil to achieve piece wise quadratic reconstruction for smooth data preserving accuracy at local extrema (something that we have as an example for the thermal pressure or magnetic field magnitude at very small areas i.e. the crosspoint area inside and outside the interface with the vacuum at later simulation times).

4.3.5 Time stepping scheme

Here we present the time stepping scheme that controls the time step evolution along the simulation run. It uses a combination of different time-marching algorithms, the determination of the Courant-Friedrichs-Lewy (CFL) number, the CFL parabolic number, the Explicit Time Stepping integration and the Super-time-Stepping (STS) technique.

4.3.5.1 Time stepping algorithms

PLUTO has several time-marching algorithms, which can be used in either a spatially split or unsplit fashion, that are analytically described in references [1] and [26]. These are :
EULER: 1st (explicit) Euler algorithm.
RK2, RK3: 2nd or 3rd-order TVD Runge Kutta is used to advance the solution to the next time level.
CHARACTERISTIC TRACING, HANCOCK: The input states for the Riemann solver are computed by Taylor expansion of the primitive variables at half-time step. They are 2nd order accurate in space and time and less dissipative than the previous multi-step algorithms. HANCOCK should be combined with linear reconstruction, while CHARACTERISTIC TRACING which does a more sophisticated characteristic limiting, can be combined with all reconstruction algorithms [1,26].

The choice for our work is usually the RK2 algorithm along with the WENO3 reconstruction scheme. The extra switch here is the **DIMENSIONAL_SPLITTING**, where it can be set to YES or NO. If it is active, the operator $\mathcal{L}$ that denotes the discretized spatial operator in equation 4.44 is one-dimensional. If it is deactivated, the contribution includes all the directions simultaneously [1]. Due to the intense dissipative nature of our simulations, the high spatiotemporal derivatives of the physics variables (i.e. in resistivities and thermal conductivities or in magnetic induction) and the topology of our plasma configurations, the unsplit scheme is preferred. Generally dimensionally unsplit schemes avoid the errors due to operator splitting and are generally preferred in all problems (astrophysical and laboratory). Unsplit implementation of the Runge-Kutta algorithms usually requires a more restrictive CFL condition. This is something that we discuss right away.

4.3.5.2 Time stepping determination (Courant-Friedrichs-Lewy (CFL) number)

The time step Δt^n is computed using the information available from the previous integration time step algorithms and it can be controlled by the Courant-Friedrichs-Lewy (CFL) number C_a. The dimensional unsplit scheme along with Runge Kutta integration sets a higher limit to the choice of the C_a number that is practically $C_a \leq 1/N_{dim}$ [1,26], where N_{dim} in our case is three. An extra number controlling the

ratio of two consecutive steps is the CFL_max_var that sets the maximum value allowed for $\Delta t^n / \Delta t^{n-1}$. For our case we take a value approximating unity (~1.1).

4.3.5.3 Numerical integration of diffusion terms

Parabolic terms introduce second-order spatial derivatives and their treatment requires the solution of diffusion equations. Typical examples include electric resistivity, thermal conductivity and viscosity terms. These terms may be included in the original conservation law with the further time step limitation $\Delta t=\min(\Delta t^{adv}, \Delta t^{par})$, where the Δt^{adv} and Δt^{par} are the advective and parabolic time step respectively.

There are two different integration schemes when the diffusion terms of the right hand side in equation 4.44 are included: the Explicit Time Stepping and the Super-Time-Stepping (STS) [1]. The first treats the parabolic and hyperbolic fluxes at the same time in an unsplit fashion. In our problems, high resolution and large diffusion coefficients lead to drastic reduction of the time step along the simulation runs thus making the computation impracticable. This is fixed if we choose the STS integration scheme. In this case, the parabolic terms are treated in a separate step using operator splitting and the solution vector is evolved over a super time step, equal to the advective one. It is less accurate but way more efficient than the explicit one. It is mentioned [26] that in diffusion dominated problems with high resolution the parabolic time step will eventually drop below the advection term. Without the STS contribution, our configurations due to their demanding dissipative nature produce a very low value time step making practically impossible the execution of the simulation.

Two extra coefficients are set to control the time step evolution when the STS module is activated. The first one is the Cp (parabolic Courant number) that should be $Cp \leq 1/N_{dim}$ and is declared as CFL_par. The second parameter controls the scale disparity between advection and diffusion time scales by restricting the time step Δt_n to be at most $r_{max}\Delta t_{par}$, where r_{max} is a free parameter (rmax_par in PLUTO language) [1].

A typical set of the CFL number related variables we use for the X-pinch configuration are:

CFL=0.25-0.3

CFL_max_var=1.1

CFL_par=0.25

rmax_par=50.0-60.0

4.3.6 Solenoidal Constraint

The solution to the MHD equations must fulfil the solenoidal constraint of the magnetic induction, $\boldsymbol{\nabla \cdot \mathbf{B} = 0}$ (no magnetic monopoles at the computational domain). This is practically impossible to be true for the whole spatiotemporal evolution in the computational domain. The three formalisms PLUTO adopts are: the Eight-Wave-Formulation, the Hyperbolic Divergence Cleaning and the Constrained Transport (CT) [1,26]. The first two are usually used for the Z-pinch configurations, while the second one is the more robust for the X-pinch configurations. The second one couples the induction equation to a Generalized Lagrange Multiplier (GLM). A slightly different version, called the

extended GLM formulation is better for our problems, especially at the X-pinch cases. This is used for the X-pinch configuration at the next Chapter.

4.3.7 Ntracer-passive scalar process

A more sophisticated technique is the Ntracer-passive scalar multi-material process that is implemented in PLUTO by the NTRACER switch [1]. It is a common technique in HD turbulent mixing flows [34]. Similar situations are also studied in Astrophysics i.e. in the turbulent interstellar material mixing flows [35]. The existence of the vacuum region in this MHD simulation is modelled using a low-density background, as we already have mentioned. Thus, a multimaterial approximation is adopted for the transition zone, which is identified using a passive scalar function. This approach results to a mixing process of the two materials and is adopted to monitor nonphysical transitions. Selecting the mass density ρ as the origin of the passive scalar variable, we introduce a function TRC in the code that is advected through equation (4.43). As MHD is a more complex and diffusive evolution process than the fluid HD cases, the passive scalar treatment introduces a better mixing procedure of the two plasma materials, the plasma temperature and the magnetic field evolution, avoiding this way early shock waves and jump conditions. The PDE that is used in a conservative form is:

$$\frac{\partial(\rho Q)}{\partial t} + \nabla \cdot (\rho Q \mathbf{u}) = 0 \tag{4.43}$$

where Q is the passive scalar variable. The mixing material procedure and the passive scalar treatment are analytically discussed at the second and third sections of the next Chapter respectively. If the Riemann solver is deactivated at the vacuum region, as we discuss at the next section, this is not an active approach.

4.3.8 Boundaries

Pluto has a variety of embodied sets of boundary conditions. The user can also code their own boundary conditions if it is necessary for the physical problem [1]. Here we present the appropriate boundary modules of our needs for the Z-pinch single cable, Z-array and X-pinch configurations. Most of the models at the next Chapter are a symmetric part of the experimental devise and the boundary conditions are crucial for the correct plasma evolution. These are:

i. outflow

Sets zero gradient across the boundary for the scalar and the vector variables. They are the typical set for a Z-pinch or an X-pinch configuration considering a large computational box, having the boundary planes as far as possible from the main plasma evolution. This set is valid for every boundary plane only if we simulate the whole geometry configuration (not necessarily the whole experimental) and not a symmetric part.

ii. reflective

Reflective (rigid walls) boundary conditions. Variables are symmetrized across the boundary and normal components of vector fields flip signs. This set is used for the xy (z=0) boundary plane of the

1/8 volumetric modelling of the X-pinch configuration due to the specific X symmetry of the **B** field, the vector velocities and the scalar variables at this plane (see figure 4.20).

iii. eqtsymmetric

Sets equatorial/mirror symmetry with respect to a given plane. It is similar to reflective, but with reversed sign for the magnetic field, we use it at the xz (y=0) and yz (x=0) planes to simulate the previous model (figure 4.20). This is also valid for the Z-array configuration, modeling only one of the four plasma cables or a Z-pinch single wire simulating 1/4 of the plasma cable (figure 4.20).

iv. periodic

Sets periodic boundary conditions on both sides of the computational domain. This is valid for the Z-pinch single wire or array configuration at the interface of the boundaries and the plasma cylinder (figure 4.20).

v. User defined boundaries at the interface of the X-pinch cable and the boundary surface. We set there zero the normal components, similarly with the outflow case, for all the primitive quantity values, constraining the cable end along the simulation run (figure 4.20).

The boundary conditions set for the radiation solver, follow the same assumptions described above.

vi. Internal boundary conditions

The user has full control over the solution array enabling this option. This feature can be used to adjust the value of selected cell-centered primitive variables inside a specific region of the computational domain rather than at boundaries. We can isolate a spatial area making it time-independent, where variables are fixed in time and do not evolve by the algorithm. This is an option tested at the next Chapter along with a similar technique used by GORGON. The threshold value is the vacuum mass density. All the primitive variables have a fixed value at the vacuum area except the magnetic field spatiotemporal evolution that is still active in the whole computational domain.

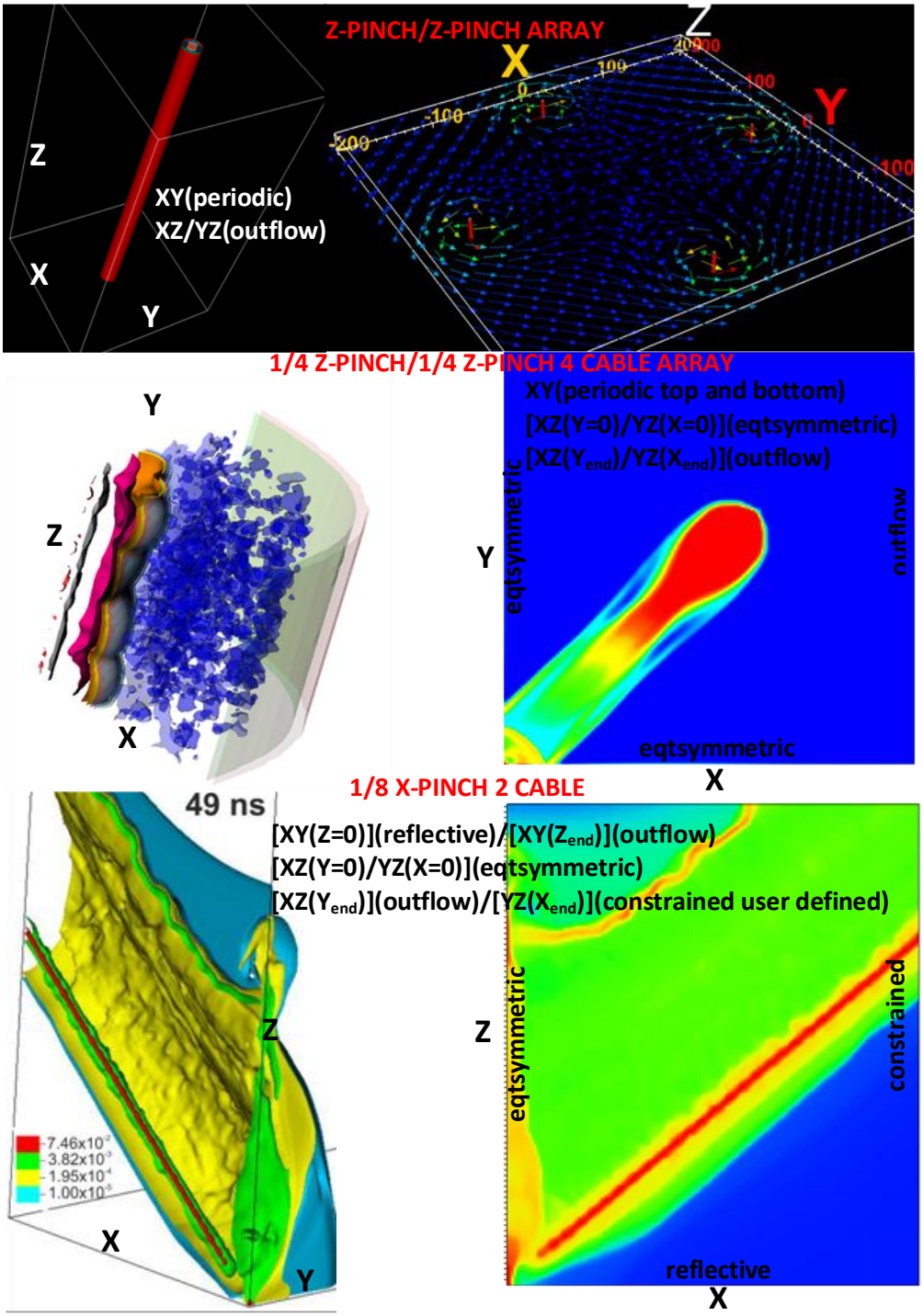

Figure 4.20: *PLUTO models of Z-pinch, Z-pinch array and X-pinch configurations. The first row depicts the whole configuration and the other two 1/4 and 1/8 symmetric models respectively presenting the set of boundary conditions for each case. The 2D pictures are at the mid plane of the computational box.*

4.3.9 Dimensionalizing the physical variables of PLUTO

Pluto by default works without unit dimensions. This way, it avoids that flow quantities can be properly scaled to “reasonable” numbers in order to avoid occurrences of extremely small or large numbers

that may be misinterpreted by numerical algorithms [1]. For our case, dimensionalization is necessary due to the dissipative nature of our problem and the experimental estimation of the spatiotemporal evolution of all the physics variables. We return to the scale invariant description of our variables at the last section of the next Chapter, where we present the Laboratory-Astrophysical scaling.

PLUTO requires three fundamental units to be specified through the definitions of the following symbolic constants ρ_o, u_o and l_o, which are the unit density, velocity and length in c.g.s units [1]. A typical set for our case are $\rho_o = 10^{-6} gr/cm^3$, $u_o = 10^6 cm/s$ and $l_o = 10^{-3} cm$. All the other unit variables are a combination of these three i.e. $t_o = l_o/u_o = 1ns$ (a typical time for our case that the timescale is a few tens of nanoseconds). This is also the unit value n_o for the resistivity. The thermal pressure and magnetic field units are: $P_o = \rho_o u_o^2 = 10^6 dyn/cm^2$ (through the definition of the Bernoulli pressure) and $B_o = (4\pi \rho_o u_o^2)^{0.5} \sim 3.5 \cdot 10^3$ Gauss (through the Alfvén velocity definition).

All the physics variables can be dimensionalized from the unit values through the equation, $A_{cgs} = A \cdot A_o$, where the A is the dimensionless PLUTO variable and A_o the relevant unit variable in c.g.s metric system.

4.4 Summary/Conclusions

PLUTO is a very powerful numerical tool, with a lot of different switches and numerical schemes that offer flexible combinations to simulate the physical problem. The variety of 7 Riemann solvers, 5 Reconstruction schemes, 8 different boundary condition implementations (including the user defined and internal boundary module for more and better choices for the outer and inner boundaries respectively), 5 different marching algorithms for the time step determination, are among other alternatives that this code offers. These are only for the 4.2 version while the 4.3 has additional modules i.e. particle-related options and the Hall MHD term in the dissipative form [36,37,38]. The flexibility of the code also relies on the C programming language and the numerous subroutines implemented for each MHD or dissipative term. This way we can directly modify the relevant terms adjusting them to the physical problem of interest.

Now PLUTO is capable of simulating satisfactory (see next Chapters for the results detailed analysis) laboratory metal plasmas of all different material and magnetic field geometries. For the time being the only metal plasma implemented in the code is tungsten but it can be (and will be) implemented to any metal plasma with known tabular data from the FLYCHK code [30,31] and the SESAME/MGGB EOS [29,30].

The mathematical and physical model using the Local to Global and vise versa physics variable correlation, as we described in section 4.1, provide a useful technique for the initial condition topology of all the physics variables, including the magnetic field, of any plasma configuration of a Z-pinch, X-pinch and Z-pinch array, as we analytically presented. This modelling is also used in GORGON code for the mass density and temperature profiles presenting similar results with the simulation runs of PLUTO with the same geometry modelling (this is examined thoroughly at the Result Chapter as we already mentioned and at this Chapter at the preliminary results section of the "cold" start model).

The preliminary results from the X-pinch tangent wires with the GORGON code and the Z-array with PLUTO are very promising and insightful according to the initial stages of the plasma evolution (i.e. at the "cold" start of two tungsten wires and their matching with the experimental description) for a

more detailed future work. The validation of the simulations results from the PLUTO (considering experimental data) and GORGON models for the Z-pinch and X-pinch configurations is the subject of the next Chapter.

References

[1] http://plutocode.ph.unito.it/PLUTO User's Guide v.4.2.

[2] Jackson J D 1975 Classical Electrodynamics (New York, John Wiley and Sons) pp 298, 481.

[3] Hank Childs et al, " VisIt: An End-User Tool For Visualizing and Analyzing Very Large Data", 2012 Oct, pp 357-372.

[4] G W Collins et al, "Effect of the global to local magnetic field ratio on the ablation modulations on X-pinches driven by 80 kA peak current", New Journal of Physics **14** (2012) 043021.

[5] Ning Ding et al, "Theoretical and Numerical Research of Wire Array Z-pinch and Dynamic Hohlraum in the IAPCM", Volume 1, Issue 3, May 2016, pp 135-152.

[6] C. J. Garasi et al, **"**Multi-dimensional high energy density physics modeling and simulation of wire array Z-pinch physics", PHYSICS OF PLASMAS VOLUME 11, NUMBER 5 MAY 2004.

[7] Felipe Veloso et al, **"**Ablation dynamics in wire array Z-pinches under modifications on global magnetic field topology", PHYSICS OF PLASMAS 22, 072509(2015). https://doi.org/10.1063/1.4926581

[8] S. A. Pikuz et al, X-Pinch. Part I, PLASMA PHYSICS REPORTS Vol. 41 No. 4 2015.

[9] T. A. Shelkovenko et al, "Evolution of the structure of the dense plasma near the cross point in exploding wire X pinches", PHYSICS OF PLASMAS VOLUME 6, NUMBER 7 JULY 1999.

[10] G V Ivanenkov et al, "Experimental study of X-pinch dynamics", Plasma Physics Reports, Vol 22, No 5., 1996, pp 363-378.

[11] I. H. Mitchell, "Investigation of the plasma jet formation in X-pinch plasmas using laser interferometry", PHYSICS OF PLASMAS VOLUME 7, NUMBER 12 DECEMBER 2000.

[12] R. Aliaga-Rossel et al, "Plasma Jet Formation in X-pinch Plasmas", AIP Conference Proceedings **563**, 270 (2001); doi: 10.1063/1.1374920.

[13] Richard Fitzpatrick, "Magnetic reconnection in weakly collisional highly magnetized electron-ion plasmas", PHYSICS OF PLASMAS **17**, 042101 (2010).

[14] G. S. Jaar and R. K. Appartaim, "Axial plasma jet characterization on a microsecond x-pinch", JOURNAL OF APPLIED PHYSICS 123, 213301 (2018).

[15] A. Ciardi et al, "The evolution of magnetic tower jets in the laboratory", PHYSICS OF PLASMAS **14**, 056501 (2007).

[16] J. P. Chittenden, "The effect of lower hybrid instabilities on plasma confinement in fiber Z pinches", Physics of Plasmas **2**, 1242 (1995); doi: 10.1063/1.871401.

[17] S.I Braginskii , "Transport processes in a plasma", Reviews of Plasma Physics, Volume 1, 206-311 (1965).

[18] J. P. Chittenden et al, "Two-dimensional magneto-hydrodynamic modeling of carbon fiber Z -pinch experiments", Phys. Plasmas **4** (12), December 1997.

[19] M. Tatarakis et al, "Optical probing of fiber z -pinch plasmas", PHYSICS OF PLASMAS VOLUME 5, NUMBER 3 MARCH 1998.

[20] J. P. Chittenden et al, "One-, two-, and three-dimensional modelling of the different phases of wire array Zpinch evolution", PHYSICS OF PLASMAS VOLUME 8, NUMBER 5 MAY 2001.

[21] V. I. Oreshkin et al, "X-pinch dynamics: Neck formation and implosion", PHYSICS OF PLASMAS 21, 102711 (2014).

[22] HPC| National HPC Infrastructure - http://doc.aris.grnet.gr/system/hardware/.

[23] J. Ruiz-Camacho et al, "Z-pinch discharges in aluminum and tungsten wires", PHYSICS OF PLASMAS VOLUME 6, NUMBER 6 JUNE 1999.

[24] J. P. Chittenden et al**,** "X-ray generation mechanisms in three dimensional simulations of wire array Z-pinches", Plasma Phys. Control. Fusion **46** (2004) B457–B476.

[25] A. Mignone et al, "PLUTO: A NUMERICAL CODE FOR COMPUTATIONAL ASTROPHYSICS", The Astrophysical Journal Supplement Series, 170:228Y242, 2007 May.

[26] A. Mignone, "The PLUTO code for astrophysical gasdynamics", Mem. S.A.It. Suppl. Vol. 13, 67.

[27] T-4 Handbook of Material Properties Data Bases, Vol Ic: Equations of State, LA-101 SO-MS, UC-34, Issued November 1984.
[28] SESAME THE LOS ALAMOS NATIONAL LABORATORY EQUATION OF STATE DATABASE, LA-UR_92_3407.
[29] Kashiwa B.A., "The MGGB Equation-of-State for Multifield Applications: A Numerical Recipe for Analytic Expression of Sesame EOS Data", LA-1442 ,September 2010. http://www.doe.gov/bridge
[30] Tungsten Charge State Distribution by FLYCHK NLTE Kinetics Calculation at NIST by International Atomic Energy Agency- Atomic Molecular Data Services provided by the Nuclear Data Section.
[31] H.-K. Chung et al, "FLYCHK: Generalized population kinetics and spectral model for rapid spectroscopic analysis for all elements", High Energy Density Physics 1 (2005) 3-12.
[32] A. Mignone et al, "THE PLUTO CODE FOR ADAPTIVE MESH COMPUTATIONS IN ASTROPHYSICAL FLUID DYNAMICS", The Astrophysical Journal Supplement Series, 198:7 (31pp), 2012 January.
[33] Stefan M. Kolb, Matthias Stute, Wilhelm Kley, Andrea Mignone, "Radiation hydrodynamics integrated in the code PLUTO", A&A 559, A80 (2013).
[34] P. Ouro et al., "Instantaneous transport of a passive scalar in a turbulent separated flow", Environ Fluid Mech , 4 December 2017, https://doi.org/10.1007/s10652-017-9567-3.
[35] Matthew J. Colbrook et al., "Scaling laws of passive-scalar diffusion in the interstellar medium", MNRAS 467, 2421–2429 (2017) , doi:10.1093/mnras/stx261.
[36] http://plutocode.ph.unito.it/PLUTO User's Guide v.4.3.
[37] A. Mignone et al, "A Particle Module for the PLUTO Code. I. An Implementation of the MHD–PIC Equations", The Astrophysical Journal, 859:13 (22pp), 2018 May 20.
[38] B. Vaidya et al, "A fluid-particle hybrid framework for the PLUTO code: applications to non-thermal emission in jets", ASTRONUM-2015 Journal of Physics: Conference Series **719** (2016) 012023.

CHAPTER 5

NUMERICAL RESULTS AND COMPARISON WITH EXPERIMENTS-ASTROPHYSICAL SCALING

5.1 Experimental setup and diagnostics

The X-pinch experiments were carried out at the Institute for Plasma Physics and Lasers (IPPL) in Rethymno, Crete. IPPL is one of the access points of the National Research Infrastructure "ELI-LASERLAB Europe Synergy, HiPER & IPERION-CH.gr" (HELLAS-CH) and was the leader of the "Fundamental Science Program " of the ESFRI research infrastructure HiPER. The three main research fields of the institute are: **i.** Laser Matter Interactions, **ii.** Plasma Science & Technology, **iii.** Numerical Modeling & Simulations [1,2].

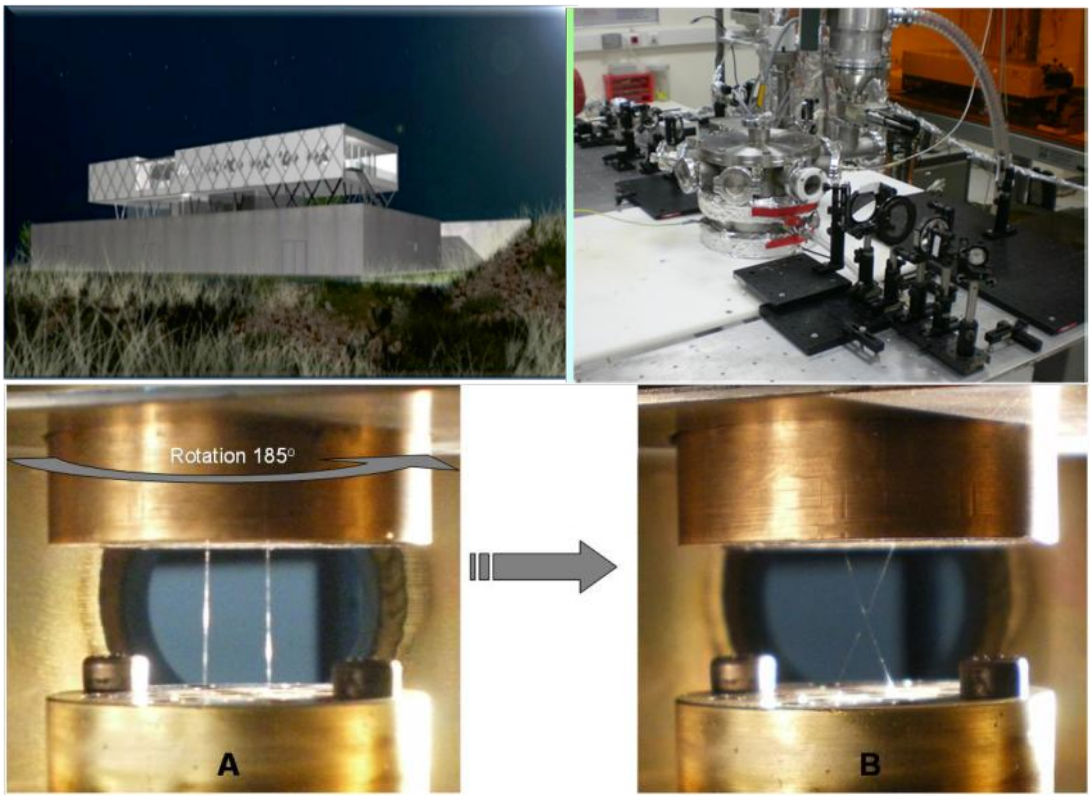

Figure 5.1.1: *Top left: the building of IPPL, Top right: An external picture of the X-pinch setup with the vacuum chambers. Bottom left (A): The initial position of the two wires inside the vacuum chamber connecting the anode and the cathode. Bottom right (B): the final geometry of the two wires after 185^o rotation of the anode for the creation of the X-pinch configuration.*

The X-pinch experiments are carried out using a table-top X-pinch pulsed powered plasma generator implemented in a mode of producing peak currents of ~45-46 kA with a rise time (10%-90%) of ~50 ns, loaded with thin pure metallic tungsten wires. The distance between anode-cathode is 15 mm and the X-pinch wires are set to a wide angle of ~100^o at the third subsection simulations and

experiments and at a sharp angle of 50^{o} at the fourth subsection of the two MHD codes (PLUTO-GORGON) for comparison reasons.

The design and construction of the X-pinch device has been implemented during a funded EU Marie-Curie Transfer of Knowledge Excellence Grant “DAIX” (Development of an Innovative X-ray source) on pulsed power X-pinch plasma devices [3].

The device is a Capacitive Energy Storage Generator type (CESG) that consists (see Figure 5.1.2) of a high voltage pulsed power supply (Known as Marx generator), a high voltage & current coaxial wiring, a pulse forming line (PFL), a self-breaking spark gap switch (SBS) and a load chamber (vacuum chamber).

It is operated by the Marx bank containing four capacitors (0.22 μF, up to 50 kV each) which then couples the electrical energy into a water dielectric pulse-forming coaxial line having an impedance of ~2 Ohms (figure 5.1.2).

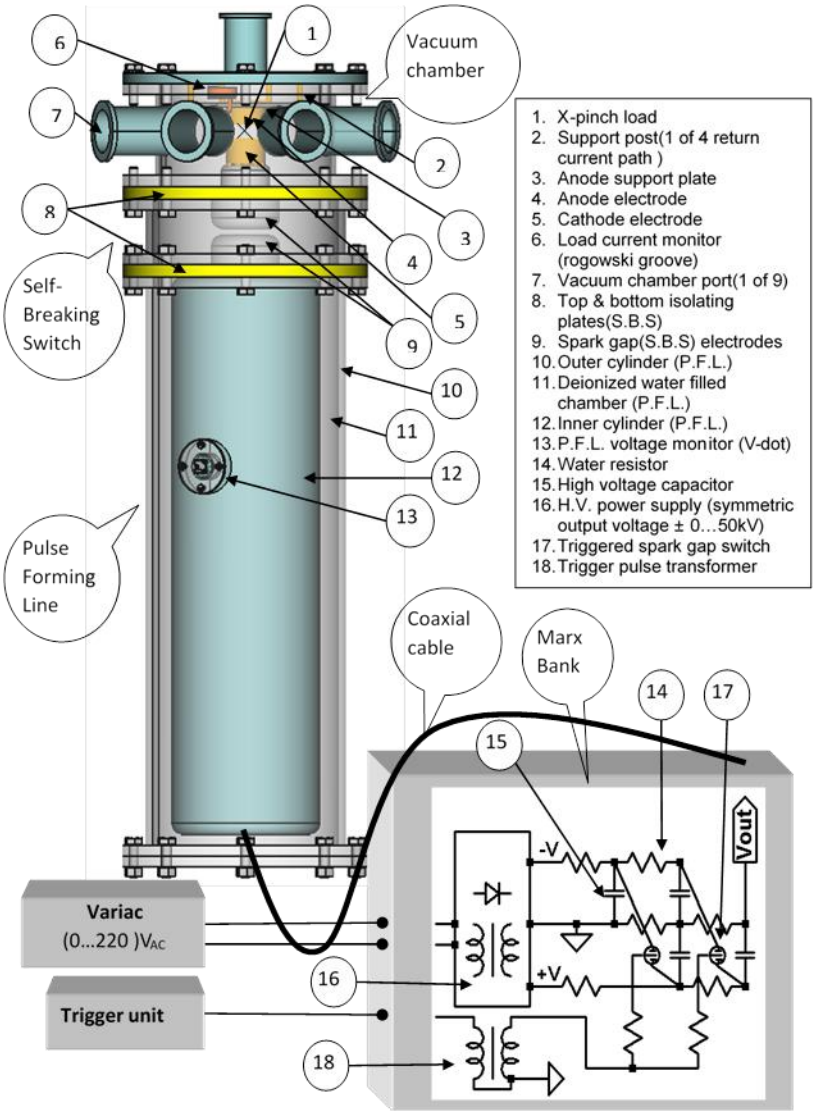

Figure 5.1.2: Schematic presentation of the CESG electrical circuits involved in pulse compression.

The Marx bank charged at 37 kV has a deposited energy of 600J and provides a high voltage negative polarity output to PFL when triggered. After reaching the breakdown voltage of the final spark-gap switch, the current begins to flow through the wire to the anode. The breakdown threshold can be controlled from the buffer gas (SF6) pressure that filled the vacuum chamber that contains the switch. A V-dot probe and a Rogowski groove are used to measure the time derivatives of the voltage at the PFL and, of the current passing through the wire respectively. These signals are recorded by a fast digital oscilloscope (LeCroy, Waverunner 6100A) located inside a home-made Faraday-shielded room. Their time integrations provide the corresponding voltage and current waveforms. The V-dot signal is also used to drive the trigger/delay unit for the laser pulse output. In this way, the jitter due the Marx bank does not affect significantly the time arrival of the laser pulse on the target wire.

The pressure of the SF6 gas is adjusted to the optimum value so that the circuit breaks at the desired voltage (160-220 kV). The load chamber is under high vacuum ($<6\times10^{-4}$mbar), thus ensuring that there is no air-plasma generated. Voltage (V-dot) and current (Rogowski groove) monitors are attached at the end of the pulse forming line and at the anode (fit around one of the four current return posts) of the load chamber, respectively. The load chamber has eight viewing ports allowing multiple diagnostics for single shot [4,5,6,7].

Indicative recorded signals and their integrated waveforms are shown in figure 5.1.3. The V-dot signal corresponds to the derivative of the voltage at the PFL, while its integral corresponds to the PFL voltage. The Rogowski-groove signal corresponds to the derivative of the current, while its integral corresponds to the current waveform [4].

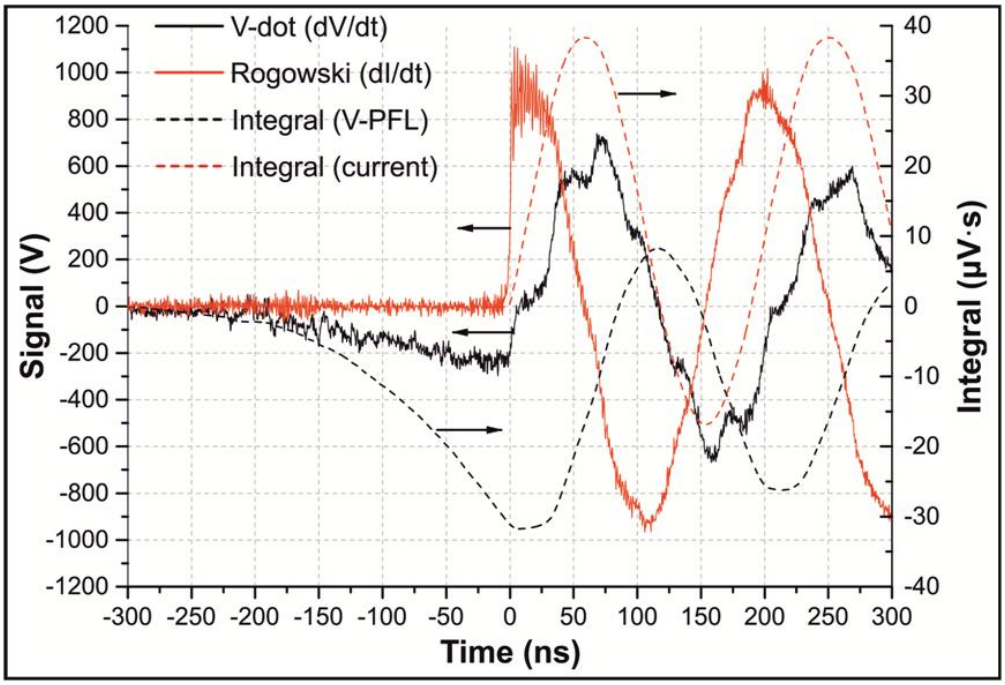

Figure 5.1.3: *Oscilloscope recorded signals and their computed integrals. Arrows indicate the corresponding vertical axis. The current waveform presents a peak current of ~46 kA [4,5].*

The values of the voltage at the PFL and the current are obtained by the multiplication of the integrals by proper coefficients (1.05 kA/μV·sec for current in kilo-amperes and 5.32 kV/μV·sec for voltage in

kilo-volts). Thus we take a current waveform of ~46kA initial magnitude with a period of ~200ns. This is the integral current we use for the code updating along the simulation run (as we already mentioned earlier and analytically discuss at the 5.3 section).

To study the temporal evolution of the plasma in the X-pinch configuration a three frame Mach–Zender type interferometer (or a shadowgraphy set up) is developed and used. A frequency doubled, Q-switched Nd-YAG laser (532 nm) with a backward stimulated Brillouin scattering (SBS) pulse compression generating a pulse of 150 ps duration (FWHM of the Gaussian-like temporal profile), is used as a probing light source. First, as shown in figure 5.1.4, the laser beam diameter is expanded and collimated by a combination of negative (L_1) and positive (L_2) lenses. Then, the broaded spatially beam is directed to a network of two time-delay lines and the beams 1, 2 and 3 are produced. Due to the adjusted differences in the light paths, there are time delays of 6.5 ns between beams 1 and 2, and 7.8 ns between beams 2 and 3. When the probing light beams 1, 2 and 3 with different delays pass though the plasma (cross the same plasma volume), they are (are not) combined with three reference beams and thus, creating a sequence of three frames of plasma interferogram (shadowgram) that are recorded with three CCD cameras respectively. The imaging system is implemented by a single lens (L_3) so that the magnification in the plane of observation is equal to ~0.8. Also, for the suppression of plasma illumination a combination of interference and neutral filters are stacked at the front side of each camera.

This setup was introduced as a single frame diagnostic in [4] and is here modified to capture three plasma images with a temporal delay of ~7ns and ~8 ns. When laser optical probing diagnostics experiments are executed, there is a limitation for the maximum detectable electron density. A characteristic opaque area is formed on shadowgraphy and interferometry plasma images. This opaque area is formed due to a) the plasma critical density effect where the probing laser pulse experiences a cut-off at the critical density and therefore cannot propagate further into the plasma [8,9,10],b) refraction of the probing laser pulse due to the steep plasma density gradients which leads laser rays outside of the acceptance angle of the optical system and c) absorption of the probing laser pulse in the plasma.

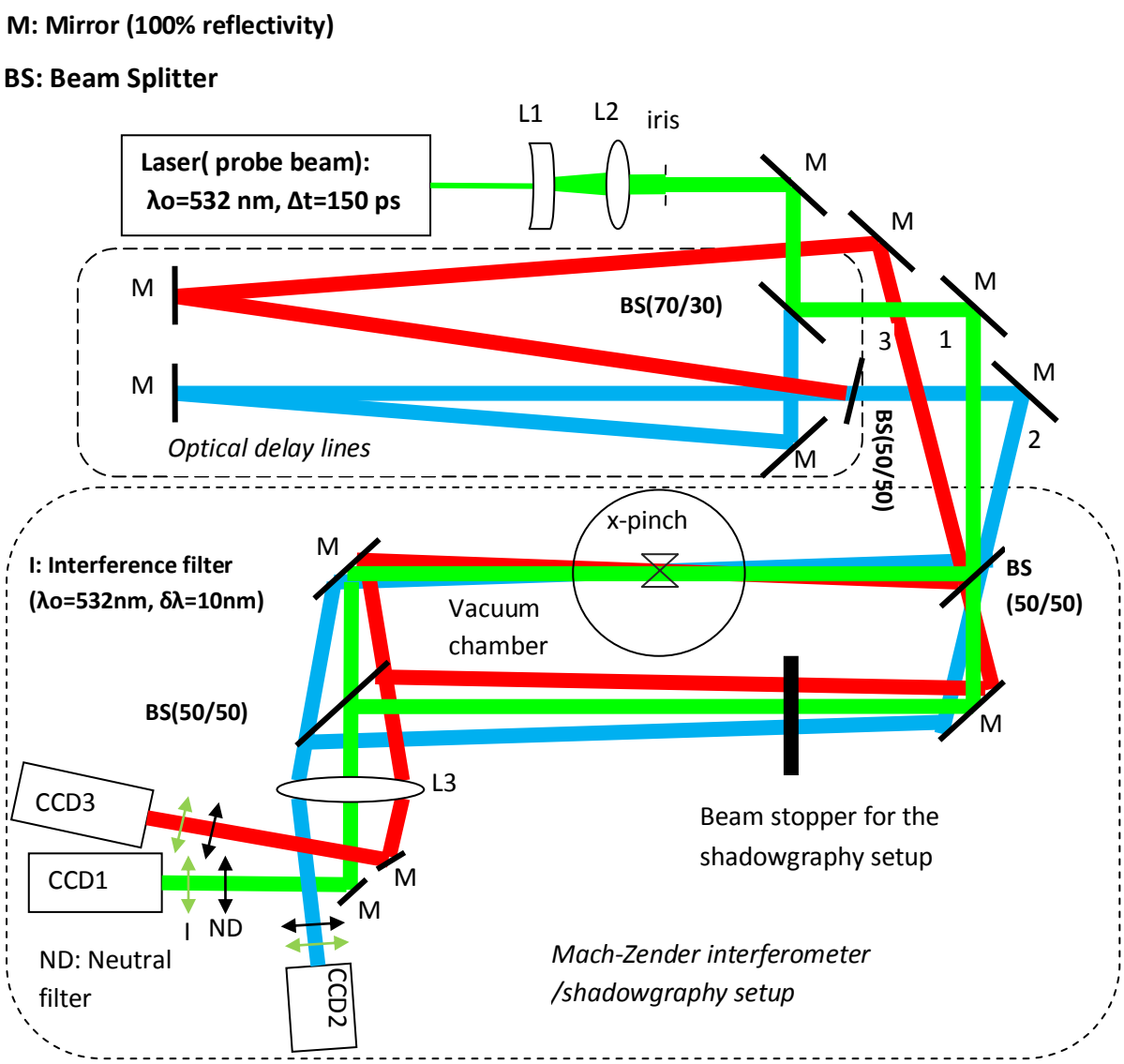

Figure 5.1.4: *2D schematic presentation of the interferometer/shadowgraphy experimental setup.*

In order to gain information concerning the refractive index and hence the electron density of a plasma we have to estimate the critical density n_c. For the calculation of n_c we use the expression for the plasma frequency. Light can only propagates through a plasma if the frequency of the plasma ω_p is lower than that of the probe beam ω_{light}. To determine the maximum density which can be probed, known as the critical density n_c, the frequency of the light is set equal to the plasma frequency:

$$\omega = \omega_p = \sqrt{\frac{4\pi n_c e^2}{m_e}} \tag{5.1.1}$$

Solving for n_c we get:

$$n_c = 1.113 \cdot 10^{21} \lambda^{-2} (cm^{-3}), \text{wavelength } \lambda \text{ in } \mu m \tag{5.1.2}$$

In our case the critical plasma density as it results from the 532nm (=0.532 μm) laser wavelength is n_c = $4.4 \cdot 10^{21} cm^{-3}$ [11,12].

For the detection of the upper and lower limits of the a real electron density we use the interferometry images. The interferometry technique is used to determine the electron density distribution, since the refractive index is related to free electron density. The refractive index in a plasma is given by:

$$n^2 = 1 - \frac{n_e}{n_c} \tag{5.1.3}$$

where n_e is the electron density and n_c is given from 5.1.2 equation. If the plasma electron density is much smaller than the critical one, we get through a Taylor approximation:

$$n \simeq 1 - \frac{1}{2}\frac{n_e}{n_c} \tag{5.1.4}$$

and the phase shift simplifies to:

$$\Delta\phi = \frac{\omega}{2cn_c}\int n_e \, dl \tag{5.1.5}$$

where c is the speed of light and integration in over the spatial dimension of the plasma propagated by the laser beam. For a phase shift $\Delta\phi = 2\pi$ the fringe shift *f* is one. Thus, it is possible to obtain the fringe shift distribution as a function of radius [10,11,12].

Considering a probe beam traveling a distance *l* through the plasma, the line density can be expressed as:

$$\int n_e(cm^{-3})\, dl = 4.0 \cdot 10^{17} f \text{ (areal density in } (cm^{-2})) \tag{5.1.6}$$

For equation 5.1.6 to be true, n_e approximated to be constant through the plasma. If this is not the case, then n_e may be taken as the average electron density along the probe beam path [11]. In most experimental circumstances this is an unrealistic assumption and the density profile can only be recovered through an Abel Inversion [10].

Consequently, the calculation for the determination of the electron density can be performed in the areas of density lower than the density of the opaque area. The upper limit which corresponds to the density border of the opaque area is determined by the analysis of interferograms and correspond to a fringe shift *f* equal to 2.5, before the saturation within the opaque area. This fringe shift corresponds to an areal electron density value equal to $1 \cdot 10^{18}$ cm^{-2} for our 532 nm laser wavelength as obtained by the equation 5.1.5. The lower limit of $2 \cdot 10^{16}$ cm^{-2} corresponds to a fringe shift of ~1/20 of their period, determined by the spatial resolution of the image (figure 5.3.2 at the third section).

The interferometry data are analyzed using the software package IDEA [13]. Prior to each shot, we take a background interferogram to use as the reference for the plasma interferogram. After the plasma discharge, both the background and the plasma interferograms were imported into IDEA and processed identically. IDEA first performs a Fast-Fourier transform (FFT), producing a zero frequency.

This zero frequency is selected, and the program then performs a reverse FFT to recreate the image, which then allows IDEA to determine the phase shift of the fringes relative to a point selected near the center of the image. The contours of the phase-shift data are then smoothed to create a continuous profile. At this point, we subtract the background phase-shift image from the phase shift image of the X-pinch discharge, giving a difference profile. The areal electron density mapping is produced via a simple rescaling that sets the minimum value in the image to zero and then multiplies by a constant specific to the wavelength of the laser used. Through the use of the interferogram analysis program IDEA it is possible to generate a continuous areal density plot which provides a more complete picture when compared with measuring densities at discrete location (see the third section and [11] and [14] for further discussion).

The simulated areal electron density at the yz plane for the X-pinch plasma formation is obtained by integrating the volumetric electron density along the x-axis. A multiplication by 2 delivers the total electron density considering the negative x-axis octant due to the 1/8 symmetry of the PLUTO models. The areal densities of the simulation are extracted using the well known software programming language MATLAB by MathWorks (experimental and simulation areal densities are at the 5.3.4 figure in section three of this Chapter).

The shadowgraphy experimental imaging technique is the second image type in this work. The focused shadowgraphy channel is sensitive to record the second derivative of the density gradients and is used for qualitative analysis only (see the relative third section and figure 5.3.2).

A similar experimental setup, as in figure 5.1.2, was used also in the experiments of the Z-pinch tungsten configuration at the next section. The current generator (IMP) used to drive the fiber Z-pinch consists of a high voltage Marx bank (eight capacitors, each of 0.7 mF, 100 kV), which charges the pulse forming line. The transmission line is coaxial with a water dielectric. It has impedance of 4V and a single transit time of 40 ns. The pulse forming line voltage is applied to a Z-pinch load via a fast self-breaking SF6 switch. The load is isolated from the switch inductance using a matched transfer section. The generator provides a peak current of 160 kA with a 10%–90% rise time of 65 ns [15].

References

[1] Hellenic Mediterranean University Institute of Plasma Physics & Lasers, *www.ippl.hmu.gr.*

[2] E. Kaselouris et al, "Plasma instabilities: the influence on plasma instabilities during the solid-plasma phase transition",*27th Symposium on Plasma Physics and Technology (Prague/*Czech*/ 20-23 June 2016).*

[3] Marie Curie ToK Programme 'Development of An Innovative X-ray source'–DAIX, Project No.1442.3.

[4] E Kaselouris et al, "Preliminary investigation on the use of low current pulsed power Z-pinch plasma devices for the study of early stage plasma instabilities", Plasma Phys. Control. Fusion 60 (2018) 014031 (8pp).

[5] E. Kaselouris et al, "The influence of the solid to plasma phase transition on the generation of plasma instabilities", NATURE COMMUNICATIONS | DOI: 10.1038/s41467-017-02000-6.

[6] G. Koundourakis et al, "Experimental and numerical investigation of the plasma dynamics and jet formation in low current table-top X-pinch plasma devices", *Proceedings of the SCinTE-VOL 3-pg 19-22 ,SCience in TEchnology 2015 (SCinTE /Athens/5-7 November 2015).*

[7] G. Koundourakis et al, "A numerical study on laboratory plasma dynamics validated by low current X-pinch experiments", Plasma Phys. Control. Fusion **62** (2020) 125012 (14pp) (https://iopscience.iop.org/article/10.1088/1361-6587/abbebf).

[8] M. Tatarakis et al, "Optical probing of fiber z -pinch plasmas", PHYSICS OF PLASMAS VOLUME 5, NUMBER 3 MARCH 1998.

[9] Chen F F 2016 *Introduction to Plasma Physics and Controlled Fusion* (Cham: Springer International Publishing) pp 75–144.
[10] Hutchinson I H 2002 *In Principles of Plasma Diagnostics* (Cambridge: Cambridge University Press) pp 1–10.
[11] Haas D M 2011, " Investigation of the dynamics and emission characteristics of x-pinch plasmas", PhD thesis University of California San Diego.
[12] E Kaselouris, "Study of matter behavior dynamics governed by the interaction with laser pulses and external strong currents", PhD thesis TECHNICAL UNIVERSITY OF CRETE SCHOOL OF PRODUCTION ENGINEERING & MANAGEMENT.
[13] Hipp M 2004 *Measurement* **36** 53.
[14] G W Collins IV et al, "Effect of the global to local magnetic field ratio on the ablation modulations on X-pinches driven by 80 kA peak current", New Journal of Physics **14** (2012) 043021.
[15] Ruiz-Camacho, J. et al. (1999), “Z-pinch discharges in aluminum and tungsten wires”, *Physics of Plasmas*, Vol. 6, pp. 2579-2587.

5.2 Computational study of a single wire Z-pinch plasma dynamic evolution through four different EOS models-Comparison of two different Riemann solvers and two different vacuum temperature evolution modeling

In this section we will clarify the affection of the different Riemann solvers at the numerical plasma evolution estimation and diffusion they cause mainly in the magnetic field topology. It is important also to evaluate the influence of the environmental thin air plasma, oftenly characterized in this work as low density background or in other words, plasma vacuum. It is crucial to understand whether we can have a realistic approximation modeling, with an active second plasma material the thin air plasma or we should have a vacuum plasma area that does not literally evolve along the simulation run. For this purpose, we choose a very simple approximation of a plasma Z-load material tungsten wire. The experimental data we use are from the literature experiment (experimental setup is shown at the previous section) evaluating the plasma evolution of aluminum and tungsten plasma Z-loads of single wires [1].

For this specific calculations we utilize :

i. the PVTE (Pressure-Volume-Temperature-Energy) Equations of state – EOS which are modified using tabulated data by SESAME Database [2,3] (analysis in Chapter 3/Part I).

ii. the electrical resistivity from the simple modified formula of Spitzer equation as presented in equations 3.52-3.55 in Chapter 3.

iii. the optically thin radiative losses module is taken into account using tabulated data by the help of the FLYCHK code[4] (Chapter 3/Part I).

iv. a modified radiation transport module is used, described analytically at the Chapter 3/ Part I relative section [5].

v. plasma density is determined using the effective ionization charge state, by the help of tabulated values that FLYCHK code provides [4,6] (Chapter 3/Part I).

The MHD scheme used here is presented in detail at the first section of Part I in Chapter 3. Note that the only dissipative term we use, beside radiation losses, is the electrical resisistivity.

The modeling of the interface region is based on four approximations and two different PLUTO solvers are used in the simulations. The simulations are repeated with the temperature of vacuum constrained resulting to sixteen simulation cases. The comparison of the simulations with the experimental results provides insights to the influence of our code modifications to the dynamic approximations of physical quantities such as, material density, magnetic field, plasma temperature and plasma energy. The simulation duration time we use is 22ns from the current start, representing the first moment of experimental results [1,7].

5.2.1 MHD material modeling

The PLUTO MHD code [8,9] is able to model the solution domain consisted of different materials by the help of user-defined functions. The existence of two materials in the solution domain is modeled by four approximations: **i.** approximation **mat**, where the solution domain consists of the tungsten material. **ii.** approximation **vac**, where two individual material regions of tungsten and vacuum are considered. The materials interface is defined by approximately seven orders lower value ρ_{lim} of

density compared to the density of the solid tungsten. The other two (**iii**) **lin** and (**iv**) **exp** approximations are implemented. A new density threshold $\rho_{vac}=\rho_{lim}/2$ in conjunction with ρ_{lim} is used to simulate the three regions for the connection of the pure vacuum **Region I** with the dense tungsten **Region III**. **Region II** is their transition region. In approximation **lin,** the linear mixing function Q for the pressure, internal energy, temperature and radiative cooling coefficient is defined by:

$$Q = f_w 10^{\log Q(w)} + (1-f_w) 10^{\log Q(air)} \tag{5.2.1}$$

where logQ(w) and logQ(air) are the logarithmic data from the SESAME tables for tungsten and air respectively and f_w is a weighted function. Likewise, for the fourth approximation **exp**, an exponential function is used:

$$Q = 10^{f_w \log Q(w) + (1-f_w)\log Q(air)} \tag{5.2.2}$$

The weighted function for the approximations **iii. lin** and **iv. exp**, is expressed as:

$$f_w = \begin{cases} \textbf{Region ID} & \textbf{Range} & \textbf{lin or exp} \\ \text{I} & \rho \le \rho_{vac} & 0 \\ \text{II} & \rho_{vac} \le \rho \le \rho_{lim} & (\rho - \rho_{vac})/(\rho_{lim} - \rho_{vac}) \\ \text{III} & \rho_{lim} \le \rho & 1 \end{cases} \tag{5.2.3}$$

The effective ionization charge state, is calculated by linear interpolation using the weighted function of Equation 5.2.3. A schematic presentation of the sixteen different cases are at the next flow chart.

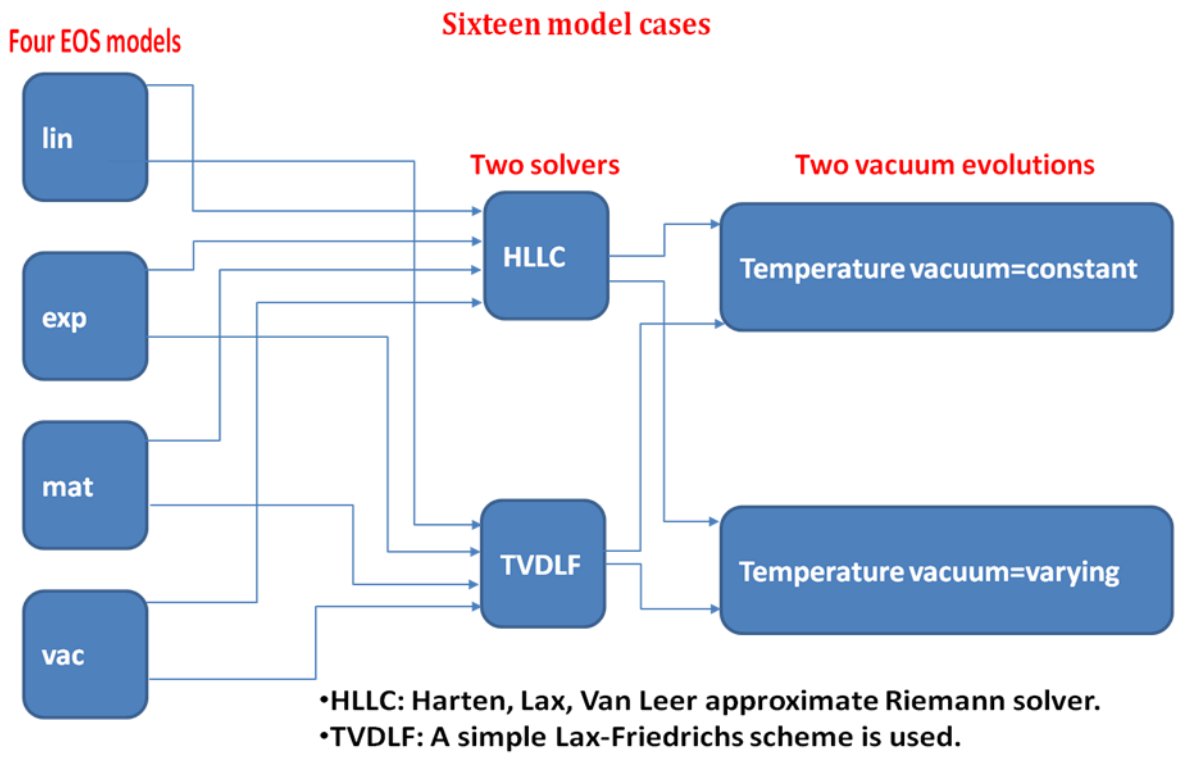

Figure 5.2.1: *Flow chart of the 4 EOS, the two Riemann solvers [8,9] and the two vacuum temperature evolutions used at this study, resulting in 16 different model cases.*

5.2.2 Computational results

The physical Z-pinch experiment, studied in this work, has a load of a single cylindrical tungsten wire with a diameter of 5 μm [1]. Based on the quarter symmetry of the model only the first quarter of the domain is modeled, and the 3D solution domain has the size of 5000x5000x80 μm^3. The numerical results are presented on the xy plane cross section of the model at the midpoint of the wire and are spatially focused on the region of interest having a size of 200x200 μm^2. Eqtsymmetric boundary conditions are used on the symmetry planes while outflow is set for the outer xz and yz boundary planes and periodic for the top and bottom xy planes of the domain [8] (see Chapter 4/boundary section). The size of the solution domain was determined by sensitivity analysis. In relation to the solution time of the model these dimensions prevent the reflections of the shock waves on the xz and yz outer boundaries.

The initial distributions of material density ρ, thermal pressure p, the magnitude of the magnetic field B_{mag}, temperature T (eV), the electron density N_e and radiation energy density E_{rad} are illustrated in figure 5.2.2. The material density and thermal pressure are approxiated by a Gaussian spatial distribution profile, in order to provide a smooth transition from the core of the wire to the rest of the outward domain. The amplitudes and widths of these Gaussian distributions are selected in accordance to the experimental observations and represent the physical conditions at the initial time-steps of the plasma generation. As it is observed by figure 5.2.2, the maximum value of the material density approaches the value of 0.53 gr/cm^3, being 40 times smaller than tungsten's solid density and asymptotically approaches the value of ρ_{vac}. The maximum value of the mass density is at ~20μm. The

maximum value of thermal pressure approaches the value of 1.7×10^6 dyn/cm^2 and asymptotically approaches the vacuum pressure of the experimental chamber. The temperature distribution is related to the physical quantities of the EOS, follows the distribution of pressure and density, while at the coronal plasma a thermal shock wave is observed and is in accordance with the experimental findings. The temperature at the core of the wire approaches the melting temperature of tungsten and asymptotically approximates the environmental temperature. The component of the magnetic field that is considered is the azimuthal one and is computed based on the assumption of existence of current density only on the z direction and the skin effect is also included. The magnetic field increases proportionally to the radial distance to a maximum value. For a radius of 20 μm, where the core and coronal plasma meet, the magnetic field decreases and expands to the domain following the 1/radius law (see similar magnetic field and current density lineout profiles at figure 4.8/Chapter 4). The temporal evolution of the magnetic field follows the form of the current with a peak of 160 kA and a rise time (10%–90%) of 65 ns [1]. The radiation energy density is computed using the Stefan–Boltzmann law (black-body radiation). It may be observed that the radiation energy density follows the distribution of temperature. The electron density occurs from the contributions of the physical quantities of the EOS and the effective ionization charge state following a shifted Gaussian distribution having a maximum value where core and coronal plasma meet. In the sub-figure of electron density, the discretization of the finite volume scheme is presented, having a size of 700x700 x8 cells for the solution domain with a unit length of ~7μm for x,y axes and 10μm for the z (rectangular cells).

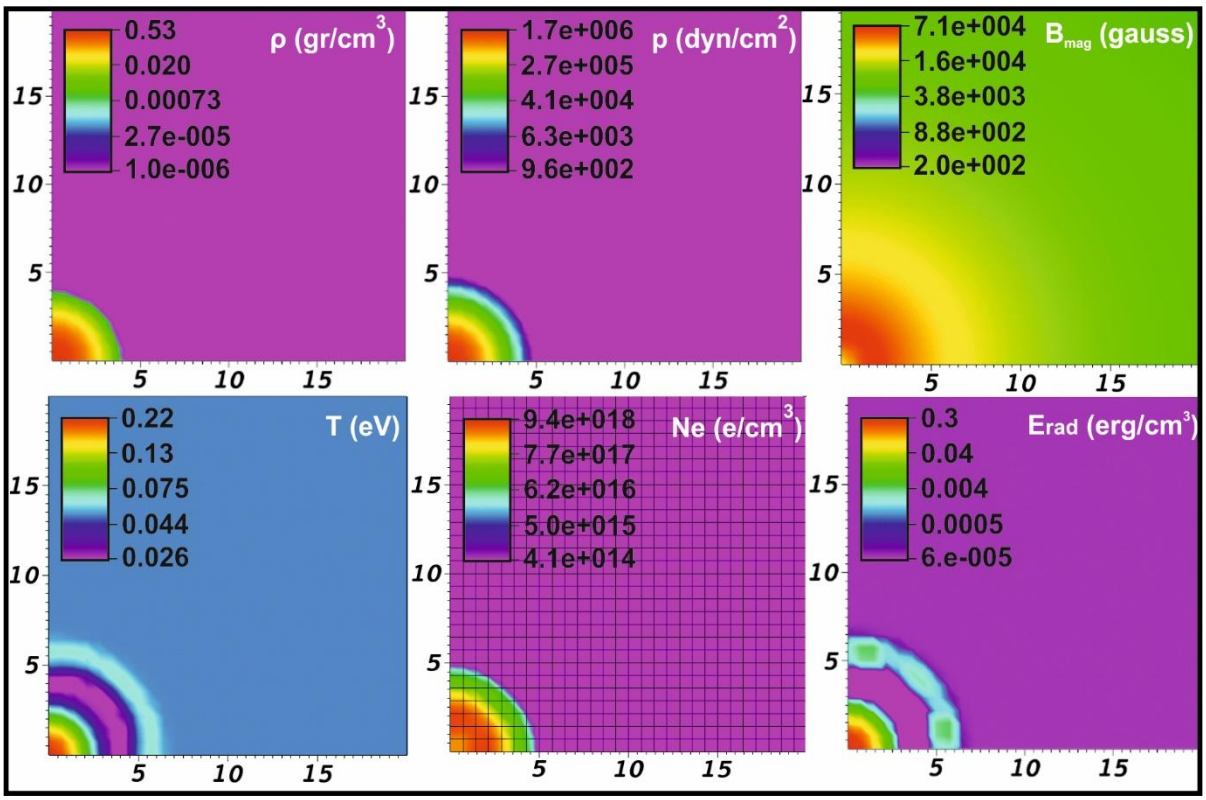

Figure 5.2.2: *Initial distributions of material density ρ, thermal pressure p, magnitude of magnetic field B_{mag}, temperature T(eV), electron density Ne and radiation energy density E_{rad} over XY plane cross*

section. Spatial resolution is ~7μm at x,y dimensions and 10μm at the z. Unit length in all graphs is 10μm.

Two different Riemann solvers are tested, the **hllc** solver and the **tvdlf** solver for the flux computation [8,9] (see Chapter 4/solver section). The prevention of the diffusion of the magnetic field in the vacuum region is obtained by preserving the resistivity value at a high level. This is achieved by setting the vacuum temperature at a constant low value, i.e. 50 meV for this study and for densities having values lower than the ρ_{lim}. Therefore, the approximations **lin**, **exp**, **mat**, **vac** solved by two solvers and constant **const temp** or varying **var temp,** vacuum temperature, result to 16 different test cases. With regard to the expected results the cylindrical symmetry of the model should prescribe a correspondent evolution of the physical phenomena without any azimuthal variations. In figures 5.2.3-5.2.5 three representative physical quantities of the electron density, the magnetic field, and the temperature, respectively, are selected to demonstrate the performance of the 16 model cases for a problem temporal time of t=22 ns. This is the first temporal moment of the experimental results in [1]. Two test cases, the **vac** approximation with constant vacuum temperature and the **mat** approximation with varying vacuum temperature and for the **hllc** solver had an early termination time at 17 and 21 ns respectively.

In figure 5.2.3, for the majority of the investigated test cases, the computed electron density is in very good agreement with the experimental results measured in [1] where the corona plasma expands to a radius of ~70μm for an electron density of about 3×10^{18} cm^{-3} at 22 ns from the current start. In more particular, the majority of the investigated test cases present **slight deviations** from the ideal cylindrical symmetry, while **large deviations** are presented for the **exp** approximation using the **hllc** solver and for **varying vacuum temperature**. For all the approximations with constant temperature a shock wave appears in the corona regime (corona "ring").

The radial expansion of plasma cylinder is 65μm to 85 μm, having the higher values at all **const temp** models and the lowest at the **var temp** models except for the **mat** model with the **tvdlf** solver that presents the higher expansion of ~85μm. A mean value velocity till this early expansion temporal moment is ~3-4μm/ns or ~3-4km/s, a reasonable estimation according to the experiments that give a mean expansion velocity ~10km/s till ~130ns from the current start [1].

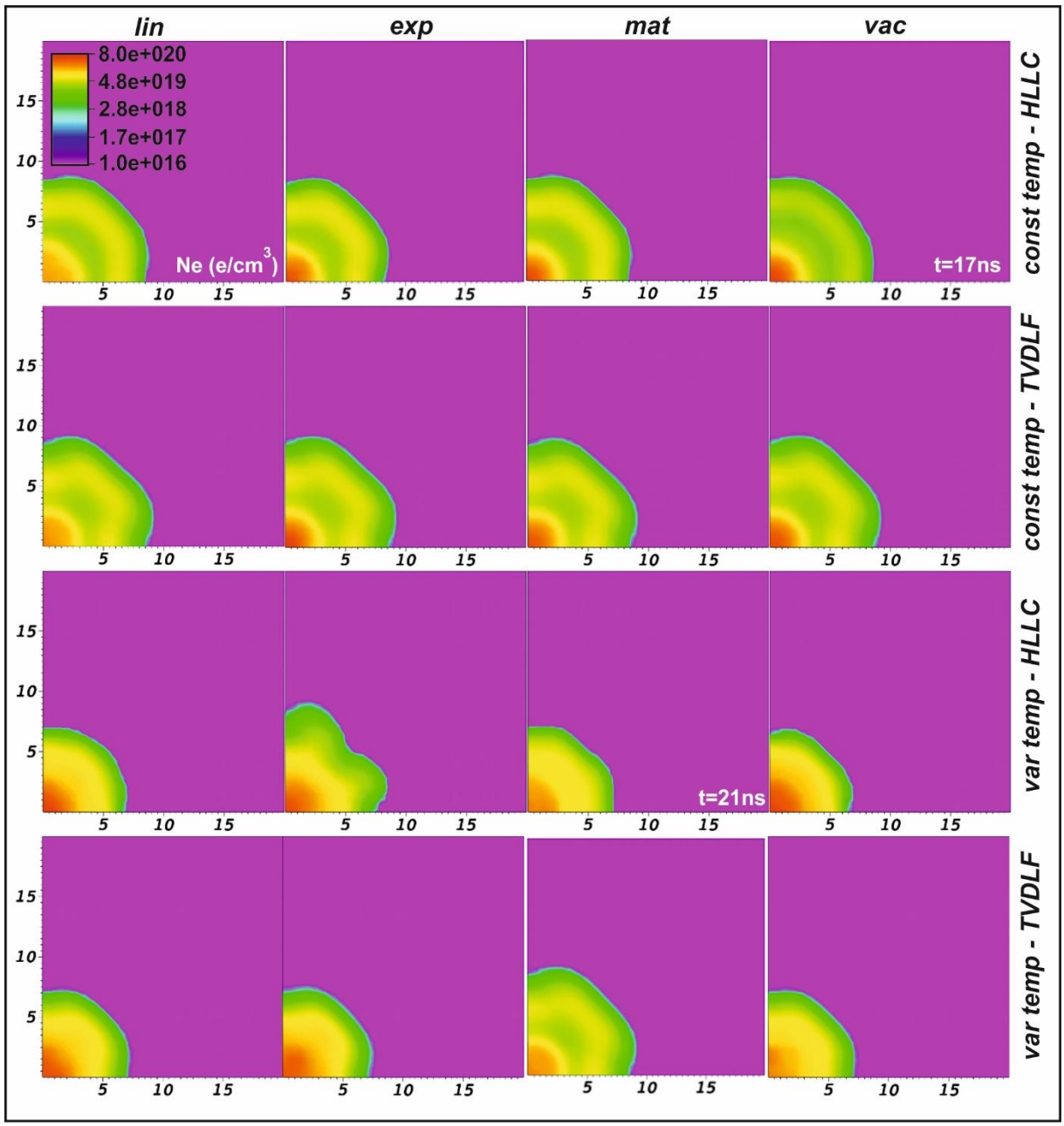

Figure 5.2.3: *Electron density for the 16 different test cases at 22ns from the current start. Unit length in all graphs is 10μm.*

In figure 5.2.4, for all the test cases, the diffusion of the magnetic field is apparent since the maximum value of the magnetic field is located in a radius of 80±20 μm, in relation to the initial radius. The form of the diffusion of the magnetic field is not realistic for the approximations lin and vac using the two solvers and for varying temperature. The exp approximation using the hllc solver and for varying vacuum temperature presents azimuthal variations in the magnetic field topology while the tvdlf solver does not but has a more diffusive behavior. Smaller variations are also present for the mat model and the hllc solver for the var temp case.

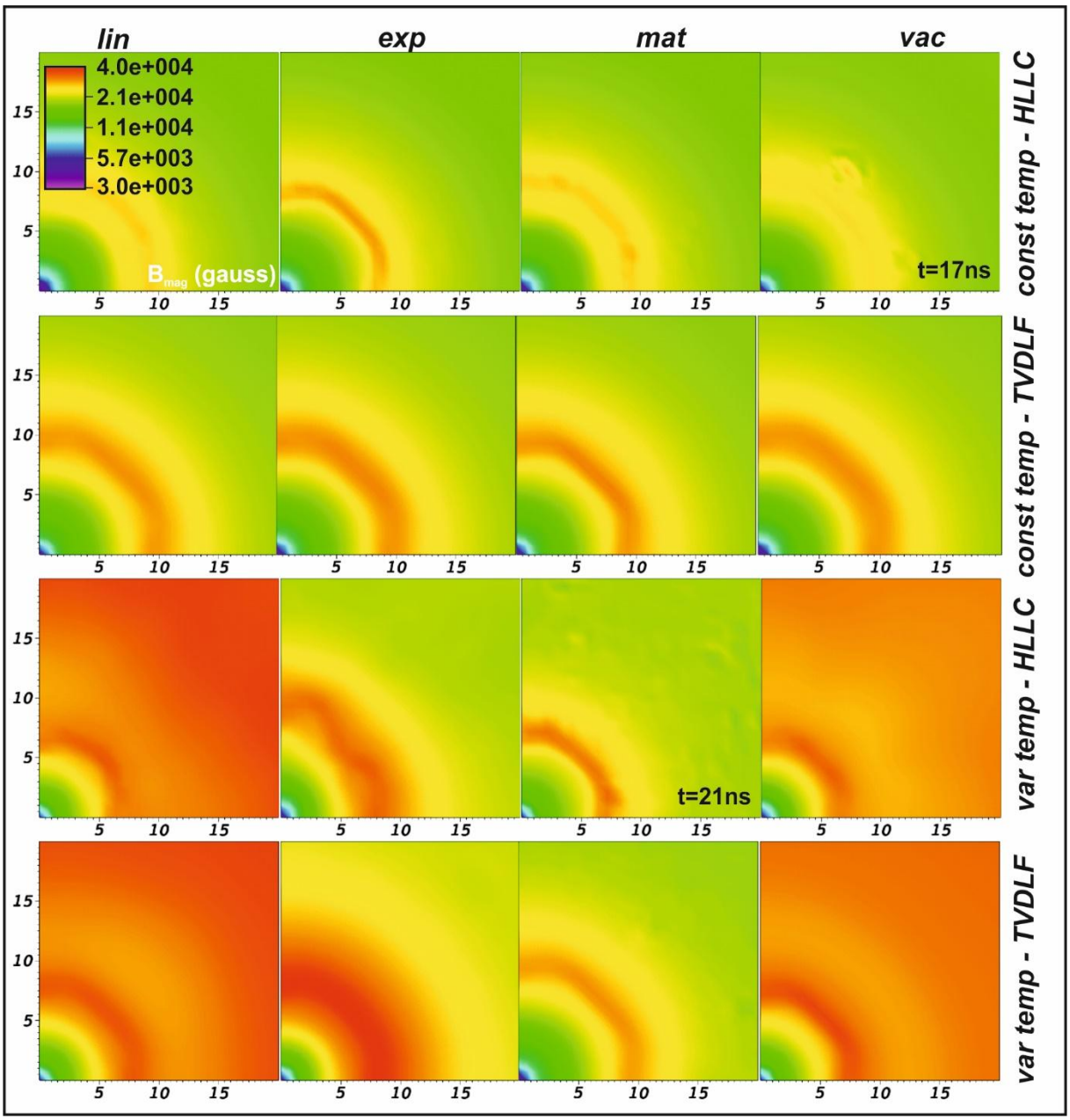

Figure 5.2.4: *Magnitude of magnetic field for the 16 different test cases at 22ns from the current start. Unit length in all graphs is 10μm.*

In figure 5.2.5, the test cases with constant vacuum temperature provide a more realistic approximation of the temperature distribution than the ones with the vacuum varying temperature. A temperature range of 1-40 eV is apparent in the corona regime, while the core temperature increases to about 0.9 eV.

The temperature profiles of the varying temperature environment are not realistic for the **lin** and **var** models for both solvers, presenting temperatures of ~100eV at the corona and vacuum regime. The other two models **exp** and **mat** present lower temperatures at the same regions having also "islands" of ~40eV temperatures at the periphery of the corona "ring" for both solvers while the **tvdlf** presents a smoother behavior. The **exp** model for the **hllc** solver presents deformations to the temperature ring and much bigger spatial temperature "islands".

The temperatures of a cold core of ~1eV to a hotter corona of a maximum value of ~40eV are consistent with other tungsten plasmas simulations and experiments of similar current loads that support the cold core temporal evolution of some eV till late experimental times [10,11].

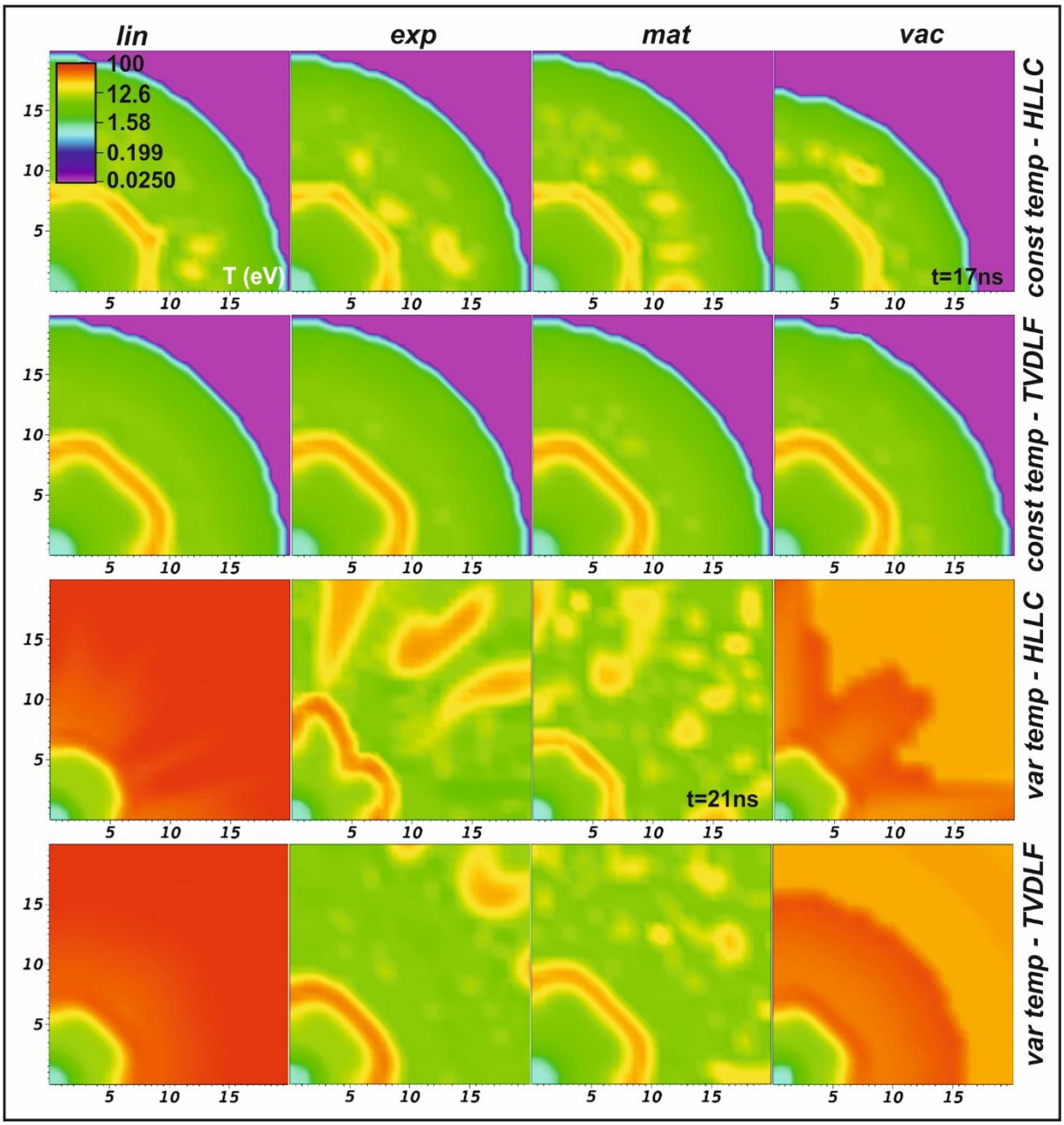

Figure 5.2.5: *Temperature distribution for the 16 test cases at 22ns from the current start. Unit length in all graphs is 10μm.*

In figure 5.2.6 is presented the influence of the radiation transport model on the plasma evolution for a representative test case. Results of electron density, thermal pressure, plasma temperature, material density and radiation energy density are depicted for the **lin** approximation using the **tvdlf** solver and constant temperature of the vacuum. It is observed that the radiation transport terms remove energy from the plasma and provide better expansion and cooling results. The model with no radiation presents: i. deviations from the cylindrical symmetry for both electron and material density,

ii. The expansion of the thermal pressure is very large and iii. The plasma temperature of ~200eV is not physical in the corona regime. The core and corona expansion for the model with radiation is located in a radius of 30μm and 75μm respectively. Furthermore, regarding the energy radiation density, the maximum value appears near the outer limit of the corona region. The diffusion nature of tvdlf solver in combination with the mixing lin-EOS may lead to the radial deformation profiles of electron density, temperature and mass density when there in no radiation transport (bottom row). Models of mat-EOS and vac-EOS, lacking the transition Region II, do not present this deformation behavior but are more diffusive.

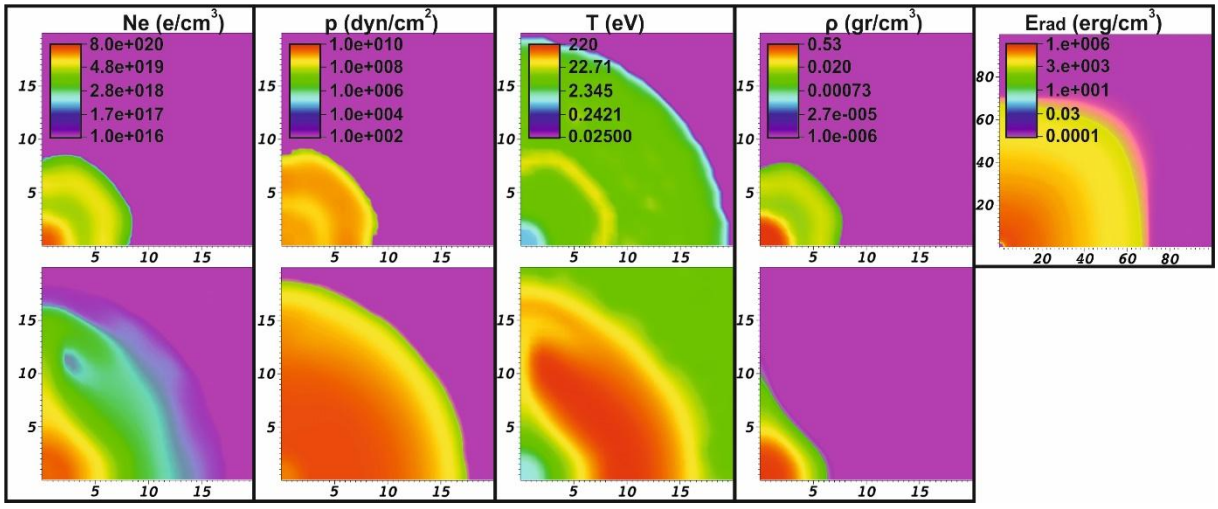

Figure 5.2.6: *Influence of the radiation transport model. The results including the radiation transport are depicted on the top row. The temporal moment is 22ns from the current start. Unit length in all graphs is 10μm.*

5.2.4 Conclusions

The inclusion of the radiation transport is significant for the spatiotemporal evolution of electron density, pressure and temperature to be consistent with literature results. The majority of the investigated test cases simulate the plasma expansion with small variations from the experimental reference measurements for the 22ns experimental time at the xy plane at z=0. Regarding the necessary preservation of the expected cylindrical shape of the computed physical quantities, qualitative results are obtained using the approximations with constant vacuum temperature. **Tvdlf** solver provides smoother but more diffusive results. From now on the **lin-EOS**, **constant vacuum temperature** and the **tvdlf** solver is the standard implementation scheme of the next sections models.

The inclusion of a passive scalar function for the multi-material approximation **lin**, **exp** and **vac**, identifying the transition zone will help to have a smoother behavior at the tungsten plasma-vacuum air interface, avoiding deformations, allowing for smaller computational boxes. This is presented at the next subsection for a two wire X-pinch load.

A different approximation of this two-component plasma evolution, consists the deactivation of the Riemann solver technique using the **internal boundary** switch (see the relative boundary condition

subsection at the 4 Chapter) at the fourth section of this Chapter where there is no need of this mixture scheme.

References

[1] Ruiz-Camacho, J. et al. (1999), “Z-pinch discharges in aluminum and tungsten wires”, Physics of Plasmas, Vol. 6, pp. 2579-2587.

[2] SESAME THE LOS ALAMOS NATIONAL LABORATORY EQUATION OF STATE DATABASE, LA-UR_92_3407.

[3] Kashiwa B.A., "The MGGB Equation-of-State for Multifield Applications: A Numerical Recipe for Analytic Expression of Sesame EOS Data", LA-1442 ,September 2010. http://www.doe.gov/bridge

[4] Tungsten Charge State Distribution by FLYCHK NLTE Kinetics Calculation at NIST by International Atomic Energy Agency-Atomic Molecular Data Services provided by the Nuclear Data Section.

[5] Stefan M. Kolb, Matthias Stute, Wilhelm Kley, Andrea Mignone, "Radiation hydrodynamics integrated in the code PLUTO", A&A 559, A80 (2013).

[6] H.-K. Chung et al, "FLYCHK: Generalized population kinetics and spectral model for rapid spectroscopic analysis for all elements", High Energy Density Physics 1 (2005) 3-12.

[7] Alekos Skoulakis et al, "PRELIMINARY COMPUTATIONAL STUDY OF PLASMA DYNAMIC EVOLUTION PRODUCED BY LOW CURRENT TABLE-TOP PINCH PLASMA DEVICES", 9th GRACM International Congress on Computational Mechanics Chania, 4-6 June 2018.

[8] http://plutocode.ph.unito.it/PLUTO User's Guide v.4.2.

[9] A. Mignone et al, "PLUTO: A NUMERICAL CODE FOR COMPUTATIONAL ASTROPHYSICS", The Astrophysical Journal Supplement Series, 170:228Y242, 2007 May.

[10] J. P. Chittenden et al, "Plasma formation in metallic wire Z pinches", PHYSICAL REVIEW E VOLUME 61, NUMBER 4 APRIL 2000.

[11] G. S. Sarkisov et al, "Transformation of a tungsten wire to the plasma state by nanosecond electrical explosion in vacuum", PHYSICAL REVIEW E **77**, 056406 (2008).

5.3 A numerical study of a two wire X-pinch plasma dynamics and jet formation validated by experiment

The capabilities of PLUTO code, as we discussed earlier, are extended now to enable the investigation of low current produced X-pinch plasmas. The numerical and physical modules of the code used and appropriately modified are presented and discussed at Chapters three and four. The simulations results are compared to experiments, carried out on a table-top pulsed power plasma generator implemented in a mode of producing a peak current of ~46kA with a rise time (10%-90%) of 50ns, loaded with tungsten wires. This experimental setup is presented at the first section of this Chapter. The structural evolution of plasma density is studied, and the influence of the magnetic field is analyzed with the help of the new simulation data. The concept of the global and the local magnetic field is discussed.

The numerical results are found to be consistent with experimental measurements using laser probing diagnostics. A three frame per shot laser shadowgraphy and interferometry setup allows for the measurement of the plasma expansion velocity and the time evolution of the plasma electron density (section 5.1). The spatiotemporal plasma jet formation and evolution is presented and discussed here. The simulated areal mass density is compared with the experimentally measured dense opaque region to enlighten the dense plasma evolution. In addition, the experimental measured areal electron density is compared to the simulation results (details in the experimental setup at 5.1 section). Moreover, the new simulation data offer valuable insights to the main jet formation mechanisms**,** that are further analyzed and discussed in relation to the influence of the **J**×**B** force and the momentum density**.**

The X-pinch configuration consists of two regions, that of tungsten (load) and that of the low-density background. The lin model with the tvdlf solver and a constant temperature vacuum are used as we described in the previous section. The novelty from the previous models is the activation of a passive scalar function used for the intermediate transition zone for a smoother transition among these two regions. The implementation description follows at the next subsection.

The MHD scheme with the set of equations is the same as the one of the Z-pinch load of the previous section. The set of equations and the radiation module are described in Chapter 3/PART I. The smooth transition of resistivity from the plasma to the vacuum regions follows the equation of 3.58 in Chapter 3/Part II. The skin effect is considered following the 2.9-2.11 equations in Chapter 2.

5.3.1 Multi-material mixing procedure

As we already discussed the existence of the vacuum region in this MHD simulation is modeled using a low-density background of plasma air. Thus, a multi-material approximation (the **lin** module) is adopted for the transition zone which is identified using a passive scalar function. This approach results to a mixing process of the two materials and is adopted to monitor nonphysical transitions.

A mass fraction Y_i, i = 1,2 is introduced, with: $Y_1 = \rho_1/\rho$ and $Y_2 = \rho_2/\rho$, where ρ_1 is the tungsten mass density and ρ_2 the dry air mass density, while $\rho = \rho_1 + \rho_2$ is the total mass density. In this approach the values of the two mass densities are calculated. To determine the value of Y_1 a passive scalar trace (f_{y1})

is used, with $Y_1 = (f_{y1}+1)/2$ and $-1 \le f_{y1} \le 1$. This trace is advected by the following equation (see equation 4.43 of Chapter 4):

$$\frac{\partial(\rho f_{y1})}{\partial t} + \nabla \cdot (\rho f_{y1}\mathbf{u}) = 0 \tag{5.3.1}$$

The initial mass fraction $Y_1(0)$ is expressed as:

$$Y_1(0) = \begin{cases} \textbf{Region ID} & \textbf{Range} & \textbf{Value} \\ \text{I} & \rho \le \rho_{vac} & 0 \\ \text{II} & \rho_{vac} \le \rho \le \rho_{lim} & (\rho - \rho_{vac})/(\rho_{lim} - \rho_{vac}) \\ \text{III} & \rho_{lim} \le \rho & 1 \end{cases} \tag{5.3.2}$$

The lower mass density value (ρ_{lim}) for tungsten plasma is defined to be six orders of magnitude lower than the solid density of tungsten. For the initialization, a density threshold value ($\rho_{vac} = \rho_{lim}/10$) is used to create three regions: Region III of pure tungsten, Region I of low-density air background and Region II being the transition region between I and III.

The linear mixing function for primitive to conservative (and vice versa) transformations (V represents p or ρe) is defined by:

$$V = \sum\nolimits_{k=1,2} Y_k \, V_k(V_k', \rho) \tag{5.3.3}$$

where V_1 and V_2 are the interpolated data from the SESAME data tables for tungsten and dry air respectively and V'=p or V'=ρe. For k species (e.g. k = 1 for tungsten and k = 2 for dry air) the total ion density N_i is:

$$N_i = \sum_{k=1,2} N_{ik} = \sum_{k=1,2} \frac{\rho_k}{m_u M_k} = \frac{\rho}{m_u \bar{M}} \tag{5.3.4}$$

where: m_u is the atomic mass unit, M_k is the molecular weight for each of the k species and $\bar{M}$ is the average molecular weight, defined as:

$$\frac{1}{\bar{M}} = \sum_{k=1,2} \frac{Y_k}{M_k} \tag{5.3.5}$$

The total electron density (N_e) is:

$$N_e = \sum_{k=1,2} Z_k N_{ik} \tag{5.3.6}$$

where Z_k is the mean ionization charge for each of the k species defined by tabulated data as:

$$Z_k = Z_k(Y_k \rho, T) \tag{5.3.7}$$

The effective mean ionization charge Z_{ef} of plasma is defined as:

$$Z_{eff} = \frac{N_e}{N_i} \tag{5.3.8}$$

and finally, the cooling function (of equation 3.23 in CHAPTER 3/PART I) is:

$$\Lambda = \sum_{k=1,2} N_{ik}{}^{2} \Lambda_k(\rho_k, T) \tag{5.3.9}$$

5.3.2 Numerical modeling

The updating numerical technique of the magnetic field along the simulation is analytically presented here and it is explained why it is important for the correct spatiotemporal evolution description of plasma in the current problems.

The induction equation (equation 3.7 in Chapter 3) is used by PLUTO and therefore for the solution of this magnetic-field-driven problem the time dependent magnetic field boundary conditions are used to impose the correct current density and energy flow to the system. Thus, a transient time duration is required for the steady state to be reached after the propagation of a numerical wave back and forth [1], several times, through the vacuum region where the induction equation relaxes to the Laplace equation. This characteristic transient time is inversely proportional to the resistivity and results to a highly increasing timestep for explicit codes such as PLUTO. Moreover, the time dependent magnetic field boundary conditions [2] become a crucial aspect in complex geometries such as X pinches. To overcome these limitations in our approach, a new procedure is proposed as we already mentioned in previous Chapters. A specific experimental time moment is considered as the simulation start-time, which corresponds to the value of the current density used. At this time, the magnetic field distribution is derived over the global computational domain using the linear superposition of each wire's calculated values, as described in the sub-section 4.1.2/A. The evolution of the magnetic field preserves the energy conservation by solving the induction equation and at every time step simple boundary conditions are applied, as described below. Moreover, instead of using a time dependent magnetic field at the boundary planes, only the magnitude of the magnetic field is updated in the whole computational domain, at the necessary time steps using the experimentally measured current (see experimental setup at the 5.1 section and figure 5.1.3) and therefore the energy inflow is imposed [3,4]. For the calculation of the initial values of the other primitive quantities, the same single superposition procedure is used (as described in 4.1.2/C subsection). This technique is also tested and evaluated for its spatiotemporal magnetic field topology evolution at the next section in comparison with a similar X-pinch simulation using the MHD code GORGON!

At the initialization of the simulation, the density and the thermal pressure have a Gaussian spatial distribution profile having a width of $1/e^2$=20 μm, equal to R_{max}, at 5ns from the current start when the full plasma state is reached since the plasma core temperature is set to 1.5eV, according to the experimentally observed plasma expansion. These profiles follow the Bennet relation, their amplitude is set to be 2.5gr/cm^3 for the mass density of tungsten and $1.5^{\times}10^{10}$dynes/cm^2 for the thermal pressure. An initial low-density background is set to be 10^{-6}gr/cm^3 to model the vacuum. The distribution of the magnetic field is calculated via the provided experimental current, which has a value of 4.5kA on each wire. Accordingly, the magnitude of the magnetic field is maximum at R_{max} and the skin depth is 1.4 R_{max} for each wire due to the skin effect.

The 3D model is 1/8 symmetric and the X legs are merged to the cross-point at the origin of the axis. The central axis of the four legs of the X-pinch lie on x=0, yz plane. The positive octant of the three-

dimensional Cartesian coordinate system is modeled. A model of size 2×1.5×3.2 mm^3 (x×y×z) preserves the solution domain, with a spatial discretization of 10×8×8 μm^3. The boundary conditions of the model are set on the six boundary planes that define the solution domain. Following the PLUTO code "terminology", the y=0, xz and x=0, yz planes of symmetry are set to "eqtsymmetric", the z=0, xy plane is set to "reflective", the x=max, yz and z=max, xy planes are set to "outflow", while for the y=max, xz plane "user defined" conditions are considered. The "user defined" boundary conditions are used to set the spatial derivatives of the primitive quantity values to zero, on the direction of the axis of the wires. The boundary conditions set for the radiation solver, follow the same assumptions described above. The detailed presentation of the boundary scheme is in Chapter 4.

The tvdlf solver is used as we mentioned earlier. The Riemann states are defined by a high-order finite difference weighted essentially non-oscillatory (WENO) reconstruction scheme [5]. Moreover, with respect to time evolution, a 2^{nd}-order explicit Runge Kutta (RK2) is used to advance the solution to the next time level. The control strategy to enforce the divergence free constraint is achieved by the extended generalized Lagrangian multiplier (GLM). The numerical integration of diffusion terms, due to resistivity, is performed by using a super time stepping technique (STS), to accelerate the standard explicit treatment of parabolic terms. For the radiation transport system of equations, the built in successive over relaxation (SOR) method is used [6] (it is the same method of the radiation transport's module of the previous subsection). All these numerical modules are mentioned and discussed in the relative section of Chapter 4.

In the vacuum region the temperature is kept constant to a very small value of 580K, in every timestep, to eliminate the thermal shock waves (constant temperature model).

5.3.3 Results and discussion

Four characteristic images at different times of the plasma density spatiotemporal evolution accompanied by the corresponding magnetic field lines are illustrated in Figure 5.3.1. The simulation results are computed at the positive octant of the domain of the X-pinch configuration.

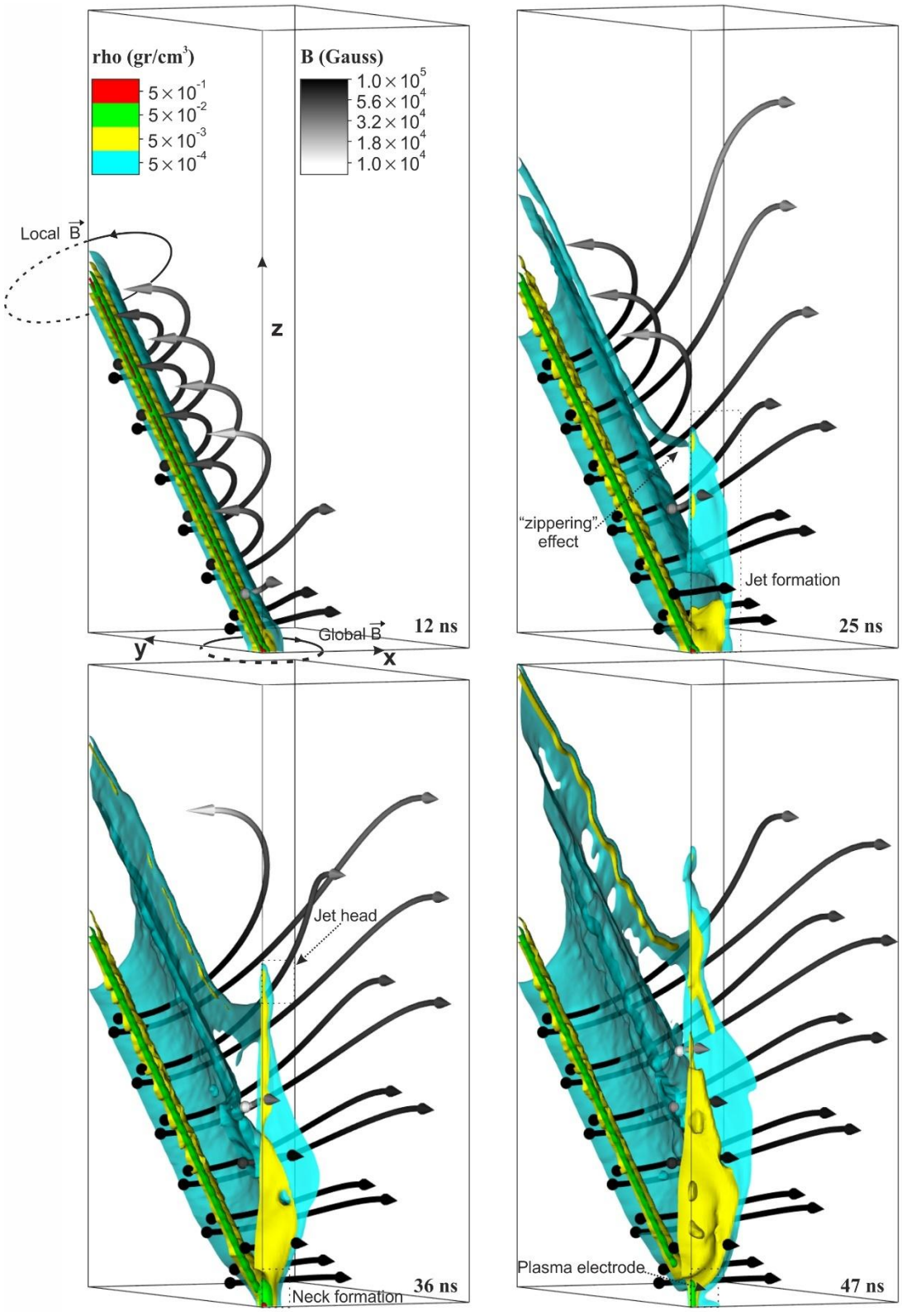

Figure 5.3.1: *Characteristic images of the plasma density spatiotemporal dynamics and of the magnetic field lines evolution, at four different times from the current start. A section of 0.8×1.5×2.2mm³ of the entire solution domain is presented.*

A global magnetic field is considered, that is generated from the superposition of the local fields due to the current flow in each wire, thus the tail and head of the magnetic lines lie on different boundary planes. Away from the cross-point, the local magnetic field dominates, thus the tail and head of the magnetic lines lie on the same boundary plane. Close to the cross-point a merging region is developed, where a global magnetic field is generated by the total current flow. It can be observed that while time increases, the global magnetic field is extended far away from the cross-point, due to advection in the plasma ablation region. At 12ns, the cylindrical symmetry of the plasma density distribution around the wire axis is preserved, while it radially expands. Near the cross-point the plasma jet formation is initiated, and the global magnetic field governs. At 25ns, the thermal plasma expansion dominates at the cross-point and the plasma jet is formed along the Z-axis. Ablation generates coronal plasma streams which contribute for the plasma jet frontal evolution, a phenomenon known as the "zippering effect" [7]. Jets are continuously confined on the y=0, xz mid-plane by the kinetic pressure of the ablated plasma flow. A new azimuthal global magnetic field is generated on the plasma jet. At 36ns, the magnetic compression of the plasma governs and hence neck formation occurs in the wire crossing region. The head of the jet becomes clearly visible above the confining region since it is accelerated to higher velocities in relation to the effective velocity of the confining region along the z-axis. Furthermore, at 47ns when plasma electrodes formation is apparent at the top and bottom of the neck, the maximum value of mass density in the neck region is reduced by two orders of magnitude, in relation to the moment that pinching occurs. This is mainly attributed to ablation rather than radiative explosion which is responsible for the neck breaking. Radiative explosion leads to the generation of electron and ion beams which are not included in our model [8].

For the reasons explained in experimental section 5.1, in laser optical probing diagnostics experiments an opaque region is formed on shadowgraphy and interferometry images. In our experimental setup, only light rays having refraction angles less than 40 mrads which is the acceptable angle of the optical system, contribute to the formation of the image. It is a fact that the ion density in plasmas of high nuclear charge material depends slightly on the electron temperature, while the absorption seems to be the most efficient in the very dense core [9]. Thus, the contribution of absorption in the generation of the opaque region is restricted in the dense plasma core, while the opaque region-plasma border, is generated due to refraction. In other words, only the refracted rays that escape from the underdense plasma create the highlighted boarders of the opaque region due to the relatively large acceptable angle. Additionally, the relative short characteristic plasma size, of several tens of microns observed, allow only to an insignificant deviation of the light rays to pass through plasma. These assumptions enable the correlation of the mass areal density with the experimental opaque region that is considered to have the size of the plasma extended normal to the ray's axis, thus providing an estimation of the coronal plasma cut-off density [10].

Figure 5.3.2 presents the simulated areal mass density contour map in relation to the optical probing experimentally recorded images at various times. The comparison of the images allows for the determination of the cut-off density boarder evolution of the dense opaque region. Thus, a qualitative and quantitative comparison between experiments and simulations can be performed. An yz plane section of $1.5\times1.75mm^2$ size presents the front view of the simulation and the experimental results at the left column of the figure, while a xz plane of the same size shows the side view at the right column

of the figure. The areal mass density (gr/cm^2) presented is determined from the volumetric mass density, obtained by the simulation in the cubic cells of the discretized solution domain, by integrating the simulated values over the x-axis to the front view. To highlight the jet opaque area, during the jet formation, a selective integration is performed along the y-axis for 240μm towards the origin for the side view.

In the front view, for the legs of the X-pinch the lower limits of the experimental dense opaque region are approximately from ~10^{-5} to ~$3.16^{\times}10^{-5}$ gr/cm^2 in relation to the simulation results. The simulation results present a near uniform coronal plasma expansion, such us uniform plasma stream since no initial random perturbation is considered [11]. A close observation of the simulation results identifies a non-smooth plasma expansion, in the form of plasma disturbances, i.e. at 41ns, which are attributed to the numerical approximation and the discretization of the model. Ablation flares are observed on the experimental images, close to the cross-point after the 33ns and indicate the low growth rate of the instabilities. The limitations of the imaging diagnostics do not allow for further conclusions away from the cross-point in relation to the shape of the plasma front, at initial times. Additionally, the opaque areas on the experimentally retrieved images do not allow for further conclusions concerning the plasma dynamics inside the opaque area. It should be noticed here that a good agreement is achieved between experiments and simulations for the formation of the jet dynamics, since the mass transfer is very well predicted. Regarding the cross-point, a sharp density gradient is apparent, defining a similar width for the simulation and the experimental results. In the side view, the expansion of the opaque region corresponds to areal densities in the range between $3.16^{\times}10^{-6}$ and $3.16^{\times}10^{-5}gr/cm^2$, thus defining the simulated boarder of the opaque area. These computations are valid and secure in the area extending up to 0.9 mm on the z-axis, since above this length, the plasma expands out of the simulation domain. This is clearly demonstrated in the front view image at 41 ns. Regarding the cross-point, a sharp density gradient follows a similar to the front view behavior, indicating strong compression. The maximum radial expansion observed indicates the jet formation as show by the simulation results. The results are in agreement with similar investigations of other relevant studies [12,13].

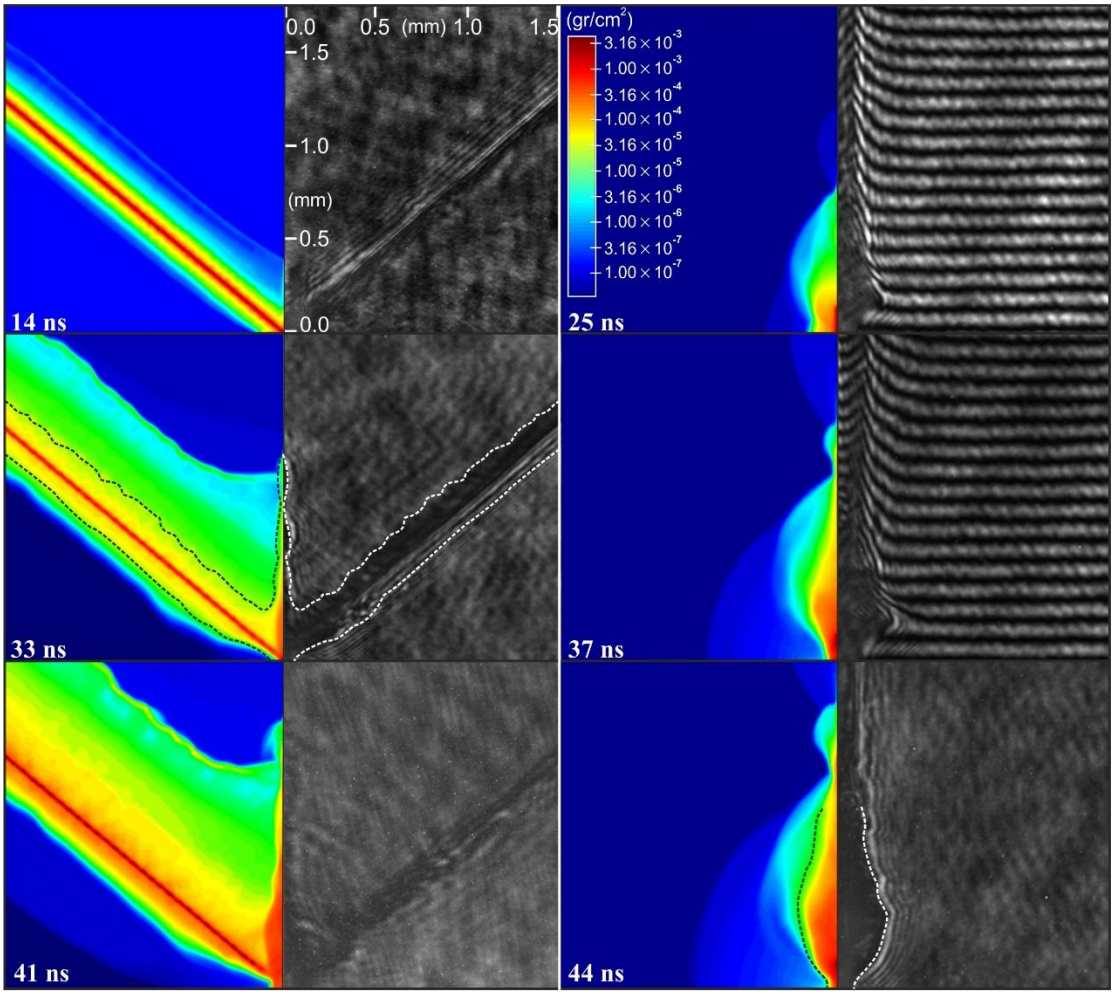

Figure 5.3.2: *Simulation vs Experimental results of the front (left column) and side (right column) views of the areal mass density evolution. The dashed lines indicate the opaque region boarders.*

The spatiotemporal evolution of the plasma areal mass density and the opaque area dynamics described above, are further analyzed by the introduction of five characteristic plasma lengths. Figure 3 demonstrates the experimental and the simulation results of the evolution of $\mathbf{L_f}$, $\mathbf{D_{f0}}$, $\mathbf{D_{s0}}$, $\mathbf{D_s}$, $\mathbf{L_s}$ lengths, that are defined on the X-pinch layout presented as inset in figure 5.3.3. The cut off density contour line (boarder) where the opaque area begins is $2^{\times}10^{-5}$gr/cm^2. The front view presents the length $\mathbf{L_f}$ of the jet and the width $\mathbf{D_{f0}}$ of the cross-point area. The side view presents the width $\mathbf{D_{s0}}$ of the cross-point area. $\mathbf{D_s}$ and $\mathbf{L_s}$ are the maximum jet width and its maximum distance from the cross-point respectively.

The average expansion velocity of the jet is approximated by linear fitting on the experimental data for $\mathbf{L_f}$ is 39km/s. The simulation results show exactly the same expansion velocity. This is an effective velocity, due to the contribution of the coronal plasma ablation in the jet bulk density, that compared to the simulated sound speed at the jet tip results to a Mach number equal to 4, that is consistent to relative works [14,15].

In the frame of time, the cross-point area width (demonstrated by the $\mathbf{D_{f0}}$ parameter**)** expands due to the thermal pressure for about 20 ns. The compression phase is initiated when the magnetic pressure becomes higher than the thermal pressure. This phase lasts until the 40thns when pinching

occurs. In the time period between 40^{th} and 45^{th} ns the simulated $\mathbf{D_{f0}}$ increases in contrast to the experimental data. This discrepancy is justified by the fact that the radiative explosion effect which takes place in this time period of the plasma dynamics is not considered in the simulation. However, the compression velocity (~11.5km/s) is very well predicted in agreement with the experimental data of this study and also of other studies [14].

Regarding the plasma jets formation shape, as simulations predict in agreement with the experiments the plasma jets almost lie on the normal plane to the one defined by the two wire straight lines (y=0, xz plane) and as a result their shape is almost flat. This is demonstrated by the $\mathbf{D_s}$ parameter values as shown in figure 5.3.3. The "flat" shape of the plasma jets is explained due to the faster expansion of the plasma on the y=0, xz plane, under the force of the kinetic pressure by the converging of the jets' plasma streams. The effective velocity of the plasma jets on the x axis demonstrated by the linear fitting of the experimental and simulation data of the parameter $\mathbf{D_s}$ is 9 km/s and 10km/s as predicted by the experimental and the simulation data, respectively. This velocity corresponds to the ~25% of the effective jets' average velocity on the z axis. The cross-point spatiotemporal dynamics demonstrated by the plasma parameters $\mathbf{D_{s0}}$ and $\mathbf{D_{f0}}$ is dominated by the same behavior of these two parameters until the 35^{th}ns slightly before the pinching time. Afterwards, effective expansion occurs due to the plasma ablation of the legs that causes the shading of the neck region at the cross-point, as can be observed in the front view of figure 2 at 41ns. The compression velocity is very well predicted by the simulation since it agrees with the compression velocity of $\mathbf{D_{f0}}$ and $\mathbf{D_{s0}}$. The uniform compression dynamics predicted by the equal velocities of $\mathbf{D_{f0}}$ and $\mathbf{D_{s0}}$ is explained from the azimuthal nature of the global magnetic field around the neck area. The distance $\mathbf{L_s}$ corresponds to the height of the region (from the wire cross-point) where the global magnetic field dominates. $\mathbf{L_s}$ increases with time having an effective velocity of ~9km/s as predicted by the experiments and ~11km/s as predicted by the simulations.

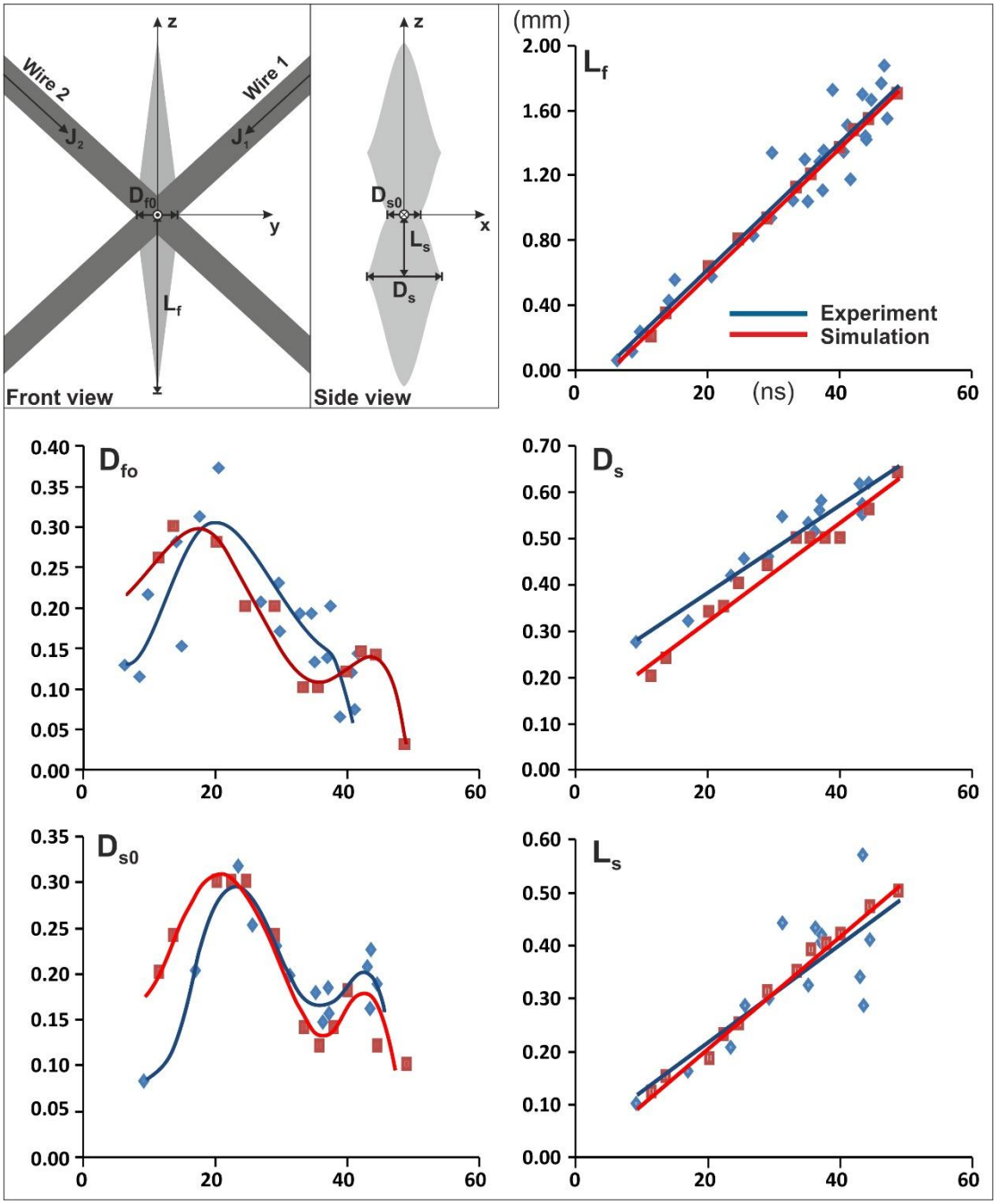

Figure 5.3.3: *Spatiotemporal evolution of five geometrical plasma lengths which support the demonstration of the spatiotemporal plasma dynamics.* ***L_f****: Plasma jet length in front view,* ***D_{f0}****: Plasma front width at cross-point,* ***D_{s0}****: Plasma side width at cross-point,* ***D_s****: Maximum jet width and* ***Ls****: Distance of* ***D_s*** *from the cross-point.*

Figure 5.3.4 shows a time sequence of simulation versus experimentally measured interferometry results for the areal electron density on the yz (front view) plane. The evolution of the ionization characteristics of plasma are demonstrated and validated in accordance with the spatiotemporal dynamics of mass density presented in the previous analysis. The simulated areal electron density is obtained at the corresponding plane by integrating the volumetric electron density along the x-axis. A multiplication by 2 delivers the total electron density considering the negative x-axis octant. The

experimentally captured interferograms are processed with the help of the IDEA software package (as described at the 5.1 section) [16].

As presented in figure 5.3.4, at 15ns from the current start, the simulated electron density deviates from the corresponding experimentally measured, especially along the jet z axis. The difference is attributed to the merging phase at the cross-point, which is not simulated, where the two wires merge to a common volume. The images at 29 and 38ns show a good agreement between the experimental and simulation results. The coronal plasma expansion is found using the $6^{\times}10^{16}cm^{-2}$ density contour as a reference which is three times higher than the minimum experimentally detectable density. At 29ns the maximum radial plasma expansion is 0.48 mm for the simulation and 0.35mm for the experiment while at 38 ns the maximum radial expansion is 0.62mm for the simulation and 0.50mm for the experiment. These lengths are represented by the white arrows on Figure 4 which indicate the length from the wire axis to the $6^{\times}10^{16}cm^{-2}$ density contour which is taken as reference. The average expansion velocity is calculated to be 16km/sec for the simulation and 17km/sec for the experiment. These velocities correspond to a density ionization front with a constant value, that exhibit simulation and experimental velocities of ~43% of the jet effective average velocity. This observation indicates that plasma with lower electron density is there apparent, which expands faster and contributes to the jet formation. Moreover, the areal electron density of the jet region is accurately computed for these two temporal moments.

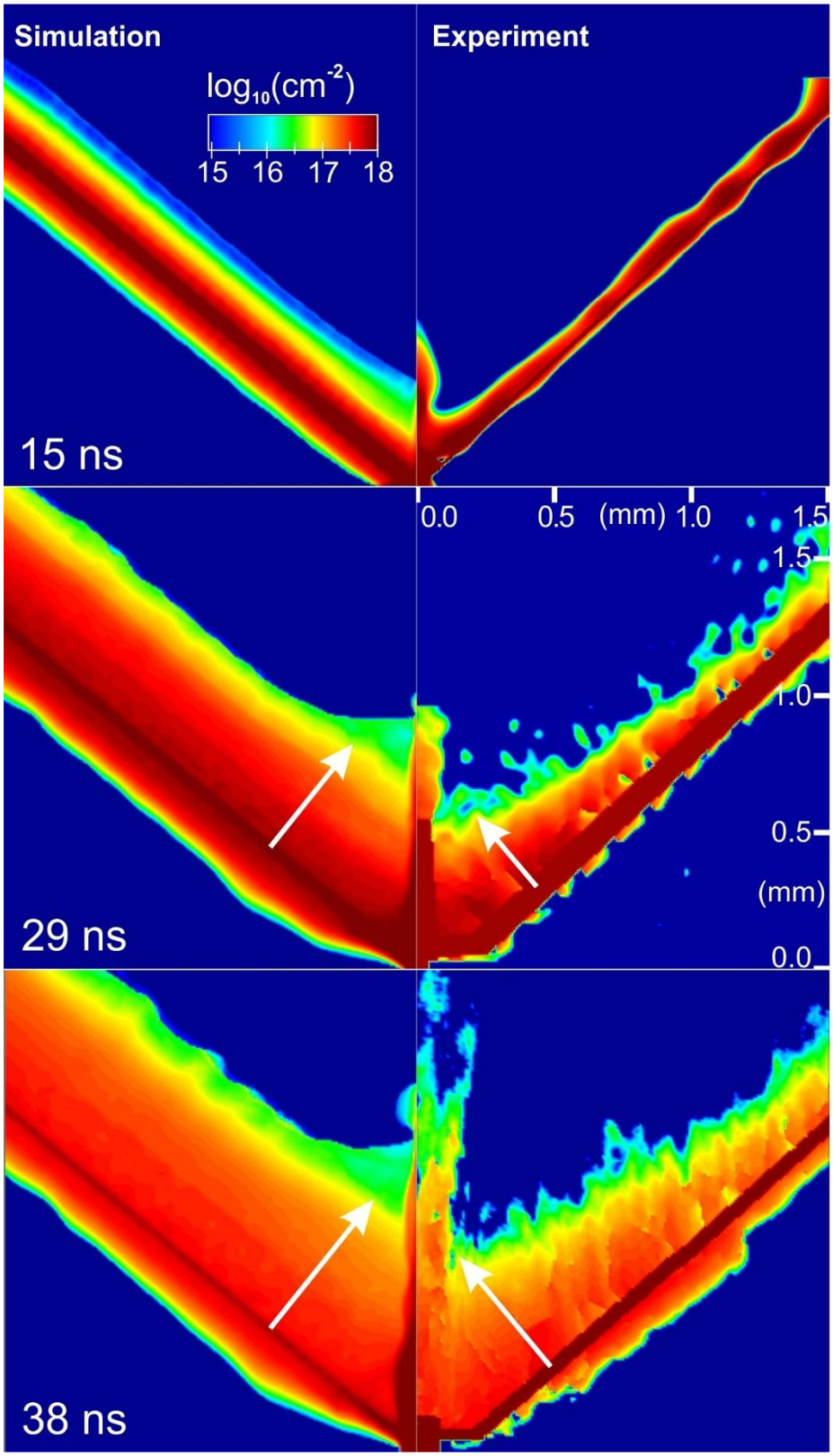

Figure 5.3.4: *Simulation vs Experimental results of the areal electron density on yz plane (front view). The white arrows indicate the simulation and experimental expansion lengths from the axis of the wire to the 6 × 10^{16} cm^{-2} density contour which is taken as reference.*

The jet formation dynamics is further analyzed and discussed here. As figure 5.3.1 shows, the actual jet is formed when the jet-tip expansion exceeds the merging point [11]. The analysis of the jet evolution is performed and presented in figure 5.3.5a. The instantaneous axial velocity Vz of the plasma fluid is calculated along the z-axis at specific temporal moments. In addition, in figure 5.3.5b the force produced by the thermal pressure gradient gradP, which acts on the opposite direction, is presented as the projection of the -gradP force on the xz, y=0 plane at 36ns. The temperature grayscale map is in the range between 0.05eV and 50eV. The vectors of the -gradP force are colored according to their magnitude. In figure 5.3.5a, the maximum fluid velocities are calculated to be 27km/s and 34km/s, at 7ns and 12ns, respectively. These velocity values are 30% and 13% lower than the effective jet velocity, which was previously calculated to be 39km/s, in the analysis of $\mathbf{L_f}$. At 12ns, the effective velocity is not the actual jet convection velocity, because it is prevented by the "zippering" effect as discussed previously. Therefore, there is mass transfer towards the z-axis due to ongoing coronal plasma ablation from the wires legs. After 20ns the maximum value of the velocity approaches the effective jet velocity and the actual jet has been formed, as observed in figure 5.3.1 at 25ns. The maximum velocity remains constant until 49ns, as the orange and yellow curves show. In figure 5.3.5b, it is observed that the plasma temperature at the core of the wire, and far from the cross-point, remains cold at a temperature of ~1.5eV. The temperature is linearly increased to reach a value of ~14eV along the transverse to the wire axis direction. This temperature remains constant until the plasma stream front. At this area, the thermal pressure force is acting on the corona-core plasma interface on both sides of the wire compressing it, as cyan arrows indicate. Far from this interface, the blue arrows denote the contribution of the pressure force to the plasma ablation. The temperature at the cross-point is ~ 8eV and along the jet axis increases linearly up to ~ 20eV and is decreased again to ~ 5eV at the tip of the jet. The maximum temperature of ~ 50eV is observed at the region of the neck. The existence of a region of strong acceleration is responsible for the axial velocities observed and is attributed to the thermal pressure force, along the z-axis for ~ 400μm.

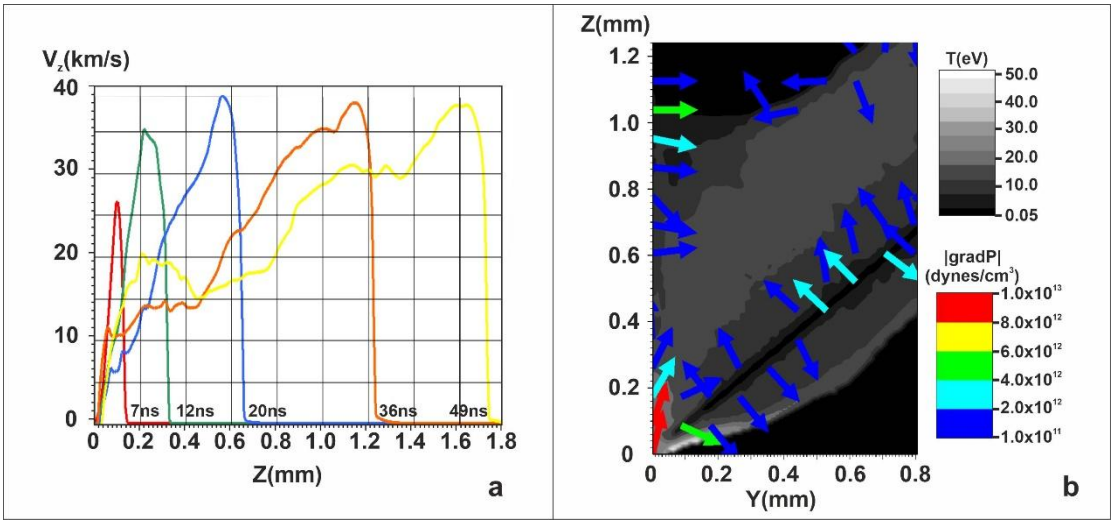

Figure 5.3.5: *(a) Graph of four evolution curves of the axial fluid jet velocity Vz, along the z-axis at 12, 20,36 and 49ns. (b) The temperature grayscale map (0.05 - 50 eV) and the vectors of the thermal pressure force (-gradP) are colored according to their magnitude (1.0×10^{11}-1.0×10^{13} dyn/cm^3).*

The mechanisms of mass transfer as well as the origin of mass which is transferred in order to form the axial plasma jet is a scientific topic of great interest. Two mass origins are considered by most of the studies. These suggest that the jet is formed by a) the coronal plasma ablated from the X legs and b) the plasma which is ejected from the cross-point pinching area [11,17-20]. Our study demonstrates that both mechanisms contribute to the jet formation. Figure 5.3.6 presents characteristic mass density contour plots at 36 ns over four characteristic plane views: the yz, x=0, plane (front view, figure 5.3.6a), the xz plane, y=0 (side view, figure 5.3.6b) and the xy plane top views, at z=400μm (figure 5.3.6c) and at z=800 μm (figure 5.3.6d). The **J×B** force and the momentum density ρ**u** are shown in a vector form. The momentum and the **J×B** force have a common origin located at the tail of the arrows. The influence of the **J×B** force is discussed, considering the local and global magnetic field dynamics [11,19,21]. The **J×B** force units are in Gauss^2 and the scaling factor used is $c\Delta l/4\pi$, where *c* is the speed of light (in CGS) and Δl=0.001cm is the unit length used in the simulation.

In figure 5.3.6a (see also figure 5.3.1), the direction of the momentum vectors represents the perpendicular to the wire axis mass flow (due to the plasma ablation), having magnitude values ≤ 2500 gr/cm^{2}s. The highest momentum values are observed along the z-axis reaching the maximum value at the tip of the jet (~5$^{\times}$10^{4}gr/cm^{2}s). This is because of the vertical momentum conservation. The contribution of the axial momentum from the ablated flow and the strong axial pressure gradient (presented in figure 5.3.5) results to the jet acceleration. These findings are in agreement with other studies for the jet formation in X-pinch plasmas [15,19,20]. In addition, the J×B force also contributes to the transverse to the wire axis mass transfer ranging between 10^8 and 10^{9}Gauss^2. This behavior changes near the plasma stream front, where the force direction is reversed since the local magnetic field changes to the opposite direction, as demonstrated in figure 5.3.1.

In figure 5.3.6b, the momentum vectors are directed towards the z-axis and indicate the plasma compression and its expansion on the direction of the jet. At this time instant, the J×B force contributes to the plasma compression reaching a maximum value of ~ 10^{9}Gauss^2 at the cross-point. On this cross-section an “egg-like” shape is observed in the jet geometry as also shown in figure 5.3.1. This shape is initiated by the influence of both the local and global magnetic fields topology. Figures 5.3.6c and 5.3.6d denote a similar behavior of the direction of the momentum on the xy, z=400 μm and z=800 μm planes. As time progresses, the mass flow which emerges from lower z levels, forms the shape of the plasma. The angles formed between the J×B and the momentum show that the J×B force tends to change the flow direction, almost normal to the velocity. Along the y-axis the J×B force contributes to the plasma compression on the x-axis.

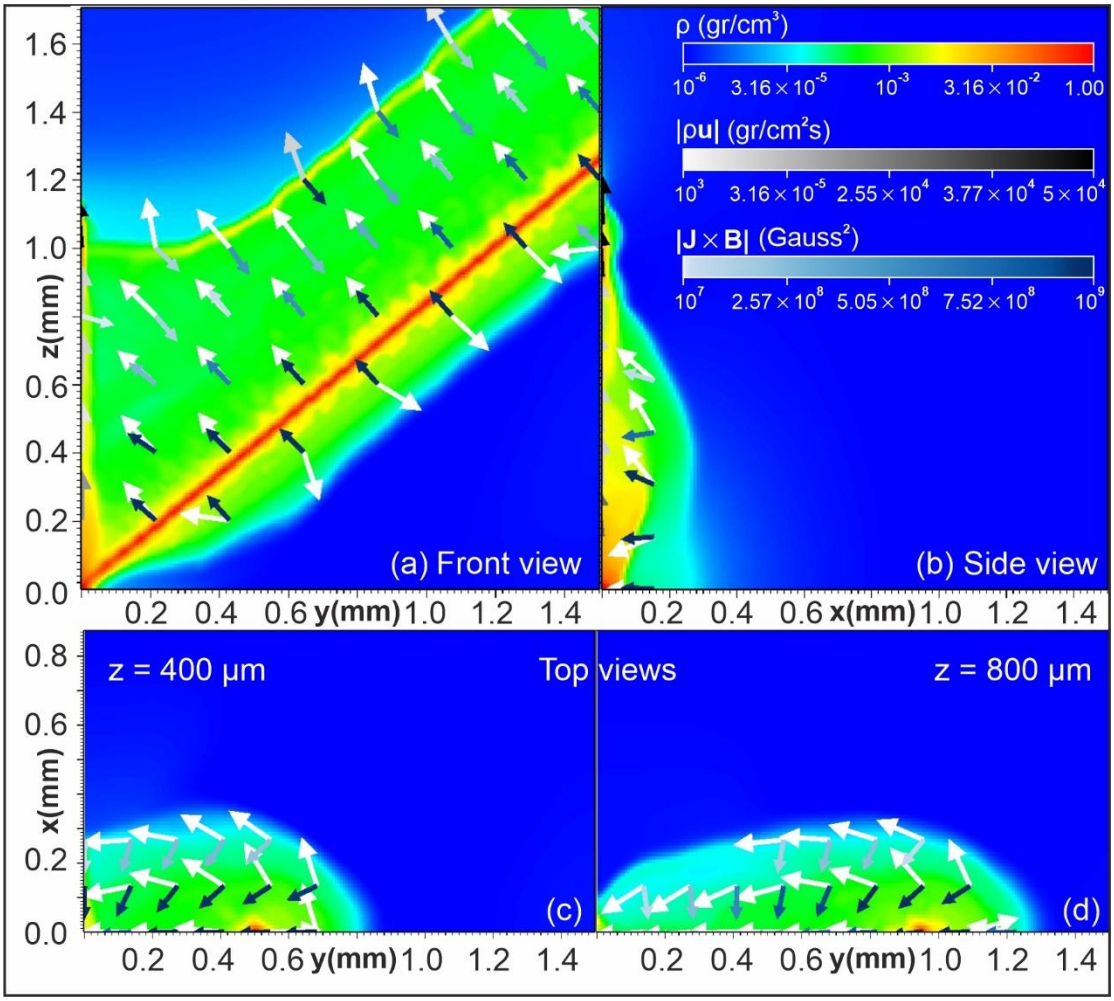

Figure 5.3.6: *Characteristic plasma volume mass density contour plots 36 ns after the starting point of current flow. The **J×B** force and momentum ρ**u** are represented in a vector form. The grayscale arrows represent the momentum and are longer than the **J×B** force arrows, which are colored by the blue-white colormap. (a) Front view, (b) side view, (c) and (d) top views at z=400 and 800 μm, respectively. The density colormap (1.0×10^{-6} - 1.0 gr/cm^3), the magnitude colormap of the momentum (1.0×10^3 - 5.0×10^4 gr/cm^2 s) and the **J×B** force (1.0×10^7 - 1.0×10^9 Gauss^2) apply to all views.*

5.3.4 Conclusions

The capabilities of the MHD code PLUTO are tested via the experimental comparison for the investigation of laboratory magnetically compressed plasmas driven by pulsed power generators. The developed numerical modules of the code were analyzed and discussed in relation to the physics they represent. The 3D MHD simulations are performed to provide a detailed description of the associated X-pinch experiments which were carried out using Tungsten wires of 5 μm diameter.

The new method was developed and applied to overcome the magnetic field boundary conditions aspect without affecting the efficiency of the code. The energy inflow was imposed by the update of the magnetic field values, in accordance with the experimental current, over the total computational domain simultaneously. This updated field was used for the integration of the conservation laws system.

The 3D simulation results of the X-pinch model were compared to the corresponding experimental results. The plasma evolution at the initial times of the experiment was accurately predicted. The jet formation and its spatiotemporal dynamics were clearly described, while the physics involved including the neck, the plasma electrodes formation as well as the “zippering” effect were identified, in respect to the concept of the global and local magnetic fields. Furthermore, the mass density and the plasma ionization front dynamics were investigated, and the plasma geometrical characteristics were determined. The results were found to be in agreement with the experiments as well as with similar research works in the literature. Moreover, the actual plasma jet velocity was computed from the simulations and compared to the experimental findings, thus the effective jet velocity was determined. The influence of the thermal pressure gradient on the jet formation was also studied in relation to the strong acceleration of the jet. Finally, the “egg”-like profile of the jet was explained and associated to the **J**×**B** force and the momentum of the ablated mass from the X pinch legs.

Our studies substantially contribute to the understanding of the interplay mechanisms associated to the generation of the supersonic plasma jet formation, enlightening the critical role of the **J**×**B** force and of the momentum transfer dynamics. The code development is enriching the laboratory magnetically compressed plasma studies.

References

[1] Fuyuan Wu et al, "A conservative MHD scheme on unstructured Lagrangian grids for Z-pinch hydrodynamic simulations" , Journal of Computational Physics, Volume 357, 15 March 2018, pp. 206-229 (2018).

[2] Wang X-G et al 2019 Chin. Phys. B **28** 035201.

[3] Kaselouris E. et al (2017), “The influence of the solid to plasma phase transition on the generation of plasma instabilities”, Nature Communications, Vol 8, pp. 1713.

[4] T. A. Shelkovenko et al., "Evolution of the structure of the dense plasma near the cross point in exploding wire X pinches", Phys. Plasmas, Vol. 6, No. 7, July 1999.

[5] Yamaleev N K and Carpenter M H 2009 J. Comput. Phys. Volume 228, Issue 11, 20 June 2009, pp 4248-4272.

[6] Kolb, S.M., Stute, M. Kley, W. and A. Mignone (2013), “Radiation hydrodynamics integrated in the PLUTO code”, Astronomy and Astrophysics, Vol. 559, pp. A80.

[7] Mitchell M 2007, "X-Pinch plasma dynamics studied with high temporal resolution diagnostics", PhD Thesis Cornell University.

[8] Pikuz S A et al, "X-Pinch. Part I", Plasma Physics Reports, 2015, Vol. 41, No. 4, pp. 291–342.

[9] Kalinin, Y. G. et al 2005 Laser diagnostics of the plasma in the S-300 pulsed power generator Proc. SPIE 5777, XV International Symposium on Gas Flow, Chemical Lasers, and High-Power Lasers pp 808-811

[10] Chittenden J P et al, "Two-dimensional magneto-hydrodynamic modeling of carbon fiber Z-pinch experiments", Physics of Plasmas 4, 4309 (1997); https://doi.org/10.1063/1.872593

[11] F. N. Beg et al., "Jet Formation and Current Transfer in X-Pinches**",** IEEE TRANSACTIONS ON PLASMA SCIENCE, VOL. 34, NO. 5, OCTOBER 2006.

[12] Pikuz S A et al, "Density measurements in exploding wire-initiated plasmas using tungsten wires", Physics of Plasmas **6**, 4272 (1999); https://doi.org/10.1063/1.873695

[13] Bott S C et al (2006), "Dynamics of cylindrically converging precursor plasma flow in wire-array Z -pinch experiments", Phys. Rev. E **74** 046403.

[14] Jaar G S et al, "Axial plasma jet characterization on a microsecond x-pinch", J. Appl. Phys. 123, 213301 (2018).

[15] D.M. Haas et al., "Supersonic jet formation and propagation in x-pinches", Astrophys Space Sci (2011) 336:33–40.

[16] Wiley Hipp M, Woisetschlager J, Reiterer P, Neger T (2004),"Digital evaluation of interferograms. Measurement 36", pp 53–66.

[17] I. H. Mitchell et al., "Investigation of the plasma jet formation in X-pinch plasmas using laser interferometry", Phys. Plasmas, Vol. 7, No. 12, December 2000.
[18] R. Aliaga-Rossel, et al., "Plasma Jet Formation in X-pinch Plasmas", AIP Conference Proceedings **563**, 270 (2001).
[19] J. P. Chittenden et al., "Structural Evolution and Formation of High-Pressure Plasmas in X Pinches", PRL **98,** 025003 (2007).
[20] Haas D M 2011, "Investigation of the dynamics and emission characteristics of x-pinch plasmas", PhD Thesis University of California San Diego.
[21] G W Collins IV et al, "Effect of the global to local magnetic field ratio on the ablation modulations on X-pinches driven by 80 kA peak current", New Journal of Physics **14** (2012) 043021.

5.4 High performance simulations of a single X-pinch using two sophisticated numerical approximations for the preparation of experiments on the generation and growth of laboratory plasma jets

Plasma production from pulsed power plasma devices loaded as Z-pinch and X-pinch is essential for plasma physics studies and for a variety of plasma applications. The investigation of laboratory plasmas demands the development of advanced computational models and numerical methods, able to describe and even substitute the real experiments. Many numerical approaches have been developed to describe the complex behavior of plasmas.

Especially the GORGON Eulerian code is ideal for MHD plasma applications such as laser-produced magnetized jets [1-3], Z and X-pinch wire configurations [4-6], Z-pinch wire arrays [7-12], conical arrays, radial wire arrays and foils that create magnetically driven outflows which are studied in laboratory astrophysics experiments mainly for Young Stellar Objects (YSO) and Herbig-Haro (HH) jets [13-17,2,3]. The PLUTO also [18,19-22] was recently used [23] to simulate the plasma expansion in two wire tungsten load X-pinch experiments. The distance between anode-cathode was 15 mm and the X-pinch wires were set to an angle of 100^{o}. The code successfully described the "zippering" effect, the pinch generation and the jet initiation, formation, and evolution as we describe at the previous section while the simulation results are validated by experimental results.

In this section, these two codes validated for X-pinch plasma generated studies, are used to simulate a sharp two-wire tungsten load X-pinch geometry. The study is carried out as the first step for an experimental campaign aiming to the detailed understanding of the phenomena related to the development of plasma jets using tabletop pulsed power X-pinch devices. The generation of the jets in such plasma devices is affected by the development of MHD/MRT instabilities. The detailed understanding of the seed and growth of these instabilities studied in relation to the associated physics parameters can lead to a more efficient plasma jet formation suitable for laboratory astrophysics as well as for plasma particle acceleration studies. The parameters used in this simulation study are based on the characteristics of the pulsed power X-pinch plasma generator located at the (IPPL) of the HMU research Centre as presented at the 5.1 section.

The distance between anode-cathode is 15 mm and the wires are set to a sharp angle of 50^{o}. Their configuration consists of two regions, namely, the tungsten (load) and the low-density background (vacuum). Two high resolution spatiotemporal MHD models are developed to describe the structural evolution of the plasma density and its influence on the magnetic field topology. The physics and numerical modeling differences of GORGON and PLUTO and their influence on the simulation results are demonstrated and analyzed. The computational data, resulting from both codes, provide valuable information on the improvement of accurate and efficient X-pinch models and offer crucial insights on the mechanisms of plasma evolution and jet formation.

5.4.1 Physical modeling in GORGON and PLUTO

In order to have a complete estimation of the physical modeling, we give a side-by-side presentation of the physical and computational schemes of the two codes. GORGON and PLUTO are single fluid 3D Eulerian MHD codes that both solve a system of conservation laws of the form:

$$\frac{\partial \mathbf{U}}{\partial t} + \nabla \cdot \mathbf{T}(\mathbf{U}) = \mathbf{S}(\mathbf{U}) \tag{5.4.1}$$

where **U** represents a set of conservative quantities, **T**(**U**) is the flux tensor and **S**(**U**) defines the source terms [17,19] (equations 3.1-3.13 in the third Chapter/PART I). This set concerns the conservation of mass, momentum and energy equations that are analytically presented in literature research works [17,19,23]. Furthermore, the GORGON code treats the ion and electron components separately allowing them to be out of thermodynamic equilibrium with respect to each other, while their internal energy equations are solved independently. The energy exchange rates Δ_{ei}=-Δ_{ie} between ions and electrons couple the two energy equations [17]. The PLUTO code has a single fluid component, and it is assumed that a thermodynamic equilibrium is always achieved, thus T_e=T_i=T. GORGON and PLUTO are built on the SI and the Gaussian metric system, respectively.

The temperature profile in PLUTO is the common variable profile correlating the mass density ρ, the thermal pressure p = p(ρ,T), and the internal energy density ε≡ρe=ρe(ρ,T) through tabulated data of the modified SESAME EOS [24] for tungsten and the original SESAME library for dry air [25]. Thus the "vacuum" area (low density background [23]) is modeled by a very thin plasma air component of initial value 10^{-6} gr/cm^3. Therefore, the computational domain is initially separated in three different regions of pure tungsten plasma, air plasma and the intermediate transition zone. The density threshold value (ρ_{vac}=ρ_{lim}/10) is used to implement the lower ρ_{vac} and upper value ρ_{lim} of the transition zone [23] (detailed presentation at the third Chapter/PART I). The GORGON code on the other hand uses similar EOS for the two plasma components (ions and electrons) by adopting the ideal approximation for the ions and by adding the ionization potential to the electrons according to:

$$\varepsilon_i = \frac{p_i}{\gamma - 1} \text{ and } \varepsilon_e = \frac{p_e}{\gamma - 1} + Q(Z_{eff}) \tag{5.4.2}$$

where ε_i and ε_e are the ion and electron internal energy densities, respectively. $Q(<Z>)$ is the ionization potential energy for tungsten plasma [26] which depends on the average ionization charge <Z> that is calculated from an average-ion Thomas-Fermi model and the adiabatic index is γ=5/3. A similar process for the definition of three zones is also adopted by GORGON. This process defines the pure vacuum region, the main tungsten plasma region and a dynamically evolving intermediate zone of one cell, which is used to separate the other two regions and envelop the outer plasma.

In GORGON, the Hydro-Dynamic (HD) solver is deactivated at the vacuum region, where the Maxwell equations are solved. The evolution of the magnetic field follows the magnetic potential **A** and the magnetic induction is calculated through the **B**=**∇**x**A** equation ensuring the **divB**=0 constraint is preserved [17]. By the same means, and without loss of the generality of the numerical approximation, the Riemann solver of PLUTO is deactivated in the vacuum region [27]. The magnetic induction **B** is computed from the Ampere's law including the skin effect in the calculation of the current density J=J(r) and its spatiotemporal update and evolution is discussed in detail in [23]. The density values that define the three zones for both codes are set to be the same in this work.

The ionization level in GORGON is defined by the help of the Thomas-Fermi model [28], that is determined by a function of mass density and plasma temperature expression fitted to the numerical solution of:

$$Z_{eff} = Z\,\frac{y}{1+y+\sqrt{1+2y}} \tag{5.4.3}$$

For the tungsten loads used here, it holds that Z = 74 and further details for the function y may be found in [28] (also detailed presentation in 3.3.1.2 at the third Chapter and in figure 3.6). The mean ionization charge state in PLUTO is a function of electron density and temperature and is determined by tabulated data of the FLYCHK code [23,29,30] (figure 3.3 in the third Chapter).

Both codes include the dissipative term of Ohmic heating where the resistivity n is measured in seconds in PLUTO and $\Omega\cdot$m in GORGON. The resistivity in GORGON has an anomalous component and is Braginskii like [17,31-33]:

$$n = \frac{m_e}{N_e e^2 (\tau_e)_{total}}\left(1-\frac{3.1\chi_e+1.89}{{\chi_e}^2+6.2\chi_e+2.8}\right) \tag{5.4.4}$$

where m_e is the electron mass, N_e is the electron density and χ_e is a dimensionless factor. The total collision time is:

$$(\tau_e)_{total} = \frac{1}{\frac{1}{\tau_e}+3Q_{en}N_n\left(\frac{3k_B T_e(K)}{m_e}\right)^{0.5}} \tag{5.4.5}$$

with

$$Q_{en}=5\times10^{-19}\,m^2$$

where Q_{en} is the electron-neutral cross-section, τ_e the collision time, N_n the neutral density and k_B the Boltzmann's constant. The $(\tau_e)_{total}$, is the total collision time, which is calculated through the τ_e collision time and a second term that includes the contribution of the neutrals density N_n. This population is calculated as the subtraction of the ion density from the heavy particles' density N_H, where the threshold value of Z_{eff}, that defines the neutrals from the ions, is user defined [31]. The dimensionless factor χ_e [equals $(\tau_e)_{total}\cdot\omega_{ce}$, with ω_{ce} the electron cyclotron frequency], is a standard parameter for the Braginskii magnetized formulas [34]. This resistivity formula prevents large discontinuities in transport coefficients at the vacuum/plasma boundary [33] while the resistivity value increases significantly for large magnetic field values and for the dilute plasma regions (2D and 3D relevant graphs in figures 3.20-3.22 at the 3.4.1.4). An analytic presentation of a similar approach is presented and discussed at the third Chapter PART II at the 3.4.1.3 subsection, with two differences. The first one is the use of an approximation of the non-ideal Saha-equation for the determination of the neutrals and the second is the effective quantum Coulomb logarithm as calculated from the Born approximation and Debye potential instead of the classical form of the Coulomb logarithm that GORGON uses, which is:

$$\ln\Lambda = 29.9 - \ln\left(Z_{eff}\cdot {T_e}^{-1.5}{N_e}^{0.5}\right) \text{ where } N_e \text{ in } m^{-3} \text{ and } T_e \text{ in eV} \tag{5.4.6}$$

with a cut-off value of 2. A similar approximation is adopted by PLUTO that considers the linear mixture formula [35]:

$$\mathrm{n_{total}} = \mathrm{n_{ei}} + \mathrm{n_{en}} \tag{5.4.7}$$

where n_{en} is the electron-neutral resistivity and n_{ei} is the electron-ion resistivity. The analytic presentation is at the 3.4.1.3 in the third Chapter. The difference in this approach lies to the estimation of the neutral population density N_n in the second term. It holds:

$$\mathrm{N_H} = \mathrm{N_i} + \mathrm{N_n}, \text{where } \mathrm{N_n} = \mathrm{N_H} - \mathrm{N_H}\tanh(\mathrm{Z_{eff}}) \tag{5.4.8}$$

N_H is the total heavy particles population, with $N_H = N_e/Z_{eff} = \rho/m_{ion}$, N_i and N_e are the ion and electron densities respectively, ρ is the mass density and m_{ion} is the ion mass. The hyperbolic function is used to provide a smooth transition near $Z_{eff} = 1$. Z_{eff} is calculated and correlated to the N_e and temperature T according to the FLYCHK code data [23,29,30].

As we already presented at the third Chapter the thermal conduction in PLUTO is contributing to the energy equation by the introduction of the additional divergence flux term:

$$\frac{\partial \mathrm{E_t}}{\partial \mathrm{t}} + \boldsymbol{\nabla} \cdot \left[\left(\mathrm{E_t} + \mathrm{P} + \frac{1}{2}\mathrm{B}^2\right)\mathbf{u} + (\mathbf{u}\cdot\mathbf{B})\mathbf{B}\right] = \boldsymbol{\nabla}\cdot\mathbf{F_c} \tag{5.4.9}$$

The resistivity and viscosity dissipative terms are ignored at the right-hand side of equation 8. E_t is the total energy density provided by: E_t=1/2ρu^2+ρe+**B**^{2}/2, where **B**=**B**cgs/$\sqrt{4\pi}$ is the magnetic field [23]. The flux $\mathbf{F_c}$ is defined by:

$$\mathbf{F_c} = \mathbf{F}_{\mathrm{class}}\left(\frac{\mathrm{F_{sat}}}{\mathrm{F_{sat}} + |\mathbf{F}_{\mathrm{class}}|}\right) \tag{5.4.10}$$

where

$$\mathbf{F}_{\mathrm{class}} = \mathrm{k}_{||}\frac{\mathbf{B}(\mathbf{B}\cdot\boldsymbol{\nabla}\mathrm{T})}{\mathrm{B}^2} + \mathrm{k}_{\perp}\left(\boldsymbol{\nabla}\mathrm{T} - \frac{\mathbf{B}(\mathbf{B}\cdot\boldsymbol{\nabla}\mathrm{T})}{\mathrm{B}^2}\right) + \mathrm{k}_{\times}\left(\frac{\mathbf{B}}{\mathrm{B}}\times\boldsymbol{\nabla}\mathrm{T}\right) \tag{5.4.11}$$

and

$$\mathrm{F_{sat}} = 5\varphi\rho\mathrm{c_s}^3 \tag{5.4.12}$$

$\mathbf{F}_{class}$ and F_{sat} are the classic and saturated thermal conduction regimes, where c_s is the isothermal sound speed, and ϕ a number of the order of unity (0< ϕ<1) [27,36,37]. The standard expression in the code includes the $k_{||}$ and $k_{\perp}$ terms that are the thermal conduction coefficients along and across the magnetic field. The $k_{\times}$ is the component coefficient of the thermal conduction flux, transverse to the plane of **B** and **∇**T, which is added to the source files of the code to approximate better the metal plasma temperature and the energy exchange spatiotemporal profile. The classical Braginskii components are used for the aforementioned three coefficients using a linear sum of the electron and ion component for the parallel and normal coefficients and the subtraction of the two for the transverse one according to the MHD equations form [34,38,39] (equations 3.74-3.82 in 3.4.2.3

subsection of the third Chapter). The k_x electron and ion components are presented in 5.4.13 and 5.4.14 respectively:

$$k_x{}^e = \frac{N_e K_B{}^2 T_e \tau_e}{m_e} \cdot (\chi_e \frac{\gamma_1'' \chi_e{}^2 + \gamma_0''}{\Delta_e}) \quad (5.4.13)$$

$$k_x{}^i = \frac{N_i K_B{}^2 T_i \tau_i}{m_i} \cdot (\frac{2.5\chi_i{}^2 + 4.65}{\Delta_i}) \quad (5.4.14)$$

where the values of γ_1'' and γ_0'' are correlated to Z_{eff} and have a mean value at the simulations [34]. All the other constants in the two equations are presented in the 3.4.2.3 subsection. On the other hand, the GORGON code uses independently the ion and electron heat flux terms $\mathbf{q}$=-k$\boldsymbol{\nabla}$**T** at the corresponding MHD equations, where the same with PLUTO parallel and normal expressions for the thermal conduction coefficients are used [17]. The transverse term is neglected in GORGON.

The radiation losses are implemented in PLUTO through an optically thin and an optically thin/thick radiation transport scheme [23,40] (presented analytically at the third Chapter PART I). Optically thin radiation losses are implemented in GORGON by using the free-bound contribution term:

$$\frac{\partial \rho e}{\partial t} = -1.69 \cdot 10^{-38} < Z >^2 N_e N_i \frac{E_\infty{}^{Z-1}}{T_e(eV)^{0.5}} (SI) \quad (5.4.15)$$

here $E_\infty{}^{Z-1}$ is the ionization energy of the recombined state in eV [39]. The absence of the free-free term is important only at very high temperatures and when the ions are fully ionized. The absence mainly of the bound-bound term is taken into consideration using a correction factor [17,41] (analytically presented and evaluated at the 3.3.1.2 subsection and demonstrated in figure 3.6).

5.4.2 Numerical modeling in GORGON and PLUTO

The numerical models are developed, aiming to describe with the maximum accuracy the physical models discussed in subsection 5.4.1, in GORGON and PLUTO. The X-pinch plasma device implemented for the experiments and used as a reference here is presented in the first section of this Chapter. This machine is a table-top pulsed powered plasma generator, implemented in a downscaled mode of producing a peak current of ~46 kA with a rise time (10% - 90%) of 50 ns. The machine is loaded with two thin tungsten wires of 5 μm initial diameter, that form an X-pinch load. The distance between anode-cathode is 15 mm and the X-pinch wires are set to a sharp angle of 50°. Figure 5.4.1 presents the computational domains of both MHD codes and their discretization, the geometrical characteristics of the wire loads and the initial density distributions of the numerical models. The complete X geometry of the load is modeled in GORGON. Thus, a spatial domain of size 12×12×6 mm (X×Y×Z) is developed. A uniform discretization of 10 μm is generated and the boundary conditions are set to "free flow" [17]. The advantage of the 1/8 symmetry is taken in the model developed in PLUTO. The positive octant of the three-dimensional Cartesian coordinate system in a spatial domain with size 1.4× 1.4×4mm (*x*-*y*-*z*) is used. The computational domain is discretized uniformly again by the same cubic cells. The boundary conditions on the *xy* plane are "reflective" and "eqtsymmetric" on the *xz* and *yz*

planes. For the x=1.4mm and z=4mm planes "outflow" boundary conditions are applied. Finally, the “user defined” boundary conditions are used to set the spatial derivatives of the primitive quantity values to zero, along the direction of the axis of the wires, on the y=1.4 mm plane [23,27].

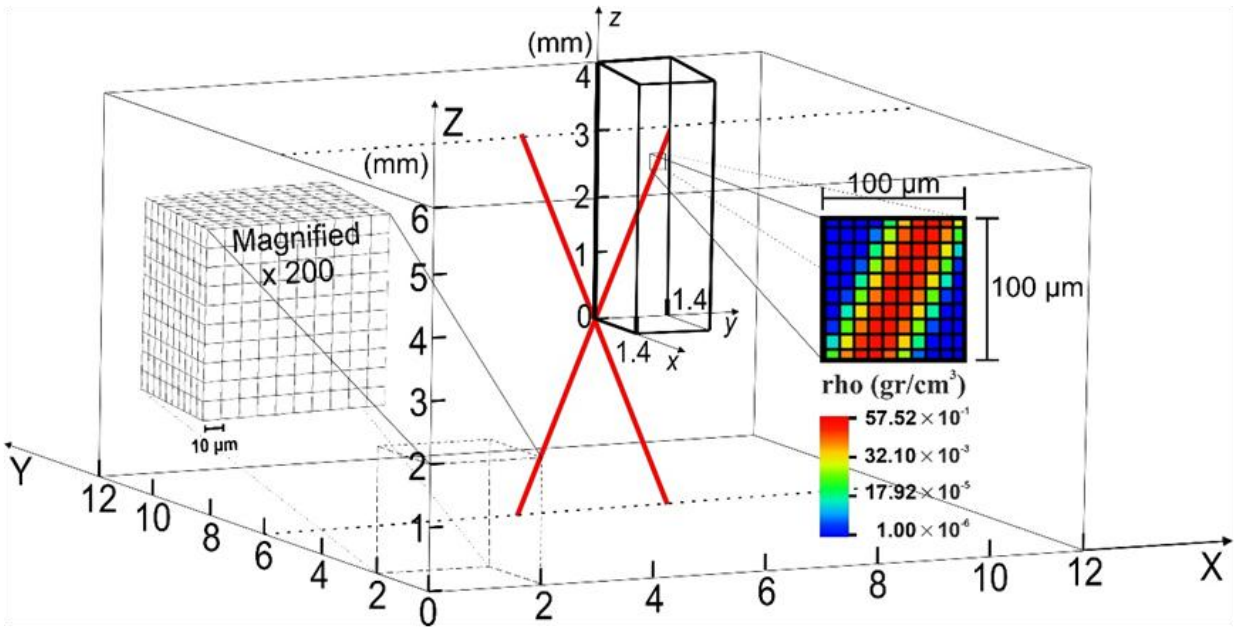

Figure 5.4.1: *The computational domains of GORGON (XYZ) and PLUTO (xyz). The magnified section of the X leg presents the 100 × 100 μm cross section of the mass density distribution at the simulation start. A magnified by 200 times detail of the models common grid, is demonstrated.*

The simulation initiates at 5 ns from the current start for both models. The density and the thermal pressure have a Gaussian spatial distribution profile with a width of $1/e^2$ = 20 μm, equal to the maximum plasma radius R_{max}. The amplitude of the mass density tungsten profile is 5.75 gr/cm^3 and a full plasma state is considered. The plasma wire temperature has a varying radius profile, starting form a cold core of 0.2 eV that increases to 4.5 eV at the outer wire radius, according to the experimental analysis presented in the previous section [23]. The initial low-density background is 10^{-6} gr/cm^3. In GORGON, an approximation of the experimental current is imposed by properly setting the magnetic field on the boundaries [17]. In PLUTO the distribution of the magnetic field is calculated via the provided experimental current of 4.5 kA on each wire. The magnitude of the magnetic field is maximum at R_{max} while the skin depth is 1.0 R_{max} for each wire [23].

The standard finite volume version of the PLUTO code is used. A Total Variation Diminishing (TVD) Riemann solver is set for the computation flux, that is based on a Lax-Friedrichs scheme (TVDLF) [19]. GORGON uses a second order Van-Leer advection numerical scheme. In the vacuum region the temperature is constant (300 K) for both codes.

5.4.3 Results

5.4.3.1 Computational results of the GORGON and PLUTO models

Our simulations were performed on the THIN node island of the HPC facility of GRNET ARIS (facilities/reference presented at the Introduction Chapter in figure 1.1) that consists of 426 computational nodes with a theoretical peak performance of 190.85 TFlops and a sustained performance of 179.73 TFlops on the Linpack benchmark. Each node is equipped with 2 Ivy Bridge - Intel® Xeon® E5-2680 v2 processors with 64 GB memory. Each processor has 20 cores making up a total of 8520 cores. After scaling and convergence test runs the numerical models presented reserved 1960 and 300 cores for 15 and 26 hours that for the simulation time of 60ns resulted to 29.4×10^3, 7.8×10^3 core-hours for the GORGON and the PLUTO codes, respectively.

Figure 5.4.2 shows the simulation results of the plasma density distributions on the XZ, Y=6 plane (see figure 5.4.1). The computational results provided by the GORGON code are presented for $4 \leq X \leq 8$ and the simulation results of PLUTO code are plotted over them. For the convenience of the reader, the symmetric results obtained by PLUTO are mirrored on the central symmetry dashed-dot line, in the dashed window of size 2.8x3 mm. The plasma density distribution is presented at six sequential characteristic times (10,20,30,40,50 and 60ns), to provide representative insights on the plasma evolution from the current start, until the late times of the pinching effect and the plasma electrode gap formation [23,32,42,43-47].

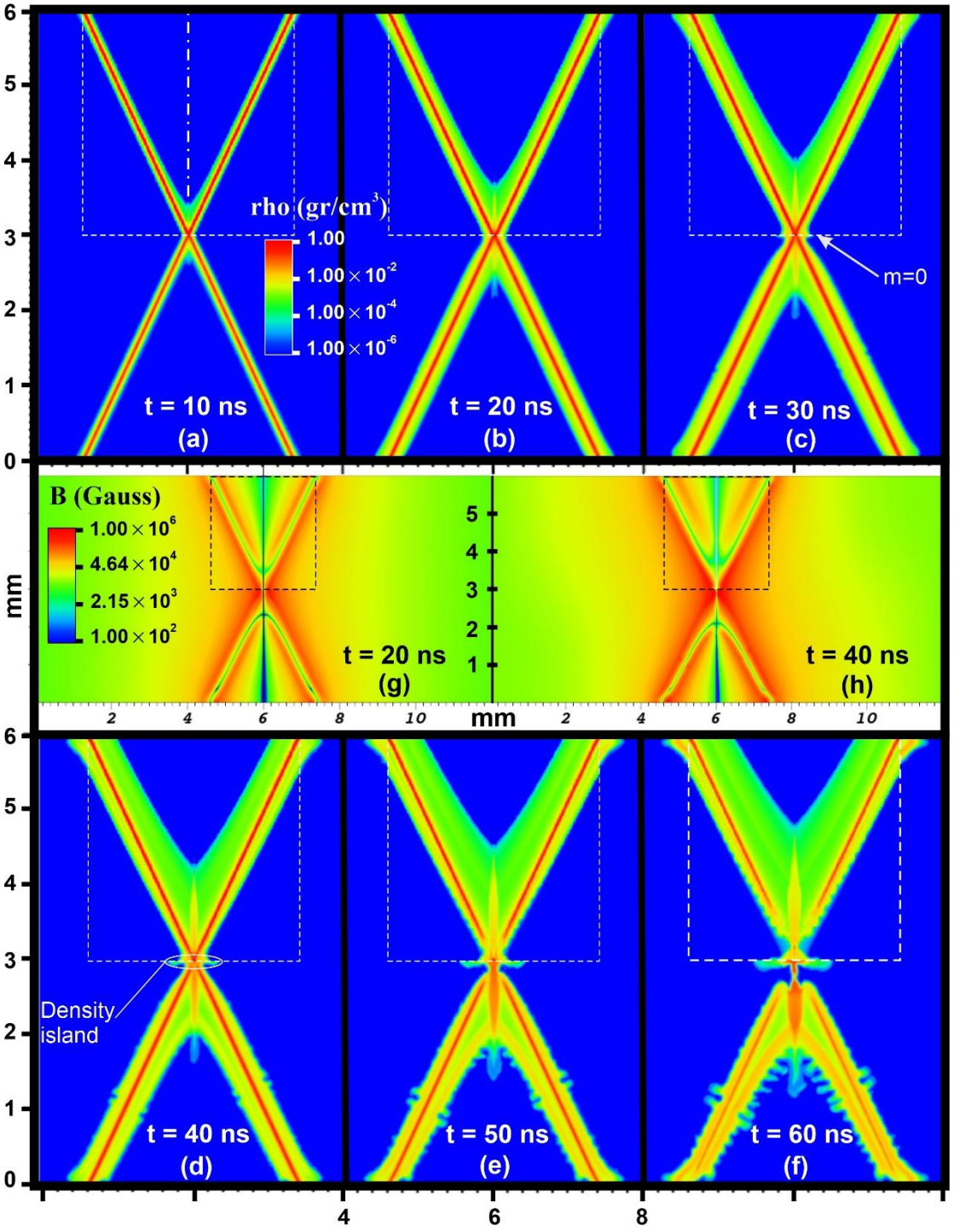

Figure 5.4.2. *Plasma density spatiotemporal dynamics representative results, on the XZ, Y=6 plane, at 10,20,30,40,50 and 60ns respectively. The symmetric results obtained by PLUTO are plotted and mirrored on the central symmetry dashed-dot line (see 2a), within the dashed window of size 2.8x3 mm, over the computational results provided by the GORGON code (4≤X≤8). The magnetic field is presented for both codes at 20 and 40ns in (2g) and (2h), respectively.*

According to the results of both codes, at 10ns the formation of the jet is initiated, and the mass transfer is mainly attributed to the continuous coronal plasma ablation from the wires' legs [31,32,49]. At 20ns, the jet tip is clearly visible and expands vertically, while the radial expanding corona plasma is

sweeping and converging to the central Z axis. The magnitude of the magnetic field, shown in figure 2g, has a similar morphology and topological distribution at both approximations, preserving low values along the wires' core and lower values along the jet axis, as expected [32]. At 30ns, two tightly compressing regions with an isolated island of plasma at the center are formed, due to the action of the Lorentz force on the smaller mass areas of the neck, at a distance of 200μm from the cross point. The formation of the density island is highlighted in figure 2d and is further observed at the temporal times that follow [42,32,43,46,47]. At 40ns, the expansion of the density island is computed by GORGON to have a width of 600μm and a height of 150μm while the PLUTO simulation results demonstrate a width of 400μm and a height of 200μm. Flaring structures are developed by GORGON while a uniform plasma expansion is simulated by PLUTO. Later on, at 50ns and 60ns, PLUTO simulation results demonstrate magneto-Rayleigh–Taylor (MRT) instability that appears at the outer plasma–vacuum interface, where the driving magnetic pressure plays a role analogous to a light fluid pushing on a heavy fluid (the coronal plasma) [48,49]. In our case, a magnetic field, having a peak value greater than ~5.0×10^{5}Gauss triggers and reinforces the initial spatial modulation of the MRT, that is shaped by the finite size of the cells grid (presented in the inset details of figure 5.4.1) [4,6,23,32]. At 50 ns two micro-Z pinches are formed and at 60 ns the expansion of the density island, results to a width of 1000μm and a height of 200μm and to a width of 680μm and a height of 400μm for GORGON and PLUTO, respectively. The half plasma electrode gap is computed to be approximately ~300 μm for both models. The PLUTO code at 50ns forms a denser central spot that is displaced at z=3.15mm at 60 ns and can possibly evolve to a hot-spot formation. The GORGON code at 50ns forms a dense plasma neck which breaks on the hot-spot formation position at 60ns, due to the intense pinching effect [32,43,46,47]. However, our study does not focus on the evolution of the hot spot, since the generation of x-rays, electron, and ion beams [32,41,46] are neglected in the simulations of this study.

A threshold value of ~10^{-5}gr/cm^3 (cyan legend color) is adopted for measuring the jet's length, that reaches the values of 0.4mm and 0.45mm at 10ns, and 1.85mm and 1.8mm at 60 ns for GORGON and PLUTO, respectively. According to these values, a mean jet tip velocity of ~29km/s and ~27km/s is computed correspondingly. As expected, this velocity is ~27% lower than the velocity computed for an X-pinch angle of 100^{o} case (~39km/s) in [23] (also presented at the previous section). The jet's length and width are almost identical for both simulations, but we observe a denser jet formation in the GORGON model results, where more mass is transferred to the jet axis due to the higher mass ablation rate of the wires legs. Figures 2g and 2h show the magnetic field at 20ns and 40ns. Even if the magnetic field has a different initial spatial implementation and its spatiotemporal evolution is approximated by different MHD numerical schemes [17,23,44], the agreement of the results presented is very satisfactory. The topology of the magnetic field demonstrates the convection and diffusion terms of the induction equation along with the ablated mass and follows the rules of the global and local magnetic field described in [23]. This enhances the observed agreement in the jet's evolution and morphology for both codes and additionally explains the computed higher density values along the jet axis and the narrower neck by GORGON [19,21,27

5.4.3.2 Numerical enhancements of the X-pinch model in PLUTO

The MHD model developed in PLUTO is further studied in relation to the physics and numerical parameters that affect its behavior and influence the resulting plasma dynamics. To evaluate the influence of these parameters on the spatiotemporal plasma evolution, five new models are developed, and their simulation results are used for their characterization. This computational analysis aims to provide valuable insights regarding the influence of the electrical resistivity, thermal conductivity, and radiation, on the performance of the X-pinch MHD simulations, on the dynamics of the evolving plasma features. Table 5.4.1 demonstrates the parameters and the coefficients adopted in the five new models in relation to the reference model **Mod.ref**, presented in the previous subsections. The Riemann solver is deactivated at the vacuum area of the simulations and thus the tungsten plasma interaction with vacuum is the same for each model.

Model	Electrical Resistivity	Thermal Conduction Coefficients	Radiation Transport	Optically Thin Losses	Vacuum Resistivity Coefficient	Random Density Perturbation
Mod.ref	linear mixture	$k_{\|\|}$, $k_{\perp}$, $k_{\times}$	YES	NO	10	NO
Mod.1	linear mixture	$k_{\|\|}$, $k_{\perp}$, $k_{\times}$	YES	NO	10	YES
Mod.2	linear mixture	$k_{\|\|}$, $k_{\perp}$	YES	NO	10	NO
Mod.3	linear mixture	$k_{\|\|}$, $k_{\perp}$	NO	YES	10	NO
Mod.4	Spitzer	$k_{\|\|}$, $k_{\perp}$	NO	YES	10	NO
Mod.5	Spitzer/10	$k_{\|\|}$, $k_{\perp}$	NO	YES	24	NO

Table 5.4.1: *Five numerical models are shown, differentiated from the reference **Mod.ref** model according to the implemented physics parameters.*

The electrical resistivity is approximated by the linear mixture formula of equation 5.4.7 and additionally the transverse Spitzer's resistivity formula is adopted in Mod.4 and 5. In Mod.5 the 10% of the Spitzer resistivity value is considered in combination with a higher vacuum resistivity coefficient (value of 24), according to the work presented in [23]. The thermal conductivity scheme used in Mod.1 is identical to Mod.ref, while in Mod.2-5 the parallel ($k_{||}$) and normal ($k_{\perp}$) thermal conductivity schemes are implemented from Braginskii's transport equations for a simple plasma [34] and follow the scheme used in the GORGON model. The radiation transport and the optically thin losses modules are applied sequentially to the models, to enable the study of their effects on the computational results. In Mod.1 and 2 the radiation transport module is activated while in Mod.3-5 the optically thin losses module is activated [23]. Furthermore, a random perturbation with a maximum magnitude of ± 10% of the actual mass density, is activated only in Mod. 1. The rest of the boundary and initial

conditions of the five models are the same and identical to the PLUTO model described in the previous subsections.

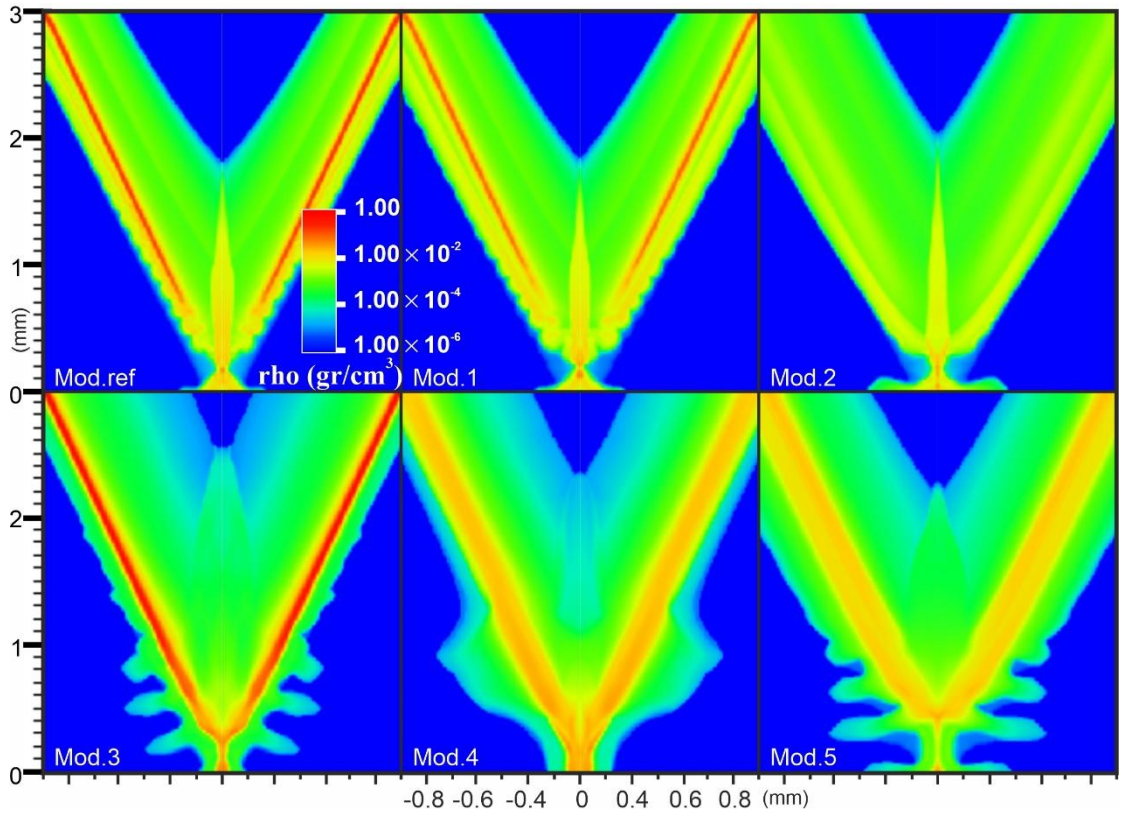

Figure 5.4.3: *Characteristic results of the plasma mass density spatiotemporal dynamics for six different PLUTO models 60ns from the current start.*

Figure 5.4.3 shows the mass density evolution of the X-pinch configuration for the five new models in relation to the reference model at 60ns from the current start. Mod.1 has an identical spatial mass density evolution as to the Mod.ref, and only slight differences are observed on the plasma modulations along the wires. These modulations have a slightly longer wavelength and an enhanced amplitude due to the activation of the initial random perturbations, having the same behavior as in Mod.ref. The jet tip height is 1.8mm and the density island formed has a length of 680μm, similarly to Mod.ref. In Mod.1 the denser area at the plasma neck appears at $0.15 \leq z \leq 0.2$ mm and is elongated along the z-axis in relation to the Mod.ref. In Mod.2 the density island expands to 1100μm and a thin plasma neck is formed. The jet's tip approximates the 2mm height, being ~10% longer than the jet produced in Mod.ref. Furthermore, the perturbations at the corona-vacuum interface are almost absent. This is attributed to the adoption of the Braginskii's high order $k_{\perp}$ thermal conductivity value that increases the heat conduction in the plasma from the coronal plasma to the core. In Mod.2, the core of the wires is heated faster and very early, since the radiation transport among the core and coronal plasma interface develops high thermal pressure. Therefore, the radial plasma expansion is enhanced in relation to Mod.ref and 1 and the peak value of the magnetic field is lower since it

depends on the coronal plasma radius, which is quickly increased due to the efficient thermal transport.

The simulation results of Mod.3, 4 and 5 present significant differences compared to Mod.ref, 1 and 2. The plasma density island at the cross-point area is eliminated in Mod.3 and 4, where a dense Z-neck core, having a density of 0.03gr/cm^3 and a height of 300μm, is developed. In Mod.3, the deactivation of the radiation transport module prevents the heating of the plasma core of the wires that remains relatively cold with a temperature of ~2eV and a density of 0.5gr/cm^3, even if the normal component of the heat conduction is high. The hot coronal plasma expands fast, and a wide jet profile is formed. The value of the plasma density (0.001gr/cm^3) of the jet in Mod.3 is an order of magnitude lower than the first three models, having a height of 2.5mm. Additionally, near the cross-point, high amplitude density perturbations are observed along the wire's corona-vacuum interface, which are attributed to the characteristic time for the magnetic field B diffusion into plasma, which is inversely proportional to the resistivity being several times greater in relation to Mod.ref-Mod.2. The coronal plasma close to the cross point, has temperature values that approach the 160eV, while in Mod.1 and 2 approach the 50eV.

In Mod.4 the Spitzer resistivity is considered instead of the linear mixture used in Mod.3. The activation of Spitzer resistivity results to a high radial expansion in relation to Mod.3 and to very low mass density values. The density distribution of the jet and the coronal plasma has the lowest values among the six models (~10^{-4}gr/cm^3). The height of the jet tip approximates the value of 2.3mm. The density island at the cross-point is not even formed, while the pinching effect on the plasma neck is reduced compared to the previous models. This behavior is attributed to the expression of the Spitzer's resistivity adopted, which for temperatures above the threshold of ~2eV is overestimating the resistivity values. Thus, even if the coronal plasma is overheated due to the Ohmic heating and reaches the maximum temperature of ~270eV close to the cross point, the resistivity values remain high. Therefore, the resistivity enhances the diffusion of the magnetic field into the coronal plasma and mitigates the development of the perturbations that were observed in Mod. 3. On the contrary, the thermal plasma expansion dominates, and high resistive plasma electrodes are formed. In Mod.5, the same to Mod.4 modules are activated, with the Spitzer resistivity being ten times lower, approximating electrical resistivity values even lower than the values obtained by the linear mixture scheme, while the vacuum resistivity coefficient is increased to 24. Therefore, the resulting plasma evolution has the morphology of Mod.3, where high amplitude density perturbations, near the cross-point area, are developed. The jet height is 2.35mm and the cross-point density island has a width of 1300μm. The maximum density is one order of magnitude lower in relation to Mod.ref, 1 and 2. The density of the jet is ~10^{-3}gr/cm^3, like Mod.3. The pinching at the cross-point area is more intense in relation to Mod.3, while the cross-point and the wire's core have similar mass density values. The temperature value at the cross-point corona area and at the density island is 110eV. The results of Mod.3-5 are characterized by a highly expanding plasma behavior that leads to the formation of wide jet profiles and generate high amplitude density perturbations along the wire's corona-vacuum interface having high valued temperatures.

The Mod.ref and 1 where the linear mixture resistivity, the three components of the thermal conductivity and the radiation transport module are activated, provide a computational description of

the spatiotemporal plasma dynamics that strictly agrees with the presented GORGON model simulation. Furthermore, although the seeding of random perturbation, that was investigated by the Mod.1 simulation, resulted to higher amplitudes and wavelengths of the corona plasma instabilities, the global dynamics of the plasma evolution were not affected. This comparison highlights the optimal selection of the physics and numerical parameters used in Mod.ref and determines their impact on the X-pinch plasma MHD simulations performed by the PLUTO code [31,32].

5.4.4 Discussion/Conclusions

In this section two state-of-the-art high parallelized Magneto-Hydro-Dynamic codes, GORGON and PLUTO, are used to simulate the evolution of laboratory magnetically compressed plasma driven by an X-pinch pulsed power generator and describe its key dynamic features. Since GORGON and PLUTO codes are built on different approximation schemes, the simulation results obtained from both codes are further discussed and analyzed, in relation to the physics and mathematics adopted. The MHD simulations focus on the reliable description of the spatiotemporal dynamic evolution of the plasma density and the magnetic field magnitude of an X-pinch configuration using Tungsten wires of 5μm diameter, set at an angle of 50^{o}.

Both codes manage to accurately handle the numerical demands of the X-pinch plasma evolution physics and provide precise details on the mechanisms of the plasma expansion, the mass-transport, the jet-formation, and the pinch generation. The physics and numerical parameters that affect and influence the simulated plasma dynamics are evaluated by five new models developed in PLUTO. The results are used for comparison with the verified GORGON code. The radiation transport module is proven to be significant for the energy exchange, providing a perturbation profile with low growth rates along time, reducing the plasma temperature and the radial expansion rate compared to the models which only consider the optically thin losses. The optically thin losses module results to a more diffusive spatiotemporal behavior regardless the resistivity implementation scheme. The seeding of random perturbations in PLUTO does not affect the global dynamics of plasma evolution but only slightly the wavelength and the amplitude of the developed modulations. The numerical study presented is important for the studies of laboratory jets formation using X-pinches and the studies for the seeding mechanisms of plasma instabilities and their subsequent growth rate evolution. The identification of the parameters that influence the dynamic expansion of plasma provides valuable information for the modeling scenarios where proper seeding, considering the solid to plasma phase transition, is simulated (as we already discussed at the Z-pinch presentation in Chapter 2).

References

[1] D. P. Higginson et al, "Enhancement of Quasi-stationary Shocks and Heating via Temporal Staging in a Magnetized Laser-Plasma Jet", PRL 119, 255002 (2017).

[2] A. Ciardi et al, Astrophysics of Magnetically Collimated Jets Generated from Laser-Produced Plasmas, PRL 110, 025002 (2013).

[3] G. Revet et al, "Laboratory disruption of scaled astrophysical outflows by a misaligned magnetic field", https://www.researchgate.net/publication/340826509

[4] F N Beg et al, "Jet Formation and Current Transfer in *X*-Pinches", IEEE TRANSACTIONS ON PLASMA SCIENCE, VOL. 34, NO. 5, OCTOBER 2006.
[5] D.M. Haas et al, "Supersonic jet formation and propagation in x-pinches", Astrophys Space Sci(2011) 336:33–40/DOI 10.1007/s10509-011-0599-8
[6] G W Collins IV et al, "Effect of the global to local magnetic field ratio on the ablation modulations on X-pinches driven by 80 kA peak current", 2012 New J. Phys. 14 043021.
[7] C. A. Jennings et al, "3D Resistive, Radiative MHD Modeling of Z-pinches" AIP **808**, 57 (2006); doi: 10.1063/1.2159319.
[8] Derek Mariscal et al, "Investigation of Current Transport in 2 × 2 Wire Array Plasmas", IEEE TRANSACTIONS ON PLASMA SCIENCE, VOL. 43, NO. 8, AUGUST 2015.
[9] Felipe Veloso et al ,"Ablation dynamics in wire array Z-pinches under modifications on global magnetic field topology", Phys. Plasmas 22, 072509 (2015)//doi.org/10.1063/1.4926581
[10] G. F. Swadling et al, Oblique shock structures formed during the ablation phase of aluminium wire array z-pinches, PHYSICS OF PLASMAS 20, 022705 (2013).
[11] J P Chittenden *et al* 2004 *Plasma Phys. Control. Fusion* **46** B457
[12] B. Jones et al, "Doppler measurement of implosion velocity in fast *Z*-pinch x-ray sources", PHYSICAL REVIEW E **84**, 056408 (2011).
[13] Ciardi, A., *Laboratory Studies of Astrophysical Jets*. Lect. Notes Phys. **793**, 31–50 (2010).
[14] S. V. Lebedev et al, "Exploring astrophysics-relevant magnetohydrodynamics with pulsed-power laboratory facilities", REVIEWS OF MODERN PHYSICS, VOLUME 91, APRIL–JUNE 2019.
[15] Matteo Bocchi et al, "Numerical simulations of Z-pinch experiments to create supersonic differentially-rotating plasma flows", High Energy Density Physics 9 (2013) 108-111.
[16] F Suzuki-Vidal et al, Laboratory astrophysics experiments studying hydrodynamic and magnetically-driven plasma jets, Journal of Physics: Conference Series 370 (2012) 012002.
[17] A. Ciardi et al, "The evolution of magnetic tower jets in the laboratory", PHYSICS OF PLASMAS **14**, 056501 (2007).
[18] E. Kaselouris et al, "The influence of the solid to plasma phase transition on the generation of plasma instabilities", NATURE COMMUNICATIONS | DOI: 10.1038/s41467-017-02000-6.
[19] A. Mignone et al, "PLUTO: A NUMERICAL CODE FOR COMPUTATIONAL ASTROPHYSICS", The Astrophysical Journal Supplement Series, 170:228Y242, 2007 May.
[20] G. Koundourakis et al, 2018, Computational study of plasma dynamic evolution produced by low current table-top pinch plasma devic.es *ECLIM Abstract book* pp 118.
[21] A. Skoulakis et al, 2018, Preliminary computational study of plasma dynamic evolution produced by low current table-top pinch plasma devices *9th GRACM International Congress on Computational Mechanics* pp 294-303.
[22] Xiao-Guang Wang et al, "Numerical study on magneto-Rayleigh–Taylor instabilities for thin liner implosions on the primary test stand facility", Chin. Phys. B Vol. 28, No. 3 (2019) 035201.
[23] G. Koundourakis et al, "A numerical study on laboratory plasma dynamics validated by low current X-pinch experiments", Plasma Phys. Control. Fusion **62** (2020) 125012 (14pp) (https://iopscience.iop.org/article/10.1088/1361-6587/abbebf.
[24] Kashiwa B A 2010 The MGGB Equation-of-State for Multifield Applications: A Numerical Recipe for Analytic Expression of Sesame EOS Data *LA-1442 Los Alamos National Laboratory Technical Report* http://www.doe.gov/bridge.
[25] T-4 Handbook of Material Properties DataBases Vol. Inc. Equations of State 1984 *LA-10160-MS Los Alamos National Laboratories Technical Report* (Ed. K. S. Holian).
[26] P. Beiersdorfer et al, "Atomic physics and ionization balance of high-Z Ions: Critical ingredients for characterizing and understanding high-temperature plasmas", High Energy Density Physics 8 (2012) 271-283.
[27] http://plutocode.ph.unito.it/PLUTO User's Guide v.4.2 and v.4.3.
[28] J. Larsen Ionization, "In Foundations of High-Energy-Density Physics: Physical Processes of Matter at Extreme Conditions" 2017 (pp. 122-184), Cambridge University Press, doi:10.1017/9781316403891.005.
[29] Tungsten Charge State Distribution by FLYCHK NLTE Kinetics Calculation at NIST by International Atomic Energy Agency- Atomic Molecular Data Services provided by the Nuclear Data Section.

[30] H.-K. Chung et al., "FLYCHK: Generalized population kinetics and spectral model for rapid spectroscopic analysis for all elements", High Energy Density Physics 1 (2005) 3-12.
[31] J. P. Chittenden, "The effect of lower hybrid instabilities on plasma confinement in fiber Z pinches", Physics of Plasmas **2**, 1242 (1995); doi: 10.1063/1.871401.
[32] J. P. Chittenden, "Structural Evolution and Formation of High-Pressure Plasmas in X Pinches", PRL **98,** 025003 (2007).
[33] J. P. Chittenden et al, "Plasma formation in metallic wire *Z* pinches", PHYSICAL REVIEW E VOLUME 61, NUMBER 4 APRIL 2000.
[34] S.I Braginskii, "Transport processes in a plasma", Reviews of Plasma Physics, Volume 1, 206-311 (1965).
[35] Zhijian Fu et al, "Electrical conductivity of warm dense tungsten", High Energy Density Physics , Volume 9, Issue 4, December 2013, Pages 781-786.
[36] L. Spitzer Jr., "Physics of Fully Ionized Gases" Interscience Publishers ING, New York, 1962.
[37] Lennox L. Cowie and Christopher F. McKee, "THE EVAPORATION OF SPHERICAL CLOUDS IN A HOT GAS. I. CLASSICAL AND SATURATED MASS LOSS RATES", The Astrophysical Journal, 211:135-146, 1977 January 1.
[38] Frank Modica et al, "The Braginskii model of the Rayleigh-Taylor instability. I. Effects of self-generated magnetic fields and thermal conduction in two dimensions", High Energy Density Physics 9 (2013) 767-780.
[39] Richardson A S 2019 NRL Plasma Formulary.
[40] Stefan M. Kolb, Matthias Stute, Wilhelm Kley, Andrea Mignone, "Radiation hydrodynamics integrated in the code PLUTO", A&A 559, A80 (2013).
[41] Nicolas-Pierre Louis Niasse, "Development of a Pseudo Non-LTE model for Z-pinch simulations", *PhD Thesis* The Blackett Laboratory Imperial College London, September 2011.]
[42] G. S. Jaar and R. K. Appartaim, "Axial plasma jet characterization on a microsecond x-pinch", JOURNAL OF APPLIED PHYSICS 123, 213301 (2018).
[43] S. A. Pikuz et al, "X-Pinch. Part I", Plasma Physics Reports, 2015, Vol. 41, No. 4, pp. 291–342.
[44] R. E. Madden et al, "Cross-point coronal plasma dynamics in two- and four-wire x-pinches", PHYSICS OF PLASMAS **15**, 112701 (2008).
[45] G.V. Ivanenkov et al, "The dynamics of non equilibrium plasmas of the neck of X-pinch", 31st EPS Conference on Plasma Phys. London, 28 June - 2 July 2004 ECA Vol.**28G**, P-5.040 (2004).
[46] A. P. Artyomov et al, "Experimental study of the neck formation in an X pinch", Journal of Physics: Conference Series 552 (2014) 012011.
[47] V. I. Oreshkin et al, "X-pinch dynamics: Neck formation and implosion", PHYSICS OF PLASMAS 21, 102711 (2014).
[48] Sinars D B et al 2010 *Phys. Rev. Lett.* **105** 185001.
[49] Sinars D B et al 2011 *Phys. Plasmas* **18** 056301.

5.5 Astrophysical correlation of laboratory jets with X-pinch low current plasma devises

Nowadays experiments on pulsed power facilities like Z-pinch wire arrays, conical arrays, radial wire arrays and high-power lasers are leading the way in studying astrophysical phenomena in the laboratory as already is mentioned in the previous section's introduction [1-11]. There is a minor gap to the scalability and jet astrophysical relevancy estimation for an X-pinch pulsed power configuration. This study contributes to the estimation of the scalability factors and all the relevant numbers and parameters for a low current X-pinch tungsten plasma configuration, the same as the one of section 5.3.

5.5.1 Scale invariant constants and estimation of dimensionless parameters- Comparison with astrophysical entities

The scaling invariant relations that have to be satisfied for the laboratory and astrophysical cases are:

$$V_{Lab}\left(\frac{\rho_{Lab}}{P_{Lab}}\right)^{0.5} = V_{Ast}\left(\frac{\rho_{Ast}}{P_{Ast}}\right)^{0.5} \text{ or } M_{Lab} = M_{Ast}$$

and

$$\frac{B_{Lab}}{(P_{Lab})^{0.5}} = \frac{B_{Ast}}{(P_{Ast})^{0.5}} \text{ or } \beta_{Lab} = \beta_{Ast} \tag{5.5.1}$$

These are known as the Euler and Alfvén numbers/similarity relations, respectively [1-4]. P is the thermal pressure, V is a characteristic velocity, ρ the mass density and B the magnitude of the magnetic field. If these scaling constraints are preserved along the simulation run, then the plasma evolution should be optically similar for both astrophysical and laboratory case [2]. The first one holds for a pure HD case with low or no magnetic field while the second constraint is extra implemented for the MHD case [3].

The first set of dimensionless numbers that are important to consider for both cases are [3-11]:

$$R_m = \frac{|\nabla \times (\mathbf{V} \times \mathbf{B})|(\text{advection})}{|\nabla \times (n_d \nabla \times \mathbf{B})|\,(\text{diffusion})}\,, \qquad \text{magnetic Reynolds number}$$

$$R_e = \frac{Vd\rho}{\nu_\mu}\,, \qquad \text{Reynolds number} \tag{5.5.2}$$

$$P_e = \frac{V\rho L_{char}}{k_{th}} c_p\,, \qquad \text{Peclet number}$$

where V is the plasma velocity, d the jet diameter, L_{char} jet length, n_d the magnetic diffusivity, ν_μ the dynamic viscosity, k_{th} thermal conductivity coefficient and c_p the constant pressure specific heat capacity. These estimate the microphysical flow jet properties evaluating the importance of dissipative effects for the dynamics of the jet evolution [3-5]. They have to be much larger than unity if we want

to ignore the resistivity, viscosity and thermal conduction. This is the ideal MHD approximation. While this is true for the astrophysical cases , the same numbers are much smaller for the laboratory cases. Nevertheless the MHD jets simulations, due to numerical transaction errors, are not of that high value numbers reaching within the mean value laboratory regime of ~50-100000 especially at many cases of Young Stellar Objects (YSOs) [3].

The next set of equations, that holds for our model, are dimensionless numbers that refer to global properties of the jets [5,8]:

$$M = \frac{V}{V_s} = \frac{V}{\left(\Gamma \frac{P}{\rho}\right)^{0.5}} \text{ with } \Gamma = \frac{P}{\rho e} + 1, \qquad \text{Mach number}$$

$$M_A = \frac{V}{V_A} = \frac{V}{\frac{B}{(4\pi\rho)^{0.5}}}\ , \qquad \text{Alfvén Mach number}$$

$$M_f = \frac{V}{V_f}, \qquad \text{Fast magnetosonic Mach number}$$

$$M_s = \frac{V}{V_s}, \qquad \text{slow magnetosonic Mach number} \tag{5.5.3}$$

$$\text{where } V_{s,f} = \left(\frac{1}{2}\left[{V_A}^2 + {V_s}^2 \mp \left(({V_A}^2 + {V_s}^2)^2 - 4{V_A}^2{V_s}^2\cos^2\theta\right)^{0.5}\right]\right)^{0.5} \textit{ and}$$

$$\beta = \frac{P}{P_{mag}} = \frac{P}{\frac{B^2}{8\pi}}\ , \qquad \text{plasma } \beta \text{ parameter}$$

$$\chi = \frac{V \cdot t_{cool}}{r_{jet}}\left(\frac{\text{cooling length}}{\text{jet radius}}\right) = \frac{V \cdot P}{(\Gamma - 1) r_{jet} \cdot P_{rad}}, \qquad \text{cooling parameter}$$

$$\delta = \frac{\lambda_{mpf}}{r_{jet}} = \frac{u_{th}\tau_i}{r_{jet}} = \frac{3 \cdot (K_B T_e)^2}{4\pi^{0.5} N_e \ln\Lambda \cdot {Z_{eff}}^3 e^4} \cdot \frac{1}{r_{jet}} \text{ localization parameter}$$

The characteristic velocities that have to be considered are the sound speed V_s, the Alfvén plasma velocity V_A and the slow/fast magnetosonic $V_{s,f}$ while the relative dimensionless numbers are M, M_A and $M_{s,f}$ respectively, corresponding all to Mach plasma numbers. The θ angle is between the direction of the wave vector **k** and the magnetic field **B.** The P_{rad} is the power density radiation energy losses and r_{jet} is the radius of plasma jet [8,10]. The collimation parameter that is important is δ that has to be much smaller than unity for collimated jets while the λ_{mfp} is the ion mean free path [7,11].

The first estimation is for the characteristic plasma velocities. The following 3D figure depicts all the important wave and plasma velocities at 49ns from the current start (a few ns after the current peak of 44 kA). It is a 1/8 spatial computational box depiction where the X-Y-Z lengths are 2.0mm-1.5mm-3.2mm respectively. The unit length corresponds to 10μm at each axis. The jet propagates along Z axis. All units are in C.G.S. metric system.

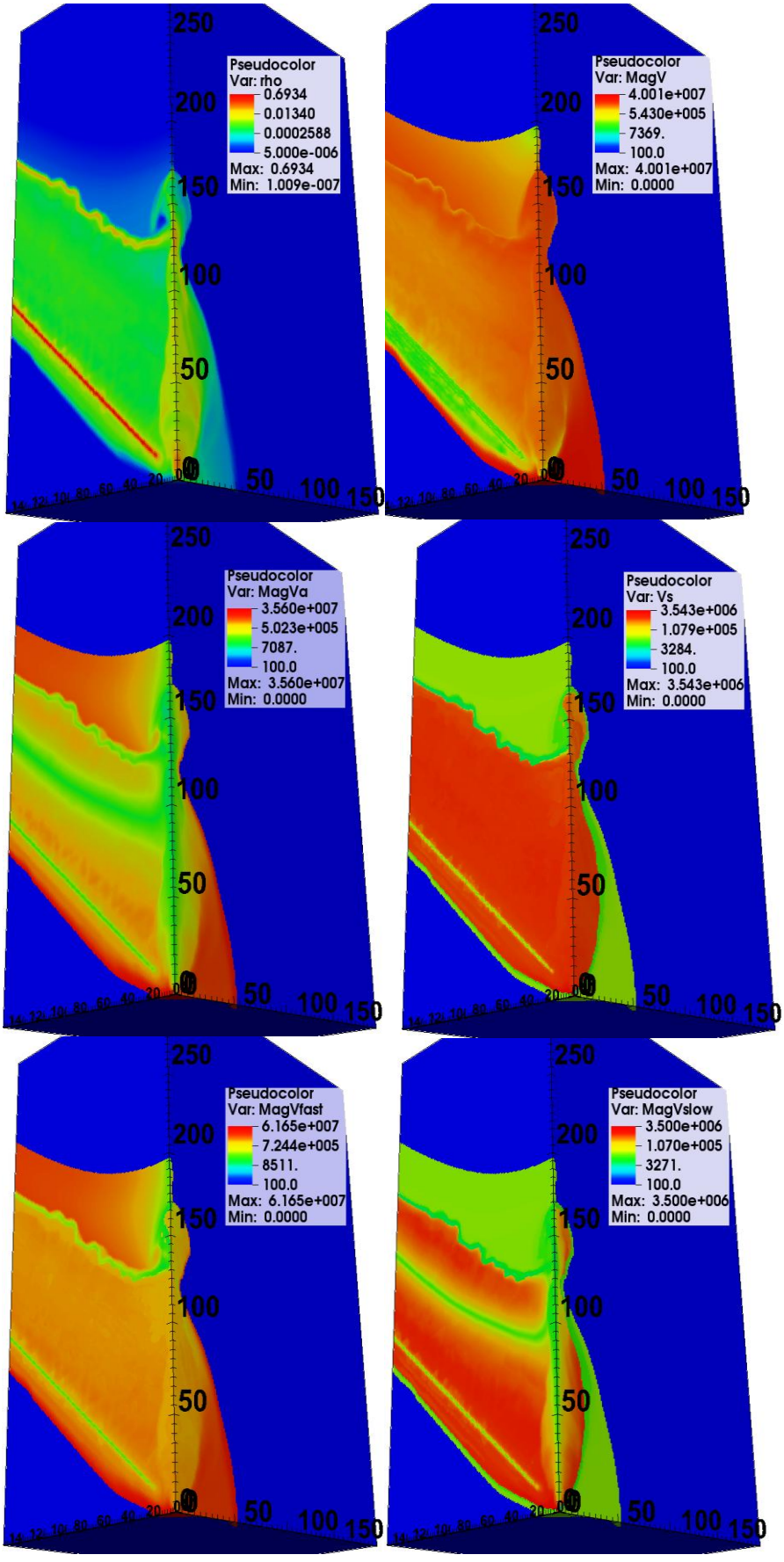
Pseudocolor
Var: rho
0.6934
0.01340
0.0002588
5.000e-006
Max: 0.6934
Min: 1.009e-007
Pseudocolor
Var: MagV
4.001e+007
5.430e+005
7369.
100.0
Max: 4.001e+007
Min: 0.0000
Pseudocolor
Var: MagVa
3.560e+007
5.023e+005
7087.
100.0
Max: 3.560e+007
Min: 0.0000
Pseudocolor
Var: Vs
3.543e+006
1.079e+005
3284.
100.0
Max: 3.543e+006
Min: 0.0000
Pseudocolor
Var: MagVfast
6.165e+007
7.244e+005
8511.
100.0
Max: 6.165e+007
Min: 0.0000
Pseudocolor
Var: MagVslow
3.500e+006
1.070e+005
3271.
100.0
Max: 3.500e+006
Min: 0.0000

Figure 5.5.1: *The main plasma velocities at 49ns from the current start. The 3D pictures present a XYZ 1/8 spatial computational box. From the left to the right and from the top to the bottom are: mass density, bulk, Alfvén, sound, fast and slow magnetosonic speeds. The lower cut-off value is 100cm/s for the velocities and for the density the* $5 \cdot 10^{-6}$ *gr/cm*^{3} *. The unit length at each axis is 0.01mm. All units are in c.g.s. The plasma vacuum has, by hand, zero values.*

The separation of the main plasma column and the low-density air background plasma is achieved through a threshold value of $5 \cdot 10^{-6}$ gr/cm^3. The main plasma jet has a mean velocity value ~40km/s that is approximately the Z axis plasma bulk velocity also (section 5.3). The highest velocity is the fast magnetosonic one that is mainly of the order of 1km/s to 100km/s remaining approximately 1000 times smaller than the speed of light making the non-relativistic approach suitable for this case. The highest sound speed is 10 times lower and its main value is ~1-10km/s.

The second estimation is for the dimensionless Mach numbers. The depiction at the next graph gives a better estimation for the supersonic regime of the plasma jet (especially at the lineout graphs along Z axis), presenting the Alfvénic, fast magnetosonic and slow magnetosonic Mach numbers. The lowest values are for the fast and the higher for the slow as expected. The slow magnetosonic and the sound Mach numbers are almost of the same highest values while the sound is of a little higher value than the slow one. The Alfvénic has lower values than the sound in general but at the main jet axis there are regions that its value is much higher than the sound's. The main jet has M from 0.1 to 30-40 and Ma from 0.1 to several hundreds. The fast magnetosonic is lower than the others and goes up to the value of ~10.

As we can see the higher values of Mach numbers are at the jets top while the lower plasma area is compressed, due to the **jxB** forces from the cross point and the surrounding area (analysis in section 5.3) with sub-Machian speeds that are rising as we are moving along the jet Axis from bottom to the top. This is best depicted at the bottom row of figure 5.5.2 that we see two lineout curves of the Mach number, one at the jets top (green one) and one at the jets main upper body (blue line). The Mach number is of the order of 10 to 20 rising to higher values at the jet's top while at the main upper parts has values from 5 to 8.

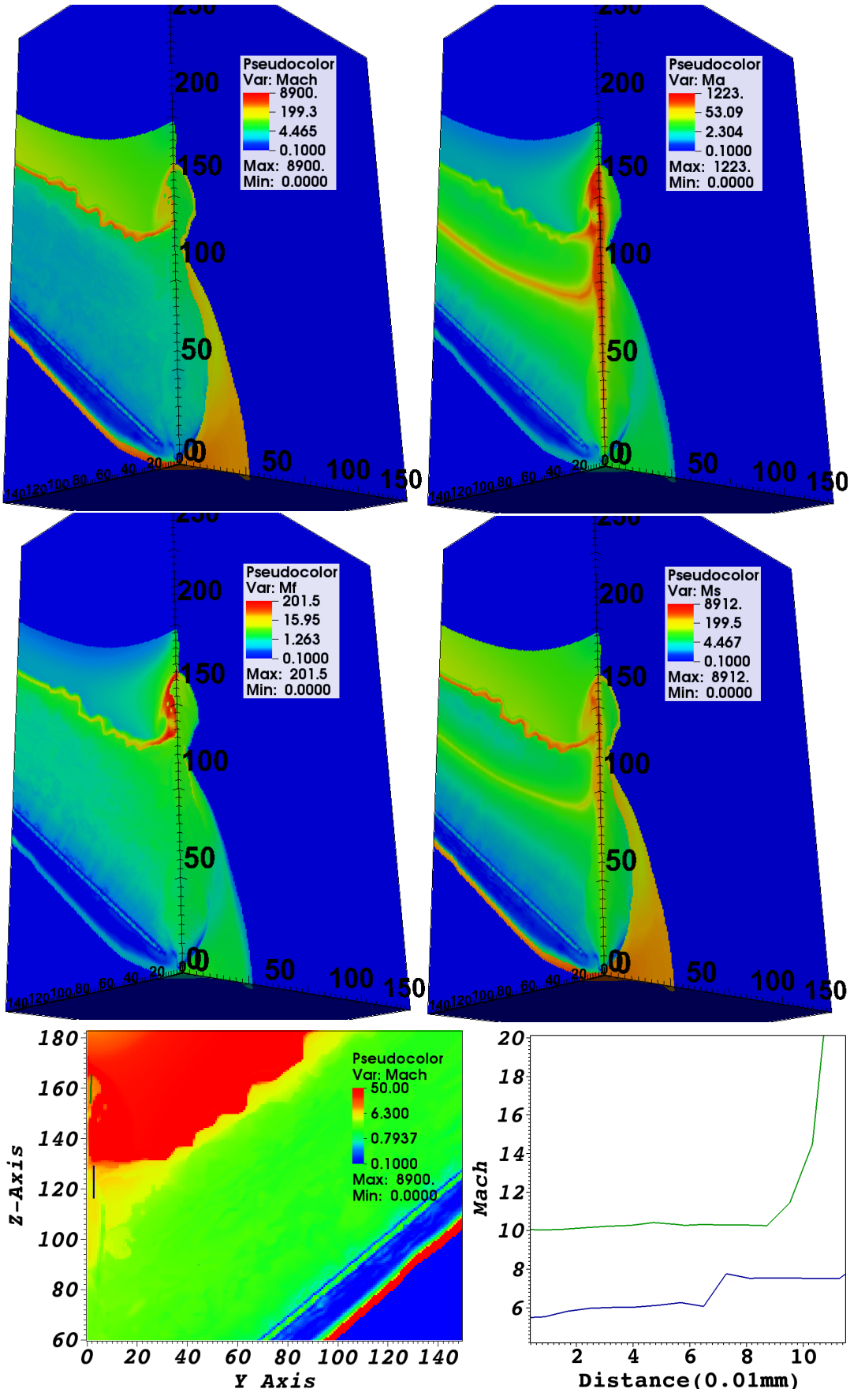
Pseudocolor
Var: Mach
8900.
199.3
4.465
0.1000
Max: 8900.
Min: 0.0000
Pseudocolor
Var: Ma
1223.
53.09
2.304
0.1000
Max: 1223.
Min: 0.0000
Pseudocolor
Var: Mf
201.5
15.95
1.263
0.1000
Max: 201.5
Min: 0.0000
Pseudocolor
Var: Ms
8912.
199.5
4.467
0.1000
Max: 8912.
Min: 0.0000
Pseudocolor
Var: Mach
50.00
6.300
0.7937
0.1000
Max: 8900.
Min: 0.0000
Z-Axis
Y Axis
Mach
Distance(0.01mm)

Figure 5.5.2 Top and second row: *The plasma sound M, Alfvénic M_a, fast magnetosonic M_f and slow magnetosonic M_s Mach numbers at 49 ns from the current start. The lower cut-off values of the Mach numbers is 0.1 . The plasma vacuum has, by hand, zero Mach value.*
Bottom row: *The YZ plane of the Mach number focusing at the jet's upper part. The lineouts are taken at the jet's top (green line) and upper main body (blue line) at the left picture while the lineout curves are depicted at the right.*

This speed acceleration has two main component mechanisms that contribute to the formation of the plasma jet and are both dominant at this time (section 5.3):
i. The **jxB** forces compress the cross point area and eject plasma to the inside area of the jet which pushes the upper layers making them to accelerate.
ii. The plasma cables continue to eject plasma streams that collide to the main plasma jet and hydro-dynamically contribute to the jet collimation and acceleration preserving the momentum along Z axis.

The third estimation is for the dimensionless parameters that are relevant to the dissipative effects of magnetic diffusion, plasma viscosity and thermal conductivity. The magnetic Reynolds number is evaluated from the original expression of equations (5.5.2) set, giving a more realistic spatiotemporal profile. The unit length that is used to the partial space derivative is 0.01mm that corresponds to the discretization unit length of the code.

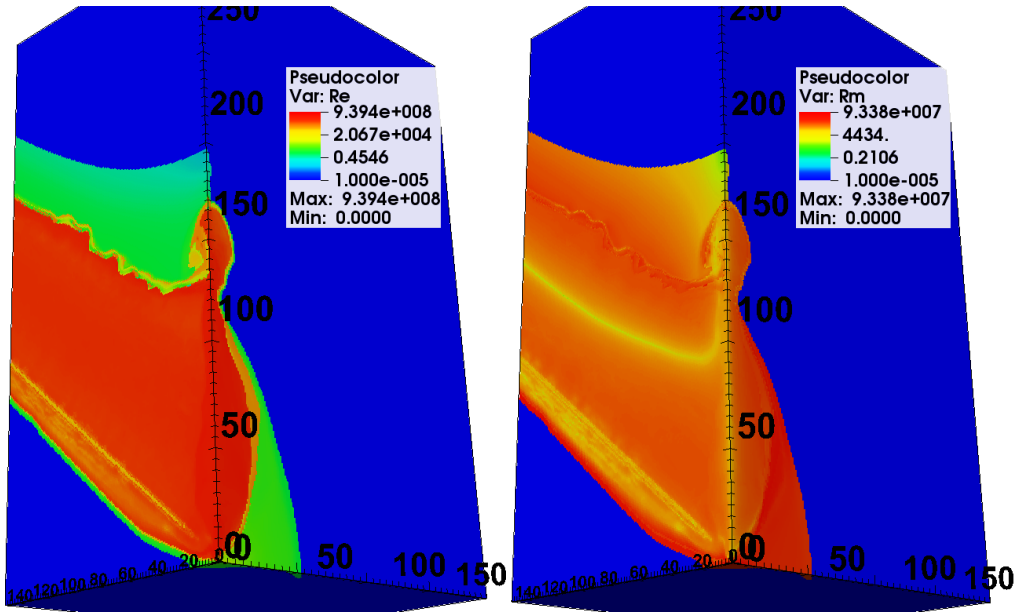

Figure 5.5.3: *The Reynolds and magnetic Reynolds number evaluated at 49ns from the current start. The plasma vacuum is set zero by hand.*

The main plasma volume has R_m numbers ~10^4-~10^5 much larger than unity giving a satisfactory value estimation according to literature [3-11].

Even though this model has no viscosity term implementation we can evaluate the simple Reynolds number from a classical dynamic viscosity coefficient i.e. Braginskii's original work [12]. The estimation of course will give high Reynolds numbers setting this model to the Ideal MHD regime. The picture estimation is depicted at figure 3.25 in sub-section 3.4.3 while the relative dynamic viscosity formula is

the one described at the same sub-section [13-15]. The relative physical values are the original from the simulation run except for the jets diameter that we set 1mm and the lnΛ that we used a constant value of 10. As we can see for the main plasma jet the previous allegation is correct giving values from ~10^4 to ~10^7.

A more thorough examination of the Reynolds number is presented right away independently from this simulation model taking in consideration a larger density range and temperature regime. This is depicted at the figure 5.5.4 graph as a function of mass density isotherms. The temperature range is from 0.52eV to 165eV and the mass density from ~10^{-11}gr/cm^3 to 10^2gr/cm^3. The jets bulk velocity is considered as the mean jet value of 40km/s at later simulation times and the jets diameter as 1 mm.

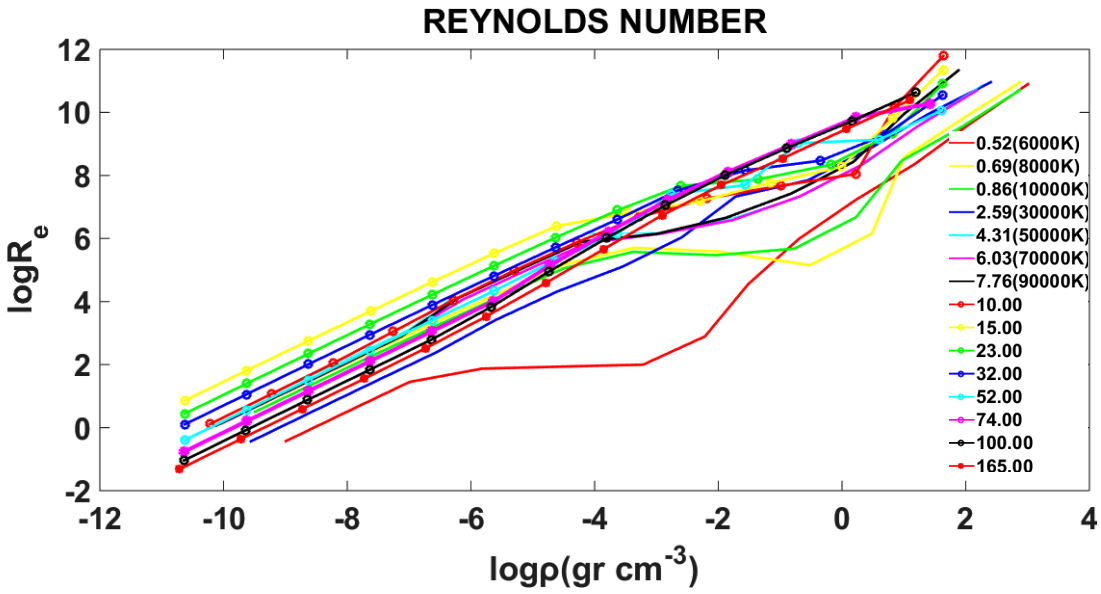

Figure 5.5.4: *The Reynolds number isotherms for temperatures 0.52eV to 165eV.*

As we can see for densities of ~10^{-6}gr/cm^3 to ~10^{-1}gr/cm^3 that is the plasma density regime, the Reynolds number is ~10^3 to ~10^8 having high values and is in good agreement with the other studies and the figure 5.5.3 picture [3-11]. It is lower at the dilute plasma region and rises linear like as density goes to higher values. From the top graph of figure 3.25 in Chapter 3 we see a value range for the viscosity coefficient from 10^{-6}dyn·s·cm^{-2} to 10^{-3}dyn·s·cm^{-2} that is valid for all plasma densities except for the local maxima for 6000K, 8000K and 10000K isotherms. This explains the rising behavior of this graph due to the Reynolds formula of equation (5.5.2) that is proportional to the mass density and the local minima for the small temperatures due to the inverse proportional relation with the viscosity coefficient.

This model does not include thermal conduction explicitly, but all the radiation phenomena are included through modules of optically thin losses and radiation transport (as described at section 5.3). Nevertheless, we can calculate the Peclet number from the formula of equations (5.5.2) set, while the specific heat capacity is taken constant and of the order of 3.10^6erg·gr^{-1}·K^{-1} [16]. The parallel component of Braginskii's electron thermal conductivity is used for thermal conductivity coefficient due to the higher values than all the other components. The parallel component is evaluated from equation 3.74 in sub-section 3.4.2. The Coulomb logarithm $\ln\Lambda$ is set 10 again and Z_{eff} is calculated

similarly as to the previous study of Reynolds number. The characteristic velocity is bulk velocity of plasma at 49 ns and the characteristic length is taken 2mm due to the jets length. The simulation estimation is at figure 5.5.5.

The thermal conductivity coefficient has values that are from ~10^{6}erg·(s·K·cm)$^{-1}$ to ~10^{8}erg·(s·K·cm)$^{-1}$. They are in good validity range for the temperatures and plasma density for our case. A more thorough estimation of the Peclet number will be presented right away similar to the one that we saw for the Reynolds number.

The Peclet number is smaller at the bottom area of the jet, takes higher values at the middle of the order of 100 (blue line and curve) and goes to much higher values at the top approximately to 1000 (red line and curve). The very top of the jet has one order higher value but it is not depicted here.

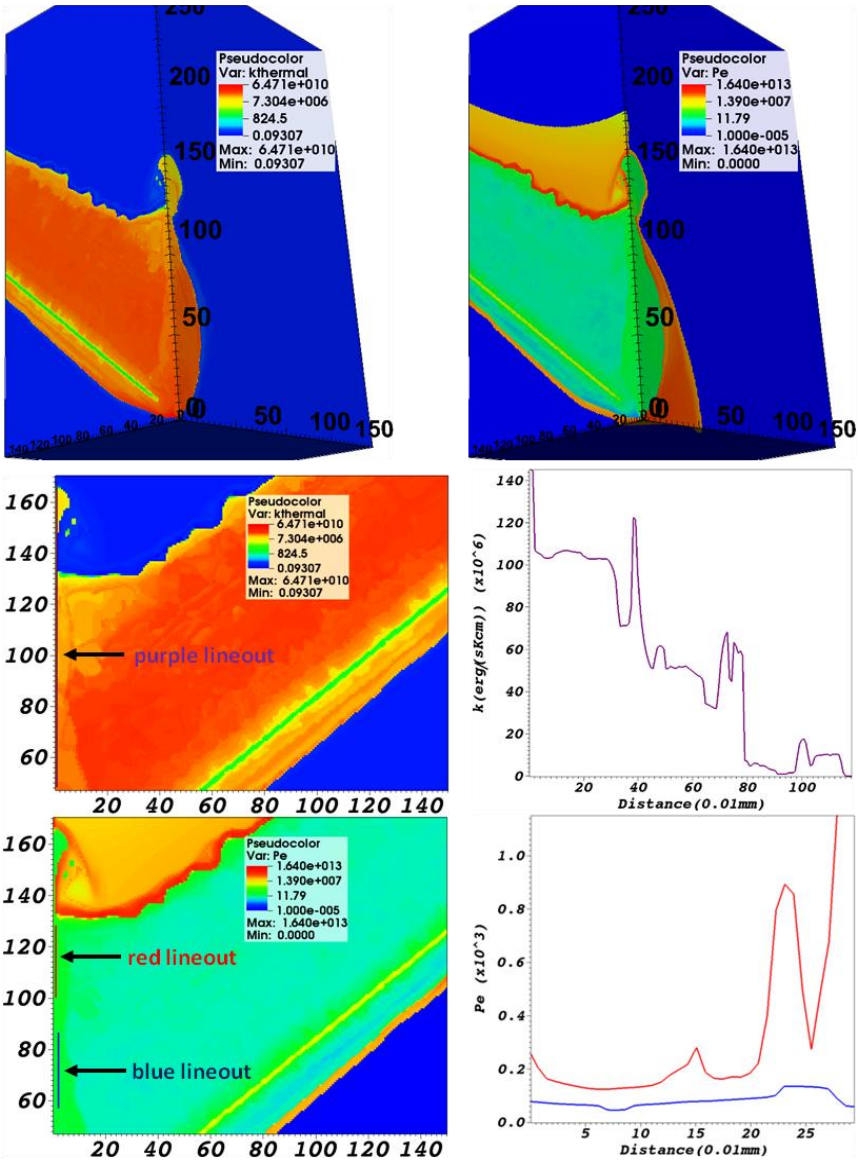

Figure 5.5.5 Top row: *3D graphs of the Braginskii's electron parallel component at the left and the Peclet number at the right 49ns from the current start.*
Second row: *The YZ plane of the thermal conductivity at the left and the lineout curve along Z axis from the near bottom area of the jet till its top (purple line).*

Third row: *The YZ plane of the Peclet number at the same moment and two displaced lineout curves along Z axis. The first (blue line) is at the middle and the second (red line) at the jet top.*

The analytical calculation of the Peclet number at the whole density and temperature range is presented using the aforementioned Braginskii formula. The jet's characteristic velocity is 40km/s and the characteristic length is the same of 2mm at 49ns. The Coulomb logarithm that is used here is the one proposed by Ebeling et al, representing the effective quantum Coulomb logarithm as calculated from the Born approximation and Debye potential [17] (analytic presentation in equation 3.64 in subsection 3.1.4.3). Experimental data at the WDM region for thermal conductivity is quite in a good agreement with the predictions of the Braginskii's formula (as presented in the second graph of figure 3.24 in Chapter 3) while the linear like rise and temperature independence mentioned in literature study [18] is achieved. The Peclet number also is affected from this linear rise at the dense matter regime lowering its value (figure 5.5.6).

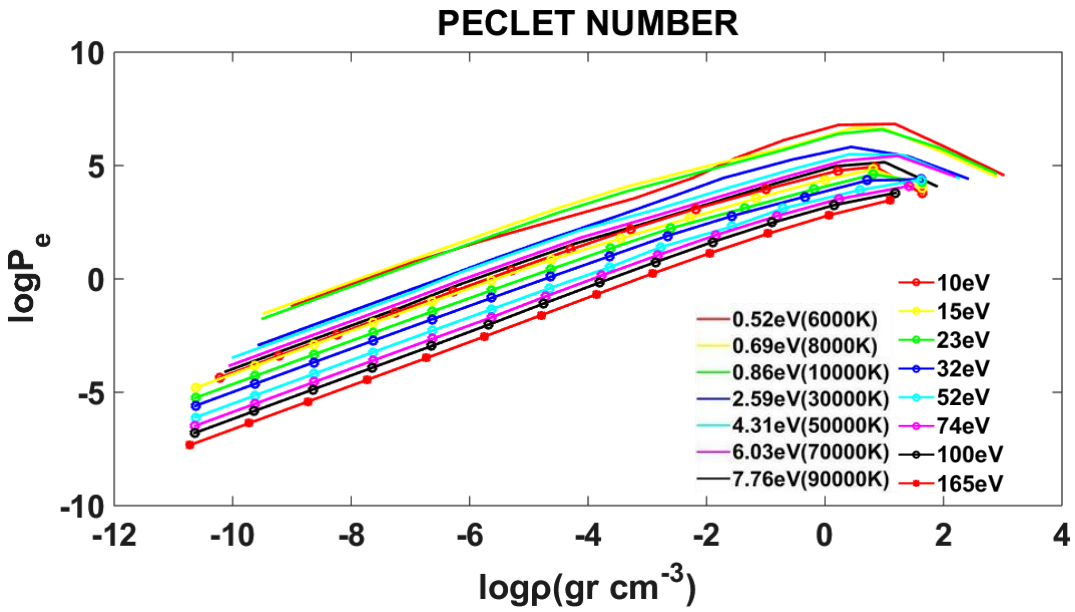

Figure 5.5.6: *The Peclet's number isotherms from 0.52eV to 165eV.*

The thermal conductivity is in the range of ~10^{6}erg·(s·K·cm)$^{-1}$ to ~10^{9}erg·(s·K·cm)$^{-1}$ for almost every plasma density and temperature (figure 3.24 in Chapter 3/PART II). Exceptions are the very low 6000K, 8000K and 1000K that have smaller values at the dilute plasma regions but are in quite good accordance to the experimental data of 10000K [18,19]. The linear rise that gives higher values of the thermal conductivity is at the very dense region that is out of this study's regime. This estimation is in perfect agreement to 5.5.5 figures along plasma jet as we saw and discussed earlier.

The Peclet number goes from ~10^{-7} to ~10^{7} from the very thin to the very dense region. The density range of the simulation study at the time of 49ns has a density of ~10^{-3}gr/cm^3 to ~10^{-1}gr/cm^3 according to figure 1. The Pe numbers according to these densities are higher than unity and reach ~10^{5} for the 10^{-1}gr/cm^3 densities and lower temperatures range. They are in good agreement to 3D, 2D and lineout depiction of the figure 5.5.5 pictures. The laboratory literature gives constant numbers above unity

[3,5,8,20] but not of the very high astrophysical cases that are ~10^4 for YSO [5] and goes to 10^6 and 10^8 for HH and SNRs object respectively [20].

The temperature range of the simulation for the 49ns is from ~1eV to ~100eV, in the range estimation of the previous graphs of viscosity and thermal conductivity. This is depicted with a 2D picture and lineout curve along Z and central jet axis at figure 5.5.7.

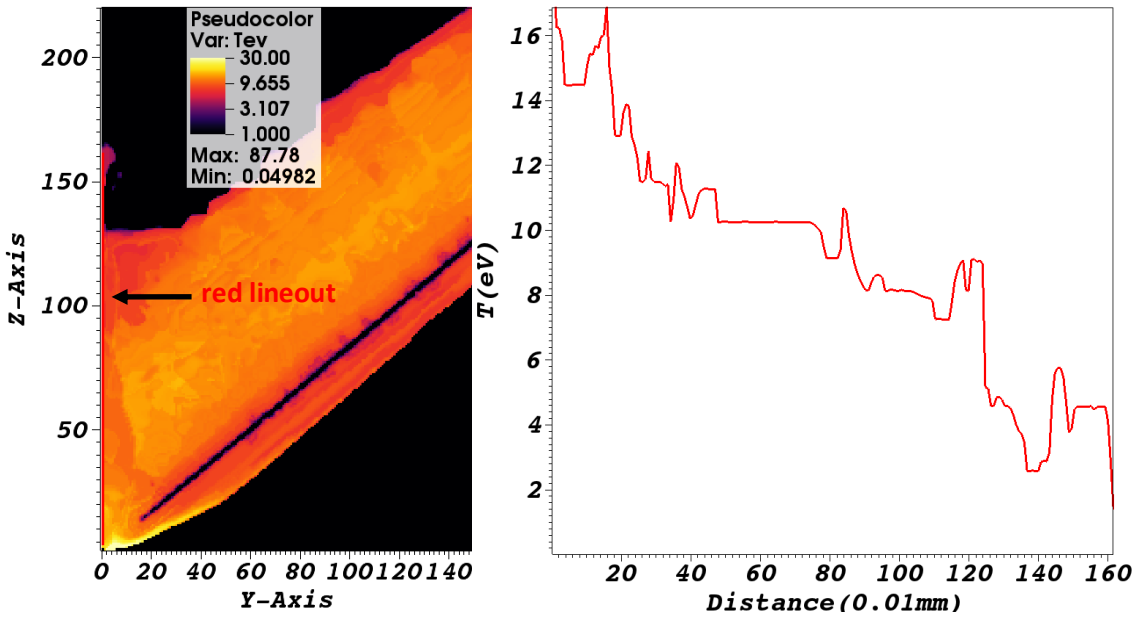

Figure 5.5.7: *The temperature profile at 49ns from the current start. The left picture is a YZ plane of the temperature taking 1eV and 30 eV as the lower and upper limit depicting the jets range of interest. The vacuum plasma has a constant temperature of 0.05eV. The lineout is taken along the jets main axis producing the right temperature curve.*

As we can observe the main temperature goes from some eV at the middle and upper parts to ~20eV to the bottom area. This is due to the efficient radiative losses from the radiation transport phenomena that give a dominant cooling mechanism (section 5.3). Also, it is inversely proportional to the jets Mach number having higher values at the cooler domains and vice-versa. The temperature regime is very close to the ones of YSO jets that are of some eV [5] and close to literature laboratory experiments for plasma tungsten [7,11,20].

The fourth estimation of the jets properties have to do with the study of the role of collision and cooling rates [3-11,20]. Two dimensionless parameters that should be evaluated and these are the cooling parameter χ and the collisionality parameter δ. If they are smaller than unity, we have collimated jets that radiation cooling is important [3,5,20]. Conically convergent flows produce stagnation of plasma on the axis of symmetry and form a standing conical shock effectively collimating the flow in the axial direction that is similar to the hydrodynamic mechanism for jet formation in astrophysical systems [5].

A lot of experiments concerning conical wire arrays [1-3,5-11], magnetic tower jets from radial wire arrays[3] and ablating plasma jets generated from a solid target by a high-power laser [5], have experimentally investigated the validity of laboratory jet formation and evolution and their relevance

to the jets of Young Stellar Objects (YSO) [1-11], formation and evolution of astrophysical phenomena such as Herbig-Haro (HH) objects and Supernova Remnants (SNRs) [5,20].

The effectiveness of collisionality and radiation cooling increase with the Atomic number of the plasmas material [3,5,20]. The plasma Tungsten of our case is the perfect candidate to have these two parameters in accordance with the astrophysical plasmas numbers. The high Mach numbers of the W flows makes them a better match to SNRs while the radiative cooling plays an important role at the jet flows giving very high cooling parameter [20].

The cooling parameter χ is estimated from the relevant equation of equation system (5.5.3), taking the jet radius 0.5mm. Thermal pressure and bulk velocity are from the simulation output data at the 49ns.

The radiation power density is proportional to the heating-cooling term [21] according to:

$$P_{rad} = \frac{\partial(\rho e)}{\partial t} = -k_P \rho c(a_R T^4 - E_{rad}) \tag{5.5.4}$$

where k_p is the Planck mean opacity, a_R the radiation constant, c the speed of light and E_{rad} the radiation energy density (Chapter 3/PART I, (3.31) and (3.37) equations) [22]. If we use this equation for the P_{rad} we have the following pictures of figure 5.5.8.

The electron density of the plasma jet varies from ~10^{16}gr·cm^{-3} to ~10^{21}gr·cm^{-3}. The radiation power density as we see at the right picture is of the order ~10^{18}egr·s^{-1}·cm^{-3} and goes up to ~10^{21}egr·s^{-1}·cm^{-3} at the bottom areas. Only the jets top is at the ~10^{14}egr·s^{-1}·cm^{-3} , much smaller than the rest of the plasma column having also the smallest temperature according to the temperature profile of figure 5.5.7. Also, we observe power density's islands of increasing and decreasing, creating thermal "islands" along Z axis that are interpreted as fluctuations to the temperature profile at figure 5.5.7 along Z axis. These values are quite in good agreement compared to the MHD estimation of figure 3.4 in Chapter 3. We see for the electron density regime of our interest and for temperatures from 1eV to 100eV, the MHD prediction is ~10^{14}egr·s^{-1}·cm^{-3}<P_{rad}<~10^{21}egr·s^{-1}·cm^{-3}, exactly the power range we mentioned earlier. Also this rate could be used to a complementary definition of the Peclet number [23].

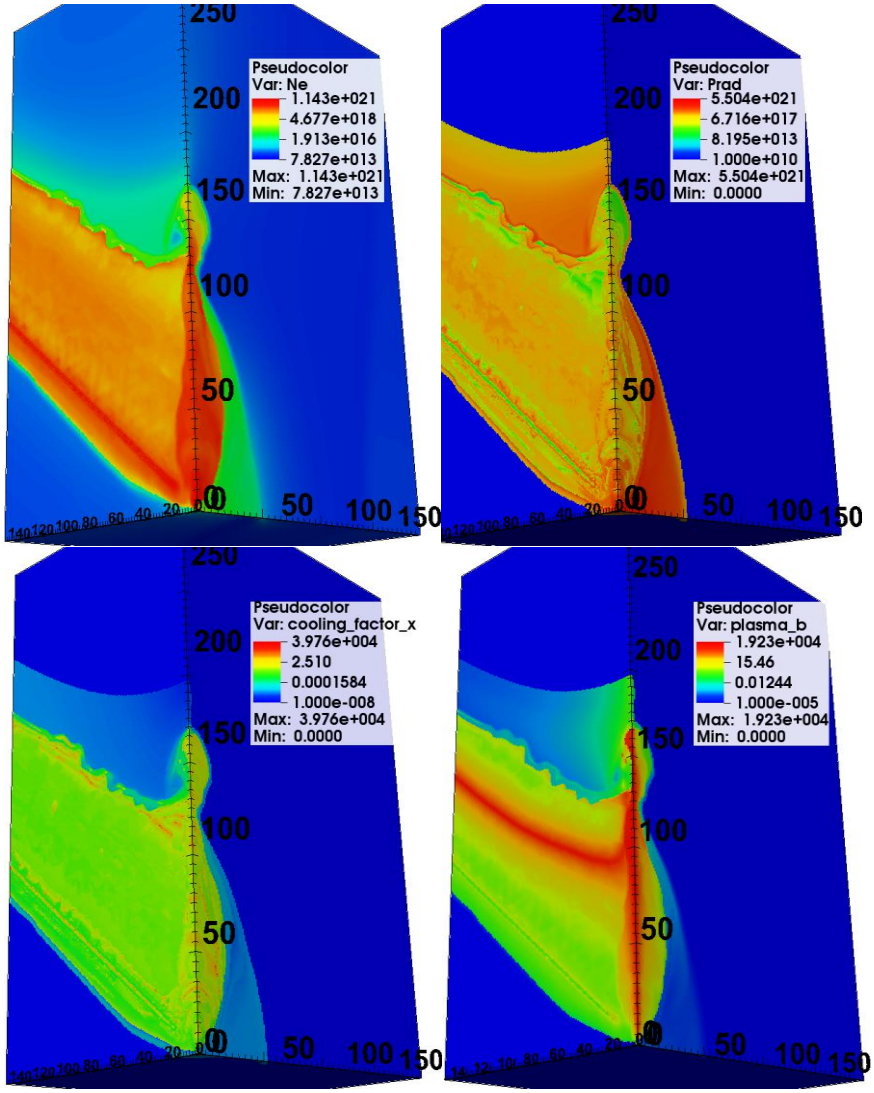

Figure 5.5.8: *The top row presents the electron density at the left and the radiation power density at the right. The lower value depiction at the power density is 10^{10} erg·s^{-1}·cm^{-3}. The bottom pictures are the dimensionless cooling parameter χ at the left and plasma β at the right. The lower value depiction is $10^{-8}$and 10^{-5} respectively. The time is 49ns from the current start. The vacuum values are set by hand zero except for the electron densities.*

The cooling parameter χ for the main plasma jet is near one giving both smaller and higher values. So to clarify this estimation a 2D YZ plane picture is presented having also three lineouts curves depiction for the bottom, middle and upper part of the jet along Z axis.

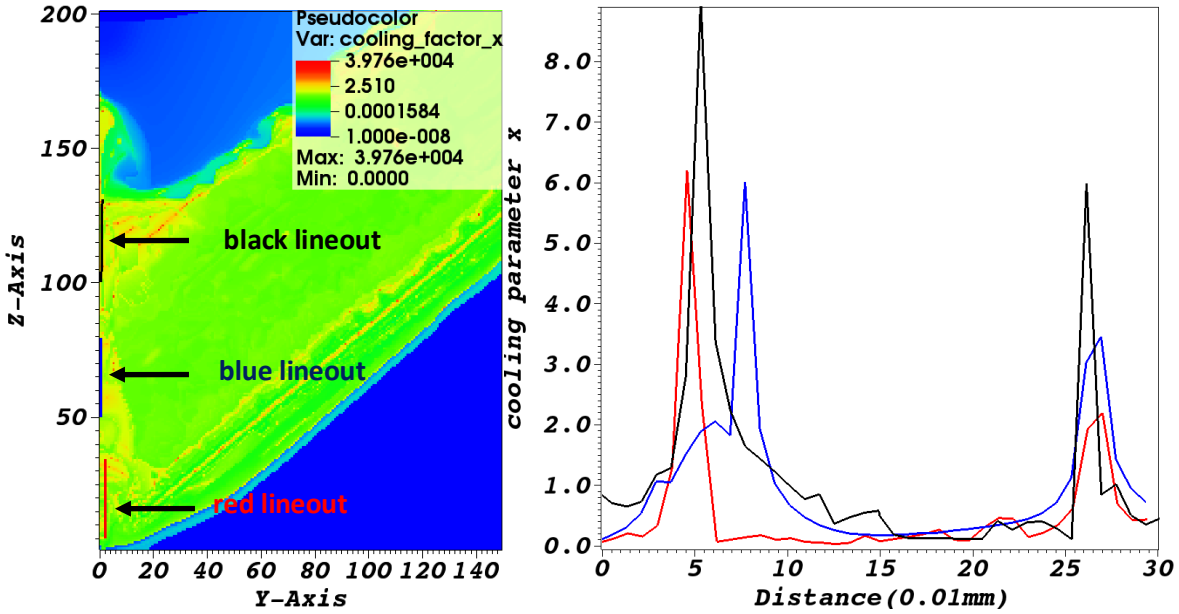

Figure 5.5.9: *A YZ plane depiction of the cooling parameter χ. The three lineouts are taken along Z axis for the jet at the bottom, middle and top area having approximately the same spatial length of 0.3mm. The right picture depicts the three lineout curves.*

The spatial length is approximately 0.3mm for each one. The lower curve has smaller values than the middle which it has smaller values than the top. We observe a main lower than unity value (~0.1 or smaller) for each curve, but we see peaks from 3 to 9 values with a periodic behavior of ~0.2mm. The maxima of the cooling parameter have the same spatial distribution as the peaks of the radiation power density (figure 9). The literature values for the cooling parameter gives an estimation of 0.1-10 for plasma tungsten that is in good agreement with this presentation [5,7,10,20]. The Z-pinch devices are generally with 0.01-10 numbers while for the YSOs are smaller than one [3]. The HH and SNRs objects have 0.01-1 and 0.1-1 respectively [20].

The plasma β parameter is much larger than unity inside the jet, along Z axis while it goes smaller than one to the bottom branch part, at the corona plasma of the branch and the jet. The thermal pressure is dominant at the denser plasma regions while at the dilute ones it goes magnetically driven. Also, we see at the cross point area the green color is the main color confirming the high magnetic pressure that was mentioned before. The red line across the plasma branch also confirms a local domination of the thermal pressure that rises due to the collimation from the upper and lower plasma layers that are magnetically driven. The laboratory have usual ~10^{-2} to ~10^{2} the same as the YSO [3]. The Astrophysical Environments are from ~10^{5} to ~10^{-8} [23].

Now we take the final formula for the localization parameter using the ion mean free path of [11]. The estimation will be again both from the MHD equations using the FLYCHK data and from the simulation at 49ns from the current start. The plasma tungsten due to the high Atomic number has higher radiation cooling rate as we discussed before and produces more collimated jets than the other smaller Atomic number metal plasmas (i.e. aluminum, iron) [5]. This way a small collisionality parameter is expected from both MHD and simulation.

For the simulation run we take lnΛ constant again as a 10 value and the radius of the jet 0.5mm.

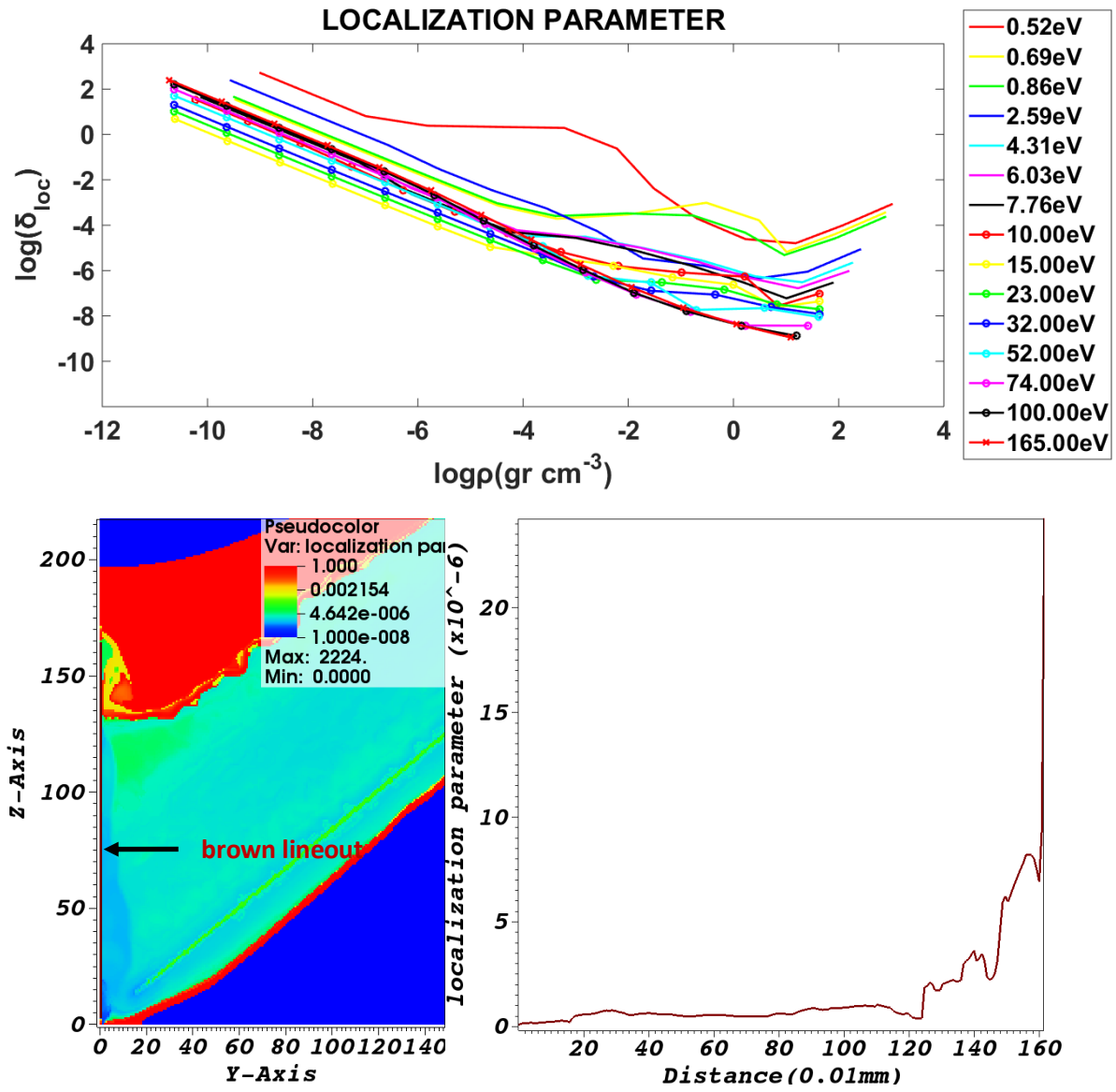

Figure 5.5.10: *The top picture presents the MHD prediction for the localization parameter. The isotherms are from 0.52eV to 165 eV and the density range is ~10^{-11}gr/cm^3 to 10^3gr/cm^3. The bottom row depicts a YZ plane of the localization parameter (left picture) at 49ns while a lineout is taken along Z jet's axis presenting the outcome at the right picture. The lower and higher values are 10^{-8} and 10^0 respectively presenting the parameters range interest for the jet. The vacuum values have been set zero by hand.*

The isotherm curves of figure 5.5.10 uses the FLYCHK data [13,14] while the lnΛ is evaluated from the formula of equation (3.64) in Chapter 3.

The simulation calculates values of ~10^{-8} to ~10^{-3} for the whole main plasma area while the lineout curve along the central jet axis gives values ranging from ~10^{-7} to ~10^{-5} having the higher values at the jet's top. Also, we observe that the denser (figure 5.5.1) and hotter (figure5.5.7) bottom parts of the jet are the ones with the lower values while they rise along the jet's Z axis at the more dilute and cooler upper parts. This prediction is exactly what the top picture of figure 11 presents. The isotherm curves that correspond to the jet temperature (some eV) and density regime (~10^{-6}gr/cm^3 to ~0.5gr/cm^3)

predict numbers from ~10^{-8} to ~10^{-2}. The main isotherm body of 10eV to 165eV has isotherms of approximately the same value range along the density axis while the bigger discrepancies are the ones of the very low temperature values of 0.52eV, 0.69eV and 0.86eV where the MHD lucks for the plasma description.

The main stellar objects have a main localization parameter ~10^{-6} to ~10^{-9} [3,20]. Specifically, for YSOs is smaller than 10^{-6} [3] and for HHs and SNRs is ~10^{-9} [20]. The laboratory experiments give a <10^{-3} [7] to <10^{-4} prediction [3,5]. The mean value of our simulation is at the YSOs and all Laboratory Astrophysics experiments regime.

5.5.2 Comparison with Laboratory, YSO jets and other astrophysical entities

The next table summarizes the results of the previous analysis and gives the Laboratory Astrophysics and Astrophysics relevant estimations.

	This study		Laboratory Astrophysical jets	Astrophysical jets and Environments
	Simulation jet	MHD		
$\rho(gr/cm^3)$	~10^{-6}-~10^{-1}	~10^{-6}-~10^{-1}	10^{-4}-10^{-6}[3,4]	10^{-18}-10^{-20}(YSO)[3,4]
T(eV)	~1-~20	~1-~20	5-300 [3,4] <10-20 (W)[20]	0.5-100(YSO)[3,4]
V_{bulk}(Km/s)	~0.1-~100	-	100-400 [3]	100-500(YSO)[3]
V_{jet}(km/s)	~40	-	33 [7] 164 (W)[20]	-
V_{sound}(km/s)	~1-~10	-	10^3-10^4 [3] 5.5 [7]	10^3-10^4(YSO)[3]
V_{alfven}(km/s)	~0.1-~50	-	180 [4]	-
V_{fast}(km/s)	~0.1-~100	-	-	-
V_{slow}(km/s)	~0.1-~5	-	-	-
Mach	~0.5-~500	-	5-40 [3,7] >10(W) [20]	>>5 (YSO)[3] 5-30 (HH) [20] 10-100 (SNRs) [20] ~10 (Astr. Env.) [23]
$(Mach)_{Alfven}$	~0.5-~1000	-	3 [4]	5 [4]
$(Mach)_{fast}$	~0.1-~100	-	-	-
$(Mach)_{slow}$	~0.5-~1200	-	-	-
Plasma β	~0.1-~1000	-	10^{-2}-10^2[3]	10^{-2}-10^2(YSO)[3] <10^{-1} (Astr. Env.)[23]
R_e	~10^4-~10^7	~10^3-~10^8	>10^4 [3,4] 10^6(W) [20]	>10^8 (YSO)[3] 10^{10}(HH) [20] 10^{11} (SNRs) [20] >10^7 (Astr. Env.)[23]

R_m	~10^4-~10^5	-	10^1-10^3[3,4]	>10^{15} (YSO)[3] >10^9 (Astr. Env.) [23]
$k_{thermal}$(erg/(sKcm))	~10^5-~10^8	~10^5-~10^9	-	-
P_e	~10^1-~10^5	~10^{-1}-~10^5	50-10^4[3] 2 [4] 20 (W) [20]	>10^7 (YSO)[3] 10^8 (HH)[20] 10^9 (SNRs)[20]
P_{rad}(ergs^{-1}cm^{-3})	~10^{14}-~10^{21}	~10^{14}-~10^{21}	-	-
$\chi_{cooling}$	~10^{-1}-~10^1	-	10^{-2}-10^1 [3,7] 0.1-1(W) [20]	<1 (YSO) [3] 0.01-1(HH) [20] 0.1-1(SNRs) [20]
$\delta_{localization}$	~10^{-7}-~10^{-5}	~10^{-8}-~10^{-2}	<10^{-4}[3] <10^{-3}[7] 10^{-3} (W) [20]	<10^{-6}[3] 10^{-9} (HH) [20] 10^{-9} (SNRs) [20]

Table 5.5.1: *The first column is for the simulation at 49ns from the current start. The second presents, for the same range of densities and temperatures, the MHD equations evaluation using the Zeff=f(ρ,T) FLYCHK data for tungsten. The third is the estimations of the Laboratory Astrophysics experiments and the fourth the Astrophysics estimations for YSOs, HHs and SNRs entities. The third and fourth column have also the literature references at the end of each estimation.*

The last thing that has to be clarified is the scaling factor consistency. The equation (5.5.1) system has two equation constraints that have to be satisfied while extra constraints are in order to evaluate extra physical phenomena i.e. radiation [3,23].

The first is for the hydrodynamic consistency and is practical the Mach numbers of the two systems to be equal along examination time for the plasma evolution. In our case the Mach number has a mean spatiotemporal value ~10 and is in range of HHs entities and at the lower limits of YSOs and SNRs. An example is YSO DG Tau A object , that has a Mach number of 11, a jet temperature of 3eV and a flow velocity of ~250km/s [4,24,25]. Since this Mach number is near our own, we can use this Astrophysical entity as scaling example. We want to take three independent variables to make the scaling dimensionless factors. Thus, we take:

$$L_{Lab} = aL_{Ast} \text{ and } \rho_{Lab} = b\rho_{Ast} \text{ and } V_{Lab} = cV_{Ast}$$

$$P_{Lab} = \frac{\rho_{Lab}}{\rho_{Ast}} \frac{{V_{Lab}}^2}{{V_{Ast}}^2} \cdot P_{Ast} = bc^2 \cdot P_{Ast} \tag{5.5.5}$$

$$\text{and } t_{Lab} = \frac{L_{Lab}}{V_{Lab}} \frac{V_{Ast}}{L_{Ast}} t_{Ast} = \frac{a}{c} \cdot t_{Ast}$$

where the a, b, c are the scaling dimensionless constants for the characteristic lengths L, mass densities ρ and plasma velocity V of the Laboratory and Astrophysical systems. This way we can compute the scaling of time for the two systems and the scaling for thermal pressure [1,2,3]. There is clearly some arbitrariness on the choice of some of the scaling parameters and for the case presented

here we assume the flow to be close to the YSO source. The next table presents the characteristic values used in our system and the astrophysical case:

Characteristic variables	X-pinch plasma tungsten simulation	DG Tau A object/HH158
V(km/s)	50	250
$\rho(gr/cm^3)$	$\sim10^{-3}$-$\sim10^{-1}$	10^{-18}
$L_{characteristic}$	0.1 cm	10 AU=$1.5\cdot10^{13}$cm
$t_{characteristic}$	50ns	~4.75 years
$P(dyn/cm^2)$	10^8-10^9	$\sim2.5\cdot10^{-7}$-$\sim2.5\cdot10^{-6}$
B(gauss)	$\sim10^4$-$\sim10^5$	$\sim5\cdot10^{-3}$

Table 5.5.2: *The first column depicts the characteristic variables of the X-pinch plasma. The right column is for the same variables of an YSO object considering the scaling factors a, b, c for the characteristic time, thermal pressure and magnetic field.*

where $a=6.67^{\times}10^{-15}$, $b=10^{16}$, if we take lab mass density $\sim10^{-2}$ gr/cm^3 and c=0.2. A characteristic time of the simulation lab experiment is ~50 ns that is the time from the current start to its peak. The Astrophysical simulation time that corresponds to the scaling relation comes from the c/a ratio of the (5.5.5) relation and is $3^{\times}10^{14}$ times higher, giving $1.5^{\times}10^8$ seconds as a result (approximately 1736 days or ~4.75 years). This is a rough estimation if we consider the density and velocity range. Similar predictions by A. Ciardi give for a 200ns simulation run a 10-year Astrophysical scalability that is very close to this prediction [3]. Another prediction gives that 10ns of the Laboratory experiment corresponds to 7.5 months of the Astrophysical evolution [4]. This prediction is also very close to our own findings.

The thermal pressure of our simulation gives an Astrophysical scalability estimation of $\sim2.5^{\times}10^{-7}$dyn/cm^2-$\sim2.5^{\times}10^{-6}$dyn/cm^2 originating from the relevant equation of the (5.5.5) set. This results for the magnetic field scaling from the second equation of the (1) set of equations, to roughly 5mG. It is also a very close estimation to the [3] and [4]. But we have to be very careful due to the discrepancy of the plasma β of our study and the usual Astrophysical that is one or two orders of magnitude smaller.

5.5.3 Discussion and Conclusions

The average Mach number of ~10 demonstrates that the jets discussed in this study show a potential scalability to Astrophysics. It is in the range value of the YSO jets and HH objects. The scaling is very close to the ones of other laboratory devises with similar current and magnetic field initial values.

A recent experimental study of G. S. Jaar and R. K. Appartaim [26] for jets produced on a microsecond X-pinch through light-field schlieren imaging and optical framing photographs across 4 different materials, Al, Ti, Mo, and W, suggests that the multi-structure axial jets formations and the kinks observed along temporal plasma evolution have some similarities with astrophysical jets. Specifically bending and deflection of jets have also been observed in astrophysical systems, where these phenomena are thought to be caused by the interaction of the jet with ambient clouds and by

radiation from nearby stars [27]. The bombardment by the plasma from the limbs could cause a standing shock on the axis and result in the multi-structure jet formation when the plasma from the crossing point is ejected up into the base of the jet [28-30]. It is the same multi-component structure and the formation mechanism that is discussed in 5.3 section and is also observed through the physical values analysis of this section. In astrophysical jets (such as He 3–1475), hydrodynamic radiative shocks are thought to provide mechanisms that contribute to their longstanding collimation and some simulations (including the ones in this study) of this phenomenon appear to have a similar form to what is observed in the X-pinch [31-35], considering numerical and physical diffusivity [34] .

This study presents a promising laboratory scalability estimation for specific X-pinch jet's parameters. The inclusion of proper viscous terms, "cold" start initial conditions transferring angular momentum from the crosspoint area to the plasma jets (similar to the ones in 4.2.3), interaction of the main plasma jet with the plasma vacuum and thorough study of the simulation till the current peak, are goals for the future work, hoping for further conclusions of the underlying formation mechanisms and potential connections to astrophysical phenomena.

References

[1] Mariscal Derek Alexander, "Investigation of Magnetic Field and Current Topology in Z- pinch Plasmas", PhD, UC San Diego Electronic Theses and Dissertations,2015, http://escholarship.org/uc/item/2x23b718.

[2] Haas David Michael, "Investigation of the dynamics and emission characteristics of x-pinch plasmas", PhD, UC San Diego Electronic Theses and Dissertations, 2011, http://escholarship.org/uc/item/8qk2k8kg.

[3] Andrea Ciardi, "Laboratory Studies of Astrophysical Jets", Lect. Notes Phys. **793**, 31–50 (2010).

[4] G. Revet et al, "Laboratory disruption of scaled astrophysical outflows by a misaligned magnetic field", NATURE COMMUNICATIONS | (2021) 12:762 | https://doi.org/10.1038/s41467-021-20917-x.

[5] S. V. Lebedev et al, "LABORATORY ASTROPHYSICS AND COLLIMATED STELLAR OUTFLOWS: THE PRODUCTION OF RADIATIVELY COOLED HYPERSONIC PLASMA JETS", THE ASTROPHYSICAL JOURNAL, 564:113-119, 2002 January 1.

[6] P. M. Bellan et al, "Astrophysical jets: Observations, numerical simulations, and laboratory experiments", PHYSICS OF PLASMAS **16**, 041005 (2009).

[7] D.M. Haas et al, "Supersonic jet formation and propagation in x-pinches", Astrophys Space Sci (2011) 336:33–40.

[8] S. V. Lebedev et al, "Exploring astrophysics-relevant magnetohydrodynamics with pulsed-power laboratory facilities", REVIEWS OF MODERN PHYSICS, VOLUME 91, APRIL–JUNE 2019.

[9] M. Belan et al, "The hydrodynamics of astrophysical jets: scaled experiments and numerical simulations", A&A 554, A99 (2013) .

[10] S V Lebedev et al, "Production of radiatively cooled hypersonic plasma jets and links to astrophysical jets", Plasma Phys. Control. Fusion **47** (2005) B465–B479.

[11] Dmitri D. Ryutov, "Characterizing the Plasmas of Dense *Z*-Pinches", IEEE TRANSACTIONS ON PLASMA SCIENCE, VOL. 43, NO. 8, AUGUST 2015.

[12] S.I Braginskii , "Transport processes in a plasma", Reviews of Plasma Physics, Volume 1, 206-311 (1965).

[13] Tungsten Charge State Distribution by FLYCHK NLTE Kinetics Calculation at NIST by International Atomic Energy Agency- Atomic Molecular Data Services provided by the Nuclear Data Section.

[14] H.-K. Chung et al., "FLYCHK: Generalized population kinetics and spectral model for rapid spectroscopic analysis for all elements", High Energy Density Physics 1 (2005) 3-12.

[15] A. S. Richardson, NRL PLASMA FORMULARY, 2019.

[16]. P. Tolias, "Analytical expressions for thermophysical properties of solid and liquid tungsten relevant for fusion applications", Nuclear Materials and Energy 13 (2017) 42–57.

[17] W. Ebeling et al "Thermophysical Properties of Hot Dense Plasmas", Teubner-Verlag, Stuttgart, 1991, Chap. 6, Sec. 5.

[18] Satoshi Sugimoto et al, " Observation of the thermal conductivity of warm dense tungsten plasma generated by a pulsed-power discharge using laser-induced fluorescence", PHYSICS OF PLASMAS **24**, 072703 (2017).
[19]. Toru Sasaki et al, "A Semiempirical Evaluation of the Thermal Conductivity in Ablated Dense Tungsten Plasma" , IEEE TRANSACTIONS ON PLASMA SCIENCE, vol. 40, NO. 12, DECEMBER 2012, pp. 3455-3457.
[20] G.W.Collins et al ,"Role of collisionality and radiative cooling in supersonic plasma jet collisions of different materials", PHYSICAL REVIEW E **101**, 023205 (2020).
[21] Stefan M. Kolb et al, "Radiation hydrodynamics integrated in the code PLUTO", A&A 559, A80 (2013).
[22] G.D. TSAKIRIS and K. EIDMANN, "AN APPROXIMATE METHOD FOR CALCULATING PLANCK AND ROSSELAND MEAN OPACITIES IN HOT, DENSE PLASMAS", J. Quant. Spectrosc. Radiat. Transfer Vol. 38, No. 5, pp. 353-368, 1987.
[23] John I. Castor , "Astrophysical Radiation Dynamics: The Prospects for Scaling", Astrophys Space Sci (2007) 307:207–211.
[24] Rachael E. Ainsworth et al, "TENTATIVE EVIDENCE FOR RELATIVISTIC ELECTRONS GENERATED BY THE JET OF THE YOUNG SUN-LIKE STAR DG Tau", The Astrophysical Journal Letters, 792:L18 (5pp), 2014 September 1, doi:10.1088/2041-8205/792/1/L18.
[25] L. Maurri et al, "Physical properties of the jet from DG Tauri on sub-arc second scales with HST/STIS",A&A 565, A110 (2014), DOI: 10.1051/0004-6361/201117510.
[26] G. S. Jaar and R. K. Appartaim, "Axial plasma jet characterization on a microsecond x-pinch", JOURNAL OF APPLIED PHYSICS 123, 213301 (2018).
[27] J. Bally and B. Reipurth, Astrophys. J. 546, 299 (2001).
[28] I. H. Mitchell et al., "Investigation of the plasma jet formation in X-pinch plasmas using laser interferometry", Phys. Plasmas, Vol. 7, No. 12, December 2000.
[29] R. Aliaga-Rossel, et al., "Plasma Jet Formation in X-pinch Plasmas", AIP Conference Proceedings **563**, 270 (2001).
[30] J. P. Chittenden et al., "Structural Evolution and Formation of High-Pressure Plasmas in X Pinches", PRL **98,** 025003 (2007).
[31] K. J. Borkowski et al, Astrophys. J. 482, L97 (1997).
[32] G. Mellema and A. Frank, Mon. Not. R. Astron. Soc. 292, 795 (1997).
[33] T. Matsakos et al, "Two-component jet simulations I. Topological stability of analytical MHD outflow solutions", A&A 477, 521–533 (2008)/DOI: 10.1051/0004-6361:20077907.
[34] Čemeljić et al, "Resistive jet simulations extending radially self-similar magnetohydrodynamic models," in *Monthly Notices of the Royal Astronomical Society*, vol. 389, no. 3, pp. 1022-1032, Sept. 2008.
[35] O. O. Teşileanu et al, "Young stellar object jet models: From theory to synthetic observations", A&A 562, A117 (2014)/DOI: 10.1051/0004-6361/201322627.

CHAPTER 6

Conclusions

The work presented in this thesis can be conceptually divided into three main parts, investigating the physical phenomena that occur during the dynamic plasma evolution of pinch plasma devices and their analogies with astrophysical plasmas in the macro-scale.

The **first part** investigates the validity of physical MHD schemes that could be applied to any pinch plasma configuration for any plasma temperature, thermal pressure and magnetic field strength. The MGGB/SESAME based EOS for thermal pressure $P=f(\rho,T)$ and internal energy $E=f(\rho,T)$ are suitable tabulated functions for the MHD scheme, considering the transition plasma state phases and the coexistence regions. An appropriate modified tabulated introduction of the mean ionization state Z_{eff} to the numerical code from the FLYCHK code, appear to be quite satisfactory for every plasma regime. The optically thin losses power density presents a remarkable agreement with the experiment and literature. The tabulated FLYCHK data are used. There is a discrepancy between the experiment and theory if we use an analytical function, taking into account only the free-free (Bremsstrahlung from hydrogen-like plasma) and free-bound (recombination) contribution to the optically thin radiation energy density rate neglecting the bound-bound radiation contribution. The FLYCHK code considers all three contributions. The radiation transport module uses two extra differential equations to the main MHD equation set, using the grey approximation in which all radiative quantities, including the opacities, are integrated over all frequencies. All the scattering phenomena are included at the constants a_R, k_p and k_R, which are the radiation constants, Planck mean opacity and Rosseland mean opacity respectively. The two opacities are calculated using an exponential fit, appropriate for tungsten plasma, providing a good approximation for any plasma temperature. The radiation transport module plays a key role to the plasma energy spatiotemporal distribution and provides a proper dynamic plasma evolution according to the experimental results, preventing the unnatural temperature rise as presented at chapter 5.

Due to the wide value range of the primitive physical variables and the coexistence of different material phases, piece wise and tabulated data functions have been used. The novelty of this approach is the flexibility of the numerical work. It could be applied to any plasma material presenting in most cases more than one approaches for the initial condition and execution scheme. It provides functional and tabulated options for the main physical dissipative terms like electrical resistivity, thermal conductivity and viscosity. These terms are introduced by piece-wise fittings from the solid phase density and temperature of 0.1 eV till temperatures of hundreds (or more) of eV and densities from the dense/overdense matter ~10^2gr/cm^3 to the very dilute region of ~10^{-11}gr/cm^3. The classical theory of the Coulomb logarithm is not valid at the dense matter region for low temperatures (WDM) presenting non-physical values. Introducing the Born approximation, we overcome this discrepancy and we achieve the anticipated experimental and literature behavior for the dissipative terms functions, without needing a lower cut-off value of the classical Coulomb logarithm formula. This is valid both in electrical and thermal conductivity piece wise formulas. It can be also used to the piece wise viscosity formulas improving even further the Braginskii and MD based formulas behavior at the

WDM regime. All these alternatives, equations, functions and tabular data are compatible and have been or could be implemented in PLUTO, upgrading the capabilities of the original astrophysical code, making it suitable for any plasma state and geometry from the astrophysical to the laboratory configurations.

The **second part** analyzes and evaluates the appropriate numerical scheme. The appropriate boundaries conditions are crucial for the spatiotemporal computational behavior till the end of the simulation time, especially when the magnetic field is involved. The magnetic field initial topology and the correct updating along the simulation run are amongst the most important things for the dynamic plasma evolution, pinching procedures and the interplay between thermal and magnetic pressure. The magnetic field topology is seeded at the very first moment of the simulations for PLUTO code, satisfying the Ampere's law and the Stokes theorem along the execution run for the whole volumetric computational territory, correlating the magnetic induction with the current density, updating the induction magnitude along time accordingly with the temporal sinusoidal form of the experimental current. This is a novel computational procedure, aiming for the appropriate physical spatiotemporal magnetic field diffusion, pinching effect and expansion. It is validated for a single Z-pinch wire and an X-pinch two wire configuration at Chapter 5 with very promising results.

A novel technique for the initial condition topology of all the physics variables, including the magnetic field, of any plasma configuration i.e. Z-pinch, X-pinch and Z-pinch array is used. This is due to the mathematical and physical modeling using the Local to Global coordinate system and vise versa physics variable correlation, employing the displacement and rotation matrices. This approach has the advantage of producing any displaced wire geometry like the "cold" start model where the tangent metal wires are not yet merged at the initial conditions, providing a useful mathematical tool for a more detailed and physically correct initial condition modeling. The preliminary results from the X-pinch tangent wires with the GORGON code and the Z-array with PLUTO are very promising and insightful according to the initial stages of the plasma evolution i.e. at the "cold" start of two tungsten wires and their matching with the experimental description or the angular momentum plasma transfer, from the X-pinch crosspoint area to the formed jets which could be scale associated even with Young Stellar Objects (YSOs) similar formation mechanisms from the accretion disk to the plasma jets**.**

At the **third part** the simulation results and evaluations for the Z-pinch and X-pinch configurations are discussed and analyzed, for PLUTO and GORGON codes. The activation and deactivation of the radiation transport module, of PLUTO, is investigated for a single Z-pinch plasma tungsten configuration. The inclusion of the radiation transport is significant for the spatiotemporal evolution of electron density, pressure and temperature to be consistent with literature results. The inclusion of a passive scalar function for the multimaterial approximation identifying the transition zone presents a smoother behavior at the tungsten plasma-plasma vacuum air interface, avoiding deformations, allowing for smaller computational boxes.

These new capabilities of the MHD code PLUTO are also tested via the experimental comparison for the investigation of laboratory magnetically compressed plasmas of X-pinch experiments which were carried out using Tungsten wires of 5 μm diameter, set at an angle of 100^{o}. The jet formation and its spatiotemporal dynamics are clearly described, while the physics involved including the neck, the

plasma electrodes formation as well as the “zippering” effect are identified, in respect to the concept of the global and local magnetic fields. The results are in good agreement with the experiments as well as with similar research works in the literature. Our studies substantially contribute to the understanding of the interplay mechanisms associated to the generation of the supersonic plasma jet formation, enlightening the critical role of the **J**×**B** force and of the momentum transfer dynamics.

In this thesis, GORGON and PLUTO, are used to simulate the evolution of laboratory magnetically compressed plasma, driven by a X-pinch pulsed power generator, and describe its key dynamic features. The developed MHD models focus on the simulation of a reliable description of the spatio-temporal dynamic evolution of the plasma density and the magnetic field magnitude of a X-pinch configuration . Even though GORGON and PLUTO codes are built on different approximation schemes, both codes manage to accurately handle the numerical demands of the X-pinch plasma evolution physics and provide precise details on the mechanisms of the plasma expansion, the mass-transport, the jet-formation, and the pinch generation. In addition, the method of the time-depended forced current value adopted in PLUTO has been proven to provide accurate results as demonstrated by the comparison with the GORGON simulations. Without loss of the generality of the numerical approximation, the Riemann solver of PLUTO is deactivated in the vacuum region, providing a more flexible numerical tool, avoiding the numerical discrepancies of the vacuum region. Although the general aspects in relation to the plasma evolution have been well recognized from both codes, the various physical models, which are implemented to capture the non-ideal effects are crucial and result to remarkable differences. Comparing the results of both codes for the magnetic field the agreement is satisfactory since a similar morphology and topological distribution is observed. The jet’s length and width are almost identical for both simulations, but a denser jet formation is observed in GORGON, since more mass is transferred to the jet axis due to the higher mass ablation rate of the wires legs. Flaring structures are developed in GORGON while a uniform plasma expansion is simulated using the radiation transport model of PLUTO. High temperature values are observed in the cross-point area for both codes. An isolated island of plasma is also generated at the center of the cross-point by both codes. At later times, PLUTO simulates the formation of two denser central spots, which further evolve to the formation of hot-spot, while a dense plasma neck which breaks on the hot-spot formation position due to the intense pinching effect is formed in GORGON. Five models are developed in PLUTO in order to evaluate the influence of the electrical resistivity, radiation transport and optically thin losses on the spatio-temporal plasma evolution. The radiation transport module is proven to be significant for the energy exchange, providing a perturbation profile with low growth rates along time, reducing the plasma temperature and the radial expansion rate compared to the models which only consider the optically thin losses. The optically thin losses module results to a more diffusive spatio-temporal behaviour regardless the resistivity implementation scheme, since high amplitude density perturbations along the wire’s corona-vacuum interface are developed with higher temperature distribution. This detailed numerical study is important for the studies of laboratory jets formation using X-pinches and for the seeding mechanisms of plasma instabilities and their subsequent growth rate evolution. The identification of the basic parameters and their weight of influence on the dynamic expansion of plasma provides valuable information to the modelling scenarios, especially when the solid to plasma phase transition is simulated and the proper seeding is demanded.

This thesis also presents a promising laboratory scalability estimation for specific X-pinch jet's parameters. It contributes to the estimation of the scalability factors and all the relevant numbers and parameters for a low current X-pinch tungsten plasma configuration. The average Mach number of ~10 , demonstrates that the jets discussed in this thesis show a potential scalability to Astrophysics. It is in the range value of the YSO jets and HH objects. The dimensionless numbers that refer to global properties of the jets are presented and discussed. The scaling is very close to the ones of other laboratory devises with similar current and magnetic field initial values.

Introduction to PLUTO the EOS and Z_{eff} of other metal materials like copper, aluminum and molybdenum is a right away task. This way we will expand the usability of the code to all our laboratory experiments. We will also be able to simulate X-pinch and Z-pinch plasmas using both GORGON and PLUTO, compare and evaluate the MHD schemes, since the former has already embodied all these materials. Multiple cable Z-pinch and X-pinch devises can be simulated with both codes providing better laboratory and simulation environments for astrophysical studies. Also the inclusion of proper viscous terms, "cold" start initial conditions, transferring angular momentum from the crosspoint area to the plasma jets, interaction of the main plasma jet with the plasma vacuum and thorough study of the simulation till the current peak, are goals for the future work, hoping for further conclusions of the underlying formation mechanisms and potential connections to astrophysical phenomena.

PUBLICATIONS RESULTED FROM THIS WORK

[1] **G. Koundourakis et al,** "Experimental and numerical investigation of the plasma dynamics and jet formation in low current table-top X-pinch plasma devices", Proceedings of the SCinTE 2015, VOL.3, 19-22.

[2] A. Skoulakis **- G. Koundourakis** et al, 2018, 9th GRACM International Congress on Computational Mechanics pp 294.

[3] **G. Koundourakis** et al, 2018, Computational study of plasma dynamic evolution produced by low current table-top pinch plasma devic.es *ECLIM Abstract book* pp 118.

[4] **G. Koundourakis** et al, "A numerical study on laboratory plasma dynamics validated by low current X-pinch experiments", Plasma Phys. Control. Fusion 62 (2020) 125012 (14pp).

[5] A. Skoulakis **- G. Koundourakis et al**, " High performance simulations of a single X-pinch", Plasma Phys. Control. Fusion 64 (2022) 025003 (11pp).